

# **HL/HE-LHC Physics Workshop Report**

## **Higgs physics opportunities**

*Conveners:* *Maria Cepeda*<sup>1</sup>, *Stefania Gori*<sup>2</sup>, *Phil Iltgen*<sup>3</sup>, *Marumi Kado*<sup>4</sup>, *Francesco Riva*<sup>5</sup>

*Contributors:*

<sup>1</sup> CERN

<sup>2</sup> Institute 2

<sup>3</sup> Laboratoire de l'Accélérateur Linéaire

<sup>4</sup> Institute 4

<sup>5</sup> Département de Physique Théorique, Université de Genève, 24 quai Ernest-Ansermet, 1211 Genève 4,  
Switzerland

### **Abstract**

## Contents

1	Introduction . . . . .	6
1.1	Bibliography . . . . .	7
2	Higgs boson precision measurements . . . . .	8
2.1	Introduction . . . . .	8
2.2	Theoretical predictions for the Higgs boson production at 14 and 27 TeV . . . . .	8
2.2.1	PDF uncertainty expectations at the HE/HL-LHC . . . . .	8
2.2.2	Progress on Higgs boson specific MC generators . . . . .	12
2.3	Overview of experimental analysis for the Higgs boson measurement channels . . . . .	12
2.3.1	Extrapolation assumptions . . . . .	12
2.3.2	$H \rightarrow \gamma\gamma$ . . . . .	13
2.3.3	$H \rightarrow Z\gamma \rightarrow 2\ell\gamma$ . . . . .	14
2.3.4	$H \rightarrow ZZ^* \rightarrow 4\ell$ . . . . .	15
2.3.5	$H \rightarrow WW^* \rightarrow \ell\nu\ell\nu$ . . . . .	15
2.3.6	$H \rightarrow \tau\tau$ . . . . .	16
2.3.7	$H \rightarrow bb$ . . . . .	17
2.3.8	$H \rightarrow \mu\mu$ . . . . .	19
2.4	Fiducial and differential cross-section measurements . . . . .	19
2.4.1	Measurements using $H \rightarrow \gamma\gamma$ , $H \rightarrow ZZ^* \rightarrow 4\ell$ , (boosted) $H \rightarrow b\bar{b}$ decay channels . .	19
2.4.2	Measurement of $p_T(H)$ spectrum in $t\bar{t}H$ production mode . . . . .	20
2.5	Direct and indirect probing of top Yukawa coupling . . . . .	21
2.5.1	Measurements in $t\bar{t}H$ and $tH$ production modes . . . . .	21
2.5.2	Constraints from differential measurements . . . . .	25
2.6	Combination of Higgs boson measurement projections . . . . .	26
2.6.1	Signal strength per-decay mode . . . . .	27
2.6.2	Signal strength per-production mode . . . . .	28
2.7	Kappa interpretation of the combined Higgs boson measurement projections . . . . .	28
2.8	Kappa-formalism and the nonlinear EFT . . . . .	32
2.9	Higgs couplings precision overview in the Kappa-framework and the nonlinear EFT . . . . .	36
2.9.1	The fit to HL/HE-LHC Higgs precision data . . . . .	37
2.9.2	Results . . . . .	37
2.10	Projections of Higgs boson measurements to the HE-LHC . . . . .	39
2.11	Probing of anomalous HVV interactions . . . . .	39
2.11.1	Probes using differential distributions of CP sensitive observables . . . . .	39
2.11.2	Experimental constraints on anomalous HVV couplings . . . . .	44
2.12	Summary . . . . .	44
3	Di-Higgs production and Higgs self couplings . . . . .	45
3.1	NLO cross sections . . . . .	45
3.1.1	SM Calculation . . . . .	45
3.1.2	Di-Higgs production in the non-linear EFT with full $m_t$ -dependence at NLO QCD . .	46
3.2	Double Higgs measurements and trilinear coupling . . . . .	49

3.2.1	Measurements with the ATLAS experiment . . . . .	49
3.2.2	Measurements with the CMS experiment . . . . .	50
3.3	New ideas . . . . .	52
3.3.1	Prospects for $hh \rightarrow (b\bar{b})(WW^*) \rightarrow (b\bar{b})(\ell^+\ell^-\nu_\ell\bar{\nu}_\ell)$ . . . . .	52
3.3.2	Prospects for $bb\gamma\gamma$ : Bayesian optimization and BDT . . . . .	54
3.4	HE prospects . . . . .	56
3.4.1	Theory studies . . . . .	56
3.4.2	ATLAS studies . . . . .	62
3.5	Indirect probes . . . . .	62
3.5.1	Indirect probes of the trilinear coupling through differential distributions measurements . . . . .	62
3.5.2	Indirect probes through single Higgs boson production . . . . .	62
3.5.3	Global fit . . . . .	65
3.6	Implications . . . . .	67
3.6.1	Implications for flavor models . . . . .	67
3.6.2	Implications for theories of electroweak phase transition . . . . .	69
4	High Energy Probes . . . . .	70
4.1	$t\bar{t}h$ differential measurements . . . . .	70
4.2	WH/ZH at high energy/luminosity . . . . .	70
4.3	Electroweak Precision Tests in High-Energy Diboson Processes . . . . .	73
4.4	Novel measurements of anomalous triple gauge couplings for the HE and HL-LHC . . . . .	77
4.4.1	Introduction . . . . .	77
4.4.2	Solutions . . . . .	78
4.4.3	Results . . . . .	79
4.4.4	Higgs pair production in vector-boson fusion at the HL-LHC . . . . .	80
4.5	Same-sign WW scattering at HL-LHC: a new strategy for the EFT-based analysis . . . . .	83
4.6	Testing the universal Higgs nonlinearity . . . . .	85
4.7	Same-sign WW scattering: A comparison of the HL- and HE-LHC reach for the selected Dim8 operators within the EFT approach . . . . .	85
4.8	Dimension-6 EFT effects on Vector Boson Scattering at high energies . . . . .	86
5	Higgs boson mass and width . . . . .	106
5.1	Theory review . . . . .	106
5.2	Measurement of the Higgs boson mass . . . . .	109
5.3	Direct constraints from the Higgs boson lineshape . . . . .	109
5.4	Direct constraints from the Higgs boson lifetime measurements . . . . .	109
5.5	Width from the diphoton interference rate . . . . .	109
5.6	Mass shift from the diphoton interference: constraints on the width . . . . .	112
5.7	Width from Off-Shell higgs boson couplings . . . . .	112
6	Invisible decays of the Higgs boson . . . . .	113
6.1	Main channels for direct searches . . . . .	114
6.2	Interpretation and combination with precision Higgs boson measurements . . . . .	116
6.2.1	Experimental input . . . . .	116

6.2.2	Effective description of Higgs portal models . . . . .	118
6.3	Higgs portal interpretations . . . . .	120
6.3.1	Minimal Higgs Portal . . . . .	120
6.3.2	Scalar singlet portal . . . . .	121
6.4	Conclusions . . . . .	125
7	Higgs flavor and rare decays . . . . .	126
7.1	Introduction . . . . .	126
7.2	Flavor aspects Yukawa modifications in flavor models . . . . .	127
7.2.1	New Physics benchmarks for modified Higgs couplings . . . . .	127
7.3	Exclusive Higgs decays . . . . .	133
7.4	Flavor tagging (charm and strange) . . . . .	135
7.4.1	Strange quark tagging . . . . .	139
7.5	LFV decays of the Higgs . . . . .	140
7.6	Yukawa constraints from Higgs distributions . . . . .	140
7.6.1	Determinations of Higgs boson coupling modifiers using differential distributions . . . . .	142
7.7	$W^\pm h$ charge asymmetry . . . . .	143
7.8	Summary . . . . .	145
8	Global view of Higgs couplings at the HL/HE-LHC . . . . .	146
8.1	Introduction . . . . .	146
8.2	Standard Model Effective Field Theory . . . . .	146
8.3	Fit Setup and Current Results . . . . .	147
8.4	Future Projections . . . . .	148
9	Searches for beyond the standard model Higgs physics . . . . .	155
9.1	Production of $t\bar{t}h$ and $t\bar{t}hh$ at the LHC in Composite Higgs models . . . . .	155
9.1.1	Introduction . . . . .	155
9.1.2	Theoretical Framework . . . . .	155
9.1.3	Parameter Space and Results . . . . .	158
9.1.4	Experimental perspectives . . . . .	162
9.2	Exotic decays of the Higgs boson . . . . .	164
9.2.1	First Level Track Jet Trigger for Displaced Jets at High Luminosity LHC . . . . .	164
9.2.2	Exotic decays of the Higgs to $2b2\mu$ . . . . .	169
9.2.3	Exotic Higgs decays to ALPs: $h \rightarrow Za$ and $h \rightarrow aa$ . . . . .	172
9.2.4	$h \rightarrow aa \rightarrow \mu\mu\mu\mu$ . . . . .	178
9.3	Searches for additional Higgs bosons in fermionic final states . . . . .	181
9.3.1	Projection of Run-2 CMS searches for MSSM and other heavy Higgs bosons . . . . .	181
9.3.2	Projection of Run-2 ATLAS searches for MSSM heavy Higgs bosons . . . . .	185
9.3.3	HL-LHC projections of LHCb searches for 2HDM+S pseudoscalars . . . . .	189
9.4	Searches for additional Higgs bosons in diboson final states . . . . .	192
9.5	MSSM charged Higgs bosons . . . . .	192
9.5.1	Prospects for the observation of MSSM charged Higgs in the $\tau_h\nu$ channel at HL-LHC and HE-LHC . . . . .	192

9.6	Interference effects in heavy Higgs searches . . . . .	194
9.7	All contributions below: Move your contribution to a separate file! . . . . .	199
9.8	Interpretation of the Higgs couplings in terms of Composite Higgs models . . . . .	199
9.8.1	Introduction . . . . .	199
9.8.2	Modified Higgs couplings . . . . .	199
9.9	Interpretation of the Higgs couplings in terms of SUSY models . . . . .	201
9.10	Direct and indirect sensitivity to heavy Higgs bosons using MSSM benchmark scenarios	201
9.11	Searches for low mass Higgs bosons (below 120 GeV) . . . . .	203
9.11.1	Introduction . . . . .	203
9.11.2	Experimental constraints on light Higgs bosons . . . . .	204
9.11.3	Models with light Higgs bosons . . . . .	204
9.11.4	Phenomenology of light anti-aligned Higgs bosons . . . . .	205
9.12	Sensitivity to heavy Higgs bosons from the 2HDM in "Higgs-to-Higgs" decays . . . . .	207
9.12.1	Introduction . . . . .	207
9.12.2	2HDM Summary . . . . .	208
9.12.3	$m_A > m_H$ : searches for $A \rightarrow ZH$ . . . . .	208
9.12.4	$m_H > m_A$ : searches for $H \rightarrow ZA$ and $H \rightarrow AA$ . . . . .	209
9.12.5	Interplay with $H/A \rightarrow \tau\tau$ . . . . .	209
10	Conclusions and Outlook . . . . .	210

## 1 Introduction

### Check

The main repository of the report material is Overleaf. If you are not registered with Overleaf as yet, you can do so. Use your cern.ch mail account, as this will give you, for free, the Professional license. This is needed if you want to access the full functionality, including the ability to grant editing rights to many people.

You can create the project for your section by just cloning this project. It's important that you do it using your professional Overleaf account (namely with your cern.ch email credentials), since the project inherits the functionalities available to its owner. After creating the project, make sure you set the proper administration rights, listing people who will have editing rights. You can do this clicking on the "share" button on top of the overleaf project page. You are given various options, such as making the project read/write accessible to anyone who has the url, or just readable to anyone who has a (different) url, or restricted to users selected in a list. The same button gives you the git repository url, to download the project locally. Notice that those you give rights to cannot further assign rights to others. Only the owner of the project can grant access rights. Of course section editors can clone a new version of the whole chapter, leave alone the other sections to focus on their own, and grant access to it to their co-editors. At the end they just put things back into the master project. I understood that it should be possible to grant rights to a CERN e-group, but I am not sure this is working already, I'm waiting for confirmation.

You can work directly on the Overleaf version, or you can download the whole package locally from the git repository. You can then use the standard git tools to commit updated versions. Working locally is almost essential at the beginning of the project, when you want to create a complete subfolder structure to contain the various sections of your report. Some scripts are available (see below) to facilitate this task.

This document can be compiled in its entirety, using the

```
> pdflatex report
```

command from the main directory. In alternative, you can compile individual sections, with the command

```
> pdflatex section
```

issued from the section subdirectory. This will generate the complete section, including its bibliography. I am not sure this is possible when working directly on the web with Overleaf. But this works in your local version, if you input the pdflatex commands yourself.

For this to work, you must preserve the template structure of the section.tex file in the directory of each section. You should also make sure that all style files contained in the main directory are present in the section directories. The simplest way to create a new section is to issue the command

```
> make newsection newfolder=new_folder_name
```

from the main directory. Here new\_folder\_name is the name of the directory you want to create to host the new section. A template section file will be created there, together with the img and bib directories (for figures and for the section.bib file, resp). All necessary style files are copied over. Now you just need to input the new\_folder\_name/section.tex file into the main driver file, report.tex, with the syntax:

```
\newpage
\subfile{\main/newdirectory/section}
```

When editing the new section.tex file, please pay attention to the header of the template. There are a few weird commands, and an apparently odd \begin{document} statement. These are required to be able to compile the section as a stand alone object. To this end, it is important that the command \providecommand{\main}{...} points \main to the directory containing the main driver file, report.tex. The file paths to figures (Fig. 1) must all include this absolute reference, as in

```
\includegraphics[width=0.45\textwidth]{\main/section1/img/hgg.pdf} .
```

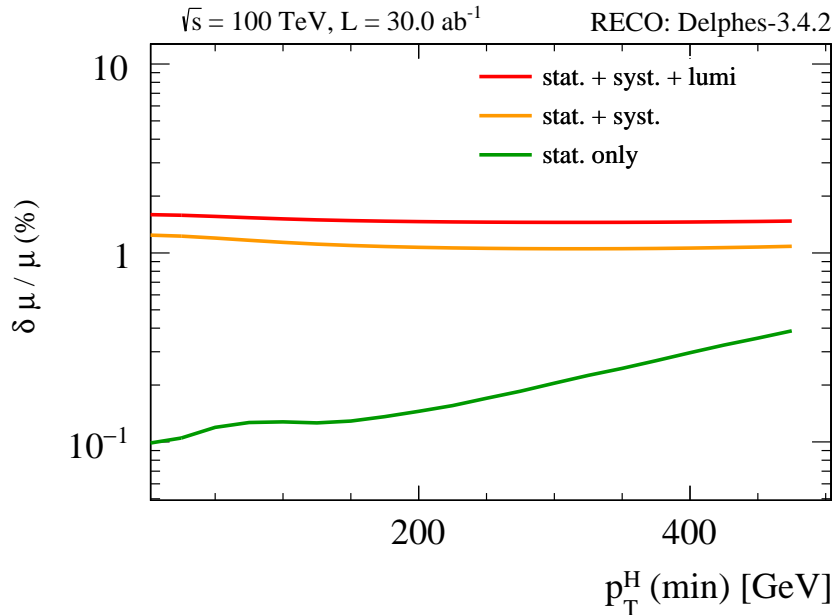


Fig. 1: Caption of the figure.

As for tables, please use the standard tabular environment, with the caption on top of the table. For cross referencing, try use labels such as `\label{eq: eqname}`, `\label{tab: tablename}` and `\label{fig: figname}`.

If you need subsections, you can include them here directly, or input them as files, which can live in their own subdirectory. If including a subsection from a file, import them with the command

```
\subfile{\main/section1/sub1/mysubsec}
```

where `mysubsec.tex` would start of course with the statement `\begin{subsection}`. In this case, make sure you define properly the path to figures and other files. This is crucial to guarantee compatibility of compilation of the whole Chapter and or the individual section. The fact that a Section compiles doesn't imply that the Chapter will compile, if paths are entered inaccurately. At this time I have not foreseen the ability to compile subsections standalone, I hope it is not necessary.

## 1.1 Bibliography

Keep each Section totally selfcontained, with its own folder(s) for figures, and its own file for bibliography [1]. Use bibtex format. Please get the bibtex from Inspire, other sources may generate conflicts with the bibliography style file. For internal notes of the LHC experiments, get the bibtex input from CDS (the CERN Document Service). Each section must have its own bib files. These are called `section.bib`, and should stay in the folder `\main/mysection/bib/section.bib`. When you create a new section, add the bib file to the string

```
\def\bibfiles{\main/bib/chapter,\main/section1/bib/section,\main/section2/bib/section}
```

that is included in the main driver, `report.tex`.

## 2 Higgs boson precision measurements

### 2.1 Introduction

*To be written by: S. Alioli, M. Duehrssen, P. Milenovic*

The large number of events expected in almost all Higgs boson measurement channels for the HL-LHC and HE-LHC will allow very precise measurements of Higgs boson cross section and coupling properties. In many channels, the expected overall statistical, experimental and theoretical uncertainties will be similar in size. Therefore, a close interaction between the experimental and theory communities will be needed in order to reach the best measurements.

Section 2.2 provides an overview of theoretical predictions for Higgs boson production at 14 and 27 TeV and of the uncertainties that are expected to be reached by the time of the final HL-LHC and HE-LHC measurements. These predictions are used as input to the studies of the sensitivity of ATLAS and CMS Higgs boson cross section and coupling measurements in individual channels that are summarized in Section 2.3 and for the expectations for differential cross section measurements presented in Section 2.4. Section 2.5 puts emphasis on all measurements related to the top Yukawa coupling, as this is the largest Yukawa couplings in the Standard Model with a value close to unity and hence of special interest in understanding the Higgs mechanism and its relation to fermions (TO EDIT: shall we expand this argument?). The combination of the expected measurements in ATLAS and CMS are presented in Section 2.6 together with an interpretation in the kappa-model [2, 3].

### 2.2 Theoretical predictions for the Higgs boson production at 14 and 27 TeV

*To be written by: F. Caola, J. Campbell et al.*

#### 2.2.1 PDF uncertainty expectations at the HE/HL-LHC

*Rabah Abdul Khalek, Shaun Bailey, Jun Gao, Lucian Harland-Lang, and Juan Rojo.*

**PDFs in the HL-LHC era.** The detailed understanding of the quark and gluon structure of the proton, quantified by the parton distribution functions (PDFs) [?, 4, 5], is an essential ingredient for the theoretical predictions at hadron colliders. PDF uncertainties represent one of the dominant theoretical systematic errors both for direct searches of new physics beyond the Standard Model (bSM) [6] as well as in the profiling of the Higgs boson sector [7]. Therefore, improving our knowledge of the proton structure is an essential task for the high-precision physics program to be carried out at future runs of the LHC, including the HL-LHC era.

Modern global PDF fits [?, ?, 8, 9] include a wide range of LHC measurements in processes such as the production of jets, weak gauge bosons, and top quark pairs, among others. Recent breakthroughs in the calculation of NNLO QCD and NLO QED and electroweak corrections to most PDF-sensitive processes have been instrumental in allowing for the full exploitation of the information provided by the LHC measurements. The impact of high-precision LHC data combined with state-of-the art perturbative calculations has been quantified for many of the processes of interest, such as top-quark pair production [?, 10], the transverse momentum spectrum of  $Z$  bosons [?], direct photon production [?, 11],  $D$  meson production in the forward region [?, 12, 13],  $W$  production in association with charm quarks [?, ?, ?], and inclusive jet production [?, ?].

From the point of view of PDF determinations, the availability of the immense data samples at the HL-LHC will permit a significant extension of the kinematic coverage of PDF-sensitive measurements as well as a marked improvement in their statistical and systematic uncertainties. In this contribution, we summarise the main results of our PDF projections for the HL-LHC era presented in [14]. The main idea is to quantify the impact of the future HL-LHC measurements on the proton PDFs and their uncertainties, with emphasis on their implications for Higgs physics. Specifically, we quantify the constraints

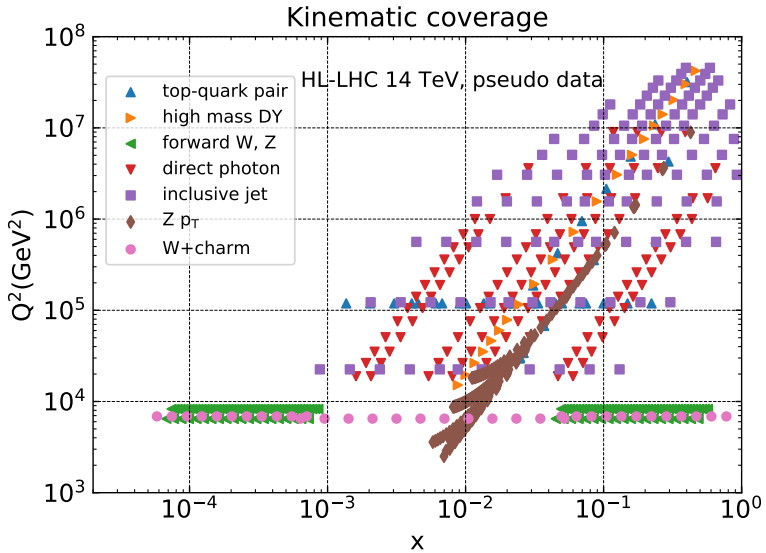


Fig. 2: The kinematical coverage in the  $(x, Q^2)$  plane of the HL–LHC pseudo-data.

of the HL–LHC pseudo-data on the PDF4LHC15 set [?, ?, ?, 15] by means of the Hessian Profiling method [?] (see also [?]). We choose the PDF4LHC15 set since it broadly represents the state-of-the-art understanding of the proton structure.

In Fig. 2 we show the kinematical coverage in the  $(x, Q^2)$  plane of the HL–LHC pseudo-data included in this analysis. As indicated there, we have simulated pseudo-data for the following processes: top quark pair production, high-mass and forward Drell-Yan  $W, Z$  production, direct photon and inclusive jet production, the transverse momentum of  $Z$  bosons, and the production of  $W$  bosons in association with charm quarks. The HL–LHC pseudo-data therefore spans a wide region in the kinematic plane, namely  $6 \times 10^{-5} < x < 0.7$  and  $40 \text{ GeV} < Q < 7 \text{ TeV}$ . In particular, one sees that the HL-LHC coverage of the large- $x$  region, where current PDF fits exhibit large uncertainties, is markedly improved as compared to available LHC measurements.

**Results.** As an illustration of the impact of individual sets of HL-LHC pseudo-data, in Fig. 3 we show the comparison between the HL–LHC projected measurements and the theoretical predictions for the lepton rapidity distribution in forward  $W+\text{charm}$  production and for the invariant mass  $m_{t\bar{t}}$  distribution in top-quark pair production. These two particular datasets probe the poorly-known strange quark and the gluon at large- $x$ , respectively. The theory calculations are shown both before (PDF4LHC15) and after profiling. In the bottom panel, we show the same results normalised to the central value of the original theory calculation. In both cases we see that the expected precision of the HL-LHC measurements is rather higher than the current PDF uncertainties, and therefore we observe a marked improvement once they are included in PDF4LHC15 via the Hessian profiling.

In this study we have considered three different scenarios for the experimental systematic uncertainties of the HL–LHC pseudo-data. These scenarios, ranging from more conservative to more optimistic, differ among them in the reduction factor applied to the systematic errors of the reference 8 TeV or 13 TeV measurements, see [14] for more details. In particular, in the optimistic scenario we assume a reduction of the systematic errors by a factor 2.5 (5) as compared to the reference 8 TeV (13 TeV) measurements, while for the conservative scenario we assume no reduction in systematic errors with respect to the 8 TeV reference. Reassuringly, we obtain that the main results of our study depend only mildly in the specific assumption for the values of this reduction factor.

In Fig. 4 we compare the PDF4LHC15 set with the strange quark and gluon PDFs obtained once

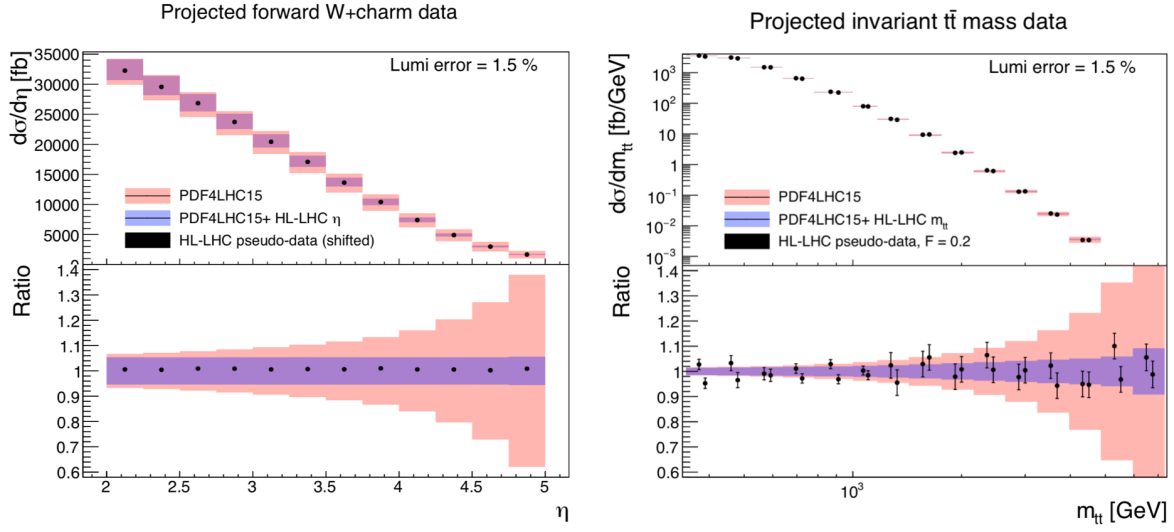


Fig. 3: Comparison between the HL–LHC pseudo-data and the theoretical predictions for forward  $W$ +charm production (left) and for the invariant mass  $m_{t\bar{t}}$  distribution in top-quark pair production (right). The theory calculations are shown both before (PDF4LHC15) and after profiling.

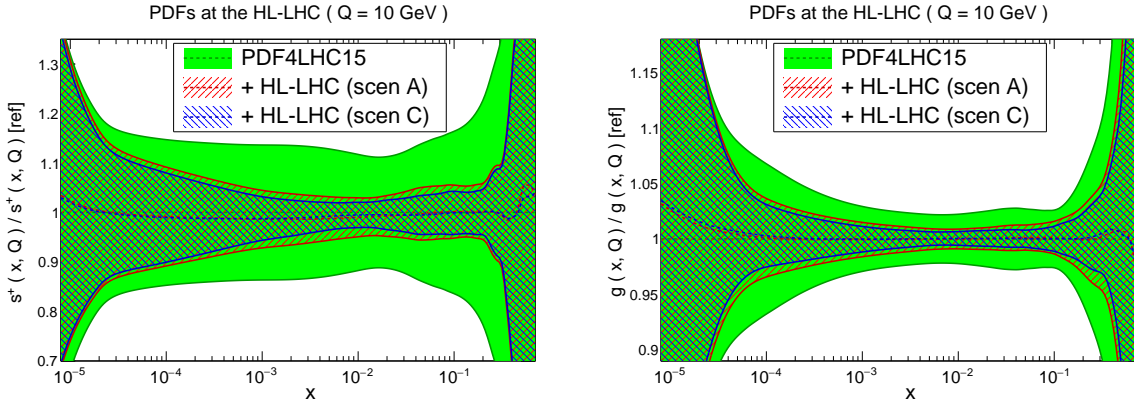


Fig. 4: Comparison of the PDF4LHC15 set with the profiled sets with HL–LHC pseudo-data. We show the strange (left) and gluon (right) PDFs normalized to the central value of the baseline.

the entire set of HL-LHC pseudo-data summarised in Fig. 2 has been included via profiling. We show results both in the conservative (A) and optimistic (C) scenarios for the projections of the experimental systematic uncertainties. We observe that the impact of the HL–LHC pseudo-data is reasonably similar in both scenarios. This is due to the fact that we have chosen those processes which will benefit from a significant improvement in statistics, independent of the specific assumption about the systematic errors. These then tend to lie in kinematic regions where the PDFs themselves are generally less well determined. We also observe a marked reduction of the PDF uncertainties in all cases. In the case of the gluon PDF, there is an improvement of uncertainties in the complete relevant range of momentum fraction  $x$ . This is a direct consequence of the fact that we have included several HL–LHC processes that have direct sensitivity to the gluon content of the proton, including jet, direct photon, and top quark pair production, as well as the transverse momentum of  $Z$  bosons. As we discuss next, this has direct implications for the phenomenology of Higgs boson production.

**Implications for Higgs physics.** In Table 1 we indicate the reduction of the PDF uncertainties in

Ratio to baseline	$10 \text{ GeV} \leq M_X \leq 40 \text{ GeV}$	$40 \text{ GeV} \leq M_X \leq 1 \text{ TeV}$	$1 \text{ TeV} \leq M_X \leq 6 \text{ TeV}$
gluon-gluon	0.50 (0.60)	0.28 (0.40)	0.22 (0.34)
quark-quark	0.74 (0.79)	0.37 (0.46)	0.43 (0.59)
quark-antiquark	0.71 (0.76)	0.31 (0.40)	0.50 (0.60)

Table 1: The reduction of the PDF uncertainties as compared to the PDF4LHC15 baseline for different initial partonic combinations in the optimistic (conservative) scenario.

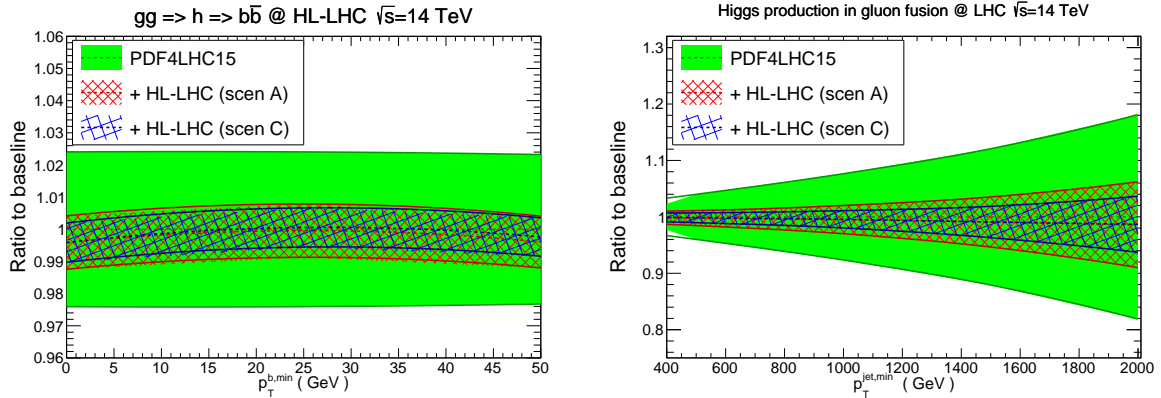


Fig. 5: Comparison of the predictions for SM Higgs production cross-sections at  $\sqrt{s} = 14 \text{ TeV}$  between the PDF4LHC15 baseline and the profiled PDF sets with HL-LHC pseudo-data.

comparison to the PDF4LHC15 baseline for different initial partonic combinations (that is, a value of 1 corresponds to no improvement). Results are presented for three different bins of the invariant mass  $M_X$  of the produced system for the three initial states relevant for Higgs production: gluon-gluon (for  $gg \rightarrow h$  and  $t\bar{t}h$ ), quark-quark (for vector boson fusion) and quark-antiquark (for associated  $Wh$  and  $Zh$  production). The values shown outside (inside) the brackets correspond to the optimistic (conservative) scenario. We can see that for the  $M_X$  region relevant for the SM Higgs boson production, as well as for related bSM Higgs-like scalars, namely  $40 \text{ GeV} \leq M_X \leq 1 \text{ TeV}$ , the HL-LHC pseudo-data leads to a reduction by almost a factor four in the optimistic scenario in the  $gg$  channel, and around a factor three in the  $q\bar{q}$  and  $qq$  channels. This implies that precision calculations of Higgs production at the HL-LHC should be possible with significantly reduced PDF uncertainties compared to current state-of-the-art predictions.

To illustrate this improvement, in Fig. 5 we present the comparison of the predictions for SM Higgs production at  $\sqrt{s} = 14 \text{ TeV}$  between the PDF4LHC15 baseline and the profiled PDF sets. Specifically, we show Higgs boson production in gluon fusion with heavy top quark effective theory, both inclusive and decaying into  $b\bar{b}$  as a function of  $p_T^{b,\min}$  (left), and then in association with a hard jet as a function of its transverse momentum  $p_T^{\text{jet},\min}$  (right). The calculations have been performed using MCFM8.2 with leading-order matrix elements. The marked reduction of PDF uncertainties is consistent with the values reported in Table 1.

Finally, there are two caveats to be added concerning this study. First we have only considered a subset of all possible measurements of relevance for PDF fits at HL-LHC. Second, possible data incompatibility has not been accounted for fully. These may strengthen and weaken, respectively, the

constraining powers of future LHC data on PDFs.

The results of this study are made publicly available in the LHAPDF6 format [16], for the three scenarios that have been considered, and can be downloaded from:

[https://data.nnpdf.science/HLLHC\\_YR/PDF4LHC15\\_nnlo\\_hllhc\\_scen1.tgz](https://data.nnpdf.science/HLLHC_YR/PDF4LHC15_nnlo_hllhc_scen1.tgz)  
[https://data.nnpdf.science/HLLHC\\_YR/PDF4LHC15\\_nnlo\\_hllhc\\_scen2.tgz](https://data.nnpdf.science/HLLHC_YR/PDF4LHC15_nnlo_hllhc_scen2.tgz)  
[https://data.nnpdf.science/HLLHC\\_YR/PDF4LHC15\\_nnlo\\_hllhc\\_scen3.tgz](https://data.nnpdf.science/HLLHC_YR/PDF4LHC15_nnlo_hllhc_scen3.tgz)

### 2.2.2 Progress on Higgs boson specific MC generators

*To be written by: Simone Alioli, Stefan Höche, Fabio Maltoni and Stefan Prestel*

Here goes the text

Monte Carlo's for Higgs Physics.

High-Lumi and High-energy

General purpose Monte Carlo's Total and differential cross section calculators Dedicated MC's

What are the improvements that are foreseen in the coming years that could change the field.  
Where the most of the results can be expected? For what? NNLO+PS?

Collecting references for MINLO, Sherpa so that people can find where to look.

Table?

Instead of showing an actual plot, we show a mock-plot where the various features which are most important are summarized.

What can we say it would be needed and in the ball park of the feasible stuff. Examples for main channels.

- approx rapidity at N3LO for gluon-fusion
- N3LO VBF is available inclusive => exclusive?
- NNLO+NLL as the next revolution for ggH, VH, VBF,...
- top / bottom mass effects

Organise it in terms of methods and developments and then physics channels.

Fabio: Simone: StefanP: StefanH:

## 2.3 Overview of experimental analysis for the Higgs boson measurement channels

*To be written by: M. Delmastro, P. Francavilla, A. de Wit*

### 2.3.1 Extrapolation assumptions

The results presented in this Section are based on the extrapolation to an expected integrated luminosity of  $3000 \text{ fb}^{-1}$  at  $\sqrt{s} = 14 \text{ TeV}$  of the corresponding ATLAS and CMS Run-2 results. For some of the Higgs decay final states (ATLAS:  $WW^*$ ,  $Z\gamma$ ,  $t\bar{t}H$ ,  $\tau\tau$ ; CMS: ...) the extrapolation is performed on results obtained with the 2015-2016  $36 \text{ fb}^{-1}$  datasets; the remaining final state analyses (ATLAS:  $\gamma\gamma$ ,  $ZZ^*$ ,  $b\bar{b}$  and  $\mu\mu$ ; CMS: ...) use the results based on the 2015+2016+2017  $80 \text{ fb}^{-1}$  data samples. The starting points of the extrapolated results are measurements based on datasets of size  $\mathcal{O}(1\%)$  of the expected HL-LHC integrated luminosity. The extrapolations are in this respect very limited with respect to the potential reach of the real HL-LHC analyses, which large statistics will allow to probe corners of the phase space inaccessible at the LHC Run-2.

In addition to the increase in integrated luminosity, the extrapolations account for the increase of signal and background cross-sections from  $\sqrt{s} = 13$  TeV to 14 TeV. The signal yields have been scaled according to the Higgs boson production cross sections values at 13 and 14 TeV, as reported in Ref. [7]. The background yields have been scaled according to the parton luminosity ratio between 13 and 14 TeV, as reported in Ref. [3], by taking into account whether the background process is predominantly quark pair or gluon pair initiated.

Object reconstruction efficiencies, resolutions and fake rates are assumed to be similar in the Run-2 and HL-LHC environments, based on the assumption that ATLAS and CMS upgraded detectors will compensate for the at HL-LHC higher pile-up environment. For the systematic uncertainties which include experimental, signal and background components, two scenarios have been considered. The first scenario (S1) assumes the same values as those used in the published Run-2 analyses. The second scenario (S2) implements a reduction of the systematic uncertainties according to the improvements expected to be reached at the end of HL-LHC program in twenty years from now: the correction factors follow the recommendations from Ref. [17]. Some systematics uncertainties are specifically treated in the individual analysis, and will be discussed in each dedicated section. In all analyses, the theory uncertainties for signal and background are generally halved, except where more precise extrapolated values have been provided. The uncertainty on the luminosity is set to 1%. The uncertainty related to Monte Carlo samples statistics is assumed to be negligible.

The extrapolated results are generally limited by systematic uncertainties. It is worth noting that, despite all efforts to design proper projections, the values of the systematic uncertainties of the Run-2 analyses cannot fully account for the HL-LHC conditions and process understanding. In this sense, they are to be considered an approximation. Future analyses will exploit and gain sensitivity from phase space regions that are not accessible yet, or use analysis techniques that reduce the impact of systematic uncertainties.

In the following, all analyses segment the selected events according to the objects campaigning the main Higgs decay products and their topology, in order to maximize the sensitivity to the main Higgs production modes ( $ggH + b\bar{b}H$ , VBF,  $VH = qqZH + ggZH + WH$  and top =  $t\bar{t}H + tH$ ) and to reduce the uncertainties on the respective cross sections. Details on how this segmentation is performed, and on the event selection and categorisation in the various analyses, are found in the Run-2 analysis references quoted in each section.

$$H \rightarrow WW^* \rightarrow e\nu\mu\nu$$

### 2.3.2 $H \rightarrow \gamma\gamma$

The measurement of the Higgs boson properties in the  $H \rightarrow \gamma\gamma$  channel is extrapolated from the most recent measurements by ATLAS with  $80\text{ fb}^{-1}$  [18] and CMS with  $XX\text{ fb}^{-1}$  [19]. Events are selected to contain two isolated photon candidates passing good quality requirements in the precision regions of the detectors. The Higgs production cross sections are measured for a Higgs boson absolute rapidity  $|y_H|$  smaller than 2.5, and with further requirements on the objects campaigning the diphoton system (e.g. jet  $p_T$ ). The  $H \rightarrow \gamma\gamma$  signal is extracted by means of a combined signal-plus-background fit of the diphoton invariant mass spectra in the various event categories, where both the continuous background and the signal resonance are parameterized by analytical functions. The shape properties of the signal PDF are obtained by MC simulation, and constrained by performance studies of the photon energy scale and resolution. The background PDF is completely determined by the fit on data, with systematic uncertainties attributed to the specific choice of functional form following the procedure described in Ref. [19] or using the discrete profiling method [20].

The main systematic uncertainties affecting the results are the background modelling uncertainty, QCD scale uncertainties causing event migrations between the bins, photon isolation efficiencies and jet uncertainties. On top of the common assumptions mentioned in Section 2.3.1, the ATLAS  $H \rightarrow \gamma\gamma$  results include a 10% increase of the background modeling systematic uncertainties, to account for the

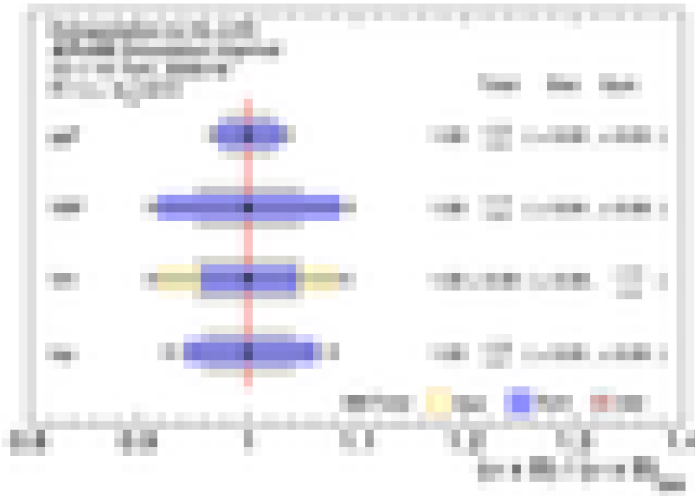


Fig. 6: Ratio of the cross-section times branching fraction measurements of the main four Higgs production modes in the  $H \rightarrow \gamma\gamma$  decay channel to their respective theoretical SM predictions, as extrapolated at the HL-LHC for scenario S2 by ATLAS.

potentially worst knowledge of the background composition in each analysis category at HL-LHC: this assumption has anyway negligible impact. In the Run-2 analyses, a conservative 100% uncertainty on the heavy flavour resonant background in top-sensitive categories is applied. Measurements by ATLAS and CMS of the heavy flavour content, or the  $b$ -jet multiplicity, are expected to better constrain these contributions: for the S2 scenario extrapolation, this uncertainty is therefore halved.

Figure 6 show the ratio of the extrapolated  $H \rightarrow \gamma\gamma$  ATLAS measurements of the main four Higgs production modes to their respective theoretical SM predictions in the scenario S2. The reduction of the total uncertainty with respect to the  $80 \text{ fb}^{-1}$  results ranges from a factor of about 2(3) for the S1 (S2) scenario for the  $ggH + b\bar{b}H$ , VBF, top cross sections, to a factor of about 5(6) for the  $VH$  cross section.

### 2.3.3 $H \rightarrow Z\gamma \rightarrow 2\ell\gamma$

Due to the small branching fraction in the SM, the  $H \rightarrow Z\gamma$  decay has not yet been observed at the LHC. The experimental observed limits at the 95% confidence level are currently 6.6 times the SM prediction for a Higgs boson mass of 125.09 GeV by ATLAS, based on the analysis of  $36.1 \text{ fb}^{-1}$  of  $pp$  collision at  $\sqrt{s} = 13 \text{ TeV}$  [?], and XX times the SM prediction by CMS, based on ... [].

The analyses select event with an isolated photon candidate passing good quality requirements in the precision regions of the detectors, and a dilepton system with properties compatible with that of the decay of a  $Z$  boson. Events are separated according to lepton flavour, the event kinematical properties, and the present of jets compatible with the VBF production of the Higgs boson, in order to maximize the signal sensitivity. The signal is sought for by means of a combined signal-plus-background fit of the photon-dilepton invariant mass spectra in various event categories, where both the continuous background and the signal resonance are parameterized by analytical functions. The Run-2 analyses are strongly driven by statistical uncertainty, and the main systematic uncertainties are from the bias associated to the background modeling.

The extrapolations to HL-LHC are performed with a simple scaling approach, assuming the same signal and background modeling used in the Run-2 analyses. All experimental and systematic uncertainties are considered to remain the same, except the uncertainty associated to the background modeling, which is taken to be negligible.

The ATLAS expected significance to the SM Higgs boson decaying in  $Z\gamma$  is  $4.9 \sigma$  with  $3000 \text{ fb}^{-1}$ .

Assuming the SM Higgs production cross section and decay branching ratios, the signal strength is expected to be measured with a  $\pm 0.24$  uncertainty. The cross section times branching ratio for the  $pp \rightarrow H \rightarrow Z\gamma$  process is projected to be measured as  $1.00 \pm 0.23$  times the SM prediction. Even at the HL-LHC scenario S1, the analysis sensitivity to  $H \rightarrow Z\gamma$  will remain driven by the statistical uncertainty. The dominant source of systematic uncertainty in the extrapolation is that associated to the QCD scale variations.

### 2.3.4 $H \rightarrow ZZ^* \rightarrow 4\ell$

The measurement of the Higgs boson properties in the  $H \rightarrow ZZ^* \rightarrow 4\ell$  is extrapolated from the most recent measurements by ATLAS with  $80\text{ fb}^{-1}$  [21] and CMS with  $XX\text{ fb}^{-1}$  [22]. Events are selected to contain at least two same-flavour opposite-sign dilepton pairs, chosen from isolated electrons and muons candidates passing good quality requirements in the precision regions of the detectors. Additional constraints on the kinematical properties of the pair associated with the decay the on-shell  $Z$  boson, and on the global topology of the event, helps to improve the signal to background ratio. The four-lepton invariant mass resolution is improved by correcting for the emission of final-state radiation photons by the leptons. The  $H \rightarrow ZZ^* \rightarrow 4\ell$  signal is extracted from the four-lepton invariant mass spectra in the different event categories, after having evaluated the background components using simulation to constrain their shapes, and data control region to extrapolate their normalization in the signal regions.

The dominant systematic uncertainties affecting the extrapolation of the ggH cross section measurement are the lepton reconstruction and identification efficiencies and pile-up modeling uncertainties. The VBF and VH cross-sections are primarily affected by the uncertainty on the jet energy scale and resolution, and by the QCD scale uncertainties. The theory uncertainties related to QCD scale and parton shower modeling primarily affects the extrapolated top cross section.

The VBF, VH and top measurements in the  $\tilde{2}\tilde{1}$  decay channel remain largely dominated by statistical uncertainty when extrapolated to  $3000\text{ fb}^{-1}$  while the  $ggH + b\bar{b}H$  cross section is dominated by systematic uncertainties both in scenario S1 and S2. Figure 7 show the ratio of the extrapolated  $H \rightarrow ZZ^* \rightarrow 4\ell$  ATLAS measurements of the main four Higgs production modes to their respective theoretical SM predictions in the scenario S2. The  $H \rightarrow ZZ^* \rightarrow 4\ell$  HL-LHC measurements are expected to reach a level of precision comparable to the projected uncertainty on the corresponding theory predictions.

### 2.3.5 $H \rightarrow WW^* \rightarrow \ell\nu\ell\nu$

The measurement of the Higgs boson properties in the  $H \rightarrow ZZ^* \rightarrow 4\ell$  is extrapolated from the most recent measurements by ATLAS in the  $H \rightarrow WW^* \rightarrow e\nu\mu\nu$  channel using  $80\text{ fb}^{-1}$  [22], and by CMS in the  $XX$  channel using  $XX\text{ fb}^{-1}$  [22]. Events are selected to contain two opposite-charged isolated leptons passing good quality requirements in the precision region of the detectors and missing transverse momentum. Additional requirements on the event kinematical properties (e.g. on the dilepton transverse mass and invariant mass, on the azimuthal separation between the leptons) are applied to reduce the various background components. Events are categorized as a function of the jet multiplicity, in order to extract the Higgs ggH and VBF production cross sections. The normalization of (non-resonant)  $WW$ , top ( $t\bar{t}$  and  $Wt$ ), and  $Z \rightarrow \tau\tau$  backgrounds is set using dedicated control regions of the same jet multiplicity as the signal category to which the normalization is transferred.

The measurements are completely dominated by systematic uncertainties, and their extrapolation to the S2 scenario shows the expected reduction by a factor two. The measurement of the ggH cross section by branching fraction is dominated by theoretical PDF uncertainty, followed by experimental uncertainties affecting the signal acceptance, including uncertainties on the jet energy scale and flavour compositing, and lepton misidentification; the VBF result suffers of similar dominant uncertainties. Figure 8 shows the ratio of the extrapolated  $H \rightarrow WW^* \rightarrow e\nu\mu\nu$  ATLAS measurements of the main four

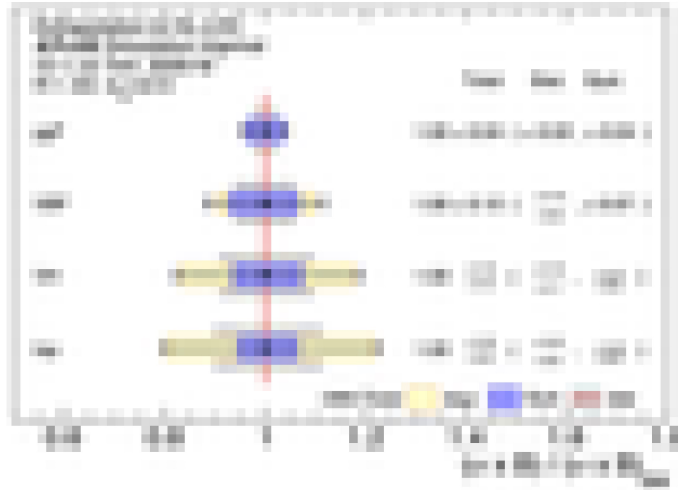


Fig. 7: Ratio of the cross-section times branching fraction measurements of the main four Higgs production modes in the  $H \rightarrow ZZ^* \rightarrow 4\ell$  decay channel to their respective theoretical SM predictions, as extrapolated at the HL-LHC for scenario S2 by ATLAS.

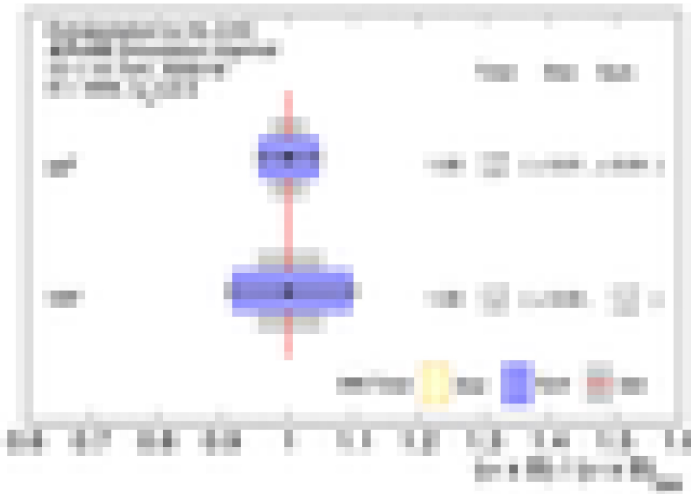


Fig. 8: Ratio of the cross-section times branching fraction measurements of the main four Higgs production modes in the  $H \rightarrow WW^* \rightarrow e\nu\mu\nu$  decay channel to their respective theoretical SM predictions, as extrapolated at the HL-LHC for scenario S2 by ATLAS.

Higgs production modes to their respective theoretical SM predictions in scenario S2.

### 2.3.6 $H \rightarrow \tau\tau$

*To be written by: P. Francavilla, ?*

The studies presented here are performed based on a previous analysis, in which the ATLAS Collaboration analyzed the 2015/2016 proton-proton collision dataset collected at  $\sqrt{s} = 13$  TeV, which corresponds to an integrated luminosity of  $36.1 \text{ fb}^{-1}$  [1]. For the Higgs boson decay products all the leptonic ( $\tau_{lep}$ ) and hadronic ( $\tau_{had}$ ) decays of the  $\tau$ 's are considered. The analysis is done by splitting events into three categories depending on the three tau final states of the decay products:  $(\tau_{lep}, \tau_{lep})$ ,  $(\tau_{lep}, \tau_{had})$  and  $(\tau_{had}, \tau_{had})$ .

### 2.3.7 $H \rightarrow bb$

*To be written by: P. Francavilla, A. de Wit*

**TODO: Text currently reflects CMS studies only. Should be updated to reflect ATLAS and CMS studies. Differences for ATLAS: -> the analysis is the observation (78.9 fb-1) -> tagger is named MVa, and we use a 70% WP -> mbb is improved with muon in jet correction and ptReco, + kinematic fit for 2 leptons -> add the mu for ATLAS -> Add the results from ATLAS** The ATLAS and CMS Collaborations have both reported the observation of the  $H \rightarrow bb$  decay [?, 23]. The studies presented here are performed based on a previous analysis, in which the CMS Collaboration reported evidence for the  $H \rightarrow bb$  decay in the VH production mode using the 2016 proton-proton collision dataset collected at  $\sqrt{s} = 13$  TeV, which corresponds to an integrated luminosity of  $35.9 \text{ fb}^{-1}$  [24]. This analysis makes use of leptonic decays of the vector boson which is produced in association with the Higgs boson. The final states of the VH system covered in this analysis always contain two b-jets and either zero, one or two electrons or muons. Both leptons are required to have the same flavour in the two lepton selection. The b-jets are identified using a combined multivariate (CMVA) tagging algorithm. The inputs include track impact parameter and secondary vertex information from the jet. Three thresholds on the CMVA discriminant are used in the analysis, denoted tight, medium and loose, which have efficiencies for tagging b-jets ranging from 50–75% and for light quark or gluon jets from 0.15–3%.

Major backgrounds arising from SM production of vector boson plus heavy- or light-flavour jets, in addition to  $t\bar{t}$  production, are controlled and constrained for each vector boson decay channel independently via dedicated control regions. Multivariate energy regression techniques are used to improve the b-jet energy resolution, and a boosted decision tree is used to improve the discrimination between signal and background. The distribution of this multivariate discriminator is used as the discriminating variable in the signal extraction fit. The signal strength observed in this analysis is  $\mu_{VHbb} = 1.19^{+0.21}_{-0.20} \text{ (stat)}^{+0.34}_{-0.32} \text{ (syst)}$ . Here the projected uncertainty on the signal strength up to  $3000 \text{ fb}^{-1}$  is reported, assuming  $\mu_{VHbb} = 1$ .

Figure 9 shows the uncertainty on  $\mu_{VHbb}$  as a function of integrated luminosity, for scenario S1 (green points), scenario S2 (red points) and a scenario where all systematic uncertainties are ignored (blue points). In both scenarios S1 and S2 systematic uncertainties start to dominate very quickly, thus moving the projected uncertainty away from the statistical-only scaling curve.

Figure 10 shows the per-process and per-channel signal strength uncertainty, showing results for all three scenarios described above. The large improvement in the signal strength uncertainty for the 1-lepton channel, which is most sensitive to the WH production mode, is caused by the integrated luminosity scaling of an uncertainty in the modelling of the W boson  $p_T$  distribution. This uncertainty dominates this channel in scenario S1.

The contributions of different sources of uncertainty in scenarios S1 and S2 are shown in Table 2. Both in scenario S1 and S2 the largest component of the systematic uncertainty is theoretical. Moving from S1 to S2 the total signal theoretical uncertainty reduces to half its size. This is expected as in scenario S2 the input uncertainties are scaled down to half the current size. In the case of the background theory, where the input uncertainties are also scaled to half their original size when going from scenario S1 to scenario S2, the total uncertainty due to this component is not halved. This is because at  $3000 \text{ fb}^{-1}$  some of the theoretical uncertainties on the backgrounds can be constrained in the fit. The same is true for the experimental uncertainties, which in some cases are already moderately constrained in the current analysis.

Looking in more detail at the dominant signal theoretical uncertainties, the largest component in the uncertainty arises from the uncertainty in the gluon-induced ZH (ggZH) production cross section due to QCD scale variations. The ggZH process contributes a small fraction of the total ZH process. Despite this, the uncertainty in the production cross section for this process due to QCD scale variations

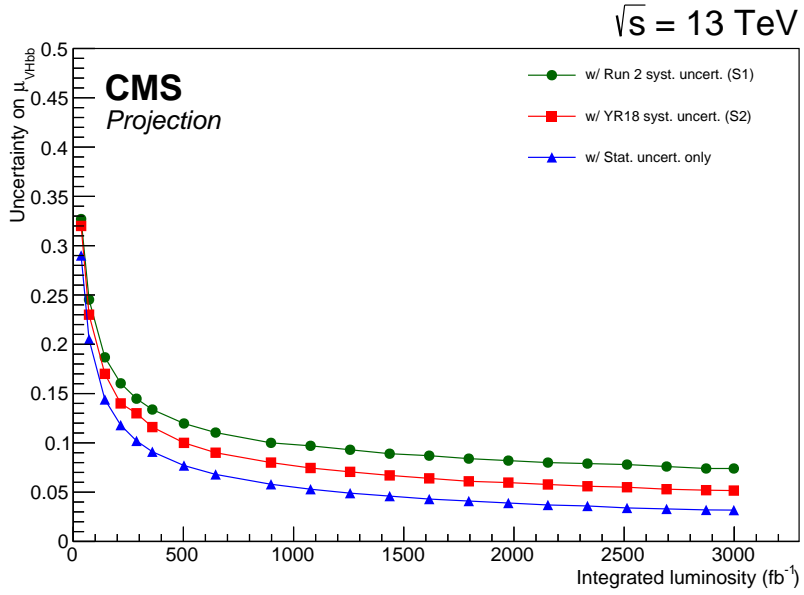


Fig. 9: Uncertainty on the signal strength  $\mu_{VHbb}$  as a function of integrated luminosity for S1 (with Run 2 systematic uncertainties [24]) and S2 (with YR18 systematic uncertainties).

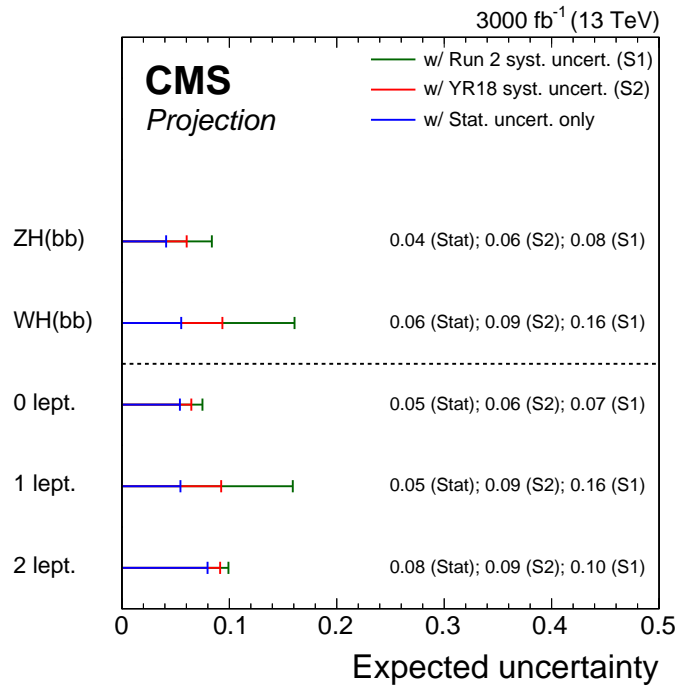


Fig. 10: Uncertainties in the per-process and per-channel signal strengths. Values are given for the S1 (with Run 2 systematic uncertainties [24]) and S2 (with YR18 systematic uncertainties) scenarios, as well as a scenario in which all systematic uncertainties are removed.

becomes dominant because it is very large: 25% for the ggZH process, compared to approximately 4% for the ZH process [7]. The next most important uncertainties are category-acceptance uncertainties in the dominant Z+bb and W+bb backgrounds due to QCD scale variations, as well as the uncertainty

in the ZH and WH production cross section due to QCD scale variations. In scenario S2 these four most important uncertainties contribute 1.6%, 1.5%, 1.3% and 1.2% (absolute) to the total uncertainty of 5.1%, respectively. To improve the precision of the measurement it is therefore important to improve these theoretical uncertainties.

Table 2: Contributions of particular groups of uncertainties in S1 (with Run 2 systematic uncertainties [24]) and S2 (with YR18 systematic uncertainties). The total uncertainty is decomposed into four components: signal theory, background theory, experimental and statistical. The signal theory uncertainty is further split into inclusive and acceptance parts, and the contributions of the b-tagging and JES/JER uncertainties to the experimental component are also given.

	S1	S2
Total uncertainty	0.073	0.051
Signal theory uncertainty	0.054	0.026
Inclusive	0.046	0.022
Acceptance	0.027	0.013
Background theory uncertainty	0.028	0.023
Experimental uncertainty	0.026	0.022
b-tagging	0.022	0.020
JES and JER	0.007	0.006
Statistical uncertainty	0.032	0.032

In the future, and at the HL-LHC in particular, the b-tagging efficiency may change. The conditions could worsen the efficiency, but at the same time new detectors and new techniques could also lead to an improvement in the b-tagging efficiency. The effect of changes in b-tagging efficiency on the overall signal strength uncertainty is evaluated. Changes in the b-tagging efficiency are emulated by scaling the rates of processes with a single b-tag by the change in b-tagging efficiency, and scaling the rates of processes with two b-tags by the change in b-tagging efficiency squared. The modifications are applied only to the efficiency to select genuine b-jets; the mistagging rates for light quark and gluon jets remain unchanged.

Figure 11 shows the results of the projection assuming various reductions and improvements in the b-tagging efficiency relative to the performance of the three CMVA working points used in the analysis. A 10% improvement in the b-tagging efficiency leads to a relative improvement in the signal strength uncertainty of up to 6%. The improvements on the signal strength precision are limited because the uncertainty is dominated by theoretical sources. When neglecting inclusive signal theory uncertainties this improvement becomes up to 8%. **TODO: Results at 300 fb<sup>-1</sup> will be removed from the plot.**

### 2.3.8 $H \rightarrow \mu\mu$

*To be written by: P. Francavilla, ?*

## 2.4 Fiducial and differential cross-section measurements

*To be written by: M. Delmastro, T.Klijnsma*

### 2.4.1 Measurements using $H \rightarrow \gamma\gamma$ , $H \rightarrow ZZ^* \rightarrow 4\ell$ , (boosted) $H \rightarrow b\bar{b}$ decay channels

*Written by: T. Klijnsma*

This section now closely follows FTR-18-011, and describes only CMS results.

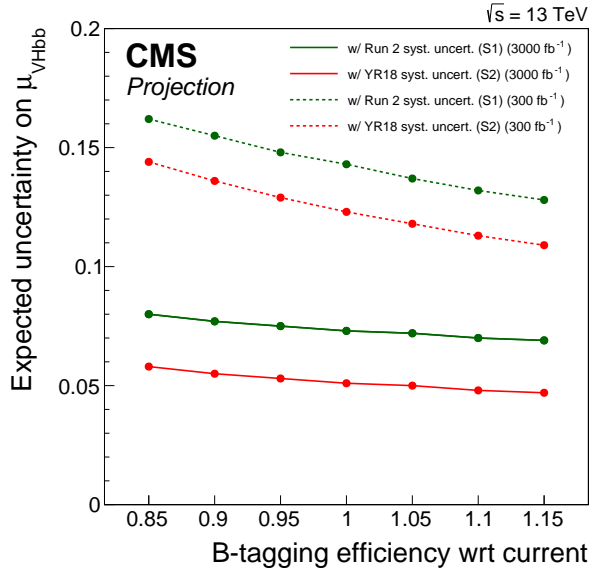


Fig. 11: Effect of varying the b-tagging efficiency on the uncertainty in the signal strength measurement when considering all systematic uncertainties.

In the context of Higgs boson property measurements, one of the main goals of HL-LHC, differential measurements provide a probe of various Higgs boson properties by looking at distortions of differential distributions. The  $p_T^H$  distribution is of particular interest, as potential new physics may reside in the tails of the distribution, which cannot be measured in inclusive measurements [?, ?, 25]. Differential Higgs boson production cross section measurements are available for a range of observables from both the ATLAS [?, ?, ?, ?, ?, ?, ?] and CMS [?, ?, ?, ?, ?, ?, ?] Collaborations at  $\sqrt{s} = 8$  and 13 TeV. The most recent  $p_T^H$  spectra at  $\sqrt{s} = 13$  TeV from both the ATLAS [?] and CMS [?] Collaborations are projected to an integrated luminosity of  $3000 \text{ fb}^{-1}$ . The projection of the  $p_T^H$  spectrum at  $3000 \text{ fb}^{-1}$  by the CMS Collaboration is shown in Fig. 12, for both S1 and S2. The corresponding relative uncertainties for both scenarios are given in Tables 3 and 4. With respect to the uncertainties at the current integrated luminosity of  $35.9 \text{ fb}^{-1}$ , the uncertainties at  $3000 \text{ fb}^{-1}$  in the higher  $p_T^H$  region are about a factor of ten smaller. This is expected, as the uncertainties in this region remain statistically dominated. The uncertainties in the lower  $p_T^H$  region are no longer statistically dominated however, as can be seen by comparing Table 3 with Table 4, where the reduced systematic uncertainties in S2 yield a reduction in the total uncertainty of up to 25% compared to S1.

$p_T^H$ (GeV)	0-15	15-30	30-45	45-80	80-120	120-200	200-350	350-600	600- $\infty$
$H \rightarrow \gamma\gamma$	7.2%	6.8%	7.1%	6.9%	7.1%	6.7%	7.1%	9.9%	32.5%
$H \rightarrow ZZ$	6.2%	5.7%	5.0%		5.5%			9.6%	
$H \rightarrow b\bar{b}$				None				38.2%	37.1%
Combination	4.7%	4.4%	5.0%	4.7%	4.8%	4.7%	5.2%	8.5%	25.4%

Table 3: Relative uncertainties on the projected  $p_T^H$  spectrum under S1 (with Run 2 systematic uncertainties [?]) at  $3000 \text{ fb}^{-1}$ .

#### 2.4.2 Measurement of $p_T(H)$ spectrum in $t\bar{t}H$ production mode

To be written by: N. Wardle

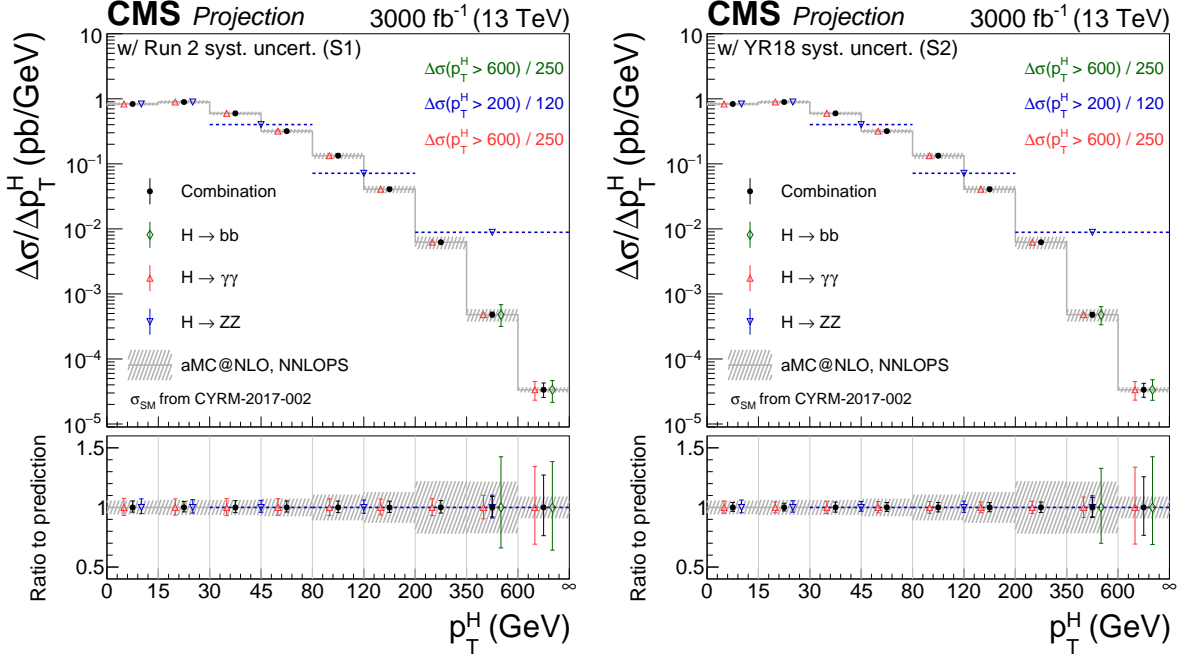


Fig. 12: Projected differential cross section for the  $p_T^H$  spectrum at an integrated luminosity of  $3000 \text{ fb}^{-1}$ , under S1 (upper, with Run 2 systematic uncertainties [?]) and S2 (lower, with YR18 systematic uncertainties).

$p_T^H$ (GeV)	0-15	15-30	30-45	45-80	80-120	120-200	200-350	350-600	600- $\infty$
$H \rightarrow \gamma\gamma$	5.1%	4.6%	5.1%	4.8%	4.9%	4.5%	5.1%	8.6%	32.2%
$H \rightarrow ZZ$	5.4%	4.8%		4.1%		4.7%		9.1%	
$H \rightarrow b\bar{b}$					<i>None</i>			31.4%	36.8%
Combination	3.7%	3.3%	4.2%	3.7%	4.0%	3.8%	4.4%	8.0%	24.5%

Table 4: Relative uncertainties on the projected  $p_T^H$  spectrum under S2 (with YR18 systematic uncertainties) at  $3000 \text{ fb}^{-1}$ .

## 2.5 Direct and indirect probing of top Yukawa coupling

### 2.5.1 Measurements in $t\bar{t}H$ and $tH$ production modes

by A. Calandri, M. Schröder

One of the main targets of the High-Luminosity LHC (HL-LHC) upgrade is to achieve precision measurements of the Higgs boson properties. The Yukawa coupling of the Higgs boson to the top quark is expected to be of the order of unity and could be partially sensitive to effects beyond the Standard Model (SM). Therefore, a direct measurement of the coupling of the Higgs boson to top quarks is extremely important to access possible deviations in the top quark’s Yukawa couplings due to couplings to new particles. Such a measurement can be performed by measuring the rate of the process where the Higgs boson is produced in association with a pair of top quarks ( $t\bar{t}H$ ) or a single top quark ( $tH$ ). Even though the  $t\bar{t}H$  process is characterised by a small cross section compared to the dominant gluon fusion Higgs boson production (approximately two orders of magnitude smaller), the signature with top quarks in the final state can be exploited to reconstruct the event and gives access to many Higgs boson decay modes. The SM  $tH$  production cross-section is yet smaller by a factor five, but due to interference effects between diagrams with top-Higgs and W-boson-Higgs couplings, the process allows access to the sign of

Table 5: Breakdown of the contributions to the expected uncertainties on the  $t\bar{t}H$  signal-strength  $\mu$  in the  $H \rightarrow b\bar{b}$  channel at different luminosities for the scenarios S1 and S2 at CMS. The uncertainties are given in percent relative to  $\mu = 1$ . Results with  $35.9 \text{ fb}^{-1}$  are intended for comparison with the projections to higher luminosities and differ in parts from [?] for consistency with the projected results: uncertainties due to the limited number of Monte Carlo statistics have been omitted and the assumptions in S1/S2 on the theory uncertainties are applied.

Source	S1		S2	
	$35.9 \text{ fb}^{-1}$	$3000 \text{ fb}^{-1}$	$35.9 \text{ fb}^{-1}$	$3000 \text{ fb}^{-1}$
Total	48.7	11.1	46.1	7.3
Stat	26.7	2.9	26.7	2.9
SigTh	10.8	8.7	5.0	4.4
BkgTh	28.6	4.1	25.6	3.5
$t\bar{t} + \text{HF XS}$	14.6	0.8	16.5	0.7
Exp	17.4	4.2	16.6	2.6
Luminosity	1.6	1.8	0.5	0.8
B tagging	12.0	2.8	10.8	1.6
JES	10.9	1.6	11.3	1.6

the top-Higgs Yukawa coupling. The ATLAS and CMS Collaborations have searched for the  $t\bar{t}H$  and  $tH$  production with LHC Run 2 data of 2015, 2016, and 2017, and observed the Higgs boson production in association with a top-quark pair [26, 27]. The analyses are sensitive to a large variety of final-state event topologies,  $H \rightarrow WW^*$ ,  $H \rightarrow ZZ^*$ ,  $H \rightarrow \tau^+\tau^-$ ,  $H \rightarrow b\bar{b}$  and  $H \rightarrow \gamma\gamma$ . Dedicated multivariate analysis techniques, including boosted decision trees and deep neural networks, that combine the information of several discriminating variables, as well as classifiers based on a matrix element method are utilised to identify the signal against the background.

In this Section, projections based on dedicated analyses with  $36 \text{ fb}^{-1}$  of Run-II data of 2016 are presented, which target the  $t\bar{t}H$ ,  $H \rightarrow b\bar{b}$  channel with leptonic decays of the  $t\bar{t}$  system [28, 29] and the  $t\bar{t}H$  multi-lepton final state [30], where the Higgs boson decays into a pair of Z and W vector bosons or into  $\tau$  leptons. Furthermore, results are presented for the projection of a search for  $tH$  production that considers all of the above decay channels.

### 2.5.1.1 Sensitivity to $t\bar{t}H$ production in the $b\bar{b}$ and multi-lepton final states

The  $t\bar{t}H$  analyses in the  $H \rightarrow b\bar{b}$  final state benefit from the large branching ratio. At the same time, the relatively poor  $b$  jet energy resolution, the large jet combinatorics, and the sizeable background of SM processes with large modelling uncertainties, in particular  $t\bar{t} + \text{heavy-flavour jet}$  ( $t\bar{t} + \text{HF}$ ) production, pose major challenges. The expected relative precision of the  $t\bar{t}H$ ,  $H \rightarrow b\bar{b}$  signal strength ( $\mu$ ) measurement for the ATLAS and CMS analyses [31, 32] reach the level of XX–XX% and 7–11% at  $3000 \text{ fb}^{-1}$  for ATLAS and CMS, respectively, depending on the scenario and the assumptions of the  $t\bar{t} + \text{HF}$  background modelling, as detailed below.

Table 5 shows a breakdown of the contributing sources of uncertainty in the CMS analysis; their evolution with integrated luminosity is depicted in Fig. 13. Compared to the result at  $35.9 \text{ fb}^{-1}$ , the relative contribution of the experimental uncertainties, such as the  $b$ -tagging uncertainty, remains approximately the same, while the signal-theory uncertainty component increases and becomes the major uncertainty component, mostly driven by the inclusive cross-section uncertainty on the SM prediction entering  $\mu$ . The statistical uncertainty becomes small compared to the systematic components. A similar behaviour is observed in the ATLAS analysis.

In both analyses, a rather sizeable reduction of the uncertainties related to the modelling of the

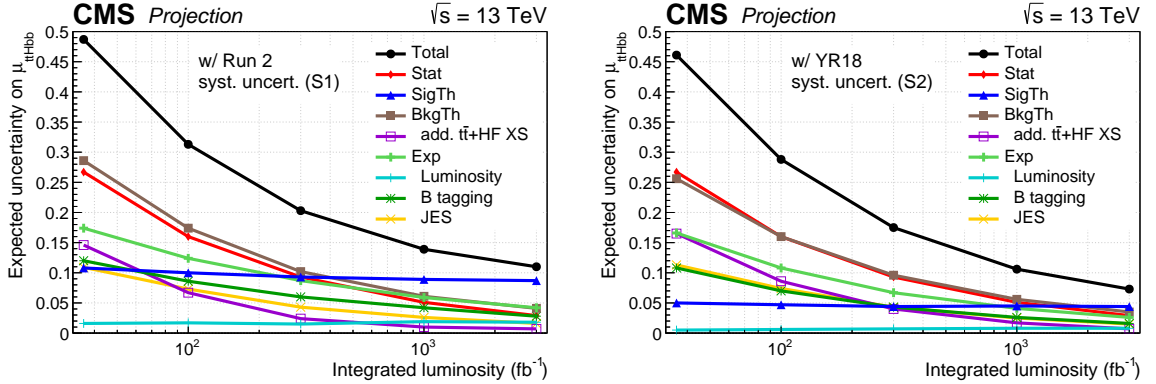


Fig. 13: Expected uncertainties on the  $t\bar{t}H$  signal strength in the  $H \rightarrow b\bar{b}$  channel as a function of the integrated luminosity under the S1 (left) and S2 (right) scenarios at CMS. Shown are the total uncertainty (black) and contributions of different groups of uncertainties. Results with  $35.9 \text{ fb}^{-1}$  are intended for comparison with the projections to higher luminosities and differ in parts from [?] for consistency with the projected results: uncertainties due to the limited number of MC events have been omitted and the assumptions in S1/S2 on the theory uncertainties are applied.

Fig. 14: Ranking of the ten most significant systematics uncertainties under S2 in the single lepton (a) and dilepton (b) final states at ATLAS listed in accordance to their post-fit impact on the  $t\bar{t}H$  cross section.

$t\bar{t} + \text{HF}$  background, which relies on MC simulation, is observed. Relevant nuisance parameters are constrained to a few percent, such as the nuisance parameters describing the difference between four and five-flavour scheme calculations which is treated as a 2-point systematic uncertainty in the ATLAS analysis (Fig. 14) or the nuisance parameters describing the additional  $t\bar{t} + \text{HF}$  cross-section uncertainties in the CMS analysis (Table 5 and Fig. 13). This is attributed to the increasing power of the profile likelihood fit to constrain the uncertainties.

The results illustrate that the background modelling, which has been designed to work well with  $35.9 \text{ fb}^{-1}$  of data, will need to be refined at  $3000 \text{ fb}^{-1}$ , requiring improved simulations or in-situ measurements of the  $t\bar{t} + \text{HF}$  processes themselves. The observed constraints on the  $t\bar{t} + \text{HF}$  background model systematics uncertainties shown in Fig. 14 demonstrate that there will be enough data at the HL-LHC to obtain further information about the background beyond the current modelling. The level at which the nuisance parameters are constrained at  $3000 \text{ fb}^{-1}$ , corresponding to a few percent cross-section uncertainty, demonstrate the level of sensitivity at which the data will be able to distinguish different models and sets a benchmark for the required precision. Monte Carlo prediction will thus need to improve sufficiently to match the data within the uncertainties expected at  $3000 \text{ fb}^{-1}$ .

Following the expected improvement in the theoretical uncertainties on the  $t\bar{t} + \text{HF}$  cross-section calculation described in Section ??, ATLAS and CMS have also performed the  $t\bar{t}H$ ,  $H \rightarrow b\bar{b}$  extrapolation assuming that the reduction of the  $t\bar{t} + \text{HF}$  modelling uncertainties is limited to factors of two (in scenario S1) and three (in scenario S2) relative to the uncertainty at  $35.9 \text{ fb}^{-1}$ . In this case, the obtained relative  $t\bar{t} + \text{HF}$  modelling uncertainties are approximately 23% (S1) and 15% (S2) in the ATLAS analysis as reported in Table 7 and approximately 15% (S1) and 10% (S2) in the CMS analysis. These results enter the combined coupling measurement presented in Section ???. The impact of limiting the constraints of the  $t\bar{t} + \text{HF}$  uncertainties on the total uncertainties on the extracted parameters is relatively small, e.g. the uncertainty on  $\kappa_t$  increases by approximately 10% and 15% in CMS and ATLAS, respectively.

In conclusion,  $t\bar{t}H$  production in the  $H \rightarrow b\bar{b}$  final state will provide a powerful channel to probe the top-Higgs Yukawa coupling at the HL-LHC. The control of the  $t\bar{t} + \text{HF}$  background is crucial, and

Table 6: Breakdown of the contributions to the expected uncertainties on the  $t\bar{t}H$  cross section in the  $H \rightarrow b\bar{b}$  channel at different luminosities for the scenarios S1 and S2 at ATLAS. As discussed in the text, the extrapolation assumes the limitations on the reduction of the  $t\bar{t} + \text{HF}$  modelling to a factor 2 and a factor 3 of the Run 2 prior uncertainties (Section ??). Therefore, the additional modelling uncertainty used for the extrapolation is 23% in S1 and 15% in S2. Uncertainties due to the limited number of Monte Carlo statistics have been omitted and the assumptions in S1/S2 on the theory uncertainties are applied.

Table 7: Breakdown of the contributions to the expected uncertainties on the  $t\bar{t}H$  cross section in the multilepton channel at different luminosities for the scenarios S1 and S2 at ATLAS. Uncertainties due to the limited number of Monte Carlo statistics have been omitted and the assumptions in S1/S2 on the theory uncertainties are applied.

Fig. 15: Ranking of the ten most significant systematics uncertainties under S2 in the  $t\bar{t}H$  final state with (a) and without (b)  $\tau$  leptons in the ATLAS analysis listed in accordance to their post-fit impact on the  $t\bar{t}H$  cross section.

it is expected to benefit from measuring relevant quantities from data, thus mitigating the impact of theoretical uncertainties.

ATLAS performs the extrapolation to HL-LHC also for the  $t\bar{t}H$  multilepton final state [31] where the Higgs boson decays into a pair of Z and W vector bosons or into  $\tau\tau$ s. Table ?? shows the results on the extrapolation to  $3000 \text{ fb}^{-1}$  under S1 and S2. As shown in the ranking plot in Figure 15, in the  $\tau$  final state, the dominant uncertainty pertains to the object reconstruction for such a channel. It is also worth noting that the main theoretical systematics concerns the modelling of the  $t\bar{t}+V$  background. Finally, fake lepton uncertainties are moderately constrained as well: this is due to the absence of reduction factor of prior uncertainties for such a source of systematics under S1 and S2.

### 2.5.1.2 Sensitivity to $tH$ production

The sensitivity to the  $tH$  process at the HL-LHC is determined by extrapolating a combination of Run 2 analyses based on  $35.9 \text{ fb}^{-1}$  of data at  $\sqrt{s} = 13 \text{ TeV}$  [33]. Two of these analyses are dedicated searches for  $tHq$ : one targets a multi-lepton final state [34] in which the Higgs boson decays to WW, ZZ or  $\tau\tau$  pairs, and the other targets the  $H \rightarrow b\bar{b}$  decay [35]. In both analyses the presence of at least one central b tagged jet and an isolated lepton from the top quark decay is required. Furthermore, the presence of a light quark jet at high pseudorapidity, a unique feature of the  $tHq$  production mode, is exploited. Both analyses also rely heavily on multivariate techniques to discriminate the signal against the large  $t\bar{t}+\text{jets}$  background. The  $\gamma\gamma$  final state is also utilised, via a reinterpretation of the inclusive  $H \rightarrow \gamma\gamma$  analysis [?]. In this analysis the  $tHq$  and  $tHW$  processes primarily contribute to the “ $t\bar{t}H$  leptonic” and “ $t\bar{t}H$  hadronic” event categories, and these are included in the combination.

In Figure 16 the variation of the expected upper limits on  $\mu_{tH}$  is shown as a function of the integrated luminosity for the S1 and S2 scenarios. The limits are determined assuming a background-only hypothesis in which the  $tH$  process is considered as following the SM expectation ( $\mu_{ttH} = 1$ ). In order to minimize further assumptions on the rate of  $tH$  production,  $\mu_{tH}$  is treated as a free parameter in the fit. In the S1 scenario the expected median upper limit on  $\mu_{tH}$  at  $3000 \text{ fb}^{-1}$  is determined to be 2.35. The corresponding value in S2 is 1.51. With the  $3000 \text{ fb}^{-1}$  dataset and foreseen reduction in systematic uncertainties in S2, the expected upper limit on  $\mu_{tH}$  improves by about a factor of eight with respect to the current exclusion.

The evolution of the expected uncertainty on the measurement of  $\mu_{tH}$ , assuming the SM rate, is

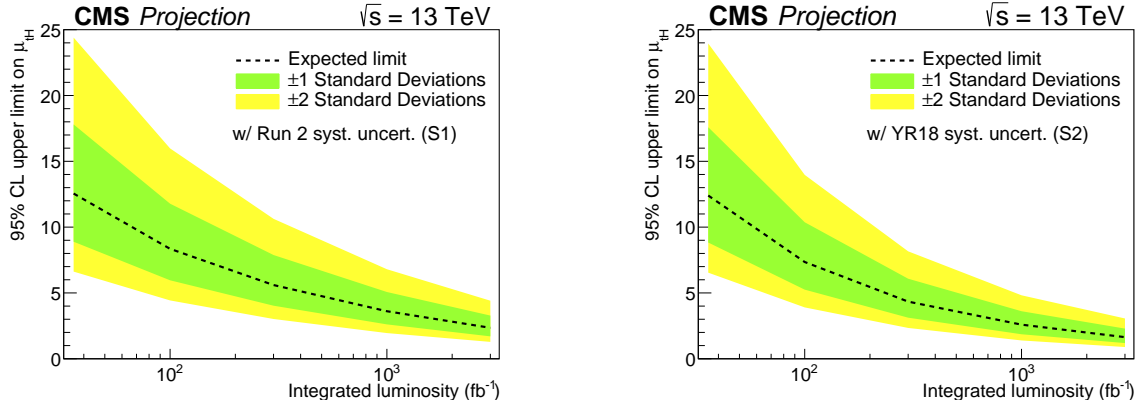


Fig. 16: The variation of expected upper limit on  $\mu_{t\bar{t}H}$  with integrated luminosity for two projection scenarios S1 (with Run 2 systematic uncertainties [33]) and S2 (with YR18 systematic uncertainties).

given in Table 8. Values are given for two cases of background: one in which  $\mu_{t\bar{t}H}$  is unconstrained in the fit, and one in which it is fixed to the SM value of 1. In the latter case the uncertainties are reduced by around 10% at  $3000 \text{ fb}^{-1}$ , indicating that a precise simultaneous measurement of the  $t\bar{t}H$  signal strength will be needed to obtain the optimal sensitivity to the  $t\bar{t}H$  channel. In both cases it is found that the reduced systematic uncertainties in S2 improve the precision by up to 30%.

Table 8: The  $\pm 1\sigma$  uncertainties on expected  $\mu_{t\bar{t}H}=1$  for scenarios S1 (with Run 2 systematic uncertainties [33]) and S2 (with YR18 systematic uncertainties) at all three luminosities, considering also the case when  $\mu_{t\bar{t}H}$  is fixed at the SM value 1.

		$\mu_{t\bar{t}H}$ floating	$\mu_{t\bar{t}H}$ fixed
S1	$35.9 \text{ fb}^{-1}$	+6.2 -5.8	+5.8 -5.4
	$300 \text{ fb}^{-1}$	+2.9 -2.8	+2.5 -2.4
	$3000 \text{ fb}^{-1}$	+1.2 -1.2	+1.1 -1.0
S2	$35.9 \text{ fb}^{-1}$	+6.2 -5.8	+5.8 -5.3
	$300 \text{ fb}^{-1}$	+2.2 -2.2	+2.0 -2.0
	$3000 \text{ fb}^{-1}$	+0.9 -0.9	+0.8 -0.8

### 2.5.2 Constraints from differential measurements

Written by: T. Klijnsma

Higgs boson couplings can be constrained by fitting theoretical predictions for  $p_T^H$  [?, ?, ?] to data, exploiting not only the overall normalization (as is done in inclusive measurements [?, ?, 25]), but also the shape of the distribution. One of the first constraints on Higgs boson couplings using differential Higgs boson production cross sections was made in Ref. [?]. The limits  $\kappa_c \in [-16, 18]$  at 95% CL were found, using data collected by the ATLAS Collaboration at  $\sqrt{s} = 8 \text{ TeV}$  [?], corresponding to an integrated luminosity of  $20.3 \text{ fb}^{-1}$ . More recently, the CMS Collaboration performed a similar fit using data [?] collected at  $\sqrt{s} = 13 \text{ TeV}$ , corresponding to an integrated luminosity of  $36.1 \text{ fb}^{-1}$ . The limits on  $\kappa_b$  and  $\kappa_c$  are discussed in Section , whereas the interpretation in terms of  $\kappa_t$  and  $c_{ggh}$ , the anomalous direct coupling to the gluon field, is discussed here. The projected simultaneous limits on  $\kappa_t$  and  $c_{ggh}$  at  $3000 \text{ fb}^{-1}$  are shown in Fig. 18, assuming branching fractions that scale according to SM predictions. It

is expected to observe the loop in the gluon-fusion production process, which is clear from the fact that heavy top mass limit, given by the point ( $\kappa_t = 0, c_{ggh} = \sim 1/12$ ), is excluded.

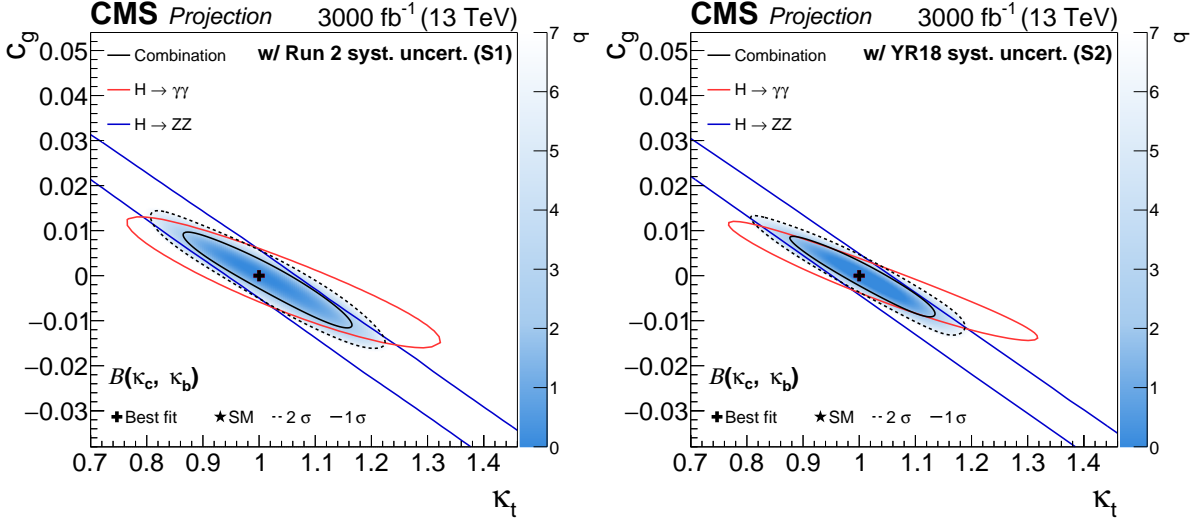


Fig. 17: Projected simultaneous fit for  $\kappa_t$  and  $c_{ggh}$ , assuming a coupling dependence of the branching fractions for Scenario 1 (left) and Scenario 2 (right). The one standard deviation contour is drawn for the combination ( $H \rightarrow \gamma\gamma$ ,  $H \rightarrow ZZ$ , and  $H \rightarrow b\bar{b}$ ), the  $H \rightarrow \gamma\gamma$  channel, and the  $H \rightarrow ZZ$  channel in black, red, and blue, respectively. For the combination the two standard deviation contour is drawn as a black dashed line, and the shading indicates the negative log-likelihood, with the scale shown on the right hand side of the plots.

In order to determine solely the constraint obtained from the distribution (and not the overall normalization), the fit is repeated with the branching fractions implemented as nuisance parameters with no prior constraint, effectively profiling the overall normalization. With this parametrization, the sensitivity to the sign of  $\kappa_t$  coming from the  $H \rightarrow \gamma\gamma$  branching fraction is lost. The fits obtained this way are shown in Fig. 18; although less significantly, the loop is still distinguished from the point-like coupling to the gluon field, using only the information in the shape of the distribution.

## 2.6 Combination of Higgs boson measurement projections

*To be written by: R. Di Nardo, A. Gilbert, H. Yang*

**TODO: Text to be updated to reflect ATLAS+CMS combination.**

The projections documented in this section are based on extrapolations of the following analyses:

- $H \rightarrow \gamma\gamma$ , with ggH, VBF, VH and ttH production [?],
- $H \rightarrow ZZ^{(*)} \rightarrow 4\ell$ , with ggH, VBF, VH and ttH production [36],
- $H \rightarrow WW^{(*)} \rightarrow \ell\nu\ell\nu$ , with ggH, VBF and VH production [37],
- $H \rightarrow \tau\tau$ , with ggH and VBF production [38],
- VH production with  $H \rightarrow b\bar{b}$  decay [24],
- Boosted H production with  $H \rightarrow b\bar{b}$  decay [39],
- ttH production with  $H \rightarrow$  leptons [?],
- ttH production with  $H \rightarrow b\bar{b}$  [40, 41],
- $H \rightarrow \mu\mu$ , with ggH and VBF production [42].

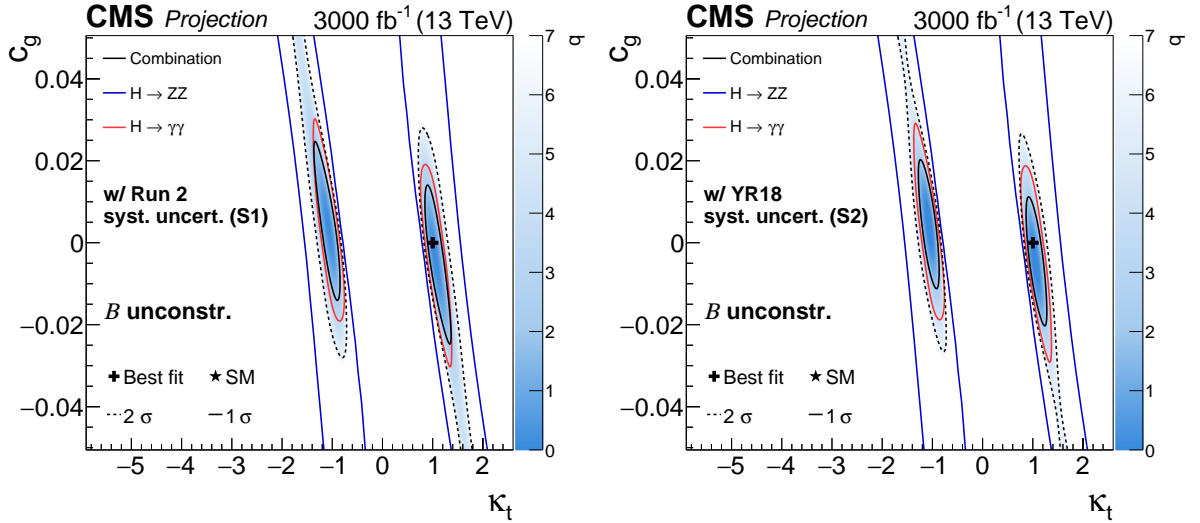


Fig. 18: Projected simultaneous fit for  $\kappa_t$  and  $c_{ggh}$  with the branching fractions implemented as nuisance parameters with no prior constraint for Scenario 1 (left) and Scenario 2 (right). The one standard deviation contour is drawn for the combination ( $H \rightarrow \gamma\gamma$ ,  $H \rightarrow ZZ$ , and  $H \rightarrow b\bar{b}$ ), the  $H \rightarrow \gamma\gamma$  channel, and the  $H \rightarrow ZZ$  channel in black, red, and blue, respectively. For the combination the two standard deviation contour is drawn as a black dashed line, and the shading indicates the negative log-likelihood, with the scale shown on the right hand side of the plots.

The projected results given in this section are based on the combined measurement of these channels [43]. In the following results the signal model in the  $H \rightarrow \mu\mu$  channel is modified to account for the improved dimuon mass resolution in the Phase-2 CMS tracker upgrade [?]. It is estimated that the reduced material budget and improved spatial resolution of the upgraded tracker will yield a 40% improvement in the relative di-muon mass resolution, for example a reduction from 1.1% to 0.65% for muons in the barrel region.

**TODO: Switch to cross section and branching ratio results without inclusive theory uncertainties.** Projections are given for two parametrisations of the signal, based on signal strength modifiers  $\mu$ , defined as the ratio between the measured Higgs boson yield and its SM expectation. One set of parameters  $\mu^f$ , where  $f = ZZ, WW, \gamma\gamma, \tau\tau, b\bar{b}$  and  $\mu\mu$ , are introduced to scale the branching fractions of each decay mode independently, assuming the SM cross sections for the production modes. Another set,  $\mu_i$ , where  $i = ggH, VBF, WH, ZH$  and  $t\bar{t}H$ , scale each production cross section independently, assuming the SM values of the branching fractions.

### 2.6.1 Signal strength per-decay mode

The expected  $\pm 1\sigma$  uncertainties on the per-decay-mode signal strength parameters in S1 and S2 are summarised in Figure 19 with numerical values given in Table 9. The table additionally gives the breakdown of the uncertainty into four components: statistical, signal theory, background theory and experimental. The S2 uncertainties range from 3–4%, with the exception of that on  $\mu^{\mu\mu}$  at 10%. The S1 uncertainties are up to a factor of 1.5 larger than those in S2, reflecting the larger systematic component. The dominant uncertainty contribution is found to vary with the scenario and the integrated luminosity of the projection. The systematic uncertainties generally dominate in both S1 and S2. In S2 the signal theory uncertainty is the largest, or joint-largest, component for all parameters except  $\mu^{\mu\mu}$ , which remains limited by statistics due to the small  $H \rightarrow \mu\mu$  branching fraction. The  $\mu^{\mu\mu}$  uncertainty using the Run 2 dimuon mass

resolution instead of the Phase-2 expectation is 14%.

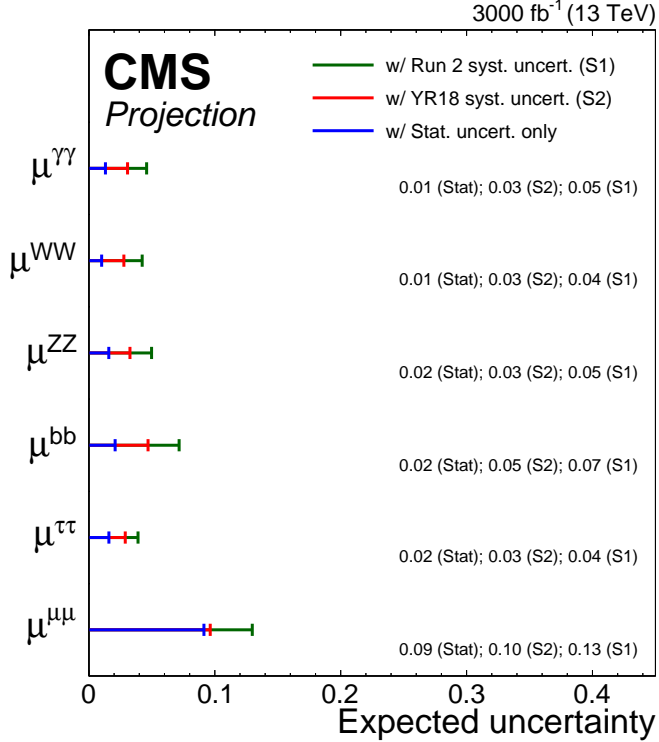


Fig. 19: Summary plot showing the total expected  $\pm 1\sigma$  uncertainties in S1 (with Run 2 systematic uncertainties [43]) and S2 (with YR18 systematic uncertainties) on the per-decay-mode signal strength parameters. The statistical-only component of the uncertainty is also shown.

Another important aspect of the projected measurements is how the correlations between the measured parameters are expected to evolve. Correlations arise when analysis channels are sensitive to more than one production or decay mode and the chosen fit observables do not fully distinguish between these. In addition, correlations may arise when the same systematic uncertainties apply to multiple production or decay modes. Figure 20 shows the correlation coefficients between the signal strength parameters in S2. The correlations range up to +0.44, and are largest between modes where the sensitivity is dominated by gluon-fusion production. This reflects the impact of the theory uncertainties affecting the SM prediction of the gluon-fusion production rate.

### 2.6.2 Signal strength per-production mode

The expected  $\pm 1\sigma$  uncertainties on the per-production-mode signal strength parameters in S1 and S2 are summarised in Figure 21 with numerical values given in Table 10. In S1 the signal theory is the main contribution for all modes except WH which remains limited by statistics. In S2  $\mu_{VBF}$  and  $\mu_{WH}$  are also statistically limited.

Figure 22 shows the correlation coefficients between the signal strength parameters in S2. The correlations in this case are small compared to the per-decay measurements since production modes are generally well-isolated by independent analysis categories and the main theoretical uncertainties on the SM signal expectation are uncorrelated.

## 2.7 Kappa interpretation of the combined Higgs boson measurement projections

*To be written by: R. Di Nardo, A. Gilbert, H. Yang*

Table 9: The expected  $\pm 1\sigma$  uncertainties, expressed as percentages, on the per-decay-mode signal strength parameters. Values are given for both S1 (with Run 2 systematic uncertainties [43]) and S2 (with YR18 systematic uncertainties). The total uncertainty is decomposed into four components: statistical (Stat), signal theory (SigTh), background theory (BkgTh) and experimental (Exp).

		3000 fb <sup>-1</sup>				
		Total	Stat	SigTh	BkgTh	Exp
$\mu^{\gamma\gamma}$	S1	4.6	1.3	3.5	0.3	2.6
	S2	3.1	1.3	2.1	0.3	1.7
$\mu^{WW}$	S1	4.2	1.0	3.7	1.0	1.4
	S2	2.8	1.0	2.2	0.9	1.1
$\mu^{ZZ}$	S1	5.0	1.6	3.5	1.9	2.5
	S2	3.3	1.6	2.1	0.7	1.7
$\mu^{bb}$	S1	7.2	2.1	5.4	3.6	2.3
	S2	4.7	2.1	2.5	2.9	1.7
$\mu^{\tau\tau}$	S1	3.9	1.6	2.6	1.5	1.9
	S2	2.9	1.6	1.8	0.6	1.4
$\mu^{\mu\mu}$	S1	13.0	9.1	5.2	0.8	7.6
	S2	9.6	9.1	2.6	0.8	1.7

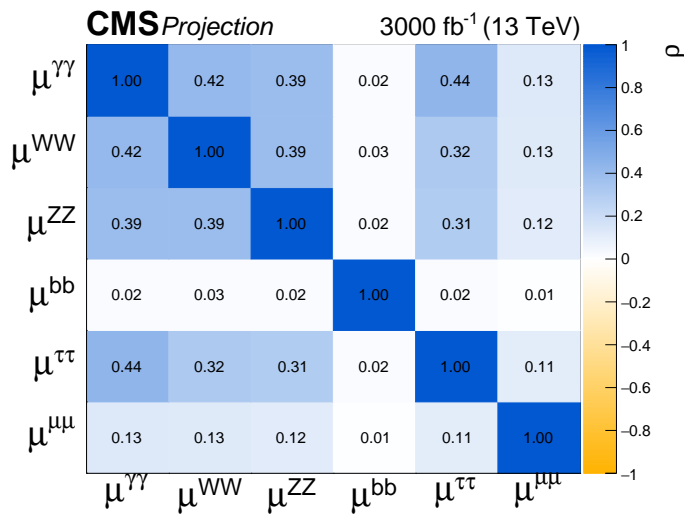


Fig. 20: Correlation coefficients ( $\rho$ ) between parameters in the signal strength per-decay-mode parametrisation for S2 (with YR18 systematic uncertainties).

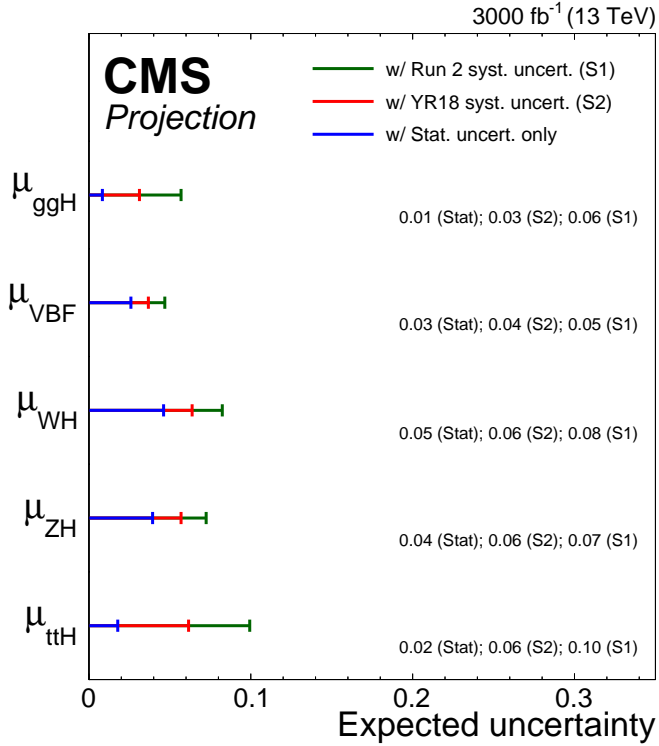


Fig. 21: Summary plot showing the total expected  $\pm 1\sigma$  uncertainties in S1 (with Run 2 systematic uncertainties [43]) and S2 (with YR18 systematic uncertainties) on the per-production-mode signal strength parameters. The statistical-only component of the uncertainty is also shown.

Table 10: The expected  $\pm 1\sigma$  uncertainties, expressed as percentages, on the per-production-mode signal strength parameters. Values are given for both S1 (with Run 2 systematic uncertainties [43]) and S2 (with YR18 systematic uncertainties). The total uncertainty is decomposed into four components: statistical (Stat), signal theory (SigTh), background theory (BkgTh) and experimental (Exp).

		3000 $\text{fb}^{-1}$				
		Total	Stat	SigTh	BkgTh	Exp
$\mu_{ggH}$	S1	5.7	0.8	5.4	0.9	1.2
	S2	3.1	0.8	2.8	0.6	0.9
$\mu_{VBF}$	S1	4.7	2.6	3.0	1.3	2.1
	S2	3.7	2.6	2.1	0.3	1.6
$\mu_{WH}$	S1	8.2	4.6	2.9	3.3	5.2
	S2	6.4	4.6	1.4	2.7	3.2
$\mu_{ZH}$	S1	7.2	3.9	5.1	2.5	2.1
	S2	5.7	3.9	3.0	2.3	1.7
$\mu_{ttH}$	S1	9.9	1.8	8.3	4.1	3.1
	S2	6.2	1.8	4.2	3.4	2.4

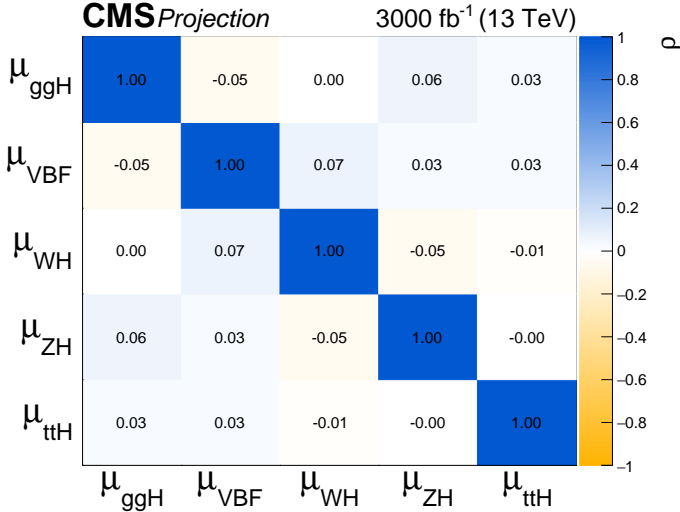


Fig. 22: Correlation coefficients ( $\rho$ ) between parameters in the signal strength per-production-mode parametrisation for S2 (with YR18 systematic uncertainties) at  $300 \text{ fb}^{-1}$  (left) and  $3000 \text{ fb}^{-1}$  (right).

In this section combination results are given for a parametrisation based on the coupling modifier, or  $\kappa$ -framework [3]. A set of coupling modifiers,  $\vec{\kappa}$ , is introduced to parametrize potential deviations from the SM predictions of the Higgs boson couplings to SM bosons and fermions. For a given production process or decay mode  $j$ , a coupling modifier  $\kappa_j$  is defined such that,

$$\kappa_j^2 = \sigma_j / \sigma_j^{\text{SM}} \quad \text{or} \quad \kappa_j^2 = \Gamma_j / \Gamma_{\text{SM}}^j. \quad (1)$$

In the SM, all  $\kappa_j$  values are positive and equal to unity. Six coupling modifiers corresponding to the tree-level Higgs boson couplings are defined:  $\kappa_W$ ,  $\kappa_Z$ ,  $\kappa_t$ ,  $\kappa_b$ ,  $\kappa_\tau$  and  $\kappa_\mu$ . In addition, the effective coupling modifiers  $\kappa_g$  and  $\kappa_\gamma$  are introduced to describe ggH production and  $H \rightarrow \gamma\gamma$  decay loop processes. The total width of the Higgs boson, relative to the SM prediction, varies with the coupling modifiers as  $\Gamma_H / \Gamma_H^{\text{SM}} = \sum_j B_{\text{SM}}^j \kappa_j^2 / (1 - B_{\text{BSM}})$ , where  $B_{\text{SM}}^j$  is the SM branching fraction for the  $H \rightarrow jj$  channel and  $B_{\text{BSM}}$  is the Higgs boson branching fraction to BSM final states. In the results for the  $\kappa_j$  parameters presented here  $B_{\text{BSM}}$  is fixed to zero and only decays to SM particles are allowed. Projections are also given for the upper limit on  $B_{\text{BSM}}$  when this restriction is relaxed, in which an additional constraint that  $|\kappa_V| < 1$  is imposed. A constraint on  $\Gamma_H / \Gamma_H^{\text{SM}}$  is also obtained in this model by treating it as a free parameter in place of one of the other  $\kappa$  parameters.

The expected uncertainties for the coupling modifier parametrisation are summarised in Figure 23 with numerical values given in Table 11. The largest uncertainty component is generally the signal theory in S1, whereas in S2 all four components contribute at a similar level for  $\kappa_\gamma$ ,  $\kappa_W$ ,  $\kappa_Z$  and  $\kappa_\tau$ . The signal theory remains the main component for  $\kappa_t$  and  $\kappa_g$ , and  $\kappa_\mu$  is limited by statistics.

Table 11 also gives the expected uncertainties on  $B_{\text{BSM}}$  and  $\Gamma_H / \Gamma_H^{\text{SM}}$  for the parametrisation with  $B_{\text{BSM}} \geq 0$  and  $|\kappa_V| \leq 1$ . The  $1\sigma$  uncertainty on  $B_{\text{BSM}}$  is 0.035 in S1 and 0.027 in S2, where in the latter case the statistical uncertainty is the largest component. The corresponding 95% CL expected upper limit is  $B_{\text{BSM}} = 0.077(0.057)$  in S1 (S2). The uncertainty on  $\Gamma_H / \Gamma_H^{\text{SM}}$  is 0.05 in S1 and 0.04 in S2, equivalent to 0.16 and 0.21 MeV respectively, assuming the SM width of 4.1 MeV. The main contribution is the statistical uncertainty, followed by the experimental one.

Figure 24 gives the correlation coefficients for the coupling modifiers for S2. In contrast to the per-decay signal strength correlations in Figure 20 the correlations here are larger, up to +0.74. One reason for this is that the normalisation of any signal process depends on the total width of the Higgs

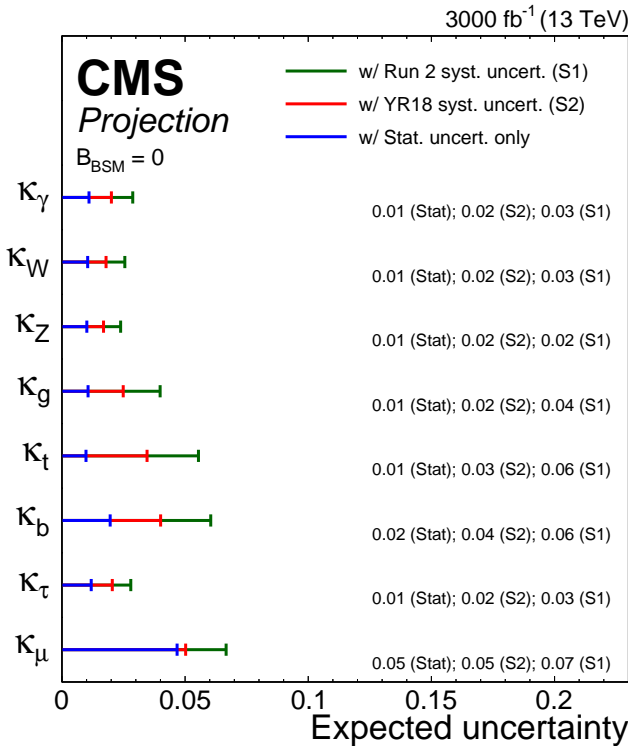


Fig. 23: Summary plot showing the total expected  $\pm 1\sigma$  uncertainties in S1 (with Run 2 systematic uncertainties [43]) and S2 (with YR18 systematic uncertainties) on the coupling modifier parameters. The statistical-only component of the uncertainty is also shown.

boson, which in turn depends on the values of the other coupling modifiers. The largest correlations involve  $\kappa_b$ , as this gives the largest contribution to the total width in the SM. Therefore improving the measurement of the  $H \rightarrow b\bar{b}$  process will improve the sensitivity of many of the other coupling modifiers at the HL-LHC.

## 2.8 Kappa-formalism and the nonlinear EFT

by Claudio Krause and Oscar Catà

The  $\kappa$ -formalism was introduced in [2, 3] as an interim framework to report on the measurements of the Higgs-boson couplings and characterize the nature of the Higgs boson. The  $\kappa_i$  are defined as ratios of measured cross sections and decay widths with respect to their SM expectation, *i.e.*

$$\kappa_X^2 = \frac{\sigma(X_i \rightarrow h + X_f)}{\sigma(X_i \rightarrow h + X_f)_{\text{SM}}}, \quad \kappa_Y^2 = \frac{\Gamma(h \rightarrow Y)}{\Gamma(h \rightarrow Y)_{\text{SM}}}, \quad (2)$$

so that the SM is recovered for  $\kappa_i = 1$ .

The  $\kappa$ -framework, defined at the level of signal strengths, was appropriate for the observables under study at Run I, which tested deviations in event rates. For Run II and the analyses required at the HL-LHC, differential distributions are needed. In order to study event shapes the formalism, as defined by eq. (2), is clearly insufficient and has to be extended.

A closely related issue is how to relate the  $\kappa$ -framework to a QFT description. A naive interpretation of the  $\kappa$  factors as rescalings of SM Higgs couplings has been attempted, but this prescription is not necessarily consistent with QFT principles and has limitations that obstruct a successful implementation. More precisely, the following caveats apply:

Table 11: The expected  $\pm 1\sigma$  uncertainties, expressed as percentages, on the coupling modifier parameters, as well as  $B_{\text{BSM}}$  and  $\Gamma_H/\Gamma_H^{\text{SM}}$ . Due to the constraint  $B_{\text{BSM}} \geq 0$  the values for this parameter correspond to the  $\pm 1\sigma$  uncertainties only. Values are given for both S1 (with Run 2 systematic uncertainties [43]) and S2 (with YR18 systematic uncertainties). The total uncertainty is decomposed into four components: statistical (Stat), signal theory (SigTh), background theory (BkgTh) and experimental (Exp).

3000 fb <sup>-1</sup>						
	Total	Stat	SigTh	BkgTh	Exp	
$B_{\text{BSM}} = 0$						
$\kappa_\gamma$	S1	2.9	1.1	1.8	1.0	1.7
	S2	2.0	1.1	0.9	0.8	1.2
$\kappa_W$	S1	2.6	1.0	1.7	1.1	1.1
	S2	1.8	1.0	0.9	0.8	0.8
$\kappa_Z$	S1	2.4	1.0	1.7	0.9	0.9
	S2	1.7	1.0	0.9	0.7	0.7
$\kappa_g$	S1	4.0	1.1	3.4	1.3	1.2
	S2	2.5	1.1	1.7	1.1	1.0
$\kappa_t$	S1	5.5	1.0	4.4	2.7	1.6
	S2	3.5	1.0	2.2	2.1	1.2
$\kappa_b$	S1	6.0	2.0	4.3	2.9	2.3
	S2	4.0	2.0	2.0	2.2	1.8
$\kappa_\tau$	S1	2.8	1.2	1.8	1.1	1.4
	S2	2.0	1.2	1.0	0.9	1.0
$\kappa_\mu$	S1	6.7	4.7	2.5	1.0	3.9
	S2	5.0	4.7	1.3	0.8	1.1
$B_{\text{BSM}} \geq 0,  \kappa_V  \leq 1$						
$B_{\text{BSM}}^{(+1\sigma)}$	S1	3.8	1.9	2.4	1.5	1.7
	S2	2.7	1.9	1.0	1.2	1.3
$\Gamma/\Gamma_{\text{SM}}$	S1	5.8	2.7	3.6	2.4	2.7
	S2	4.3	2.7	1.9	1.8	2.1

1. In this prescription, only QCD corrections, which are factorizable, can be taken into account. Electroweak corrections cannot be implemented consistently.
2. Gauge invariance and unitarity are generically broken by ad-hoc variations of the SM couplings.
3. In processes that are loop-induced in the SM, such as  $h \rightarrow \gamma\gamma$  or  $gg \rightarrow h$ , care has to be taken. A rescaled local coupling, for example for  $h \rightarrow \gamma\gamma$ , does not yield an overall  $\kappa_\gamma^2$  factor, since the process is not mediated by the local interaction only. In these loop processes the interplay of different couplings, most prominently  $\kappa_t$ , has to be consistently included.

The way to circumvent the objections above is to work not at the level of rescaled couplings but at the level of Lagrangians, where locality, unitarity and gauge invariance are automatically implemented. In order to be as general as possible, an upgrade of the  $\kappa$ -formalism should be embedded in the language of EFTs.

Here we will discuss the interpretation of the  $\kappa$  factors within the electroweak chiral Lagrangian

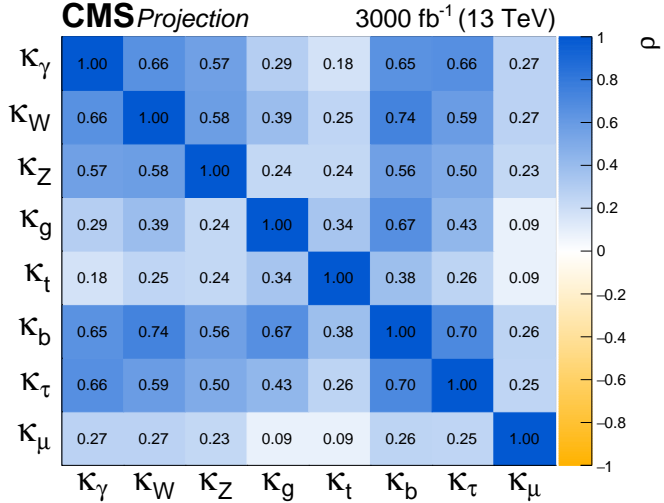


Fig. 24: Correlation coefficients ( $\rho$ ) between parameters in the coupling modifier parametrisation for S2 (with YR18 systematic uncertainties).

(EWChL), also denoted as HEFT in the literature. Within this EFT, and only projecting out the leading contributions to processes with a single Higgs, one finds [44–46]

$$\begin{aligned} \mathcal{L}_{\text{fit}} = & 2c_V \left( m_W^2 W_\mu^+ W^{-\mu} + \frac{1}{2} m_Z^2 Z_\mu Z^\mu \right) \frac{h}{v} - \sum_{\psi} c_\psi m_\psi \bar{\psi} \psi \frac{h}{v} \\ & + \frac{e^2}{16\pi^2} c_\gamma F_{\mu\nu} F^{\mu\nu} \frac{h}{v} + \frac{e^2}{16\pi^2} c_{Z\gamma} Z_{\mu\nu} F^{\mu\nu} \frac{h}{v} + \frac{g_s^2}{16\pi^2} c_g \langle G_{\mu\nu} G^{\mu\nu} \rangle \frac{h}{v}, \end{aligned} \quad (3)$$

where  $m_i$  is the mass of particle  $i$ ,  $\psi \in \{t, b, c, \tau, \mu\}$ , and the  $c_i$  describe the modifications of the Higgs couplings.

The previous Lagrangian differs from a naive rescaling of Higgs couplings, even though superficially it might seem to be equivalent. In particular, the Standard Model is consistently recovered in eq. (3) for

$$c_i^{\text{SM}} = \begin{cases} 1 & \text{for } i = V, t, b, c, \tau, \mu \\ 0 & \text{for } i = g, \gamma, Z\gamma. \end{cases} \quad (4)$$

which is not the case for a naive coupling rescaling. The crucial point is that the coupling modifiers in eq. (3) are not the full EFT, but just the relevant projection for the processes under study at non-trivial leading order in unitary gauge. Since the couplings differ from the SM ones, the previous Lagrangian, taken in isolation, would be non-renormalizable and break unitarity. These requirements are reinstated once eq. (3) is understood as part of the EWChL.

The EWChL [47–64] is a bottom-up effective field theory (EFT), constructed with the particle content and symmetries of the SM. These are the same requirements adopted in the construction of the SMEFT. The main difference between both EFTs concerns the Higgs particle. In the EWChL, the Higgs particle,  $h$ , is included as a scalar singlet, with couplings unrelated to the ones of the Goldstone bosons of EWSB. Therefore,  $h$  is not necessarily part of an SU(2) doublet and consequently the leading-order Lagrangian is non-renormalizable, i.e. loop divergences require the addition of new counterterms. The inclusion of the (finite) number of counterterms at each loop order makes the theory consistent. The procedure is analogous to the one employed in Chiral Perturbation Theory, whence the name EWChL. Counterterms needed for the 1-loop renormalization [65–67] are included as NLO operators [63] and are

therefore suppressed by a loop factor with respect to the leading order. The theory is thus renormalizable order by order in the loop expansion. The embedding of the EFT as a loop expansion can equivalently be expressed as an expansion in chiral dimensions [64], which allows to identify the counterterms in a straightforward way. Further details and justifications of the expansion are discussed in [45, 63, 64, 68].

Focussing on the leading effects of the measured processes only, the full EWChL reduces to the Lagrangian in eq. (3). Note that it includes only single-Higgs processes, as the  $\kappa$ -formalism also describes only single-Higgs processes. If needed, eq. (3) can also be extended to describe other processes, simply by projecting the relevant operators already present in the EWChL. For instance, for double-Higgs production from gluon fusion three more operators should be added, corresponding to the interactions  $h^3, \bar{t}th^2, ggh^2$  [7, 69–71]. Double-Higgs production is discussed in more details in section 3.1.2.1. Since the observed processes are mediated by both tree level and one-loop amplitudes at the first non-vanishing order, operators of leading order in the EFT (first line of eq. (3)) and next-to-leading order in the EFT (second line of eq. (3)) have to be included [45]. Corrections beyond the leading ones, both strong and electroweak, can also be incorporated to arbitrary order in the description of Higgs processes. These corrections involve additional operators, not present in eq. (3), but contained in the EWChL.

Understood as corrections to the SM, the  $\kappa$  factors can also be generated with the SMEFT (see e.g. [72] and the discussion in [73]). The main differences between both EFT descriptions are the following: (i) in the EWChL, deviations from the SM appear at leading order, and  $\mathcal{O}(1)$  corrections to the  $\kappa$  factors can be easily accommodated. In the SMEFT, the corrections to the SM appear at NLO, and therefore smaller effects, typically at the present level, are expected; (ii) In the SMEFT the Higgs is assumed to be a weak doublet. The EWChL instead describes a generic scalar and is therefore closer to the spirit of the  $\kappa$  formalism of testing the nature of the Higgs boson.

As stated above, the couplings in eq. (3) can receive a priori large contributions and have to be considered as  $\mathcal{O}(1)$  numbers. This is the expectation if new physics contains strongly-coupled new interactions. In some of these scenarios, new-physics interactions can be progressively decoupled from the SM, and it is therefore useful to understand the Wilson coefficients in eq. (3) as functions of the parameter  $\xi = v^2/f^2$ , where  $v \approx 246$  GeV is the electroweak vacuum expectation value, and  $f$  is the scale of new physics. The latter could correspond, for example, to the scale of global symmetry breaking in composite Higgs models. The SM is then recovered for  $\xi = 0$ . For  $\xi \ll 1$ , one can perform an expansion in  $\xi$  on top of the loop expansion in the EWChL. This yields a double expansion in  $\xi$  and  $1/16\pi^2$  [74], in the spirit of the strongly-interacting light Higgs (SILH) [75]. The expected size of the Wilson coefficients is then

$$c_i = c_i^{\text{SM}} + \mathcal{O}(\xi). \quad (5)$$

The mapping of the Wilson coefficients  $c_i$  to the  $\kappa_i$  parameters is done using the relations of the signal strengths computed from the Lagrangian in eq. (3). The necessary formulas can be found in [44, 46]. These relations can be written as

$$\kappa_i = |f_i(c_j)| \equiv \frac{|\mathcal{A}_i(c_j)|}{|\mathcal{A}_i(c_j^{\text{SM}})|}, \quad (6)$$

where  $\mathcal{A}$  is the corresponding transition amplitude of each process. The absolute value on the right hand side is necessary, as the loop functions of the light fermions ( $b, \tau, \mu, \dots$ ) for the  $\kappa_\gamma$  and  $\kappa_g$  are complex.

The inverse of eq. (6) is, however, not a well-defined function. We can still obtain an approximate inverse, to connect both formalisms in the opposite direction. This can be easily obtained if we assume that all the imaginary parts are negligible. While this is a good approximation for some of the coefficients in  $f_i(c_j)$ , for example for the coefficient of  $c_t$ , it is not the case for the coefficients of the light fermion loops, where real and imaginary parts are of similar size. Nevertheless, as long as the Wilson coefficients stay relatively close to the SM value, neglecting the imaginary parts completely is still a good approximation, because in  $\kappa_g$  ( $\kappa_\gamma$ ) the real part of the top loop (top and  $W$  loops) contribution dominates over all the other terms.

With the assumption of vanishing imaginary parts, eq. (6) becomes

$$\begin{pmatrix} \kappa_V \\ \kappa_t \\ \kappa_b \\ \kappa_\ell \\ \kappa_g \\ \kappa_\gamma \end{pmatrix} = \begin{pmatrix} 1 & 0 & 0 & 0 & 0 & 0 \\ 0 & 1 & 0 & 0 & 0 & 0 \\ 0 & 0 & 1 & 0 & 0 & 0 \\ 0 & 0 & 0 & 1 & 0 & 0 \\ 0 & 1.055 & -0.055 & 0 & 1.3891 & 0 \\ 1.2611 & -0.2683 & 0.0036 & 0.0036 & 0 & -0.3039 \end{pmatrix} \cdot \begin{pmatrix} c_V \\ c_t \\ c_b \\ c_\tau \\ c_g \\ c_\gamma \end{pmatrix}. \quad (7)$$

These numbers also include the leading QCD corrections of the  $h \rightarrow \gamma\gamma$  and  $gg \rightarrow h$  amplitude. An explicit comparison of this approximation and the full formulas shows only negligible numerical differences. The inverse of eq. (7) is

$$\begin{pmatrix} c_V \\ c_t \\ c_b \\ c_\tau \\ c_g \\ c_\gamma \end{pmatrix} = \begin{pmatrix} 1 & 0 & 0 & 0 & 0 & 0 \\ 0 & 1 & 0 & 0 & 0 & 0 \\ 0 & 0 & 1 & 0 & 0 & 0 \\ 0 & 0 & 0 & 1 & 0 & 0 \\ 0 & -0.76 & 0.04 & 0 & 0.72 & 0 \\ 4.15 & -0.88 & 0.012 & 0.012 & 0 & -3.29 \end{pmatrix} \cdot \begin{pmatrix} \kappa_V \\ \kappa_t \\ \kappa_b \\ \kappa_\ell \\ \kappa_g \\ \kappa_\gamma \end{pmatrix}. \quad (8)$$

With these relations one can translate the results of a  $\kappa_i$  fit into the EWChL formalism and vice-versa. In order to do so, however, it is important to have all the relevant information about the fits. In particular, the median and errors of the parameters are not sufficient, since there may be also significant correlations between them.

## 2.9 Higgs couplings precision overview in the Kappa-framework and the nonlinear EFT

by Jorge de Blas, Otto Eberhardt, and Claudius Krause

After the discovery of the Higgs boson at the LHC, and the first exploration of the couplings of the new particle at the run 1 and 2, achieving an overall precision at the level of ten percent, one of the main goal of Higgs studies at the HL-LHC or HE-LHC will be to push such limits to a percent level. In this section we study the projected precision that would be possible at such high luminosity and high energy extensions of the LHC from a global fit to modifications of the different single Higgs couplings. Other important goals of the Higgs physics program at the HL/HE-LHC, such as extending/complementing the onshell studies with the study of differential distributions, or getting access to the Higgs trilinear coupling will be covered in other parts of this document.

Many explorations of deviation in Higgs couplings in the context of future proposed experiments are typically presented in the so called  $\kappa$  framework [2, 3]. In this phenomenological formalism one defines scaling factors, denoted  $\kappa_i$ , such that the production cross sections and decays of the Higgs boson involving the SM particle  $i$ , scale as  $\kappa_i^2$ . This is indeed a helpful approach to quantify the precision in Higgs measurements. However, it lacks robustness from the theory point of view, as it cannot be extended at NLO and, in its more general form, misses correlations derived from well established symmetry principles. A more robust[/reliable] exploration of deformations in Higgs couplings can be performed within the formalism of effective field theories. In this section we consider the general parameterization provided by non-linear Higgs effective field theory. As explained, in section 2.8, as long as we restrict to the LO effective Lagrangian and one focuses only on deviations on Higgs couplings, it is possible to connect the results of this formalism to those from the  $\kappa$  framework. We refer the reader to section 2.8 for the introduction of the non-linear Higgs effective Lagrangian and its connection with the  $\kappa$  formalism. Throughout this section we will present the expected sensitivities to deviations on the Higgs couplings at the HL/HE-LHC, and compare with the recent results obtained using current data from [46]. A more general analysis going beyond pure modifications of Higgs couplings, allowing also for new physics



on the HL-LHC, and taking the conservative S1 scenario as the reference, we observe an improvement on the knowledge of Higgs coupling of at least a factor of 2-3 with respect to current experimental limits. The improvement is more notorious for channels that benefit from very high statistics, such as the  $H \rightarrow \mu^+ \mu^-$  channel, with a precision almost 6 times better than in the current fit. Further progress is expected once we include the HE-LHC numbers, getting close to the 1% level of precision for the Higgs couplings to vector bosons and  $\tau$  leptons, assuming theory and systematic uncertainties can be kept under control at the same level at the HL-LHC. One must be careful with the interpretation of these results though, since they implicitly assume only modifications in the Higgs couplings with respect to the SM or, in other words, that any other interaction entering on the relevant Higgs processes is known to be SM-like with infinite precision. At the level of precision we observe, close to the 1%, this may not be a justified assumption given current bounds on other electroweak interactions that could modify, e.g. VBF or VH associated production. This comment applies even more for the uncertainties obtained assuming the reduced theory and systematic uncertainties which, in particular, predict a subpercent precision for the Higgs coupling to vector bosons. We believe this to be too aggressive and that a realistic assessment of the HE-LHC uncertainties requires an equally realistic study of the experimental precisions at that machine, as well as the results of a full global fit combining Higgs data with other relevant observables of the EW sector. We refer to section 8 for more details in this regard.

	Current limits [46]	HL-LHC S1	HL-LHC S2	HE-LHC S1	HE-LHC S2
$c_V$	$1.01 \pm 0.06$	$\pm 0.021$	$\pm 0.015$	$\pm 0.013$	$\pm 0.008$
$c_t$	$1.04^{+0.09}_{-0.1}$	$\pm 0.049$	$\pm 0.028$	$\pm 0.031$	$\pm 0.016$
$c_b$	$0.95 \pm 0.13$	$\pm 0.046$	$\pm 0.034$	$\pm 0.03$	$\pm 0.02$
$c_\tau$	$1.02 \pm 0.1$	$\pm 0.027$	$\pm 0.02$	$\pm 0.017$	$\pm 0.011$
$c_\mu$	$0.58^{+0.4}_{-0.38}$	$\pm 0.069$	$\pm 0.052$	$\pm 0.035$	$\pm 0.02$
$c_g$	$-0.01^{+0.08}_{-0.07}$	$\pm 0.044$	$\pm 0.025$	$\pm 0.028$	$\pm 0.14$
$c_\gamma$	$0.05 \pm 0.2$	$\pm 0.081$	$\pm 0.055$	$\pm 0.051$	$\pm 0.032$

Table 12: Current and future constraints on  $c_i$  as shown in Figure 25.

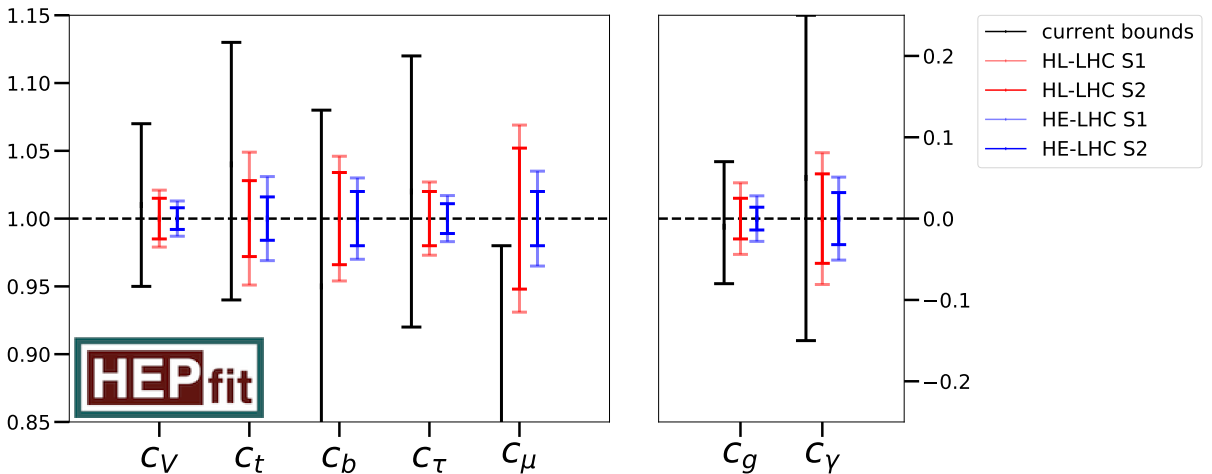


Fig. 25: Current and future constraints on  $c_i$ . The left line of each coupling is the current bound of [46]. The central line is the projection to the HL-LHC with scenario 1 in light red and scenario 2 in dark red. The right line is the projection to HE-LHC (including HL) with scenario 1 in light blue and scenario 2 in dark blue.

	Current limits [46]	HL-LHC S1	HL-LHC S2	HE-LHC S1	HE-LHC S2
$\kappa_V$	$1.01 \pm 0.06$	$\pm 0.021$	$\pm 0.015$	$\pm 0.013$	$\pm 0.008$
$\kappa_t$	$1.04^{+0.09}_{-0.1}$	$\pm 0.049$	$\pm 0.028$	$\pm 0.031$	$\pm 0.016$
$\kappa_b$	$0.94 \pm 0.13$	$\pm 0.046$	$\pm 0.034$	$\pm 0.03$	$\pm 0.02$
$\kappa_\tau$	$1.0 \pm 0.1$	$\pm 0.027$	$\pm 0.02$	$\pm 0.017$	$\pm 0.011$
$\kappa_\mu$	$0.58^{+0.4}_{-0.38}$	$\pm 0.069$	$\pm 0.052$	$\pm 0.035$	$\pm 0.02$
$\kappa_g$	$1.02^{+0.08}_{-0.07}$	$\pm 0.035$	$\pm 0.022$	$\pm 0.024$	$\pm 0.13$
$\kappa_\gamma$	$0.97 \pm 0.07$	$\pm 0.028$	$\pm 0.02$	$\pm 0.017$	$\pm 0.011$

Table 13: Current and future constraints on  $\kappa_i$  as shown in Figure 26.

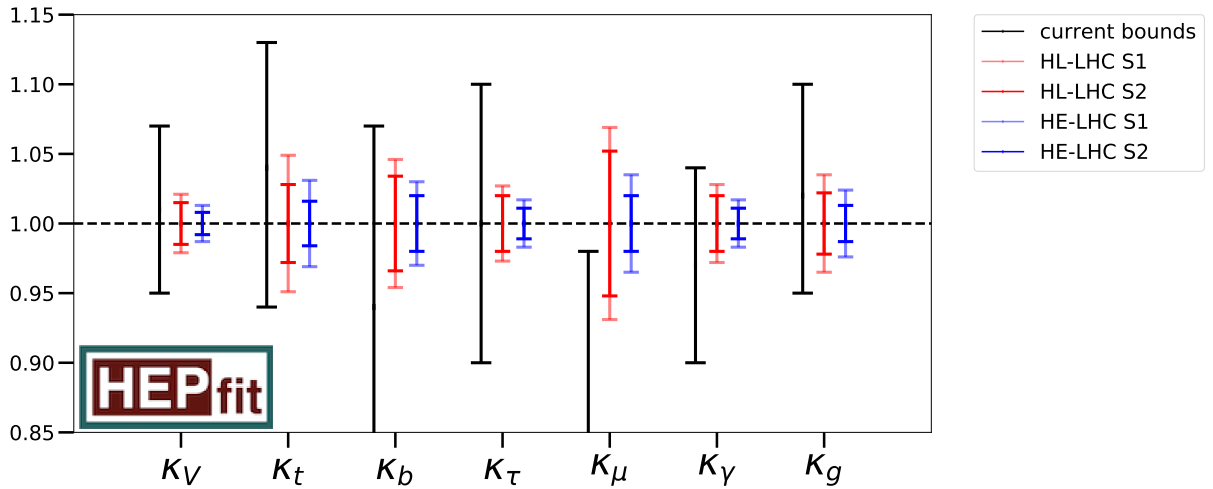


Fig. 26: Current and future constraints on  $\kappa_i$ . The left line of each  $\kappa$  is the current bound of [46]. The central line is the projection to the HL-LHC with scenario 1 in light red and scenario 2 in dark red. The right line is the projection to HE-LHC (including HL) with scenario 1 in light blue and scenario 2 in dark blue.

## 2.10 Projections of Higgs boson measurements to the HE-LHC

To be written by: J.Ellis, L.Silvestrini

## 2.11 Probing of anomalous HVV interactions

### 2.11.1 Probes using differential distributions of CP sensitive observables

To be written by: F. Piccinini, F. Yu, A. Shivaji, ???

By S. Boselli, C. M. Carloni Calame, G. Montagna, O. Nicrosini, F. Piccinini, A. Shivaji, F. Yu, Maria Moreno Llacer et al.

We present prospects for studies on  $CP$ -odd couplings in the couplings of the Higgs boson with the electroweak gauge bosons as well as in the Yukawa couplings of the Higgs boson with fermions, in particular with  $\tau^+\tau^-$  pairs.

#### 2.11.1.1 CP-odd VVH couplings

While a large number of studies assessing the impact of  $CP$ -even effective operators on Higgs physics is available in the literature (see for instance our analysis in Ref. [?] and the references therein), the present

Process	Combination	Theory	Systematic	Statistical
$H \rightarrow ZZ$	ggF	0.06	0.05	0.02
	VBF	0.17	0.10	0.10
	$WH$	0.16	0.06	0.13
	$ZH$	0.21	0.08	0.18
	$t\bar{t}H$	0.20	0.12	0.15

Table 14: Estimated relative uncertainties on the determination of single-Higgs production channels. The estimation of experimental uncertainties is for the high-luminosity LHC (14 TeV center of mass energy and  $3 \text{ ab}^{-1}$  integrated luminosity) [1]. The theoretical uncertainties are taken from [2].

analysis is focused on the impact of  $CP$ -odd effective operators on the interactions among the Higgs boson and the electroweak bosons. In the Higgs basis, the  $CP$ -violating sector of the BSM Lagrangian affecting  $VVH$  couplings is given by,

$$\mathcal{L}_{\text{CPV}} = \frac{H}{v} \left[ \tilde{c}_{\gamma\gamma} \frac{e^2}{4} A_{\mu\nu} \tilde{A}^{\mu\nu} + \tilde{c}_{Z\gamma} \frac{e\sqrt{g_1^2 + g_2^2}}{2} Z_{\mu\nu} \tilde{A}^{\mu\nu} + \tilde{c}_{ZZ} \frac{g_1^2 + g_2^2}{4} Z_{\mu\nu} \tilde{Z}^{\mu\nu} + \tilde{c}_{WW} \frac{g_2^2}{2} W_{\mu\nu}^+ \tilde{W}^{-\mu\nu} \right] \quad (9)$$

where,  $g_1$  and  $g_2$  are the  $U(1)_Y$  and  $SU(2)_L$  gauge coupling constants. Out of the above four parameters only three of them are independent. In particular,

$$\tilde{c}_{WW} = \tilde{c}_{ZZ} + 2s_\theta^2 \tilde{c}_{Z\gamma} + s_\theta^4 \tilde{c}_{\gamma\gamma}. \quad (10)$$

The processes which are sensitive to CPV operators are the Higgstrahlung processes ( $WH$  and  $ZH$ ), the vector boson fusion (VBF) and the Higgs decay into four charged leptons ( $H \rightarrow 4\ell$ ). Here we focus on angular observables which are sensitive to CPV effects. Indeed, since the total cross-section is a  $CP$ -even quantity, the  $1/\Lambda^2$  effects of CPV operators can affect the shape of some specific kinematic distributions only.

### 2.11.1.2 Global Fit

To study the sensitive on CP-violating parameters  $\tilde{c}_{Z\gamma}$  and  $\tilde{c}_{ZZ}$  at HL and HE-LHC, we perform a  $\chi^2$  fit using the signal strength ( $\mu_{i,f}$ ) as the observable. We can build a  $\chi^2$  as follows:

$$\chi^2(\tilde{c}_{Z\gamma}, \tilde{c}_{ZZ}) = \sum_{i,f} \frac{(\mu_{i,f} - \mu_{i,f}^{\text{obs.}})^2}{\Delta_{i,f}^2} \quad (11)$$

The signal strength,  $\mu_{i,f}$  is function of the BSM parameters and it is defined as,

$$\mu_{i,f} = \mu_i \times \mu_f \quad (12)$$

$$= \frac{\sigma_i^{\text{BSM}}}{\sigma_i^{\text{SM}}} \times \frac{\text{BR}_f^{\text{BSM}}}{\text{BR}_f^{\text{SM}}}. \quad (13)$$

The uncertainty,  $\Delta_{i,f}^2$  includes theoretical, experimental systematic and statistical uncertainties which are added in quadrature to obtain the total uncertainty. The one-sigma uncertainties for the high-luminosity (14 TeV center of mass energy and  $3 \text{ ab}^{-1}$  integrated luminosity) are given in table 14. Assuming same acceptance efficiency, we scale the statistical uncertainties at 14 TeV and  $3 \text{ ab}^{-1}$  luminosity appropriately to obtain the statistical uncertainties at 27 TeV and  $15 \text{ ab}^{-1}$  luminosity. The theoretical and systematic uncertainties are kept unchanged.

When considering kinematic distribution in the fit, we estimate the statistical uncertainty in each bin by scaling the overall statistical uncertainty by the fraction of number of events in each bin. On the other hand, the theoretical and systematic uncertainties are assumed to be the same in all the bins implying a very conservative scenario.

Since we are interested in the sensitivity on the CPV parameters that can be reached at HL and HE LHC for which we don't have any data, we take  $\mu_{i,f}^{\text{obs.}} = 1$  implying that the future data would be consistent with the SM hypothesis. In the current analysis we consider all the production channels and Higgs decaying to four charged-lepton that is,  $i = \text{ggF}, \text{VBF}, ZH, WH, t\bar{t}H$  and  $f = 4\ell(2e2\mu, 4e, 4\mu)$ . The projected uncertainties in these channels for HL-LHC are given in table 14. Note that only the  $H \rightarrow 4\ell$  decay mode has a non-trivial kinematic distribution and therefore other decay modes in the present analysis have been ignored. All the results in the following sections are presented taking  $M_H = 125$  GeV.

### Production signal strengths : Inclusive

The first step is to calculate the signal strengths for the relevant production channels in presence of the CP-violating parameters  $\tilde{c}_{Z\gamma}$  and  $\tilde{c}_{ZZ}$ . We use MG5 [] to obtain the inclusive cross sections in presence of these parameters. We have generated the required UFO model file for MG5 using the FeynRules package []. At 14 TeV, the production signal strengths are given by,

$$\mu_{ZH}^{14\text{TeV}} = 1.00 + 0.54 \tilde{c}_{Z\gamma}^2 + 2.80 \tilde{c}_{ZZ}^2 + 0.95 \tilde{c}_{Z\gamma} \tilde{c}_{ZZ} \quad (14)$$

$$\mu_{WH}^{14\text{TeV}} = 1.00 + 0.84 \tilde{c}_{Z\gamma}^2 + 3.87 \tilde{c}_{ZZ}^2 + 3.63 \tilde{c}_{Z\gamma} \tilde{c}_{ZZ} \quad (15)$$

$$\mu_{\text{VBF}}^{14\text{TeV}} = 1.00 + 0.25 \tilde{c}_{Z\gamma}^2 + 0.45 \tilde{c}_{ZZ}^2 + 0.45 \tilde{c}_{Z\gamma} \tilde{c}_{ZZ} \quad (16)$$

At 27 TeV, the corresponding signal strengths are given by,

$$\mu_{ZH}^{27\text{TeV}} = 1.00 + 0.63 \tilde{c}_{Z\gamma}^2 + 3.26 \tilde{c}_{ZZ}^2 + 1.11 \tilde{c}_{Z\gamma} \tilde{c}_{ZZ} \quad (17)$$

$$\mu_{WH}^{27\text{TeV}} = 1.00 + 0.98 \tilde{c}_{Z\gamma}^2 + 4.48 \tilde{c}_{ZZ}^2 + 4.16 \tilde{c}_{Z\gamma} \tilde{c}_{ZZ} \quad (18)$$

$$\mu_{\text{VBF}}^{27\text{TeV}} = 1.00 + 0.32 \tilde{c}_{Z\gamma}^2 + 0.67 \tilde{c}_{ZZ}^2 + 0.65 \tilde{c}_{Z\gamma} \tilde{c}_{ZZ} \quad (19)$$

The BSM predictions for VBF are derived using following cuts,

$$p_T(j) > 20 \text{ GeV}, |\eta(j)| < 5, \Delta\eta_{jj} > 3, m_{jj} > 130 \text{ GeV}.$$

The  $VH$  production modes are more sensitive to  $\tilde{c}_{ZZ}$  parameters. The ggF and  $t\bar{t}H$  production channels are unaffected in presence of CP-violating  $VVH$  couplings. Therefore,

$$\mu_{\text{ggF}}^{14\text{TeV}} = \mu_{\text{ggF}}^{27\text{TeV}} = 1.00 \quad (20)$$

$$\mu_{t\bar{t}H}^{14\text{TeV}} = \mu_{t\bar{t}H}^{27\text{TeV}} = 1.00. \quad (21)$$

In the present analysis we do not consider any kinematic distribution in the production channels.

### Decay signal strength : Inclusive

Now we turn to the calculation of signal strength for the decay channel  $H \rightarrow 4\ell$ . This decay channel receives contributions from  $2e^+2e^-$  ( $4e$ ),  $2\mu^+2\mu^-$  ( $4\mu$ ) and  $e^+e^-\mu^+\mu^-$  ( $2e2\mu$ ) final states. We use the latest version of the Hto4l event generator [?] to obtain the partial decay widths in these channels

in presence of  $\tilde{c}_{Z\gamma}$  and  $\tilde{c}_{ZZ}$ . Both the  $e$  and  $\mu$  are treated massless. The ratio of the partial decay widths in BSM and in SM ( $R_\Gamma$ ) for different channels are given by,

$$R_\Gamma(H \rightarrow 2e2\mu) = 1 + 1.174 \tilde{c}_{Z\gamma}^2 + 0.00291 \tilde{c}_{ZZ}^2 + (-0.00762) \tilde{c}_{Z\gamma} \tilde{c}_{ZZ} \quad (22)$$

$$\begin{aligned} R_\Gamma(H \rightarrow 4e) &= R_\Gamma(H \rightarrow 4\mu) \\ &= 1 + 1.106 \tilde{c}_{Z\gamma}^2 + 0.00241 \tilde{c}_{ZZ}^2 + (-0.00595) \tilde{c}_{Z\gamma} \tilde{c}_{ZZ}. \end{aligned} \quad (23)$$

The above expression for Higgs decay into  $4e$  is obtained after applying a selection cut of 4 GeV on the leading and subleading lepton pairs of opposite sign.

In the present analysis, we also assume that total Higgs decay width remains unchanged in presence of BSM. In this case, the signal strength for decay is just the ratio of decay widths in BSM and in SM.

$$\begin{aligned} \mu_{4\ell} &= \frac{\Gamma_{4\ell}^{\text{BSM}}}{\Gamma_{4\ell}^{\text{SM}}} \\ &= 1 + 1.138 \tilde{c}_{Z\gamma}^2 + 0.00265 \tilde{c}_{ZZ}^2 + (-0.00674) \tilde{c}_{Z\gamma} \tilde{c}_{ZZ} \end{aligned} \quad (24)$$

We note that, the dependence of the  $4\ell$  decay signal strength on the parameter  $\tilde{c}_{ZZ}$  is very weak.

### Decay signal strength : Differential

In our analysis, we are interested in assessing the role of kinematic distributions in  $H \rightarrow 4\ell$  decay channel which are affected by CP-violating  $VVH$  couplings, in improving the sensitivity on  $\tilde{c}_{Z\gamma}$  and  $\tilde{c}_{ZZ}$  at HL and HE-LHC. The Higgs rest frame angle  $\phi$  between the decay planes of the two intermediate gauge bosons is one of the most sensitive kinematic observables to the CP-Violating  $VVH$  couplings. We have considered 50 bins of  $\phi$ -distribution to perform the fit at differential level. For each bin, we calculate the signal strength ( $\mu_{4\ell}^j, j = 1 \rightarrow 50$ ) corresponding to Eq. 24 which is also sensitive to linear terms in  $\tilde{c}_{Z\gamma}$  and  $\tilde{c}_{ZZ}$ .

#### 2.11.1.3 Result: HL and HE-LHC Analysis

The results of the  $\chi^2$  fit are displayed in Fig. 27 and Fig. 28. In these results, *incl.* refers to the fit obtained using the total partial decay width information in the  $H \rightarrow 4\ell$  channel, while *diff.* refers to the fit obtained using  $\phi$ -distribution in  $H \rightarrow 4\ell$  decay. In Fig. 27, we show  $1\sigma$  and  $2\sigma$  bounds on  $\tilde{c}_{Z\gamma}$  and  $\tilde{c}_{ZZ}$  in a one parameter (1P) analysis. At the inclusive level we gain better sensitivity on  $\tilde{c}_{ZZ}$  than on  $\tilde{c}_{Z\gamma}$  when going from HL-LHC to HE-LHC. However, due to a stronger dependence of  $\mu_{4\ell}$  on  $\tilde{c}_{Z\gamma}$  the effect of using  $\phi$ -distribution in the fit is larger for  $\tilde{c}_{Z\gamma}$  than for  $\tilde{c}_{ZZ}$ .

In Fig. 28, we provide  $1\sigma$  contour lines in the  $\tilde{c}_{Z\gamma} - \tilde{c}_{ZZ}$  plane. We can see that the parameters  $\tilde{c}_{Z\gamma}$  and  $\tilde{c}_{ZZ}$  are weakly correlated. Once again we find that using  $\phi$ -distribution in the fit improves our sensitivity on CP-violating parameters significantly. The parameter  $\tilde{c}_{ZZ}$  is mainly constrained by the production channels  $VH$  and  $VBF$ . We have given a summary of  $1\sigma$  bounds on  $\tilde{c}_{Z\gamma}$  and  $\tilde{c}_{ZZ}$  obtained from our analysis for HL and HL-LHC in Table 15.

#### 2.11.1.4 $h \rightarrow \tau^+ \tau^-$

The most promising direct probe of CP violation in fermionic Higgs decays is the  $\tau^+ \tau^-$  decay channel, which benefits from a relatively large  $\tau$  Yukawa giving a SM branching fraction of 6.3%. Measuring the CP violating phase in the tau Yukawa requires a measurement of the linear polarizations of both  $\tau$  leptons and the azimuthal angle between them. This can be done by analyzing tau substructure, namely the angular distribution of the various components of the tau decay products.

Parameter Analysis	$\tilde{c}_{Z\gamma}$	$\tilde{c}_{ZZ}$	Case
HL-LHC ( $4\ell$ , incl.)	[-0.20,0.20]	[-0.19,0.19]	1P
HL-LHC ( $4\ell$ , incl.)	[-0.26,0.26]	[-0.26,0.26]	1P <sub>marg.</sub>
HL-LHC ( $4\ell$ , diff.)	[-0.10,0.10]	[-0.17,0.17]	1P
HL-LHC ( $4\ell$ , diff.)	[-0.13,0.13]	[-0.22,0.22]	1P <sub>marg.</sub>
HE-LHC ( $4\ell$ , incl.)	[-0.17,0.17]	[-0.14,0.14]	1P
HE-LHC ( $4\ell$ , incl.)	[-0.22,0.22]	[-0.20,0.20]	1P <sub>marg.</sub>
HE-LHC ( $4\ell$ , diff.)	[-0.04,0.04]	[-0.07,0.07]	1P
HE-LHC ( $4\ell$ , diff.)	[-0.06,0.06]	[-0.10,0.10]	1P <sub>marg.</sub>

Table 15: Summary of  $1\sigma$  bounds on  $\tilde{c}_{Z\gamma}$  and  $\tilde{c}_{ZZ}$  from various analysis considered here. 1P refers to the case where only one parameter is non-zero while 1P<sub>marg.</sub> refers to the case in which one of the two parameters is marginalized. **Preliminary**

The main  $\tau$  decay modes studied include  $\tau^\pm \rightarrow \rho^\pm(770)\nu$ ,  $\rho^\pm \rightarrow \pi^\pm\pi^0$  [?, ?, ?, ?, ?, ?] and  $\tau^\pm \rightarrow \pi^\pm\nu$  [?, ?, ?]. Assuming CPT symmetry, collider observables for CP violation must be built from differential distributions based on triple products of three-vectors. In the first case,  $h \rightarrow \pi^\pm\pi^0\pi^\mp\pi^0\nu\nu$ , angular distributions built only from the outgoing charged and neutral pions are used to determine the CP properties of the initial  $\tau$  Yukawa coupling. In the second case,  $h \rightarrow \pi^\pm\pi^\mp\nu\nu$ , there are not enough reconstructible independent momenta to construct an observable sensitive to CP violation, requiring additional kinematic information such as the  $\tau$  decay impact parameter.

In the kinematic limit when each outgoing neutrino is taken to be collinear with its corresponding reconstructed  $\rho^\pm$  meson, the acoplanarity angle, denoted  $\Phi$ , between the two decay planes spanned by the  $\rho^\pm \rightarrow \pi^\pm\pi^0$  decay products is exactly analogous to the familiar acoplanarity angle from  $h \rightarrow 4\ell$  CP-property studies. Hence, by measuring the  $\tau$  decay products in the single-prong final state, suppressing the irreducible  $Z \rightarrow \tau^+\tau^-$  and reducible QCD backgrounds, and reconstructing the acoplanarity angle of  $\rho^+$  vs.  $\rho^-$ , the differential distribution in  $\Phi$  gives a sinusoidal shape whose maxima and minima correspond to the CP-phase in the  $\tau$  Yukawa coupling.

An optimal observable using the colinear approximation was derived in [?]. Assuming 70% efficiency for tagging hadronic  $\tau$  final states, and neglecting detector effects, the estimated sensitivity for the CP-violating phase of the  $\tau$  Yukawa coupling using  $3 \text{ ab}^{-1}$  at the HL-LHC is  $8.0^\circ$ . A more sophisticated analysis [?] found that detector resolution effects on the missing transverse energy distribution degrade the expected sensitivity considerably, and as such, about  $1 \text{ ab}^{-1}$  is required to distinguish a pure scalar coupling (CP phase is zero) from a pure pseudoscalar coupling (CP phase is  $\pi/2$ ).

At the HE-LHC, the increased signal cross section for Higgs production is counterbalanced by the increased background rates, and so the main expectation is that improvements in sensitivity will be driven by the increased luminosity and more optimized experimental methodology. Rescaling with the appropriate luminosity factors, the optimistic sensitivity to the  $\tau$  Yukawa phase from acoplanarity studies is  $4\text{-}5^\circ$ , while the more conservative estimate is roughly an order of magnitude worse.

### 2.11.1.5 $t\bar{t}h$

CP violation in the top quark-Higgs coupling is strongly constrained by EDM measurements and Higgs rate measurements [?]. However, these constraints assume that the light quark Yukawa couplings and  $hWW$  couplings have their SM values. If this is not the case, the constraints the phase of the top Yukawa coupling relax.

Assuming the EDM and Higgs rate constraints can be avoided, the CP structure of the top quark Yukawa can be probed directly in  $pp \rightarrow t\bar{t}h$ . Many simple observables, such as  $m_{t\bar{t}h}$  and  $p_{T,h}$  are

sensitive to the CP structure, but require reconstructing the top quarks and Higgs.

Some  $t\bar{t}h$  observables have been proposed recently that access the CP structure without requiring full event reconstruction. These include the azimuthal angle between the two leptons in a fully leptonic  $t/bart$  decay with the additional requirement that the  $p_{T,h} > 200 \text{ GeV}$  [?], and the angle between the leptons (again in a fully leptonic  $t/\bar{t}$  system) projected onto the plane perpendicular to the  $h$  momentum [?]. These observables only require that the Higgs is reconstructed and are inspired by the sensitivity of  $\Delta\phi_{\ell^+\ell^-}$  to top/anti-top spin correlations in  $pp \rightarrow t\bar{t}$  [?]. The sensitivity of both of these observables improves at higher Higgs boost (and therefore higher energy), making them promising targets for the HE-LHC, though no dedicated studies have been carried out to date.

### **2.11.2 Experimental constraints on anomalous HVV couplings**

*To be written by: U. Sarica*

## **2.12 Summary**

*To be written by: S. Alioli, M. Duehrssen, P. Milenovic*

### 3 Di-Higgs production and Higgs self couplings

#### 3.1 NLO cross sections

##### 3.1.1 SM Calculation

###### 3.1.1.1 HH production in subdominant channels

by Eleni Vryonidou

$\sqrt{s}$ (TeV)	ZHH	WHH	VBF HH	t <sub>t</sub> HH	t <sub>j</sub> HH
14	$0.359^{+1.9\%}_{-1.3\%} \pm 1.7\%$	$0.573^{+2.0\%}_{-1.4\%} \pm 1.9\%$	$1.95^{+1.1\%}_{-1.5\%} \pm 2.0\%$	$0.948^{+3.9\%}_{-13.5\%} \pm 3.2\%$	$0.0383^{+5.2\%}_{-3.3\%} \pm 4.7\%$
27	$0.963^{+2.1\%}_{-2.3\%} \pm 1.5\%$	$1.48^{+2.3\%}_{-2.5\%} \pm 1.7\%$	$8.21^{+1.1\%}_{-0.7\%} \pm 1.8\%$	$5.27^{+2.0\%}_{-3.7\%} \pm 2.5\%$	$0.254^{+3.8\%}_{-2.8\%} \pm 3.6\%$

Table 16: Signal cross section (in fb) for HH production at NLO QCD.

Results have been obtained within the MADGRAPH5\_AMC@NLO [79] framework, as in Ref. [80]. The renormalisation and factorisation scale was set to  $m_{HH}/2$  and varied up and down by a factor of two to obtain the scale uncertainties. The 5-flavour PDF4LHC NLO Monte Carlo PDF set was used to obtain the results (LHAPDF: 90500). The WHH results are the sum of the  $W^+$  and  $W^-$  cross-sections. Similarly t<sub>j</sub>HH involves both top and anti-top production.

###### 3.1.1.2 Probing the Higgs boson self-coupling in di-Higgs production with full $m_t$ -dependence at NLO QCD

by Gudrun Heinrich, Stephen Jones, Matthias Kerner, Gionata Luisoni, Ludovic Scyboz

While the couplings of the Higgs boson to vector bosons are very well measured meanwhile, and the couplings to third generation fermions also start to be well constrained and seem to confirm the Standard Model, the Higgs boson self-coupling could still reveal clear signs of New Physics. As it is not too far-fetched to have BSM scenarios in mind where the trilinear Higgs boson coupling  $\lambda$  is different from the SM value at the  $\mathcal{O}(10\%)$  level, while the deviations in other Higgs boson couplings are at the percent level, we consider  $\lambda$  variations only in this section. In particular, we announce a version of the ggHH code [81–83] implemented in the POWHEG-BOX-V2 [84] where variations of  $\lambda$  are accessible to the user in a parton shower Monte Carlo program at full NLO.

###### 3.1.1.3 Total cross sections at different values of the trilinear coupling

In Table 17 we list total cross sections at 14 TeV and 27 TeV for various values of the trilinear Higgs coupling  $\lambda$ . The results have been obtained using the parton distribution functions PDF4LHC15\_nlo\_100\_pdfsas [?, 15, 85, 86], along with the corresponding value for  $\alpha_s$  for both the NLO and the LO calculation. The masses have been set to  $m_h = 125$  GeV,  $m_t = 173$  GeV, and the top quark width has been set to zero. The scale uncertainties are the result of a 7-point scale variation around the central scale  $\mu_0 = m_{hh}/2$ , with  $\mu_{R,F} = c_{R,F} \mu_0$ , where  $c_R, c_F \in \{2, 1, 0.5\}$ , except that the extreme variations  $(c_R, c_F) = (2, 0.5)$  and  $(c_R, c_F) = (0.5, 2)$  are omitted.

Table 17 also shows that the K-factors do vary substantially as functions of the trilinear coupling. This fact is illustrated in Fig. 29, where it is demonstrated that the K-factor takes values between 1.57 and 2.16 if the trilinear coupling is varied between  $-5 \leq c_{hh} \leq 12$ .

$\lambda_{\text{BSM}}/\lambda_{\text{SM}}$	$\sigma_{\text{NLO}} @ 14 \text{TeV} [\text{fb}]$	$\sigma_{\text{NLO}} @ 27 \text{TeV} [\text{fb}]$	K-fac. @ 14TeV	K-fac. @ 27TeV
1	$32.88^{+13.5\%}_{-12.5\%}$	$127.7^{+11.5\%}_{-10.4\%}$	1.66	1.62
2	14.91	59.10		
2.4	xx	yy		
3	19.82	69.84		
5	98.42			
0	73.84	275.29		
-1	137.69			

Table 17: Total cross sections for Higgs boson pair production at full NLO. The given uncertainties are scale uncertainties. A statistical uncertainty of about 0.3% is not included in the quoted uncertainties.

### 3.1.1.4 Differential cross sections at 14 TeV and 27 TeV

In Figs. 30 and 31 we show the  $m_{hh}$  distribution for various values of  $c_{hhh} = \lambda_{\text{BSM}}/\lambda_{\text{SM}}$ . The ratio plots show the differential K-factors.

*... add 27TeV plots including ratio plots, to be completed*

Fig. 32 shows the Higgs boson pair invariant mass distributions at NLO as a function of  $c_{hhh}$  as 3-dimensional heat maps. The other couplings are fixed to their SM values.

### 3.1.2 Di-Higgs production in the non-linear EFT with full $m_t$ -dependence at NLO QCD

by Gerhard Buchalla, Alejandro Celis, Matteo Capozi, Gudrun Heinrich, Ludovic Scyboz

#### 3.1.2.1 The Higgs sector in the non-linear EFT framework

Below we will describe the potential impact of physics beyond the Standard Model through a non-linear Effective Field Theory (EFT), also called the electroweak chiral Lagrangian including a light Higgs boson [63, 64, 66]. This framework provides us with a consistent EFT for New Physics in the Higgs sector, where the Higgs field is an electroweak singlet  $h$ , independent of the Goldstone matrix  $U = \exp(2i\varphi^a T^a/v)$ . The latter transforms as  $U \rightarrow g_L U g_Y^\dagger$  under the SM gauge group. The symmetry is non-linearly realised on the Goldstone fields  $\varphi^a$ , therefore the name non-linear EFT. More details about this framework already have been given in Section 2.8. Therefore we restrict ourselves to stating the part of the Lagrangian relevant for our study of anomalous Higgs couplings:

$$\mathcal{L} \supset -m_t \left( c_t \frac{h}{v} + c_{tt} \frac{h^2}{v^2} \right) \bar{t} t - c_{hhh} \frac{m_h^2}{2v} h^3 + \frac{\alpha_s}{8\pi} \left( c_{ggh} \frac{h}{v} + c_{gghh} \frac{h^2}{v^2} \right) G_{\mu\nu}^a G^{a,\mu\nu}. \quad (25)$$

To lowest order in the SM  $c_t = c_{hhh} = 1$  and  $c_{tt} = c_{ggh} = c_{gghh} = 0$ . In general, all couplings may have arbitrary values of  $\mathcal{O}(1)$ . Note that we have extracted a loop factor from the definition of the Higgs-gluon couplings.

The leading-order diagrams are shown in Fig. 33.

Examples for virtual diagrams at NLO are shown in Fig. 34. For further details we refer to Ref. [71].

#### 3.1.2.2 Total cross sections for 14 and 27 TeV at some benchmark points

In the following we will show results for some benchmark points, specified in Table 18, some of them having been first defined in Refs. [87]. The results at 14 TeV and 27 TeV are given in Table 19. Note

that our conventions for  $c_{ggh}$  and  $c_{gghh}$  differ from the ones in Ref. [87, 88], the relations are  $c_{ggh} = \frac{2}{3}c_g$  and  $c_{gghh} = -\frac{1}{3}c_{2g}$ , where  $c_g, c_{2g}$  are the couplings defined in Refs. [87, 88]. We also take into account recent constraints on  $c_{ggh}$  from Refs. [46, 89] and the limits on the Higgs boson pair production cross section from Refs [90, 91]. This is why we do not show results for the original benchmark point 5 anymore, as its value for  $c_{ggh}$  is outside the 2-sigma band of a combined fit of  $c_{ggh}, c_t$  from single Higgs production data [46, 89]. Benchmark point 6 is interesting because its value for  $c_{hhh}$  is near the point where maximal destructive interference takes place between triangle-type and box-type contributions if the other couplings are SM-like, leading to a total cross section which is below the SM value.

Benchmark	$c_{hhh}$	$c_t$	$c_{tt}$	$c_{ggh}$	$c_{gghh}$
5a	1	1	0	2/15	4/15
6	2.4	1	0	2/15	1/15
7	5	1	0	2/15	1/15
8a	1	1	1/2	4/15	0
SM	1	1	0	0	0

Table 18: Benchmark points used for the distributions shown below.

Benchmark	$\sigma_{NLO}$ [fb]	K-factor	scale uncert. [%]	stat. uncert. [%]	$\frac{\sigma_{NLO}}{\sigma_{NLO,SM}}$
$B_{5a}$ [14 TeV]			$+x, -y$		
$B_{5a}$ [27 TeV]			$+x, -y$		
$B_6$ [14 TeV]	24.69	1.89	$+2, -11$	2.1	0.75
$B_6$ [27 TeV]			$+x, -y$		
$B_7$ [14 TeV]	169.41	2.07	$+9, -12$	2.2	5.14
$B_7$ [27 TeV]	598.20	2.11	$+8, -10$	2.0	4.68
$B_{8a}$ [14 TeV]	41.70	2.34	$+6, -9$	0.63	1.27
$B_{8a}$ [27 TeV]	179.52	2.33	$+4, -7$	0.49	1.40
$SM$ [14 TeV]	32.95	1.66	$+14, -13$	0.1	1
$SM$ [27 TeV]	127.7	1.62	$+12, -10$	0.1	1

Table 19: Total cross sections at 14 and 27 TeV at NLO (2nd column), K-factor  $\sigma_{NLO}/\sigma_{LO}$  (3rd column), scale uncertainty (4th column), statistical uncertainty (5th column) and the ratio to the SM total cross section at NLO (6th column).

Table 19 shows that the total cross sections increase by a factor of 3.5-5 when increasing the centre-of-mass energy from 14 TeV to 27 TeV. The increase for  $B_{5a}$  is largest because of the large value of  $c_{gghh}$ , which yields a contribution growing linearly with energy.

### 3.1.2.3 HH invariant mass distributions at 14 and 27 TeV at some benchmark points

In Figs. 35 and 36 we show Higgs boson pair invariant mass distributions for the benchmark points 7 and 8a. For both of them the shape of the distribution is very different from the SM one, and the K-factor is non-homogeneous over the whole  $m_{hh}$ -range. Benchmark point 7 is characterised by a large enhancement of the low  $m_{hh}$  region, induced by the large value of  $c_{hhh}$ . The lower ratio plot shows the ratio of the two approximations “Born-improved HEFT” and “ $FT_{approx}$ ” to the full NLO, where the former denotes the  $m_t \rightarrow \infty$  limit rescaled by the  $m_t$ -dependent LO, while  $FT_{approx}$  includes the Born-improved  $m_t \rightarrow \infty$  limit for the virtual part and the full  $m_t$ -dependence for the real radiation part. One

can see from Fig. ?? that these approximations are off by about 20% even below the  $2m_t$  threshold. Therefore one cannot claim that the  $m_t \rightarrow \infty$  limit works well in the region below  $\sim 400$  GeV. As the triangle-type contributions are dominating for  $c_{hhh} = 5$ , their full  $m_t$ -dependence plays a significant role.

Benchmark point 8a shows a characteristic dip near  $m_{hh} = 2m_t$  and an enhancement in the tail compared to the SM. As the total cross section for  $B_{8a}$  is very similar to the SM one, both at 14 TeV and at 27 TeV, this is an example where the discriminating power of differential information is very important.

### 3.1.2.4 Characterising the BSM parameter space

The total cross section can be written in terms of the 15 coefficients  $A_1, \dots, A_{15}$ , at LO [87, 92] and in terms of 23 coefficients at NLO [71].

$$\begin{aligned} \sigma^{\text{NLO}} / \sigma_{SM}^{\text{NLO}} = & \\ & A_1 c_t^4 + A_2 c_{tt}^2 + A_3 c_t^2 c_{hhh}^2 + A_4 c_{ggh}^2 c_{hhh}^2 + A_5 c_{gghh}^2 + A_6 c_{tt} c_t^2 + A_7 c_t^3 c_{hhh} \\ & + A_8 c_{tt} c_t c_{hhh} + A_9 c_{tt} c_{ggh} c_{hhh} + A_{10} c_{tt} c_{gghh} + A_{11} c_t^2 c_{ggh} c_{hhh} + A_{12} c_t^2 c_{gghh} \\ & + A_{13} c_t c_{hhh} c_{ggh} + A_{14} c_t c_{hhh} c_{gghh} + A_{15} c_{ggh} c_{hhh} c_{gghh} \\ & + A_{16} c_t^3 c_{ggh} + A_{17} c_t c_{tt} c_{ggh} + A_{18} c_t c_{ggh}^2 c_{hhh} + A_{19} c_t c_{ggh} c_{gghh} \\ & + A_{20} c_t^2 c_{ggh}^2 + A_{21} c_{tt} c_{ggh}^2 + A_{22} c_{ggh}^3 c_{hhh} + A_{23} c_{ggh}^2 c_{gghh}. \end{aligned} \quad (26)$$

Based on our results for  $A_1, \dots, A_{23}$ , we produce heat maps for the ratio  $\sigma / \sigma_{SM}$ , varying two of the five parameters, while for the fixed parameters the SM values are used, along with  $\sigma_{SM}^{\text{LO}}[14 \text{ TeV}] = 19.85 \text{ fb}$ ,  $\sigma_{SM}^{\text{NLO}}[14 \text{ TeV}] = 32.95 \text{ fb}$ . The couplings are varied in a range which seems reasonable when taking into account the current constraints on the Higgs coupling measurements as well as recent limits on the di-Higgs production cross section [90, 91].

Fig. 37 shows variations of the triple Higgs coupling  $c_{hhh}$  in combination with  $c_{tt}$  and  $c_{gghh}$  at  $\sqrt{s} = 14 \text{ TeV}$ . We observe that the deviations from the SM cross section can be substantial. In Fig. 38 we show the K-factors as a function of the coupling parameters, with the others fixed to their SM values. It shows that the K-factors exhibit a much stronger dependence on the coupling parameters once the full top quark mass dependence is taken into account when compared to the results in the  $m_t \rightarrow \infty$  limit [69, 93].

Fig. 39 shows the Higgs boson pair invariant mass distributions as a function of (a)  $c_{tt}$  and (b)  $c_{gghh}$  as 3-dimensional heat maps. In case (a) the other couplings are fixed to their SM values. We can see that large values of  $|c_{tt}|$  lead to a substantial increase of the cross section, in particular at low  $m_{hh}$  values. In case (b) the other couplings are fixed to their SM values except for  $c_{hhh}$ , which is fixed to  $c_{hhh} = 2.4$  in order to demonstrate the following point: varying only  $c_{hhh}$ , the  $m_{hh}$  distribution shows a dip in the differential cross section just below  $m_{hh} \sim 2m_t$  for  $c_{hhh} \sim 2.4$ , while the low  $m_{hh}$  region gets enhanced for larger values of  $c_{hhh}$ , see Section 3.1.1.2. However, this pattern can get destroyed by non-zero Higgs-gluon contact interactions. While  $c_{ggh}$  is increasingly well constrained meanwhile,  $c_{gghh}$  still could be relatively large. We can see from Fig. 39(b) that the dip is not present for very low (negative)  $c_{gghh}$  values and also gets very shallow for values of  $c_{gghh} \sim 0.4$ . Therefore it would be premature to conclude that a dip in the  $m_{hh}$  distribution points to a value of  $c_{hhh}$  close to 2.4.

We also point out that the LO and NLO  $A_i$  coefficients for both the total cross section and the  $m_{hh}$  distributions at both 14 TeV and 27 TeV are available as ancillary files, coming with the arXiv submission. These data files allow to reconstruct the full NLO result for any point in the 5-dimensional parameter space.

## 3.2 Double Higgs measurements and trilinear coupling

### 3.2.1 Measurements with the ATLAS experiment

by N. Readioff, S. Olivares Pino, E. Petit, J. Stark, P. Bokan, D. Wardrope, M. Wielers

A direct measurement of the Higgs boson trilinear self-coupling  $\lambda_{HHH}$  can be made via the study of Higgs boson pair production. Only the dominant production mechanism at hadron colliders, gluon fusion, is considered, with the other production mechanisms being more than an order magnitude smaller. The Feynman diagram which exhibits a  $\lambda_{HHH}$  dependence interferes destructively with the box diagram that is independent of  $\lambda_{HHH}$ , thus a small increase in the value of  $\lambda_{HHH}$  decreases the expected HH production cross section, and modifies the distributions of event kinematics.

The small SM non-resonant HH production cross section means that it is necessary to consider final states where at least one of the two Higgs bosons decays into a final state with a large branching ratio, ie  $H \rightarrow b\bar{b}$ . The most promising decays channels are  $HH \rightarrow b\bar{b}b\bar{b}$ ,  $HH \rightarrow b\bar{b}\tau\tau$  and  $HH \rightarrow b\bar{b}\gamma\gamma$  with branching ratios of 33.9, 7.3 and 0.26% respectively.

#### 3.2.1.1 The $HH \rightarrow b\bar{b}b\bar{b}$ channel

Projections for this channel were made by extrapolating from the ATLAS Run 2 analysis of  $24.3 \text{ fb}^{-1}$  of 13 TeV data, described in Ref. [94]. This extrapolation assumes similar detector performance to Run 2. The largest source of systematic uncertainty comes from the ability to model the QCD multi-jet background using control regions in data. The allowed range at 95% CL for  $\kappa_\lambda$  including (without) systematic uncertainties is  $-4.1 - 8.7$  ( $-1.2 - 8.0$ ).

#### 3.2.1.2 The $HH \rightarrow b\bar{b}\tau\tau$ channel

Results [95] for this channel are computed by extrapolating from the Run 2 analysis of  $36.1 \text{ fb}^{-1}$  of 13 TeV data [96]. A multivariate analysis with a boosted decision tree (BDT) is performed on the leptonic/hadronic and hadronic/hadronic decay modes of the  $\tau$ -lepton, and the BDT score is used as final discriminant. The largest systematic uncertainty of the Run 2 analysis, the simulation statistics, is neglected in the extrapolation. The expected significance of  $XX (XX)\sigma$  including (without) systematics uncertainties can be achieved. The allowed range at 95% CL for  $\kappa_\lambda$  including (without) systematic uncertainties is  $XX - XX (XX - XX)$ .

#### 3.2.1.3 The $HH \rightarrow b\bar{b}\gamma\gamma$ channel

The analysis [95] is based on truth level particles convoluted with the detector resolution, efficiencies and fake rates computed for  $\mu = 200$  which were extracted from fully simulated samples using the detector layout described in Ref. [94]. The selection is made using a multivariate analysis with a boosted decision tree. The diphoton invariant mass distribution, used to extract the signal through an analytical fit, is shown in Figure 40a. The number of signal, single Higgs and continuum background in a 123–127 GeV window is  $XX$ ,  $XX$  and  $XX$  respectively, leading to a significance of  $XX (XX)\sigma$  including (without) systematics uncertainties. The allowed range at 95% CL for  $\kappa_\lambda$  including (without) systematic uncertainties is  $XX - XX (XX - XX)$ .

#### 3.2.1.4 Combined results

The combination of the three decay channels leads to an expected significance of  $XX (XX)\sigma$  including (without) systematics uncertainties [95]. The 95% CL upper limit on the HH production cross-section is shown in Figure 40b. The allowed range at 95% CL for  $\kappa_\lambda$  including (without) systematic uncertainties is  $XX - XX (XX - XX)$ . A measurement of  $\lambda_{HHH}$  is also performed, improved by the use of the  $m_{HH}$

shape in the  $HH \rightarrow b\bar{b}b\bar{b}$  and  $HH \rightarrow b\bar{b}\gamma\gamma$  analyses. The trilinear coupling is measured to be:

$$1^{+XX}_{-XX} [{}^{+XX}_{-XX} (stat) {}^{+XX}_{-XX} (syst)] \text{ at 68% CL}$$

$$1^{+XX}_{-XX} [{}^{+XX}_{-XX} (stat) {}^{+XX}_{-XX} (syst)] \text{ at 95% CL}$$

### 3.2.2 Measurements with the CMS experiment

by N. De Filipis, M. Gouzevith, A. Carvalho

The estimations of the di-Higgs production in the HL-LHC is done by studying the possible analyses improvements based on Delphes [?] simulations. The Delphes framework was tuned to simulate the geometry of HL-LHC. Five channels are studied:  $HH \rightarrow b\bar{b}b\bar{b}$ ,  $HH \rightarrow b\bar{b}\tau\tau$  and  $HH \rightarrow b\bar{b}\gamma\gamma$ ,  $HH \rightarrow b\bar{b}l\bar{l}\nu\nu$ , where one of the  $H$  decays as  $H \rightarrow Z(l\bar{l})Z(\nu\bar{\nu})$  or  $H \rightarrow W(l\nu)W(\nu)$ , and  $HH \rightarrow b\bar{b}ZZ(4l)$ , the last two has a branching ratio of 2.1% and XX% respectively.

#### 3.2.2.1 The $HH \rightarrow b\bar{b}b\bar{b}$ channel

Two regimes are exploited on the  $b\bar{b}b\bar{b}$  final state. The first consider a resolved situation, where four b-tagged jets are reconstructed as the  $H$  pair. The second considers the case where two fat jets are each one reconstructed as a boosted  $H$ .

In the resolved scenario events are pre-selected by requiring four jets with  $p_T > 45$  GeV and  $|\eta| < 3.5$  that satisfy the medium b-tagging working point. We assume the situation of 100% trigger, what is compatible with upgrades studies of the CMS trigger system, both at L1 and HLT, and the improvement and harmonization of online and offline b-tagging algorithms that are being considered [?]. Four b-tagged jets are selected and paired accordingly with proximity to the Higgs boson mass (the efficiency of the pairing exceeds 95%), a selection around 40 GeV window around the Higgs boson mass on each di-jet pair is used to reduce background. As this is one of the analyses that most suffers with the huge size of its background, but it is also the region where most of the SM-like signal lives. To overcome this, multivariate variable (BDT) is used to best separate signal as signal extraction variable.

In the boosted scenario is typically a good handle to investigate other  $H$  couplings that not the trilinear coupling (see the comparison of the sensibility of this channel compared with the other channels on the combination of the 2016  $HH$  analyses from CMs []). For that reason, for this specific channel we will show the prospected sensitivity on the shape benchmarks already described on section XXX. The two leading-pT AK8 jets in the event, to be reconstructed each one as a Higgs boson, are required to have  $p_T > 300$  GeV and lie within  $|\eta| < 3.0$ . The soft-drop [42, 43] jet grooming algorithm and n-subjetiness [XXXX] are used to remove soft and collinear components of the jet and retain the two subjets associated with the showering and hadronization of the two b quarks from the  $H \rightarrow bb$  decay and background. The background estimation follows closely the approach in Ref. [46]. The background obtained from simulations is scaled by 0.7 based on comparisons with the LHC data at  $\sqrt{s} = 13$  TeV. The main discriminating variable between the signal and the background is the invariant mass of the two selected jets and the  $M_{JJ}$ , which is correlated with the  $HH$  invariant mass. **FIXME: Explain better the signal extraction variables**

#### 3.2.2.2 The $HH \rightarrow b\bar{b}\tau\tau$ channel

The  $b\bar{b}\tau\tau$  final state is experimentally favourable thanks to its sizable branching fraction of 7.3% and the moderate background contamination. The decay of the Higgs boson to  $\tau\tau$  gives rise to six possible combinations of decay channels for the signal:  $e\tau_h$ ,  $\mu\tau_h$ ,  $\tau_h\tau_h$ ,  $\mu\mu$ ,  $e\mu$ , and  $ee$ . For this investigation, we only consider the three most frequent final states, i.e. those involving at least one  $\tau_h$ , that correspond to about 88% of the total decays of the  $\tau\tau$  system and provide the largest sensitivity to the  $HH$  process. Events in all the three categories above are then required to contain at least two b-tagged jets with  $p_T >$

30 GeV and  $|\eta| < 2.4$ . As for the case of resolved  $b\bar{b}b\bar{b}$  analysis a multivariate variable is used for signal extraction. The final discriminant consists however of an ensemble of fully-connected deep neural networks (DNN), each consisting of three hidden layers of 100 neurons.

### 3.2.2.3 The $HH \rightarrow b\bar{b}\gamma\gamma$ channel

The  $b\bar{b}\gamma\gamma$  channel was the most sensitive to a SM-like signal at CMS with data [?] and remains the most sensitive for the projections. The excellent resolution of the di-photon mass, clean trigger signature with 2 high  $p_T$  isolated photons, over-constrained and fully reconstructed final state is a strong asset to reduce the background contamination. The branching fraction is low compared to other channels, but still high enough to observe few 100-th of events after  $3 \text{ ab}^{-1}$ .

The two leading photons satisfying the loose working point  $p_{T,1} > m_{\gamma\gamma}/3$  GeV and  $p_{T,2} > m_{\gamma\gamma}/4$  GeV and  $|\eta| < 2.5$  are selected and we constraint  $100 < m_{\gamma\gamma} < 150$  GeV. Fiducial region between the barrel and endcap calorimeters is rejected. For this selection defined as is Run II [?] the trigger is expected to be fully efficient. The working point chosen for photon identification and isolation selects about 90% of photons within the required kinematic region.

The  $H \rightarrow bb$  candidate is built from the two leading jets that satisfy  $p_T > 25$  GeV and  $|\eta| < 2.5$ . The fiducial acceptance if this defined by Run II analysis. The Phase II tracker allows to extend the b-tagging region up to  $|\eta| = 4$ , but the impact on this analysis is very limited. The background from light flavour jets is suppressed by requiring both jets to satisfy a loose working point of the b tagging algorithm, corresponding to a 90% efficiency for a genuine b-jet (and 10% misidentification efficiency). The dijet invariant mass is required to be between 80 and 190 GeV. The main background to this analysis is coming from nonresonant production of  $\gamma\gamma + 2$  jets. A contribution of  $\approx 10\%$  of the events is expected, for the photon identification working point chosen in this analysis, from  $\gamma$  jet +2 jets where a jet is identified as photon

A multivariate variable (BDT) is constructed to separate the  $HH$  signal from  $t\bar{t}H \rightarrow \gamma\gamma$ . This latter contribution is the dominant source of single  $H \rightarrow \gamma\gamma$  background that have the same properties than  $HH$  production for the main discriminating variable  $m_{\gamma\gamma}$ . The BDT is trained to identify the presence of decay products from W bosons originating from top quark decays. The working point used allows to reject 75% of  $t\bar{t}H \rightarrow \gamma\gamma$  events, while preserving 95% of the signal.

The signal extraction procedure is performed in purity categories obtained by training a classification BDT. This latter try to separate  $\gamma\gamma + 2$  jets from the signal using kinematic (helicity angles,  $p_T$  and directions of the  $\gamma$ s and jets) and b-tagging variables. We define 2 categories, the high purity with the best ration signal over background and the medium purity one. The lowest purity events similar to  $\gamma\gamma + 2$  jets are rejected.

We also define 3 categories in  $m_{HH}$  variable that is well approximated by  $M_X = M_{\gamma\gamma bb} - M_{\gamma\gamma} - M_{bb} + 250$  GeV (see ??):  $250 < M_X < 350$  GeV,  $350 < M_X < 480$  GeV and  $480 < M_X$  GeV. The first one have no impact on SM-like  $HH$  analysis but helps to constrain the Higgs self-coupling.

In each of the  $3 \times 2$  categories the signal is extracted by a parametric maximum likelihood fit of the signal and background in 2 dimensions:  $m_{\gamma\gamma} \times m_{\text{jetjet}}$ .

### 3.2.2.4 The $HH \rightarrow b\bar{b}ll\nu\nu$ channel

### 3.2.2.5 The $HH \rightarrow b\bar{b}ZZ(4l)$ channel

Up to now, the low signal rate leads to consider mostly final states with a sizable branching ratio. In view of HL-LHC, some rare but clean processes have been re-considered because of the increasing available statistics and the challenging conditions due to the enormous number of pile-up events.

Events are required to have at least four identified and isolated (isolation  $< 0.7$ ) muons (electrons) with  $p_T > 5(7)$  GeV and  $|\eta| > 2.8$ , where muons (electrons) are selected if passing the Loose (Medium)

Working Point identification. Z boson candidates are formed from pairs of opposite-charge leptons (...) requiring a minimum angular separation between two leptons of 0.02. At least two di-lepton pairs are required. The Z candidate with the invariant mass closest to the nominal Z mass is denoted as Z1; then, among the other opposite-sign lepton pairs, the one with the highest  $p_T >$  is labelled as Z2. In order to improve the sensitivity to the Higgs boson decay, Z candidates are required to have an invariant mass in the range [40, 120] GeV (Z1) and [12, 120] GeV (Z2), respectively. At least one lepton is required to have  $p_T > > 20$  GeV and a second is required to have  $p_T > > 10$  GeV. On figure 41 we show the resolution of the reconstructed  $H \rightarrow ZZ \rightarrow 4l$  after baseline selections. The four leptons invariant mass is requested to be in the range [120,130] GeV. At least two (but not more than three) identified b-jets, reconstructed with the anti-kT algorithm inside a cone of radius  $R = 0.4$ , are required; a B-Tag Medium working point, exploiting the presence of the MIP Timing Detector (MTD) [], is assumed. The di-jet mass is required to be in the range [80, 160] GeV and the angular distance between the 2 b-jets has to be between 0.5 and 2.3. The signal is them extracted with a cut-and-count analysis.

### 3.2.2.6 Combination

## 3.3 New ideas

### 3.3.1 Prospects for $hh \rightarrow (b\bar{b})(WW^*) \rightarrow (b\bar{b})(\ell^+\ell^-\nu_\ell\bar{\nu}_\ell)$

by Jeong Han Kim, Minho Kim, Kyoungchul Kong, Konstantin T. Matchev, Myeonghun Park

In this section, we discuss the discovery prospects for double Higgs production in the  $hh \rightarrow (b\bar{b})(WW^*)$  channel. In order to increase sensitivity in the dilepton channel [97–99], we propose a novel kinematic method, which relies on two new kinematic functions, *Topness* and *Higgsness* [100]. They characterize features of the major ( $t\bar{t}$ ) background and of  $hh$  events, respectively. The method also utilizes two less commonly used variables, the subsystem  $M_{T2}$  (or subsystem  $M_2$ ) [101–103] for  $t\bar{t}$  and the subsystem  $\sqrt{s}_{min}$  (or subsystem  $M_1$ ) [103–105] for  $hh$  production. For any given event, Topness [100, 106] quantifies the degree of consistency to dilepton  $t\bar{t}$  production, where there are 6 unknowns (the three-momenta of the two neutrinos,  $\vec{p}_\nu$  and  $\vec{p}_{\bar{\nu}}$ ) and four on-shell constraints, for  $m_t$ ,  $m_{\bar{t}}$ ,  $m_{W^+}$  and  $m_{W^-}$ , respectively. The neutrino momenta can be fixed by minimizing the quantity

$$\chi_{ij}^2 \equiv \min_{\vec{p}_T = \vec{p}_{\nu T} + \vec{p}_{\bar{\nu} T}} \left[ \frac{(m_{b_i \ell^+ \nu}^2 - m_t^2)^2}{\sigma_t^4} + \frac{(m_{\ell^+ \nu}^2 - m_W^2)^2}{\sigma_W^4} + \frac{(m_{b_j \ell^- \bar{\nu}}^2 - m_t^2)^2}{\sigma_t^4} + \frac{(m_{\ell^- \bar{\nu}}^2 - m_W^2)^2}{\sigma_W^4} \right], \quad (27)$$

subject to the missing transverse momentum constraint,  $\vec{p}_T = \vec{p}_{\nu T} + \vec{p}_{\bar{\nu} T}$ . Since there is a twofold ambiguity in the paring of a  $b$ -quark and a lepton, we define *Topness* as the smaller of the two  $\chi^2$ s,

$$T \equiv \min(\chi_{12}^2, \chi_{21}^2). \quad (28)$$

In double Higgs production, the two  $b$ -quarks arise from a Higgs decay ( $h \rightarrow b\bar{b}$ ), and therefore their invariant mass  $m_{bb}$  can be used as a first cut to enhance the signal sensitivity. For the decay of the other Higgs boson,  $h \rightarrow WW^* \rightarrow \ell^+\ell^-\nu\bar{\nu}$ , we define *Higgsness* [100] as follows:

$$H \equiv \min \left[ \frac{(m_{\ell^+\nu}^2 - m_h^2)^2}{\sigma_{h_\ell}^4} + \frac{(m_{\nu\bar{\nu}}^2 - m_{\nu\bar{\nu},peak}^2)^2}{\sigma_\nu^4} \right] + \min \left( \frac{(m_{\ell^+\nu}^2 - m_W^2)^2}{\sigma_W^4} + \frac{(m_{\ell^-\bar{\nu}}^2 - m_{W^*,peak}^2)^2}{\sigma_{W^*}^4}, \frac{(m_{\ell^-\bar{\nu}}^2 - m_W^2)^2}{\sigma_W^4} + \frac{(m_{\ell^+\nu}^2 - m_{W^*,peak}^2)^2}{\sigma_{W^*}^4} \right), \quad (29)$$

where  $m_{W^*}$  is the invariant mass of the lepton-neutrino pair which resulted from the off-shell  $W$ . It satisfies  $0 \leq m_{W^*} \leq m_h - m_W$  and  $m_{W^*}^{peak} = \frac{1}{\sqrt{3}} \sqrt{2(m_h^2 + m_W^2) - \sqrt{m_h^4 + 14m_h^2m_W^2 + m_W^4}}$  is the peak in the  $m_{W^*}$  distribution.  $m_{\nu\bar{\nu}}^{peak} = m_{\ell\ell}^{peak} \approx 30$  GeV is the location of the peak in the  $\frac{d\sigma}{dm_{\nu\bar{\nu}}}$  or  $\frac{d\sigma}{dm_{\ell\ell}}$  distribution [100, 107].

The  $\sigma$  values in Eqs. (27) and (29) result from the experimental uncertainties and intrinsic particle widths. In principle, they can be treated as free parameters and tuned using a neutral network (NN), a boosted decision tree (BDT), etc. In our numerical study, we use  $\sigma_t = 5$  GeV,  $\sigma_W = 5$  GeV,  $\sigma_{W^*} = 5$  GeV,  $\sigma_{h_\ell} = 2$  GeV, and  $\sigma_\nu = 10$  GeV. The main contribution in Eq. (29) comes from the on-shell conditions for the Higgs and the  $W$ , while the effects of the invariant mass of the two neutrinos and the off-shell  $W$  are minor.

Along with Higgsness and Topness, we adopt the subsystem  $\hat{s}_{min}^{(\ell\ell)}$  for  $h \rightarrow W^\pm W^{*\mp} \rightarrow \ell^+ \ell^- \nu\bar{\nu}$  [104, 105] and the subsystem  $M_{T2}$  for the  $b\bar{b}$  system ( $M_{T2}^{(b)}$ ) and the lepton system ( $M_{T2}^{(\ell)}$ ) [102]. The variable  $\hat{s}_{min}^{(v)}$  is defined as  $\hat{s}_{min}^{(v)} = m_v^2 + 2 \left( \sqrt{|\vec{P}_T^v|^2 + m_v^2} |\vec{p}_T| - \vec{P}_T^v \cdot \vec{p}_T \right)$  [103–105], where (v) represents a set of visible particles under consideration, while  $m_v$  and  $\vec{P}_T^v$  are their invariant mass and transverse momentum, respectively. It provides the minimum value of the Mandelstam invariant mass  $\hat{s}$  which is consistent with the observed visible 4-momentum vector. The  $M_{T2}$  is defined as  $M_{T2}(\tilde{m}) \equiv \min \{ \max [M_{TP_1}(\vec{p}_{\nu T}, \tilde{m}), M_{TP_2}(\vec{p}_{\bar{\nu} T}, \tilde{m})] \}$  where  $\tilde{m}$  is the test mass for the daughter particle and the minimization over the transverse masses of the parent particles  $M_{TP_i}$  ( $i = 1, 2$ ) is performed over the transverse neutrino momenta  $\vec{p}_{\nu T}$  and  $\vec{p}_{\bar{\nu} T}$  subject to the  $\vec{p}_T$  constraint [101–103, 108–111].

Events for the signal and all relevant background processes were simulated as described in Ref. [100]. After basic selection cuts, we use the kinematic information discussed above for further background suppression. Distributions of  $M_{T2}^{(b)}$ ,  $M_{T2}^{(\ell)}$  and  $\sqrt{\hat{s}_{min}^{(\ell\ell)}}$  are shown in Fig. 42, while scatter distributions of Topness and Higgsness are displayed in Fig. 43. The right panel in Fig. 43 shows the expected signal significance at the HL-LHC as a function of the triple Higgs coupling  $\kappa_3$ . We obtain each curve by applying the same set of cuts optimized for the SM point ( $\kappa_3 = 1$ ) to non-SM points ( $\kappa_3 \neq 1$ ) for  $N_{sig}^{SM} = 35$  in black,  $N_{sig}^{SM} = 20$  in red and  $N_{sig}^{SM} = 10$  in blue. The three symbols  $\diamond$ ,  $\circ$  and  $\square$  show the signal significance using CMS-NN [97], CMS-BDT [98] and BDT [99], respectively.

Finally Fig. 44 shows the significance for observing an anomalous Higgs self-coupling at the 14 TeV LHC with an integrated luminosity of  $3 \text{ ab}^{-1}$  and at 27 TeV with  $15 \text{ ab}^{-1}$ , respectively. For the HL-LHC, we follow the analysis presented in Ref. [100]. The red solid curves are obtained with nominal efficiencies for  $b$  (mis-)tagging ( $\epsilon_{b \rightarrow b} = 0.7$ ,  $\epsilon_{c \rightarrow b} = 0.2$  and  $\epsilon_{j \rightarrow b} = 0.01$ ) [112]. The HL-LHC will rule out the Higgs self-coupling outside the range  $(-0.5, 3.2)$ . The four vertical dashed lines in the left panel represent the expected 95% CL exclusion of  $\kappa_3$  in the  $bbbb$  channel (black, from Ref. [113]), in the  $bb\gamma\gamma$  channel (blue, from Ref. [114] and green from Ref. [115]) and in the  $bb\tau\tau$  channel (cyan, from Ref. [70]). We notice that the sensitivity in the  $bbWW^*$  channel is comparable to the sensitivity in those other channels. For the 27 TeV study, we normalize our signal cross section to 139.9 fb [116], and use  $K$  factors of  $K = 1.56$  for  $t\bar{t}$  production [117],  $K = 1.28$  for  $t\bar{t}h$  [118],  $K = 1.54$  for  $t\bar{t}V$  and a conservative  $K = 2$  for  $\ell\ell b\bar{b}$  and  $\tau\tau b\bar{b}$  [100]. Our result shows that the 27 TeV collider could observe double Higgs production at  $5\sigma$  for a wide range of values for  $\kappa_3$  and would be able to exclude  $\kappa_3$  outside the range  $(0.2, 1.8)$  (for a comparative study in the  $bb\gamma\gamma$  channel, see Ref. [119] (vertical, dashed lines in the middle panel)).

In summary, we obtained a significant increase in the signal sensitivity for  $hh$  production in the dilepton channel compared to previous analyses [97–99]. The method can be easily incorporated into more advanced algorithms for further improvement. For example, using deep learning (convolutionary neural network) slightly improves the discovery significance, see the right panel of Fig. 44. The discussed method is very general and can be easily applied to other processes such as the semi-leptonic

final state, resonant  $hh$  production, non-resonant production with more than one Higgs boson, etc. It is straightforward to generalize the idea to different topologies in searches for other BSM particles as well.

### 3.3.2 Prospects for $bb\gamma\gamma$ : Bayesian optimization and BDT

by Alexandre Alves, Tathagata Ghosh, and Kuver Sinha

Searches for double Higgs pair production in the  $b\bar{b}\gamma\gamma$  channel are an important target for the future. In this section, we study this problem at the 14 TeV LHC in two steps, following [120]:

(i) We first propose a Bayesian optimization approach to select cuts on kinematic variables and study its performance compared to manual and random cuts, taking into account systematic uncertainties. We demonstrate our results with the Python algorithm Hyperopt .

(ii) We next perform a joint optimization of kinematic cuts and boosted decision trees (BDT) hyperparameters to further discriminate signal and background events. For our calculations, we use the XGBoost implementation of BDTs for Python.

#### 3.3.2.1 Signal and Backgrounds

For the simulation of the signal, we use MadGraph5\_aMC@NLO\_v2.3.3 [?], to generate  $pp \rightarrow hh$  process exclusively at the leading order (LO). The simulation of our signal include both the triangle and box diagrams. We scale our LO cross-section by the partial NNLO K-factor of 2.27 [121], calculated in the large quark mass limit and use the resulting production cross section of 36.8 fb.

The following backgrounds were taken into account in our study: (i)  $b\bar{b}\gamma\gamma$ ; (ii)  $Zh$  with  $Z \rightarrow b\bar{b}$  and  $h \rightarrow \gamma\gamma$ ; (iii)  $b\bar{b}h$  with  $h \rightarrow \gamma\gamma$ ; (iv)  $t\bar{t}h \rightarrow b\bar{b} + \gamma\gamma + X$ ; (v)  $jj\gamma\gamma$  where the light-jets  $jj$  are mistaken for a  $b$ -jet pair in the detector; (vi)  $b\bar{b}jj$ , where the light-jets  $jj$  are mistaken for a photon pair; (vii)  $c\bar{c}\gamma\gamma$ , where a  $c$ -jet is mistagged as a  $b$ -jet; (viii)  $b\bar{b}\gamma j$ , where one light-jet is mistaken for a photon; (ix)  $c\bar{c}\gamma j$  where the  $c$ -jets are mistagged as bottom jets and the light-jet as a photon. We note that the  $b\bar{b}\gamma j$ ,  $c\bar{c}\gamma\gamma$ , and  $c\bar{c}\gamma j$  backgrounds were neglected in several early studies.

The cross section normalizations for the backgrounds from (i) - (v) are taken from ref. [92], which we consider reliable. In order to obtain the distributions of the kinematic variables of interest, we pass our simulated events to PYTHIA\_v6.4 [?] for showering, hadronization and underlying event and finally to DELPHES\_v3.3 [?] for detector simulation. For all further details of our signal and background simulation, we refer to our paper [120].

The following basic cuts were applied on both signal and background:

$$\begin{aligned} p_T(j) &> 20 \text{ GeV}, \quad p_T(\gamma) > 20 \text{ GeV}, \quad |\eta(j)| < 2.5, \quad |\eta(\gamma)| < 2.5 \\ 100 \text{ GeV} &< |M_{jj}| < 150 \text{ GeV}, \quad 100 \text{ GeV} < |M_{\gamma\gamma}| < 150 \text{ GeV} . \end{aligned} \quad (30)$$

The number of backgrounds events after imposing the basic cuts for  $3 \text{ ab}^{-1}$  of integrated luminosity is shown in Table 20.

signal	$b\bar{b}\gamma\gamma$	$c\bar{c}\gamma\gamma$	$jj\gamma\gamma$	$b\bar{b}\gamma j$	$t\bar{t}h$	$c\bar{c}\gamma j$	$b\bar{b}h$	$Zh$	total backgrounds
42.6	1594.5	447.7	160.3	137	101.1	38.2	2.4	1.8	2483

Table 20: The number of signal and the various types of backgrounds considered in this work after imposing the basic cuts of eq. (30) for  $3 \text{ ab}^{-1}$  of data. We found  $b\bar{b}jj$  negligible after cuts and after estimating the probability of the jet pair faking a photon pair.

### 3.3.2.2 Bayesian Optimization

The  $b\bar{b}\gamma\gamma$  channel has been studied by several groups using cut and count strategies. Once signal and background cross sections are normalized to the proper values, one finds that the analysis of any particular group does not radically outperform that of any other. For a detailed comparison, we refer to Table 2 of [120].

Bayesian optimization offers a systematic way to obtain the most optimal cuts on a set of kinematic variables. The algorithm we utilize is implemented in the Python library HyperOpt , based on the so-called sequential model-based optimization (SMBO) technique [122–124].

The kinematic variables used in our study are: (*i*) transverse momentum of  $b$ -jets and photons:  $p_T(b)$  and  $p_T(\gamma)$ ; (*ii*)  $b\bar{b}$  and  $\gamma\gamma$  invariant masses:  $M_{bb}$  and  $M_{\gamma\gamma}$ , where signal events exhibit resonance peaks at  $m_h$ ; (*iii*) transverse momentum of  $b\bar{b}$  and  $\gamma\gamma$ :  $p_T(bb)$  and  $p_T(\gamma\gamma)$ ; (*iv*) invariant mass of two  $b$ -jets and two photons:  $M_{bb\gamma\gamma}$ ; (*v*) distance between pairs of  $b$ -jets and photons:  $\Delta R(bb)$ ,  $\Delta R(\gamma\gamma)$  and  $\Delta R(b\gamma)$ , where  $\Delta R = \sqrt{(\Delta\eta)^2 + (\Delta\phi)^2}$  in the pseudo-rapidity and azimuthal angle plane  $(\eta, \phi)$ ; (*vi*) the fraction  $E_T/M_{\gamma\gamma}$  for the two hardest photons in the event; these are variables used in experimental searches as in ref. [?, 125].

In Figure 45, we display the results obtained from the Bayesian optimization of cuts on the above kinematic variables. We see that after 100-200 trials, the signal significance does not change much and the optimized cuts achieved a significance of  $2.81\sigma$  against  $2.1\sigma$  of the manual search of ref. [92], a 34% improvement. If  $b\bar{b}\gamma j$ ,  $c\bar{c}\gamma\gamma$ , and  $c\bar{c}\gamma j$  backgrounds are incorporated, the Bayesian search reached  $2.48\sigma$  against  $1.85\sigma$  of the cuts of ref. [92], again roughly the same improvement. The performance of the Bayesian algorithm is also displayed in Figure 45.

### 3.3.2.3 BDT Analysis

We now turn to a discussion of the BDT analysis, for which we utilize the XGBoost implementation of BDTs for Python. XGBoost is chosen for its good discrimination performance, speed and capacity of parallelization. For our analysis we simulated  $\sim 880000$ ; depending on the cuts, however, the total number of events usually drops to around 100000–300000 events which also turned out to be a sufficient number of samples to keep overfitting under control.

Using HyperOpt, we perform a joint optimization of the kinematic variables introduced previously in conjunction with the following BDT hyperparameters: the number of boosted trees, the learning rate, the maximum depth of the trees, and the minimum sum of instance weight needed in a child to continue the splitting process of the trees, `min_child_weight`. All the BDT results were obtained from a 5-fold cross validation by randomly splitting training and testing samples at the proportion of 2/3 and 1/3 of the total sample, respectively. We allowed for 300 trials in HyperOpt.

Hyperparameters like the number of boosted trees, maximum depth of the trees and the `min_child_weight` are directly related to the complexity of the algorithm by controlling the number, size and configuration of the trees. The learning rate, also known as shrinkage in this context, is a parameter that controls the weight new trees have to further model the data. A large value permits a larger effect from new added trees and might lead to more severe overfitting. There are other parameters which can be eventually used to prevent overfitting and loss of generalization power, but we found that tuning these parameters was sufficient to achieve a good performance.

A comparative result of a simple cut and count analysis and a sequential optimization of cuts and BDT hyperparameters are presented Table 21. We note that BDT outperforms simple cut and count, even when cutting is performed using Bayesian optimization. This is due to the better discrimination between the signal and background classes achieved by the machine learning algorithms as they find more profound correlations among the kinematic features and those classes. These correlations cannot be fully explored in simple/manual rectangular cut-and-count analyses.

systematics (%)	Cut-and-count	BDT
0	2.34[1.76]	3.88
10	<b>1.93</b> [1.43]	<b>3.57</b>
20	1.51[1.0]	3.10

Table 21: Signal significances for cut-and-count and BDT for 0, 10 and 20% systematics. We took all backgrounds into account for the computation of the AMS with optimized cuts and an integrated luminosity of  $3 \text{ ab}^{-1}$  at the 14 TeV LHC. The bold-face numbers represent the significances expected with the level of systematics anticipated by the experimental collaborations in refs. [?, ?, ?]. The numbers inside brackets are the significances computed with the default cuts of Azatov *et. al.*, ref. [92], which we took as baseline results.

However, there is a trade-off between the efficiency of the cuts and the ML performance which is usually neglected in phenomenological works where these tools are employed. The reasoning is simple: cutting harder cleans up more backgrounds but weakens the correlations between the kinematic variables and the event classes, thereby decreasing the ML performance. On the other hand, relaxing the cuts makes the correlations stronger helping to boost ML but the discrimination power gained might not be enough to get a good significance with a large number of surviving background events. Hence, a joint optimization of cuts and BDT hyperparameters improve the performance of our analysis further.

The maximum AMS significance is  $4.0\sigma$  for a joint optimization analysis of cuts and BDT hyperparameters. The final selections of the kinematic variables and BDT hyperparameters are the following  $p_T(1) > 72 \text{ GeV}$ ,  $p_T(2) > 20 \text{ GeV}$ ;  $\Delta R_{ij} > 0.15$ ,  $\Delta R_{ii} < 3.6$ ;  $M_{b\bar{b}\gamma\gamma} > 370 \text{ GeV}$ ,  $p_{T_{ii}} > 145 \text{ GeV}$ ,  $M_{b_1\gamma_1} > 100 \text{ GeV}$ ;  $|M_{bb} - m_h| < 27 \text{ GeV}$ ,  $|M_{\gamma\gamma} - m_h| < 11 \text{ GeV}$ ; number of trees = 157; learning rate = 0.101; maximum tree depth = 14; min\_child\_weight = 5. We have denoted  $p_T(1)$  as the leading  $b$ -jet or photon, and  $p_T(2)$  as the next-to-leading  $b$ -jet or photon.

The results are shown in Figure 46. The left panel shows the normalized  $\Delta R_{b_1\gamma_1}$  histograms for the signal and the  $b\bar{b}\gamma\gamma$  continuum background, the signal efficiency (background rejection) is the red (blue) line, and the area under the Receiver-Operator curve (ROC), AUC, is the dashed line. The bigger the AUC, the better the performance of a cut-and-count analysis based on that distribution. On the right panel, we show the histogram of number of cut strategies producing a given significance interval in a BDT-aided joint optimization analysis. Finding this optimal performance from the competition between hard cuts and an ML algorithm is the core of the method presented in the section.

### 3.4 HE prospects

#### 3.4.1 Theory studies

by Dorival Gonçalves, Tao Han, Felix Kling, Tilman Plehn and Michihisa Takeuchi

Higgs pair production  $pp \rightarrow hh$  offers a direct path to pin down the Higgs self-coupling  $\lambda$  at a hadron collider [?, ?]. Theoretical studies as well as current analyses point to the  $b\bar{b}\gamma\gamma$  decay as the most promising signature at the LHC [?]. For the high-luminosity LHC (HL-LHC), ATLAS and CMS projections indicate a very modest sensitivity to the Higgs self-coupling [?]. In the optimistic scenario that we can neglect systematic uncertainties, those studies indicate that the LHC will probe the coupling at 95% confidence level  $-0.8 < \kappa_\lambda < 7.7$ , where the SM value is  $\kappa_\lambda = \lambda/\lambda_{SM} = 1$ , falling short in precision in comparison to other Higgs property measurements at the LHC, and far from satisfactory in probing the Higgs potential. For example,  $\mathcal{O}(1)$  determination of  $\kappa_\lambda$  would be required to test some of the EW Baryogenesis models [?].

Because of the rapidly growing gluon luminosity at higher energies, the  $hh$  production cross section increases by about a factor of 4 (40) at 27 (100) TeV. This means that at the HE-LHC with the

anticipated integrated luminosity of  $15 \text{ ab}^{-1}$  the number of events in the  $b\bar{b} \gamma\gamma$  channel increases by a factor  $4 \times 5 = 20$  to around 5k events. A 100 TeV hadron collider with a projected integrated luminosity of  $30 \text{ ab}^{-1}$  features another increase by a factor  $10 \times 2 = 20$ , to around 100k expected Higgs pair events in the Standard Model. This estimate shows how the combination of increased energy and increased luminosity slowly turns Higgs pair production into a valid channel for precision measurements [?].

### 3.4.1.1 Information in Distributions

Previous studies have shown that multivariate analysis, taking into account kinematic distributions, gives a substantially better reach on the Higgs self coupling over the purely rate-based analysis [?, ?, ?, ?]. In the following, we therefore summarize which kinematic features include information about the Higgs self-coupling.

At leading order, Higgs pair production receives contributions both from a triangular loop diagram sensitive to the Higgs-self coupling and from a box or continuum diagram. The box contribution completely dominates the total rate over most of the phase space, making the Higgs coupling measurements a challenge. While we can define a number of kinematic observables describing the continuum backgrounds, the measurement of the Higgs self-coupling relies on a simple  $2 \rightarrow 2$  process with two independent kinematic variables.

Three distinct phase space regions provide valuable information on a modified Higgs self-coupling, all from a large destructive interference between the triangle and box contributions. First, there is the threshold [?, ?] in the partonic center of mass energy  $m_{hh} \approx 2m_h$ . Based on the effective Higgs-gluon Lagrangian [?] we can therefore write the corresponding amplitude for Higgs pair production as

$$\frac{\alpha_s}{12\pi v} \left( \frac{\kappa_\lambda \lambda_{\text{SM}}}{s - m_h^2} - \frac{1}{v} \right) \rightarrow \frac{\alpha_s}{12\pi v^2} (\kappa_\lambda - 1) \stackrel{\text{SM}}{=} 0 . \quad (31)$$

While the heavy-top approximation is known to give a poor description of the signal kinematics as a whole, it does describe the threshold dependence correctly [?]. This indicates that we can search for a deviation of the Higgs self-coupling by looking for an enhancement of the rate at threshold. Second, an enhanced sensitivity to the self-coupling appears as top mass effect. For large positive values of  $\lambda$  absorptive imaginary parts lead to a significant dip in the combined rate at the threshold  $m_{hh} \approx 2m_t$  [?, ?]. The sharpest interference dip takes place near  $\kappa_\lambda \approx 2$  while for negative values of  $\kappa_\lambda$  the interference becomes constructive. Finally, the triangular and box amplitudes have a generally different scaling in the limit  $m_{hh} \gg m_h, m_t$  [?, ?]. While the triangle amplitude features an explicit suppression of either  $m_h^2/m_{hh}^2$  or  $m_t^2/m_{hh}^2$  at high invariant mass, the box diagrams drops more slowly towards the high-energy regime. This explains why a rate based analysis focussing on the high di-Higgs mass region only has limited sensitivity. The impact of all three kinematic features can be quantified statistically and indicate that essentially the full information on the Higgs self-coupling can be extracted through a shape analysis of the  $m_{hh}$  distribution [?].

In Fig. 47 we present the signal and background distributions for three relevant kinematic variables:  $m_{hh}$ ,  $p_{T,h}$  and  $\Delta R_{\gamma\gamma}$ . Using the MADMAX approach [?], based on the Neyman Pearson Lemma we also estimate the maximum significance with which any multi-variate analysis will be able to extract an anomalous self-coupling  $\kappa_\lambda \neq 1$ . The corresponding differential distribution of maximum significance are shown as solid lines in Fig. 47. In addition to the signal features, the significance is limited by the rapidly dropping backgrounds, covering both of the above-mentioned regions with an enhanced dependence on the triangle diagram. In the absence of background, the significance indeed peaks between the production threshold and the top-mass threshold [?]. The drop towards large values of  $m_{hh}$  is a combination of the dominance of the box diagram in the signal and the limited number of expected signal events. The significance with which we can extract modified self-couplings either smaller ( $\kappa_\lambda = 0$ ) or larger ( $\kappa_\lambda = 2$ ) than in the Standard Model shows a similar phase space dependence. The only difference is a slightly harder significance distributions for  $\kappa_\lambda = 2$ , an effect of the dip at  $m_{hh} \approx 2m_t$ .

### 3.4.1.2 Detector-Level Analysis

Based on our findings above, we now design a detailed analysis strategy to extract the Higgs self-coupling with a focus on the shape of the  $m_{hh}$  distribution [?]. Our signal is  $pp \rightarrow hh + X \rightarrow b\bar{b} \gamma\gamma + X$ . The signal and background samples are generated with MADGRAPH5+PYTHIA8 [?, ?], including one extra jet using the MLM scheme [?].

In the final state we demand two  $b$ -tagged jets and two isolated photons with the minimal acceptance and trigger cuts

$$p_{T,j} > 30 \text{ GeV}, \quad |\eta_j| < 2.5, \quad p_{T,\gamma} > 30 \text{ GeV}, \quad |\eta_\gamma| < 2.5, \quad \Delta R_{\gamma\gamma,\gamma j,jj} > 0.4. \quad (32)$$

The background to our  $b\bar{b} \gamma\gamma$  signal consists of other Higgs production modes ( $t\bar{t}h, Zh$ ) with  $h \rightarrow \gamma\gamma$ , continuum  $b\bar{b}\gamma\gamma$  production, and of multi-jet events with light-flavor jets faking either photons or  $b$ -jets ( $jj\gamma\gamma, b\bar{b}\gamma j$ ) [?].

The proper simulation of efficiencies and fake rates are a key ingredient for a realistic background estimate in this analysis. For the HE-LHC and the future 100 TeV collider we follow the ATLAS projections [?]. The efficiency for a tight photon identification can be well parametrized by

$$\epsilon_{\gamma \rightarrow \gamma} = 0.863 - 1.07 \cdot e^{-p_{T,\gamma}/34.8 \text{ GeV}}, \quad (33)$$

and a jet-to-photon mis-identification rate by

$$\epsilon_{j \rightarrow \gamma} = \begin{cases} 5.30 \cdot 10^{-4} \exp(-6.5(p_{T,j}/(60.4 \text{ GeV}) - 1)^2) & \text{for } p_{T,j} < 65 \text{ GeV}, \\ 0.88 \cdot 10^{-4} [\exp(-(p_{T,j}/(943 \text{ GeV})) + 248 \text{ GeV}/p_{T,j}] & \text{for } p_{T,j} > 65 \text{ GeV}. \end{cases} \quad (34)$$

This leads to a photon efficiency of about 40% at  $p_{T,\gamma} = 30$  GeV, saturating around 85% for  $p_{T,\gamma} > 150$  GeV. Note that the Higgs decay products tend to be soft,  $p_{T,\gamma} \sim m_h/2$ . For  $b$ -tagging, we adopt an efficiency with  $\epsilon_b = 0.7$  associated with mis-tag rates of 15% for charm quarks and 0.3% for light flavors. These flat rates present a conservative estimate from the two dimensional distribution on  $(p_{T,j}, \eta_j)$  shown in the HL-LHC projections [?]. Encouragingly, the small light flavor fake rate projections result in a strong suppression for the initially dominant  $jj\gamma\gamma$  background.

To control the continuum backgrounds, we require two Higgs mass windows,

$$|m_{bb} - m_h| < 25 \text{ GeV}, \quad |m_{\gamma\gamma} - m_h| < 1 \text{ GeV}. \quad (35)$$

An obvious way to enhance the Higgs pair signal is to improve the resolution on the reconstructed photons and  $b$ -jets from the Higgs decays. We adopt the rather conservative resolution for  $m_{bb}$  as in Eq. (35). Any improvement on it in experiments would be greatly helpful for the signal identification and background separation.

To take the information in the differential distribution  $m_{hh}$  into account, we employ a binned log-likelihood analysis based on the  $CL_s$  method, using the full  $m_{hh}$  distribution to extract  $\kappa_\lambda$  [?]. As a starting point, we show the  $5\sigma$  determination on the Higgs pair signal strength for the SM hypothesis  $\kappa_\lambda = 1$  as a function of the luminosity in the left panel of Fig. 48. Here we require two  $b$ -tagged jets among the two or three leading jets. We decompose the latter case in two sub-samples ( $bb, bbj$ ) and ( $jbb, bjbj$ ). We see how exploring the extra-jet emission significantly improves the significance as compared to the standard procedure adopted in the literature. The  $5\sigma$  measurement for HE-LHC is pushed from  $2.8 \text{ ab}^{-1}$  to below  $2.3 \text{ ab}^{-1}$ .

In the right panel of Fig. 48 we show the discovery reach for the Higgs pair signal at HE-LHC and a 100 TeV collider for three di-photon invariant mass resolutions described by a Gaussian width of 0.75, 1.5, 2.25 GeV and corresponding Higgs mass windows  $|m_{\gamma\gamma} - m_h| < 1, 2, 3$  GeV. As resolution

of 1.5 GeV has already been achieved at the LHC [?]. Higgs pair production will be discovered at the HE-LHC with approximately  $2.5 \dots 5 \text{ ab}^{-1}$  and at the 100 TeV collider with  $0.2 \dots 0.3 \text{ ab}^{-1}$  of data, in both cases well below the design luminosity.

As commented in the introduction, there exist physics scenarios in which the Higgs self-coupling could be modified at the level of order one deviation from the SM value. The accurate measurement of the Higgs self-coupling via Higgs pair production at future colliders has the best promise to uncover the new physics associated with the Higgs sector. In Fig. 49, we show the accuracy on this measurement. We find that the Higgs self-coupling can be measured with a precision

$$\begin{aligned} \kappa_\lambda &\approx 1 \pm 15\% \text{ at } 68\% \text{ CL} & \kappa_\lambda &\approx 1 \pm 30\% \text{ at } 95\% \text{ CL} & (\text{HE-LHC, } 27 \text{ TeV, } 15 \text{ ab}^{-1}), \\ \kappa_\lambda &\approx 1 \pm 5\% \text{ at } 68\% \text{ CL} & \kappa_\lambda &\approx 1 \pm 10\% \text{ at } 95\% \text{ CL} & (100 \text{ TeV, } 30 \text{ ab}^{-1}). \end{aligned} \quad (36)$$

While our conclusions on the determination of Higgs-self-interaction at future hadron colliders are robust and important, there is still room to improve. Although the final state  $b\bar{b}\gamma\gamma$  is believed to be the most sensitive channel because of the background suppression and signal reconstruction, there exist complementary channels such as  $gg \rightarrow hh \rightarrow b\bar{b}\tau^+\tau^-$ ,  $b\bar{b}W^+W^-$ ,  $b\bar{b}b\bar{b}$ , etc. The kinematics-based measurement and the all features related to QCD radiation at higher energies should be equally applicable to all of them.

*by Samuel Homiller and Patrick Meade*

The Higgs self-coupling plays a central role in the spontaneous breaking of electroweak symmetry, and governs a pure elementary scalar interaction – one that has never been observed in nature. Unfortunately, due to the small rate of  $hh$  production, measuring the Higgs self-coupling at a 14 TeV appears exceedingly difficult unless it deviates substantially from the Standard Model value [115, 126]. A precision measurement of the Higgs self-coupling is thus one of the primary goals of any higher energy collider. In this section we use the convention

$$V_{\text{int}} = \lambda_3 \frac{m_h^2}{2v} h^3 + \lambda_4 \frac{m_h^2}{8v^2} h^4 \quad (37)$$

such that in the SM  $\lambda_3 = 1$ .

While the prospects of a 100 TeV collider in measuring the self-coupling have been well studied [127], relatively less attention has been paid to intermediate energy colliders such as HE-LHC. Previous studies indicate that the  $hh \rightarrow b\bar{b}\gamma\gamma$  channel has the most promising signature at hadron colliders, and this is expected to be true at 27 TeV as well. However, the  $b\bar{b}\gamma\gamma$  channel still suffers from significant backgrounds from particle misidentification in the detector, making a dedicated detector study including these effects essential. Finally, as discussed below, single-Higgs production – including through gluon-fusion – is a significant background that must be properly understood to accurately project the capabilities of HE-LHC. In what follows, we present a projection of the capabilities of a HE-LHC to measure the self-coupling with these intricacies carefully considered.

#### 3.4.1.3 Signal and Background Simulations

The signal and background samples generated for this study are summarized in Table 22. We also show the cross sections of 14 TeV samples generated for validation with previous projections.

The details of the signal and background simulations mimic those in Ref. [128]. The  $pp \rightarrow hh \rightarrow b\bar{b}\gamma\gamma$  signal is simulated at leading order using `MADGRAPH5_AMC@NLO` [79, 129] using the NNPDF2.3LO PDF set [130] including all finite top mass effects. The `MADSPIN` package [131] was used for the Higgs boson decays and `PYTHIA 8` [132] for the showering and hadronization of events. The LO signal is normalized to match the state of the art NNLO/NNLL calculation with finite top mass

Process	Generator	$\sigma \cdot BR [\text{fb}]$		Order QCD	Expected Events (27 TeV, 15 ab $^{-1}$ )
		14 TeV	27 TeV		
$h(b\bar{b})h(\gamma\gamma)$	MADGRAPH/PYTHIA 8	0.11	0.41	NNLO/NNLL	209.6 $\pm$ 0.2
$tth(\gamma\gamma)$	PYTHIA 8	1.40	6.54	NLO	286.8 $\pm$ 1.6
$Zh(\gamma\gamma)$	PYTHIA 8	2.24	5.58	NLO	67.1 $\pm$ 0.7
$ggF(\gamma\gamma)$	MADGRAPH/PYTHIA 8	83.2	335.1	$N^3\text{LO}$	349.7 $\pm$ 9.5
$b\bar{b}\gamma\gamma$	MADGRAPH/PYTHIA 8	$3.4 \times 10^2$	$9.5 \times 10^2$	LO	414.6 $\pm$ 10.3
$c\bar{c}\gamma\gamma$	MADGRAPH/PYTHIA 8	$4.4 \times 10^2$	$1.5 \times 10^3$	LO	185.7 $\pm$ 4.2
$jj\gamma\gamma$	MADGRAPH/PYTHIA 8	$5.9 \times 10^3$	$1.4 \times 10^4$	LO	63.3 $\pm$ 3.8
$bbj\gamma$	MADGRAPH/PYTHIA 8	$1.1 \times 10^6$	$3.4 \times 10^6$	LO	199.6 $\pm$ 9.4
$c\bar{c}j\gamma$	MADGRAPH/PYTHIA 8	$4.8 \times 10^5$	$1.6 \times 10^6$	LO	25.3 $\pm$ 3.0
$bbjj$	MADGRAPH/PYTHIA 8	$3.7 \times 10^8$	$1.5 \times 10^9$	LO	155.4 $\pm$ 8.2
$Z(b\bar{b})\gamma\gamma$	MADGRAPH/PYTHIA 8	2.61	5.23	LO	21.5 $\pm$ 0.4
$t\bar{t}$	MADGRAPH/PYTHIA 8	$6.7 \times 10^5$	$2.9 \times 10^6$	NNLO	11.6 $\pm$ 3.3
$t\bar{t}\gamma$	MADGRAPH/PYTHIA 8	$1.7 \times 10^3$	$7.9 \times 10^3$	NLO	145.0 $\pm$ 10.3
Total Background					1925.8 $\pm$ 22.7
Significance ( $S/\sqrt{B}$ )					4.77 $\pm$ 0.14

Table 22: List of signal and background processes, the event generator used to simulate the matrix element and parton shower, and the cross section of each process along with the corresponding order in QCD at which the cross section is normalized. In the right-most column we show the expected number of events after all the event selection criteria have been applied.

effects included at NLO in QCD [116]. Additional samples with the self-coupling modified to values between  $-1$  and 10 times the SM value were also generated. Representative kinematic distributions of the signal at parton level are shown in Fig. 50.

Backgrounds to the  $b\bar{b}\gamma\gamma$  decay channel include single Higgs production modes, non-resonant QCD backgrounds, as well as  $Z(b\bar{b})\gamma\gamma$  and  $t\bar{t}(+\gamma)$  production. We include all backgrounds where up to two additional photons or  $b$ -jets can arise from either misidentified light jets or electrons misidentified as photons.

The background from single Higgs production via gluon fusion ( $ggF(\gamma\gamma)$ ) was generated in MADGRAPH with up to two extra partons allowed in the matrix element, with no additional  $k$ -factor due to the already present real emissions. Events from other single Higgs production modes were generated directly in PYTHIA 8 at LO and normalized based on the recommendations in Ref. [7]. The remaining backgrounds were generated in MADGRAPH interfaced with PYTHIA 8 for showering and hadronization, with one additional jet allowed in the matrix element with MLM matching [133, 134] to the parton shower.

#### 3.4.1.4 Detector Simulation

To approximate the effects of detector resolution and reconstruction efficiencies, we use DELPHES 3 with a dedicated card developed to approximate the performance of ATLAS and CMS at HL-LHC. We take this as a reasonable benchmark for the expected performance after the HE-LHC upgrade.

With respect to the DELPHES setup used in [128], the card here has an improved E-Cal resolution and assumes a higher photon identification efficiency, but a somewhat degraded dijet mass resolution. Aside from resolution and efficiency effects, particle misidentification in the detector is also an important source of backgrounds to  $hh \rightarrow b\bar{b}\gamma\gamma$ . To avoid issues with MC statistics, we implement  $b$ -tagging and jet mistagging rates at analysis level using a reweighting scheme, with probabilities taken as functions of the jet  $p_T$  as in Ref. [128]. These probabilities correspond to roughly  $p_{b \rightarrow b} \approx 70\%$ ,  $p_{c \rightarrow b} \approx 20\%$  and  $p_{j \rightarrow b} \lesssim 1\%$ . The probability for a light jet to fake a photon in the detector is also included via

reweighting at analysis level as a function of  $p_T$  (see [128]) which peaks at  $5 \times 10^{-4}$  for  $p_{T,j} \sim 60$  GeV before falling exponentially to  $\sim 1 \times 10^{-4}$ .

#### 3.4.1.5 Results and Limits on the Self-Coupling

To isolate the  $hh \rightarrow b\bar{b}\gamma\gamma$  signal, we implement selection cuts as follows:

- At least 2 isolated photons and b-tagged jets with leading  $p_T > 60$  GeV and sub-leading  $p_T > 35$  GeV, all with  $|\eta_{\gamma,b}| < 2.5$ .
- $p_{T,\gamma\gamma}, p_{T,b\bar{b}} > 125$  GeV.
- $\Delta R_{b\bar{b}}, \Delta R_{\gamma\gamma} < 3.5$ .
- $|m_{\gamma\gamma} - 125.0 \text{ GeV}| < 4.0 \text{ GeV}$ .
- $|m_{b\bar{b}} - 125.0 \text{ GeV}| < 25 \text{ GeV}$ .
- $n_{\text{jets}} < 6$  for jets with  $p_T > 30$  GeV,  $|\eta| < 2.5$ .
- No isolated leptons with  $p_T > 25$  GeV.
- $|\cos \theta_{hh}| < 0.8$ .

where  $\cos \theta_{hh}$  is the decay angle of the Higgs boson pair evaluated in the lab frame (see Fig. 51).

Note that cuts on the  $p_T$  and  $\Delta_R$  of the  $\gamma\gamma$  and  $b\bar{b}$  pair are tightly correlated with the invariant mass of the  $hh$  system. As seen in Fig. 51 the photon pair  $p_T$  has strong discriminating power for the SM  $hh$  signal, but for non-SM values of  $\lambda_3$ , the signal and background become more degenerate.

The final selection efficiency is 3.4%, and the expected number of events from each signal/background channel after applying all the cuts and detector effects is given in Table 22 assuming  $15 \text{ ab}^{-1}$  integrated luminosity at HE-LHC. The uncertainty for each sample is estimated by partitioning the full event sample in to subsamples and computing the standard deviation of the results from each subsample.

The largest backgrounds are from continuum  $bb\gamma\gamma$  and single Higgs production and decay to  $\gamma\gamma$ . Particularly, we see that the  $ggF$  induced mode contributes an  $\mathcal{O}(1)$  background, despite being neglected in previous studies. The accurate modeling of the extra jets that arise in the hadron collision is a necessity for properly understanding this contribution. Other large backgrounds arise from processes where a jet is reconstructed as a photon – even when two fake photons are needed. Finally, we see that  $t\bar{t}$  and  $t\bar{t}\gamma$  are not insignificant backgrounds with the set of cuts we've applied. Several of these backgrounds might be mitigated by exploring the additional kinematic information in events with multiple jets, but the single-Higgs production backgrounds are difficult to reduce in light of the true  $h \rightarrow \gamma\gamma$  present.

To understand the attainable precision on  $\lambda_3$ , we assume a hypothetical observation of  $S+B$  events after all selection cuts with  $S$  and  $B$  as in Table 22. This allows us to derive 68 and 95% confidence intervals on the expected number of signal events using a likelihood scan, including only the MC and statistical uncertainties. The expected number of signal events with  $15 \text{ ab}^{-1}$  integrated luminosity is plotted in Fig. 52 along with the  $1\sigma$  ( $2\sigma$ ) regions in green (yellow).

We can also compute the expected number of events at  $15 \text{ ab}^{-1}$  as a function of  $\lambda_3$ , taking into account both the varying  $\sigma_{hh}$  cross section and the modified acceptance due to changes in the signal kinematics. The resulting curve is shown in red in Fig. 52. The intersection of this curve with the  $1$  and  $2\sigma$  regions indicate the expected precision on  $\lambda_3$  in the absence of systematic uncertainties. We find

$$\lambda_3 \in [0.58, 1.45] \quad \text{at 68\% C.L.} \quad (38)$$

Note that, as a result of the destructive interference between the triangle and box diagrams leading to  $hh$  production, there is a degeneracy in the expected number of events around  $\lambda_3 \sim 5$ . However, the kinematic structure of the  $hh$  signal is very different at large values of  $\lambda_3$ , and such values could be easily rejected using differential measurements (e.g, with  $m_{hh} = m_{b\bar{b}\gamma\gamma}$  or  $p_{T,hh}$ ), so the degeneracy can be safely ignored for the purposes of this work.

In conclusion, we find that with a full account of the detector effects and backgrounds to  $hh \rightarrow b\bar{b}\gamma\gamma$ , a cut based analysis leads to an expected significance of  $4.77 \pm 0.14\sigma$ , corresponding to a 45% measurement of the Higgs self-coupling at 27 TeV with  $15 \text{ ab}^{-1}$ . Future improvements can be made

both by considering other decay channels (e.g.,  $hh \rightarrow b\bar{b}b\bar{b}, b\bar{b}\tau\tau$ , and  $b\bar{b}WW$ ) and by exploiting the additional information present in the  $hh$  invariant mass distribution, as discussed elsewhere in this report.

### 3.4.2 ATLAS studies

*by P. Bokan, E. Petit, M. Wielers*

The results presented in Section 3.2.1 were extended to provide estimates of the prospects at the HE-LHC, assuming a centre of mass collision energy of 27 TeV and  $15 \text{ ab}^{-1}$  of data.

The assumption is made that the detector performance will be the same as of the HL-LHC ATLAS detector. Comparisons between simulation at centre of mass energy of 14 and 27 TeV show that the kinematic of the Higgs boson decay particles, as well as the  $m_{HH}$  distribution are similar. However the pseudorapidity of the particle tends to point more frequently in the forward region, which would decrease the acceptance by around 10%. This effect is not taken into account and the impact is expected to be small.

The event yields for the various background processes are scaled by the luminosity increase and the cross-section ratio between the two centre of mass energies. For the signal the cross-section of 139.9 fb is used.

Without including systematic uncertainties a significance of XX and XX standard deviations is expected for the  $b\bar{b}\gamma\gamma$  and  $b\bar{b}\tau\tau$  channels respectively. The hypothesis of no Higgs self-coupling can be excluded with a significance of XX and XX standard deviations respectively. Finally the  $\kappa_{lambda}$  parameter is expected to be measured with a precision of XX% and XX% respectively.

## 3.5 Indirect probes

### 3.5.1 Indirect probes of the trilinear coupling through differential distributions measurements

### 3.5.2 Indirect probes through single Higgs boson production

*Bizon, Gorbahn, Haisch, Maltoni, Pagani, Shivaji, Zanderighi, Zhao*

In this section we discuss the possibility of indirectly extracting information on the trilinear self interactions of the Higgs boson via precise measurements of single-Higgs production [135–143] at the HL-LHC and HE-LHC. This strategy is complementary to the direct measurement via double-Higgs production (see section ??), which already at leading order, i.e. at one loop in the case of  $gg \rightarrow HH$ , depends on the trilinear Higgs self interaction. In the case of single-Higgs production, on the contrary, the Higgs self interactions enter only via one-loop corrections, i.e., at the two-loop level for the gluon-fusion ( $ggF$ ) production mode. The effects of modified Higgs self interactions are therefore generically much smaller, but for single-Higgs production processes the precision of the experimental measurements is and will be much better than for double-Higgs production. This, and the fact that for single-Higgs production many different final states and both inclusive as well as differential measurements are possible will lead to competitive indirect determinations of the trilinear Higgs self coupling. In [144, 145] also electroweak (EW) precision observables have been considered to this purpose.

In the following subsection, we will briefly recall the calculation framework introduced in [136, 137]. We also provide numerical results for the effects due to a modified trilinear Higgs coupling in the most important inclusive and differential single-Higgs production cross sections as well as the Higgs branching ratios. Based on these results, we will analyse in section ?? the sensitivity of the HL-LHC and HE-LHC in constraining the trilinear Higgs self interactions.

#### 3.5.2.1 Theoretical framework

The effects of anomalous Higgs interactions can be extracted from experimental data via the signal strength parameters  $\mu_i^f$ , which are defined for any specific combination of production and decay channel

$i \rightarrow H \rightarrow f$  as follows

$$\mu_i^f \equiv \mu_i \times \mu^f = \frac{\sigma(i)}{\sigma^{\text{SM}}(i)} \times \frac{\text{BR}(f)}{\text{BR}^{\text{SM}}(f)}. \quad (39)$$

Here the quantities  $\mu_i$  and  $\mu^f$  are the production cross sections  $\sigma(i)$  ( $i = ggF, \text{VBF}, WH, ZH, t\bar{t}H, tHj$ ) and the branching ratios  $\text{BR}(f)$  ( $f = \gamma\gamma, ZZ, WW, b\bar{b}, \tau\tau$ ) normalised to their SM values, respectively. Assuming on-shell production, the product  $\mu_i \times \mu^f$  therefore corresponds to the rate for the  $i \rightarrow H \rightarrow f$  process normalised to the corresponding SM prediction.

The quantities  $\mu_i$  and  $\mu^f$  that enter the definition of  $\mu_i^f$  in (39) can be expressed as

$$\mu_i = 1 + \delta\sigma_{\lambda_3}(i), \quad \mu^f = 1 + \delta\text{BR}_{\lambda_3}(f), \quad (40)$$

where  $\delta\sigma_{\lambda_3}(i)$  and  $\delta\text{BR}_{\lambda_3}(f)$  are the deviations induced by an anomalous trilinear Higgs self interaction to the production cross sections and branching ratios, respectively. This definition can be straightforwardly extended to the differential level and one has  $\mu_i^f = \mu_i = \mu^f = 1$  in the SM.

In single-Higgs production, the trilinear Higgs self interactions start to enter only at the one-loop level in the case of vector boson fusion (VBF),  $WH, ZH, t\bar{t}H, tHj$  production, while in the case of  $ggF$  production and the decays  $H \rightarrow gg, \gamma\gamma$  one has to calculate two-loop EW corrections. The appearance of the quadrilinear Higgs self coupling in single-Higgs processes is further delayed by one loop order.

For the strategy discussed here, the anomalous trilinear Higgs self interactions can be equivalently parameterised either via an anomalous trilinear coupling

$$\lambda_3 \equiv \kappa_3 \lambda_3^{\text{SM}} \quad (41)$$

where  $\lambda_3^{\text{SM}} = m_H^2 / (2v^2)$  with  $v = (\sqrt{2}G_F)^{-1/2} \simeq 246 \text{ GeV}$  the EW vacuum expectation value, or via the corresponding dimension-six operator

$$\mathcal{O}_6 = -\frac{\lambda_3^{\text{SM}} c_6}{v^2} |\Phi|^6, \quad (42)$$

with  $\Phi$  denoting the usual SM Higgs doublet. In the normalisation adopted in (42), the simple relation

$$\kappa_3 = 1 + c_6, \quad (43)$$

is obtained and allows to translate constraints on the coupling modifier  $\kappa_3$  into bounds on the Wilson coefficient  $c_6$  and vice versa.

In the presence of modified trilinear Higgs self interactions, all single-Higgs production and decay channels receive two types of contributions [136, 137]: firstly, a process and kinematic dependent one, denoted as  $C_1$  hereafter, which is linear in  $c_6$  or  $\kappa_3$  and second, a universal one proportional to the Higgs wave function renormalisation constant  $Z_H$ , which is proportional to  $\kappa_3^2$  and therefore contains both a linear and quadratic piece in  $c_6$ . The quantity  $\delta\sigma_{\lambda_3}(i)$  introduced in (40) as well as any differential distribution related to it can thus be written as<sup>2</sup>

$$\delta\sigma_{\lambda_3}(i) = (\kappa_3 - 1) C_1^\sigma + \left(\kappa_3^2 - 1\right) \delta Z_H = c_6 C_1^\sigma + \left(2c_6 + c_6^2\right) \delta Z_H, \quad (44)$$

where  $\delta Z_H$  denotes the one-loop correction to the Higgs wave function renormalisation constant associated to modifications of the trilinear Higgs self coupling. In the case of the decays, the effects due to Higgs wave function renormalisation cancel in the branching ratios, and as a result the quantities  $\delta\text{BR}_{\lambda_3}(f)$  defined in (40) take the following form

$$\delta\text{BR}_{\lambda_3}(f) = (\kappa_3 - 1) (C_1^\Gamma - C_1^{\Gamma_{\text{tot}}}) = c_6 (C_1^\Gamma - C_1^{\Gamma_{\text{tot}}}). \quad (45)$$

---

<sup>2</sup>This equation is in reality a linearised version of the complete formula that is used for extracting the results in Section ... and involves the Higgs wave function resummation [137, 141]. Also (45) is a linear expansion.

$C_1^\sigma$ [%]	ggF	VBF	WH	ZH	ttH	tHj
13 TeV	0.66	0.64	1.03	1.19	3.51	0.91
14 TeV	0.66	0.64	1.03	1.18	3.47	0.89
27 TeV	0.66	0.62	1.01	1.16	3.20	0.79

Table 23:  $C_1^\sigma$  coefficients for inclusive single-Higgs production cross sections at different CM energies.

$p_T(H)$ [GeV]	[0, 25]	[25, 50]	[50, 100]	[100, 200]	[200, 500]	> 500
VBF	0.97	0.88	0.73	0.58	0.45	0.29
ZH	2.00	1.75	1.21	0.51	0.01	-0.10
WH	1.70	1.49	1.04	0.44	0.01	-0.09
tH	5.31	5.07	4.38	3.00	1.27	0.17
tHj	1.23	1.18	1.02	0.74	0.33	-0.06

Table 24:  $C_1^\sigma$  coefficients for single-Higgs production processes at 13 TeV in different  $p_T(H)$  bins.

$p_T(H)$ [GeV]	[0, 25]	[25, 50]	[50, 100]	[100, 200]	[200, 500]	> 500
VBF	0.65	0.65	0.65	0.62	0.52	0.29
ZH	2.00	1.74	1.21	0.50	0.00	-0.10
WH	1.70	1.49	1.04	0.44	0.01	-0.09
tH	5.00	4.78	4.14	2.86	1.23	0.22
tHj	1.06	1.03	0.91	0.69	0.33	0.02

Table 25: Same as table 24 but for a CM energy of 27 TeV.

$C_1^\Gamma$ [%]	$\gamma\gamma$	$ZZ$	$WW$	$gg$
on-shell $H$	0.49	0.83	0.73	0.66

Table 26:  $C_1^\Gamma$  coefficients for the phenomenologically relevant decay modes of the Higgs boson.

Here  $C_1^{\Gamma_{\text{tot}}}$  is an effective term that describes the process dependent corrections to the total decay width of the Higgs boson.

In the following we provide the values of the  $C_1$  coefficients that are used in the numerical analyses presented in section ???. The given values correspond to the input

$$G_F = 1.1663787 \times 10^{-5} \text{ GeV}^{-2}, \quad m_W = 80.385 \text{ GeV}, \\ m_Z = 91.1876 \text{ GeV}, \quad m_H = 125 \text{ GeV}, \quad m_t = 172.5 \text{ GeV}. \quad (46)$$

For these parameters one finds numerically [137]

$$\delta Z_H = -1.536 \times 10^{-3}, \quad C_1^{\Gamma_{\text{tot}}} = 2.3 \times 10^{-3}. \quad (47)$$

In the calculations of production cross sections and distributions, the renormalisation and factorisation scales are taken to be  $\mu_R = \mu_F = \frac{1}{2} \sum_f m_f$  with  $m_f$  the masses of the particles in the final state and PDF4LHC2015 [15] parton distribution functions are used. On the other hand, the dependence of the  $C_1$  coefficients on  $\mu_R$ ,  $\mu_F$  and the PDF set is negligible.

In table 23 we list the values of  $C_1^\sigma$  for the various production modes at different centre of mass (CM) energies. One first notices that  $WH$ ,  $ZH$  and especially  $t\bar{t}H$  production depend stronger on the anomalous trilinear Higgs self coupling than the  $ggF$ , the VBF and the  $tHj$  channel. Furthermore, in the case of  $WH$ ,  $ZH$  and  $t\bar{t}H$  production the loop corrections contributing to  $C_1^\sigma$  feature a Sommerfeld enhancement, which results in an increased sensitivity to anomalous trilinear Higgs self interactions at low energies [137, 138, 141]. This feature is illustrated in tables 24 and 25 where we give the values of  $C_1^\sigma$  in bins of the Higgs transverse momentum  $p_T(H)$  for  $pp$  collisions at 13 TeV and 27 TeV, respectively.<sup>3</sup> Table 26 finally provides the values of the  $C_1^\Gamma$  coefficients for the decay modes of the Higgs boson that are relevant in our numerical study.

Notice that all the formulas and numbers presented in this subsection take into account only effects associated to an anomalous trilinear Higgs self coupling. The extension to more general and physically motivated scenarios that include also other new-physics effects is simple and has been worked out in [139, 141]. It consists in adding to (44) and (45) the effects of other anomalous interactions such as a modified top Yukawa coupling or altered/new gauge-Higgs vertices. In the next subsection, we perform a global analyses of the constraints on  $\lambda_3$  that the HL-LHC and the HE-LHC should be able to set. We thereby follow the lines of the study [139], using the results for the coefficients  $C_1$  provided above.

As discussed in refs. [139, 141], the constraints that can be set on  $c_6$  critically depend on the interplay between the following aspects:

- The number of additional parameters related other anomalous interactions.
- The number of independent measurements considered in the analysis.
- The inclusion of differential information.
- The assumptions on the theoretical and experimental (statistical and systematic) errors.

In the next section we explore this interplay for the cases of the HL- and HE-LHC following the lines of the study presented in refs. [139] augmented with the new results provided in this section. Independent analyses performed by the ATLAS and CMS collaborations with a full-fledged treatment of all the correlations among experimental uncertainties are desirable. It is worth noting that, when other anomalous interactions are also considered, the effects of  $Z_H^{\text{BSM}}$  are degenerate with those in general affecting the Higgs wave-function normalisation, typically parameterised via the Wilson coefficient  $C_H$ . Thus, the coefficients  $C_1^\sigma$  and therefore the differential distributions have a primary role in the extraction of the information on  $\kappa_3$  from measurements of single Higgs production.

We also recall that limits on  $\kappa_3$  or equivalently  $c_6$  obtained with this strategy are sensible only when  $|\kappa_3| < 20$ ; as discussed in refs. [137] this limit guarantees that the perturbative loop expansion is converging and that the leading missing higher orders depending on  $\kappa_3 - 1 = c_6$  are below 10% level. On the contrary, as discussed in refs. [143, 146], when the information from double Higgs production is considered a more cautious limit  $|\kappa_3| < 6$  should be adopted in order to achieve both perturbative unitarity and the convergence of the loop expansion.

### 3.5.3 Global fit

*Stefano Di Vita, Gauthier Durieux, Jiayin Gu, Zhen Liu, Giuliano Panico, Marc Riembau, Thibaud Vantalon*

In the previous chapter (cite) it as been shown that assuming the trilinear is the only coupling deviating from its SM value that single Higgs observable can give competitive bound with double Higgs production, see also Refs. [136–138, 141, 144], electroweak process where the Higgs trilinear enter at the two loop level have also been studied in [145]. Nevertheless, departures of the Higgs self-coupling

---

<sup>3</sup>Results for a different binning or different observables can be easily obtained with the code presented in [141].

from its SM prediction signal the existence of new dynamics that, in general, would leave an imprint on other Higgs couplings as well which have a strong impact on the bound as shown by Ref. [139]. The importance of a global fit is therefore two-fold, namely to assess the robustness of the studies that take into account deformations exclusively in the Higgs trilinear, and to single out the sensitivity on the single-Higgs couplings that is required to minimize the impact of the possible correlations.

To include the effect of the different deformations away from the SM, we use the EFT framework described in Ref. [139], where 9 parameters describe the deviations of the single-Higgs couplings. In particular, we consider three<sup>4</sup> parameters for the Yukawa interactions ( $\delta y_t$ ,  $\delta y_b$ ,  $\delta y_{\tau}$ ), two for the contact interactions with gluons and photons ( $c_{gg}$ ,  $c_{\gamma\gamma}$ ), rescalings of the SM  $hZZ$  and  $hWW$  interactions (parametrized by one coefficient,  $\delta c_z$ , if custodial symmetry is unbroken), and three coefficients ( $c_{zz}$ ,  $c_{z\Box}$ ,  $c_{z\gamma}$ ) parametrizing interactions of the Higgs with the electroweak bosons that have non-SM tensor structures. Note that two combinations of the last three parameters are constrained by diboson data, showing an interesting interplay between the gauge and the Higgs sectors. A global fit on the Higgs self-coupling, parametrized by  $\delta\kappa_\lambda$  (which is zero in the SM) using only inclusive single Higgs observables, and taking into account the additional 9 EFT deviations described above, suffers from a flat direction. To lift it, it is necessary to include data from differential measurements of those processes, since the single-Higgs deformations and  $\delta\kappa_\lambda$  tend to affect the distributions in complementary ways.

The global fit for the HL-LHC is summarized in Fig. 53. In the left plot, we show in green the  $\Delta\chi^2$  including only single-Higgs data, both in an exclusive study (dotted), and after profiling over all the other parameters (solid). The width of the lines corresponds to different assumptions on the extrapolation of the projected experimental sensitivities on the inclusive signal strengths, to differential ones. We can see that, in a global fit, the constraint on the trilinear is worsened due to correlations (mainly with the top yukawa  $\delta y_t$  and the contact interaction with gluons  $c_{gg}$ , and, to a lesser degree, between  $\delta y_b$  and  $\delta c_z$  **refer to fig4 if we include it**). The fit to differential double-Higgs data and inclusive single-Higgs measurements, taken from the study in Ref. [92], is depicted in blue. In the right plot we can see that, while double-Higgs is clearly driving the bound, differential single-Higgs data is nonetheless relevant as it can help lift the degenerate minima around  $\delta\kappa_\lambda \sim 5$ .

We now discuss projections for the HE-LHC at 27 TeV with  $15 \text{ ab}^{-1}$  of integrated luminosity. For the uncertainties we perform a simple extrapolation where the theory and systematic uncertainties are kept the same as in the HL-LHC projections, while the statistical uncertainty is rescaled accordingly [119]. We show the results in Fig. 54. In the left plot, in pink, we present the  $\chi^2$  analysis using the projections for the single-Higgs channels at HE-LHC at the inclusive level. Inclusive measurements are able to lift the flat direction due to the measurement of the  $th + j$  production and the  $z\gamma$  decay. The combination with the full HL-LHC analysis closes the flat direction and the second minimum can be excluded at  $\sim 95\%$  CL. In the right plot the fit using differential observables in single-Higgs production at HE-LHC is shown in blue. The differential information is enough to lift the flat directions and the single-Higgs data is more constraining than the full HL-LHC combination, even in the global fit. Combination with HL-LHC gives a constraint of about  $|\delta\kappa_\lambda| \lesssim 2$  at 95% CL. Moreover, the combination (in red) reduces the impact of the correlations.

Since it is expected that the theory and systematic uncertainties will change over time, in Fig. 55 we explore how our findings are affected if both uncertainties are rescaled by a common factor. Getting more than a factor two improvement on those uncertainties, which is a rather reasonable benchmark, does not significantly improve the constraints, and we conclude that the precision is limited by statistics.

---

<sup>4</sup>If other fermionic decay channels can be observed, further parameters can be included, with no effect on the number of degrees of freedom.

### 3.6 Implications

#### 3.6.1 Implications for flavor models

by Martin Bauer, Marcella Carena and Adrián Carmona

In 2HDMs, the term  $H_1 H_2 \equiv H_1^T (i\sigma_2) H_2$  is a SM singlet which can however be charged under an additional  $U(1)$  flavor symmetry. This is an interesting possibility that allows to generate the different fermion masses with a Froggatt-Nielsen (FN) mechanism where the flavon is replaced by the  $H_1 H_2$  operator. In this way, the new physics scale  $\Lambda$  where the higher dimensional FN operators are generated is tied to the electroweak scale, leading to much stronger phenomenological consequences. Let us assume for concreteness a type-I like 2DHM with the following Yukawa Lagrangian

$$\mathcal{L}_Y \supset y_{ij}^u \left( \frac{H_1 H_2}{\Lambda^2} \right)^{n_{u_{ij}}} \bar{q}_L^i H_1 u_R^j + y_{ij}^d \left( \frac{H_1^\dagger H_2^\dagger}{\Lambda^2} \right)^{n_{d_{ij}}} \bar{q}_L^i \tilde{H}_1 d_R^j + y_{ij}^e \left( \frac{H_1^\dagger H_2^\dagger}{\Lambda^2} \right)^{n_{e_{ij}}} \bar{\ell}_L^i \tilde{H}_1 e_R^j + \text{h.c.}, \quad (48)$$

where  $\tilde{H}_1 \equiv i\sigma_2 H_1^*$  as usual and the charges  $n_{u,d,e}$  are a combination of the  $U(1)$  charges of  $H_1$ ,  $(H_1 H_2)$  and the different SM fermion fields. For simplicity, we set the flavor charges of  $(H_1 H_2)$  and  $H_2$  to 1 and 0, respectively, such that

$$n_{u_{ij}} = a_{q_i} - a_{u_j}, \quad n_{d_{ij}} = a_{q_i} - a_{d_j}, \quad n_{e_{ij}} = a_{\ell_i} - a_{e_j}, \quad (49)$$

if we denote by  $a_{q_i}, a_{u_i}, \dots$ , the  $U(1)$  charges of the SM fermions. In general, the fermion masses are given by

$$m_\psi = y_\psi \varepsilon^{n_\psi} \frac{v}{\sqrt{2}} \quad \varepsilon = \frac{v_1 v_2}{2\Lambda^2} = \frac{t_\beta}{1 + t_\beta^2} \frac{v^2}{2\Lambda^2}, \quad (50)$$

with the vacuum expectation values  $\langle H_{1,2} \rangle = v_{1,2}$  and  $t_\beta \equiv v_1/v_2$ . Besides being able to accommodate the observed hierarchy of SM fermion masses and mixing angles for the right assignment of flavor charges [], this framework can lead to enhanced diagonal Yukawa couplings between the Higgs and the SM fermions while having suppressed FCNCs. If we denote by  $h$  and  $H$  the two neutral scalar mass eigenstates, with  $h$  being the observed 125 GeV Higgs, the couplings between the scalars  $\varphi = h, H$  and SM fermions  $\psi_{L_i, R_i} = P_{L,R} \psi_i$  in the mass eigenbasis read

$$\mathcal{L} = g_{\varphi \psi_{L_i} \psi_{R_j}} \varphi \bar{\psi}_{L_i} \psi_{R_j} + \text{h.c.} \quad (51)$$

with  $i$ , such that  $u_i = u, c, t$ ,  $d_i = d, s, b$  and  $e_i = e, \mu, \tau$ . This induces flavor-diagonal couplings

$$g_{\varphi \psi_{L_i} \psi_{R_i}} = \kappa_{\psi_i}^\varphi \frac{m_{\psi_i}}{v} = \left( g_{\psi_i}^\varphi(\alpha, \beta) + n_{\psi_i} f^\varphi(\alpha, \beta) \right) \frac{m_{\psi_i}}{v}, \quad (52)$$

as well as flavor off-diagonal couplings

$$g_{\varphi \psi_{L_i} \psi_{R_j}} = f^\varphi(\alpha, \beta) \left( \mathcal{A}_{ij} \frac{m_{\psi_j}}{v} - \frac{m_{\psi_i}}{v} \mathcal{B}_{ij} \right). \quad (53)$$

The flavor universal functions in (52) and (53) read

$$g_{\psi_i}^h = \frac{c_{\beta-\alpha}}{t_\beta} + s_{\beta-\alpha}, \quad g_{\psi_i}^H = c_{\beta-\alpha} - \frac{s_{\beta-\alpha}}{t_\beta}, \quad (54)$$

and

$$f^h(\alpha, \beta) = c_{\beta-\alpha} \left( \frac{1}{t_\beta} - t_\beta \right) + 2s_{\beta-\alpha}, \quad f^H(\alpha, \beta) = -s_{\beta-\alpha} \left( \frac{1}{t_\beta} - t_\beta \right) + 2c_{\beta-\alpha}, \quad (55)$$

where  $c_x \equiv \cos x$ ,  $s_x \equiv \sin x$ . One can see that, unless all flavor charges for a given type of fermions are equal, the off-diagonal elements in matrices  $\mathcal{A}$  and  $\mathcal{B}$  lead to FCNCs which are chirally suppressed by powers of the ratio  $\varepsilon$ , see [147] for more details.

The scalar couplings to the different gauge bosons are the same as in a normal type-I 2HDM while the scalar coupling between the heavy Higgs  $H$  and two SM Higgs scalars  $h$ , as well as the triple Higgs coupling can be expressed as [148, 149]

$$g_{Hhh} = \frac{c_{\beta-\alpha}}{v} \left[ (1 - f^h(\alpha, \beta) s_{\beta-\alpha}) (3M_A^2 - 2m_h^2 - M_H^2) - M_A^2 \right], \quad (56)$$

$$g_{hhh} = -\frac{3}{v} \left[ f^h(\alpha, \beta) c_{\beta-\alpha}^2 (m_h^2 - M_A^2) + m_h^2 s_{\beta-\alpha} \right], \quad (57)$$

where  $M_A$  is the pseudoscalar mass. The  $U(1)$  flavor symmetry restricts the number of allowed terms in the scalar potential forbidding e.g. terms proportional to  $H_1 H_2$ . The interesting feature is that one can rewrite such self scalar interactions with the help of the function  $f^h(\alpha, \beta)$ , since it is somehow related to the combination  $H_1 H_2^\dagger$  appearing in both the scalar potential and the higher dimensional operators generating the different Yukawa couplings. Therefore, the parameter space for which  $f^h(\alpha, \beta) \gamma\gamma 1$  and  $c_{\beta-\alpha} \neq 0$  leads to maximally enhanced diagonal couplings of the SM Higgs to fermions (52) as well as to an enhancement of the trilinear couplings (56) and (57). For maximally enhanced Yukawa couplings, the mass of the heavy Higgs  $H$  cannot be taken arbitrarily large and resonant Higgs pair production has to be present. This correlation between the enhancement of the Higgs Yukawa couplings  $\kappa_\psi^h$  and  $\text{Br}(H \rightarrow hh)$  is illustrated for  $M_H = M_A = M_{H^\pm} = 500$  GeV in Fig. 56 where we plot the dependence of  $\text{Br}(H \rightarrow hh)$  on  $c_{\beta-\alpha}$  and  $t_\beta$ . The dashed contours correspond to constant values of  $|\kappa_\psi^h|$  for  $n_\psi = 1$ . This correlation does not depend of the factor  $n_\psi$ , although  $n_\psi > 1$  leads to a larger enhancement. The two exceptions for which this correlation breaks down are the limits  $c_{\beta-\alpha} \approx 0$  and  $c_{\beta-\alpha} \approx \pm 1$ . Whereas the second case is strongly disfavoured by SM Higgs couplings strength measurements, the first one (which corresponds to the decoupling limit) is at odds with the flavor model, for it requires large values of the spurion  $\mu_3 \propto M_A$  which softly breaks the  $U(1)$  flavor symmetry.

The enhancement in  $\text{Br}(H \rightarrow hh)$  shown in Figure 56 is partially cancelled in the production cross section  $\sigma(gg \rightarrow H)$  for large values of  $t_\beta$  due to the fact that  $\sigma(gg \rightarrow H) \propto 1 + 1/t_\beta^2 - (\kappa_t^h)^2$ , with  $\kappa_t^h \approx 1$ . However, the cross-section  $\sigma(gg \rightarrow h \rightarrow hh)$  is not suppressed for such values of  $t_\beta$  and the combination of both contributions leads to a continuous enhancement in the di-Higgs cross-section. There is therefore a non-trivial interplay between resonant and non-resonant contributions, which we illustrate in the left panel of Fig. 57, where we plot both contributions assuming as a function of  $\kappa_\psi^h$  for fixed values of  $c_{\beta-\alpha}$  (which is a monotonic function of  $t_\beta$ ). We assume a center-of-mass energy of  $\sqrt{s} = 27$  TeV and set  $M_A = 450$  GeV and  $M_H = M_{H^\pm} = 550$  GeV, while choosing two different values of  $c_{\beta-\alpha} = -0.45$  and  $-0.4$ . Dashed (dotted) lines correspond to the non-resonant (resonant) contributions, whereas the solid lines represent the full  $\sigma(gg \rightarrow hh)$  in the 2HDM in units of the SM prediction, both at LO and NLO. Solid lines show the NLO results, while the solid shaded lines mark the values of  $\kappa_\psi$  excluded by perturbativity and unitarity constraints [150]. More details about the calculation of the signal and plots for  $\sqrt{s} = 13$  TeV can be found in Ref. [147]. The values of  $\kappa_\psi^h$  in Fig. 57 correspond to  $n_\psi = 1$  but values of  $\mathcal{O}(10)$  and larger are obtained for  $n_\psi > 1$ . We also show in the right panel of Fig. 57 the invariant mass distribution for the different contributions to the di-Higgs signal for  $c_{\beta-\alpha} = -0.45$  and three different values of  $\kappa_\psi^h = 3, 4$  and  $5$ . The interesting feature is that, when the enhancement in the Higgs Yukawa couplings is large enough, the interference between both non-resonant and resonant contributions turns the broad peak into a shoulder in the  $d\sigma/dm_{hh}$  distribution for the total cross section, as shown for the case  $\kappa_\psi^h = 5$  by the blue line in the right panel of Fig. 57. Resolving such shape in the invariant mass distribution can be quite challenging. We encourage a dedicated analysis considering the corresponding  $d\sigma/dm_{hh}$  templates to maximize the sensitivity to features in the di-Higgs invariant mass distribution from the simultaneous enhancement of  $g_{hhh}$ ,  $g_{Hhh}$  and  $\kappa_\psi^h$ .

### *3.6.2 Implications for theories of electroweak phase transition*

## 4 High Energy Probes

### 4.1 tt differential measurements

### 4.2 WH/ZH at high energy/luminosity

Shankha Banerjee<sup>a</sup>, Rick S. Gupta<sup>a</sup>, Christoph Englert<sup>b</sup> and Michael Spannowsky<sup>a</sup>

<sup>a</sup>*Institute of Particle Physics Phenomenology, Durham University, Durham DH1 3LE, UK*

<sup>b</sup>*SUPA, School of Physics and Astronomy, University of Glasgow, Glasgow G12 8QQ, UK*

## Introduction and EFT analysis

In this note we perform a collider study of the Higgs-strahlung process,  $pp \rightarrow Z(\ell^+\ell^-)h(b\bar{b})$  in the Standard Model Effective Field Theory (SMEFT) framework. We will see that the leading high energy contribution to the  $pp \rightarrow Zh$  process comes from the four contact interactions  $hZ_\mu \bar{u}_{L,R} \gamma^\mu u_{L,R}$  and  $hZ_\mu \bar{d}_{L,R} \gamma^\mu d_{L,R}$  that appear in the dimension-6 Lagrangian. These are the same four EFT directions, the so called “high energy primaries” that control high energy  $Wh$ ,  $WW$  and  $WZ$  production (see Ref. [151]). The (pseudo-)observables involved in these diboson processes (anomalous TGCs and  $Z$ -pole observables) have already been constrained at LEP. We show in this note that because of the higher energies accessible at the LHC one can obtain bounds on these observables that are at least an order of magnitude stronger than those obtained at LEP.

The vertices in the dimension 6 Lagrangian that contribute to the  $ff \rightarrow Vh$  (where  $V = W, Z$ ) process in unitary gauge are as follows,

$$\begin{aligned} \Delta\mathcal{L}_6 \supset & \sum_f \delta g_f^Z Z_\mu \bar{f} \gamma^\mu f + \delta g_{ud}^W (W_\mu^+ \bar{u}_L \gamma^\mu d_L + h.c.) + g_{VV}^h h \left[ W^{+\mu} W_\mu^- + \frac{1}{2c_{\theta_W}^2} Z^\mu Z_\mu \right] \\ & + \delta g_{ZZ}^h h \frac{Z^\mu Z_\mu}{2c_{\theta_W}^2} + \sum_f g_{Zf}^h \frac{h}{v} Z_\mu \bar{f} \gamma^\mu f + g_{Wud}^h \frac{h}{v} (W_\mu^+ \bar{u}_L \gamma^\mu d_L + h.c.) + \kappa_{Z\gamma} \frac{h}{v} A^{\mu\nu} Z_{\mu\nu} \\ & + \kappa_{WW} \frac{h}{v} W^{+\mu\nu} W_{\mu\nu}^- + \kappa_{ZZ} \frac{h}{2v} Z^{\mu\nu} Z_{\mu\nu}. \end{aligned} \quad (58)$$

Here we have used the Lagrangian presented in Ref. [152, 153], where  $\alpha_{em}$ ,  $m_Z$  and  $m_W$  have been used as input parameters and any corrections to the SM vector boson propagators have been traded in favor of the vertex corrections. After summing over all  $V$ -polarizations, the leading piece in the high energy cross-section deviation for  $ff \rightarrow Vh$ , is proportional to the four contact interactions:  $g_{Zf}^h$ , with  $f = u_L, u_R, d_L$  and  $d_R$ .<sup>5</sup> Table 27, shows the linear combinations of Wilson coefficients contributing to the four  $g_{Zf}^h$  couplings in different EFT bases. The aforementioned directions are shown in the BSM Primary basis of Ref. [152], where the Wilson coefficients are already constrained pseudo-observables. In this basis we see that these can be written in terms of already constrained LEP (pseudo)observables.

Given the inability to control the polarization of the initial state partons in a hadron collider, the process, in reality, only probes two of the above four directions. Taking only the interference term, we find these directions to be

$$g_{\mathbf{u}}^Z = g_{Zu_L}^h + \frac{g_{u_R}^Z}{g_u^Z} g_{Zu_R}^h, \quad g_{\mathbf{d}}^Z = g_{Zd_L}^h + \frac{g_{d_R}^Z}{g_{d_L}^Z} g_{Zd_R}^h. \quad (59)$$

---

<sup>5</sup>There exists a basis independent constraint at the dimension-6 level,  $\sqrt{2} g_{Wud}^h = (g_{Zd_L}^h - g_{zu_L}^h)$ .

	EFT directions probed by high energy $ff \rightarrow Vh$ production
Warsaw Basis [154]	$-\frac{2g}{c_{\theta_W}} \frac{v^2}{\Lambda^2} ( T_3^f  c_L^1 - T_3^f c_L^3 + (1/2 -  T_3^f ) c_f)$
BSM Primaries [152]	$\frac{2g}{c_{\theta_W}} Y_f t_{\theta_W}^2 \delta \kappa_\gamma + 2 \delta g_f^Z - \frac{2g}{c_{\theta_W}} (T_3^f c_{\theta_W}^2 + Y_f s_{\theta_W}^2) \delta g_1^Z$
SILH Lagrangian [75]	$\frac{g}{c_{\theta_W}} \frac{m_W^2}{\Lambda} (2 T_3^f  \hat{c}_W - 2t_{\theta_W}^2 Y_f \hat{c}_B)$
Universal observables	$\frac{2g}{c_{\theta_W}} Y_f t_{\theta_W}^2 (\delta \kappa_\gamma - \hat{S} + Y) - \frac{2g}{c_{\theta_W}} (T_3^f c_{\theta_W}^2 + Y_f s_{\theta_W}^2) \delta g_1^Z - \frac{2g}{c_{\theta_W}} T_3^f W$
High Energy Primaries [151]	$- \frac{2m_W^2}{gc_{\theta_W}} ( T_3^f  a_q^{(1)} - T_3^f a_q^{(3)} + (1/2 -  T_3^f ) a_f)$

Table 27: The linear combinations of Wilson coefficients contributing to the contact interaction couplings  $g_{Zf}^h$  where  $f = u_L, d_L, u_R, d_R$ . the direction for a given  $f$  can be read off from this table by substituting the corresponding value of the  $SU(2)_L$  and  $U(1)_Y$  quantum numbers  $T_3^f$  and  $Y_f$ . Here  $\hat{c}_W = c_W + c_{HW} - c_{2W}$  and  $\hat{c}_B = c_B + c_{HB} - c_{2B}$ . For the nomenclature of the operators, their corresponding Wilson coefficients and observables see for eg. Ref. [151].

At a given energy, a linear combination of the up-type and down-type coupling deviations, enters the interference term for the  $pp \rightarrow Z h$  process,  $g_{\mathbf{p}}^Z = g_{\mathbf{u}}^Z + \frac{\mathcal{L}_d(\hat{s})}{\mathcal{L}_u(\hat{s})} g_{\mathbf{d}}^Z$ , where  $\mathcal{L}_{u,d}$  is the  $u\bar{u}$ ,  $d\bar{d}$  luminosity at a given partonic centre of mass energy. The luminosity ratio changes very little with energy: between 0.65 and 0.59 as  $\sqrt{\hat{s}}$  is varied from 1 to 2 TeV. Thus, to a good approximation,  $pp \rightarrow Z h$  probes the single direction,

$$g_{\mathbf{p}}^Z = g_{Zu_L}^h - 0.76 g_{Zd_L}^h - 0.45 g_{Zu_R}^h + 0.14 g_{Zd_R}^h. \quad (60)$$

using  $\hat{s} = (1.5 \text{ TeV})^2$ . Using Tab. 27, one can now write this in terms of the LEP-constrained pseudo-observables,

$$\begin{aligned} g_{Z\mathbf{p}}^h &= 2 \delta g_{Zu_L}^h - 1.52 \delta g_{Zd_L}^h - 0.90 \delta g_{Zu_R}^h + 0.28 \delta g_{Zd_R}^h \\ &\quad - 0.14 \delta \kappa_\gamma - 0.89 \delta g_1^Z \\ g_{Z\mathbf{p}}^h &= -0.14 (\delta \kappa_\gamma - \hat{S} + Y) - 0.89 \delta g_1^Z - 1.3 W \end{aligned} \quad (61)$$

where the first and second lines apply respectively to the general and universal case (third and fourth row of Table 27).

To estimate the cut-off for our EFT, note that the  $g_{Vf}^h$  couplings arise from current-current operators that can be generated, for instance, by integrating out at tree-level a heavy  $SU(2)_L$  triplet (singlet) vector  $W'^a$  ( $Z'$ ) that couples to SM fermion currents,  $\bar{f} \sigma^a \gamma_\mu f$  ( $\bar{f} \gamma_\mu f$ ) with a coupling  $g_f$  and to the Higgs current  $iH^\dagger \sigma^a \overset{\leftrightarrow}{D}_\mu H$  ( $iH^\dagger \overset{\leftrightarrow}{D}_\mu H$ ) with a coupling  $g_H$ . This gives  $g_{Zf}^h \sim g_H g g_f v^2 / \Lambda^2$ , where  $\Lambda$  is the mass of the massive vector and thus the cut-off for our EFT description. A universal coupling to the SM fermions can arise via kinetic mixing of the heavy vector with the SM gauge bosons; this would give  $g_f = g/2$  ( $g_f = g' Y$ ), such that,

$$g_{Zu_L, d_L}^h \sim \frac{g_H g^2 v^2}{2\Lambda^2}, \quad g_{Zu_R, d_R}^h \sim \frac{g_H g g' Y_{u_R, d_R} v^2}{\Lambda^2}. \quad (62)$$

For a given set of couplings  $\{g_{Zu_L}^h, g_{Zd_L}^h, g_{Zu_R}^h, g_{Zd_R}^h\}$ , the cut-off is evaluated using Eq. 62 with  $g_H = 1$  (note that this is somewhat larger than the value corresponding to the SM  $hZZ$  coupling) and taking the smallest of the four values.

## Collider Analysis

For our collider analysis, we consider  $Z(\ell^+\ell^-)h$  production from a pair of quarks as well as from a pair of gluons. For the decay of the Higgs boson, we find that at an integrated luminosity of  $300 \text{ fb}^{-1}$ , the diphoton mode is not feasible as it yields less than 5 events at high energies ( $p_{T,Z} > 150 \text{ GeV}$ ). We thus focus on the decay  $h \rightarrow b\bar{b}$  to obtain large statistics. The dominant backgrounds are then  $Zb\bar{b}$  and the irreducible  $Zh$  production in SM. Reducible contributions also arise from  $Z + \text{jets}$  production (where we include  $c$ -quarks but do not require that they are explicitly tagged). We employ the BDRS approach [155] and demand a fat jet with a cone radius of  $R = 1.2$ . More details of the Monte-Carlo analysis, the QCD corrections, the detailed cut-based and multivariate analyses (MVA) can be found in Ref. [156]. Finally, we find a cut-based (MVA) SM  $Zh$  to  $Zb\bar{b}$  ratio of  $\sim 0.26$  (0.50).

To discriminate between the EFT signal and the irreducible SM  $Zh(b\bar{b})$  background we study the growth of the EFT cross-section at high energies. This can be seen in Fig. 58 where we show the differential distribution with respect to  $M_{Zh}$ , the invariant mass of the leptons and the fat jet, for the EFT signal as well as for the different backgrounds. The EFT signal corresponds to a point that can be excluded in our analysis but is allowed by the LEP constraint. To fully utilise the shape deviation of the EFT signal with respect to the background, we perform a binned log likelihood analysis assuming a 5% systematic error taking only events below the cut-off (evaluated as explained below Eq. 62). To obtain the 95% CL exclusion curve, we assume that the observed number of events would agree with the SM.

## Discussion and Conclusions

Taking into account only the SM-BSM interference term, we find the following per-mille level bounds for  $300$  ( $3000$ )  $\text{fb}^{-1}$ ,

$$g_{Z\mathbf{p}}^h \in [-0.004, 0.004] \quad ([ -0.001, 0.001]) \quad (63)$$

The above bounds translate to a lower bound on the scale of new physics given by  $2.4 \text{ TeV}$  ( $4.4 \text{ TeV}$ ) at  $300 \text{ fb}^{-1}$  ( $3000 \text{ fb}^{-1}$ ) using Eq. 62. To compare the above projections with existing LEP bounds, one can now extract bounds on the LEP observables contributing to  $g_{Z\mathbf{p}}^h$  in Eq. 61 by turning them on one by one. We show the results in Tab. 28. For the TGCs  $\delta g_1^Z$  and  $\delta \kappa_\gamma$ , our projections are much stronger than the LEP bounds and in the case of the  $Z$ -pole observables  $\delta g_f^Z$ , that parametrize the deviations of the  $Z$  coupling to quarks, they are comparable.

For the universal case, we perform a more detailed analysis. The results are shown in the  $\delta \kappa_\gamma - \hat{S}$  vs.  $\delta g_1^Z$  plane in Fig. 59 for the interesting class of models where  $W = Y = 0$  [151]. The direction related to the  $pp \rightarrow Zh$  interference term, *i.e.*,  $g_{Z\mathbf{p}}^h = 0$  (see Eq. 60 and the second line of Eq. 61) is shown by the dashed blue line, whereas the direction orthogonal to it is shown by the dotted red line. Once the LEP II bounds [157] from the  $e^+e^- \rightarrow W^+W^-$  process are imposed, the allowed region that remains is shown by the grey shaded area. We show the results of this work in blue (light (dark) blue for results at  $300$  ( $3000$ )  $\text{fb}^{-1}$ ). The shape of the allowed region arises due to the fact that the interference term vanishes along the dashed blue line and the squared term increases in magnitude as we move away from the origin. This curves the allowed region away from the dashed line as we move away from the origin. The accidental cancellation of the interference term means that our bounds are susceptible to dimension-8 effects along this direction. On the other hand our bounds are more robust and not susceptible to such effects in the orthogonal direction shown by the red dotted line.

As  $VV$  production constrains the same set of operators as the  $Vh$  production in Fig. 59, we also show the projected bound from the  $WZ$  process at  $300 \text{ fb}^{-1}$  obtained in Ref. [151]. Only the purple region remains when both these bounds are combined at  $300 \text{ fb}^{-1}$ . This shrinks further to the green region at  $3000 \text{ fb}^{-1}$ . A drastic reduction in the allowed LEP region is thus possible by considering the  $pp \rightarrow Zh$  at high energies.

	Our Projection	LEP Bound
$\delta g_{u_L}^Z$	$\pm 0.002 (\pm 0.0007)$	$-0.0026 \pm 0.0016$
$\delta g_{d_L}^Z$	$\pm 0.003 (\pm 0.001)$	$0.0023 \pm 0.001$
$\delta g_{u_R}^Z$	$\pm 0.005 (\pm 0.001)$	$-0.0036 \pm 0.0035$
$\delta g_{d_R}^Z$	$\pm 0.016 (\pm 0.005)$	$0.0016 \pm 0.0052$
$\delta g_1^Z$	$\pm 0.005 (\pm 0.001)$	$0.009^{+0.043}_{-0.042}$
$\delta \kappa_\gamma$	$\pm 0.032 (\pm 0.009)$	$0.016^{+0.085}_{-0.096}$
$\hat{S}$	$\pm 0.032 (\pm 0.009)$	$0.0004 \pm 0.0007$
$W$	$\pm 0.003 (\pm 0.001)$	$0.0000 \pm 0.0006$
$Y$	$\pm 0.032 (\pm 0.009)$	$0.0003 \pm 0.0006$

Table 28: Comparison of the bounds obtained in this work with existing LEP bounds obtained by turning on the LEP observables in Eq. 61 one by one and using Eq. 63. The LEP bounds on the  $Z$  coupling to quarks has been obtained from Ref. [158], the bound on the TGCs from Ref. [157], the bound on  $\hat{S}$  from Ref. [159] and finally the bounds on  $W, Y$  have been obtained from Ref. [160]. Except for the case of the bounds on  $\delta g_f^Z$ , all of the bounds in the last column were derived by turning on only the given parameter and putting all other parameters to zero. The numbers outside (inside) brackets, in the second column, denote our bounds with  $\mathcal{L} = 300$  (3000)  $\text{fb}^{-1}$ .

### 4.3 Electroweak Precision Tests in High-Energy Diboson Processes

Roberto Franceschini<sup>a</sup>, Giuliano Panico<sup>b</sup>, Alex Pomarol<sup>b,c</sup>,  
Francesco Riva<sup>d</sup> and Andrea Wulzer<sup>d,e,f</sup>

<sup>a</sup>*Dipartimento di Matematica e Fisica, Università di Roma Tre and INFN, 00146 Rome*

<sup>b</sup>*IFAE and BIST, Universitat Autònoma de Barcelona, 08193 Bellaterra, Barcelona*

<sup>c</sup>*Dept. de Física, Universitat Autònoma de Barcelona, 08193 Bellaterra, Barcelona*

<sup>d</sup>*Theoretical Physics Department, CERN, Geneva, Switzerland*

<sup>e</sup>*Institut de Théorie des Phénomènes Physiques, EPFL, Lausanne, Switzerland*

<sup>f</sup>*Dipartimento di Fisica e Astronomia, Università di Padova and INFN Padova, Italy*

#### High-Energy Primary Effects in Diboson Production

Diboson production processes provide a very good sensitivity to a large set of new-physics effects and can be effectively used to test interesting classes of BSM theories. In this section we classify the leading new-physics effects that can be tested in these channels, showing that they can be encapsulated in four real “high-energy primary” (HEP) parameters [161]. We also assess the reach on these parameters at the HL-LHC and at future hadronic colliders, focusing in particular on the fully leptonic  $WZ$  channel that appears particularly promising.

We are interested in processes which fulfill two conditions. First, their amplitudes must receive BSM contributions that grow with  $E^2$  at the leading order (i.e.,  $d = 6$ ) in the EFT operator expansion. Second, the SM amplitudes must be constant and sizable at high energy, in such a way that, at the linear order in the EFT Wilson coefficient, the  $E^2$ -growth of the BSM amplitudes results into a  $E^2$ -growth of the differential cross-sections thanks to the SM-BSM interference. As explained in detail in Ref. [161], only  $pp \rightarrow V_L V_L$  and  $pp \rightarrow V_L h$  production processes enjoy quadratic energy growth at the interference level; we thus focus on these in the rest of the section.<sup>6</sup> The study of longitudinally-polarized

<sup>6</sup>Notice however that promising strategies to circumvent the non-interference problem have been recently proposed [162, 163], which allow for instance to “resurrect” interference effects in transverse vector bosons production.

Amplitude	High-energy primaries	Low-energy primaries
$\bar{u}_L d_L \rightarrow W_L Z_L, W_L h$	$\sqrt{2} a_q^{(3)}$	$\sqrt{2} \frac{g^2}{m_W^2} \left[ c_{\theta_W} (\delta g_{uL}^Z - \delta g_{dL}^Z)/g - c_{\theta_W}^2 \delta g_1^Z \right]$
$\bar{u}_L u_L \rightarrow W_L W_L$ $\bar{d}_L d_L \rightarrow Z_L h$	$a_q^{(1)} + a_q^{(3)}$	$-\frac{2g^2}{m_W^2} \left[ Y_L t_{\theta_W}^2 \delta \kappa_\gamma + T_Z^{u_L} \delta g_1^Z + c_{\theta_W} \delta g_{dL}^Z/g \right]$
$\bar{d}_L d_L \rightarrow W_L W_L$ $\bar{u}_L u_L \rightarrow Z_L h$	$a_q^{(1)} - a_q^{(3)}$	$-\frac{2g^2}{m_W^2} \left[ Y_L t_{\theta_W}^2 \delta \kappa_\gamma + T_Z^{d_L} \delta g_1^Z + c_{\theta_W} \delta g_{uL}^Z/g \right]$
$\bar{f}_R f_R \rightarrow W_L W_L, Z_L h$	$a_f$	$-\frac{2g^2}{m_W^2} \left[ Y_{f_R} t_{\theta_W}^2 \delta \kappa_\gamma + T_Z^{f_R} \delta g_1^Z + c_{\theta_W} \delta g_{fR}^Z/g \right]$

Table 29: Parameter combinations (in the high- and in the low-energy primary bases) that control  $E^2$ -enhanced effects in each polarized longitudinal diboson production process. Here,  $T_Z^f = T_3^f - Q_f s_{\theta_W}^2$  and  $Y_{L,f_R}$  is the hypercharge of the left-handed and right-handed quark (e.g.,  $Y_L = 1/6$ ).

dibosons production in the high-energy limit  $E\gamma\gamma m_W$  is greatly simplified by using the Equivalence Theorem [164, 165]. In this formalism, external longitudinally-polarized vector states are represented in Feynman diagrams as the corresponding scalar Goldstone bosons, up to corrections of order  $m_W/E$  from diagrams with gauge external lines. In order to assess the leading energy behavior, it is sufficient to study the amplitude in the unbroken phase, where the EW bosons are massless and the  $G_{\text{SM}} = \text{SU}(2)_L \times \text{U}(1)_Y$  symmetry is exact. Given that the Goldstone bosons live in the Higgs doublet  $H$ , together with the Higgs particle,  $G_{\text{SM}}$  implies that the high-energy behavior of the former ones are connected with the latter. This is the reason why  $V_L V_L$  and  $V_L h$  production processes, collectively denoted as  $\Phi\Phi'$  in what follows, should be considered together.

Focusing our interest to the production of  $\Phi\Phi'$  out of a quark  $q'$  with helicity  $\lambda'$  and an anti-quark  $\bar{q}$  with helicity  $\lambda$  we can restrict the form of the BSM amplitudes that interfere with SM one. At order  $E^2/M^2$  in the EFT expansion the relevant BSM effects can be parametrized as corrections to the  $J = 1$  partial wave amplitudes [161], namely

$$\delta\mathcal{A}(q'_\pm \bar{q}_\mp \rightarrow \Phi\Phi') = f_{q'_\pm \bar{q}_\mp}^{\Phi\Phi'}(s) \sin \theta = \frac{1}{4} A_{q'_\pm \bar{q}_\mp}^{\Phi\Phi'} E^2 \sin \theta^*, \quad (64)$$

where  $\theta^*$  is the scattering angle in the  $\Phi\Phi'$  center of mass, and  $E = \sqrt{s}$  is the center of mass energy.

Eq. (64) shows that at the leading order in the SM EFT expansion each diboson process is sensitive at high energy to a single constant new-physics parameter  $A_{q'_\pm \bar{q}_\mp}^{\Phi\Phi'}$  for every combination of initial or final states. This can be taken real since its imaginary part does not interfere with the SM. In addition, the SM symmetry group, which is restored in the high-energy limit, as previously explained, implies several relations among these parameters [161]. As a consequence, only 4 HEP parameters are enough to parametrize the BSM effects we are interested in. This is very non-trivial from an EFT perspective, since a total of 6 anomalous couplings coming from  $d = 6$  effective operators contribute to longitudinal diboson processes. These couplings can be identified as  $\delta g_{uL}^Z, \delta g_{uR}^Z, \delta g_{dL}^Z, \delta g_{dR}^Z, \delta g_1^Z$  and  $\delta \kappa_\gamma$  in the notation of Ref. [152].

The relations between the HEP parameters and the 4 combinations of the low-energy primaries that produce growing-with-energy effects are reported in the third column of table 29.

The relations between the HEP and the Wilson coefficients in the SILH basis [75] are given by

$$a_q^{(3)} = \frac{g^2}{M^2} (c_W + c_{HW} - c_{2W}), \quad a_q^{(1)} = \frac{g'^2}{3M^2} (c_B + c_{HB} - c_{2B}), \quad (65)$$

and

$$a_u = -2a_d = 4a_q^{(1)}. \quad (66)$$

These relations can also be written using the  $\hat{S}$ ,  $\hat{T}$ ,  $W$  and  $Y$  parameters (we follow the notation of Ref. [160]) in addition to the two anomalous triple gauge couplings (aTGC),  $\delta g_1^Z$  and  $\delta\kappa_\gamma$ . We have

$$a_q^{(3)} = -\frac{g^2}{m_W^2} \left( c_{\theta_W}^2 \delta g_1^Z + W \right), \quad a_q^{(1)} = \frac{g'^2}{3m_W^2} \left( \hat{S} - \delta\kappa_\gamma + c_{\theta_W}^2 \delta g_1^Z - Y \right), \quad (67)$$

which can be useful in order to compare HEP analyses from LHC with other experiments, such as LEP.

In the Warsaw basis [154], the HEP are transparently identified with contact interactions between quarks and scalars<sup>7</sup>

$$a_u = 4\frac{c_R^u}{M^2}, \quad a_d = 4\frac{c_R^d}{M^2}, \quad a_q^{(1)} = 4\frac{c_L^{(1)}}{M^2}, \quad a_q^{(3)} = 4\frac{c_L^{(3)}}{M^2}. \quad (68)$$

### LHC Primaries Sensitivity: The $WZ$ Channel

To illustrate the HE-LHC reach on the high-energy primaries we focus on  $WZ$  production. This channel gives access to the  $a_q^{(3)}$  primary and has a very high sensitivity to new physics [161]. We consider the fully leptonic final state

$$pp \rightarrow W^\pm Z + \text{jets} \rightarrow \ell\nu\ell'\bar{\ell}' + \text{jets}, \quad \text{with } \ell, \ell' = e, \mu,$$

which is likely to be measured with good accuracy and can benefit from a straightforward reconstruction of the final-state leptons and a very low reducible background [166]. At the experimental level the situation might not be too much different from the neutral Drell-Yan process, in which a measurement with 2% relative systematic uncertainty of the differential cross-section was performed, with run-1 LHC data, up to TeV energies [167]. A systematic uncertainty of 5% might be considered as a realistic goal for the differential cross-section measurement in the leptonic  $WZ$  channel.

The main obstacle to obtain sensitivity to new physics is the potentially large contribution of the other polarizations, which for our purposes constitute a background, since they are insensitive to the new physics parameter  $a_q^{(3)}$ . In the  $WZ$  channel these effects are automatically under control in the high- $p_T$  region and they can be further reduced by suitable selection criteria, as we will discuss later.

Due to the symmetry structure, the emission of transversely polarized  $W$  and  $Z$  bosons in the central rapidity region is disfavored [161]. No suppression is instead expected for longitudinally polarized gauge bosons, therefore it is advantageous to concentrate our analysis on central scattering region,  $|\cos\theta^*| \sim 0$ , or, equivalently, at large  $p_{T,V}$  ( $p_{T,V} > 1$  TeV). We stress that other diboson processes, e.g.  $pp \rightarrow WW$ , do not enjoy this suppression of transverse vector boson emission, therefore are expected to be less sensitive probes of the high energy primaries. The interested reader can find estimates of the results achievable with the other diboson channels in Ref. [161].

### Analysis

We now estimate the reach on  $a_q^{(3)}$  based on a full NLO simulation of the  $pp \rightarrow 3\ell\nu$  process. We report the analysis of Ref. [161] to which we refer for more details. We consider generation-level leptons momenta, but we include an overall detector efficiency for reconstructing the three leptons that we estimate

---

<sup>7</sup>These relations, as well as those in eq. (65), are obtained by computing the diboson helicity amplitudes in the presence of the EFT operators, and matching with the results of the low energy primaries. See Ref. [161] for details.

acceptance cuts	$p_{T,\ell} > 30 \text{ GeV}, \quad  \eta_\ell  < 2.4$
analysis cuts	$p_{T,VV}/p_{T,V} < 0.5$ $ \cos \theta^*  \leq 0.5$

Table 30: List of acceptance and analysis cuts.

around 50% [168]. We furthermore apply standard acceptance cuts on the leptons (see Table 30). The same-flavor and opposite-charge lepton pair with invariant mass closer to the  $Z$  boson mass is taken as the  $Z$  candidate and the remaining lepton is taken to be the decay product of the  $W$  boson. The missing transverse energy vector of the event ( $\vec{E}_T$ ) is estimated from the generation-level transverse neutrino momentum, to which we apply a Gaussian smearing with standard deviation  $\sigma_{\vec{E}_{T_i}}^2 = (0.5)^2 \cdot \sum_f |p_i| \cdot \text{GeV}$ .

In order to highlight the production of longitudinally polarized vector bosons in the central rapidity region is useful to eliminate events with hard real radiation, which tend to be more abundant for our background of transverse polarized gauge bosons. To tame real radiation events in a controlled way we employ a selection on the transverse momentum of the  $WZ$  system, denoted by  $p_{T,VV} = |\vec{p}_{T,W} + \vec{p}_{T,Z}|$ .<sup>8</sup> We require  $p_{T,VV}$  to be smaller than 50% of the transverse momentum of the gauge bosons in the event,  $p_{T,V} = \min(p_{T,W}, p_{T,Z})$ . We also impose a cut on the scattering angle in the  $WZ$  center of mass frame  $|\cos \theta^*| \leq 0.5$ . The cuts are summarized in Table 30.

The kinematical variables described so far allow us to determine  $p_{T,Z}$  and  $p_{T,W}$ , and in turn  $p_{T,V}$  and  $p_{T,VV}$ , used to construct the binned distribution and for the selection cuts. In order to extract  $|\cos \theta^*|$  the neutrino rapidity is reconstructed by the standard technique of imposing the invariant mass of the neutrino plus lepton system to be as close as possible to the physical  $W$  boson mass. A twofold ambiguity in the reconstruction is resolved by imposing the  $|\cos \theta^*|$  cut on both solutions, i.e. by retaining for the analysis only events such that both the possible neutrino configurations satisfy the selection criteria.

We study the 3 collider energy options that correspond to the LHC (14 TeV), to the High-Energy LHC (HE-LHC, 27 TeV) and to the FCC-hh (100 TeV). In each case we consider suitably designed  $p_{T,V}$  bins, namely

$$\begin{aligned} \text{LHC: } p_{T,V} &\in \{100, 150, 220, 300, 500, 750, 1200\}, \\ \text{HE-LHC: } p_{T,V} &\in \{150, 220, 300, 500, 750, 1200, 1800\}, \\ \text{FCC: } p_{T,V} &\in \{220, 300, 500, 750, 1200, 1800, 2400\}. \end{aligned} \tag{69}$$

The binning is chosen such as to cover the kinematical regime that is accessible at each collider and it is taken as fine as possible in order to maximize the BSM sensitivity. On the other hand, a minimum bins size  $\Delta p_{T,V}/p_{T,V} \gtrsim 30\%$  is required in order to avoid a degradation of the accuracy due to the  $p_{T,V}$  resolution.

The predicted cross-sections are used to construct the  $\chi^2$ , under the assumption that observations agree with the SM, and are eventually used to derive 95% CL bounds on  $a_q^{(3)}$ . The uncertainties in each bin are the sum in quadrature of the statistical error, obtained from the SM expected events yield, and of a systematical component (uncorrelated across bins) which we take as a fixed fraction ( $\delta_{\text{syst}}$ ) of the SM expectations. With this procedure we obtain, for different collider energies and luminosities and for  $\delta_{\text{syst}} = 5\%$

$$\begin{aligned} \text{HL-LHC, } 3 \text{ ab}^{-1}: \quad a_q^{(3)} &\in [-4.9, 3.9] 10^{-2} \text{ TeV}^{-2} \\ \text{HE-LHC, } 10 \text{ ab}^{-1}: \quad a_q^{(3)} &\in [-1.6, 1.3] 10^{-2} \text{ TeV}^{-2} \\ \text{FCC-hh, } 20 \text{ ab}^{-1}: \quad a_q^{(3)} &\in [-7.3, 5.7] 10^{-3} \text{ TeV}^{-2} \end{aligned} \tag{70}$$

<sup>8</sup>Alternatively, a jet veto might be considered, which however could lead to lower accuracy because of the experimental and theoretical uncertainties in jets reconstruction. See also Ref. [169] for a different approach.

We see that the HE-LHC will improve the HL-LHC reach by a factor of 3, while a gain of nearly one order of magnitude would be possible with the FCC-hh collider. The FCC-hh reach is comparable with the one of CLIC, as extracted from the analysis in Ref. [170].

The results of eq. (70) rely on BSM cross-section predictions obtained by integrating up to very high center of mass energies, formally up to the collider threshold. Therefore these limits assume that the description of the underlying BSM model offered by the EFT is trustable in the whole relevant kinematical regime, i.e. that the cutoff  $M$  of the BSM EFT is high enough. We quantify how large  $M$  concretely needs to be for our results to hold by studying [171–173] how the limit deteriorates if only events with low  $WZ$  invariant mass,  $m_{WZ} < m_{WZ}^{\max}$  are employed. This obviously ensures that the limit is consistently set within the range of validity of the EFT provided the EFT cutoff  $M$  is below  $m_{WZ}^{\max}$ . The results are reported in figure 60. Since the 95% CL interval is nearly symmetric around the origin only the upper limit is reported in the figure for shortness.

Several conclusions can be drawn from figure 60. First of all we see that the reach saturates for  $m_{WZ}^{\max}$  below around 1.5 TeV at the HL-LHC if the systematic uncertainties are low, meaning that the limits obtained without  $m_{WZ}$  cut apply to theories with cutoff  $M$  above that threshold. The threshold grows to around 3 and 4 TeV at the HE-LHC and at the FCC-hh, respectively. The figures show that  $\delta_{\text{syst}} = 5\%$  is sufficient to probe “Weak” theories in all cases, but it also shows that the impact of larger or smaller uncertainties on the reach can be significant. Systematic errors at the  $\delta_{\text{syst}} = 5\%$  level already make an appreciable difference with respect to  $\delta_{\text{syst}} = 1\%$ . This is due to the fact that the low- $p_{T,V}$  bins have small statistical error and the reach in those bins benefits from lower systematics. The effect is even more pronounced at the HE-LHC and at the FCC-hh, where even with  $\delta_{\text{syst}} = 2\%$  the reach deteriorates significantly with respect the ideal case  $\delta_{\text{syst}} = 1\%$ . The fact that more accurate measurements would improve the reach of future colliders is an element that should be taken into account in the design of the corresponding detectors.

## 4.4 Novel measurements of anomalous triple gauge couplings for the HE and HL-LHC

A. Azatov, D. Barducci, J. Elias-Miró and Elena Venturini

*SISSA and INFN sezione di Trieste, Via Bonomea 265; I-34137 Trieste, Italy*

### 4.4.1 Introduction

In this work we are interested in the measurement of the Standard Model (SM) Triple Gauge Couplings (TGCs). This is a classic test of the SM and a possible measurement of deviations from its expectations would signify an invaluable piece of information for the theory beyond the SM. A consistent way to parametrize such possible deviations is through the SM Effective Field Theory (EFT) approach. We are going to consider the SM EFT as defined in [163], in particular we are going to focus on the measurement of the EFT operator

$$\mathcal{O}_{3W} = \frac{g}{3!} \epsilon^{abc} W^{a,\mu\nu} W_{\nu\rho}^b W_{\mu}^{c,\rho}, \quad (71)$$

which is associated to the the anomalous triple gauge coupling (aTGC)  $\lambda_z$ .

A precise determination of the TGC stems from the measurement of the  $2 \rightarrow 2$  cross section  $\sigma(q\bar{q} \rightarrow VV)$  [?, 166]. Naive dimensional analysis and standard EFT reasoning predicts that the energy

scaling of such cross-section is given by

$$\sigma(q\bar{q} \rightarrow VV) \sim \frac{g_{\text{SM}}^4}{E^2} \left[ 1 + \underbrace{c_i \frac{E^2}{\Lambda^2}}_{\text{BSM}_6 \times \text{SM}} + \underbrace{c_i^2 \frac{E^4}{\Lambda^4}}_{\text{BSM}_6^2} + \dots \right], \quad (72)$$

where the first factor  $g_{\text{SM}}^4/E^2$  accounts for the energy flux of the initial quarks,  $c_i$  are the relevant Wilson coefficients, and we have omitted numerical factors. In (72) we have explicitly indicated dimension six squared ( $\text{BSM}_6^2$ ) and SM-dimension six interference terms ( $\text{BSM}_6 \times \text{SM}$ ).<sup>9</sup> The ellipses in (72) are due to corrections from operators of dimension  $\geq 8$ , which we will neglect. The leading such term is an interference term of the type  $\text{BSM}_8 \times \text{SM}$  and it is of order  $O(E^4/\Lambda^4)$ .

A closer inspection however reveals that the  $2 \rightarrow 2$  diboson production through the dimension six operator  $\mathcal{O}_{3W}$  has an interference piece with a suppressed energy scaling. Indeed, the energy scaling of such process is

$$\sigma(q\bar{q} \rightarrow VV) \sim \frac{g_{\text{SM}}^4}{E^2} \left[ 1 + C_{3W} \frac{m_V^2}{\Lambda^2} + C_{3W}^2 \frac{E^4}{\Lambda^4} + O(E^4/\Lambda^4) \right]. \quad (73)$$

This is a consequence of the helicity selection rules, see [?, 162, 163, 174]. The suppressed energy scaling can be problematic for the correct EFT interpretation of the  $\sigma(q\bar{q} \rightarrow VV)$  measurement. Namely, in view of (73), the sensitivity on  $C_{3W}$  is largely dominated by the quadratic piece  $\text{BSM}_6^2$ , which is  $O(E^4/\Lambda^4)$ . Furthermore, in this case, the measurements become insensitive to the sign of the Wilson coefficient. The main objective of the present work is to improve the sensitivity to the linear piece  $\text{BSM}_6 \times \text{SM}$ . We will present two classes of solutions to achieve this goal. Firstly, in section 4.4.2 we will show that the differential angular cross-section of the process  $q\bar{q} \rightarrow VV \rightarrow 4\psi$  has a large sensitivity on  $\text{BSM}_6 \times \text{SM}$  compared to the inclusive cross-section. Secondly, in section 4.4.2 we will show that accounting for extra radiation  $q\bar{q} \rightarrow VV + j$  also results in an improved sensitivity on the leading piece  $\text{BSM}_6 \times \text{SM}$ . These measurements are specially interesting in a HL/HE phase of the LHC, for which we show the prospects in section 4.4.3.

#### 4.4.2 Solutions

Next we will present two ways to improve the sensitivity to the aTGC  $\lambda_z$  by restoring the energy growth  $g_{\text{SM}}^4/E^2 \left[ 1 + c_i E^2/\Lambda^2 + \dots \right]$  of the interference piece  $\text{BSM}_6 \times \text{SM}$  of the  $\mathcal{O}_{3W}$  operator.

##### *Interference resurrection via angular distributions*

The first way of enhancing the interference term is by noting that in a collider experiment instead of the  $2 \rightarrow 2$  process we actually measure a  $2 \rightarrow 4$  scattering, i.e. vector bosons decay into fermions  $q\bar{q} \rightarrow V_1 V_2 \rightarrow 4\psi$ .

Let us start by considering the differential cross section for the production of the polarized particles  $W_{T+} Z_T \rightarrow W_{T+} l_+ \bar{l}_-^{10}$

$$\frac{d\sigma(q\bar{q} \rightarrow W_{T+} l_- \bar{l}_+)}{d\text{LIPS}} = \frac{1}{2s} \frac{\left| \sum_i (\mathcal{M}_{q\bar{q} \rightarrow W_{T+} Z_i}^{\text{SM}} + \mathcal{M}_{q\bar{q} \rightarrow W_{T+} Z_i}^{\text{BSM}}) \mathcal{M}_{Z_i \rightarrow l_- \bar{l}_+} \right|^2}{(k_Z^2 - m_Z^2)^2 + m_Z^2 \Gamma_Z^2}, \quad (74)$$

where sum runs over intermediate Z polarizations and  $d\text{LIPS} \equiv (2\pi)^4 \delta^4(\sum p_i - p_f) \prod_i d^3 p_i / (2E_i (2\pi)^3)$  is the Lorentz Invariant differential Phase Space. Then in the narrow width approximation the leading contribution to the interference, i.e. the cross term  $\text{SM} \times \text{BSM}_6$  in 74, is given by  $d\sigma_{\text{int}}(q\bar{q} \rightarrow$

<sup>9</sup>Note that operators of dimension 7 necessarily violate either baryon or lepton number. We assume the scale of such symmetry violation to be very large and therefore irrelevant for diboson physics at the LHC.

<sup>10</sup>We ignore the longitudinal Z polarization which is subdominant at the LHC [175].

$W_{T_+} l_- \bar{l}_+)/d\phi_Z \propto E^2/\Lambda^2 \cos(2\phi_Z)$ , where  $\phi_Z$  is the azimuthal angle between the plane defined by the decaying leptons and the plane defined by the collision and WZ momenta, see Fig. 61. Note that  $d\sigma_{\text{int}}(q\bar{q} \rightarrow W_{T_+} l_- \bar{l}_+)/d\phi_Z$  has the energy growth expected from naive dimensional analysis, see Eq. 72. An analogous derivation goes through if we also consider the decay of the W gauge boson. The differential interference term for the process  $q\bar{q} \rightarrow WZ \rightarrow 4\psi$  is unsuppressed and modulated as

$$\frac{d\sigma_{\text{int}}(q\bar{q} \rightarrow WZ \rightarrow 4\psi)}{d\phi_Z d\phi_W} \propto \frac{E^2}{\Lambda^2} (\cos(2\phi_Z) + \cos(2\phi_W)), \quad (75)$$

where  $\phi_{W,Z}$  are the corresponding azimuthal angles. Integrating 75 over the fermion phase space the interference term vanishes as expected from the discussion in section 4.4.1. Since the dependence on the two azimuthal angles is additive, integrating over  $\phi_W$  leads to a differential cross-section that is modulated by  $\cos(2\phi_Z)$  and that features  $E^2/\Lambda^2$  energy growth. We will use the result in Eq. 75 to prove the aTGC  $\lambda_Z$ , with an increased overall sensitivity to both the magnitude and sign of the Wilson coefficient.

### Angle ambiguities [162]

Let us make a few remarks on the experimental measurement of  $\phi_{Z,W}$  in Eq. 75. The angle  $\phi_Z$  can be determined up to an ambiguity  $\phi_Z \leftrightarrow \phi_Z \pm \pi$ , since experimentally we can only measure the charges but not the helicities of the leptons from Z decay. The reconstruction of the W azimuthal angle  $\phi_W$  in the  $l\nu$  final state suffers from an ambiguity  $\phi_W \leftrightarrow \pi - \phi_W$  due to the twofold ambiguity in the determination of the neutrino momentum. Interestingly, none of these ambiguities affects Eq. 75.

### Interference resurrection via jet emission

A second way to resurrect the expected energy growth of the interference term is based on the observation that the helicity selection rule holds only at tree-level [163]. So the next-to-leading-order (NLO) effects will necessarily lead to the enhancement of the interference. Virtual effects are expected to be suppressed by a factor  $\mathcal{O}(\alpha_s/4\pi)$  with respect to the contributions coming from azimuthal modulation discussed in the previous section. Alternatively we will consider processes with an extra hard jet emission, which will improve on the signal over the background ratio. In this case, since we are dealing with the hard  $2 \rightarrow 3$  process, the same polarization configuration  $q\bar{q} \rightarrow V_\pm V_\pm g_\mp$  is allowed both in SM and in the BSM five point amplitude with the  $\mathcal{O}_{3W}$  insertion. Therefore the interference is not suppressed and the leading quadratic energy scaling is restored by requiring an extra (hard) QCD radiation.

#### 4.4.3 Results

##### HL-LHC

In order to test the sensitivity of the High-Luminosity (HL) phase of the LHC on the  $\mathcal{O}_{3W}$  with the proposed solution to the non-interference behaviour we proceed in the following way. We generate with MadGraph5 aMC@NLO [79] parton level events for  $pp \rightarrow W^\pm Z$  decaying into a four leptons (electron and muon) final state together with events for the same process where we allow for a jet emission in the initial state. We perform two different analyses (see [163] for more details): an inclusive one where we restrict to events up to  $p_T^j < 100$  GeV and do not bin on the  $\phi_Z$  variable and an exclusive one where we bin both on the jet transverse momentum and on  $\phi_Z$ , where for the latter we define two bins with the threshold  $|\cos(\phi_Z)| = 1/\sqrt{2}$ . All together the results for the bound on the  $C_{3W}$  Wilson coefficient are reported in Fig. 62 as a function of the maximum transverse mass of the WZ system, which allows to have an estimate of the validity of the EFT computation, see again [163] for a detailed discussion<sup>11</sup>.

One might wonder if a simulation beyond the parton level accuracy might spoil these results. To this end we have performed a more detailed simulation by showering the events through PYTHIA 8 [79]

---

<sup>11</sup>These results are obtained by keeping both the linear and the quadratic terms in the cross section determination.

and simulating the detector response via `Delphes` 3 [176]. By analysing the density of events in the two azimuthal bins we found that with respect to the parton level case the relative difference is of at most a few %, thus making our parton level analysis solid, see ref. [?].

## **HE-LHC**

We now estimate the reach of a future HE phase of the LHC with  $\sqrt{s} = 27$  TeV. For these preliminary results we adopt the same binning, both in  $\phi_Z$  and in jet transverse momentum, of the previous section. We show the results in Fig. 63. We found a slight increase of order 30% on the reach on  $C_{3W}$ . We expect that a dedicated HE analysis will lead to a further improvement of these bounds; this can be done by exploiting in a more efficient way the high energy tails of the differential distributions.

### **4.4.4 Higgs pair production in vector-boson fusion at the HL-LHC**

by Fady Bishara, Roberto Contino, and Juan Rojo

#### *4.4.4.1 Introduction.*

While the dominant production channel of Higgs boson pairs at hadron colliders is the gluon-fusion mechanism, other channels are also of phenomenological relevance. In particular, Higgs pair production in weak vector-boson fusion [?] is interesting since it probes the strength of the Higgs non-linear interactions with vector bosons at high energies. This process can therefore provide unique information to test the nature of the Higgs boson, whether it is a composite or elementary state, and whether or not it emerges as a Nambu-Goldstone boson (NGB) of some new dynamics at the TeV scale [?, 75, 177].

The production of Higgs pairs in the VBF channel [?, ?, 75, 177–179] proceeds via the soft emission of two vector bosons from the incoming protons followed by the hard  $VV \rightarrow hh$  scattering, with  $V = W, Z$ . In the SM, the VBF inclusive cross section at 14 TeV is around 2 fb, more than one order of magnitude smaller than in gluon fusion. Higher order QCD corrections are moderate ( $\sim 10\%$ ) as expected for an electroweak process. Despite the small rate, Higgs pair production via VBF is relevant since even small modifications of the SM couplings induce a striking increase of the cross section as a function of the di-Higgs mass, for instance in models where the Higgs is a composite pseudo-NGB (pNGB) of new strong dynamics at the TeV scale [?]. In these theories, the Higgs anomalous couplings imply a growth of the  $VV \rightarrow hh$  cross section with the partonic center-of-mass energy,  $\hat{\sigma} \propto \hat{s}/f^4$ , where  $f$  is the pNGB decay constant [75]. This enhanced sensitivity to the underlying strength of the Higgs interactions makes double Higgs production via VBF a key process to test the nature of the electroweak symmetry breaking dynamics and to constrain the  $hhVV$  quartic coupling in a model-independent way.

Here we review the feasibility of measuring and interpreting the VBF Higgs pair production at the HL-LHC in the  $hh \rightarrow b\bar{b}b\bar{b}$  final state. While QCD multi-jet backgrounds are huge, this final state turns out to be within the reach of the HL-LHC thanks to the unique VBF topology, characterized by two forward jets well separated in rapidity and with a large invariant mass and a reduced hadronic activity in the central region. In addition, the di-Higgs system will acquire a substantial boost in the presence of BSM dynamics, and jet substructure techniques [?, 180, 181] make possible to fully exploit the high-energy limit and optimize the signal significance.

Here the theoretical description of di-Higgs VBF production follows [177], where general parametrization of the couplings of a light Higgs-like scalar  $h$  to the SM vector bosons and fermions was introduced. In this formalism, assuming that the couplings of the Higgs boson to SM fermions scale with their masses

and do not violate flavor, the resulting effective Lagrangian in [177] is given by

$$\begin{aligned} \mathcal{L} \supset & \frac{1}{2}(\partial_\mu h)^2 - V(h) + \frac{v^2}{4} \text{Tr}\left(D_\mu \Sigma^\dagger D^\mu \Sigma\right) \left[1 + 2c_V \frac{h}{v} + c_{2V} \frac{h^2}{v^2} + \dots\right] \\ & - m_i \bar{\psi}_{Li} \Sigma \left(1 + c_\psi \frac{h}{v} + \dots\right) \psi_{Ri} + \text{h.c.}, \end{aligned} \quad (76)$$

where  $V(h)$  denotes the Higgs potential,

$$V(h) = \frac{1}{2}m_h^2 h^2 + c_3 \frac{1}{6} \left(\frac{3m_h^2}{v}\right) h^3 + c_4 \frac{1}{24} \left(\frac{3m_h^2}{v^2}\right) h^4 + \dots \quad (77)$$

The parameters  $c_V$ ,  $c_{2V}$ ,  $c_\psi$ ,  $c_3$ , and  $c_4$  are in general arbitrary coefficients, normalized so that they equal 1 in the SM. In this contribution we focus on the determination of  $c_{2V}$  by means of di-Higgs VBF production in the  $b\bar{b}b\bar{b}$  final state.

#### 4.4.4.2 Analysis strategy

Signal and background events are simulated at leading-order (LO) by means of matrix-element generators and then processed through a parton shower (PS). The dominant background is given by QCD multijet production, while other backgrounds, such as top-quark pair production and Higgs pair production via gluon-fusion, turn out to much smaller. After the parton shower, events are clustered with FASTJET v3.0.1 [182] using the anti- $k_t$  algorithm [?] with a jet radius  $R = 0.4$ . The resulting jets are then processed through a  $b$ -tagging algorithm, where a jet is tagged as  $b$ -jet with probability  $\varepsilon(b\text{-tag})$  if it contains a  $b$ -quark with  $p_T^b > 15$  GeV. In order to account for  $b$ -jet misidentification (fakes), jets which do not meet this requirement are also tagged as  $b$ -jets with probability  $\varepsilon(c\text{-mistag})$  or  $\varepsilon(q, g\text{-mistag})$  depending on whether they contain a  $c$ -quark or not. Only events with four or more jets, of which at least two must be  $b$ -tagged, are retained at this stage.

Subsequently to  $b$ -tagging, events are classified through a scale-invariant tagging procedure [180, 181]. This step is crucial to efficiently reconstruct the Higgs boson candidates and suppress the otherwise overwhelming QCD backgrounds while at the same time taking into account all the relevant final-state topologies. The basic idea of this method is to robustly merge three event topologies – boosted, intermediate and resolved – into a common analysis. This is particularly relevant for our study given that the degree of boost of the di-Higgs system strongly depends on the deviations of  $c_{2V}$  from its SM value.

Acceptance cuts to match detector coverage are applied to signal and background events. We require the  $p_T$  of both the light and  $b$ -tagged jets to be larger than 25 GeV, while the pseudo-rapidities of light and  $b$ -tagged jets,  $\eta_j$  and  $\eta_b$ , are limited by the coverage of the forward calorimeters and by the tracking region where  $b$ -tagging can be applied respectively. We also impose a set of selection cuts tailored to the VBF topology which is characterized by two forward and very energetic jets with little hadronic activity between them. In particular, we cut on the rapidity separation  $\Delta y_{jj} \equiv |y_j^{\text{lead}} - y_j^{\text{sublead}}|$  and the invariant mass  $m_{jj}$  of the two VBF-tagging jets, and impose a central jet veto (CJV) on the hardest non-VBF light jet in the central region. The VBF tagging jets are defined as the pair of light jets satisfying the acceptance cuts of with the largest invariant mass  $m_{jj}$ . Moreover, a CJV cut is imposed in VBF analyses to veto light jets, with pseudo-rapidity  $\eta_{j_3}$ , lying between those of the VBF-tagging jets,  $\eta_j^{\text{max}} > \eta_{j_3} > \eta_j^{\text{min}}$ , above a given  $p_T$  threshold.

Figure 64 (right) shows the  $m_{hh}$  distribution after all analysis cuts for both for the signal (SM and  $c_{2V} = 0.8$ ) and the total background. For  $c_{2V} = 0.8$ , the crossover between the resolved and boosted categories takes place at  $m_{hh} \simeq 1.5$  TeV, although this specific value depends on the choice of the jet radius  $R$  [180]. Unsurprisingly, we find that background events are always dominated by the resolved topology. The decomposition of the total background in terms of individual processes as a function of

$m_{hh}$  is shown in Fig. 64 (left), where each component is stacked on top of each other. We see how the  $4b$  background dominates for large  $m_{hh}$  while the  $2b2j$  one is instead the most important for small  $m_{hh}$ .

		Cross-sections (fb)			
		Acceptance	VBF	Higgs reco.	$m_{hh}$ cut
14 TeV	Signal SM	0.011	0.0061	0.0039	0.0020
	Signal $c_{2V} = 0.8$	0.035	0.020	0.017	0.011
	Bkgd (total)	$1.3 \times 10^5$	$4.9 \times 10^3$	569	47

Table 31: Cross sections, in fb, after the successive application of the acceptance, VBF cuts, and Higgs reconstruction cuts for signal events (SM and  $c_{2V} = 0.8$ ) and for the total background.

In Table 31 we show the cross-sections after the successive application of the acceptance, VBF cuts, and Higgs reconstruction cuts for signal events (SM and  $c_{2V} = 0.8$ ) and for the total background. We find that the VBF di-Higgs signal in the SM is rather small already after the basic acceptance cuts. On the other hand, the signal event yield is substantially increased for  $c_{2V} \neq 1$  as illustrated by the benchmark value of  $c_{2V} = 0.8$  leading to more than a factor 3(5) enhancement compared to the SM after the acceptance (all analysis) cuts. The fact that this cross-section enhancement for the  $c_{2V} = 0.8$  scenario is more marked at the end of the analysis is not a coincidence: our selection cuts have been designed so as to improve the sensitivity to  $c_{2V}$  by increasing the signal significance in the large- $m_{hh}$  region. Note however that even after all analysis cuts the background is still much larger than the signal (either SM or  $c_{2V} = 0.8$ ) at the level of inclusive rates. It is only by exploiting the large- $m_{hh}$  region that the former can be made small enough to achieve high signal significances.

#### 4.4.4.3 Projections for the HL-LHC

Following the analysis strategy outlined in the previous section, we can now estimate the expected precision on the determination of the  $c_{2V}$  coupling at the HL-LHC. In the left panel of Fig. 65 we show the posterior probabilities for  $c_{2V}$  at 14 TeV, from where we can assess the expected precision its measurement at the HL-LHC assuming SM couplings. The corresponding 68% probability intervals for the determination of  $c_{2V}$  at the HL-LHC are listed in Table 32 for two different scenarios for the background cross section.

	68% probability interval on $\delta_{c_{2V}}$	
	$1 \times \sigma_{\text{bkg}}$	$3 \times \sigma_{\text{bkg}}$
LHC <sub>14</sub>	[−0.37, 0.45]	[−0.43, 0.48]
HL-LHC	[−0.15, 0.19]	[−0.18, 0.20]

Table 32: Expected precision (at 68% probability level) for the measurement of  $\delta_{c_{2V}}$  at the HL-LHC for SM values of the Higgs couplings, for two scenarios for the background cross section.

From Table 32, we find that the  $c_{2V}$  coupling, for which there are currently no direct experimental constraints, can be measured with a precision of around  $^{+19\%}_{-15\%}$  at the HL-LHC. It is interesting to compare these results with the experimental precision expected on the fiducial VBF di-Higgs cross section after all analysis cuts, expressed in terms of  $\mu$ , the signal strength parameter normalized to the SM result. We find that the 95% CL upper limits on  $\mu$  for the nominal background cross section is  $\mu \leq 109$  with 300

$\text{fb}^{-1}$ , and  $\mu \leq 49$  at the HL-LHC. This result highlights that the high precision expected on  $c_{2V}$  can be obtained despite the loose constraints expected on the VBF di-Higgs cross section itself.

The results of Table 32 have been obtained by making full use of the information contained on the di-Higgs invariant mass distribution  $m_{hh}$ . However, the EFT expansion might break down at large enough values of  $m_{hh}$ , corresponding to large partonic center-of-mass energies, and some assessment on the validity of our procedure is thus required. In particular, results can be consistently derived within the EFT framework only if the new physics scale  $\Lambda$  is smaller than the largest value of  $m_{hh}$  included in the analysis. Indeed, constraining  $\Lambda$  requires making assumptions on the structure of the UV dynamics extending the SM [183]. For example, for the case where the new physics is characterized by a single coupling strength  $g_*$  and mass scale  $\Lambda$  [75], one expects  $\delta_{c_{2V}} \approx g_*^2 v^2 / \Lambda^2$ , so that for maximally strongly-coupled UV completions (with  $g_* \simeq 4\pi$ ) it is possible to derive the upper limit  $\delta_{c_{2V}}^{\max} \approx 16\pi^2 v^2 / \Lambda^2$  which connects  $\delta_{c_{2V}}$  with the new physics scale  $\Lambda$ . The validity of the EFT can thus be monitored by introducing a restriction  $m_{hh} \leq m_{hh}^{\max}$ , and then determining how the sensitivity on  $\delta_{c_{2V}}$  varies as a function of  $m_{hh}^{\max}$  [183]. The precision on  $\delta_{c_{2V}}$  is shown in Fig. 65 as a function of  $m_{hh}^{\max}$ , where the gray area indicates the region where  $\delta_{c_{2V}} > \delta_{c_{2V}}^{\max}$ . As expected, increasing  $m_{hh}^{\max}$  leads to stronger constraints. We therefore find that in the kinematic region accessible at the HL-LHC the EFT description of the di-Higgs VBF process should be valid.

#### 4.5 Same-sign WW scattering at HL-LHC: a new strategy for the EFT-based analysis

J. Kalinowski,<sup>a</sup> P. Kozów,<sup>a</sup> S. Pokorski,<sup>a</sup> J. Rosiek,<sup>a</sup> M. Szleper<sup>b</sup> and S. Tkaczyk<sup>c</sup>

<sup>a</sup> Faculty of Physics, University of Warsaw, Warsaw, Poland,

<sup>b</sup> National Center for Nuclear Research, Warsaw, Poland,

<sup>c</sup> Fermi National Accelerator Laboratory, Batavia, IL 60510, USA.

Although any statistically significant deviation in data from the Standard Model(SM) predictions would be a manifestation of a BSM physics, the question is what we can learn about its scale and its strength before discovering new particles. The appropriate tool for answering this question is the Effective Field Theory(EFT) approach: the information about the scale  $\Lambda$  and the strength  $C$  of new physics is encoded in the Wilson coefficients of the higher dimension operators,  $f_i = C^m / \Lambda^n$ . The usefulness of any EFT analysis of a given process relies on the assumption that only a few higher-dimension terms in the expansion  $\mathcal{L} = \mathcal{L}_{SM} + \sum_i f_i^{(6)} \mathcal{O}_i^{(6)} + \sum_i f_i^{(8)} \mathcal{O}_i^{(6)} + \dots$  provide adequate approximation to an unknown UV completion. This assumption introduces a strong model-dependent aspect and therefore it is convenient to introduce the concept of EFT "models" defined by the choice of operators and the values of their Wilson coefficients  $(\mathcal{O}_i^{(d)}, f_i^{(d)})$ . Our focus is on the proper use of the EFT "models" in their range of validity for the WW scattering in purely leptonic W decay channels where the WW invariant mass cannot be determined experimentally [184].

Following a common practice we take one operator at a time setting others to zero, which effectively defines the EFT "model", and consider the process  $pp \rightarrow 2jW^+W^+ \rightarrow 2jl^+\nu l^+\nu'$ . The EFT "model" can be maximally valid up to the invariant mass  $M$  of the  $W^+W^+$  system  $M < \Lambda \leq M^U$ , where  $M^U = M^U(f)$  is the perturbative partial wave unitarity bound in the chosen EFT "model". If the kinematic range  $M_{max}$  at the LHC is greater than  $\Lambda$ , there is necessarily a contribution to observables from the region  $\Lambda < M < M_{max}$ . Two questions arise: 1) what is the discovery region in the space  $(\Lambda, f)$  for the chosen EFT "model", 2) if a deviation from the SM predictions is indeed observed, how to verify the chosen EFT "model" by fitting it to a set of experimental distributions  $D$  and in what range of  $\Lambda, f_i$  such a fit is really meaningful?

For a given EFT "model" the unitarity bound is very different for different helicity amplitudes. As  $M^U$  we take the *lowest* value, universally for all helicity amplitudes. The BSM signal  $S$  of the EFT "model"  $(\mathcal{O}_i^{(d)}, f_i^{(d)})$  can be defined as the deviation of some observable  $D$  from the SM prediction

$S = D^{model} - D^{SM}$ . A quantitative estimate of the signal can be written as

$$D^{model} = \int_{2M_W}^{\Lambda} \frac{d\sigma}{dM} \Big|_{model} dM + \int_{\Lambda}^{M_{max}} \frac{d\sigma}{dM} \Big|_{SM} dM, \quad (78)$$

which comes uniquely from the operator that defines the “model” in its range of validity and assumes only the SM contribution in the region  $M > \Lambda$ . BSM contribution from the region above  $\Lambda$  may enhance the signal, but it may also preclude proper description of the data in the EFT “model”, which makes sense *if and only if* this additional contribution is small enough compared to the contribution from the validity region. For a quantitative estimate of this contribution we define a second estimate in which all the helicity amplitudes above  $\Lambda$  are assumed to remain constant at their respective values they reach at  $\Lambda$

$$D^{model} = \int_{2M_W}^{\Lambda} \frac{d\sigma}{dM} \Big|_{model} dM + \int_{\Lambda}^{M_{max}} \frac{d\sigma}{dM} \Big|_{A=const} dM. \quad (79)$$

For  $\Lambda = \Lambda_{max}$  this prescription regularizes the helicity amplitudes that violate unitarity at  $M^U$ . We adopt the criterion that the EFT “model” is tested for values of  $(\Lambda \leq M^U, f_i)$  when the signals computed from Eq.(78) are statistically consistent within  $2\sigma$  with the signals computed with Eq.(79).

The observability of the EFT “model” predictions imposes some minimum value of  $f_{min}$ , while the description within the EFT “model” imposes some maximum value of  $f_{max}$  such that signal estimates computed from Eqs.(78) and (79) remain statistically consistent. For  $\Lambda = M^U$  a finite interval of  $f_i$  values is possible, while for  $\Lambda < M^U$  the respective limits on  $f_i$  depend on the actual value of  $\Lambda$ . It is illustrated in a cartoon plot in Fig. 66, where the white “triangle” is bounded from above by the unitarity bound  $M^U(f_i)$ , from the left by the signal significance criterion and from the right by the consistency criterion. The EFT “model” could be the right framework to describe the BSM signal as long as the “triangle” shown in our cartoon plot is not empty.

Our preferred strategy for data analysis is as follows:

- a) Measure distributions  $D$  that offer the highest sensitivity to the studied EFT “model”,
- b) if deviations from the SM are observed, fit the values of  $(\Lambda \leq M^U, f_i)$  according to Eq.(79),
- c) using the fitted values of  $f_i$  and  $\Lambda$  recalculate  $D$  templates according to Eq.(78),
- d) check statistical consistency between estimates based on Eqs.(78) and (79).

Physics conclusions from the obtained  $(\Lambda, f_i)$  values can only be drawn if such a consistency is found. Stability of the result against alternative regularization methods would provide a measure of uncertainty of the procedure - too much sensitivity to the region above  $\Lambda$  means the procedure is destined to fail and that data cannot be described within the chosen EFT “model”.

To demonstrate our strategy we considered EFT “models” defined by one-at-a-time dimension-8 operator that affects  $WWWW$  couplings. Details of the simulation of events for the process  $pp \rightarrow jj\mu^+\mu^+\nu\nu$  (at 14 TeV with 3/ab integrated luminosity) and their processing according to our strategy can be found in [184]. Assuming  $\Lambda$  equal to the respective unitarity bounds, the lower and upper limits for the values of  $f$  for each dimension-8 operator, for positive and negative  $f$  values, as well as the applicability “triangles” in the  $(\Lambda, f_i)$  plane for each operator have been calculated. These limits define the (continuous) sets of testable EFT “models” based on the choice of single dimension-8 operators. The “triangles” turned to be rather narrow, but in most cases non-empty.

To summarize: we have introduced the concept of EFT “models” defined by the choice of higher dimension operators and values of the Wilson coefficients and analyzed “models” based on single dimension-8 operators at a time. We argue that usage of EFT “models” in the analysis of purely leptonic  $W$  decay channels requires bounding the possible contribution from the region  $M_{WW} > \Lambda$ , no longer described by the “model”, and ensuring it does not significantly distort the measured distributions compared to what they would have looked from the region of EFT validity alone and propose a data analysis strategy to satisfy the above requirements. We find that, with a possible exception of  $\mathcal{O}_{S1}$ , all dimension-8 operators which affect the  $WWWW$  quartic coupling have regions where a  $5\sigma$  BSM signal can be observed at HL-LHC with  $3 \text{ ab}^{-1}$  of data, while data could be satisfactorily described using the EFT approach.

Acknowledgments: Work partially supported by the National Science Centre (Poland) grants DEC-2015/18/M/ST2/00054, DEC-2016/23/G/ST2/04301 (SP), DEC-2015/19/B/ST2/02848 (JR) and HARMONIA project UMO-2015/18/M/ST2/00518 (JK). ST is supported by Fermi Research Alliance, LLC under Contract No. De-AC02-07CH11359 with the US DoE.

#### 4.6 Testing the universal Higgs nonlinearity

D. Liu,<sup>a</sup> I. Low,<sup>a,b</sup> Z. Yin,<sup>b</sup>

<sup>a</sup> High Energy Physics Division, Argonne National Laboratory, Argonne, IL 60439, USA

<sup>b</sup> Department of Physics and Astronomy, Northwestern University, Evanston, IL 60208, USA.

We initiate a phenomenological study of “universal relations” in composite Higgs models, which are dictated by nonlinear shift symmetries acting on the 125 GeV Higgs boson. These are relations among one Higgs couplings with two electroweak gauge bosons (HV), two Higgses couplings with two electroweak gauge bosons (HHV), one Higgs couplings with three electroweak gauge bosons (HVVV), as well as triple gauge boson couplings (TGC), which are all controlled by a single input parameter: the decay constant  $f$  of the pseudo-Nambu-Goldstone Higgs boson. Assuming custodial invariance in strong sector, the relation is independent of the symmetry breaking pattern in the UV, for an arbitrary symmetric coset  $G/H$ . The complete list of corrections to HV, HHV, HVV and TGC couplings in composite Higgs models is presented to all orders in  $1/f$ , and up to four-derivative level, without referring to a particular  $G/H$ . We then present several examples of universal relations in ratios of coefficients which could be extracted experimentally. Measuring the universal relation requires a precision sensitive to effects of dimension-8 operators in the effective Lagrangian and highlights the importance of verifying the tensor structure of HHV interactions in the standard model, which remains untested to date.

Acknowledgments: This work is supported in part by the U.S. Department of Energy under contracts No. DE-AC02-06CH11357 and No. DE-SC0010143.

#### 4.7 Same-sign WW scattering: A comparison of the HL- and HE-LHC reach for the selected Dim8 operators within the EFT approach

G. Chaudhary,<sup>a</sup> J. Kalinowski,<sup>b</sup> M. Kaur,<sup>a</sup> P. Kozów,<sup>b</sup> K. Sandeep,<sup>a</sup> M. Szleper<sup>c</sup> and S. Tkaczyk<sup>d</sup>

<sup>a</sup> University of Panjab, Chandigarh, India,

<sup>b</sup> Faculty of Physics, University of Warsaw, Warsaw, Poland,

<sup>c</sup> National Center for Nuclear Research, Warsaw, Poland,

<sup>d</sup> Fermi National Accelerator Laboratory, Batavia, IL 60510, USA.

In Sect.4.5 a new strategy for the EFT-based analysis of the same-sign WW scattering in the purely leptonic  $W$  decay channels at the LHC has been proposed. Since in this process the scale of the WW scattering cannot be reconstructed experimentally, the main idea of the proposed strategy is to require that the dominant contribution to the observed signal should come from the EFT controlled region of the phase space. As a result, for the given EFT scale  $\Lambda$  one expects a finite interval of the Wilson coefficient, from  $f_{min}$  to  $f_{max}$ , where the BSM signal is observable and the EFT description can be trusted. Together with the unitarity bound the  $f_{min}$  and  $f_{max}$  eventually will form a “triangle”, as shown in the cartoon plot Fig.66, where the BSM physics can be studied within the chosen EFT “model”.

Following the above strategy we have compared the expected reach the expected reach for the dim-8 operator  $O_{M6}$  at the HL- and HE-LHC assuming the integrated luminosities 3/ab and ??/ab, respectively. Fig.67 shows the respective “triangles”.

## 4.8 Dimension-6 EFT effects on Vector Boson Scattering at high energies

Roberto Covarelli<sup>a</sup> and Raquel Gomez-Ambrosio<sup>b</sup>

<sup>a</sup>*Università di Torino and INFN sezione di Torino, Via Pietro Giuria 1, 10125, Turin, Italy*

<sup>b</sup>*Institute of Particle Physics Phenomenology, Durham University, Durham DH1 3LE, UK*

### Introduction

In this note we assess the sensitivity of vector boson scattering (VBS) processes to different dimension-6 ( $\text{dim} = 6$ ) operators. We focus here on the  $ZZ$  final state, decaying to 4 charged leptons. This experimental channel, currently statistically limited at the LHC [185], will become more interesting at the HL-LHC because of the attainable selection purity. The full reconstruction of the final states also gives access to cleaner observables with respect to final states involving  $W$  bosons, where neutrino 4-momenta must be inferred using approximated methods. This analysis can nevertheless be repeated analogously to other VBS final states.

In [186] we studied the purely electroweak component of the  $pp \rightarrow ZZjj$  process, referred to as VBS(ZZ). Sensitivity to several  $\text{dim} = 6$  operators has been demonstrated, as well as the impact of such EFT contribution on the VBS cross-section and triple and quartic gauge couplings (TGCs and QGCs).

Here we update predictions for the HL-LHC setup and show the kinematic distributions for a handful of relevant operators. For the  $\text{dim} = 6$  parametrisations we use the *Warsaw basis* from [154], following the notation and classification from [187]. Other technical details can be found in the original publication [186].

### Effective Field Theory parametrization

We consider a standard SMEFT parametrisation:

$$\mathcal{L}_{SMEFT} = \mathcal{L}_{SM} + \sum_i \frac{c_i}{\Lambda^2} \mathcal{O}_i^{(6)} + \dots \quad (80)$$

where the  $\mathcal{O}_i^{(6)}$  represent a basis of  $\text{dim} = 6$  operators built from SM fields and respecting the known gauge symmetries<sup>12</sup>, and  $c_i$  are the Wilson coefficients of the theory. Further, the SMEFT amplitudes and cross sections can be parametrised as

$$\mathcal{A}_{EFT} = \mathcal{A}_{SM} + \frac{g'}{\Lambda^2} \mathcal{A}_6 + \frac{g'^2}{\Lambda^4} \mathcal{A}_8 + \dots \quad (81)$$

$$\sigma_{EFT} \sim |\mathcal{A}_{SM}|^2 + 2 \frac{g'}{\Lambda^2} \mathcal{A}_{SM} \mathcal{A}_6 + \frac{g'^2}{\Lambda^4} (2 \mathcal{A}_{SM} \mathcal{A}_8 + |\mathcal{A}_6|^2) + \dots \quad (82)$$

Here, we assume the linear contribution (red) of the EFT effects to be leading. Analysis of the  $\text{dim} = 6$  quadratic terms and the  $\text{dim} = 8$  interference terms (both in blue) will be subject of further studies. In particular,  $\text{dim} = 8$  are commonly associated with quartic gauge couplings and such contribution, albeit subleading, would represent some added value to the linear  $\text{dim} = 6$  prediction.

### Definition of the fiducial region

The VBS(ZZ) process has a very peculiar experimental signature, with two energetic forward jets and 4 identifiable charged leptons ( $\ell, \ell' = \mu$  or  $e$ ). The electroweak component of the process  $pp \rightarrow ZZjj \rightarrow$

<sup>12</sup>In particular, we assume CP symmetry, neglecting the CP-odd operators since their impact on VBS cross-sections and differential distributions is negligible. However it is well known that certain variables of these processes (namely spin correlations and polarizations) can be sensible to CP-violation.

$\ell\bar{\ell}\ell'\bar{\ell}'jj$  is defined and isolated through some experimental cuts. The ones used in the CMS analysis (in the measurement of the fiducial cross-section) can be found in [185]. Here we define a similarly VBS-enriched region, with a relaxed  $m_{jj}$  selection: Editors, I'd like to have this in 2 columns but I don't want to mess up anything.... usepackage{multicol} didnt work unfortunately

- $p_T(j) > 30 \text{ GeV}$
- $\Delta\eta(j_1j_2) > 2.4$
- $m_{jj} > 100 \text{ GeV}$
- *on-shell*  $Z_1, Z_2$

### EFT analysis

In tables 33 and 34 we show the sensitivities to different  $\text{dim} = 6$  operators of the VBS(ZZ) process, as well as of its main background at LHC: the diboson production channel from quark-antiquark annihilation associated to gluon radiation (studied in depth by CMS for LHC runs I and II in [188], QCD(ZZ)).

Further, in figure 69 we show differential distributions for a subset of the previous operators. In particular we chose the three operators that directly affect triple and quartic gauge couplings: this as well

- $\mathcal{O}_W = \epsilon^{ijk} W_\mu^{i\nu} W_\nu^{j\rho} W_\rho^{k\mu}$
- $\mathcal{O}_{HW} = H^\dagger H W_{\mu\nu}^I W^{\mu\nu I}$
- $\mathcal{O}_{HWB} = H^\dagger \tau^I H W_{\mu\nu}^I B^{\mu\nu}$

However, as reported in tables 33 and 34, there are other relevant operators for the VBS process, for example  $\mathcal{O}_{\ell\ell}$ , the 4-lepton operator that affects  $G_F$ , or  $\mathcal{O}_{HB}$  that enters the  $Z$  boson propagator. More details can be found for example in [72].

Figure 69 should be interpreted as follows: we select one paradigmatic operator (for example  $\mathcal{O}_W$ ), and see how much does its interference term affect the VBS and diboson signals (2.5% in this case). As the VBS(ZZ) cross section is still mostly unconstrained experimentally, while the QCD(ZZ) has a 21% uncertainty in the 2-jet bin [188], we know the bounds within which we can vary this coefficient. If we assume for example a 10% positive interference with the total cross-section, we observe that such a small contribution to the total cross-section can represent a large modification in certain bins of the differential distributions. This advantage is twofold: with this procedure we can select the optimal bin(s) for the study and fit of each EFT operator; and, by applying unitarity considerations, we can constrain the values of the Wilson coefficients further. In our example, a contribution of 10% in  $\mathcal{O}_W$ , still allowed for the total rate, has a large impact on the high energy bins of the  $p_T(Z_1)$  distribution.

### Conclusions

The VBS(ZZ) and QCD(ZZ) final states, still largely unexplored at the LHC, will be an important source of constraints on  $\text{dim} = 6$  EFT operators at the HL-LHC. We have shown the impact that values of Wilson coefficients still experimentally allowed have on differential distributions that are easily accessible experimentally in this channel.

VBS Signal	Signal strengths (Linear EFT)
Class 1:	$\mathcal{O}_W = c_W \cdot 2.5\%$
Class 3:	$\mathcal{O}_{HD} = c_{HD} \cdot 6.0\%$
Class 4:	$\mathcal{O}_{HW} = c_{HW} \cdot 5\%, \mathcal{O}_{CHB} = c_{HB} \cdot 0.2\%, \mathcal{O}_{HWB} = c_{HWB} \cdot 14\%$
Class 7:	$\mathcal{O}_{Hl^{(3)}} = c_{Hl^{(3)}} \cdot 48\%, \mathcal{O}_{Hq^{(1)}} = c_{Hq^{(1)}} \cdot 2\%,$ $\mathcal{O}_{Hq^{(3)}} = c_{Hq^{(3)}} \cdot 46\%, \mathcal{O}_{Hu} = c_{Hu} \cdot 0.8\%$
Class 8a: $(L\bar{L})(L\bar{L})$	$(G_F \rightarrow) \mathcal{O}_{\ell\ell} = c_{\ell\ell} \cdot 24\%, \mathcal{O}_{qq^{(1)}} = c_{qq^{(1)}} \cdot 12\%,$ $\mathcal{O}_{qq^{(11)}} = c_{qq^{(11)}} \cdot 14\%, \mathcal{O}_{qq^{(33)}} = c_{qq^{(33)}} \cdot 100\%, \mathcal{O}_{qq^{(31)}} = c_{qq^{(31)}} \cdot 75\%$

Table 33: Different sensitivities to each of the Warsaw basis operators. The operators that are not listed do not intervene in the process, or do it in a negligible way. Each sensitivity  $\epsilon_i$  is calculated as  $\epsilon_i = \frac{|\sigma_{EFT} - \sigma_{SM}|}{\sigma_{SM}}$ , and they include a standard EFT prefactor  $\frac{v^2}{\Lambda^2}|_{\Lambda=1TeV}$  which needs to be taken into account if substituting values for the  $c_i$  in the table. NB: we quote the absolute value for the sensitivities  $\epsilon$ .

ZZ Diboson	Sensitivities (Linear EFT)
Class 1:	$\mathcal{O}_G = 2.5\%, \mathcal{O}_W = 2.5\%$
Class 3:	$\mathcal{O}_{HD} = 6.0\%$
Class 4:	$\mathcal{O}_{CHW} = 0.2\%, \mathcal{O}_{CHG} = 8\%, \mathcal{O}_{CHB} = 0\%, \mathcal{O}_{CHWB} = 12\%$
Class 7:	$\mathcal{O}_{Hl^{(3)}} = c_{Hl^{(3)}} \cdot 25\%, \mathcal{O}_{Hq^{(1)}} = c_{Hq^{(1)}} \cdot 3\%,$ $\mathcal{O}_{Hq^{(3)}} = c_{Hq^{(3)}} \cdot 31\%, \mathcal{O}_{Hu} = c_{Hu} \cdot 1.1\%$
Class 8a: $(L\bar{L})(L\bar{L})$	$(G_F \rightarrow) \mathcal{O}_{\ell\ell} = c_{\ell\ell} \cdot 12\%, \mathcal{O}_{qq^{(1)}} = c_{qq^{(1)}} \cdot 1.0\%,$ $\mathcal{O}_{qq^{(11)}} = c_{qq^{(11)}} \cdot 1.3\%, \mathcal{O}_{qq^{(33)}} = c_{qq^{(33)}} \cdot 8.4\%, \mathcal{O}_{qq^{(31)}} = c_{qq^{(31)}} \cdot 8.0\%$

Table 34: Sensitivities to the different dim = 6 operators in the diboson production channel, main background for the VBS(ZZ) at LHC. A large sensitivity does not necessarily mean that a large EFT effect is expected, since the corresponding Wilson coefficient might as well be very small.

THIS IMAGE  
NEEDS  
TO BE  
REPLACED

THIS IMAGE  
NEEDS  
TO BE  
REPLACED

Fig. 27:  $\chi^2$  dependence on CP-violating parameters taking one parameter non-zero at a time at HL ( $3 \text{ ab}^{-1}$ ) and HE ( $15 \text{ ab}^{-1}$ ) LHC. Preliminary 89

THIS IMAGE  
NEEDS  
TO BE  
REPLACED

Fig. 28:  $1\sigma$  reach on  $\tilde{c}_{Z\gamma}$  and  $\tilde{c}_{ZZ}$  at HL ( $3 \text{ ab}^{-1}$ ) and HE ( $15 \text{ ab}^{-1}$ ) LHC. Preliminary  
90

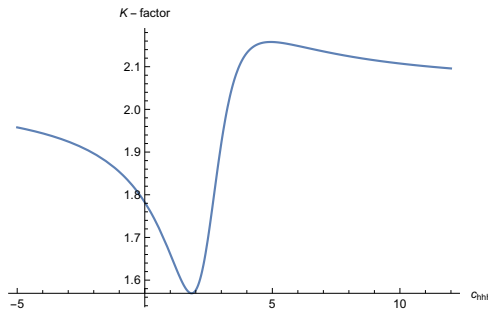
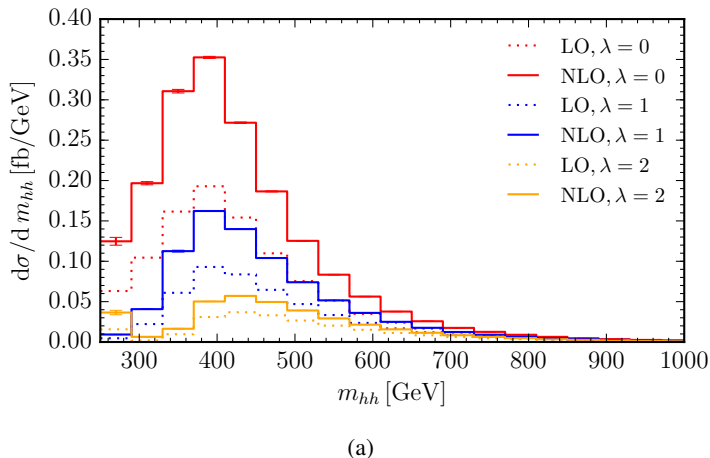


Fig. 29: Variation of the NLO K-factor with the trilinear coupling,  $\sqrt{s} = 14$  TeV.



(a)

Fig. 30: Higgs boson pair invariant mass distributions for various values of  $\lambda$  (relative to  $\lambda_{\text{SM}}$ ) at 14 TeV.

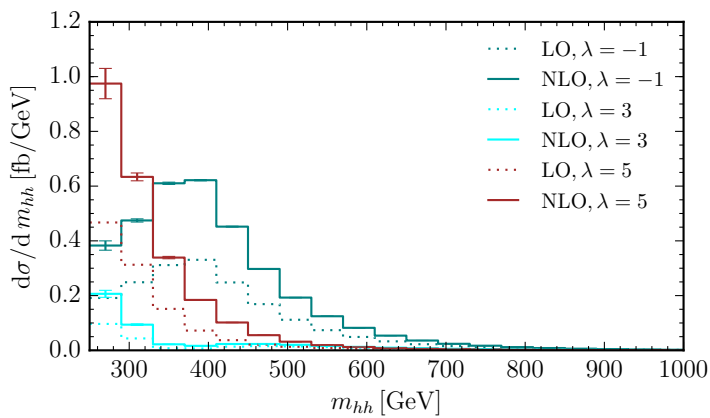


Fig. 31: Higgs boson pair invariant mass distributions for  $\lambda/\lambda_{\text{SM}} = -1, 3, 5$  at 14 TeV.

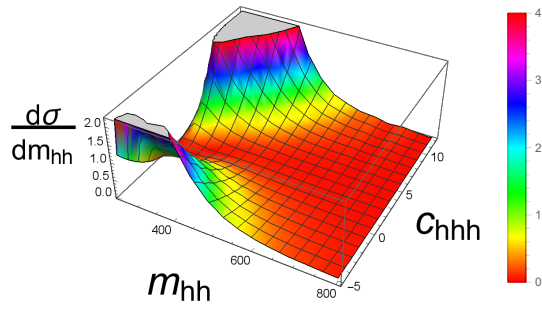


Fig. 32: 3-dimensional visualisation of the  $m_{hh}$  distribution at 14 TeV, as a function  $c_{hhh}$ .

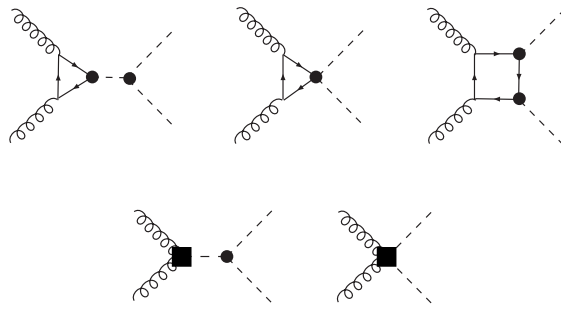


Fig. 33: Higgs-pair production in gluon fusion at leading order in the non-linear EFT Lagrangian.

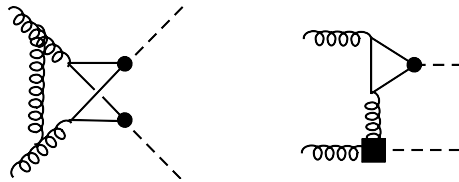


Fig. 34: Examples of virtual diagrams contributing at NLO QCD.

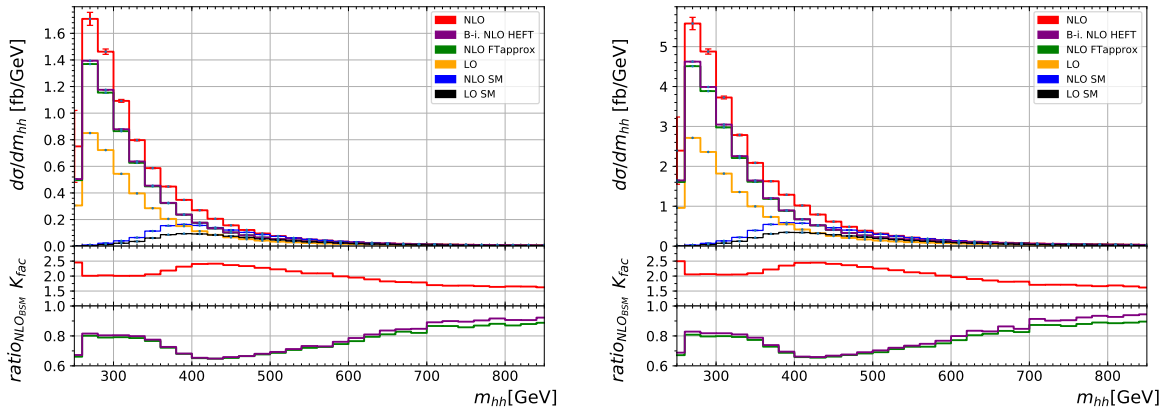


Fig. 35: Higgs boson pair invariant mass distributions for benchmark point 7,  $c_{hhh} = 5, c_t = 1, c_{tt} = 0, c_{ggh} = 2/15, c_{gghh} = 1/15$ , at 14 TeV (left) and 27 TeV (right).

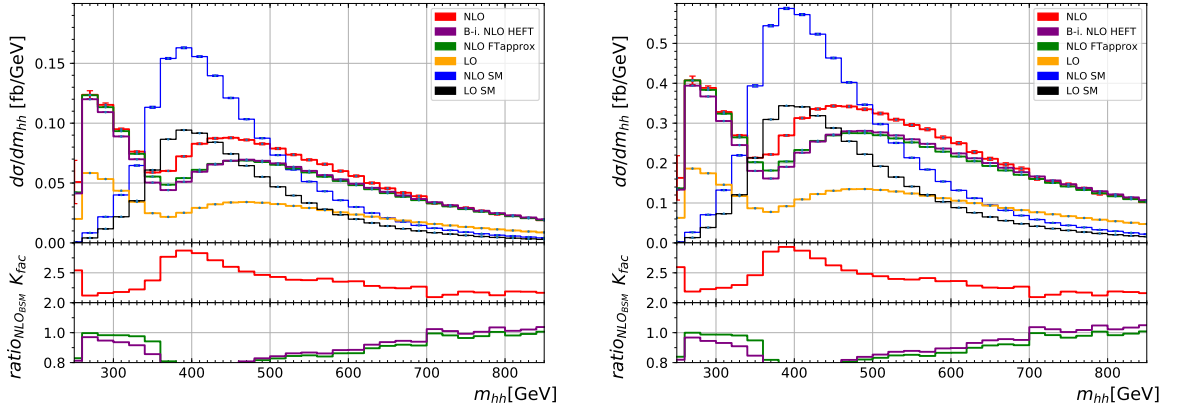


Fig. 36: Higgs boson pair invariant mass distributions for benchmark point 8a,  $c_{hhh} = 1$ ,  $c_t = 1$ ,  $c_{tt} = 0.5$ ,  $c_{ggh} = 4/15$ ,  $c_{gggh} = 0$ , at 14 TeV (left) and 27 TeV (right).

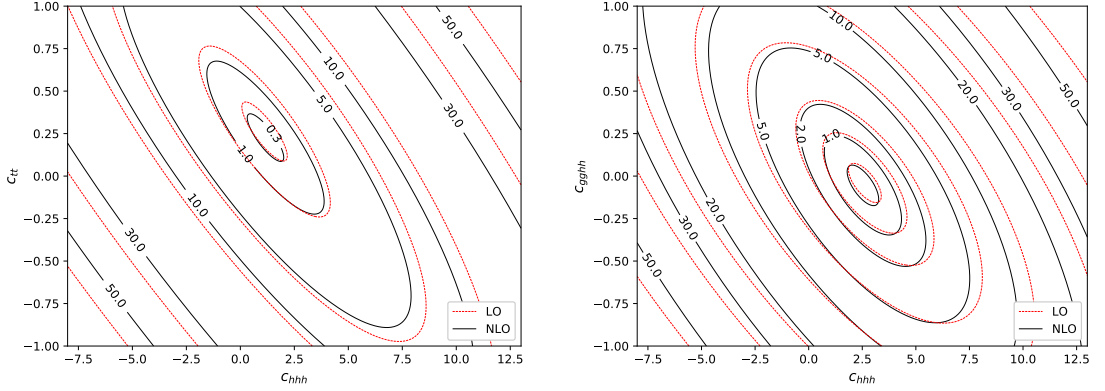


Fig. 37: Iso-contours of  $\sigma/\sigma_{SM}$ : (a)  $c_{hhh}$  versus  $c_{tt}$  and (b)  $c_{hhh}$  versus  $c_{gghh}$  at  $\sqrt{s} = 14$  TeV.

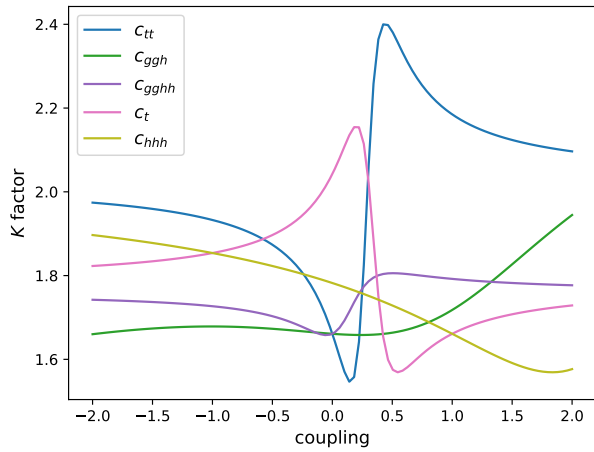


Fig. 38: K-factors for the total cross section at  $\sqrt{s} = 14$  TeV as a function of the different couplings.

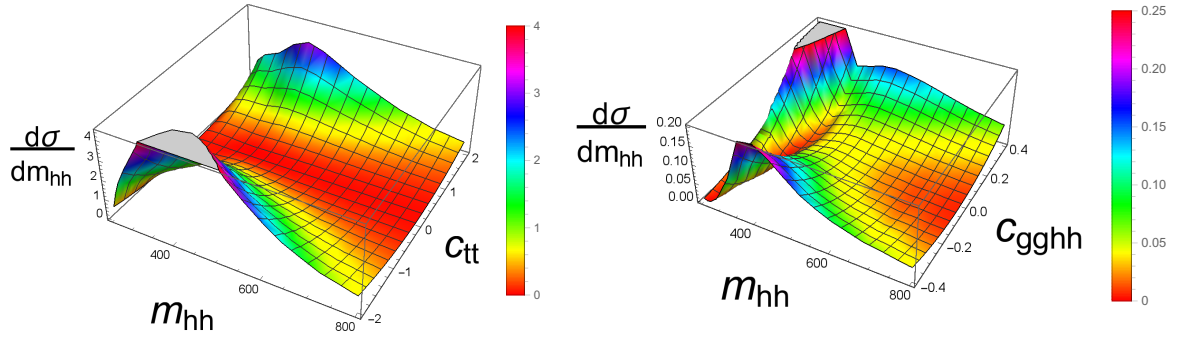


Fig. 39: 3-dimensional visualisation of the  $m_{hh}$  distribution (in units of  $\text{fb}/\text{GeV}$ ) at 14 TeV as a function of (a)  $c_{tt}$  and (b)  $c_{gggh}$ . In case (a) all other couplings are fixed to their SM values, in case (b)  $c_{hhh} = 2.4$ .

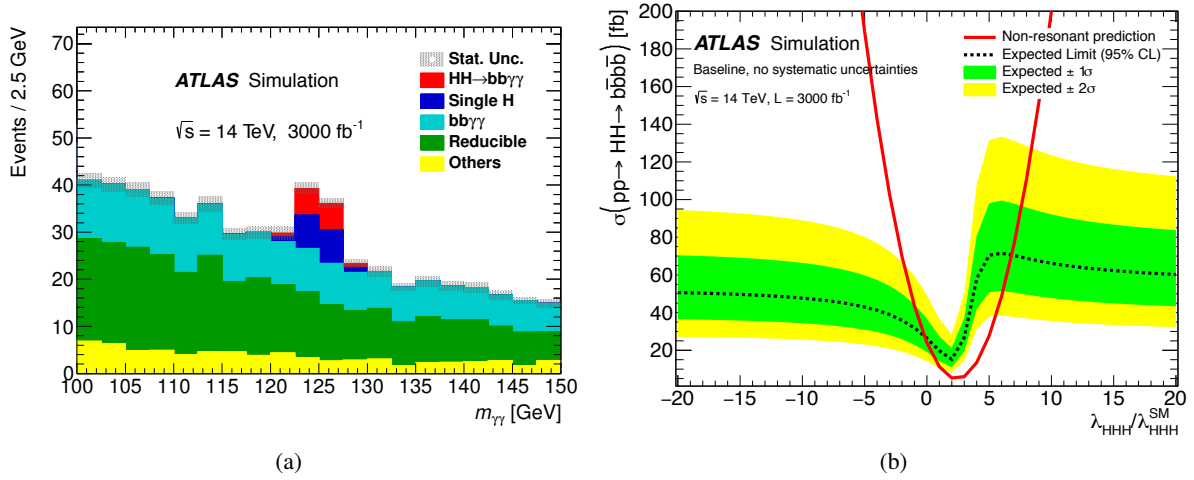


Fig. 40: (a) **PLACEHOLDER** Diphoton invariant mass distribution after selection, for the Standard Model HH signal and different background (plot from [94]). (b) **PLACEHOLDER** Expected 95% CL upper limit on the cross-section  $\sigma(\text{HH})$  with  $3000 \text{ fb}^{-1}$  of data, as a function of the Higgs self-coupling constant modifier  $\kappa_\lambda$ . The non-resonant HH prediction shows the theoretical cross-section for di-Higgs production as function of  $\kappa_\lambda$  (plot from [94]).

Fig. 41: **PLACEHOLDER** Invariant mass distribution of the four leptons selected at the end of the CMS analysis for the  $bb4l$  final state.

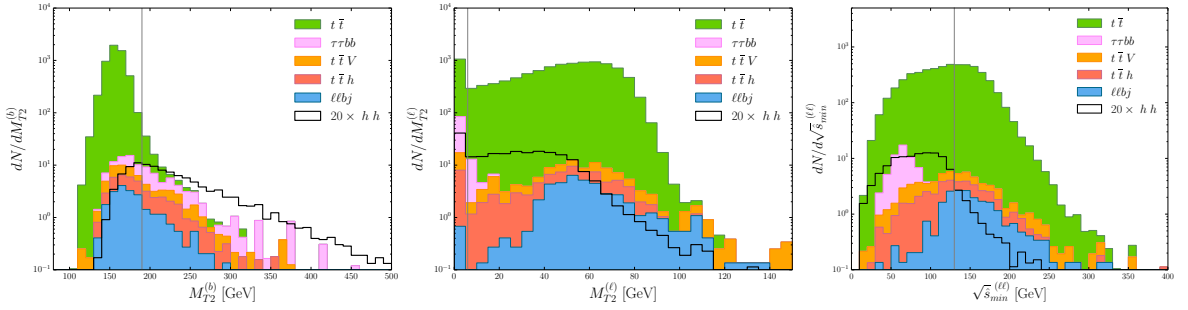


Fig. 42: Distributions for signal ( $hh$ ) and all backgrounds ( $t\bar{t}$ ,  $t\bar{t}h$ ,  $t\bar{t}V$ ,  $\ell\ellbj$  and  $\tau\taubb$ ) for  $M_{T2}^{(b)}$ ,  $M_{T2}^{(\ell)}$  and  $\sqrt{s}_{min}^{(\ell\ell)}$  after loose baseline selection cuts defined in Ref. [100]. The vertical lines at  $M_{T2}^{(b)} = 190$  GeV,  $M_{T2}^{(\ell)} = 6$  GeV and  $\sqrt{s}_{min}^{(\ell\ell)} = 130$  GeV mark the optimized cuts.

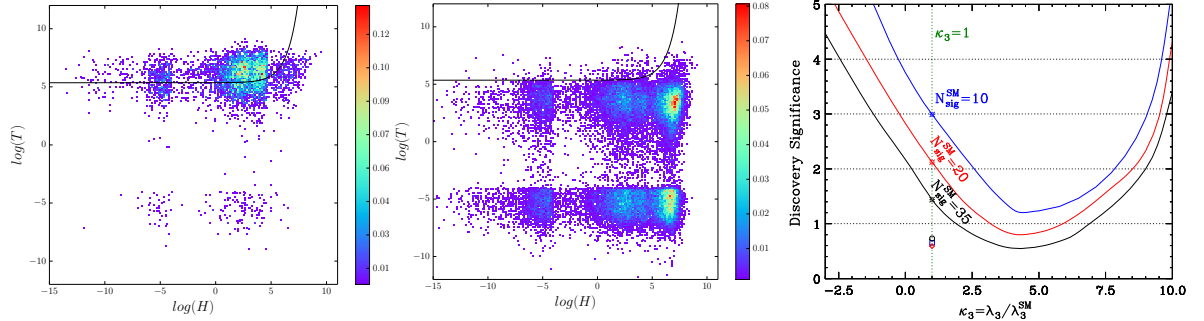


Fig. 43: Scatter distribution of  $(\log H, \log T)$  for signal ( $hh$  in the left) and backgrounds ( $t\bar{t}$ ,  $t\bar{t}h$ ,  $t\bar{t}V$ ,  $\ell\ellbj$  and  $\tau\taubb$  in the middle) after loose baseline selection cuts. The right panel shows the expected discovery significance at the 14 TeV LHC with  $3 \text{ ab}^{-1}$  as a function of the triple Higgs coupling  $\kappa_3$ . We obtain each curve by applying the same set of cuts optimized for the SM point ( $\kappa_3 = 1$ ) to non-SM points ( $\kappa_3 \neq 1$ ) for  $N_{sig}^{SM} = 35$  in black,  $N_{sig}^{SM} = 20$  in red and  $N_{sig}^{SM} = 10$  in blue. The curves in the left and middle panel are the optimized cuts for the  $N_{sig}^{SM} = 20$  case. The three symbols  $\diamond$ ,  $\circ$  and  $\square$  display the signal significance using CMS-NN [97], CMS-BDT [98] and BDT [99], respectively.

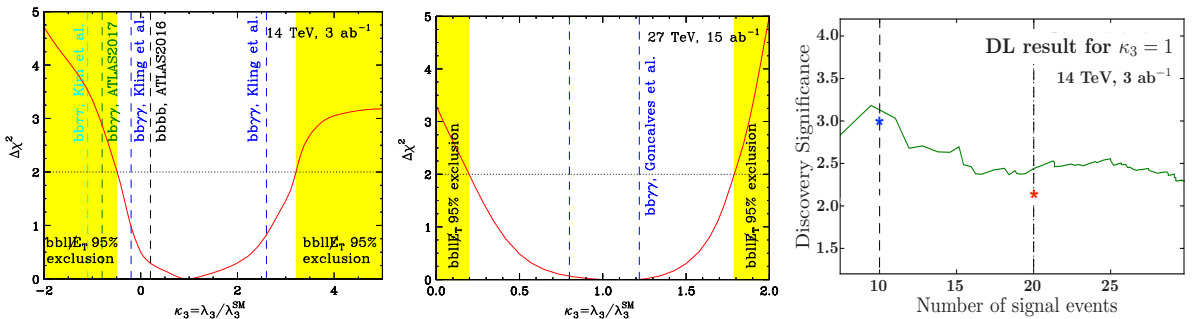


Fig. 44: Significance for observing an anomalous Higgs self-coupling at the 14 TeV LHC with an integrated luminosity of  $3 \text{ ab}^{-1}$  (left) and at 27 TeV with  $15 \text{ ab}^{-1}$  (middle). Right: the effect of using a Deep Learning algorithm to improve the discovery significance for  $\kappa_3 = 1$  shown in the right panel of Fig. 43.

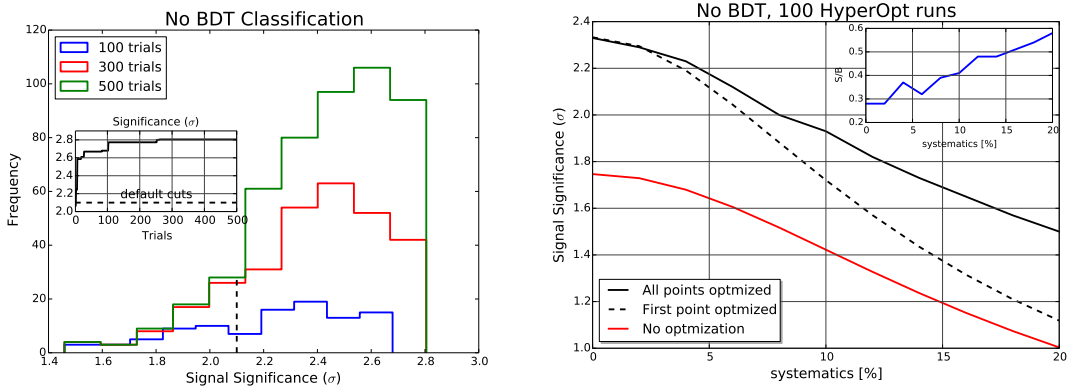


Fig. 45: **Left panel:** The left panel shows the optimized search with the TPE algorithm in HyperOpt with no systematic errors. The inset frame in the left plot shows the significance as a function of the number of trials.  $S/\sqrt{B}$  is used to compute the signal significance. The black dashed line represents the results obtained with the cuts of Azatov *et. al.*, ref. [92]. **Right panel:** The  $S/\sqrt{B + (\varepsilon_B B)^2}$  significance metric as a function of  $\varepsilon_B$ , the systematic uncertainty in the total background rate. The red line represents the default cuts of Azatov *et. al.*, the black dashed assumes an optimized strategy just for the 0% systematics point, while for the solid upper line, the algorithm was solicited to learn the best cuts for each systematics level from 0 to 20%. In the inner plot we show the  $S/B$  ratio for the point-to-point optimization case.

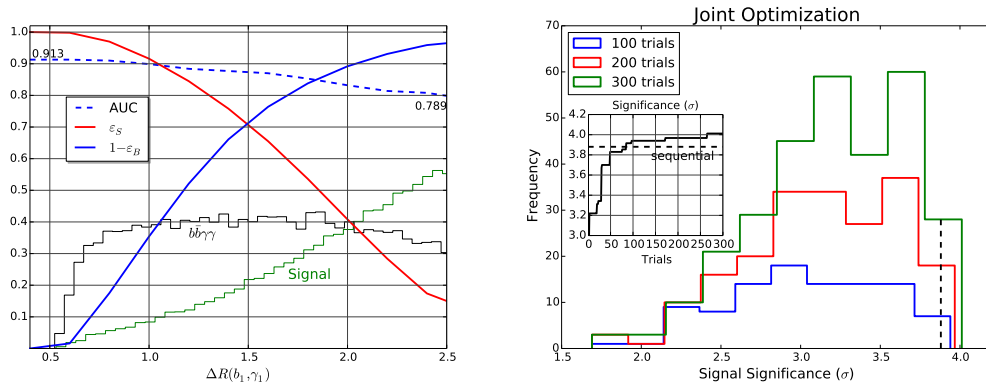


Fig. 46: **Left panel:** We show the results of the effects of imposing hard cuts on  $\Delta R_{b_1\gamma_1}$  for the BDT performance, see [120] for further details. **Right panel:** The histogram of number of cut strategies producing a given significance interval in a BDT-aided classification analysis. The inset plot shows the significance as a function of the number of HyperOpt trials. No systematics are assumed, the backgrounds are those of ref. [92] and the  $S/\sqrt{B}$  used to compute the signal significances. The black dashed line represents the results obtained with the default cuts of Azatov *et. al.*, ref. [92].

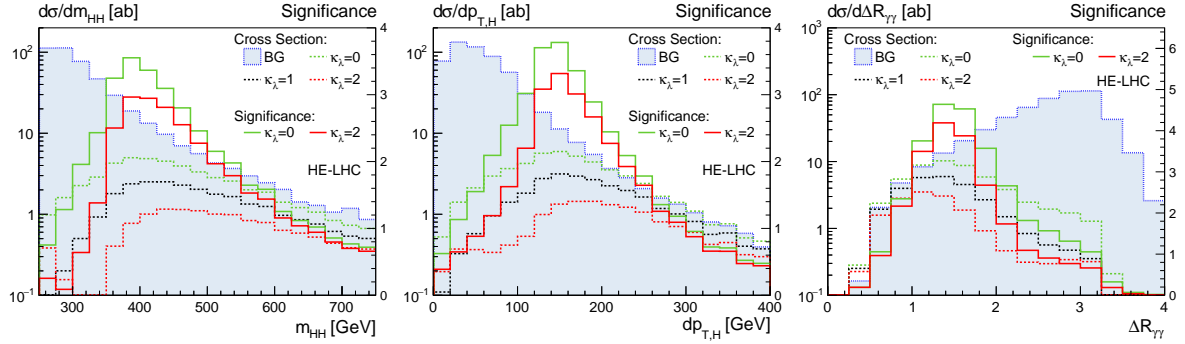


Fig. 47: Kinematic distributions (dashed lines with left vertical axes) and significance distribution (solid lines with right vertical axes) assuming a Higgs self-coupling with  $\kappa_\lambda = 0, 1, 2$  for the HE-LHC. The significance describes the discrimination of an anomalous self-coupling  $\kappa_\lambda \neq 1$  from the SM hypothesis  $\kappa_\lambda = 1$ .

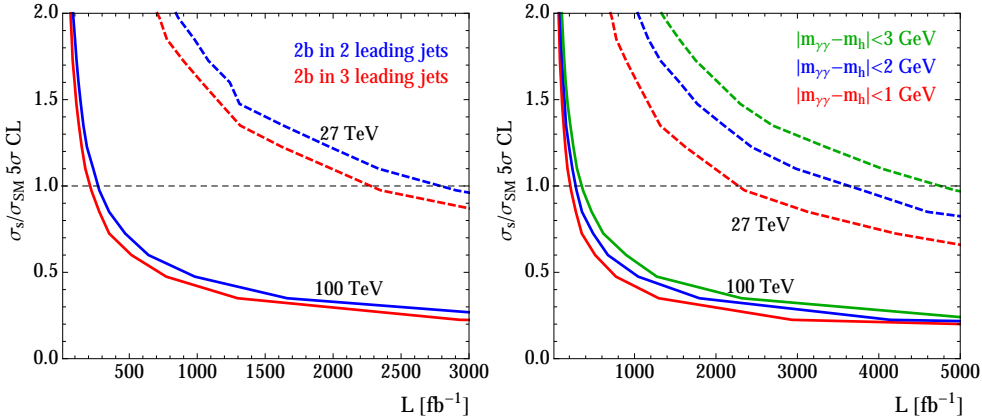


Fig. 48: Luminosity required for a  $5\sigma$  discover of Higgs pair production for the HE-LHC (dashed) and a 100 TeV collider (full). Left: sensitivity in terms of the total rate, demanding two  $b$ -tags among the two or three leading jets and assuming  $|m_{\gamma\gamma} - m_h| < 1$  GeV. Right: sensitivity for three mass windows  $|m_{\gamma\gamma} - m_h| < 1, 2, 3$  GeV. We assume the SM hypothesis with  $\kappa_\lambda = 1$  and use a binned log-likelihood analysis of the  $m_{hh}$  distribution.

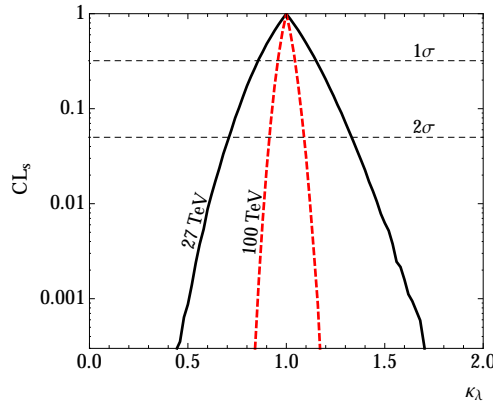


Fig. 49: Confidence level for separating an anomalous Higgs self-coupling hypothesis from the Standard Model  $\kappa_\lambda = 1$ .

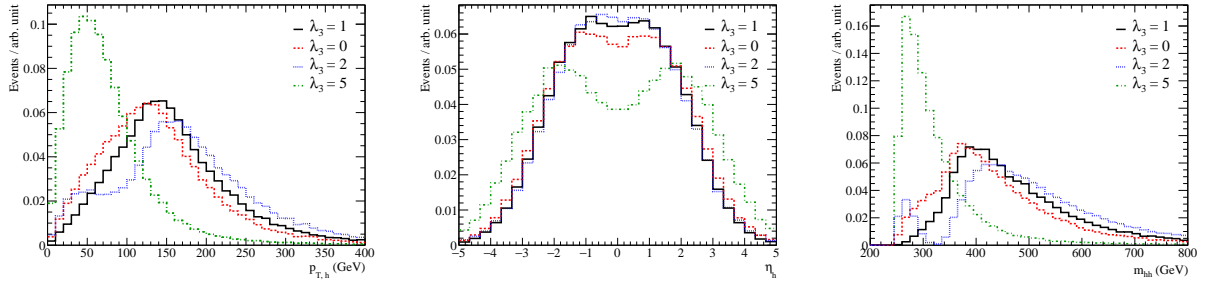


Fig. 50: (Left:) The transverse-momentum distribution of the true Higgs bosons generated in our 27 TeV samples, prior to showering and detector smearing, for several different values of  $\lambda_3$ . (Center:) The same, but for the Higgs pseudorapidity. Right: The same, but for the distribution of the true Higgs pair invariant mass.

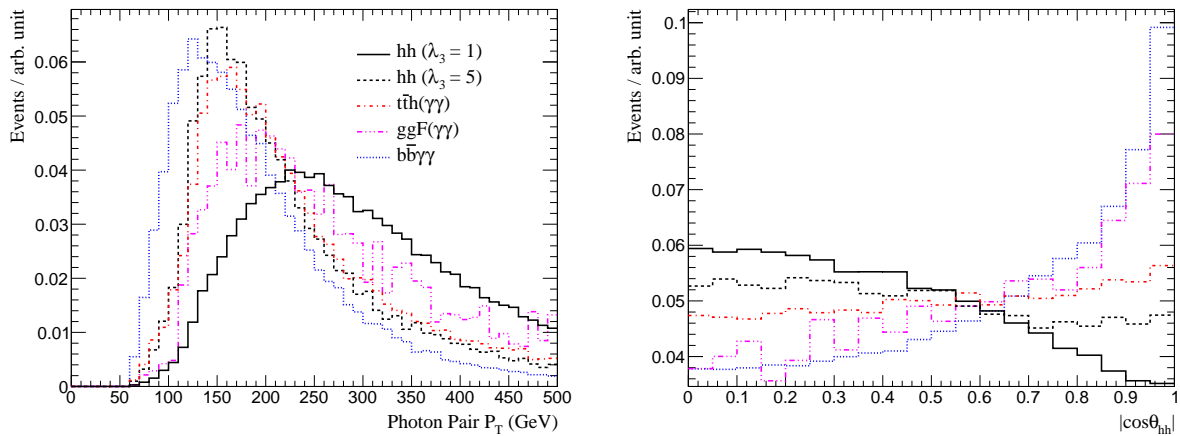


Fig. 51: Normalized distributions of (Left:) the  $p_T$  of the reconstructed  $h \rightarrow \gamma\gamma$  and (Right:) the magnitude of  $\cos\theta_{hh}$ , the Higgs decay angle defined in the text. We show the distributions for the signal with  $\lambda_3 = 1$  and 5 as well as several representative backgrounds.

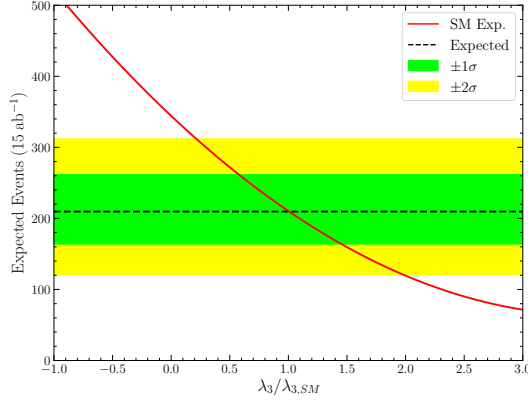


Fig. 52: The expected number of signal events in a hypothetical experiment assuming the signal and background rates computed in Table 22 at  $L = 15 \text{ ab}^{-1}$  for HE-LHC with the regular detector performance assumption. The black dashed line indicates the expected number of events from signal while the green (yellow) regions show the  $1\sigma$  ( $2\sigma$ ) uncertainty regions arising from a likelihood scan with the statistical and MC uncertainties on the signal and background counts. The red curve shows the expected number of events from signal in a background free measurement as a function of  $\lambda_3$ , accounting for the changes in the signal acceptance due to kinematic differences at different  $\lambda_3$

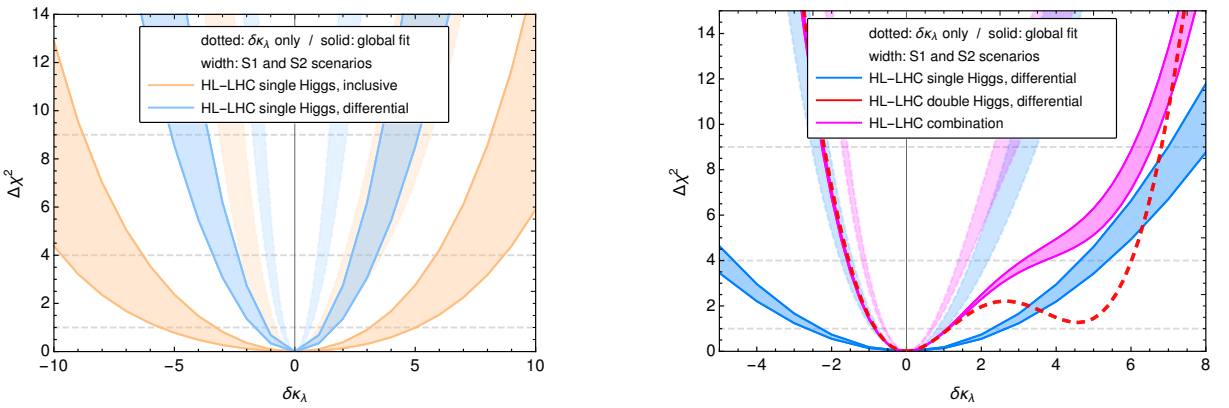


Fig. 53:  $\chi^2$  analysis of the Higgs self-coupling  $\delta\kappa_\lambda$  using single- and double-Higgs processes for the HL-LHC at 13 TeV and  $3 \text{ ab}^{-1}$ . **Left:** Comparison of the constraints obtained using differential single-Higgs processes (green), with the ones using differential double-Higgs data together with inclusive single-Higgs measurements (blue). **Right:** Comparison of the constraints from differential single- and double-Higgs (orange), with those from differential double-Higgs data together with inclusive single-Higgs measurements (blue).

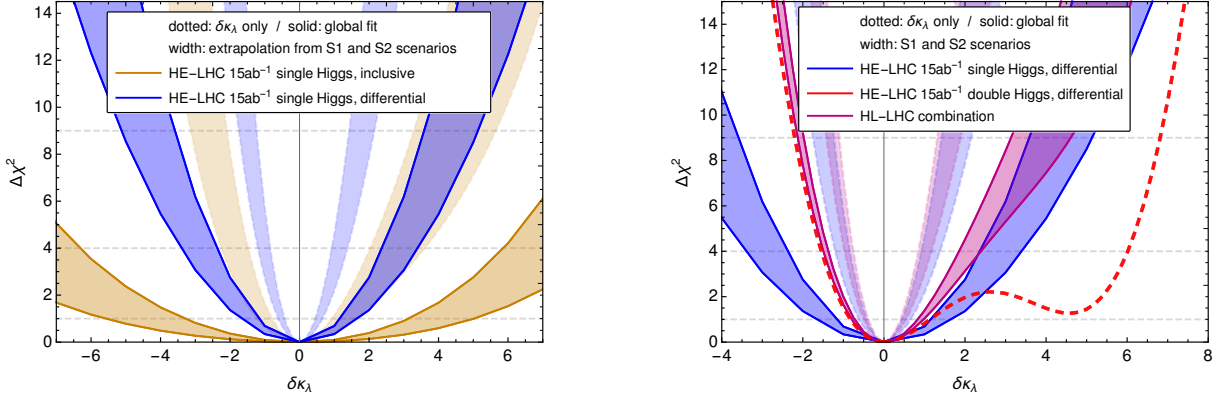


Fig. 54:  $\chi^2$  analysis of the Higgs self-coupling  $\delta\kappa_\lambda$  using single-Higgs processes for the HE-LHC at 27 TeV and  $15 \text{ ab}^{-1}$ . **Left:** Comparison of the constraints using inclusive single-Higgs processes at HE-LHC (pink) with the global fit of HL-LHC (green) and its combination (Orange). **Right:** Comparison of the constraints using differential single-Higgs processes at HE-HLC (blue) with the global fit of HL-LHC (green) and its combination (red).

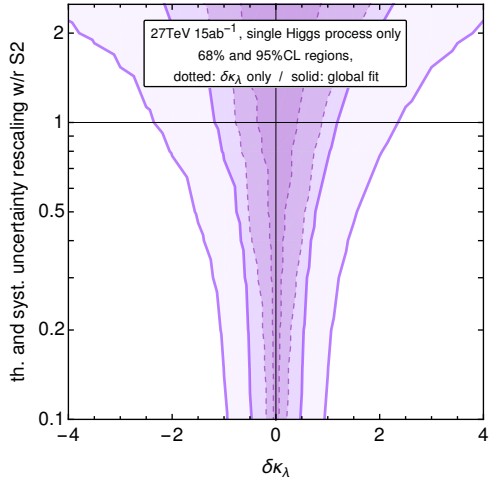


Fig. 55:  $\Delta\chi^2 = 1$  and  $\Delta\chi^2 = 3.85$  contour regions on the anomalous Higgs self-coupling  $\delta\kappa_\lambda$  for the HE-LHC projections, as a function of the common rescaling factor of both the theory and systematic uncertainties with respect to the HL-LHC projections. The dashed lines indicate the constraints for an exclusive fit to  $\delta\kappa_\lambda$ , while the solid lines indicate the constraints after profiling over the remaining parameters.

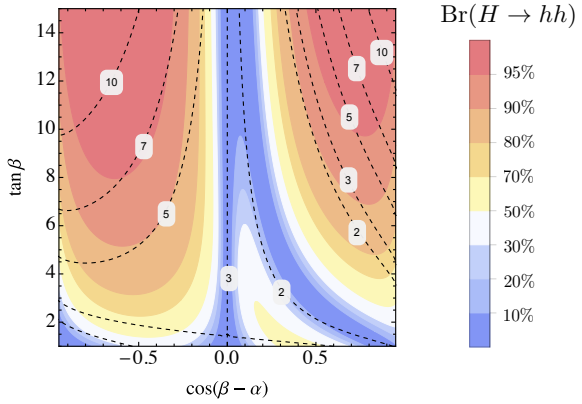


Fig. 56:  $\text{Br}(H \rightarrow hh)$  as a function of  $\cos(\beta - \alpha)$  and  $\tan \beta$  for  $M_H = M_{H^\pm} = 550$  GeV and  $M_A = 450$  GeV. The dashed contours correspond to constant values  $|\kappa_\psi^h|$  for  $n_\psi = 1$ .

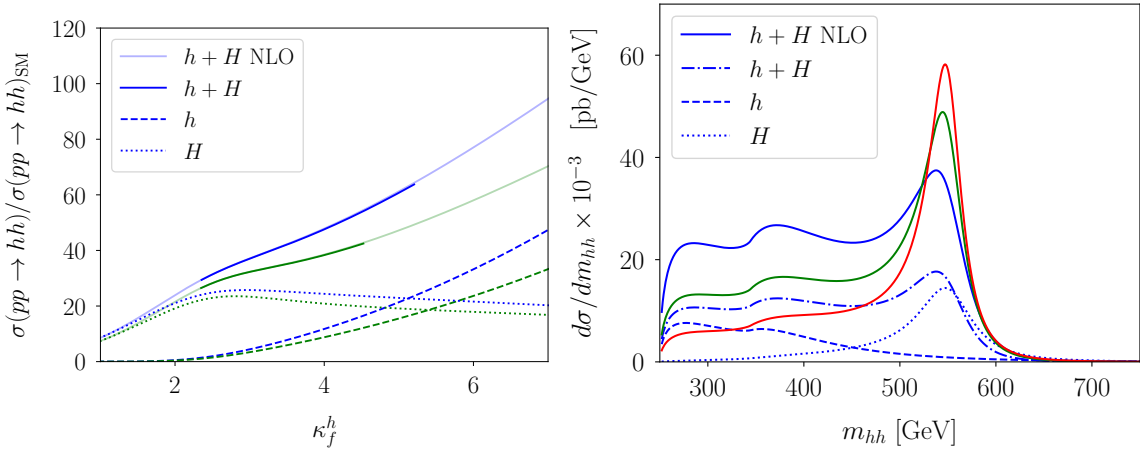


Fig. 57: Left: Cross section for Higgs pair production in units of the SM prediction as a function of  $\kappa_\psi^h$  for  $c_{\beta-\alpha} = -0.45$  ( $-0.4$ ) and  $M_A = 450$  GeV,  $M_H = M_{H^\pm} = 550$  GeV in blue (green) at  $\sqrt{s} = 27$  TeV. Right: Invariant mass distribution for the different contributions to the signal with  $c_{\beta-\alpha} = -0.45$  and  $\kappa_\psi^h = 5$  (blue),  $\kappa_\psi^h = 4$  (green) and  $\kappa_\psi^h = 3$  (red) at  $\sqrt{s} = 27$  TeV, respectively.

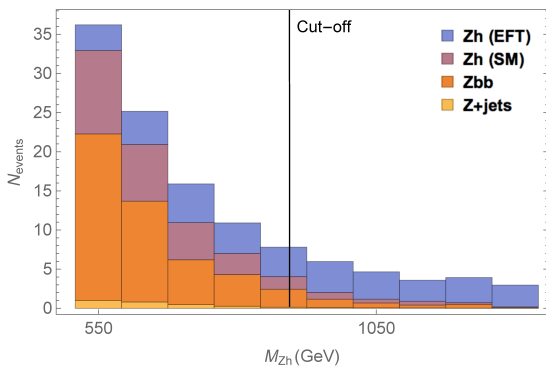


Fig. 58: The differential distribution of events at an integrated luminosity of  $300 \text{ fb}^{-1}$  with respect to  $M_{Zh}$  for the EFT signal as well as the different backgrounds. The EFT signal corresponds to the point  $\{g_{Zu_L}^h, g_{Zd_L}^h, g_{Zu_R}^h, g_{Zd_R}^h\} = \{-0.005, 0.0001, -0.010, 0.005\}$  which is allowed by LEP bounds. The vertical line shows the cut-off evaluated using Eq. 62

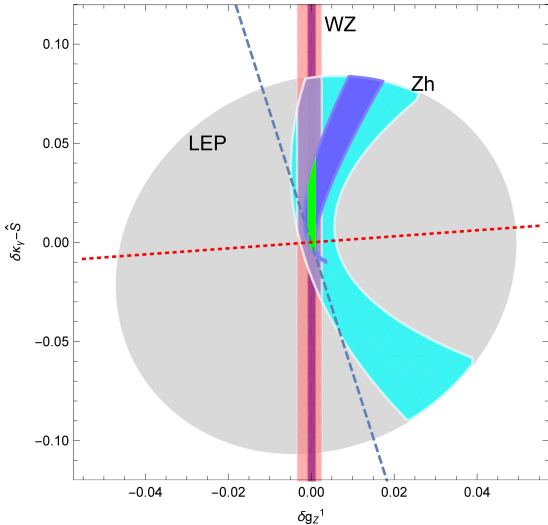


Fig. 59: The light blue (dark blue) region above shows the projection for the allowed region with  $300 \text{ fb}^{-1}$  ( $3 \text{ ab}^{-1}$ ) data from the  $pp \rightarrow Zh$  process in the  $\delta\kappa_\gamma - \hat{S}$  vs  $\delta g_z^{-1}$  plane for universal models. We show in grey the allowed region after LEP bounds (taking the TGC  $\lambda_\gamma = 0$ , a conservative choice) are imposed. In pink (dark pink) we show the region that corresponds to the projection from the  $WZ$  process with  $300 \text{ fb}^{-1}$  ( $3 \text{ ab}^{-1}$ ) data derived in Ref. [151] and the purple (green) region shows the region that survives from a combination of the  $Zh$  and  $WZ$  projections with  $300 \text{ fb}^{-1}$  ( $3 \text{ ab}^{-1}$ ) data.

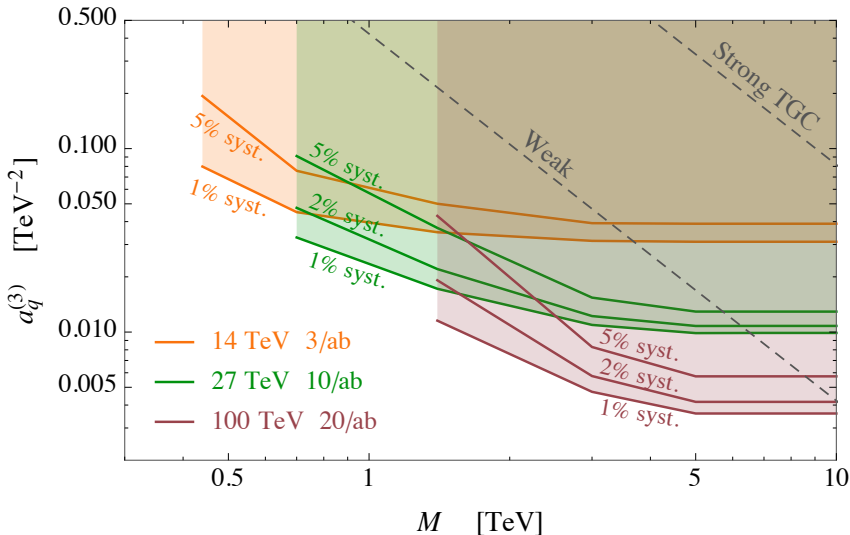


Fig. 60: Expected 95% CL bounds from fully leptonic  $WZ$  on the high-energy primary parameter  $a_q^{(3)}$  as a function of the new physics scale  $M$ . The plots reports the results for the HL-LHC (orange lines), HE-LHC (green lines) and FCC-hh (brown lines) for different values of the systematic uncertainties.

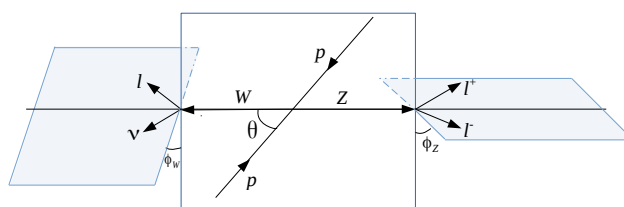


Fig. 61: Angles for  $2 \rightarrow 4$  scattering.

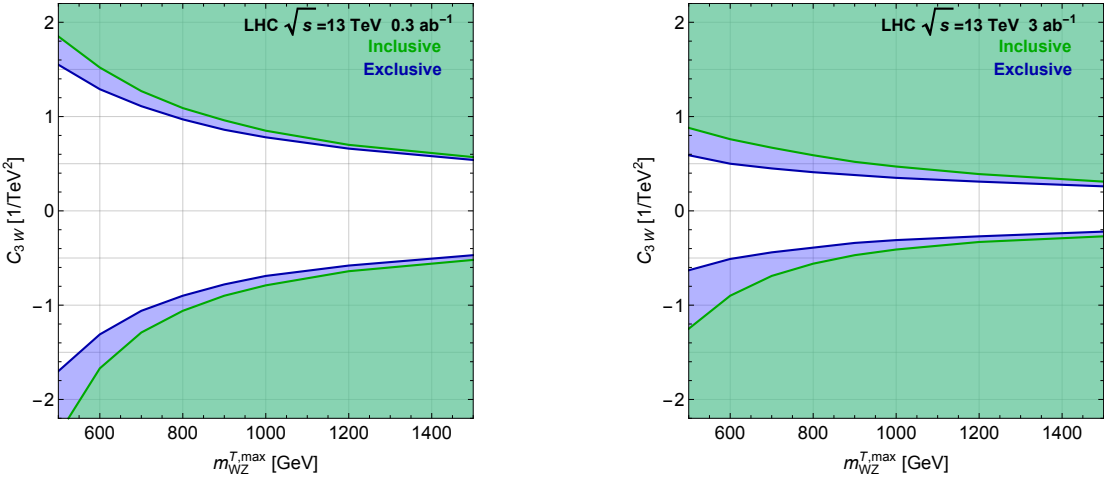


Fig. 62: Bounds on the  $C_{3W}$  Wilson coefficient for the inclusive and exclusive categories at the LHC 13 for  $300 \text{ fb}^{-1}$  (left) and  $3000 \text{ fb}^{-1}$  (right) of integrated luminosity.

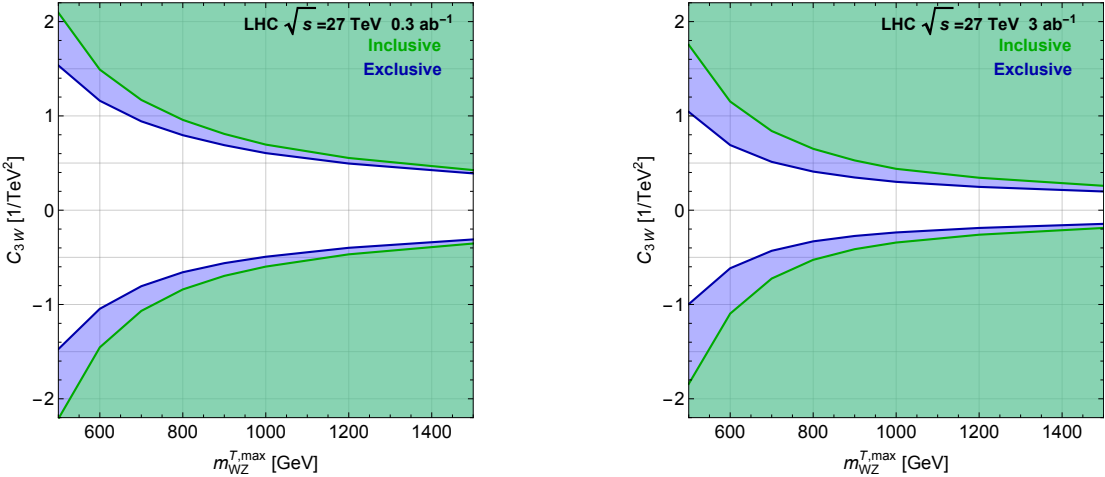


Fig. 63: Bounds on the  $C_{3W}$  Wilson coefficient for the inclusive and exclusive categories at the LHC 27 for  $300 \text{ fb}^{-1}$  (left) and  $3000 \text{ fb}^{-1}$  (right) of integrated luminosity.

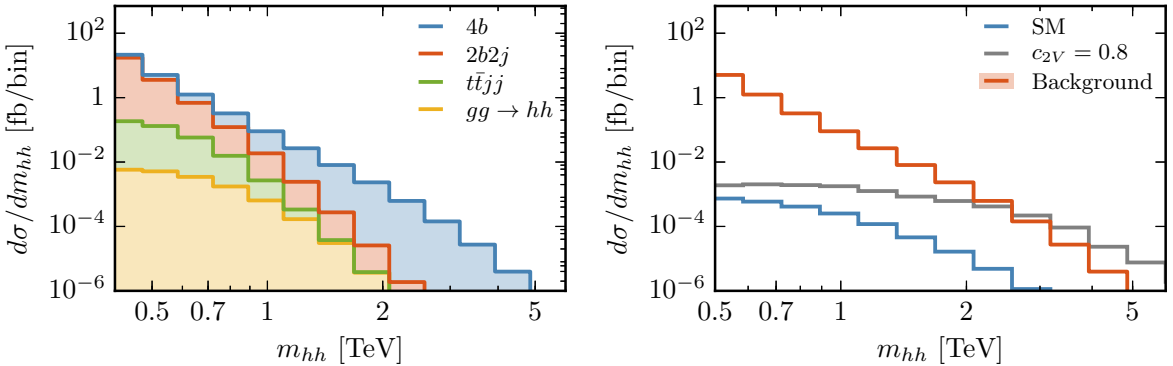


Fig. 64: Left: Decomposition of the total background into individual processes as a function of  $m_{hh}$  after all analysis cuts have been imposed. Right: the di-Higgs invariant mass distribution after all analysis cuts for the signal (SM and  $c_{2V} = 0.8$ ) and the total background.

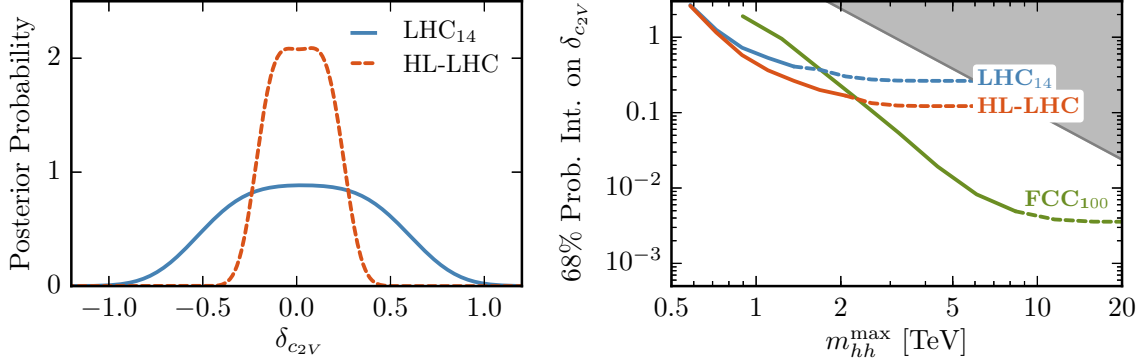


Fig. 65: Left: the posterior probability densities for  $\delta_{c_2V}$  at the HL-LHC. Right: the expected precision for a measurement of  $\delta_{c_2V}$  at the 68% CL as a function of  $m_{hh}^{\text{max}}$ , where the gray area indicates the region where  $\delta_{c_2V} > \delta_{c_2V}^{\text{max}}$ .

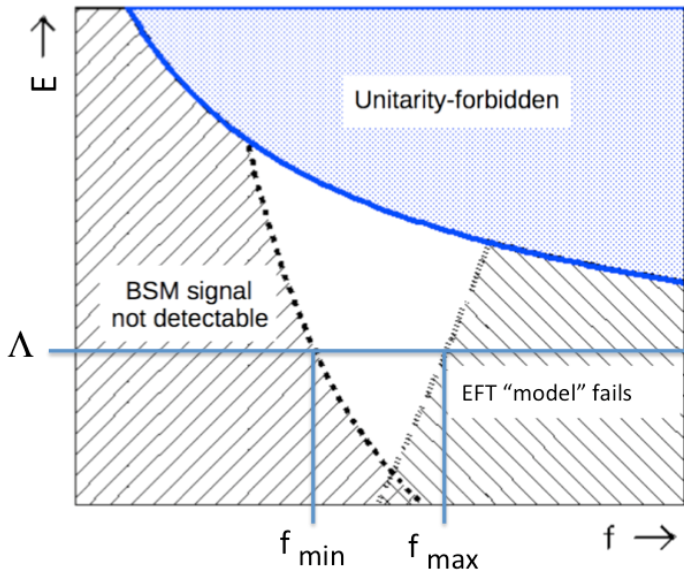


Fig. 66: Cartoon plot showing the regions in  $f_i$  and  $\Lambda$  in terms of BSM signal observability and applicability of the EFT “model” for the same-sign WW process with purely leptonic decays. The white triangle shows the region where the BSM physics can be studied within the chosen EFT “model”.

# THIS IMAGE NEEDS TO BE REPLACED

Fig. 67: Regions in  $f_{M6}$  and  $\Lambda$  in terms of BSM signal observability for the EFT “model” based on M6 operator at the HL- and HE-LHC.

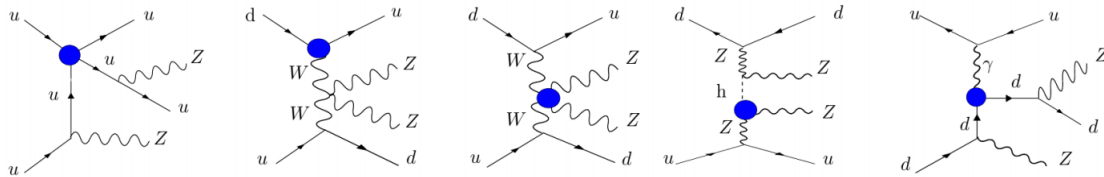


Fig. 68: Examples of some EFT diagrams for the VBS(ZZ) signal. The blobs represent dim = 6 insertions.

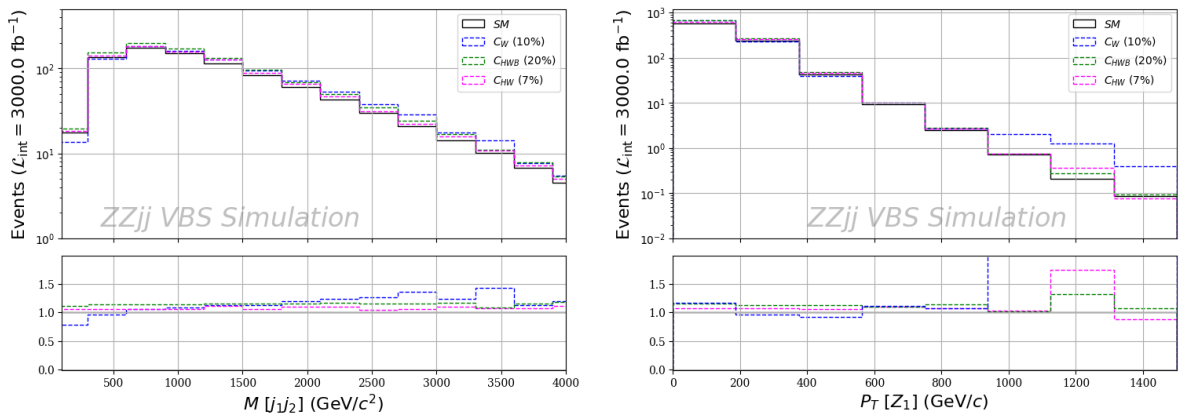


Fig. 69: Two generic simulations showing the EFT effects on key differential distributions: invariant mass of the di-jet system (left) and transverse momentum of the leading Z boson (right). We selected arbitrary values for the Wilson coefficients  $\{c_W, c_{HW}, c_{HWB}\}$

## 5 Higgs boson mass and width

### 5.1 Theory review

*F. Caola, R. Röntsch*

The total decay width is an important property of the Higgs boson, as it contains information about the interactions of the Higgs with all other fundamental particles, and is predictable both in the Standard Model and its extensions. Therefore, measuring this property is an important part of Higgs studies. Direct measurements of the Higgs width are very challenging at hadron colliders, as these require a scan of the invariant mass profile of the Higgs decay products. This is limited by detector resolution to roughly  $\sim 1$  GeV, which is three orders of magnitude larger than the SM prediction of  $\Gamma_H \sim 4$  MeV. Current LHC measurements have already attained this level of precision, and no significant improvement is anticipated.<sup>13</sup>

Given this situation, there has been considerable interest in devising indirect probes of the Higgs width. In general, a standard Higgs analysis in the  $H \rightarrow X$  decay channel measures the production cross section times branching ratio,  $\sigma \sim \sigma_{\text{prod}} \times \Gamma_{H \rightarrow X} / \Gamma_H$ , and is thus only sensitive to a combination of the coupling and the width. Schematically,

$$\sigma \sim \frac{g_{\text{prod}}^2 \times g_{\text{dec}}^2}{\Gamma_H}, \quad (83)$$

where  $g_{\text{prod}}$  and  $g_{\text{dec}}$  are the couplings that enter the Higgs production and decay channels, respectively. An independent measurement of the couplings and the decay width is therefore not possible from such analyses. The idea behind all indirect determinations of  $\Gamma_H$  is to find an observable whose dependence on  $g_i$  and  $\Gamma_H$  is different from Eq. (83), which allows one to lift the coupling/width degeneracy. Indirect determinations can be broadly separated in two classes: *on-shell* methods, which rely on delicate interference effects on the Higgs resonant peak, and *off-shell* methods, which combine on-peak and off-peak information. In the following, we provide a quick overview of these methods, emphasizing their strengths and weaknesses.

The starting point of the *on-shell methods* [?, ?, ?, ?] is the observation that measurements in the  $H \rightarrow X$  decay channel receive a contribution both from the signal  $pp \rightarrow H \rightarrow X$  process and from the continuum background  $pp \rightarrow X$ , and the two interfere. Schematically, the amplitude for the process can be written as

$$\mathcal{A}_{pp \rightarrow X} = \frac{Sm_H^2}{s - m_H^2 + im_H\Gamma_H} + B, \quad (84)$$

where  $S \propto g_{\text{prod}} \times g_{\text{dec}}$  is the signal part and  $B$  is the background contribution. This leads to

$$|\mathcal{A}_{pp \rightarrow X}|^2 = \frac{m_H^4}{(s - m_H^2)^2 + m_H^2\Gamma_H^2} \times \left[ |S|^2 + \frac{(s - m_H^2)}{m_H^2} 2\text{Re}(SB^*) + \frac{\Gamma_H}{m_H} 2\text{Im}(SB^*) \right] + |B|^2. \quad (85)$$

Here,  $|S|^2 \propto g_{\text{prod}}^2 \times g_{\text{dec}}^2$ , but  $SB^* \propto g_{\text{prod}} \times g_{\text{dec}}$ , so a combined determination of the signal  $|S|^2$  and interference  $SB^*$  contributions can lift the coupling/width degeneracy of Eq. (83), thus giving access to  $\Gamma_H$ . For this method to be effective, one needs to consider channels where the interference is large. The best candidate is then the  $gg \rightarrow H \rightarrow \gamma\gamma$  channel: indeed, in this case both the  $gg \rightarrow H$  production and the  $H \rightarrow \gamma\gamma$  are loop induced, as is the continuum contribution  $gg \rightarrow \gamma\gamma$ . This implies that at least naively there is a loop enhancement factor in the interference w.r.t. the pure signal, thus making the former noticeable.

The *real part of the interference* in Eq. (85) is antisymmetric around the Higgs peak, so it does not affect the total rate. However, it leads to a distortion in the shape of the  $m_{\gamma\gamma}$  distribution around

---

<sup>13</sup>Lower bounds on the Higgs width can be obtained from lifetime measurements, see Sec. 5.4 for details.

the Higgs peak, which in turns translates into a slight shift in the reconstructed Higgs mass [?]. The size of this mass shift is proportional to the interference contribution, whose dependence on couplings and width is different from Eq. (83). A measurement of the mass shift then allows for a determination of  $\Gamma_H$ . This can be done for example by comparing the mass extracted in the  $\gamma\gamma$  channel with that determined in the  $4l$  channel, where these interference effects are negligible. However, even if the  $4l$  channels lead to a very good mass determination once high enough statistics have been accumulated, extracting the mass shift from a  $\gamma\gamma$  vs  $4l$  comparison introduces additional systematics. Because of this, it is preferable to consider only the  $\gamma\gamma$  decay mode and to compare different kinematic regions. This is possible since the interference is strongly dependent on the transverse momentum of the Higgs [?]. In particular, hard radiation tends to lessen this effect somewhat. Another candidate for a reference mass could be obtained from studying Higgs production in association with two hard jets. Indeed, in this case there are cancellations between the  $ggF$  and  $VBF$  contributions and the net result for the interference is very small [?]. Theoretical predictions for the mass shift are under good control, with the interference being known to NLO in QCD [?, ?, ?] and matched to parton shower [?, ?]. It turns out that radiative corrections deplete the interference contribution somewhat. Although it is well known that higher order corrections are important for Higgs physics, for this analysis the main limitation comes from experimental systematics, namely the detector response, which must be properly modeled to extract the interference contribution from the measured mass shift. In the SM, the mass shift at the LHC is rather small,  $\Delta m_{\gamma\gamma} \sim \mathcal{O}(50 - 100)$  MeV. This implies that at the HL-LHC this method could lead to bounds on  $\Gamma_H$  of the order  $\Gamma_H \sim \mathcal{O}(10 - 50) \times \Gamma_{H,\text{SM}}$ . Detailed projections can be found in Sec. 5.6.

The *imaginary part of the interference* [?, ?] in Eq. (85) is symmetric around the Higgs peak, so it leads to a change in the rate. Unfortunately, because of helicity conservation this imaginary part is highly suppressed at LO. Higher order corrections provide a new mechanism to generate an imaginary part, lifting this suppression [?]. However, because the bulk of the interference effectively enters at NLO, the anticipated loop enhancement factor in the interference relative to the pure signal (mentioned above) is not present, and the actual size of the effect is quite small. In the SM, it reduces the total rate by about 2%, which makes it challenging to observe, and the effect is further diluted by additional radiation [?]. Thus this technique requires very good control on the total rate, both experimental and theoretical. To reduce the former, it is profitable to consider cross-section ratios; for example, the  $\gamma\gamma$  to  $4l$  ratio is projected to be measured at the few percent level. However, this introduces additional experimental and theoretical systematics, including theoretical model dependence since one would need to make assumptions about the structure of Higgs couplings. For this reason, it is again preferable to perform the interference effect extraction in the  $\gamma\gamma$  channel alone, by considering different kinematic regions. As with the real part of the interference, this effect is also quite sensitive to the transverse momentum of the Higgs, with the bulk of the interference effect confined to the small  $p_t$  region, as shown in an NLO analysis in Ref. [?]. However, since the interference is essentially an NLO effect, as discussed above, the residual theoretical uncertainty at this order is still quite sizable. Moreover, a fine-grained comparison of the low and high Higgs  $p_t$  regions requires very good theoretical control. For the former, this is notoriously complicated as several different effects are at play, see e.g. [?] and references therein for a recent discussion of this point. Because of this, assuming a few percent experimental accuracy, the width extraction from this method would be limited by theoretical uncertainties. Although computing higher order corrections for this effect is well beyond our current ability, it is reasonable to assume that the situation will improve on the HL/HE-LHC timescale, along the lines described in Section 2.2. Currently, it is expected that this technique would lead to bounds of the order  $\Gamma_H \sim \mathcal{O}(10) \times \Gamma_{H,\text{SM}}$ , see section 5.5 for details.

The main advantage of the on-shell width determinations discussed above is that – although being indirect measurements – they require minimal theoretical assumptions on potential BSM effects. This is because couplings are extracted at the same energy scale, ideally from the same process. Unfortunately, since interference effects scale like  $g_{\text{prod}} \times g_{\text{dec}}$  at the first power, the constraints on the width are quite mild. Indeed, if one assumes that the on-shell rates are kept fixed, a linear dependence on the coupling

translates into a square root dependence on the width.

Another option to constrain the width is off-shell methods [?, ?, ?, ?], which are based on the following observation. Schematically, the cross section can be written as

$$\sigma \sim \frac{g_{\text{prod}}^2 \times g_{\text{dec}}^2}{(s - m_H^2)^2 + m_H^2 \Gamma_H^2}. \quad (86)$$

On the resonant peak, this leads to the usual relation Eq. (83). Typically, most of the cross section is concentrated there. In the  $VV$  decay channel though there is a sizable contribution from the off-shell  $s\gamma\gamma m_H^2$  region [?]: indeed, Higgs decay to vector bosons is strongly enhanced at high energy. In the far off-shell region, Eq. (86) reduces to  $\sigma \sim (g_{\text{prod}}^2 \times g_{\text{dec}}^2)/s^4$ . Assuming that the on-peak rates are kept fixed, this quadratic dependence on the couplings translates into a linear dependence on  $\Gamma_H$ , allowing this quantity to be constrained by a comparison of on- and off-shell rates.

However, it is important to stress that to extract  $\Gamma_H$  from off-shell measurements one has to assume that on-shell and off-shell couplings are the same. Since the two are evaluated at very different energy scales, this introduces a theoretical model dependence. Indeed, there are several new physics scenarios where BSM effects decorrelate on- and off- shell couplings, see e.g. [?, ?, ?]. These include for example new light degrees of freedom coupled to the Higgs, additional Higgs states, or anomalous  $HVV$  couplings. Therefore, to constrain the width using an off-shell analysis, it is important to perform complementary measurements to control potential BSM effects. This was studied in detail for the case of  $HVV$  anomalous couplings in [?]. Projections at the HL-LHC will be presented in section 5.7. In general, off-shell measurements offer the opportunity to investigate Higgs interactions at high energy scale, thus leading to interesting information that is not limited to the width extraction. For example, in combination with measurements of boosted Higgs,  $HH$  and  $t\bar{t}H$ , an off-shell analysis can help lifting the degeneracy between  $ggH$  and  $t\bar{t}H$  couplings [?]. The off-shell program will clearly benefit from the increased statistics and energy of the HL/HE upgrade. For example, this would allow for off-shell studies in the VBF production mode [?]. Although the rate here is very small, by looking at same-sign vector boson final states one can significantly reduce backgrounds. Although it is estimated that HL-LHC measurements in this channel would lead to constraints at the same level of current ones in the  $ggF$  channel [?], the completely different production mechanism makes them complementary to the  $ggF$  constraints, thus allowing for a less model dependent interpretation. Aside from these considerations, it is interesting to study the potential of future LHC upgrades to constrain  $\Gamma_H$  under the assumption that no large decorrelations between on- and off-shell couplings occur. Because of the linear dependence on the width discussed above, such constraints are quite powerful. Indeed, assuming a reasonable reduction in the theoretical uncertainty in the HL-LHC timescale, it will be possible to probe values close to the SM value  $\Gamma_H \sim 4$  MeV. Projections under different assumptions for the theoretical uncertainty are reported in section 5.7.

A reliable theoretical description of the off-shell region is non trivial. First, there is a large  $q\bar{q} \rightarrow VV$  background, which needs to be properly subtracted to access the signal yield. More important, there is an irreducible  $gg \rightarrow VV$  continuum background that interferes with the signal process  $gg \rightarrow H \rightarrow VV$ . The interference effect is sizable and destructive, which is a consequence of the Higgs mechanism ensuring unitarity in the SM. Because of the large interference, it is necessary to have good theoretical control not only on the signal process but also on the continuum background amplitude. This is non trivial, since the  $gg \rightarrow VV$  process is loop induced, so higher order corrections – expected to be large given the  $gg$  initial state – involve multi-loop amplitudes. Moreover, at large invariant masses, the contribution of virtual top quarks to the amplitude becomes dominant. Its proper description would then require multi-loop amplitudes involving internal massive states, which are extremely challenging to compute. For this reason, exact predictions for the background amplitude are only known to LO in the off-shell region. NLO corrections are known below the top threshold, and only in an approximate form above [?, ?, ?, ?, ?, ?, 189]. Nevertheless, recent developments in numerical techniques [83] make

NLO computations for the background feasible in the near future. One subtle point in this discussion is the role of quark-initiated reactions. On the one hand, they appear naturally in the computation of NLO corrections to  $gg \rightarrow VV$  from initial state splitting. On the other hand this kind of contribution – although separately finite and gauge invariant – only forms a small subset of the whole  $qg \rightarrow VVq$  process at  $\mathcal{O}(\alpha_s^3)$ , which are part of the genuine N<sup>3</sup>LO corrections to the quark-initiated  $q\bar{q} \rightarrow VV$  process. Therefore, only including the contribution coming from initial state splitting in the  $gg \rightarrow VV$  process, although formally possible, may not entirely capture the correct physics. In general, this problem is not particularly relevant because the gluon channel provides the bulk of the contribution. This is however no longer the case if strong requirements on extra jet activities (typical e.g. for  $WW$  analysis) are imposed. Understanding this issue is an interesting theoretical problem, and the high statistics available at the HL/HE-LHC motivates its detailed investigation. Another issue that should be investigated is the impact of electroweak corrections, which can be sizable at high energy. Once again, although they are currently unknown, it is natural to expect progress in this direction within the HL-LHC timescale.

The modeling of the  $gg \rightarrow H \rightarrow VV$  process is under better control than the background one. Still, since in the far off-shell region the top loop cannot be approximated by a contact interaction, computations are still much harder than in the on-shell region, where such an approximation is justified. As a consequence, exact results are only known to NLO. A full computation of NNLO corrections would require significant advances on current technology, which are however likely to occur in the HL-LHC timescale. It is reasonable to expect [7] that the  $K$ -factor for the exact theory is rather similar to that obtained from calculations in which the top loop is integrated out. In the absence of an exact calculation, one can use this approximation to estimate rates at the HL/HE LHC.

The HL/HE-LHC upgrade will improve off-shell analysis in several ways. On the one hand, the larger statistics will allow for a better discrimination of the  $q\bar{q} \rightarrow VV$  vs  $gg \rightarrow VV$  background and – crucially – interference. Currently, this is done by using the different kinematic behavior of these contributions. Clearly, a higher statistical sample would allow for more powerful discrimination. Furthermore, increasing the collider energy would lead to a larger fraction of gluon initiated events w.r.t. quark initiated events. For example, the  $(gg \rightarrow H \rightarrow VV)/(q\bar{q} \rightarrow VV)$  ratio increases by a factor of roughly 1.5 in the off-shell region when the center-of-mass energy is increased from 14 TeV to 27 TeV. Furthermore, the increase in the total rate at the HE-LHC will lead to a significant number of off-shell events in the few-TeV region. This would allow for precise investigations of the Higgs sector in the high-energy region, which could shed light on the unitarity structure of the SM.

## 5.2 Measurement of the Higgs boson mass

## 5.3 Direct constraints from the Higgs boson lineshape

## 5.4 Direct constraints from the Higgs boson lifetime measurements

## 5.5 Width from the diphoton interference rate

14 15

The SM Higgs total decay width can be constrained from the change in on-shell Higgs rates due to interference effects between the Higgs signal and the QCD background [?]. This change in rates requires the existence of a so-called strong phase in the amplitudes, that can be present both in the Higgs signal and in the continuum background, as is the case in the SM. We shall demonstrate that, the different

---

<sup>14</sup> Authors: John Campbell<sup>a</sup>, Marcella Carena<sup>a,b,c</sup>, Roni Harnik<sup>a</sup> and Zhen Liu<sup>a,d</sup>

<sup>a</sup> Theoretical Physics Department, Fermilab, Batavia, IL 60510, USA

<sup>b</sup> Enrico Fermi Institute, University of Chicago, Chicago, IL 60637

<sup>c</sup> Kavli Institute for Cosmological Physics, University of Chicago, Chicago, IL 60637

<sup>d</sup> Maryland Center for Fundamental Physics, Department of Physics, University of Maryland, College Park, MD 20742

<sup>15</sup> This manuscript has been authored by Fermi Research Alliance, LLC under Contract No. DE-AC02-07CH11359 with the U.S. Department of Energy, Office of Science, Office of High Energy Physics.

scaling behavior between the strong phase induced interference and the Breit-Wigner parts of the on-shell Higgs rate may allow the placement of bounds on, or even measurements of, the Higgs boson total width. Both theoretical and experimental uncertainties are the leading limiting factors in this program. On the other hand, without the strong phase induced interference effects, fits to on-shell Higgs rates can only place bounds on the total width by making definite theoretical assumptions [?, ?, 2].

It is useful to write the amplitude for  $gg \rightarrow h \rightarrow \gamma\gamma$  in a form which explicitly factors out the loop-induced couplings to gluons ( $F_{gg}$ ) and photons ( $F_{\gamma\gamma}$ ),

$$A_h \equiv A_{gg \rightarrow h \rightarrow \gamma\gamma} \propto \frac{\hat{s}}{\hat{s} - m_h^2 + i\Gamma_h m_h} F_{gg} F_{\gamma\gamma}. \quad (87)$$

Both the Higgs couplings  $F_{gg}$  and  $F_{\gamma\gamma}$  as well as the background amplitude  $A_{\text{bkg}}$  receive absorptive contributions that arise from loops of particles that are sufficiently light to be on shell. The resulting induced phases are usually dubbed ‘strong phases’ in the flavor literature and we will adopt this terminology here.<sup>16</sup> In the presence of a strong phase we can write the interference term as

$$\begin{aligned} |\mathcal{M}_h|_{\text{int}}^2 &\equiv 2 \operatorname{Re}[A_h A_{\text{bkg}}^*] = \frac{2|A_{\text{bkg}}||F_{gg}||F_{\gamma\gamma}|}{(\hat{s} - m_h^2)^2 + \Gamma_h^2 m_h^2} \\ &\times \left[ (\hat{s} - m_h^2) \cos(\delta_{\text{bkg}} - \delta_h) + m_h \Gamma_h \sin(\delta_{\text{bkg}} - \delta_h) \right], \end{aligned} \quad (88)$$

where we have taken  $\delta_h = \arg[F_{gg}] + \arg[F_{\gamma\gamma}]$  and  $\delta_{\text{bkg}} = \arg[A_{\text{bkg}}]$  as the signal and background strong phases, respectively. The first term in the square bracket is the contribution to the interference term that does not modify the overall rate upon integration over  $\hat{s}$ . The second term is the subject of this work and leads to a modified rate in the presence of a strong phase. For convenience, we define  $|\mathcal{M}_h|_{\text{int}}^2 = \mathcal{R}_h^{\text{int}} + \mathcal{I}_h^{\text{int}}$  and  $\delta_s = \delta_{\text{bkg}} - \delta_h$  such that

$$\begin{aligned} \mathcal{R}_h^{\text{int}} &\equiv \frac{2|A_{\text{bkg}}||F_{gg}||F_{\gamma\gamma}|}{(\hat{s} - m_h^2)^2 + \Gamma_h^2 m_h^2} (\hat{s} - m_h^2) \cos \delta_s \\ \mathcal{I}_h^{\text{int}} &\equiv \frac{2|A_{\text{bkg}}||F_{gg}||F_{\gamma\gamma}|}{(\hat{s} - m_h^2)^2 + \Gamma_h^2 m_h^2} m_h \Gamma_h \sin \delta_s. \end{aligned} \quad (89)$$

In the SM the dominant contribution to  $\mathcal{I}_h^{\text{int}}$  comes from the phase of the background amplitude at two loops [?, ?]. The signal amplitude also contains a strong phase, mainly due to bottom quark loops. We have performed a calculation of the interference effect that accounts for absorptive effects from both signal and background. In Fig. 70 we illustrate the features of the interference effects. The line shape, the differential cross-section as a function of  $\hat{s}$ , is shown for the pure Breit-Wigner (only  $|A_h|^2$ ), and for the interference contributions  $\mathcal{I}_h^{\text{int}}$  and  $\mathcal{R}_h^{\text{int}}$  as well as for the sum of both. For visualization, the interference contribution  $\mathcal{I}_h^{\text{int}}$  has been magnified by a factor of 10. In this figure we show the lineshapes obtained including NLO effects with virtual corrections only. After summing over different interfering helicity amplitudes, we obtain averaged strong phases  $\delta_h = (\pi + 0.036)$  and  $\delta_{\text{bkg}} = -0.205$  for the signal and background, respectively.

As a concrete example that demonstrates the potential of this novel effect, without loss of generality we can consider excursions in the flat direction corresponding to,

$$\frac{|F_{gg}|^2 |F_{\gamma\gamma}|^2}{|F_{gg}^{\text{SM}}|^2 |F_{\gamma\gamma}^{\text{SM}}|^2} = \frac{\Gamma_h}{\Gamma_h^{\text{SM}}}. \quad (90)$$

---

<sup>16</sup>Strong phases, which are CP even, get their name because they often arise in flavor physics from QCD dynamics. This is in contrast with CP odd weak phases, e.g., the relative size of the Higgs couplings to  $F\tilde{F}$  versus  $FF$

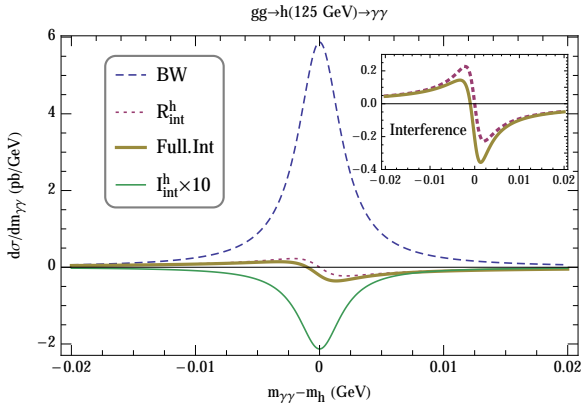


Fig. 70: The lineshape induced by various contributions to the cross-section for  $gg \rightarrow h \rightarrow \gamma\gamma$  in the SM. The Breit-Wigner line-shape, with no interference, is shown in blue (dashed) while the effect of  $\mathcal{R}_h^{\text{int}}$  and  $\mathcal{I}_h^{\text{int}}$  (multiplied by a factor of 10) are shown in red (dotted) and green (solid), respectively. The overall effect of the interference in the full NLO calculation is given by the brown (solid) line. The insert in the top right is a magnification of the corresponding interference lineshapes.

The total Higgs cross section can then be written as,

$$\sigma = \sigma_{\text{BW}}^{\text{SM}} \left( 1 + \frac{\sigma_{\text{int}}^{\text{SM}}}{\sigma_{\text{BW}}^{\text{SM}}} \sqrt{\frac{\Gamma_h}{\Gamma_h^{\text{SM}}}} \right) \simeq \sigma_{\text{BW}}^{\text{SM}} \left( 1 - 2\% \sqrt{\frac{\Gamma_h}{\Gamma_h^{\text{SM}}}} \right). \quad (91)$$

The result of a full NLO calculation of the interference effect are presented in Fig. 71, that shows the relative size of the interference effect as a function of the total width, normalized to its SM value, for parameter excursions defined by Eq. (90).<sup>17</sup> The variation of the interference effect with the total width is shown imposing a 20 GeV  $p_T^h$ -veto, with and without LHC cuts on the final state photons. Since the interference effect is largest at small scattering angles, the photon cuts reduce the expected interference. This small consideration in the SM leads to much bigger differences for  $\Gamma_h \gamma\gamma \Gamma_h^{\text{SM}}$ . Observe that in the SM the interference contribution is destructive. However, if the sign of  $F_{gg} F_{\gamma\gamma}$  were flipped, ( $\delta_s \rightarrow \pi + \delta_s$ ), the interference effect would lead to an enhancement of the diphoton rate rather than a suppression. The theoretical scale uncertainty is shown in the bottom panel of Fig. 71 and amounts to about  $\pm 50\%$ . For example, the interference effect is  $-(2.20^{+1.06}_{-0.55})\%$  without photon cuts for SM Higgs. Although a measurement at the 2% level may be challenging at the LHC, this shows that a precise measurement of the  $gg \rightarrow h \rightarrow \gamma\gamma$  rate can place a limit on the width of the Higgs boson. In this respect a measurement of the ratio of the  $\gamma\gamma$  rate to the  $4\ell$  rate is a promising route to reduce many of the systematic and theoretical, e.g. PDF and other parametric, uncertainties.

The best measured channels at the LHC,  $gg \rightarrow h \rightarrow \gamma\gamma$  and  $gg \rightarrow h \rightarrow 4\ell$ , provide the most accurate cross section ratio, projected to be measurable at the 4% level [?]. In contrast to single cross section measurements, the precision on this ratio is statistically limited. Keeping the current theoretical uncertainty band in mind, the projected sensitivity of 4% on the ratio of  $\gamma\gamma$  to  $4\ell$  yields can be translated into an upper limit of 22, 14, and 8 on  $\Gamma_h/\Gamma_h^{\text{SM}}$  at 1- $\sigma$  level, for low, central and high theoretical expectations on this interference effect, respectively.<sup>18</sup> This assumes that the couplings to photons and  $Z$  bosons maintain their SM ratio and the photon and gluon couplings respect Eq. (90). The Higgs cross section precisions are anticipated to improve by a factor of three or so from statistical improvement at the

<sup>17</sup>For details of the NLO calculation , see the supplemental material with Refs [?, ?, ?, ?, ?, ?, ?, ?, ?, ?, ?, ?, ?, ?, 190].

<sup>18</sup>This limit is worse by one order of magnitude than the off-shell Higgs measurement that constrains the Higgs total width [?, ?]. However, unlike the off-shell Higgs measurement, our effect is independent from the assumptions on the high-energy behavior of the Higgs boson and the absence of new physics contribution in the off-shell region. For more detailed discussion, see e.g., chapter I.8 of the Higgs Yellow Report [7] and Refs. [?, ?].

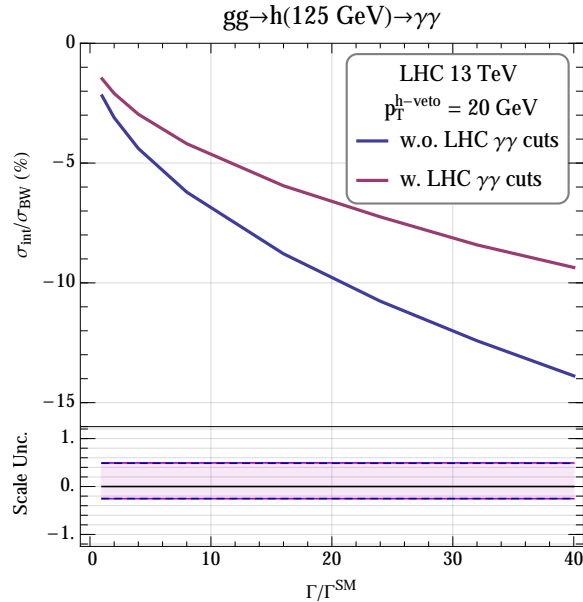


Fig. 71: The total signal rate change due to the interference effect as a function of the Higgs total width normalized to its SM value, while keeping the Breit-Wigner cross section identical to that of the SM Higgs. The magenta and blue (solid) lines represent the cases with and without LHC cuts on the final state photons, respectively. The lower panel shows the scale variation uncertainties for these interference terms as bands delimited by the blue (dashed) and magenta (solid) lines. The curves are obtained with a veto on the Higgs boson  $p_T$  at 20 GeV.

HE-LHC with 27 TeV center of mass energy and  $15 \text{ fb}^{-1}$  of integrated luminosity. This can be naively translated into lower and upper limits on the Higgs total width of  $\Gamma_h/\Gamma_h^{\text{SM}} < 5$  at  $1-\sigma$  level using the central value from our NLO theory calculation.

In summary, we discuss the change in the  $gg \rightarrow h \rightarrow \gamma\gamma$  on-shell rate, due to interference between the Higgs signal and the QCD background amplitudes, as a way to provide a novel handle to constrain - or even measure - the Higgs boson total width. We perform a full NLO calculation at order  $\alpha_s^3$  of the interference effect and find that in the standard model it leads to a reduction of the on-shell rate by  $\sim 2\%$ . The proposed method for gaining sensitivity to the Higgs boson width is complementary to other methods that have been discussed in the literature. Altogether our study aims at motivating a more thorough examination of Higgs precision physics taking into account the strong phase induced interference effect in different Higgs boson observables.

## 5.6 Mass shift from the diphoton interference: constraints on the width

## 5.7 Width from Off-Shell higgs boson couplings

## 6 Invisible decays of the Higgs boson

by Anne-Marie Magnan, Ben Nachman, Tania Robens and Tim Stefański

### Status: waiting for final experimental numbers

Invisible decays of the 125 GeV Higgs boson are a generic prediction of new physics models that feature a light dark matter (DM) particle which couples directly or indirectly to the Standard Model (SM) Higgs field. The invisible branching ratio in the SM is very small (0.1%) so any observable rate would be evidence for physics beyond the SM. LHC searches for this signature require the Higgs boson to be produced in association with a taggable object, most importantly, a  $Z$ -boson, extra forward jets (as appearing in the vector boson fusion (VBF) process), or a single high- $p_T$  jet. Furthermore, the invisible Higgs decay to the DM particles inevitably suppresses the branching fractions for the Higgs decays to SM particles. This — along with possible model-dependent alterations of the Higgs couplings — leads to a modification of the LHC Higgs signal rates of channels with SM final states with respect to their SM expectation, which can be probed with precision Higgs measurements.

In so-called *Higgs portal* models the SM Higgs field acts as a mediator between the visible SM sector and a hidden DM sector. Commonly, an additional symmetry is introduced that prohibits interactions of single hidden sector fields with SM fields, thus allowing only pair production of hidden sector particles and rendering the lightest hidden sector particle a stable DM candidate. The *Higgs portal* and its generalization to other non-SM Higgs bosons are found in many BSM scenarios (see e.g. Refs. [?, ?, ?, ?] and [?, ?, ?, ?, ?, ?] for models with and without supersymmetry).

The invisible decay of the Higgs is experimentally challenging because the missing transverse energy (MET) spectrum is relatively soft, where resolution and pileup effects are non-negligible. The issues associated with pileup, both from pileup jets and from pileup-induced resolution degradation, will only become more severe beyond Run 3. Significant recent advances in constituent-based pileup mitigation techniques will likely play a key role in maintaining and possibly improving the MET performance [?, ?, ?, ?]. Furthermore, lepton identification and pileup jet rejection will both improve with the increased tracking acceptance planned by both ATLAS and CMS [?, ?, ?, ?, ?, ?]. Current analyses with  $\sim 30 \text{ fb}^{-1}$  place limits on the invisible branching ratio of the Higgs boson at about 20–25% [?, ?, ?, ?, ?, ?]. The systematic uncertainty is about the same size as the statistical uncertainty; this means that the factor of 100 increase in statistics will not necessarily translate into an improvement by a factor of 10. Early projections from ATLAS and CMS [?, ?] predict limits that are a factor of 3–5 below the current result. The main limiting systematic uncertainty is from using  $W \rightarrow l\nu$  to estimate the  $Z \rightarrow \nu\nu$  in the dominant VBF channel. Advances in this theory input over the next decade could significantly improve the achievable precision. Already, CMS has shown that optimistic projections with reduced systematic uncertainties are realistic – the 2016 analysis [?] follows optimistic (reduced systematic uncertainties) scaling from the 2015 projection [?].

Currently, the VBF production dominates the branching ratio limit. This is because the VBF mode has a large cross-section (about 10% of the total) and the main background  $Z \rightarrow \nu\nu$  is qualitatively different (QCD production) from the same background in the  $VH$  mode (EW production). However, it is not clear which mode will dominate after Run 3, since there will be a non-trivial change in experimental conditions that will make both triggering and background rejection more difficult for both the VBF and  $VH$  modes. At the same time, there are many interesting opportunities to improve both channels from new detector capabilities (extended trackers and timing detectors) as well as new analysis techniques (e.g. quark/gluon tagging).

In this report we assess the prospects of probing *Higgs portal* models directly with future searches for invisible Higgs decays, as well as indirectly with precision Higgs rate measurements, at the LHC in the high luminosity (HL) phase with  $3 \text{ ab}^{-1}$ . Furthermore, we shall highlight the complementarity between these two probes, as well as with other constraints, e.g. with current and future limits from DM direct detection experiments and limits from LEP Higgs searches. Searches for invisible decays of

the Higgs boson also have important implications for “nearly invisible” decays into neutral long-lived particles that are predicted by many models [?]. Dedicated searches set much stronger limits [?, ?, ?], but the Higgs to invisible search is a model-independent constraint on all possibilities. Projections for dedicated searches as well as proposals for dedicated detectors at the LHC complex [?, ?] are not discussed in this section.

This contribution is organized as follows. We briefly review in Section 6.2.1 the experimental input for the HL-LHC that we use in our study. In Section 6.2.2 we first employ an effective description of the generic phenomenological Higgs features that appear in this class of models. We then focus on two specific realizations of the Higgs portal: in Section 6.3.1 we discuss the *minimal Higgs portal*, where the SM Higgs field directly couples to an additional DM field through a quartic interaction; in Section 6.3.2 we show results for the *scalar singlet portal*, where an additional scalar singlet is acting as a mediator between the visible and hidden sector. We conclude in Section 6.4.

## 6.1 Main channels for direct searches

Given the VBF production presents the best sensitivity, this channel is chosen to investigate the sensitivity of the search with the HL-LHC. The CMS phase-2 detector is simulated using Delphes [176] (fast parametrisation), with on average 200 interactions per bunch crossing. A cut-and-count approach similar to the one described in the analysis from [?] is used.

The VBF Higgs signal samples are produced using POHWEGv2.0 [?, 84] at next-to-leading order (NLO) in perturbative QCD, assuming 100% branching ratio of the Higgs boson to invisible final states, and normalised using the SM inclusive Higgs boson production cross sections taken from [7]. The gluon-fusion contribution is accounted for, depending on the selection chosen, based on the full-simulation samples produced at 13 TeV, applied as a ratio to the Delphes expected VBFH yields.

The main backgrounds are processes involving vector bosons (W,Z) produced in association with jets, either through QCD or electroweak (EWK) vertices. They are simulated at leading order (LO) using AMC@NLOv2.2.2 [79] interfaced with PYTHIAv8.205 or higher. Top processes contribute also to the backgrounds and are simulated using either POHWEG or AMC@NLO. The QCD multijet background is simulated using AMC@NLO interfaced with PYTHIA, imposing a minimum threshold of 1000 GeV on the dijet mass at parton level.

The objects studied are as defined for the analysis [?], with extended coverage to  $\eta = 3.0$  for leptons, b-tagged jets and tau jets. Electrons passing loose identification criteria, with a transverse momentum  $p_T > 10$  GeV, and pseudorapidity  $|\eta| < 2.8$  are vetoed. Similarly, muons passing loose identification criteria with  $p_T > 20$  GeV and  $|\eta| < 3.0$  are vetoed. Taus passing loose identification criteria with  $p_T > 20$  GeV and  $|\eta| < 2.8$  are vetoed. Jets are reconstructed using the anti- $k_T$  algorithm [?] with a parameter size of 0.4,  $p_T > 30$  GeV and  $|\eta| < 5.0$ , and are corrected for pile-up effects using the so-called “Puppi” scheme [?]. Jets passing a b-tagging algorithm which uses timing information, and with medium working point (b-tagging efficiency around 60% for mis-tagging rates below 1%), are vetoed if they have  $p_T > 20$  GeV and  $|\eta| < 3.0$ . The negative vectorial sum of the transverse energy of all the identified objects defines the missing transverse energy (whose magnitude is referred to as  $E_T^{\text{miss}}$  in the following), also corrected for pileup using the Puppi scheme. The two leading jets are required to have  $p_T > 80, 40$  GeV, be in opposite hemispheres, and are used to form the VBF dijet pair, with pre-selection requirements applied on its invariant mass  $M_{jj} > 1000$  GeV, and separations in pseudorapidity  $\Delta\eta_{jj} > 4.0$  or azimuthal angle  $\Delta\phi_{jj} < 1.8$ . To reject the QCD multijet background, for which the transverse missing energy arises from jet mismeasurements, the  $E_T^{\text{miss}}$  is required to not be aligned with a jet using  $\min\Delta\phi(\text{jet } p_T > 30 \text{ GeV}, E_T^{\text{miss}}) > 0.5$ . The magnitude of the vectorial sum of all jets  $p_T$  with  $p_T > 30$  GeV defines  $H_T^{\text{miss}}$ .

The analysis uses five different and non-overlapping regions: the signal region (SR) where all leptons are vetoed, and four control regions (CR) with exactly one electron or muon (W boson CR) or

exactly two electrons or two muons ( $Z$  boson CR). In the  $W$  boson CR, to further reject QCD multijet backgrounds, the lepton- $E_T^{\text{miss}}$  transverse mass is required to be less than 160 GeV. In the  $W \rightarrow e\nu$  CR also a selection on  $E_T^{\text{miss}} > 60$  GeV is applied due to higher QCD contamination than in the muon channel. In the  $Z$  boson CR, the dilepton mass is required to be between 60 and 120 GeV. To account for expected higher single-electron trigger thresholds, the leading electron  $p_T$  is required to be above 40 GeV, for both  $W \rightarrow e\nu$  and  $Z \rightarrow ee$  CR.

Lower thresholds on  $E_T^{\text{miss}}$  values are varied from 130 to 400 GeV in 10 to 50 GeV steps, and lower thresholds on  $M_{jj}$  values from 1000 to 4000 GeV in 100 GeV steps. The statistical uncertainty on the MC is considered to be negligible, assuming the available MC samples will have at least 10 times the luminosity available in the data. For each  $(E_T^{\text{miss}}, M_{jj})$  selection, the yields are extracted in the four control regions and in the signal region. A maximum likelihood fit is performed taking into account all regions simultaneously. Upper limits on the Higgs boson production cross section times  $\text{BR}(H \rightarrow \text{inv})$  are placed at 95% CL using an asymptotic CLs method [?, ?, ?], following the standard LHC Higgs combination technique [?, ?]. Systematic uncertainties are treated as nuisance parameters in a frequentist paradigm, as described in [?], and all correlations between processes are taken into account.

The scenario considered for the systematic uncertainties is described in table 35, together with the systematics that are considered for the 2016 analysis, for comparison.

Systematic	2016	YR18
e-ID	1%(gsf) $\oplus$ 1%(idiso)	1%
$\mu$ -ID	1%(reco) $\oplus$ 1%(id) $\oplus$ 0.5%(iso)	0.5%
e-veto	0.6%(gsf) $\oplus$ 1.5%(idiso)	1%
$\mu$ -veto on QCD V+jets	5%(reco) $\oplus$ 5%(id) $\oplus$ 2%(iso)	2%
$\mu$ -veto on EWK V+2jets	10%(reco) $\oplus$ 10%(id) $\oplus$ 6%(iso)	6%
$\tau$ -veto	1–1.5% for QCD–EWK	0.5–0.75%
b-tag-veto	0.1% (sig) 2% (top)	0.05% (sig) 1% (top)
JES	14%(sig) 2%(W/W) 1%(Z/Z)	4.5%(sig) 0.5%(W/W) 0.2%(Z/Z)
Lumi	2.5%	1%
QCD multijet	1.5%	1.5%
Theory on W/Z ratio	12.5%	7%
ggH normalisation	24%	20%
QCDscale_qqH	+0.4% -0.3%	+0.4% -0.3%
QCDscale_accept_qqH	2%	1%
pdf_qqbar	2%	1%
pdf_accept_qqbar	1%	1%
QCDscale_ggH2in	40%	20%
QCDscale_YR4_ggH	+4.6% -6.7%	+2% -4%
pdf_gg	3.2%	1.5%
UEPS	16.8%	9%

Table 35: Impacts on the signal and background yields from different systematic uncertainty sources considered in the run II 2016 analysis and for the HL-LHC setup (YR18).

The analysis is expected to be systematically dominated, with the dominant systematic uncertainties due to the muon and electron efficiencies, both in control and signal regions, and the jet energy scale and trigger efficiencies. In the present Run II analyses, due to limited statistics in the dilepton control regions, the knowledge of the  $W$  over  $Z$  boson ratio is used as a constraint between the two backgrounds, leading to an increased sensitivity. The theoretical uncertainty on this ratio is set at 12.5% from studies of missing higher order QCD and EWK corrections [?], on both QCD and EWK productions. Already with  $300 \text{ fb}^{-1}$ , this parameter plays a much smaller role at the HL-LHC. Its influence is studied considering

half the current theoretical uncertainty, namely 7%, will be achieved by then. It is expected to have an impact of at most 3–5% degradation for the interesting best sensitivity regions and hence the constraint has been removed. It becomes however again relevant when considering very tight selection criteria on  $E_T^{\text{miss}}$  and  $M_{jj}$ , i.e. when the statistics in the CR become again the dominant uncertainty.

The best upper limits are achieved in the regions with lower thresholds on  $M_{jj}$  of 2500 GeV and on  $E_T^{\text{miss}}$  of 190 GeV, for the  $3000 \text{ fb}^{-1}$  scenario. The minimum region is rather flat between 2300 and 3000 GeV thresholds in  $M_{jj}$  and between 170 and 220 GeV in  $E_T^{\text{miss}}$ , indicating limited impact from the native MC sample statistics. The upper limits are degrading steeply as the  $E_T^{\text{miss}}$  threshold increases above 250 GeV. The behaviour is similar for the 300 and  $1000 \text{ fb}^{-1}$  scenarios, with best thresholds found at lower values in  $E_T^{\text{miss}}$  (170 GeV) and  $M_{jj}$  (1500 and 1800 GeV respectively) due to the interplay between the statistics in the control regions and the systematics.

Distributions in  $M_{jj}$  for the leading jet pair and  $E_T^{\text{miss}}$  in the signal region are shown in figure 72, for the final  $3000 \text{ fb}^{-1}$  luminosity. The corresponding expected yields are shown in table 36. The uncertainties shown are the native uncertainties from the Delphes samples (not used in the calculations of the final limits).

Process	SR	$W \rightarrow e\nu$ CR	$W \rightarrow \mu\nu$ CR	$Z \rightarrow ee$ CR	$Z \rightarrow \mu\mu$ CR
VBFH	$47812 \pm 584$	-	-	-	-
ggH	972	-	-	-	-
$Z \rightarrow \ell\ell$ (EWK)	$103 \pm 8$	$398 \pm 16$	$641 \pm 20$	$1342 \pm 30$	$1889 \pm 35$
$Z \rightarrow \ell\ell$ (QCD)	$451 \pm 90$	$944 \pm 126$	$1048 \pm 116$	$1347 \pm 118$	$2297 \pm 158$
$Z \rightarrow \nu\nu$ (EWK)	$15275 \pm 358$	-	-	-	-
$Z \rightarrow \nu\nu$ (QCD)	$20968 \pm 599$	-	-	-	-
$W \rightarrow e\nu$ (EWK)	$3358 \pm 62$	$18986 \pm 146$	$72 \pm 9$	$33 \pm 6$	-
$W \rightarrow \mu\nu$ (EWK)	$3426 \pm 62$	$7 \pm 3$	$29360 \pm 181$	-	$17 \pm 4$
$W \rightarrow \tau\nu$ (EWK)	$3595 \pm 64$	$55 \pm 8$	$87 \pm 10$	-	-
$W \rightarrow e\nu$ (QCD)	$3994 \pm 999$	$13376 \pm 1656$	$170 \pm 168$	-	-
$W \rightarrow \mu\nu$ (QCD)	$6891 \pm 1388$	-	$23322 \pm 2096$	-	-
$W \rightarrow \tau\nu$ (QCD)	$4308 \pm 938$	-	-	-	-
Top	$2050 \pm 132$	$2171 \pm 143$	$3735 \pm 188$	$107 \pm 36$	$130 \pm 39$
QCD	-	-	-	-	-

Table 36: Number of events expected after the final selection  $M_{jj} > 2500 \text{ GeV}$  and  $E_T^{\text{miss}} > 190 \text{ GeV}$ , with  $3000 \text{ fb}^{-1}$  of integrated luminosity. The uncertainties are the native statistical uncertainties from the Delphes samples.

Final limits for  $3000 \text{ fb}^{-1}$  of luminosity are shown in figure 73, left, as a function of the thresholds applied on  $E_T^{\text{miss}}$  assuming the MC statistical uncertainties are negligible, for the final selections described above. In the best case, the lowest 95% CL limit on  $\text{BR}(\text{Hinv})$  assuming standard model production is expected to be at 3.8%, for thresholds values of 2500 GeV (190 GeV) on the dijet mass ( $E_T^{\text{miss}}$ ). If the  $E_T^{\text{miss}}$  resolution was to be a factor of 2 worse, the re-optimisation of the selection leads to minimum thresholds of 1800 GeV (250) GeV on the dijet mass ( $E_T^{\text{miss}}$ ), and similar 95%CL limit sensitivity. The limits are shown for the different luminosity scenarios in figure 73, right.

## 6.2 Interpretation and combination with precision Higgs boson measurements

### 6.2.1 Experimental input

For the VBF production channel, the projected HL-LHC limit on the invisible Higgs decay rate from the CMS experiment amounts to 4%, see Section 6.1. For the  $VH$  production channel ATLAS projected a

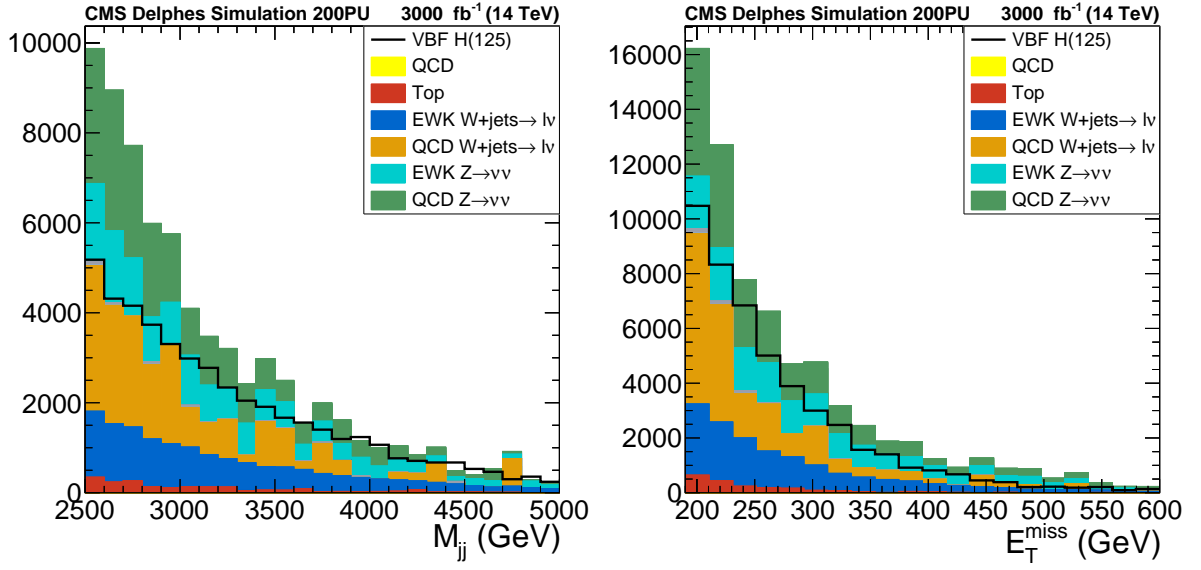


Fig. 72: Distributions of  $M_{jj}$  (left) and  $E_T^{\text{miss}}$  (right) in the signal region for the final selection  $M_{jj} > 2500$  GeV and  $E_T^{\text{miss}} > 190$  GeV.

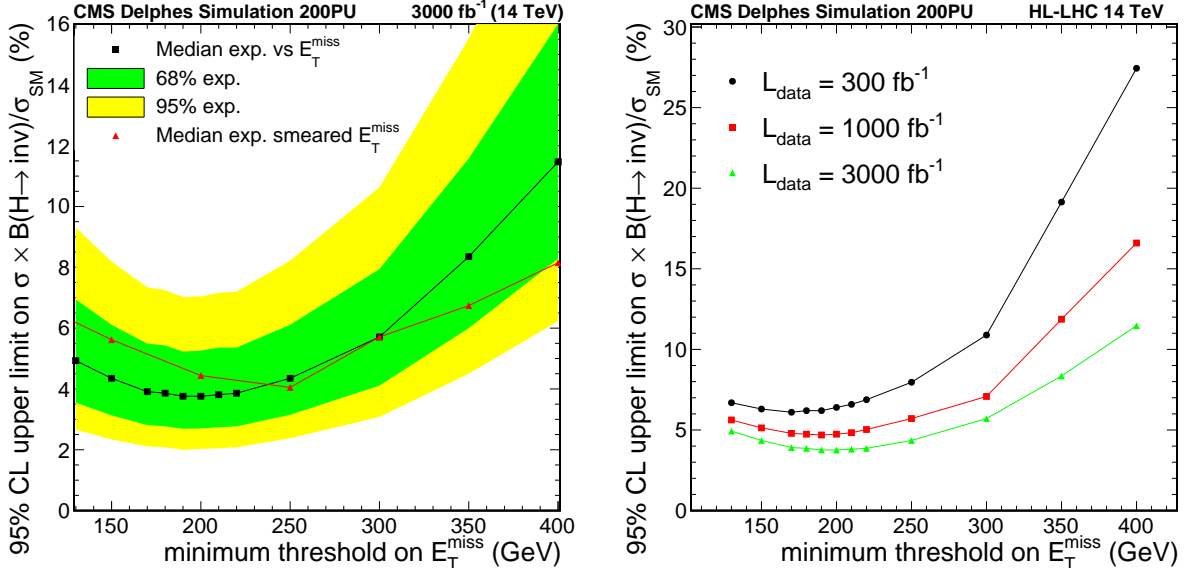


Fig. 73: Left: 95% CL limits on  $\text{BR}(\text{Hinv})$  as a function of the minimum threshold on  $E_T^{\text{miss}}$ , for  $M_{jj} > 2500$  GeV and  $3000 \text{ fb}^{-1}$  of luminosity. Right: 95% CL limits for different luminosity scenarios.

limit of around 8% in 2013 [?]. Assuming ATLAS (CMS) performs equally well as CMS (ATLAS) in the VBF ( $VH$ ) channel, and neglecting possible correlations of experimental and theoretical uncertainties, a combination of these limits results in

$$(\mu_{\text{VBF}, VH} \cdot \text{BR}_{\text{inv}})^{\text{HL-LHC}} \leq 2.5\%, \quad (92)$$

where  $\mu_{\text{VBF}, VH}$  is a common signal strength modifier of the VBF and  $VH$  production cross sections.

We implemented the CMS HL projections for Higgs signal strength measurements for the individual production times decay modes (see Section 2.9) into the public code `HiggsSignals` [?, ?]. We double the number of projections to account for the corresponding future ATLAS measurements. We consider both scenarios S1 and S2. These scenarios differ in the treatment of systematic uncertainties.

In S1, systematic uncertainties are unchanged with respect to current values; S2 employs rescaled experimental systematic uncertainties [?] and furthermore assumes a reduction of theoretical uncertainties by a factor 2. Note that correlations of theoretical rate uncertainties between the future CMS and assumed ATLAS measurements are taken into account in our fit via `HiggsSignals`.

We furthermore study the impact of a future electron-proton collider option (LHeC) at CERN [?, ?, ?], assuming a 60 GeV electron beam, a 7 TeV proton beam and an integrated luminosity of  $1 \text{ ab}^{-1}$ . We implemented the prospective signal strength measurements at the LHeC presented in Ref. [?] into HS. The projected limit on the invisible Higgs decay rate is around 5% [?, ?, ?, ?, ?, ?]<sup>19</sup>. In combination with the above CMS and ATLAS projections, we obtain

$$(\mu_{\text{VBF}, VH, \text{NC}} \cdot \text{BR}_{\text{inv}})^{\text{HL-LHC} \oplus \text{LHeC}} \leq 2.25\%$$

as upper limit on the branching ratio of an invisible Higgs decay mode. Here, we assume the common signal strength modifier  $\mu$  also applies to the neutral current (NC) Higgs production cross section at the LHeC.

### 6.2.2 Effective description of Higgs portal models

In this section we discuss the HL-LHC prospects in the context of an effective parametrization of Higgs rate modifications that are commonly predicted by Higgs portal models, using the coupling scale factor ( $\kappa$ ) framework [3]. Herein, the scale factors  $\kappa_X$  ( $X = W, Z, g, \gamma, b, \tau, \dots$ ) are introduced for every relevant Higgs coupling to SM particle  $X$ . The partial widths and cross sections associated with these Higgs couplings are then rescaled by  $\kappa_X^2$  (see Refs. [?, 3] for more details). In addition, we treat the branching fraction for invisible Higgs decays,  $\text{BR}_{\text{inv}}$ , as free parameter.

In particular, we investigate two scenarios for the Higgs coupling modifications:

- (i) a universal scale factor for all Higgs couplings to SM particles,  $\kappa \equiv \kappa_X$  ( $X = W, Z, g, \gamma, b, \tau, \dots$ );
- (ii) additional free parameters  $\kappa_g$  and  $\kappa_\gamma$  that rescale the loop-induced Higgs couplings to gluons and photons, respectively. The remaining (tree-level) Higgs couplings to SM particles are again rescaled universally with  $\kappa \equiv \kappa_X$  ( $X = W, Z, b, \tau, \dots$ ).

We employ the program `HiggsSignals` [?, ?] to perform a  $\chi^2$  fit to the projected HL-LHC and/or LHeC Higgs rate measurements (see Section 6.2.1) in each scenario. The resulting future 95% C.L. limit is shown in Fig. 74 as light and dark green area for scenario (i) and (ii), respectively. The *top panels* display the HL-LHC projections for future scenarios S1 (*left*) and S2 (*right*), while the *bottom panels* show the projections for LHeC (*left*) and the combination of LHeC with HL-LHC S2 measurements (*right*). In Tab. 37 we summarize the lower limits on the Higgs signal strength of channels with SM final states,  $\kappa^2(1 - \text{BR}_{\text{inv}})$ , as well as the upper limits on the invisible Higgs decay rate,  $\text{BR}_{\text{inv}}$ , assuming SM Higgs coupling strengths ( $\kappa \equiv 1$ ), for the four future collider scenarios and for the two global fit scenarios. Note that these results do not strictly require the additional Higgs decay mode to yield an invisible final state.

These results are compared in Fig. 74 with the prospective future limits from direct searches for invisible Higgs decays (see Section 6.2.1). At the HL-LHC, assuming scenario S1 (S2), direct invisible Higgs searches are more sensitive than Higgs rates if deviations from the SM Higgs couplings are small,  $\Delta\kappa \equiv 1 - \kappa \lesssim 2 (1)\%$ . For larger suppression of the Higgs couplings the Higgs rates will provide the strongest constraint. In contrast, if we allow for an enhancement of the Higgs couplings,  $\kappa > 1$ , the invisible Higgs searches will provide the strongest constraint (besides other bounds on the Higgs total decay width, see Sec. 5).

---

<sup>19</sup>Optimization of the signal selection, advanced background estimation techniques and details of the detector design may improve this limit down to about (3 – 4)% [?].

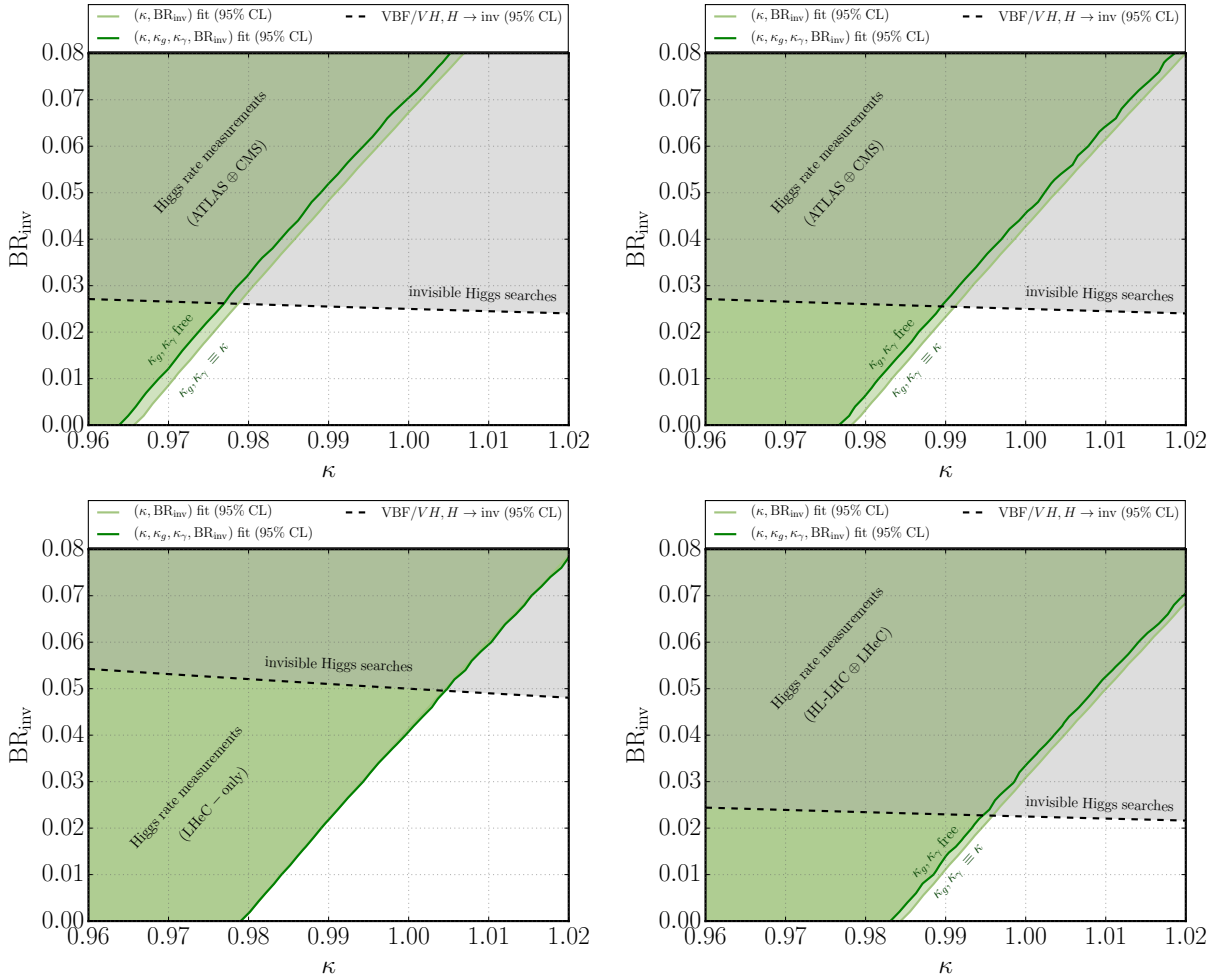


Fig. 74: Projected 95% C.L. limit in the  $(\kappa, \text{BR}_{\text{inv}})$  plane inferred from Higgs rate measurements (green regions) and direct invisible Higgs searches (black dashed line) at the HL-LHC and LHeC. We show results for the two future HL-LHC scenarios S1 (top left) and S2 (top right) (see text for details), as well as for the LHeC (bottom left) and the combination of LHeC and HL-LHC (S2) (bottom right). The light green area shows the limit from Higgs rates obtained by assuming no new physics contributions to the loop-induced Higgs couplings to gluons and photons,  $\kappa = \kappa_g = \kappa_\gamma$ , whereas for the dark green area  $\kappa_g$  and  $\kappa_\gamma$  are marginalized free parameters. These plots will be updated once ATLAS and CMS signal strength combination projections become available.

fit setup	quantity	HL-LHC S1	HL-LHC S2	LHeC	LHeC ⊕ HL-LHC S2
$(\kappa, \text{BR}_{\text{inv}})$	$\kappa^2(1 - \text{BR}_{\text{inv}})$	$\geq 0.933$	$\geq 0.957$	$\geq 0.959$	$\geq 0.969$
	$\text{BR}_{\text{inv}}(\kappa \equiv 1)$	$\leq 6.7\%$	$\leq 4.3\%$	$\leq 4.1\%$	$\leq 3.1\%$
$(\kappa, \kappa_g, \kappa_\gamma, \text{BR}_{\text{inv}})$	$\kappa^2(1 - \text{BR}_{\text{inv}})$	$\geq 0.930$	$\geq 0.954$	$\geq 0.959$	$\geq 0.966$
	$\text{BR}_{\text{inv}}(\kappa \equiv 1)$	$\leq 7.0\%$	$\leq 4.6\%$	$\leq 4.1\%$	$\leq 3.4\%$

Table 37: Comparison of prospective 95% C.L. limits on the Higgs signal strength for SM final states,  $\kappa^2(1 - \text{BR}_{\text{inv}})$ , and the invisible Higgs decay rate,  $\text{BR}_{\text{inv}}$  (assuming SM Higgs couplings,  $\kappa = 1$ ), for HL-LHC scenarios S1 and S2, LHeC, and the combination of LHeC and HL-LHC (scenario S2). First (second) row shows the results obtained in the fit parametrization (i) [(ii)].

At the LHeC the prospective indirect Higgs rate constraints are comparable to the HL-LHC S2 prospects, reaching a precision of  $\Delta\kappa \lesssim (2.1 - 2.2)\%$  independently of the invisible Higgs decay rate, in both fit parametrizations considered here.<sup>20</sup> On the other hand, the direct invisible Higgs searches at the LHeC are weaker than at the HL-LHC. In combination with the HL-LHC (assuming future scenario S2), the bounds from the Higgs rates can further be improved to coupling deviations of  $\Delta\kappa \lesssim 1.5\%$ .

Compared with the sensitivity of Higgs rate measurements during Run 1 of the LHC [25] to the invisible decay rate,  $\text{BR}_{\text{inv}} \lesssim \mathcal{O}(20\%)$  (at 95% C.L.), we find that the sensitivity improves by roughly a factor of 3–5 at the HL-LHC (depending on the evolution of systematic uncertainties). In combination with LHeC results we expect the indirect limit to improve by a factor of up to 6.5.

### 6.3 Higgs portal interpretations

#### 6.3.1 Minimal Higgs Portal

In the minimal Higgs portal model, we impose a quartic interaction of the SM Higgs doublet field  $H$  with the DM field, which could be either a scalar ( $S$ ) [?], a vector ( $V^\mu$ ) [?] or a fermion ( $\chi$ ) [?] (see Refs. [?, ?] for a comprehensive overview):

$$\mathcal{L} \supset -\frac{1}{4}\lambda_{hSS}H^\dagger HS^2 \quad (\text{scalar DM}) \quad \text{or} \quad (93)$$

$$\mathcal{L} \supset +\frac{1}{4}\lambda_{hVV}H^\dagger HV_\mu V^\mu \quad (\text{vector DM}) \quad \text{or} \quad (94)$$

$$\mathcal{L} \supset -\frac{1}{4}\frac{\lambda_{h\chi\chi}}{\Lambda}H^\dagger H\bar{\chi}\chi \quad (\text{fermion DM}), \quad (95)$$

respectively. Besides these operators the Lagrangian contains an explicit mass term of the DM field, allowing us to use the mass of the DM particle,  $M_{\text{DM}}$ , as a free model parameter. In addition, the Lagrangian  $\mathcal{L}$  contains DM self-interaction operators, however, these are irrelevant to our study.

If DM is light,  $M_{\text{DM}} < M_H/2 \simeq 62.5$  GeV, the above interactions lead to the invisible Higgs decay into two DM particles. An upper limit on  $\text{BR}_{\text{inv}}$  can therefore be translated into an upper limit on the portal coupling  $\lambda$  of above operators, Eqs. (93)–(95), depending on  $M_{\text{DM}}$ . At the same time, the portal coupling  $\lambda$  governs the DM phenomenology. For DM masses  $M_{\text{DM}} \lesssim M_H/2$  the relic abundance of the DM particles is driven by the  $s$ -channel annihilation through the exchange of the Higgs boson.<sup>21</sup> As the DM–nucleon elastic scattering amplitudes are directly proportional to the portal coupling [?], it can be additionally constrained by DM direct detection experiments. These are sensitive to the elastic scattering of the DM particles with nuclei, mediated by the Higgs boson. Hence, in turn, the upper limit on  $\lambda$  can be translated into an upper limit on the (spin-independent) DM–nucleon scattering cross section,  $\sigma_{\text{DM–nucleon}}$  (see Refs. [?, ?]).

In Fig. 75 we show the current [*left panel*] and prospective [*right panel*] upper limits on  $\sigma_{\text{DM–nucleon}}$  inferred from a current and HL-LHC prospective upper limit on  $\text{BR}_{\text{inv}}$  of 20% and 2.5%, respectively.<sup>22</sup> These are shown for scalar [*blue curve*], fermion [*red curve*] and vector [*green curve*] DM. The uncertainty bands on these curves correspond to the uncertainty in the Higgs–nucleon coupling form factor, where we use the recent result from Ref. [?]. For comparison we include in Fig. 75 current limits from DM direct detection experiments XENON10 [?], XENON100 [?] and XENON1T [?], prospective limits from XENONNT [?] and SUPERCDMS at SNOLAB [?]. For completeness, we also show the favored parameter regions from excesses seen in the DAMA/LIBRA [?], CRESST [?], CDMS II [?] and Co-

<sup>20</sup>The complementarity of LHeC and HL-LHC Higgs rate measurements is much stronger in more general coupling fit setups, e.g., when independent scale factors for the Higgs- $W$ - $W$  and Higgs- $Z$ - $Z$  couplings are considered [?].

<sup>21</sup>Assuming a standard cosmological history and thermal freeze-out dark matter, the minimal Higgs portal scenario with light DM is tightly constrained, with only a narrow mass range around  $M_{\text{DM}} \simeq M_H/2$  being allowed. However, this can be relaxed in alternative cosmological scenarios and DM production mechanisms, see e.g. Refs. [?, ?, ?].

<sup>22</sup>For current ATLAS and CMS results for the minimal Higgs portal interpretation see Refs. [?, ?, ?, ?].

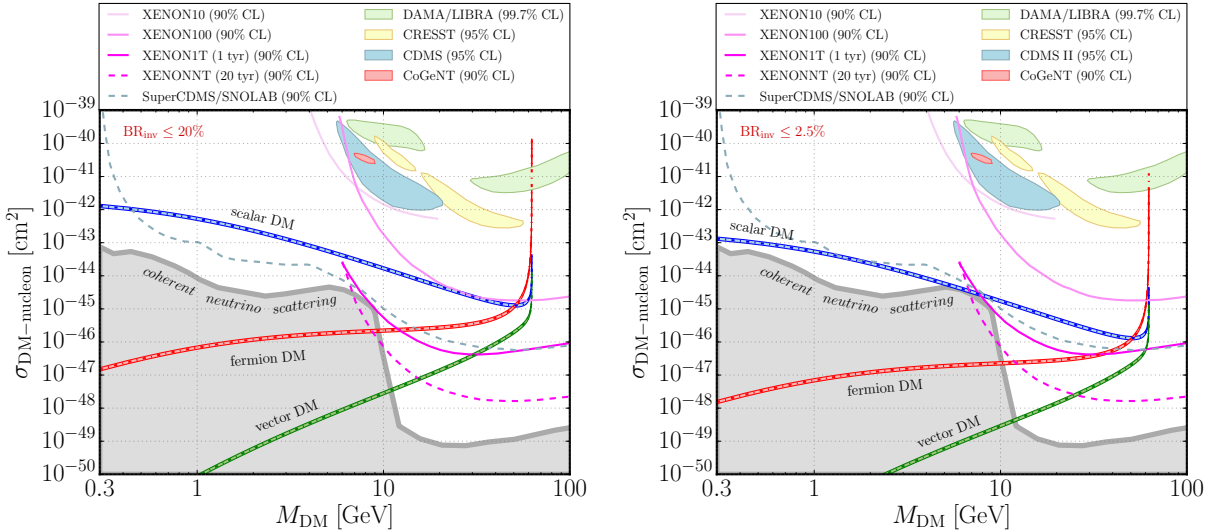


Fig. 75: Implications for the minimal Higgs portal model: Comparison of current (*left figure*) and future HL-LHC (*right figure*) limits from invisible Higgs searches with limits from DM direct detection experiments on the spin-independent DM-nucleon scattering cross section,  $\sigma_{\text{DM}-\text{nucleon}}$ , as a function of the DM mass,  $M_{\text{DM}}$ . The inferred limits from invisible Higgs searches are shown for scalar DM (blue curve), fermion DM (red curve) and for vector DM (green curve). In addition we show present limits (*solid lines*), favored regions (*filled areas*) and future sensitivity (*dashed lines*) of the DM direct detection experiments XENON10 [?], XENON100 [?], XENON1T [?], XENONNT [?], SUPERCDMS at SNOLAB [?], DAMA/LIBRA [?], CRESST [?], CDMS II [?] and COGENT [?] (*see legend*). The gray area indicates regions inaccessible to DM direct detection experiments due to the irreducible neutrino flux background [?].

GENT [?] experiments.<sup>23</sup> We furthermore indicate by the gray area in Fig. 75 the *neutrino floor*, i.e. the parameter region that is inaccessible to DM direct detection experiments due to the irreducible neutrino flux background [?].

Currently, the inferred limit from invisible Higgs searches yields the most sensitive constraint in the low mass region,  $M_{\text{DM}} \lesssim 6, 10$  and  $30$  GeV for scalar, fermion and vector DM, respectively, while at larger DM masses the XENON1T limit is more constraining. In particular, in the fermion and vector DM case, the  $\text{BR}_{\text{inv}}$  limit probes deep into the parameter region that is inaccessible to direct detection experiments. A future limit on the invisible Higgs decay rate from the HL-LHC will improve the limits on  $\sigma_{\text{DM}-\text{nucleon}}$  by almost one order of magnitude, which pushes the limit for light scalar DM close to the neutrino floor. For fermion (vector) DM in the mass range  $10 \text{ GeV} \lesssim M_{\text{DM}} \lesssim 20$  (60) GeV, in case of a future excess seen in the XENONNT data, complementary measurements of an invisible Higgs decay at the HL-LHC may be possible.

### 6.3.2 Scalar singlet portal

We now turn our discussion to a model that features an additional scalar singlet in the visible sector, which provides the portal interaction to the hidden DM sector. In contrast to the minimal Higgs portal discussed in Section 6.3.1, this model allows for a modification of the 125 GeV Higgs couplings, and thus for a non-trivial interplay between direct invisible Higgs searches and Higgs rate measurements at the HL-LHC. For illustration, we focus here on the case of scalar DM, the other cases (fermion and vector DM) can be treated analogously. The model is inspired by Refs. [?, ?].

<sup>23</sup>Note that the limits and favored regions from DM direct detection experiments assume for the incoming flux of DM particles that the observed relic density in the Universe is fully saturated by this one DM particle species.

The SM Higgs sector is extended by two real scalar singlet fields,  $S$  and  $X$ . Imposing a  $\mathbb{Z}_2$  symmetry described by the transformation  $S \rightarrow -S$ ,  $X \rightarrow -X$ , the model is characterized by the scalar potential  $\mathcal{V} = \mathcal{V}_{\text{visible}} + \mathcal{V}_{\text{hidden}}$ , where

$$\mathcal{V}_{\text{visible}} = \mu_\Phi^2 \Phi^\dagger \Phi + \lambda_\Phi (\Phi^\dagger \Phi)^2 + \mu_S^2 S^2 + \lambda_S S^4 + \lambda_{\Phi S} \Phi^\dagger \Phi S^2, \quad (96)$$

$$\mathcal{V}_{\text{hidden}} = \frac{1}{2} [\mu_X^2 X^2 + \lambda_X X^4 + \lambda_{SX} S^2 X^2]. \quad (97)$$

After electroweak symmetry breaking (EWSB) the scalar  $\text{SU}(2)_L$  doublet field  $\Phi$  is given by  $\Phi \equiv (0 \ \phi + v)^T / \sqrt{2}$ , with the vacuum expectation value (vev)  $v \approx 246$  GeV. We assume the scalar field  $S$  to acquire a non-zero vev,  $v_S$ , which softly breaks the  $\mathbb{Z}_2$  symmetry, such that the singlet field  $S$  is given by  $S \equiv (s + v_S)/\sqrt{2}$ . Through the last term in Eq. (96) the non-zero vevs induce a mixing of the physical degrees of freedom of these two fields,  $\phi$  and  $s$ ,

$$\begin{pmatrix} h \\ H \end{pmatrix} = \begin{pmatrix} \cos \alpha & -\sin \alpha \\ \sin \alpha & \cos \alpha \end{pmatrix} \begin{pmatrix} \phi \\ s \end{pmatrix}, \quad (98)$$

with the masses of the physical states  $h$  and  $H$  given by

$$M_{h/H}^2 = \lambda_\Phi v^2 + \lambda_S v_S^2 \mp \sqrt{\left(\lambda_\Phi v^2 - \lambda_S v_S^2\right)^2 + \left(\lambda_{\Phi S} v v_S\right)^2}, \quad (99)$$

and the mixing angle  $\alpha \in [-\frac{\pi}{2}, \frac{\pi}{2}]$  given by

$$\tan 2\alpha = \frac{\lambda_{\Phi S} v v_S}{\lambda_S v_S^2 - \lambda_\Phi v^2}. \quad (100)$$

In contrast,  $X$  does not acquire a vev. As a result  $X$  is stable and thus a possible DM candidate, with a mass given by  $M_X^2 = \mu_X^2 + \lambda_{SX} v_S^2 / 2$ .

In this analysis, we assume  $M_H = 125.09$  GeV, and  $M_h < M_H$ . Furthermore, we discard the quartic interaction term  $\propto \lambda_X$  in Eq. (97) as this operator is irrelevant for our study. With this, the model can then be parametrized in terms of the following input quantities:

$$M_h, \cos \alpha, v_S, M_X, \lambda_{SX}. \quad (101)$$

The couplings of the Higgs bosons  $h$  and  $H$  to SM gauge bosons and fermions are universally suppressed by the mixing,

$$g_h/g_{h,\text{SM}} = \cos \alpha, \quad g_H/g_{H,\text{SM}} = \sin \alpha. \quad (102)$$

If the DM scalar  $X$  is light enough the portal coupling  $\lambda_{SX}$  gives rise to decays of the Higgs bosons  $h$  and  $H$  to the invisible  $XX$  final state. The partial decay widths are given by

$$\begin{aligned} \Gamma(h \rightarrow XX) &= \sin^2 \alpha \cdot \Gamma_{XX}(M_h), \\ \Gamma(H \rightarrow XX) &= \cos^2 \alpha \cdot \Gamma_{XX}(M_H), \end{aligned} \quad \text{with} \quad \Gamma_{XX}(M) = \frac{\lambda_{SX}^2 v_S^2}{32\pi M} \sqrt{1 - \frac{4M_X^2}{M^2}}. \quad (103)$$

Furthermore, if  $M_h \leq M_H/2$ , the heavier Higgs boson  $H$  can decay into  $hh$ , with the partial width given by

$$\Gamma(H \rightarrow hh) = \frac{\lambda_{Hhh}^2}{32\pi M_H} \sqrt{1 - \frac{4M_h^2}{M_H^2}}, \quad (104)$$

and the effective  $Hhh$  coupling<sup>24</sup>

---

<sup>24</sup>Note that the relative sign between the two terms in Eq. (105) differs with respect to Eq. (13) in Ref. [?].

$$\begin{aligned}\lambda_{Hhh} = & -3 \sin 2\alpha [\lambda_S v_S \sin \alpha + \lambda_\Phi v \cos \alpha] \\ & - \tan 2\alpha (\lambda_S v_S^2 - \lambda_\Phi v^2) \left[ (1 - 3 \sin^2 \alpha) \frac{\cos \alpha}{v} + (1 - 3 \cos^2 \alpha) \frac{\sin \alpha}{v_S} \right].\end{aligned}\quad (105)$$

Through the successive decay of the lighter Higgs boson  $h$  into either final states with SM particles (denoted as ‘SM’) or the invisible  $XX$  final state, this gives rise to the following signatures<sup>25</sup>

$$H \rightarrow hh \rightarrow \begin{cases} (\text{SM})(\text{SM}), & (\text{visible}), \\ (\text{SM})(XX), & (\text{semi-invisible}), \\ (XX)(XX), & (\text{invisible}). \end{cases}\quad (106)$$

The branching ratio of the invisible decay of the SM-like Higgs boson  $H$  is given by

$$\text{BR}_{\text{inv}} = \text{BR}(H \rightarrow XX) + \text{BR}(H \rightarrow hh) \cdot \text{BR}(h \rightarrow XX)^2.\quad (107)$$

In Fig. 76 we show the invisible Higgs decay rate  $\text{BR}_{\text{inv}}$  in the  $(M_h, \cos \alpha)$  plane, for fixed DM mass  $M_X = 5$  GeV, and four choices  $(v_S, \lambda_{SX}) = (50v, 10^{-4})$  [top left],  $(50v, 10^{-6})$  [top right],  $(50v, 10^{-3})$  [bottom left] and  $(5v, 10^{-4})$  [bottom right]. For better illustration, the secondary y-axis shows the deviation from the SM coupling strength,  $\Delta\kappa = 1 - \sin \alpha$ , of the heavier Higgs boson  $H$ . The  $\text{BR}_{\text{inv}}$  prediction is given by the black solid contours. Various constraints (at 95% C.L.) are included in the figures: future direct invisible Higgs searches (red dashed contour/gray area), future indirect limits from Higgs rate measurements at the HL-LHC (assuming S2) using the two parametrizations of Section 6.2.2 [cf. Fig. 74] (solid pale/bright green contour and area), and LEP searches for the lighter Higgs boson  $h$  (orange contour and area), obtained via HiggsBounds [?, ?, ?]. For the latter, the relevant experimental analyses are searches for  $e^+e^- \rightarrow Zh$  production with  $h$  either decaying to invisible particles [?, ?, ?, ?] or to SM particles (in particular,  $b\bar{b}$ ) [?], as well as the decay mode independent analysis by OPAL [?].

In all four panels of Fig. 76 we can identify two kinematical thresholds for the invisible  $H$  decay: at  $M_h = M_H/2 \simeq 62.5$  GeV, where the cascade decay  $H \rightarrow hh \rightarrow (XX)(XX)$  becomes available for decreasing  $M_h$ , and at  $M_h = 2M_X = 10$  GeV, where the decay  $h \rightarrow XX$  kinematically closes for smaller  $M_h$ , and thus the  $H \rightarrow hh$  decay cannot further lead to an invisible final state. Above the first threshold,  $M_h > M_H/2$ , and below the second threshold,  $M_h < 2M_X$ , the invisible  $H$  decay is solely given by the direct decay  $H \rightarrow XX$ .

For the parameter choice  $(v_s, \lambda_{SX}) = (50v, 10^{-4})$  (top left panel), the direct invisible Higgs searches at the HL-LHC will provide similar bounds as the indirect constraints from the Higgs rates for the mass range  $M_h \in [2M_X, M_H/2]$ . However, in the mass range  $M_h \sim (10 - 40)$  GeV, the LEP searches for invisible  $h$  decays will still yield the strongest exclusion. Note that the Higgs rate measurements are always constraining the sum  $\text{BR}(H \rightarrow \text{NP}) = \text{BR}(H \rightarrow XX) + \text{BR}(H \rightarrow hh)$ , irrespectively of whether the decay  $H \rightarrow hh$  leads to an invisible final state. Hence, they remain to be sensitive in the low mass region  $M_h < 2M_X$ .

For a larger Higgs-portal interaction,  $\lambda_{SX} = 10^{-3}$  (bottom left panel), the direct decay  $H \rightarrow XX$  becomes more prominent, leading to sizable  $\text{BR}_{\text{inv}}$  even at smaller  $\cos \alpha$ . Here, direct invisible Higgs searches at HL-LHC will be most constraining and will supersede the LEP limits except in the mass range  $M_h \sim (10 - 33)$  GeV. In contrast, for very small Higgs-portal interaction,  $\lambda_{SX} = 10^{-6}$  (top right panel) the invisible Higgs decay rates are much smaller. Nevertheless, future indirect constraints from Higgs rate measurements will supersede the LEP limits in almost the entire mass range except for

---

<sup>25</sup>Note that LHC searches for the semi-invisible and visible final states are highly complementary to invisible Higgs searches in this model.

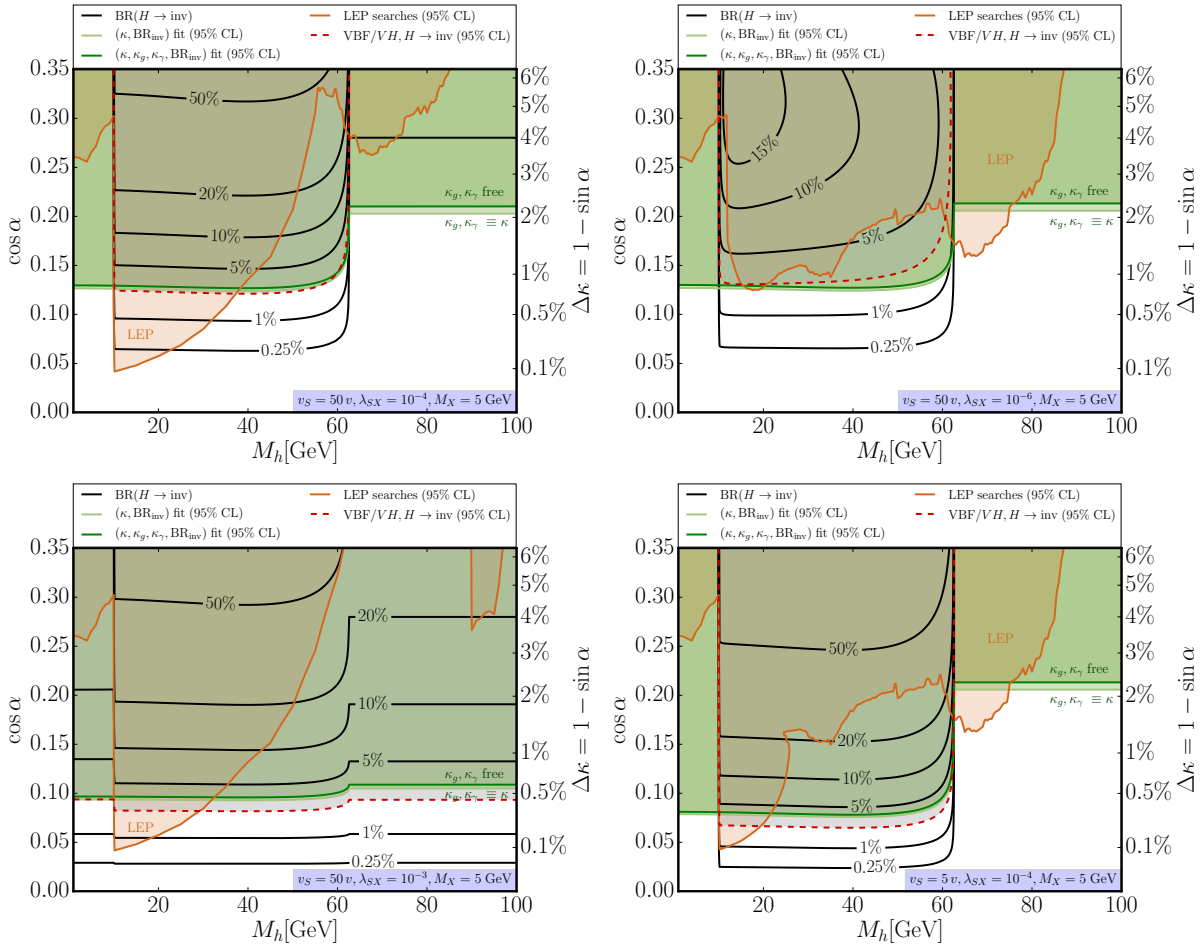


Fig. 76: Implications for the scalar singlet portal model, shown in the  $(M_h, \cos \alpha)$  parameter plane for a DM mass of  $M_X = 5$  GeV and  $(v_S, \lambda_{SX}) = (50 v, 10^{-4})$  [top left],  $(50 v, 10^{-6})$  [top right],  $(50 v, 10^{-3})$  [bottom left] and  $(5 v, 10^{-4})$  [bottom right]. Black solid contours show the invisible Higgs decay rate,  $\text{BR}(H \rightarrow \text{inv})$ , the red dashed contour/gray area indicates the expected HL-LHC limit from invisible Higgs searches, pale and bright green contours/areas indicate the indirect constraints from HL-LHC Higgs rate measurements (using the two parametrizations, see Section 6.2.2), and the orange contour/area marks the excluded region from LEP searches. See text for more details. These plots will be updated once the ATLAS and CMS signal strength combination projection becomes available.

$M_h$  values between 62 to 75 GeV. Note that the LEP exclusion arises from  $e^+ e^- \rightarrow Z h \rightarrow Z(b\bar{b})$  searches [?].

If we decrease the vev of the singlet field,  $v_s = 5 v$  (bottom right panel), the effective  $H h h$  coupling becomes larger, leading to a more pronounced  $H \rightarrow hh$  decay if kinematically accessible. Hence, in the region  $M_h < M_H/2$ , the HL-LHC constraints both from direct invisible Higgs searches and Higgs rate measurements are very strong and supersede the LEP constraints in almost the entire mass range up to  $M_h \lesssim M_H/2$ . In this case, the direct invisible Higgs searches are slightly more sensitive than the Higgs rate measurements.

In summary, the example parameter choices made in Fig. 76 illustrate an interesting interplay between past LEP searches for a light Higgs boson  $h$ , future HL-LHC searches for an invisibly decaying SM-like Higgs boson  $H$ , and future HL-LHC precision Higgs rate measurements. Depending on the parameter choice, each experimental probe can be the most sensitive/constraining one, which highlights their complementarity and strongly motivates a corresponding experimental program at the HL-LHC.

## 6.4 Conclusions

Higgs portal models are intriguing and simple new physics scenarios that contain a dark matter candidate which can be tested at collider as well as astrophysical experiments. The HL-LHC will be able to constrain the Higgs boson–dark matter coupling constant and probe the parameter regime down to an invisible Higgs decay rate of 2%. For low dark matter masses,  $M_{\text{DM}} \lesssim 30$  GeV, these bounds are typically more constraining than limits obtained from dark matter direct detection experiments. For a specific model with two visible scalar states and a scalar dark matter candidate, we presented scenarios for which future HL-LHC searches will supersede complementary constraints from LEP searches for a light scalar boson. In summary, the future HL-LHC measurements of the Higgs signal strength, as well as direct searches for the invisible decay of the observed Higgs boson, promise to provide important insight within the framework of Higgs portal models. The sensitivity can further be improved by the future electron-proton collider LHeC. In particular, the indirect constraints from Higgs rate measurements will improve substantially if HL-LHC and LHeC results are combined.

## 7 Higgs flavor and rare decays

**Staus: ready for us editors and conveners to edit. One more contribution of Maria et al.?**

### 7.1 Introduction

In this section we cover the current status and future prospects for measuring the different Higgs couplings to fermions, these go under the generic name of “Higgs and Flavor”. The Higgs mechanism of the SM predict that the Yukawa couplings are proportional to the fermion mass and CP conserving, or more precisely

$$y_f^{\text{SM}} = \sqrt{2}m_f/v, \quad (108)$$

where the tree-level flavor changing couplings are zero. Currently, only the third generation Yukawa couplings were directly measured and found to be in agreement with the SM prediction, see Refs. [] for  $h\tau\bar{\tau}$ ,  $h\bar{b}b$  and  $h\bar{t}t$  recent results. However, for the Higgs coupling to first and second generations there are only upper bounds, see [].

Below, we adapt the generalized  $\kappa$  framework to describe deviations of the Higgs couplings from their SM values due to new physics (NP). In particular, we define **YS: why different notation for the diagonal and off-diagonal  $\kappa$ 's?**

$$\mathcal{L}_{\text{eff}} = -\kappa_{f_i} \frac{m_{f_i}}{v} h \bar{f}_i f_i + i \tilde{\kappa}_{f_i} \frac{m_{f_i}}{v} h \bar{f}_i \gamma_5 f_i - \left[ \left( \kappa_{f_i f_j} + i \tilde{\kappa}_{f_i f_j} \right) h \bar{f}_L^i f_R^j + \text{h.c.} \right]_{i \neq j}, \quad (109)$$

where a sum over fermion type  $f = u, d, \ell$  and generations  $i, j = 1, 2, 3$  is understood. The first two terms are flavour-diagonal with the first term CP-conserving and the second CP-violating. The terms in square brackets are flavour violating. The real (imaginary) part of the coefficient is CP conserving (violating). In the SM, we have  $\kappa_{f_i} = 1$  while  $\tilde{\kappa}_{f_i} = \kappa_{f_i f_j} = \tilde{\kappa}_{f_i f_j} = 0$ .

**YS: short discussion explains direct and indirect** The different Higgs Yukawa couplings can be probed by direct and indirect methods. The most direct probe of the top Yukawa is by measuring the Higgs production in association with top pair. The 13 TeV result []

The Higgs production and decay strengths measured at the LHC constrain the flavour-diagonal CP-conserving Yukawa couplings to be [?, ?, ?, ?, 89] (for future prospects see also [?, ?, ?, ?, ?, ?]) **YS: update numbers, for example  $h \rightarrow b\bar{b}$  has a new result also check  $t\bar{t}h$  - make sure that there is only direct measurements here**

$$\begin{aligned} \kappa_t &= 1.09 \pm 0.14, & \kappa_b &= 1.10_{-0.33}^{+0.27}, & \kappa_c &\lesssim 6.2, \\ \kappa_s &< 65, & \kappa_d &< 1.4 \cdot 10^3, & \kappa_u &< 3.0 \cdot 10^3, \\ \kappa_\tau &= 1.01_{-0.18}^{+0.17}, & \kappa_\mu &= 0.2_{-0.2}^{+1.2}, & \kappa_e &\lesssim 630. \end{aligned} \quad (110)$$

Here,  $\kappa_{t,b,c,s,d,u,\tau}$  constraints have been obtained by allowing BSM particles to modify the  $h \rightarrow gg$  and  $h \rightarrow \gamma\gamma$  couplings, i.e.  $\delta\kappa_{g,\gamma}$  were floated, while assuming that there are no new decay channels,  $BR_{\text{BSM}} = 0$ . The  $\kappa_{\mu,e}$  were required to be non-negative and **YS: is it just bound on the absolute value of them?**, in addition, when obtaining the respective bounds,  $\delta\kappa_{g,\gamma}$  were set to zero. The upper bounds on  $\kappa_{c,s,d,u}$  roughly correspond to the size of the SM bottom Yukawa coupling and are thus much bigger than the corresponding SM Yukawa couplings. The upper bounds can be saturated only if one allows for large cancellations between the contribution to fermion masses from the Higgs vev and an equally large but opposite in sign contribution from NP. We will show that in models of NP motivated by the hierarchy problem, the effects of NP are generically well below these bounds.

**YS:check citation to new Manos paper** The CP-violating flavour-diagonal Yukawa couplings,  $\tilde{\kappa}_{f_i}$ , are well constrained from bounds on the electric dipole moments (EDMs) [?, ?, ?] under the assumption of no cancellation with other contributions to EDMs beyond the Higgs contributions. The flavour

Model	$\kappa_t$	$\kappa_{c(u)}/\kappa_t$	$\tilde{\kappa}_t/\kappa_t$	$\tilde{\kappa}_{c(u)}/\kappa_t$
SM	1	1	0	0
MFV	$1 + \frac{\Re(a_u v^2 + 2b_u m_t^2)}{\Lambda^2}$	$1 - \frac{2\Re(b_u)m_t^2}{\Lambda^2}$	$\frac{\Im(a_u v^2 + 2b_u m_t^2)}{\Lambda^2}$	$\frac{\Im(a_u v^2)}{\Lambda^2}$
NFC	$V_{hu} v/v_u$	1	0	0
F2HDM	$\cos \alpha / \sin \beta$	$-\tan \alpha / \tan \beta$	$\mathcal{O}\left(\frac{m_c}{m_t} \frac{\cos(\beta-\alpha)}{\cos \alpha \cos \beta}\right)$	$\mathcal{O}\left(\frac{m_{c(u)}^2}{m_t^2} \frac{\cos(\beta-\alpha)}{\cos \alpha \cos \beta}\right)$
MSSM	$\cos \alpha / \sin \beta$	1	0	0
FN	$1 + \mathcal{O}\left(\frac{v^2}{\Lambda^2}\right)$	$1 + \mathcal{O}\left(\frac{v^2}{\Lambda^2}\right)$	$\mathcal{O}\left(\frac{v^2}{\Lambda^2}\right)$	$\mathcal{O}\left(\frac{v^2}{\Lambda^2}\right)$
GL2	$\cos \alpha / \sin \beta$	$\simeq 3(7)$	0	0
RS	$1 - \mathcal{O}\left(\frac{v^2}{m_{KK}^2} \bar{Y}^2\right)$	$1 + \mathcal{O}\left(\frac{v^2}{m_{KK}^2} \bar{Y}^2\right)$	$\mathcal{O}\left(\frac{v^2}{m_{KK}^2} \bar{Y}^2\right)$	$\mathcal{O}\left(\frac{v^2}{m_{KK}^2} \bar{Y}^2\right)$
pNGB	$1 + \mathcal{O}\left(\frac{v^2}{f^2}\right) + \mathcal{O}\left(y_*^2 \lambda^2 \frac{v^2}{M_*^2}\right)$	$1 + \mathcal{O}\left(y_*^2 \lambda^2 \frac{v^2}{M_*^2}\right)$	$\mathcal{O}\left(y_*^2 \lambda^2 \frac{v^2}{M_*^2}\right)$	$\mathcal{O}\left(y_*^2 \lambda^2 \frac{v^2}{M_*^2}\right)$

Table 38: Predictions for the flavour-diagonal up-type Yukawa couplings in a sample of NP models (see text for details).

violating Yukawa couplings are well constrained by the low-energy flavour-changing neutral current measurements [?, ?, ?]. A notable exception are the flavour-violating couplings involving a tau lepton. The strongest constraints on  $\kappa_{\tau\mu}, \kappa_{\mu\tau}, \kappa_{\tau e}, \kappa_{e\tau}$  are thus from direct searches of flavour-violating Higgs decays at the LHC [?, ?]. **YS: what about  $t \rightarrow ch$ ?**

In the rest of this section we review the expected sizes of  $\kappa_{f_i}$  in popular models of weak scale NP, some of them motivated by the hierarchy problem.

## 7.2 Flavor aspects Yukawa modifications in flavor models

### 7.2.1 New Physics benchmarks for modified Higgs couplings

#### 7.2.1.1 Modified Yukawa couplings and electroweak New Physics

Tables 38, 39, and 40, adapted from [?, ?, ?, ?, 191], summarize the predictions for the effective Yukawa couplings,  $\kappa_f$ , in the Standard Model, multi-Higgs-doublet models (MHDM) with natural flavour conservation (NFC) [?, ?], a “flavourful” two-Higgs-doublet model beyond NFC (F2HDM) [?, ?, ?, ?] the MSSM at tree level, a single Higgs doublet with a Froggat-Nielsen mechanism (FN) [?], the Giudice-Lebedev model of quark masses modified to 2HDM (GL2) [?], NP models with minimal flavour violation (MFV) [?], Randall-Sundrum models (RS) [?], and models with a composite Higgs where Higgs is a pseudo-Nambu-Goldstone boson (pNGB) [?, ?, ?, ?]. The flavour-violating couplings in the above set of NP models are collected in Tables 41 and 42. Next, we briefly discuss each of the above models, and show that the effects are either suppressed by  $1/\Lambda^2$ , where  $\Lambda$  is the NP scale, or are proportional to the mixing angles with the extra scalars.

Dimension-Six Operators with Minimal Flavor Violation (MFV). We first assume that there is a mass gap between the SM and NP. Integrating out the NP states leads to dimension six operators (after absorbing the modifications of kinetic terms using equations of motion [?]),

$$\mathcal{L}_{\text{EFT}} = \frac{Y'_u}{\Lambda^2} \bar{Q}_L H^c u_R (H^\dagger H) + \frac{Y'_d}{\Lambda^2} \bar{Q}_L H d_R (H^\dagger H) + \frac{Y'_\ell}{\Lambda^2} \bar{L}_L H \ell_R (H^\dagger H) + \text{h.c.}, \quad (111)$$

which correct the SM Yukawa interactions. Here  $\Lambda$  is the NP scale and  $H^c = i\sigma_2 H^*$ . The fermion mass

Model	$\kappa_b$	$\kappa_{s(d)}/\kappa_b$	$\tilde{\kappa}_b/\kappa_b$	$\tilde{\kappa}_{s(d)}/\kappa_b$
SM	1	1	0	0
MFV	$1 + \frac{\Re(a_d v^2 + 2c_d m_t^2)}{\Lambda^2}$	$1 - \frac{2\Re(c_d)m_t^2}{\Lambda^2}$	$\frac{\Im(a_d v^2 + 2c_d m_t^2)}{\Lambda^2}$	$\frac{\Im(a_d v^2 + 2c_d  V_{ts(td)} ^2 m_t^2)}{\Lambda^2}$
NFC	$V_{hd} v/v_d$	1	0	0
F2HDM	$\cos \alpha / \sin \beta$	$-\tan \alpha / \tan \beta$	$\mathcal{O}\left(\frac{m_s}{m_b} \frac{\cos(\beta-\alpha)}{\cos \alpha \cos \beta}\right)$	$\mathcal{O}\left(\frac{m_s^2}{m_b^2} \frac{\cos(\beta-\alpha)}{\cos \alpha \cos \beta}\right)$
MSSM	$-\sin \alpha / \cos \beta$	1	0	0
FN	$1 + \mathcal{O}\left(\frac{v^2}{\Lambda^2}\right)$	$1 + \mathcal{O}\left(\frac{v^2}{\Lambda^2}\right)$	$\mathcal{O}\left(\frac{v^2}{\Lambda^2}\right)$	$\mathcal{O}\left(\frac{v^2}{\Lambda^2}\right)$
GL2	$-\sin \alpha / \cos \beta$	$\simeq 3(5)$	0	0
RS	$1 - \mathcal{O}\left(\frac{v^2}{m_{KK}^2} \bar{Y}^2\right)$	$1 + \mathcal{O}\left(\frac{v^2}{m_{KK}^2} \bar{Y}^2\right)$	$\mathcal{O}\left(\frac{v^2}{m_{KK}^2} \bar{Y}^2\right)$	$\mathcal{O}\left(\frac{v^2}{m_{KK}^2} \bar{Y}^2\right)$
pNGB	$1 + \mathcal{O}\left(\frac{v^2}{f^2}\right) + \mathcal{O}\left(y_*^2 \lambda^2 \frac{v^2}{M_*^2}\right)$	$1 + \mathcal{O}\left(y_*^2 \lambda^2 \frac{v^2}{M_*^2}\right)$	$\mathcal{O}\left(y_*^2 \lambda^2 \frac{v^2}{M_*^2}\right)$	$\mathcal{O}\left(y_*^2 \lambda^2 \frac{v^2}{M_*^2}\right)$

Table 39: Same as Table 38 but for down-type Yukawa couplings.

Model	$\kappa_\tau$	$\kappa_{\mu(e)}/\kappa_\tau$	$\tilde{\kappa}_\tau/\kappa_\tau$	$\tilde{\kappa}_{\mu(e)}/\kappa_\tau$
SM	1	1	0	0
MFV	$1 + \frac{\Re(a_\ell)v^2}{\Lambda^2}$	$1 - \frac{2\Re(b_\ell)m_\tau^2}{\Lambda^2}$	$\frac{\Im(a_\ell)v^2}{\Lambda^2}$	$\frac{\Im(a_\ell)v^2}{\Lambda^2}$
NFC	$V_{h\ell} v/v_\ell$	1	0	0
F2HDM	$\cos \alpha / \sin \beta$	$-\tan \alpha / \tan \beta$	$\mathcal{O}\left(\frac{m_\mu}{m_\tau} \frac{\cos(\beta-\alpha)}{\cos \alpha \cos \beta}\right)$	$\mathcal{O}\left(\frac{m_{\mu(e)}^2}{m_\tau^2} \frac{\cos(\beta-\alpha)}{\cos \alpha \cos \beta}\right)$
MSSM	$-\sin \alpha / \cos \beta$	1	0	0
FN	$1 + \mathcal{O}\left(\frac{v^2}{\Lambda^2}\right)$	$1 + \mathcal{O}\left(\frac{v^2}{\Lambda^2}\right)$	$\mathcal{O}\left(\frac{v^2}{\Lambda^2}\right)$	$\mathcal{O}\left(\frac{v^2}{\Lambda^2}\right)$
GL2	$-\sin \alpha / \cos \beta$	$\simeq 3(5)$	0	0
RS	$1 + \mathcal{O}\left(\bar{Y}^2 \frac{v^2}{m_{KK}^2}\right)$	$1 + \mathcal{O}\left(\bar{Y}^2 \frac{v^2}{m_{KK}^2}\right)$	$\mathcal{O}\left(\bar{Y}^2 \frac{v^2}{m_{KK}^2}\right)$	$\mathcal{O}\left(\bar{Y}^2 \frac{v^2}{m_{KK}^2}\right)$

Table 40: Same as Table 38 but for lepton Yukawa couplings. NP effects in the pNGB model are negligible and therefore we do not report them here.

matrices and Yukawa couplings after EWSB are

$$M_f = \frac{v}{\sqrt{2}} \left( Y_f + Y'_f \frac{v^2}{2\Lambda^2} \right), \quad y_f = Y_f + 3Y'_f \frac{v^2}{2\Lambda^2}, \quad f = u, d, \ell, \quad (112)$$

Because  $Y_f$  and  $Y'_f$  appear in two different combinations in  $M_f$  and in the physical Higgs Yukawa couplings,  $y_f$ , the two, in general, cannot be made diagonal in the same basis and will lead to flavour-violating Higgs couplings.

In Tables 38-42 we show the resulting  $\kappa_f$  assuming MFV, i.e., that the flavour breaking in the NP sector is only due to the SM Yukawas [?, ?, ?, ?, ?, ?, ?]. This gives  $Y'_d = a_u Y_u + b_u Y_u Y_u^\dagger Y_u + c_u Y_d Y_d^\dagger Y_u + \dots$ , and similarly for  $Y'_d$  with  $u \leftrightarrow d$ , while  $a_q, b_q, c_q \sim \mathcal{O}(1)$  and are in general complex. For leptons we follow [?] and assume that the SM  $Y_\ell$  is the only flavour-breaking spurion even for the neutrino mass matrix (see also [?]). Then  $Y'_\ell$  and  $Y_\ell$  are diagonal in the same basis and there are no flavour-violating couplings. The flavour-diagonal  $\kappa_\ell$  are given in Table 40.

Multi-Higgs-doublet model with natural flavour conservation (NFC). Natural flavour conservation in multi-Higgs-doublet models is an assumption that only one doublet,  $H_u$ , couples to the up-type quarks,

Model	$\kappa_{ct(tc)}/\kappa_t$	$\kappa_{ut(tu)}/\kappa_t$	$\kappa_{uc(cu)}/\kappa_t$
MFV	$\frac{\Re(c_u m_b^2 V_{cb}^{(*)})}{\Lambda^2} \frac{\sqrt{2} m_{t(c)}}{v}$	$\frac{\Re(c_u m_b^2 V_{ub}^{(*)})}{\Lambda^2} \frac{\sqrt{2} m_{t(u)}}{v}$	$\frac{\Re(c_u m_b^2 V_{ub(cb)} V_{cb(ub)}^*)}{\Lambda^2} \frac{\sqrt{2} m_{c(u)}}{v}$
F2HDM	$\mathcal{O}\left(\frac{m_c}{m_t} \frac{\cos(\beta-\alpha)}{\cos \alpha \cos \beta}\right)$	$\mathcal{O}\left(\frac{m_u}{m_t} \frac{\cos(\beta-\alpha)}{\cos \alpha \cos \beta}\right)$	$\mathcal{O}\left(\frac{m_c m_u}{m_t^2} \frac{\cos(\beta-\alpha)}{\cos \alpha \cos \beta}\right)$
FN	$\mathcal{O}\left(\frac{v m_{t(c)}}{\Lambda^2}  V_{cb} ^{\pm 1}\right)$	$\mathcal{O}\left(\frac{v m_{t(u)}}{\Lambda^2}  V_{ub} ^{\pm 1}\right)$	$\mathcal{O}\left(\frac{v m_{c(u)}}{\Lambda^2}  V_{us} ^{\pm 1}\right)$
GL2	$\epsilon(\epsilon^2)$	$\epsilon(\epsilon^2)$	$\epsilon^3$
RS	$\sim \lambda^{(-)2} \frac{m_{t(c)}}{v} \bar{Y}^2 \frac{v^2}{m_{KK}^2}$	$\sim \lambda^{(-)3} \frac{m_{t(u)}}{v} \bar{Y}^2 \frac{v^2}{m_{KK}^2}$	$\sim \lambda^{(-)1} \frac{m_{c(u)}}{v} \bar{Y}^2 \frac{v^2}{m_{KK}^2}$
pNGB	$\mathcal{O}(y_*^2 \frac{m_t}{v} \frac{\lambda_{L(R),2} \lambda_{L(R),3} m_W^2}{M_*^2})$	$\mathcal{O}(y_*^2 \frac{m_t}{v} \frac{\lambda_{L(R),1} \lambda_{L(R),3} m_W^2}{M_*^2})$	$\mathcal{O}(y_*^2 \frac{m_c}{v} \frac{\lambda_{L(R),1} \lambda_{L(R),2} m_W^2}{M_*^2})$

Table 41: Same as Table 38 but for flavour-violating up-type Yukawa couplings. In the SM, NFC and the tree-level MSSM the Higgs Yukawa couplings are flavour diagonal. The CP-violating  $\tilde{\kappa}_{ff'}$  are obtained by replacing the real part,  $\Re$ , with the imaginary part,  $\Im$ . All the other models predict a zero contribution to these flavour changing couplings.

Model	$\kappa_{bs(sb)}/\kappa_b$	$\kappa_{bd(db)}/\kappa_b$	$\kappa_{sd(ds)}/\kappa_b$
MFV	$\frac{\Re(c_d m_t^2 V_{ts}^{(*)})}{\Lambda^2} \frac{\sqrt{2} m_{s(b)}}{v}$	$\frac{\Re(c_d m_t^2 V_{td}^{(*)})}{\Lambda^2} \frac{\sqrt{2} m_{d(b)}}{v}$	$\frac{\Re(c_d m_t^2 V_{ts(td)}^* V_{td(ts)})}{\Lambda^2} \frac{\sqrt{2} m_{s(d)}}{v}$
F2HDM	$\mathcal{O}\left(\frac{m_s}{m_b} \frac{\cos(\beta-\alpha)}{\cos \alpha \cos \beta}\right)$	$\mathcal{O}\left(\frac{m_d}{m_b} \frac{\cos(\beta-\alpha)}{\cos \alpha \cos \beta}\right)$	$\mathcal{O}\left(\frac{m_s m_d}{m_b^2} \frac{\cos(\beta-\alpha)}{\cos \alpha \cos \beta}\right)$
FN	$\mathcal{O}\left(\frac{v m_{b(s)}}{\Lambda^2}  V_{cb} ^{\pm 1}\right)$	$\mathcal{O}\left(\frac{v m_{b(d)}}{\Lambda^2}  V_{ub} ^{\pm 1}\right)$	$\mathcal{O}\left(\frac{v m_{s(d)}}{\Lambda^2}  V_{us} ^{\pm 1}\right)$
GL2	$\epsilon^2(\epsilon)$	$\epsilon$	$\epsilon^2(\epsilon^3)$
RS	$\sim \lambda^{(-)2} \frac{m_{b(s)}}{v} \bar{Y}^2 \frac{v^2}{m_{KK}^2}$	$\sim \lambda^{(-)3} \frac{m_{b(d)}}{v} \bar{Y}^2 \frac{v^2}{m_{KK}^2}$	$\sim \lambda^{(-)1} \frac{m_{s(d)}}{v} \bar{Y}^2 \frac{v^2}{m_{KK}^2}$
pNGB	$\mathcal{O}(y_*^2 \frac{m_b}{v} \frac{\lambda_{L(R),2} \lambda_{L(R),3} m_W^2}{M_*^2})$	$\mathcal{O}(y_*^2 \frac{m_b}{v} \frac{\lambda_{L(R),1} \lambda_{L(R),3} m_W^2}{M_*^2})$	$\mathcal{O}(y_*^2 \frac{m_s}{v} \frac{\lambda_{L(R),1} \lambda_{L(R),2} m_W^2}{M_*^2})$

Table 42: Same as Table 41 but for flavour-violating down-type Yukawa couplings.

only one Higgs doublet,  $H_d$ , couples to the down-type quarks, and only one doublet,  $H_\ell$  couples to leptons (it is possible that any of these coincide, as in the SM where  $H = H_u = H_d = H_\ell$ ) [?, ?]. The neutral scalar components of  $H_i$  are  $(v_i + h_i)/\sqrt{2}$ , where  $v^2 = \sum_i v_i^2$ . The dynamical fields  $h_i$  are a linear combination of the neutral Higgs mass eigenstates (and include  $h_u$  and  $h_d$ ). We thus have  $h_i = V_{hi} h + \dots$ , where  $V_{hi}$  are elements of the unitary matrix  $V$  that diagonalizes the neutral-Higgs mass terms and we only write down the contribution of the lightest Higgs,  $h$ . NFC means that there are no tree-level Flavor Changing Neutral Currents (FCNCs) and no  $CP$  violation in the Yukawa interactions  $\kappa_{qq'} = \tilde{\kappa}_{qq'} = 0$ ,  $\tilde{\kappa}_q = 0$ .

There is a universal shift in all up-quark Yukawa couplings,  $\kappa_u = \kappa_c = \kappa_t = V_{hu} v / v_u$ . Similarly, there is a (different) universal shift in all down-quark Yukawa couplings and in all lepton Yukawa couplings, see Tables 38 - 40.

Higgs sector of the MSSM at tree level. The MSSM tree-level Higgs potential and the couplings to quarks are the same as in the type-II two-Higgs-doublet model, see, e.g., [?]. This is an example of

Model	$\kappa_{\tau\mu(\mu\tau)}/\kappa_\tau$	$\kappa_{\tau e(e\tau)}/\kappa_\tau$	$\kappa_{\mu e(e\mu)}/\kappa_\tau$
F2HDM	$\mathcal{O}\left(\frac{m_\mu}{m_\tau} \frac{\cos(\beta-\alpha)}{\cos\alpha\cos\beta}\right)$	$\mathcal{O}\left(\frac{m_e}{m_\tau} \frac{\cos(\beta-\alpha)}{\cos\alpha\cos\beta}\right)$	$\mathcal{O}\left(\frac{m_\mu m_e}{m_\tau^2} \frac{\cos(\beta-\alpha)}{\cos\alpha\cos\beta}\right)$
FN	$\mathcal{O}\left(\frac{vm_{\mu(\tau)}}{\Lambda^2}  U_{23} ^{\mp 1}\right)$	$\mathcal{O}\left(\frac{vm_{e(\tau)}}{\Lambda^2}  U_{13} ^{\mp 1}\right)$	$\mathcal{O}\left(\frac{vm_{e(\mu)}}{\Lambda^2}  U_{12} ^{\mp 1}\right)$
GL2	$\epsilon^2(\epsilon)$	$\epsilon$	$\epsilon^2(\epsilon^3)$
RS	$\sim \sqrt{\frac{m_{\mu(\tau)}}{m_{\tau(\mu)}}} \bar{Y}^2 \frac{v^2}{m_{KK}^2}$	$\sim \sqrt{\frac{m_{e(\tau)}}{m_{\tau(e)}}} \bar{Y}^2 \frac{v^2}{m_{KK}^2}$	$\sim \sqrt{\frac{m_{e(\mu)}}{m_{\mu(e)}}} \bar{Y}^2 \frac{v^2}{m_{KK}^2}$

Table 43: Same as Table 41 but for flavour-violating lepton Yukawa couplings.

a 2HDM with natural flavour conservation in which  $v_u = \sin\beta v$ ,  $v_d = \cos\beta v$ . The mixing of  $h_{u,d}$  into the Higgs mass-eigenstates  $h$  and  $H$  is given by  $h_u = \cos\alpha h + \sin\alpha H$ ,  $h_d = -\sin\alpha h + \cos\alpha H$ , where  $h$  is the observed SM-like Higgs. The up-quark Yukawa couplings are rescaled universally,  $\kappa_u = \kappa_c = \kappa_t = \cos\alpha/\sin\beta$ , and similarly the down-quark Yukawas,  $\kappa_d = \kappa_s = \kappa_b = -\sin\alpha/\cos\beta$ . The flavour-violating and CP-violating Yukawas are zero<sup>26</sup>. In Tables 38-40 we limit ourselves to the tree-level expectations, which are a good approximation for a large part of the MSSM parameter space.

In the alignment limit,  $\beta - \alpha = \pi/2$  [?, ?, ?, ?, ?, ?, 149], the Yukawa couplings tend toward their SM value,  $\kappa_i = 1$ . The global fits to Higgs data in type-II 2HDM already constrain  $\beta - \alpha$  to be not to far from  $\pi/2$  [?, ?, ?] so that the couplings of the light Higgs are also constrained to be close to their SM values. Note that the decoupling limit of the 2HDM, where the heavy Higgs bosons become much heavier than the SM Higgs, implies the alignment limit while the reverse is not necessarily true [?].

*Flavorful two-Higgs-doublet model.* In [?] a 2HDM setup was introduced in which one Higgs doublet couples only to top, bottom and tau, and a second Higgs doublet couples to the remaining fermions (see also [?, ?, ?, ?]). Such a 2HDM goes beyond NFC and therefore introduces FCNCs at tree level. However, the Yukawa couplings of the first Higgs doublet to the third generation fermions preserve a  $U(2)^5$  flavour symmetry, only broken by the small couplings of the second Higgs doublet. This approximate  $U(2)^5$  symmetry leads to a strong suppression of the most sensitive flavour violating transitions between the second and first generation.

The non-standard flavour structure of this ‘‘flavourful’’ 2HDM scenario leads to flavour non-universal modifications of all Higgs couplings. To be more precise  $\kappa_t \neq \kappa_c = \kappa_u$ ,  $\kappa_b \neq \kappa_s = \kappa_d$ , and  $\kappa_\tau \neq \kappa_\mu = \kappa_e$ . CP violation in Higgs couplings can arise but is strongly suppressed by small fermion masses, see Tables 38 - 40. Also potentially sizable flavour violating Higgs couplings involving the third generation fermions arise, see Tables 41 - 43. As in all 2HDMs, the Higgs couplings approach their SM values in the alignment limit,  $\beta - \alpha = \pi/2$ .

*A single Higgs doublet with Froggatt-Nielsen mechanism (FN).* The Froggatt-Nielsen [?] mechanism provides a simple explanation of the size and hierarchy of the SM Yukawa couplings. In the simplest realization this is achieved by a  $U(1)_H$  horizontal symmetry under which different generations of fermions carry different charges. The  $U(1)_H$  is broken by a spurion,  $\epsilon_H$ . The entries of the SM Yukawa matrix are then parametrically suppressed by powers of  $\epsilon_H$  as, for example, in the lepton sector

$$(Y_\ell)_{ij} \sim \epsilon_H^{H(L_i) - H(e_j)}, \quad (113)$$

where  $H(e, L)$  are the FN charges of the right- and left-handed charged lepton, respectively. The dimension 6 operators in (111) due to electroweak NP have similar flavour suppression,  $(Y'_\ell)_{ij} \sim$

<sup>26</sup>Note that beyond the tree level, in fine-tuned regions of parameter space the loops of sfermions and gauginos can lead to substantial corrections to these expressions [?].

$\epsilon_H^{H(e_j)-H(L_i)} v^2 / \Lambda^2$  [?,?]. After rotating to the mass eigenbasis, the lepton masses and mixing angles are then given by [?,?]

$$m_{\ell_i} / v \sim \epsilon_H^{|H(L_i) - H(e_i)|}, \quad |U_{ij}| \sim \epsilon_H^{|H(L_i) - H(L_j)|}, \quad (114)$$

giving the Higgs Yukawa couplings in Tables 40 and 43 in the row labeled ‘FN’ [?]. Similarly for the quarks, after rotating to the mass eigenbasis, the masses and the mixings are given by [?]

$$m_{u_i(d_i)} / v \sim \epsilon_H^{|H(Q_i) - H(u_i(d_i))|}, \quad |V_{ij}| \sim \epsilon_H^{|H(Q_i) - H(Q_j)|}, \quad (115)$$

where  $V$  is the Cabibbo-Kobayashi-Maskawa (CKM) mixing matrix and  $H(u, d, Q)$  are the FN charges of the right-handed up and down and the left-handed quark fields, respectively.

Higgs-dependent Yukawa couplings (GL2) In the model of quark masses introduced by Giudice and Lebedev [?], the quark masses, apart from the top mass, are small because they arise from higher dimensional operators. The original GL proposal is ruled out by data **YS: ref?**, while the straightforward modification to a 2HDM (GL2) is

$$\begin{aligned} \mathcal{L}_f = & c_{ij}^u \left( \frac{H_1^\dagger H_1}{M^2} \right)^{n_{ij}^u} \bar{Q}_{L,i} u_{R,j} H_1 + c_{ij}^d \left( \frac{H_1^\dagger H_1}{M^2} \right)^{n_{ij}^d} \bar{Q}_{L,i} d_{R,j} H_2 + \\ & c_{ij}^\ell \left( \frac{H_1^\dagger H_1}{M^2} \right)^{n_{ij}^\ell} \bar{L}_{L,i} e_{R,j} H_2 + \text{h.c.}, \end{aligned} \quad (116)$$

where  $M$  is the mass scale of the mediators. In the original GL model  $H_2$  is identified with the SM Higgs,  $H_2 = H$ , while  $H_1 = H^c$ . Taking  $c_{ij}^{u,d} \sim \mathcal{O}(1)$ , the ansatz  $n_{ij}^{u,d} = a_i + b_j^{u,d}$  with  $a = (1, 1, 0)$ ,  $b^d = (2, 1, 1)$ , and  $b^u = (2, 0, 0)$  then reproduces the hierarchies of the observed quark masses and mixing angles for  $\epsilon \equiv v^2/M^2 \approx 1/60$ . The Yukawa couplings are of the form  $y_{ij}^{u,d} = (2n_{ij}^{u,d} + 1)(y_{ij}^{u,d})_{\text{SM}}$ . The SM Yukawas are diagonal in the same basis as the quark masses, while the  $y_{ij}^{u,d}$  are not. Because the bottom Yukawa is largely enhanced,  $\kappa_b \simeq 3$ , this simplest version of the GL model is already excluded by the Higgs data. Its modification, GL2, is still viable, though [?]. For  $v_1/v_2 = \tan \beta \sim 1/\epsilon$  one can use the same ansatz for  $n_{ij}^{u,d}$  as before, modifying only  $b^d$ , so that  $b^d = (1, 0, 0)$ , with the results shown in Tables 38-43. For leptons we use the same scalings as for right-handed quarks. Note that the  $H_1^\dagger H_1$  is both a gauge singlet and a flavour singlet. From symmetry point of view it is easier to build flavour models, if  $H_1 H_2$  acts as a spurion in (116), instead of  $H_1^\dagger H_1$ . This possibility is severely constrained phenomenologically, though [191, 192].

Randall-Sundrum models (RS). The Randall-Sundrum warped extra-dimensional model has been proposed to address the hierarchy problem and simultaneously explain the hierarchy of the SM fermion masses [?, ?, ?, ?, ?]. Integrating out the Kaluza-Klein (KK) modes of mass  $m_{KK}$ , and working in the limit of a brane-localized Higgs, keeping only terms of leading order in  $v^2/m_{KK}^2$ , the SM quark mass matrices are given by [?] (see also [?, ?, ?, ?, ?, ?, ?, ?, 193], and Ref. [?] for a bulk Higgs scenario)

$$M_{ij}^{d(u)} = [F_q Y_{1(2)}^{5D} F_{d(u)}]_{ij} v. \quad (117)$$

The  $F_{q,u,d}$  are  $3 \times 3$  matrices of fermion wave-function overlaps with the Higgs and are diagonal and hierarchical. Assuming flavour anarchy, the 5D Yukawa matrices,  $Y_{1,2}^{5D}$ , are general  $3 \times 3$  complex matrices with  $\bar{Y} \sim \mathcal{O}(1)$  entries, but usually  $\bar{Y} \lesssim 4$ , see, e.g., [?]. At leading order in  $v^2/m_{KK}^2$  the Higgs Yukawas are aligned with the quark masses, i.e.,  $M_{u,d} = y_{u,d} v / \sqrt{2} + \mathcal{O}(v^2/m_{KK}^2)$ . The misalignments are generated by tree-level KK quark exchanges, giving

$$[y_{u(d)}]_{ij} - \frac{\sqrt{2}}{v} [M_{u,d}]_{ij} \sim -\frac{1}{3} F_{q_i} \bar{Y}^3 F_{u_j(d_j)} \frac{v^2}{m_{KK}^2}. \quad (118)$$

For the charged leptons, there are two choices for generating the hierarchy in the masses [?]. If left- and right-handed fermion profiles are both hierarchical (and taken to be similar) then the misalignment between the masses and Yukawas is  $\sim \sqrt{m_i m_j / v^2} \times \mathcal{O}(\bar{Y}^2 v^2 / m_{KK}^2)$ . If only the right-handed profiles are hierarchical the misalignment is given by (see also Tables 40 and 43)

$$[y_\ell]_{ij} - \frac{\sqrt{2}}{v} [M_\ell]_{ij} \sim -\frac{1}{3} \bar{Y}^2 \frac{v^2}{m_{KK}^2} \frac{m_j^\ell}{v}. \quad (119)$$

The Higgs mediated FCNCs are suppressed by the same zero-mode wave-function overlaps that also suppress the quark masses, (117), giving rise to the RS GIM mechanism [?, ?, ?]. Using the fact that the CKM matrix elements are given by  $V_{ij} \sim F_{q_i}/F_{q_j}$  for  $i < j$ , Eq. (118), one can rewrite the  $\kappa_i$  as in Tables 38-42. The numerical analysis of Ref. [?] found that for diagonal Yukawas typically  $\kappa_i < 1$ , with deviations in  $\kappa_{t(b)}$  up to 30%(15%), and in  $\kappa_{s,c(u,d)}$  up to  $\sim 5\% (1\%)$ . For the charged leptons one obtains deviations in  $\kappa_{\tau\mu(\mu\tau)} \sim 1(5) \times 10^{-5}$  [?]. These estimates were obtained fixing the mass of the first KK gluon excitation to 3.7 TeV, above the present ATLAS bound [?].

Composite pseudo-Goldstone Higgs (pNGB). Finally, we assume that the Higgs is a pseudo-Goldstone boson arising from the spontaneous breaking of a global symmetry in a strongly coupled sector, and couples to the composite sector with a typical coupling  $y_*$  [?, ?, ?, ?] (for a review, see [?]). Assuming partial compositeness, the SM fermions couple linearly to composite operators  $O_{L,R}$ ,  $\lambda_{L,i}^q \bar{Q}_{L,i} O_R^i + \lambda_{R,j}^u \bar{u}_{R,j} O_L^j + h.c.$ , where  $i, j$  are flavour indices [194]. This is the 4D dual of fermion mass generation in 5D RS models. The SM masses and Yukawa couplings arise from expanding the two-point functions of the  $O_{L,R}$  operators in powers of the Higgs field [?].

The new ingredient compared to the EFT analysis in (111) is that the shift symmetry due to the pNGB nature of the Higgs dictates the form of the higher-dimensional operators. The flavour structure and the composite Higgs coset structure completely factorize if the SM fields couple to only one composite operator. The general decomposition of Higgs couplings then becomes [?] (see also [?, ?, ?])

$$Y_u \bar{Q}_L H u_R + Y'_u \bar{Q}_L H u_R \frac{(H^\dagger H)}{\Lambda^2} + \dots \rightarrow c_{ij}^u P(h/f) \bar{Q}_L^i H u_R^j, \quad (120)$$

and similarly for the down quarks. Here  $f \gtrsim v$  is the equivalent of the pion decay constant, while  $P(h/f) = a_0 + a_2(H^\dagger H/f^2) + \dots$  is an analytic function whose form is fixed by the pattern of the spontaneous breaking and the embedding of the SM fields in the global symmetry of the strongly coupled sector. In (120) the flavour structure of  $Y_u$  and  $Y'_u$  is the same **YS: is it assumption?**. The resulting corrections to the quark Yukawa couplings are therefore strictly diagonal,

$$\kappa_q \sim 1 + \mathcal{O}(v^2/f^2). \quad (121)$$

For example, for the models based on the breaking of  $SO(5)$  to  $SO(4)$ , the diagonal Yukawa couplings can be written as  $\kappa_q = (1 + 2m - (1 + 2m + n)(v/f)^2)/\sqrt{1 - (v/f)^2}$ , where  $n, m$  are positive integers [?]. The MCHM4 model corresponds to  $m = n = 0$ , while MCHM5 is given by  $m = 0, n = 1$ .

The flavour-violating contributions to the quark Yukawa couplings arise only from corrections to the quark kinetic terms [?],

$$\bar{q}_L i \not{p}_L \frac{H^\dagger H}{\Lambda^2}, \bar{u}_R i \not{p}_R \frac{H^\dagger H}{\Lambda^2}, \dots, \quad (122)$$

due to the exchanges of composite vector resonances with typical mass  $M_* \sim \Lambda$ . After using the equations of motion these give (neglecting relative  $\mathcal{O}(1)$  contributions in the sum) [?, ?, ?],

$$\kappa_{ij}^u \sim 2y_*^2 \frac{v^2}{M_*^2} \left( \lambda_{L,i}^q \lambda_{L,j}^q \frac{m_{u_j}}{v} + \lambda_{R,i}^u \lambda_{R,j}^u \frac{m_{u_i}}{v} \right), \quad (123)$$

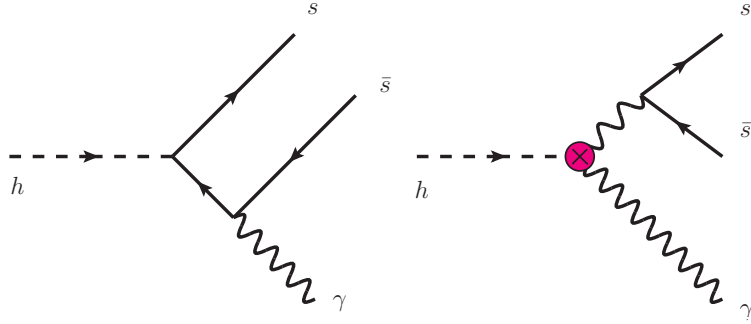


Fig. 77: The two contributions to  $h \rightarrow V\gamma$  with  $V = \rho, \omega, \phi, J/\psi, \Upsilon$ . Left: the direct amplitude, proportional to the  $q$ -quark Yukawa; Right: indirect amplitude involve the  $h\gamma\gamma$  vertex. **YS: replace  $s \rightarrow q$  the figure**

and similarly for the down quarks. If the strong sector is CP violating, then  $\tilde{\kappa}_{ij}^{u,d} \sim \kappa_{ij}^{u,d}$ .

The exchange of composite vector resonances also contributes to the flavour-diagonal Yukawa couplings, shifting the estimate (121) by  $\Delta\kappa_{q_i} \sim 2y_*^2 \frac{v^2}{M_*^2} \left[ (\lambda_{L,i}^q)^2 + (\lambda_{R,i}^u)^2 \right]$ . This shift can be large for the quarks with a large composite component if the Higgs is strongly coupled to the vector resonances,  $y_* \sim 4\pi$ , and these resonances are relatively light,  $M_* \sim 4\pi v \sim 3$  TeV. The left-handed top and bottom, as well as the right-handed top, are expected to be composite, explaining the large top mass (i.e.,  $\lambda_{L,3}^q \sim \lambda_{R,3}^u \sim 1$ ). In the anarchic flavour scenario, one expects the remaining quarks to be mostly elementary (so the remaining  $\lambda_i \ll 1$ ). If there is some underlying flavour alignment, it is also possible that the light quarks are composite. This is most easily achieved in the right-handed sector [?, ?, ?].

In the case of the lepton sector, if we assume that there are no hierarchies in the composite sector [?] (see also [?, ?, ?, ?]), then the NP effects in the flavour diagonal and off-diagonal Yukawas are negligible. For this reason, we do not report them in Tabs. 40 and 43.

### 7.3 Exclusive Higgs decays

Exclusive Higgs decays to a vector meson ( $V$ ) and photon,  $h \rightarrow V\gamma$ , directly probe the Higgs bottom, charm [?, ?] strange, down and up [?] quark Yukawas, as well as to the flavor violating couplings. For improved theory predictions see [?]. Within the LHC, the Higgs exclusive decays are the only direct probe of the  $u$ ,  $d$  and  $s$  Yukawa couplings. On the experimental side, both ATLAS and CMS report first upper bounds on  $h \rightarrow J/\psi\gamma$  [?, ?],  $h \rightarrow \phi\gamma$  and  $h \rightarrow \rho\gamma$  [?, ?]. The  $h \rightarrow VZ$ ,  $ZW$  modes as a probe of the Higgs electroweak coupling are discussed in [?]. Finally,  $Z$  exclusive decays are considered in [?, ?] and can be served as a test of QCD factorization.

The Higgs exclusive decays which involve  $V = \rho, \omega, \phi, J/\psi, \Upsilon$  are sensitive to the diagonal Yukawa couplings. These receive contributions from two amplitudes which are denoted as direct and indirect, see Fig. 77. The direct amplitude, first analyzed in [?], involves a hard  $h \rightarrow q\bar{q}\gamma$  vertex and sensitive to the  $q$ -quark Yukawa. The indirect process is mediated by  $h\gamma\gamma$  vertex which is followed by a  $\gamma^* \rightarrow V$  fragmentation. Since the indirect contribution is larger than the direct, the largest sensitivity to the Higgs  $q$ -quark coupling is via the interference between the two diagrams.

It is beneficial to consider the ratio between  $h \rightarrow V\gamma$  and  $h \rightarrow \gamma\gamma$  or  $h \rightarrow ZZ^* \rightarrow 4\ell$  as various of theoretical uncertainties and the dependence of the Higgs total width are canceled [?, ?]. Moreover, since the Higgs production is inclusive for all of these modes, it canceled in the ratio to large extension.

Thus, we can write

$$\mathcal{R}_{V\gamma,f} = \frac{\mu_{V\gamma}}{\mu_f} \frac{\text{BR}_{h \rightarrow V\gamma}^{\text{SM}}}{\text{BR}_{h \rightarrow f}^{\text{SM}}} \simeq \frac{\Gamma_{h \rightarrow V\gamma}}{\Gamma_{h \rightarrow f}}, \quad (124)$$

where  $f = ZZ^*, \gamma\gamma$ ,  $\mu_X = \sigma_h \text{BR}_X / \sigma_h^{\text{SM}} \text{BR}_X^{\text{SM}}$ , the superscript ‘‘SM’’ denotes the SM values and we assume a perfect cancellation of the production mechanism. For simplicity, we assume CP even Higgs coupling and find

$$\mathcal{R}_{V\gamma,f} = \alpha_{V,f} \left| 1 - \left( \Delta_V^R + i\Delta_V^I \right) \frac{\bar{\kappa}_V}{\kappa_{\gamma\gamma}^{\text{eff}}} + \Delta_V^U \right|^2, \quad (125)$$

with

$$\alpha_{V,\gamma\gamma} = 6 \frac{\Gamma_{V \rightarrow e^+ e^-}}{\alpha m_V} \left( 1 - \frac{m_V^2}{m_h^2} \right)^2, \quad \alpha_{V,ZZ^*} = \left| \frac{\kappa_{\gamma\gamma}^{\text{eff}}}{\kappa_Z} \right|^2 \frac{\Gamma_{h \rightarrow \gamma\gamma}^{\text{SM}}}{\Gamma_{h \rightarrow ZZ^* \rightarrow 4\ell}^{\text{SM}}} \alpha_{V,\gamma\gamma}, \quad (126)$$

where  $\kappa_X$  is the normalized coupling with respect to its SM value. Below, we adopted the numerical values of  $\Delta_V^X$  from Ref. [?]. The advantage of use  $h \rightarrow \gamma\gamma$  for the normalization is that there are only two unknown - the Higgs coupling to di-photon and the quark Yukawa. However, since  $h \rightarrow ZZ^*$  is a very clean channel is serve as a good channel to use for the normalization. Moreover, by combing the Higgs data with the electroweak precision measurements, the Higgs coupling to  $ZZ$  is known to a few precents level [?, 195], thus, there is no additional large uncertainty. We note that with the current data the bounds evaluating by using  $\mathcal{R}_{V\gamma,ZZ^*}$  are slightly stronger than the ones from  $\mathcal{R}_{V\gamma,\gamma\gamma}$ .

For the interpretation of the experimental results in term of bounds on the different Yukawa coupling we follow Refs. [?, ?]. Denoting the 95 % CL bound on the ratio  $\mathcal{R}_{V\gamma,f}$  as  $\mathcal{R}_{V\gamma,f}^{95}$  we can write

$$\frac{\Delta_V^R - \sqrt{\frac{(\Delta_V^R)^2 + (\Delta_V^I)^2}{\alpha_{V\gamma,f}} \mathcal{R}_{V\gamma,f}^{95} - (\Delta_V^I)^2}}{(\Delta_V^R)^2 + (\Delta_V^I)^2} < \frac{\bar{\kappa}_V}{\kappa_{\gamma\gamma}^{\text{eff}}} < \frac{\Delta_V^R + \sqrt{\frac{(\Delta_V^R)^2 + (\Delta_V^I)^2}{\alpha_{V\gamma,f}} \mathcal{R}_{V\gamma,f}^{95} - (\Delta_V^I)^2}}{(\Delta_V^R)^2 + (\Delta_V^I)^2}, \quad (127)$$

where we neglect  $\Delta_V^U$  as it is a small correction. Moreover, neglecting  $\Delta_V^I$  we get simplified formula, which hold to good accuracy,

$$\frac{1 - \sqrt{\mathcal{R}_{V\gamma,f}^{95} / \alpha_{V\gamma,f}}}{\Delta_V^R} < \frac{\bar{\kappa}_V}{\kappa_{\gamma\gamma}^{\text{eff}}} < \frac{1 + \sqrt{\mathcal{R}_{V\gamma,f}^{95} / \alpha_{V\gamma,f}}}{\Delta_V^R}. \quad (128)$$

Table 44 summarizes the current experimental status along with the theory interpretation in terms of light quarks Yukawa.

The prospects for probing light quark Yukawa within future LHC runs and for future colliders are estimated in Ref. [?], which we follow here. One of the important implications of the first upper bounds on the different exclusive modes is that the measurement is background dominated. Thus, even for future runs, without significant improvement of the analysis, we expect only upper bounds. Given an upper bound on  $\mathcal{R}_{V\gamma,f}^{95}(E_1, \mathcal{L}_1)$ , where  $E_1$  ( $\mathcal{L}_1$ ) stands for the collider energy (integrated luminosity), the estimated bound with  $E_2$  and  $\mathcal{L}_2$  is

$$\mathcal{R}_{V\gamma,f}^{95}(E_2, \mathcal{L}_2) = \mathcal{R}_{V\gamma,f}^{95}(E_1, \mathcal{L}_1) \sqrt{\frac{1}{R_E} \frac{\sigma_{h,E_1}^{\text{SM}} \mathcal{L}_1}{\sigma_{h,E_2}^{\text{SM}} \mathcal{L}_2}}, \quad (129)$$

mode	$\text{BR}_{h \rightarrow V\gamma} <$	$\mathcal{R}_{V\gamma, ZZ^*} <$	Yukawa range
$J/\psi \gamma$	$1.5 \times 10^{-3}$ 8 TeV [?, ?]	9.3	$-295\kappa_Z + 16\kappa_{\gamma\gamma}^{\text{eff}} < \kappa_c < 295\kappa_Z + 16\kappa_{\gamma\gamma}^{\text{eff}}$
$\phi \gamma$	$4.8 \times 10^{-4}$ 13 TeV [?, ?]	3.2	$-140\kappa_Z + 10\kappa_{\gamma\gamma}^{\text{eff}} < \bar{\kappa}_s < 140\kappa_Z + 10\kappa_{\gamma\gamma}^{\text{eff}}$
$\rho \gamma$	$8.8 \times 10^{-4}$ 13 TeV [?]	5.8	$-285\kappa_Z + 42\kappa_{\gamma\gamma}^{\text{eff}} < 2\bar{\kappa}_u + \bar{\kappa}_d < 285\kappa_Z + 42\kappa_{\gamma\gamma}^{\text{eff}}$

Table 44: The current upper bounds, assuming SM Higgs production, on the different exclusive Higgs decays and the interpretation in terms of the Higgs Yukawa couplings. Note that  $\bar{\kappa}_q = y_q/y_b^{\text{SM}}$ . The quoted bounds are at 95 CL.

mode	collider energy	$\mathcal{R}_{V\gamma, ZZ^*} <$	Yukawa range ( $\kappa_V = \kappa_{\gamma\gamma}^{\text{eff}} = 1$ )
$J/\psi \gamma$	14 TeV	$0.47\sqrt{L_3}$	$16 - 67L_3^{1/4} < \kappa_c < 16 + 67L_3^{1/4}$
	27 TeV	$0.28\sqrt{L_3}$	$16 - 52L_3^{1/4} < \kappa_c < 16 + 52L_3^{1/4}$
	100 TeV	$0.12\sqrt{L_3}$	$16 - 33L_3^{1/4} < \kappa_c < 16 + 33L_3^{1/4}$
$\phi \gamma$	14 TeV	$0.33\sqrt{L_3}$	$11 - 46L_3^{1/4} < \bar{\kappa}_s < 11 + 46L_3^{1/4}$
	27 TeV	$0.20\sqrt{L_3}$	$11 - 35L_3^{1/4} < \bar{\kappa}_s < 11 + 35L_3^{1/4}$
	100 TeV	$0.083\sqrt{L_3}$	$11 - 23L_3^{1/4} < \bar{\kappa}_s < 11 + 23L_3^{1/4}$
$\rho \gamma$	14 TeV	$0.60\sqrt{L_3}$	$44 - 93L_3^{1/4} < 2\bar{\kappa}_u + \bar{\kappa}_d < 44 + 93L_3^{1/4}$
	27 TeV	$0.36\sqrt{L_3}$	$44 - 72L_3^{1/4} < 2\bar{\kappa}_u + \bar{\kappa}_d < 44 + 72L_3^{1/4}$
	100 TeV	$0.15\sqrt{L_3}$	$44 - 47L_3^{1/4} < 2\bar{\kappa}_u + \bar{\kappa}_d < 44 + 47L_3^{1/4}$

Table 45: The projection for Yukawa range for future  $pp$  colliders with center of mass energy of 14, 27 and 100 TeV. In the above table we define  $L_3 \equiv (3/\text{ab})/\mathcal{L}$ .

where  $\sigma_{h,E_{1,2}}^{\text{SM}}$  is the SM Higgs production cross section,  $R_E = (S_{E_1}^{\text{SM}}/B_{E_1})/(S_{E_2}^{\text{SM}}/B_{E_2})$  with  $S(B)$  the number of signal (background) events, which encoded the difference in the analysis details and assumed to be 1 here. In Tabel 45We combine Eqs. (128) and (129) along with the current bounds to estimate the future projections of probing the different light quark Yukawa.

In addition to the Higgs diagonal Yukawa, in principle, Higgs exclusive decays can probe off-diagonal couplings by measuring modes such as  $h \rightarrow B_s^* \gamma$  [?]. These processes receive contribution only from the direct amplitude and there is not enhancement from interference with the relative large indirect amplitude. Moreover, the Higgs flavor violating couplings are strongly constrained by meson mixing [?, ?]. Thus, the expected rates are too small to be observe. For a detailed discussion on the  $h \rightarrow VZ, VW$  channels see [?].

#### 7.4 Flavor tagging (charm and strange)

$H \rightarrow c\bar{c}$  from charm-tagging, by Emmanuel Stamou

In the SM, the coupling of the Higgs to bottom quarks is small, i.e.,  $y_b^{\text{SM}} \simeq 0.016$  at  $\mu = m_H$ , and its coupling to charm quarks even smaller by roughly four times, i.e.,  $y_c^{\text{SM}} \simeq 0.0036$  at  $\mu = m_H$ . Nevertheless, due to phase-space the process  $H \rightarrow b\bar{b}$  is the dominant decay mode of the Higgs in the SM. This situation has not only made a roughly 30% precise measurement of such a small coupling possible at Run I of the LHC, but has also created opportunities to measure possible order one deviations in the coupling of the Higgs to charm quarks.

An important difference between the charm- and to some extend also the strange-quark (see section

??) with respect to up- and down-quarks is that it is possible to pursue an inclusive approach in identifying the flavour of the final state particles by  $c$ -tagging jets. The underlying geometrical/kinematical input necessary for  $c$ -tagging is similar to  $b$ -tagging with the most relevant one being the identification of displaced vertices due to the lifetime of  $c$ -hadrons.  $c$ -tagging has been used early on in Run I of the LHC by ATLAS in searches for supersymmetry, e.g., Refs. [?, ?]. Its usefulness in relations to Higgs physics was first discussed in Ref. [?] and subsequently used in Ref. [?] to recast ATLAS's and CMS's Run I analyses for  $h \rightarrow b\bar{b}$  to provide the first LHC constraint on the charm Yukawa.

The inclusive method of probing the charm-quark Yukawa is in many ways complementary to searches for exclusive decays (see discussion of section ??) or searches for deviations in Higgs distributions (see section ??). For example, in the inclusive approach an underlying assumption is that the Higgs coupling to  $WW$  and  $ZZ$  —entering Higgs production— is SM-like, while the interpretation of Higgs distributions assumes no additional new physics contribution that affects them in a significant way. An important difference between the inclusive and the exclusive approach is that the latter relies on interference with the SM  $H \rightarrow \gamma\gamma$  amplitude while the former not. Therefore, in principle the exclusive approach may be sensitive to the sign and  $CP$  properties of the coupling to which the inclusive approach is insensitive to. At the same time, measurements of exclusive decays of the Higgs are challenging due to the small probability of fragmenting into the specific final state and large QCD backgrounds, which is why the inclusive approach appears to be the most promising one to probe deviations in the magnitude of the Higgs to charm coupling.

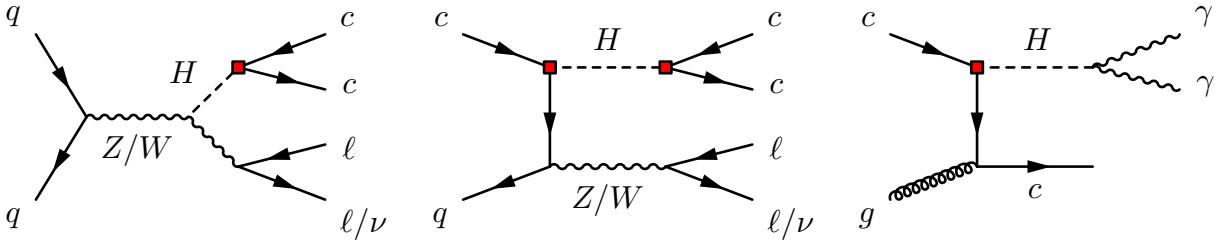


Fig. 78: Left panel, leading-order production of Higgs in association with a heavy gauge boson ( $Z/W$ ) and subsequent decays. Central panel, additional production channel of Higgs in association with a heavy gauge boson that becomes relevant for large  $y_c$  [?]. Right panel, leading-order diagram to search for non-SM  $y_c$  in Higgs production in association with a charm-quark [?].

The most straight-forward way of inclusively probing the charm-quark Yukawa is by expanding the search for  $H \rightarrow b\bar{b}$  to search for  $pp \rightarrow (Z/W \rightarrow \ell\ell/\nu)(H \rightarrow c\bar{c})$  [?] (left and central panel in Fig. 78). Another possibility discussed in Ref. [?] is to search for deviations in Higgs production in association with a charm quark in which the Higgs is produced from a charm-quark in the proton parton-distribution functions (right panel in Fig. 78). We focus here on the measurement from  $pp \rightarrow VH$  events proposed in Ref. [?] and recently performed on a  $36.1 \text{ fb}^{-1}$  sample of  $ZH$  data by ATLAS [?] at  $\sqrt{s} = 13 \text{ TeV}$ . Two key elements for this measurement, which we discuss below, are:

- i) The experimental sensitivity in discriminating between  $c$ -jets from background  $b$ - and light-jets.
  - ii) Probing the charm-quark coupling independent of the value of the bottom-quark Yukawa (breaking the degeneracy).
- i) Tagging algorithms rely on monte-carlo simulations in order to assign a probability for a given jet to be produced from a specific quark-flavour. Therefore, the efficiency / confidence in associating a jet to a specific quark is correlated with the confidence to reject other hypotheses, e.g., production from light-quarks. ATLAS's recent search [?] demonstrated that its  $c$ -tagging capabilities are significantly stronger than anticipated. For LHCb's capabilities of  $c$ -tagging and its sensitivity to  $H \rightarrow c\bar{c}$  see section ??.
- The tagging working point chosen in ATLAS's search has an approximately 41% efficiency to tag  $c$ -jets

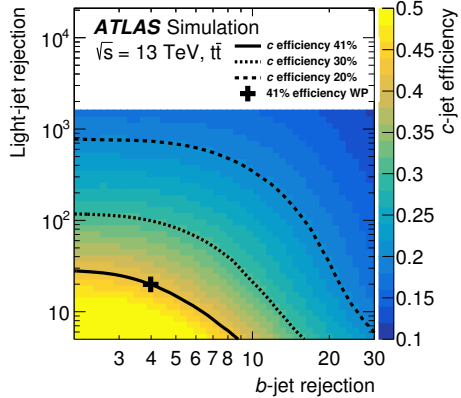


Fig. 79: Correlation of  $c$ -tagging efficiency with  $b$ - and light-quark-jet rejection in ATLAS’s  $c$ -tagger employed in the analysis of Ref. [?].

and rejection factors of roughly 4 and 20 for  $b$ - and light-quark-jets, respectively. In Figure 79 we show ATLAS’s results [?] of the correlation between  $c$ -tagging efficiency and rejection factors. This ATLAS result provides to date the most stringent limit in direct searches for the inclusive decay of Higgs boson to charm quarks,  $\sigma(pp \rightarrow ZH)\text{BR}(H \rightarrow c\bar{c}) < 2.7 \text{ pb}$  at 95% CL. To translate this cross-section bound to a non-trivial constraint on  $y_c$  it is essential to include the additional production channel from large charm Yukawa (central panel in Fig. 78) as demonstrated in Refs. [?]. The additional production channel is affected by the kinematics, e.g.,  $p_T$  of the  $Z$  and thus depends on the details of the analysis. This “unfolding” / reinterpretation of the analysis is thus best performed by the analysis itself and cannot be avoided to obtain non-trivial constraints on the Yukawa itself. Note that at the moment the systematic uncertainties are approximately a factor of two larger than the statistical uncertainties of the  $36.1 \text{ fb}^{-1}$  sample used in the analysis; the largest systematic uncertainty is associated to flavour-tagging and the tagging of  $c$ -jets in particular.

ii) Given the rather similar lifetime of  $b$  and  $c$  hadrons, there is always a non-negligible “contamination” of the  $c$ -jet sample from jets originating from  $b$  quarks [?]. An inclusive  $H \rightarrow c\bar{c}$  analysis probing  $y_c$  must thus either assume a SM value for the bottom Yukawa (as assumed in Ref. [?]) or allow the simultaneous variation of  $y_b$  and  $y_c$ , and break the degeneracy in another way. As discussed and demonstrated in Refs. [?, ?] this is possible by employing more than one tagging working points with a different ratio of  $c$ -tagging efficiency to  $b$ -jet rejection. In this way, it is possible to gain sensitivity to the two independent contributions that enter the search’s signal strength, i.e.,  $\mu_c$  and  $\mu_b$ . Though possible this has not been done in ATLAS’s latest 13 TeV search. It is, however, encouraging that the results presented there would only be mildly affected by this (see discussion within Ref. [?]).

At the moment there is one official study for the prospects of measuring the rate of  $pp \rightarrow ZH(\rightarrow c\bar{c})$  from ATLAS [?]. The study uses the Run II analysis [?] to rescale the results to the high-luminosity stage of the LHC, i.e.,  $3000 \text{ fb}^{-1}$ , and points out directions to improve on the systematic uncertainties. The analysis finds that, if there is no significant NP contribution, ATLAS will be able to set an 95% CL upper bound on the signal strength at a level of  $\mu_{ZH(c\bar{c})} < 6.3$ . Yet the collaboration has not unfolded the results to interpret them as limits on the charm Yukawa, for which the additional production mechanism must be included (see above). To illustrate this point we quote here some results from Ref. [?] in which ATLAS’s study of the prospects for measuring  $H \rightarrow b\bar{b}$  at  $\sqrt{s} = 14 \text{ TeV}$  [?] has been employed to recast the results to an inclusive measurement of  $H \rightarrow c\bar{c}$  from Higgs production in association with a  $Z$  or  $W$  boson. In Figure 80 we show the result of the analysis of Ref. [?]. In the left, right panel, a  $c$ -tagging efficiency of 30% ( $c$ -tag I), 50% ( $c$ -tag II) was employed, respectively. In both cases the  $b$ -jet rejection was chosen to be 5 and the light-jet rejection 200. These two tagging working points cover

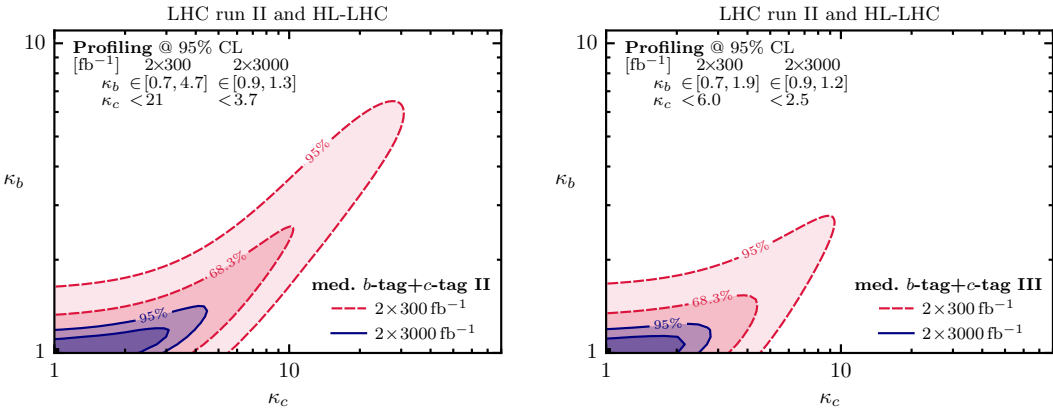


Fig. 80: Projections for measuring charm Yukawa modifications from an inclusive  $H \rightarrow c\bar{c}$  search at  $\sqrt{s} = 14$  TeV using two different  $c$ -taggers (left and right panel) [?]. In red the 95% CL region employing an integrated luminosity of  $2 \times 300 \text{ fb}^{-1}$  and in blue the region employing  $2 \times 3000 \text{ fb}^{-1}$ .

the currently employed tagging working point in which the  $c$ -tagging efficiency is approximately 41%. In the analysis both the charm and the bottom quark are treated as free variables; the bottom-Yukawa direction is profiled away to project the sensitivity to the charm-quark Yukawa. It was found that with  $2 \times 3000 \text{ fb}^{-1}$  at  $\sqrt{s} = 14$  TeV the high-luminosity stage of the LHC probes values of  $y_c/y_c^{\text{SM}} \simeq 21, 6$  with  $c$ -tag I (left panel),  $c$ -tag II (right panel) at 95% CL (the blue regions in Figure 80). The recent ATLAS analysis has studied the systematic uncertainties associated to such measurements, in particular the uncertainties associated to  $c$ -tagging. Such uncertainties could not have been included in the above initial analysis of the future study, but are to a large extend include in ATLAS's study [?].

#### $H \rightarrow c\bar{c}$ at LHCb, by Oscar Augusto De Aguiar Francisco and Lorenzo Sestini

Even though the LHCb experiments operates at lower luminosity when compared to ATLAS/CMS, it has unique capabilities for discrimination between b- and c-jets thanks to its excellent vertex reconstruction system [?]. Its acceptance covers  $\sim 5\%$  of the associated production of  $W/Z + H$  at 13 TeV. The Figure 81 shows the coverage of the LHCb for the  $b\bar{b}$  produced by the Higgs decay in association with a vector boson. When the two jets are in acceptance, the lepton from  $W/Z$  tends to be in acceptance as well ( $\sim 60\%$  of times). Due to its forward geometry, more boosted Higgs are more likely to be properly reconstructed.

During the Run I LHCb set experimental upper limits on the  $V + H(\rightarrow b\bar{b})$  and  $V + H(\rightarrow c\bar{c})$  production [?]. Neglecting any improvements in the analysis or detector, the extrapolation of the limit obtained at 8 TeV to  $300 \text{ fb}^{-1}$  at 14 TeV is  $\sim 50 \times \text{BR}(\text{SM})$  for  $H(c\bar{c})$ .

Detector improvements are expected in future upgrades, in particular in impact parameter resolution which directly affects the  $c$ -tagging efficiency. If the detector improvement is taken into account, the  $c$ -jet tagging efficiency is expected to be improved as can be seen in the Figure 82. A further improvement is expected from the electron reconstruction that will benefit from upgraded versions of the electromagnetic calorimeter. Electrons are used in the identification of the vector bosons associated with the Higgs. Therefore, with these improvements, the expected limit can be pushed down to  $5 - 10 \times \text{BR}(\text{SM})$ . In terms of Yukawa coupling this correspond to limit of 2-3 times the Standard Model prediction. These extrapolation does not include improvements on analysis techniques: as example a Deep Learning analysis can be applied to exploit the jets substructures properties to reduce the backgrounds.

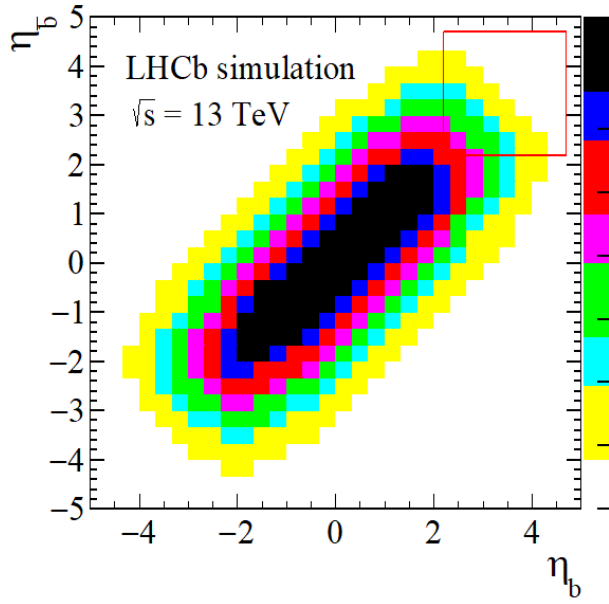


Fig. 81: 2D histogram showing the coverage of the LHCb acceptance for the  $b\bar{b}$  pair produced by the Higgs decay in associated production with a W or a Z boson.

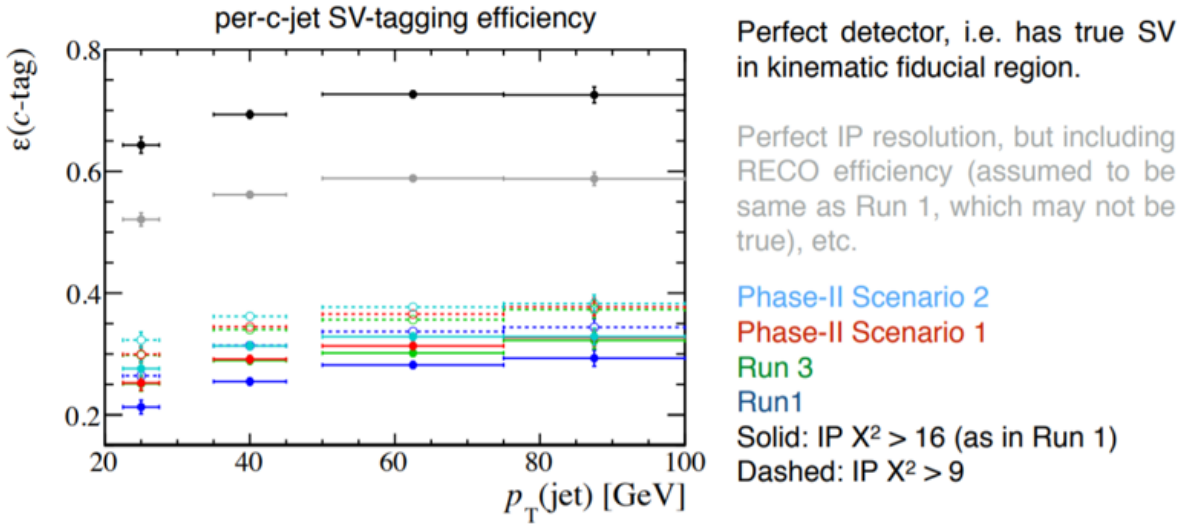


Fig. 82: c-jet tagging efficiency for different scenarios in the HL-LHC conditions.

#### 7.4.1 Strange quark tagging

Tagging strange jets from Higgs decays provides an alternative method to exclusive Higgs decays [?, ?, ?, ?, ?] for constraining the Yukawa coupling of the strange quark. See Ref. [?, ?, ?, ?] for approaches using event shape and kinematic observables. The main idea behind the strange tagger described in Ref. [?] is that strange quarks—more than other partons—hadronize to prompt kaons that carry a large fraction of the jet momentum. Based on this idea a tagger is constructed to allow for an estimate of the capabilities in measurements involving strange quarks. Although the current focus at LHC is on mainly on charm and bottom tagging, recognizing strange jets has been attempted before at DELPHI [?] and SLD [?], albeit in  $Z$  decays.

The shown results are based on an analysis of event samples of Higgs and  $W$  events generated

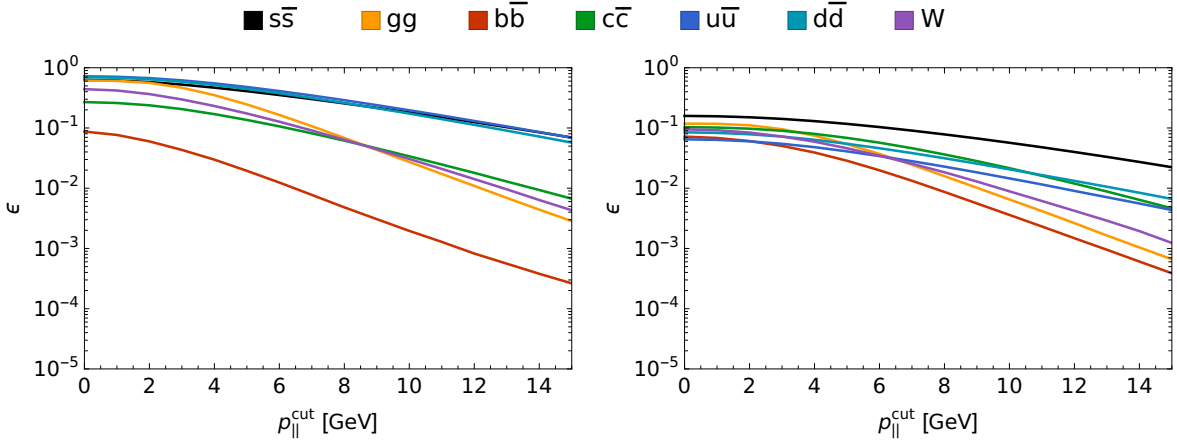


Fig. 83: Efficiencies as function of the cut on  $p_{||}$  and for  $d_0 < 14 \mu\text{m}$  to reconstruct the different Higgs decay channels and  $W$  decays as  $s\bar{s}$  event by the described tagger. The left plot shows the CC channel, the right the CN channel.

with PYTHIA 8.219 [132, 196]. In each of the two hemispheres of the resonance decay, the charged pions and kaons stemming from the resonance are selected with an assumed efficiency of 95%. Similarly,  $K_s$  are identified with an efficiency of 85% if they decay within 80 cm of the interaction point into a  $\pi^+\pi^-$  pair that allows to reconstruct the decaying neutral kaon. Among the two lists of kaon candidates—one per hemisphere—one kaon of each list is chosen for further analysis such that the scalar sum of their momenta is maximized while rejecting charged same-sign pairs. The events are separated into the categories charged-charged (CC), charged-neutral (CN) and neutral-neutral (NN) with a relative abundance of about CC:CN:NN  $\approx 9 : 6 : 1$  from isospin considerations and branching ratios by the charges of the selected kaon candidates.

All selected candidates are required to carry a large momentum  $p_{||}$  along the hemisphere axis. This cut allows to reduce the background from gluon jets as gluons radiate more than quarks and therefore tend to spread their energy among more final state particles. In addition, charged kaons need to be produced promptly, in order to reject heavy flavor jets. This latter requirement is implemented by a cut on the impact parameter  $d_0$  after the truth value has been smeared by the detector resolution.

The efficiencies obtained in the CC and CN channel for a cut of  $d_0 < 14 \mu\text{m}$  are shown in Fig. 83. While there is clearly still ample room for improvement, this simple tagger shows already a good suppression by orders of magnitude of the bottom, charm and gluon background. Due to missing particle identification, the efficiencies for first-generation jets and strange jets are degenerate in the CC channel. However, in the CN channel, due to the required  $K_s$ , a suppression of pions is achieved that breaks this degeneracy. This is particularly interesting in light of the HL-LHC, where a large background from first generation jets is expected.

## 7.5 LFV decays of the Higgs

## 7.6 Yukawa constraints from Higgs distributions

The Higgs transverse momentum,  $p_T$ , distributions have been considered before as a probe of high scale new physics running in the  $ggh$  loop, see [?, ?, ?, ?, ?, ?, ?, ?, ?, ?, 197]. In addition, the soft spectrum is an indirect probe of the Higgs coupling to light quarks [?, ?]. Quark fusion production of Higgs, which is negligible in the SM, have two effects of the Higgs kinematical distributions. First, the Sudakov peak will be at smaller  $p_T$  around 5 GeV vs 10 GeV for gluon fusion, see [?]. This is because the effective radiation strength of gluon is few times larger than of quarks,  $\alpha_s N_c$  vs.  $\alpha_s(N_c^2 - 1)/(2N_c)$ , with  $N_c = 3$ . This leads to harder  $p_T$  spectrum for gluon fusion than in the quark case. In terms of

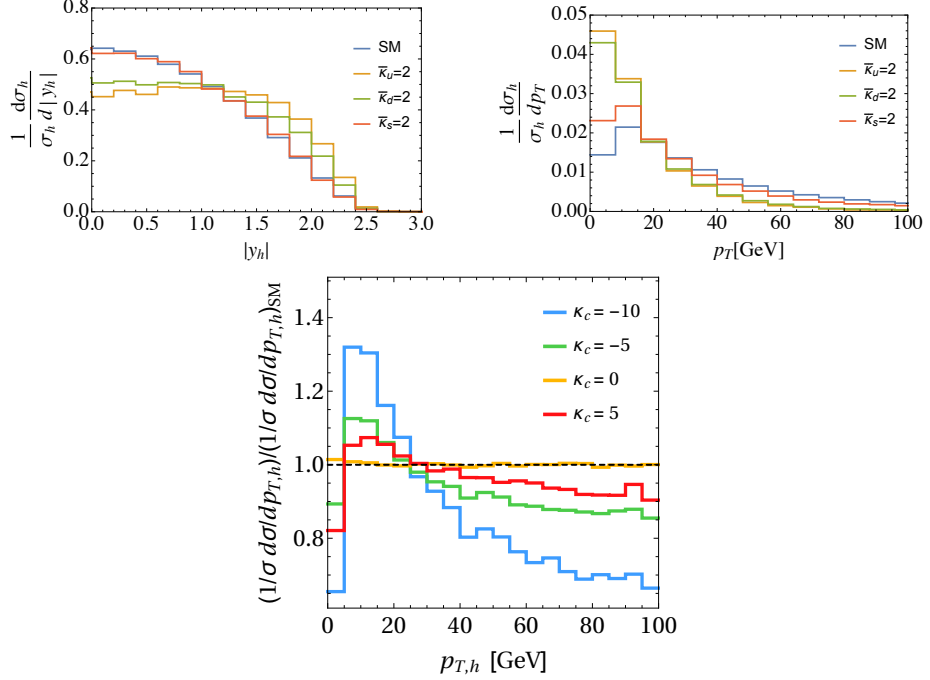


Fig. 84: The Higgs normalized distributions. Left-top (Right-top) :  $y_h$  ( $p_T$ ) distribution for enhanced  $u$ ,  $d$  and  $s$  Yukawa compared to the SM [?]; Bottom:  $p_T$  distribution for enhanced  $c$  Yukawa [?].

normalized  $p_T$  distribution, therefore, the  $u\bar{u}$  or  $d\bar{d}$  scattering leads to a much sharper peak at lower  $p_T$  compared with the  $gg$  scattering [?]. Second, in the SM, the Higgs production is dominated by a gluon fusion, where the two gluon carry similar partonic  $x$ . This leads to peak at zero Higgs rapidity. However, for  $u\bar{u}$  or  $d\bar{d}$  fusion, the valance quark will carry larger partonic  $x$  than the sea anti-quark. This leads to a peak in the forward direction. For enhanced  $s$  or  $c$  Yukawa, the dominant effect is the one loop of the quarks in the  $gg \rightarrow hj$  process, which show double logarithms behavior and peaks toward low Higgs  $p_T$  [?]. This will also resulting in a softer Higgs  $p_T$  spectrum [?], which can be used to constrain the charm and strange Yukawa. For illustration of the above effect on the different kinematical distributions see In Fig. 84. We comment that many theoretical and experimental uncertainties are canceled in the normalized kinematical distribution,  $(1/\sigma)d\sigma/dX$  with  $X = p_T, y_h$ , see for example [?]. Thus, the use of them will result in a better sensitivity for probing the light quark Yukawa.

In Ref. [?], the 8 TeV ATLAS data [?] has been used to evaluate first bound on the  $u$  and  $d$  Yukawa from the Higgs kinematical distribution. The resulting 95 % CL regions from the  $p_T$  distribution are

$$\bar{\kappa}_u = y_u/y_b^{\text{SM}} < 0.46, \quad \bar{\kappa}_d = y_d/y_b^{\text{SM}} < 0.54, \quad (130)$$

which are stronger than the fits to the inclusive Higgs production cross sections. Note that the above upper bound found to be stronger than the expected due to lower fluctuation of the data in the first  $p_T$  bin. The bounds from the 8 TeV Higgs rapidity distribution are found to be weaker. The sensitivity of the 13 TeV run of the rapidity and transverse momentum distribution is plotted in Fig. 85.

Following Ref. [?], CMS interpertated the 13 TeV Higgs  $p_T$  spectrum with luminoisty of  $35.9 \text{ fb}^{-1}$  as bounds on the  $c$  and  $b$  Yukawa [?]. In case that the branching ratio are allowed to floated (are depend on  $\kappa_c$  and  $\kappa_b$ ), the resulting 95 % CL intervals are

$$-2.8 (-0.9) < \kappa_c < 9.9 (0.9), \quad -18.0 (-4.3) < \kappa_b < 22.9 (4.3). \quad (131)$$

These bounds on the  $c$  Yukawa are weaker (stronger) then the bounds from the global fit of the 8 TeV Higgs data along with the electroweak precision data allowing all Higgs coupling to float [?]

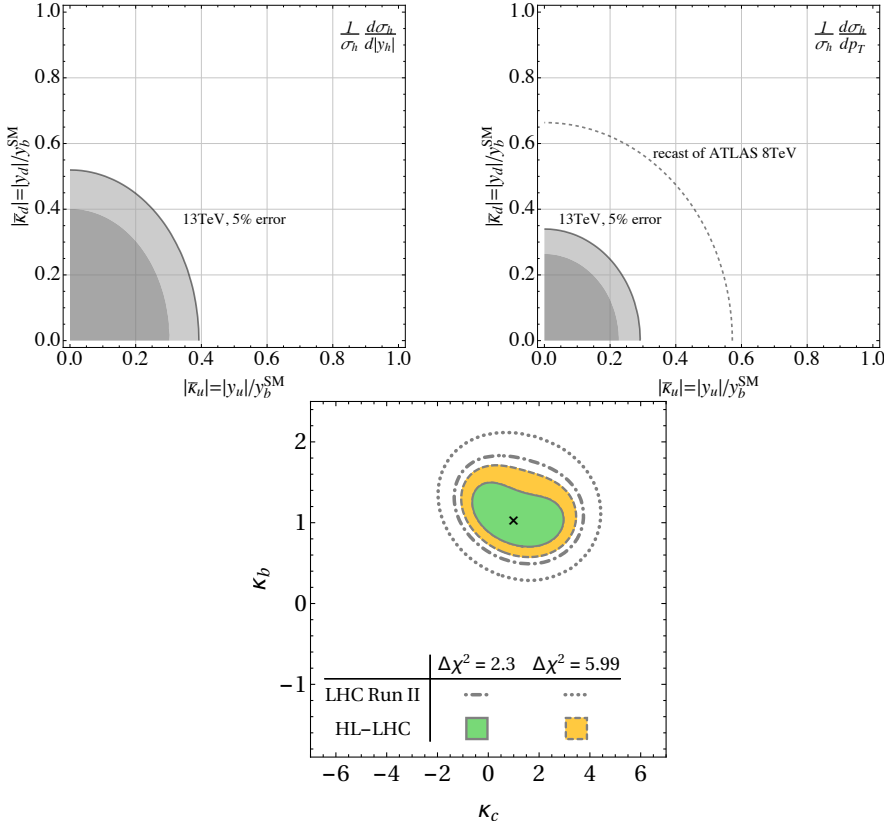


Fig. 85: The sensitivity of the different angular distribution to probe light quarks Yukawa at 13 TeV. Left-top:  $u$  and  $d$  quark Yukawa from  $y_h$  distribution [?]; Right-top:  $u$  and  $d$  quark Yukawa from  $p_T$  distribution [?]; Bottom:  $b$  and  $c$  quark Yukawa from  $p_T$  distribution [?].

### 7.6.1 Determinations of Higgs boson coupling modifiers using differential distributions

this subsection contributed by T. Kljnsma (integrated by A.Schmidt) on 5. Oct. for CMS. It still needs to be merged with the section above

Variations of Higgs boson couplings alter the SM Higgs production cross sections, both inclusively and differentially. Exploiting the deviations of the differential spectra, in particular the transverse momentum spectrum,  $pTH$ , one can constrain Higgs boson couplings using information that is not available in inclusive measurements [?, ?, 25]. As the measurements of differential cross sections are generally dominated by statistical uncertainties [?], these constraints are expected to improve drastically with the advent of more data.

The Higgs boson couplings are free parameters in the SM Lagrangian, and there are many potential extensions of the SM [?, ?] that predict deviations of their SM values. Using the transverse momentum distribution measured by the ATLAS Collaboration at  $\sqrt{s} = 8$  TeV [?], corresponding to an integrated luminosity of  $20.3 \text{ fb}^{-1}$ , for the first time limits were set on the coupling to the charm quark,  $\kappa_c$ , using differential distributions [?]. These limits are compatible with those obtained from direct limits, such as a search using the same dataset for  $H \rightarrow J/\psi\gamma$  by the ATLAS Collaboration [?], and a search for  $H \rightarrow c\bar{c}$  by the ATLAS Collaboration [?] using data collected at  $\sqrt{s} = 13$  TeV, corresponding to an integrated luminosity of  $36.1 \text{ fb}^{-1}$ . In addition to this study of the Higgs boson coupling to light quarks concerning mostly  $pTH \lesssim m_H$  (where  $m_H$  is the Higgs boson mass), a study [?, ?] involving simultaneous variations of the Higgs boson coupling to the top quark,  $\kappa_t$ , the bottom quark,  $\kappa_b$ , and an anomalous direct coupling to the gluon field,  $c_{ggh}$ , aims to exploit the tails of the  $pTH$  distribution.

Differential Higgs boson production cross section measurements are available from both the ATLAS [?, ?, ?, ?, ?, ?] and CMS [?, ?, ?, ?, ?, ?] Collaborations at  $\sqrt{s} = 8$  and 13 TeV. Recently, the theoretical predictions of the  $pTH$  distribution from Ref. [?] and Refs. [?, ?] were fitted to data [?] collected by the CMS Collaboration at  $\sqrt{s} = 13$  TeV, corresponding to an integrated luminosity of  $36.1 \text{ fb}^{-1}$ . This section concerns the projection of the constraints on Higgs boson couplings obtained in Ref. [?] to an integrated luminosity of  $3000 \text{ fb}^{-1}$ . We report projections for the simultaneous fits to data of  $\kappa_c$  and  $\kappa_b$  and of  $\kappa_t$  and  $c_{ggh}$ , using projections of the differential distributions at  $3000 \text{ fb}^{-1}$  obtained elsewhere [Ref to pure diff xs projection here].

The Higgs boson coupling fits are based a combination of  $pTH$  distributions from the  $H \rightarrow \gamma\gamma$  [?] and  $H \rightarrow ZZ^{(*)} \rightarrow 4\ell$  [?] (where  $\ell = e$  or  $\mu$ ) decay channels obtained at  $\sqrt{s} = 13$  TeV. Furthermore, a search for the Higgs boson produced with large  $p_T$  and decaying to a bottom quark-antiquark ( $b\bar{b}$ ) pair [?], which enhances the sensitivity at high  $pTH$ , is included in the  $\kappa_t/c_{ggh}$  fit. The Higgs boson coupling fits are performed using an simultaneous extended maximum likelihood fit to the diphoton mass, four-lepton mass, and soft-drop mass  $m_{SD}$  [?, ?] spectra in all the analysis categories of the  $H \rightarrow \gamma\gamma$ ,  $H \rightarrow ZZ$ , and  $H \rightarrow b\bar{b}$  channels, respectively. For more details on the treatment of the input measurements, see Ref. [?].

The treatment of the decay of the Higgs boson affects the Higgs boson coupling fits. Assuming full knowledge of how the Higgs decays, i.e., assuming no beyond-the-SM contributions, the inclusive Higgs production cross section adds a strong constraint on the Higgs boson couplings in the fit. This result is obtained by parametrizing the branching fractions as functions of the Higgs boson couplings. Likewise, the constraints on the Higgs boson couplings excluding the information from the inclusive cross section are of interest in order to evaluate the discriminating power of the differential distributions. This result is implemented by letting the branching fractions be determined in the fit without any prior constraint.

The expected one and two standard deviation contours of the  $\kappa_c/\kappa_b$  fit with the branching fractions as functions of the Higgs boson couplings at a projected integrated luminosity of  $3000 \text{ fb}^{-1}$  is shown in Fig. 86, for both scenarios of systematic uncertainty. For the  $H \rightarrow \gamma\gamma$  channel the systematic uncertainties dominate if kept at the current level (i.e., in Scenario 1), but when scaled down according to the Scenario 2 prescription the systematic uncertainties are within the same order of magnitude as the statistical ones.

The same fits, but now with the branching fractions implemented as nuisance parameters with no prior constraint, are shown in 87. As this fit is dominated by statistical uncertainties even at very high integrated luminosities, the smaller systematic uncertainties in Scenario 2 have only a minor impact.

## 7.7 $W^\pm h$ charge asymmetry

The  $W^\pm h$  charge asymmetry, introduced in [?], is a new, production-based probe for constraining the light quark Yukawa couplings. In contrast to decay-based probes, which rely on rare or subdominant Higgs decay modes, production-based probes can take advantage of the dominant Higgs decays with high signal-to-background ratios.

The main observable is the charge asymmetry between  $W^+h$  and  $W^-h$  production,

$$A = \frac{\sigma(W^+h) - \sigma(W^-h)}{\sigma(W^+h) + \sigma(W^-h)}, \quad (132)$$

In the SM, the inclusive HE-LHC charge asymmetry is expected to be 17.3%, while the HL-LHC charge asymmetry is expected to be 21.6%. In either case, the charge asymmetry is driven by the proton PDFs and the fact that the dominant  $W^\pm h$  production mode stems from Higgs bosons radiating from  $W^\pm$  intermediate lines, where the Yukawa-mediated diagrams are negligible. If the quark Yukawas are not SM-like, however, the charge asymmetry can either increase or decrease, depending on the overall weight of the relevant PDFs. In particular, the charge asymmetry will increase if the down or up quark Yukawa couplings are large, reflecting the increased asymmetry of  $u\bar{d}$  vs.  $\bar{u}d$  PDFs; the charge asymmetry will

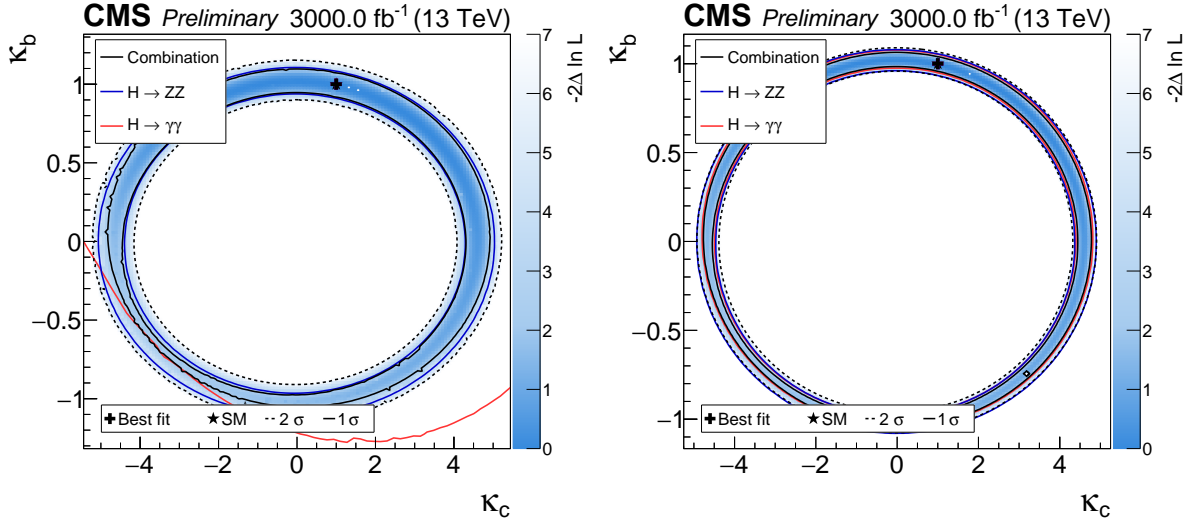


Fig. 86: Simultaneous fit to data for  $\kappa_b$  and  $\kappa_c$ , assuming a coupling dependence of the branching fractions for Scenario 1 (upper) and Scenario 2 (lower). The one standard deviation contour is drawn for the combination ( $H \rightarrow \gamma\gamma$  and  $H \rightarrow ZZ$ ), the  $H \rightarrow \gamma\gamma$  channel, and the  $H \rightarrow ZZ$  channel in black, red, and blue, respectively. For the combination the two standard deviation contour is drawn as a black dashed line, and the negative log-likelihood value on the coloured axis.

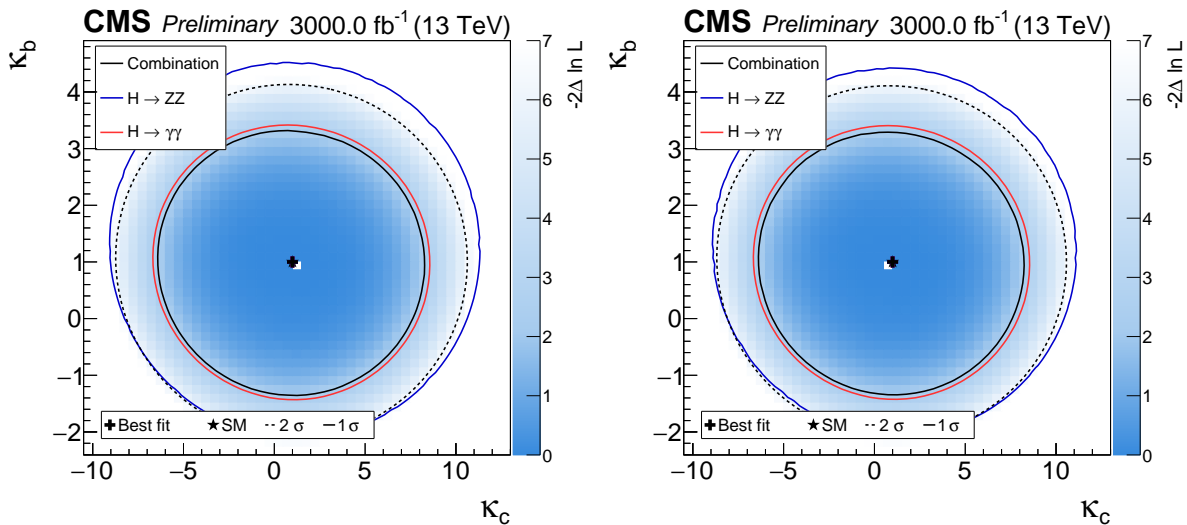


Fig. 87: As Fig. 86, but with the branching fractions implemented as nuisance parameters with no prior constraint.

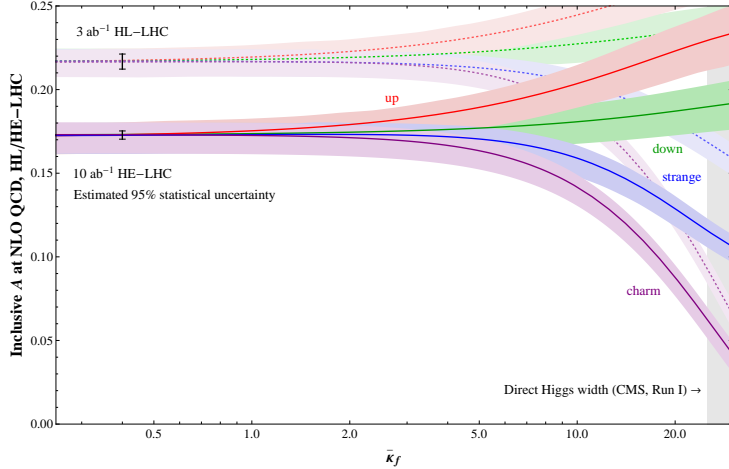


Fig. 88: Inclusive charge asymmetry for  $W^\pm h$  production at the 27 TeV HE-LHC (solid colored bands), and 14 TeV HL-LHC (dotted colored bands), calculated at NLO QCD from MadGraph\_aMC@NLO using NNPDF 2.3 as a function of individual Yukawa rescaling factors  $\bar{\kappa}_f$  for  $f = u$  (red),  $d$  (green),  $s$  (blue), and  $c$  (purple). Shaded bands correspond to scale uncertainties at  $1\sigma$  from individual  $\sigma(W^+h)$  and  $\sigma(W^-h)$  production, which are conservatively taken to be fully uncorrelated. The expected statistical errors from this measurement using  $10 \text{ ab}^{-1}$  of HE-LHC data and  $3 \text{ ab}^{-1}$  of HL-LHC data are also shown.

decrease if the strange or charm Yukawa couplings are large, reflecting the symmetric nature of  $c\bar{s}$  vs.  $\bar{c}s$  PDFs. The subleading correction from the Cabibbo angle-suppressed PDF contributions determines the asymptotic behavior for extremely large Yukawa enhancements.

The effect of individual  $d$ ,  $u$ ,  $s$ , or  $c$  quark Yukawa enhancements on the inclusive charge asymmetry is shown in Figure 88, in units of  $\bar{\kappa}_f = y_f/y_{\text{SM}, b}$ , evaluated at the Higgs mass scale. Since  $W^\pm h$  production probes lower Bjorken- $x$  at the HE-LHC compared to the HL-LHC, the expected SM charge asymmetry is lower at the higher energy collider. In Figure 88, we also display the expected 0.45% statistical sensitivity to the charge asymmetry coming from an HL-LHC simulation study [?] in the  $W^\pm h \rightarrow \ell^\pm \ell^\pm jj\nu\nu$  final state. To estimate the HE-LHC sensitivity, we simply rescale by the appropriate luminosity ratio, giving 0.25%, since we expect that the increase in both signal and background electroweak rates to largely cancel. We also indicate the constraint from the direct Higgs width constraint using Run I data from CMS [?]. The bands denote the change in the charge asymmetry from the varying the renormalization and factorization scales within a factor of 2.

We see that the expected statistical sensitivity supercedes the combined theoretical uncertainty in the PDF evaluation. Hence, in addition to being an important consistency check of the SM regarding enhanced light quark Yukawa couplings, the charge asymmetry measurement in different Higgs channels can be used to help determine PDFs at the HE-LHC, assuming light quark Yukawa couplings are SM-like. Separately, enhanced light quark Yukawa couplings would also generally be expected to decrease the Higgs signal strengths, necessitating the introduction of other new physics to be consistent with current Higgs measurements [?]. If the signal strengths are fixed to SM expectation and the central prediction is used, the HE-LHC charge asymmetry measurement could constrain  $\bar{\kappa}_f \lesssim 2 - 3$  for up and charm quarks, and  $\bar{\kappa}_f \lesssim 7$  for down or strange quarks.

## 7.8 Summary

YS: add summary

## 8 Global view of Higgs couplings at the HL/HE-LHC

Christopher W. Murphy

*Department of Physics, Brookhaven National Laboratory, Upton, New York, 11973, USA*

### 8.1 Introduction

To date there are no conclusive signals of physics beyond the Standard Model (SM) at the Large Hadron Collider (LHC). This suggests there is a separation of scales between the SM, characterized by  $v \approx 246$  GeV, and whatever may lie beyond it at some higher energy,  $\Lambda$ . Effective Field Theory (EFT) techniques are ubiquitous in physics, and are most useful when there is a separation of scales in the problem. Therefore it is not surprising that the Standard Model Effective Field Theory (SMEFT) has become one of the most powerful tools to analyze LHC results given its (near) model-independence, systematic improvability, and ability to simultaneously describe multiple datasets. Taking a global view of constraints on the Wilson coefficients of the SMEFT is of critical importance not only because these parameters often contribute to multiple datasets, but also because the LHC currently competes in precision with previous generation precision experiments. Given proposals for future runs of the LHC, High-Luminosity (HL) and High-Energy (HE), it is imperative to understand how the global picture of bounds on Wilson coefficients will change as the HL- and/or HE-LHC become the singularly dominant machine(s) in particle physics. To do so this Section uses the framework of Ref. [198], and its predecessors [?, ?, ?], to project bounds on Wilson coefficients in the SMEFT for the HL and HE runs of the LHC.

### 8.2 Standard Model Effective Field Theory

We focus on dimension-6 operators, and work to linear order in the Warsaw basis [154] yielding a consistent EFT expansion to order  $O(\Lambda^{-2})$ . We choose  $\alpha$ ,  $G_F$ , and  $M_Z$  as the input parameters for our computations. There are 2499 baryon number preserving dimension-6 Wilson coefficients in the SMEFT [?]. Here we assume a  $U(3)^5$  flavor symmetry, one power for each of the five SM fermions fields, under which the Yukawa matrices,  $y_{d,e,u}$ , are promoted to spurions transforming as bi-triplets. This reduces the number of (real) coefficients to 76. However only 20 of those parameters are relevant for the diboson, electroweak precision, and Higgs observables we consider here.

In the Warsaw basis, the 11 operators that span the set of diboson measurements and electroweak precision observables, whether through direct contributions or shifts in input parameters, can be written as

$$\begin{aligned} \mathcal{L}_{\text{SMEFT}}^{\text{Warsaw}} \supset & \frac{\bar{C}_{Hl}^{(3)}}{v^2} (H^\dagger i \overleftrightarrow{D}_\mu^I H) (\bar{l} \tau^I \gamma^\mu l) + \frac{\bar{C}_{Hl}^{(1)}}{v^2} (H^\dagger i \overleftrightarrow{D}_\mu H) (\bar{l} \gamma^\mu l) + \frac{\bar{C}_{ll}}{v^2} (\bar{l} \gamma_\mu l) (\bar{l} \gamma^\mu l) \\ & + \frac{\bar{C}_{HD}}{v^2} |H^\dagger D_\mu H|^2 + \frac{\bar{C}_{HWB}}{v^2} H^\dagger \tau^I H W_{\mu\nu}^I B^{\mu\nu} \\ & + \frac{\bar{C}_{He}}{v^2} (H^\dagger i \overleftrightarrow{D}_\mu H) (\bar{e} \gamma^\mu e) + \frac{\bar{C}_{Hu}}{v^2} (H^\dagger i \overleftrightarrow{D}_\mu H) (\bar{u} \gamma^\mu u) + \frac{\bar{C}_{Hd}}{v^2} (H^\dagger i \overleftrightarrow{D}_\mu H) (\bar{d} \gamma^\mu d) \\ & + \frac{\bar{C}_{HQ}^{(3)}}{v^2} (H^\dagger i \overleftrightarrow{D}_\mu^I H) (\bar{q} \tau^I \gamma^\mu q) + \frac{\bar{C}_{HQ}^{(1)}}{v^2} (H^\dagger i \overleftrightarrow{D}_\mu H) (\bar{q} \gamma^\mu q) + \frac{\bar{C}_W}{v^2} \epsilon^{IJK} W_\mu^{I\nu} W_\nu^{J\rho} W_\rho^{K\mu}, \end{aligned} \quad (133)$$

where Hermitian conjugate operators are implicit. The flavor indices are trivial, except for the four-lepton operator,  $C_{ll} = C_{ll}^{e\mu e\mu} = C_{ll}^{ee ee}$  [?], and are also left implicit. Additionally in Eq. (133) we define

$$\bar{C} \equiv \frac{v^2}{\Lambda^2} C. \quad (134)$$

There are an additional nine operators that affect Higgs measurements,

$$\begin{aligned} \mathcal{L}_{\text{SMEFT}}^{\text{Warsaw}} \supset & \frac{\bar{C}_{eH}}{v^2} y_e (H^\dagger H) (\bar{l} e H) + \frac{\bar{C}_{dH}}{v^2} y_d (H^\dagger H) (\bar{q} d H) + \frac{\bar{C}_{uH}}{v^2} y_u (H^\dagger H) (\bar{q} u \tilde{H}) \\ & + \frac{\bar{C}_G}{v^2} f^{ABC} G_\mu^{A\rho} G_\nu^{B\rho} G_\rho^{C\mu} + \frac{\bar{C}_{H\square}}{v^2} (H^\dagger H) \square (H^\dagger H) + \frac{\bar{C}_{uG}}{v^2} y_u (\bar{q} \sigma^{\mu\nu} T^A u) \tilde{H} G_{\mu\nu}^A \\ & + \frac{\bar{C}_{HW}}{v^2} H^\dagger H W_{\mu\nu}^I W^{I\mu\nu} + \frac{\bar{C}_{HB}}{v^2} H^\dagger H B_{\mu\nu} B^{\mu\nu} + \frac{\bar{C}_{HG}}{v^2} H^\dagger H G_{\mu\nu}^A G^{A\mu\nu}. \end{aligned} \quad (135)$$

The explicit appearance of the Yukawa matrices in Eq. (135) is necessary to formally preserve the  $U(3)^5$  flavor symmetry. A tenth operator,  $\mathcal{O}_H = (H^\dagger H)^3$  operator, is not listed here. The Wilson coefficient for this operator,  $C_H$ , can be measured in double-Higgs production, see Section 3 of this report.

Strictly speaking more than nine operators affect Higgs measurements. All of the operators in Eq. (133) except  $\mathcal{O}_W$  affect Higgs measurements at leading order. Furthermore Higgs production in association with a top-quark pair probes additional coefficients in the SMEFT [?, 198] that do not appear in our other observables. (See also Section 4.1 of this report.) The only one we explicitly consider is  $C_{uG}$ , which makes the largest contribution to  $t\bar{t}h$  production [198]. An alternative possibility would be to include all the operators by regularizing the fit as in Ref. [?].

### 8.3 Fit Setup and Current Results

We use the predictions for electroweak precision observables and  $WW$  scattering at LEP 2 in the Warsaw basis from Refs. [?, 73], whereas predictions for LHC observables are made using SMEFTsim [?]. The following data are used in our global fit, which are sensitive to 20 directions in the SMEFT parameter space.

- *pre-LHC data:* We use 11  $Z$ -pole observables from LEP 1 and 1 from SLC, which are given in Ref. [199], as well as the  $W$  mass measurement from the Tevatron [?]. In addition we use all the data for the processes  $e^+ e^- \rightarrow W^+ W^- \rightarrow 4f$ . These measurements were compiled in Ref. [?], and the original experimental papers are Refs. [?, ?, ?, ?]. These measurements also probe eleven directions in the SMEFT, which can be mapped to the operators in Eq. (133).
- *LHC Run 1 data:* We use all the 20 signal strengths from Table 8 of Ref. [25]. A signal strength is defined as the ratio of the measured cross section to its SM prediction. We also use the ATLAS and CMS combination for the  $h \rightarrow \mu^+ \mu^-$  signal strength [25], and the ATLAS  $h \rightarrow Z\gamma$  signal strength [78]. Furthermore, we include the  $W$  mass measurements from ATLAS [?].
- *LHC Run 2 data:* We use 25 measurements from CMS [?, ?, ?, ?, ?, ?, ?, ?, 29], and 23 measurements from ATLAS [?, ?, ?, ?, ?, ?, 28, 30], including experimental correlations whenever possible. In addition we include one measurement of the differential cross section for  $pp \rightarrow W^+ W^- \rightarrow e^\pm \nu \mu^\mp \nu$ , which requires  $p_T > 120$  GeV for the leading lepton, by ATLAS at 13 TeV [?].

We first present a simplified case where only the operators  $C_{HWB}$  and  $C_{HD}$  in the Warsaw basis are non-zero. In this particular case these coefficients are equivalent to the oblique parameters  $\Delta S$  and  $\Delta T$  [?]

$$\frac{v^2}{\Lambda^2} C_{HWB} = \frac{g_1 g_2}{16\pi} \Delta S, \quad \frac{v^2}{\Lambda^2} C_{HD} = -\frac{g_1 g_2}{2\pi(g_1 + g_2)} \Delta T, \quad (136)$$

Figure 89 shows the preferred parameter space for  $C_{HWB}$  and  $C_{HD}$  for three different selections of the data sets included in the fit. The blue ellipses are obtained using just pre-LHC measurements in the fit, whereas the orange ellipses use only the LHC Run-1 and -2 results. Finally, the green ellipses are obtained using all the data described in the list above. The regions shaded in darker and lighter colors are allowed at  $1$  and  $2\sigma$ , respectively.

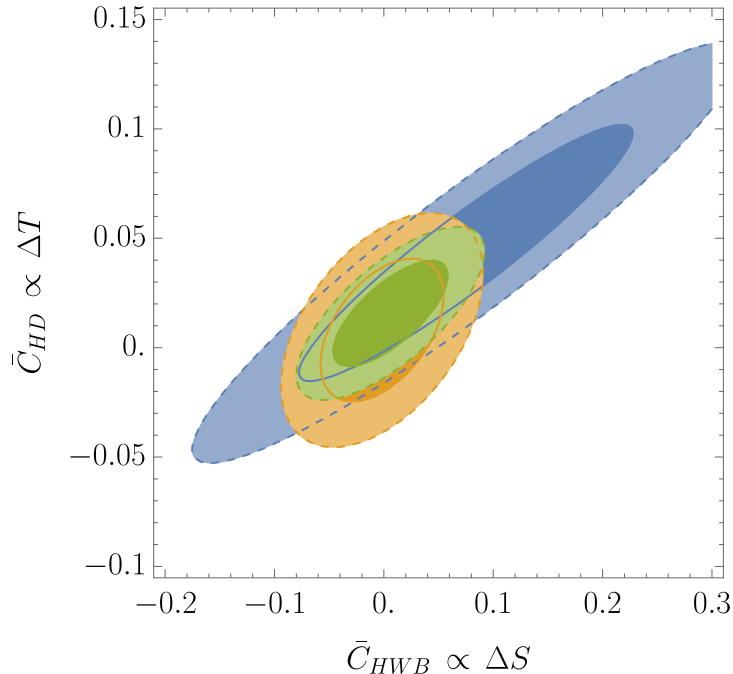


Fig. 89: *Fits to  $C_{HWB}$  and  $C_{HD}$  using pre-LHC measurements (blue), using LHC Run-1 and -2 results (orange), and all the data (green). The darker and lighter shaded regions are allowed at 1 and 2 $\sigma$ , respectively. When these are the only two non-zero coefficients in the Warsaw basis they are equivalent to the  $\Delta S$  and  $\Delta T$  parameters.*

Fig. 90 summarizes the sensitivities to the scales of the operators in the Warsaw basis. Specifically it gives the 95% CL bounds on the sensitivity in TeV for a Wilson coefficient, obtained from marginalized (yellow) and individual (brown) fits to the 20 dimension-6 operators entering in electroweak precision tests, diboson and Higgs measurements at LEP, SLC, Tevatron, and LHC Run-1 and -2. The yellow and brown bars correspond to the red and green bars of Figure 8 of Ref. [198], respectively. Shown in blue are the analogous results of the individual fits of the HEPfit Collaboration [?, 195], see also [?, ?]. For a recent fit in another basis see Ref. [?]. For a recent fit in the Nonlinear Effective Theory see instead Ref. [46].

#### 8.4 Future Projections

We project how the bounds on the Wilson coefficients of the SMEFT will change at HL- and HE-LHC using the framework of Ref. [198]. Our projection strategy is as follows. We leave all pre-LHC, and LHC Run-1 measurements unchanged. For measurements from Run-2 of the LHC we perform two extrapolations as to how the systematic uncertainties will change. The first, more pessimistic, extrapolation keeps the systematic and theoretical uncertainties fixed to their current values. This procedure is equivalent to the CMS scenario YR2018 S1 [?]. In contrast, the second, more optimistic, extrapolation scales the systematic and theoretical uncertainties as though they were statistical in nature. This procedure is more optimistic than CMS scenario YR2018 S2 where the theoretical uncertainties are only reduced by a factor of two and there are defined lower limits for the experimental systematic uncertainties [?]. In both cases the correlations between experimental measurements are assumed to be unchanged, and the statistical uncertainties are scaled as expected. In what follows we will refer to the former and the latter scenarios as ‘‘Systematics Unchanged,’’ and ‘‘ $\sqrt{N}$  Scaling,’’ respectively.

The explicit forms of the scaling we use HL- and HE-LHC for the  $i^{\text{th}}$  measurement in our dataset

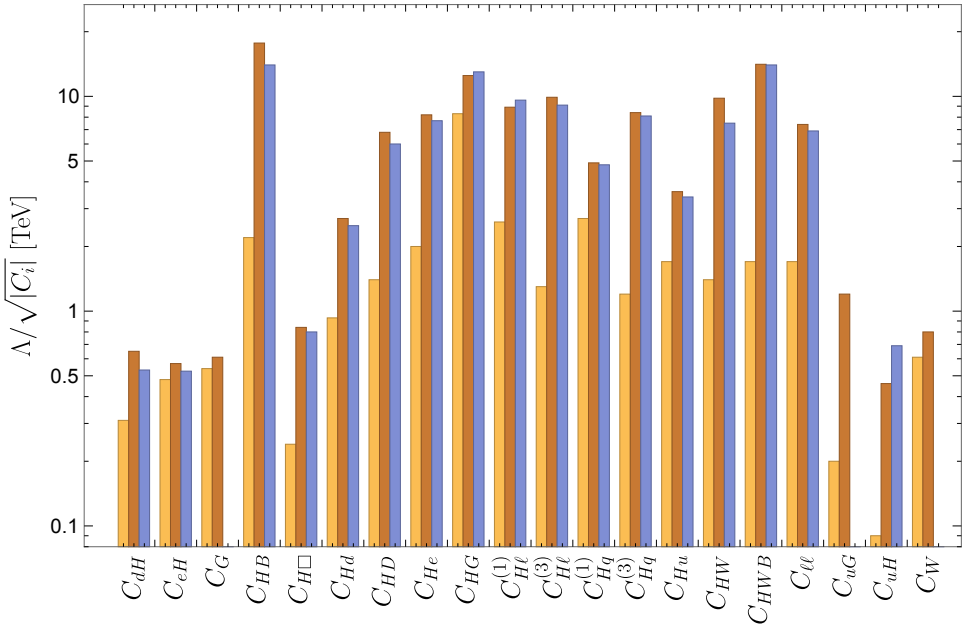


Fig. 90: Current constraints on dimension-6 operators. The yellow and brown bars are the marginalized and individual limits from Ref. [198], respectively. Shown in blue are the analogous results of the HEPfit Collaboration [?, 195] for the case where only one operator is switched on at a time.

are

$$\begin{aligned} \frac{\delta \mathcal{O}_{\text{HL},i}}{\delta \mathcal{O}_{\text{today},i}} &= \sqrt{\frac{L_{\text{today},i}}{L_{\text{HL}}}}, \\ \frac{\delta \mathcal{O}_{\text{HE},i}}{\delta \mathcal{O}_{\text{today},i}} &= \sqrt{\frac{\sigma_{13,i}}{\sigma_{27,i}} \frac{L_{\text{today},i}}{L_{\text{HE}}}}. \end{aligned} \quad (137)$$

For the overwhelming majority of the measurements by ATLAS(CMS)  $L_{\text{today},i} = 36.1(35.9) \text{ fb}^{-1}$ . We use the benchmark luminosities  $L_{\text{HL}} = 3 \text{ ab}^{-1}$ . and  $L_{\text{HE}} = 15 \text{ ab}^{-1}$  for all the measurements in the respective HL and HE extrapolations. The cross sections  $\sigma_{13,i}$  and  $\sigma_{27,i}$  refer to the SM cross section in the signal region for a given measurement at 13 and 27 TeV, respectively.

We stress that both our projection scenarios are pessimistic in the sense that they do not take into account the additional channels [?] and fining binning [?, ?, 7] that will become available as more data are collected. Furthermore our projections under-utilize LHC diboson scattering measurements, see Sections 4.3 and 4.4 of this report.

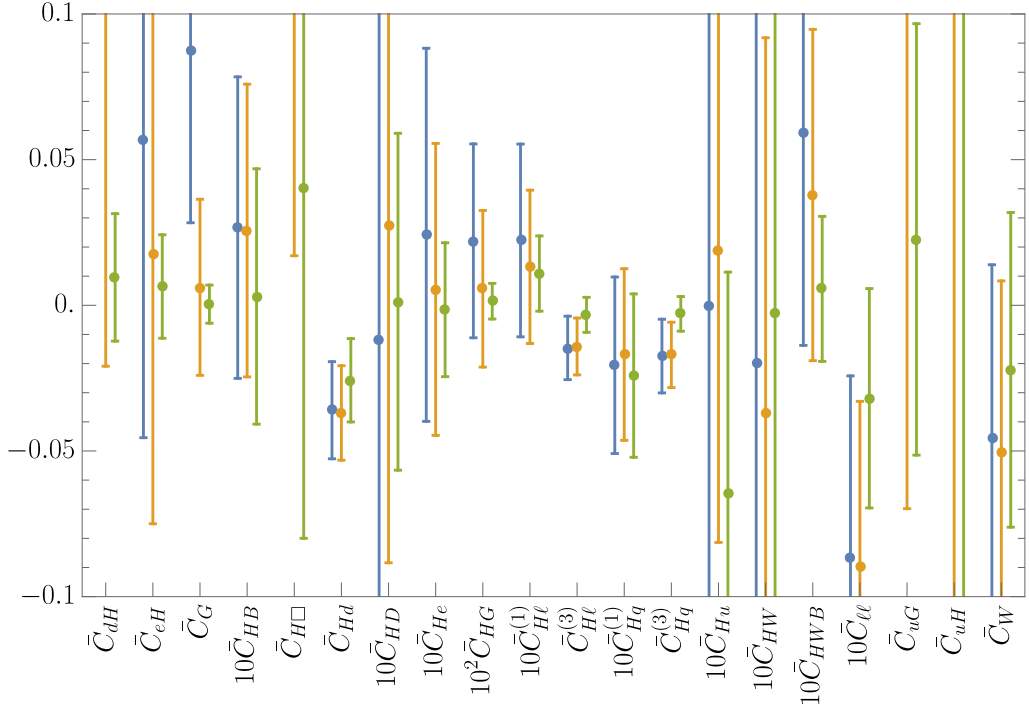
The results of our projections are shown in Figures 91, 92, 93, and 94. In all four figures the upper panel is a projected fit including all operators simultaneously, whereas the lower panel are projected fits switching each operator on individually. We display the best-fit values and 95% CL ranges. The color coding is consistent throughout the four figures: current bounds (blue), HL-LHC with Systematics Unchanged (orange), HL-LHC with  $\sqrt{N}$  Scaling (green), HE-LHC with Systematics Unchanged (red), and HE-LHC with  $\sqrt{N}$  Scaling (purple). The current bounds are displayed in all four figures. Fig. 91 shows projections for HL-LHC. Fig. 92 shows projections for HE-LHC. Fig. 93 shows projections with Systematics Unchanged. Fig. 94 shows projections with  $\sqrt{N}$  Scaling. Although Figs. 91 and 92 contain all the information from our projections, Figs. 93 and 94 are included to make comparisons between different scenarios easier, and vice versa.

In the individual fits there is a large spread in the improvement on the bounds on the Wilson

coefficients. In this scenario some bounds, including those on  $C_{dH}$  and  $C_{eH}$ , improve by an order of magnitude or more, while other bounds, such as those on  $C_{He}$  and  $C_{He}^{(1)}$ , are still dominated by pre-LHC measurements in this particular scenario. Conversely, when fitting to all operators simultaneously, the general trend is that there is some improvement on the bounds of all of the Wilson coefficients. Under the  $\sqrt{N}$  Scaling scenario HE-LHC clearly outperforms HL-LHC in terms of sensitivity to Wilson coefficients, or equivalently on how large of a cutoff scale  $\Lambda$  can be probed. On the other hand, under the Systematic Unchanged scenario the HL- and HE-LHC perform approximately equally as well as each other in terms of their sensitivity to Wilson coefficients.

Acknowledgments: CM thanks John Ellis, Verónica Sanz, and Tevong You for collaborations on Ref. [198]. The work of CM was supported by the United States Department of Energy under Grant Contract DE-SC0012704.

Marginalized Bounds at HL-LHC w/  $3 \text{ ab}^{-1}$



Individual Bounds at HL-LHC w/  $3 \text{ ab}^{-1}$

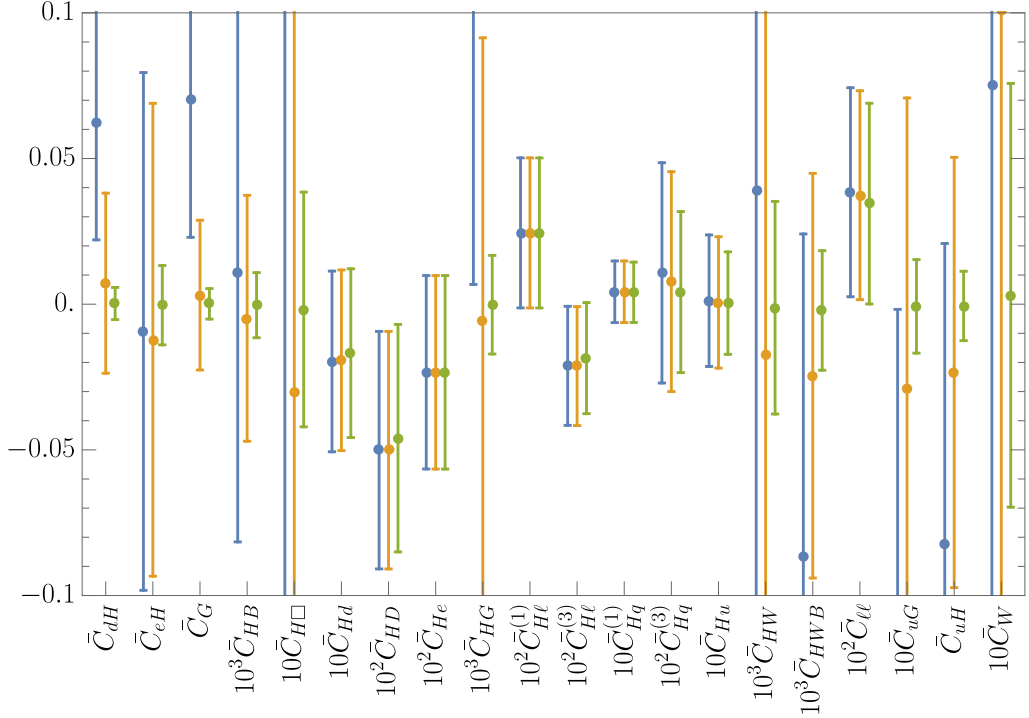


Fig. 91: Current bounds (blue), and projections for HL-LHC with Systematics Unchanged (orange) and  $\sqrt{N}$  Scaling (green) including all operators simultaneously (upper panel) and switching each operator on individually (lower panel). We display the best-fit values and 95% CL ranges.

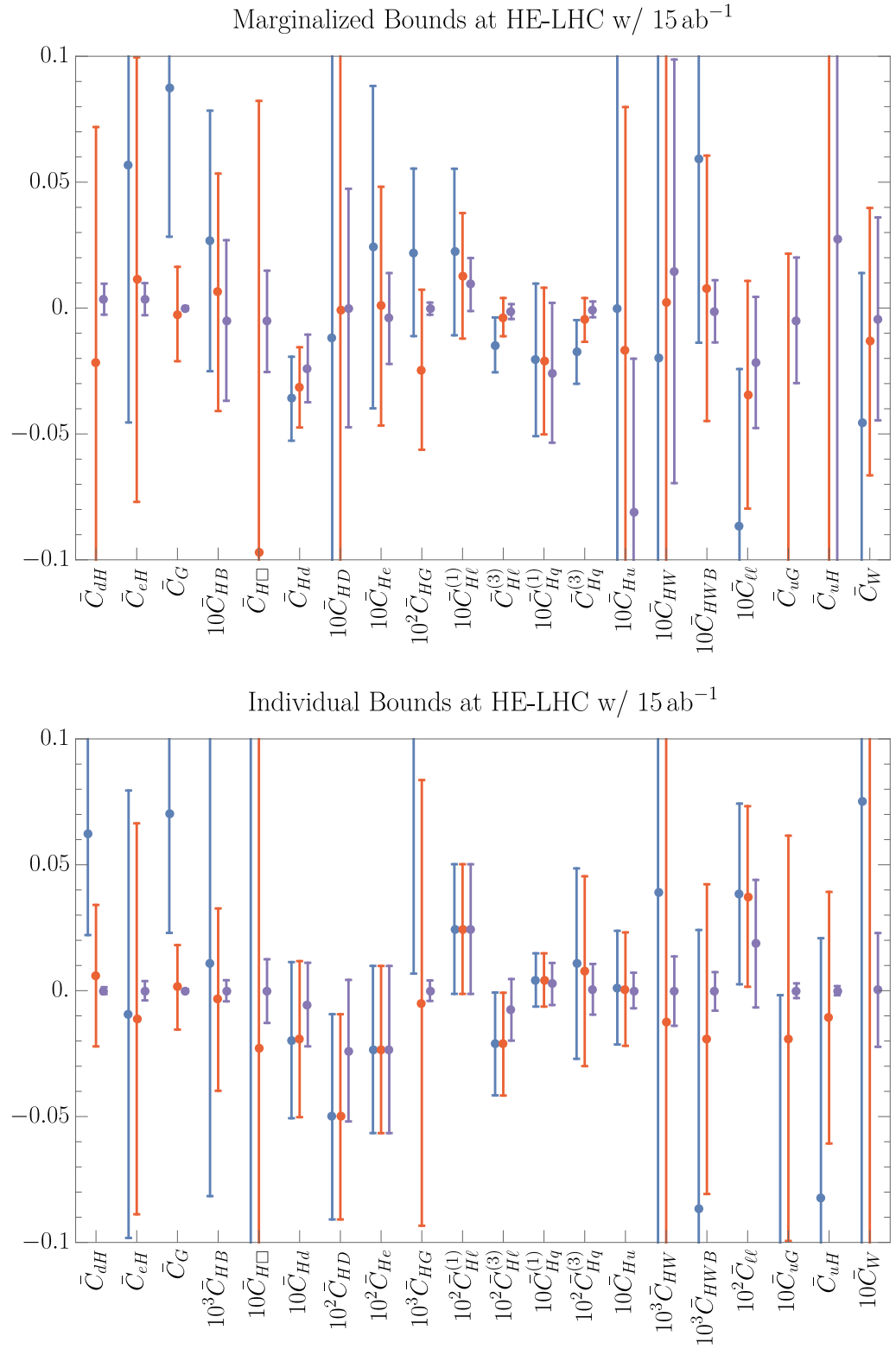
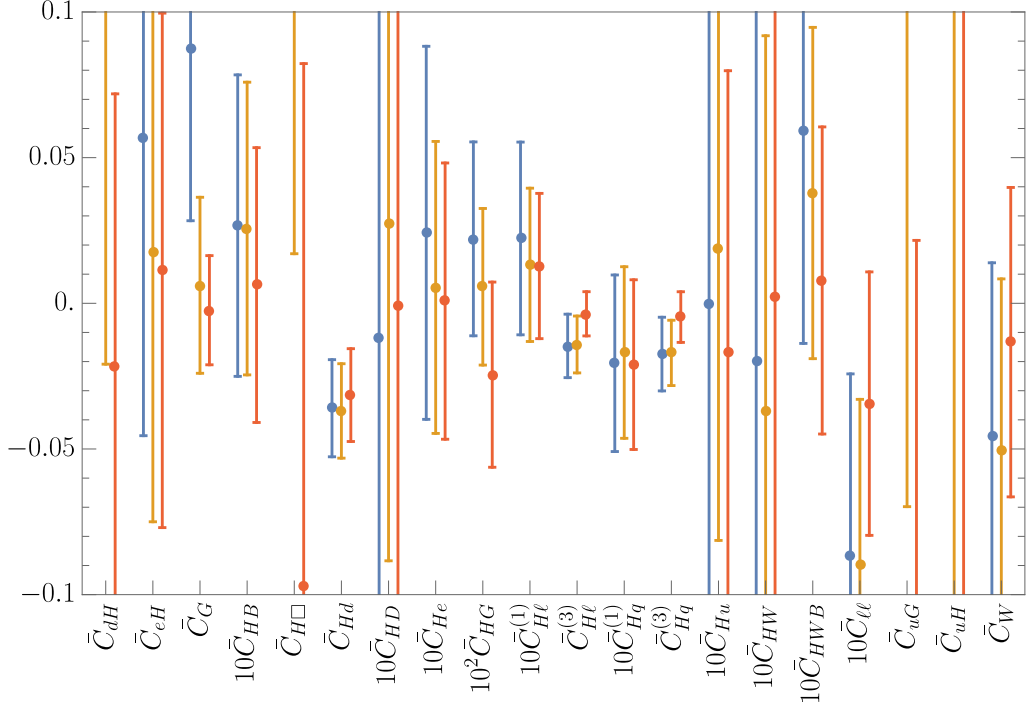


Fig. 92: Current bounds (blue), and projections for HE-LHC with Systematics Unchanged (red) and  $\sqrt{N}$  Scaling (purple) including all operators simultaneously (upper panel) and switching each operator on individually (lower panel). We display the best-fit values and 95% CL ranges.

Marginalized Bounds w/ Systematics Unchanged



Individual Bounds w/ Systematics Unchanged

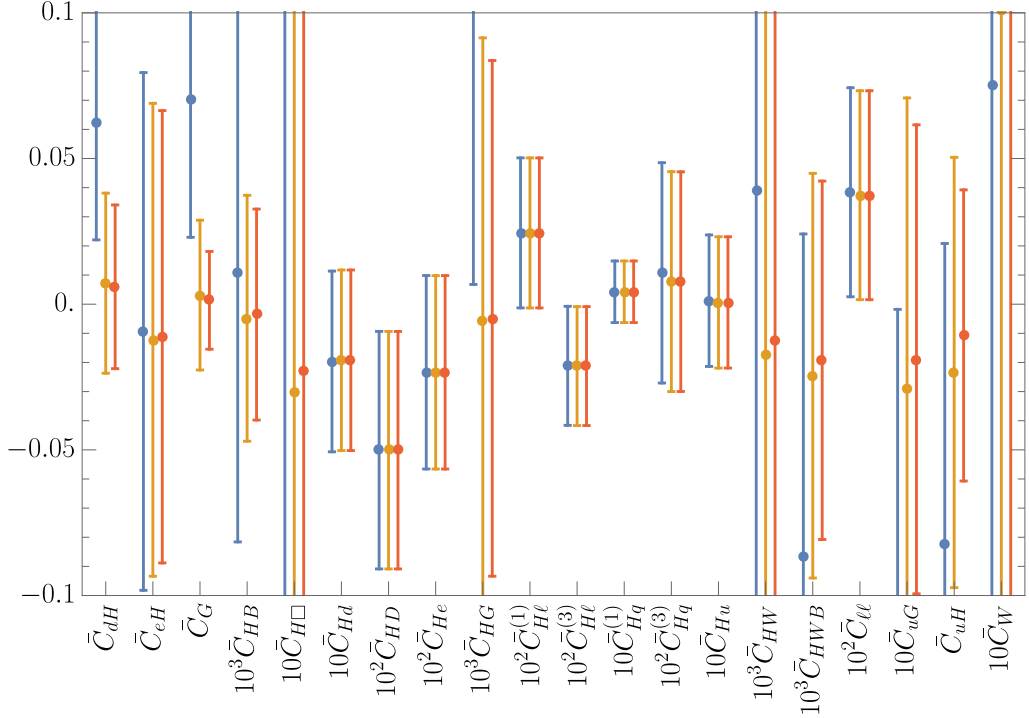


Fig. 93: Current bounds (blue), and projections with Systematics Unchanged for HL-LHC (orange) and HE-LHC (red) including all operators simultaneously (upper panel) and switching each operator on individually (lower panel). We display the best-fit values and 95% CL ranges.

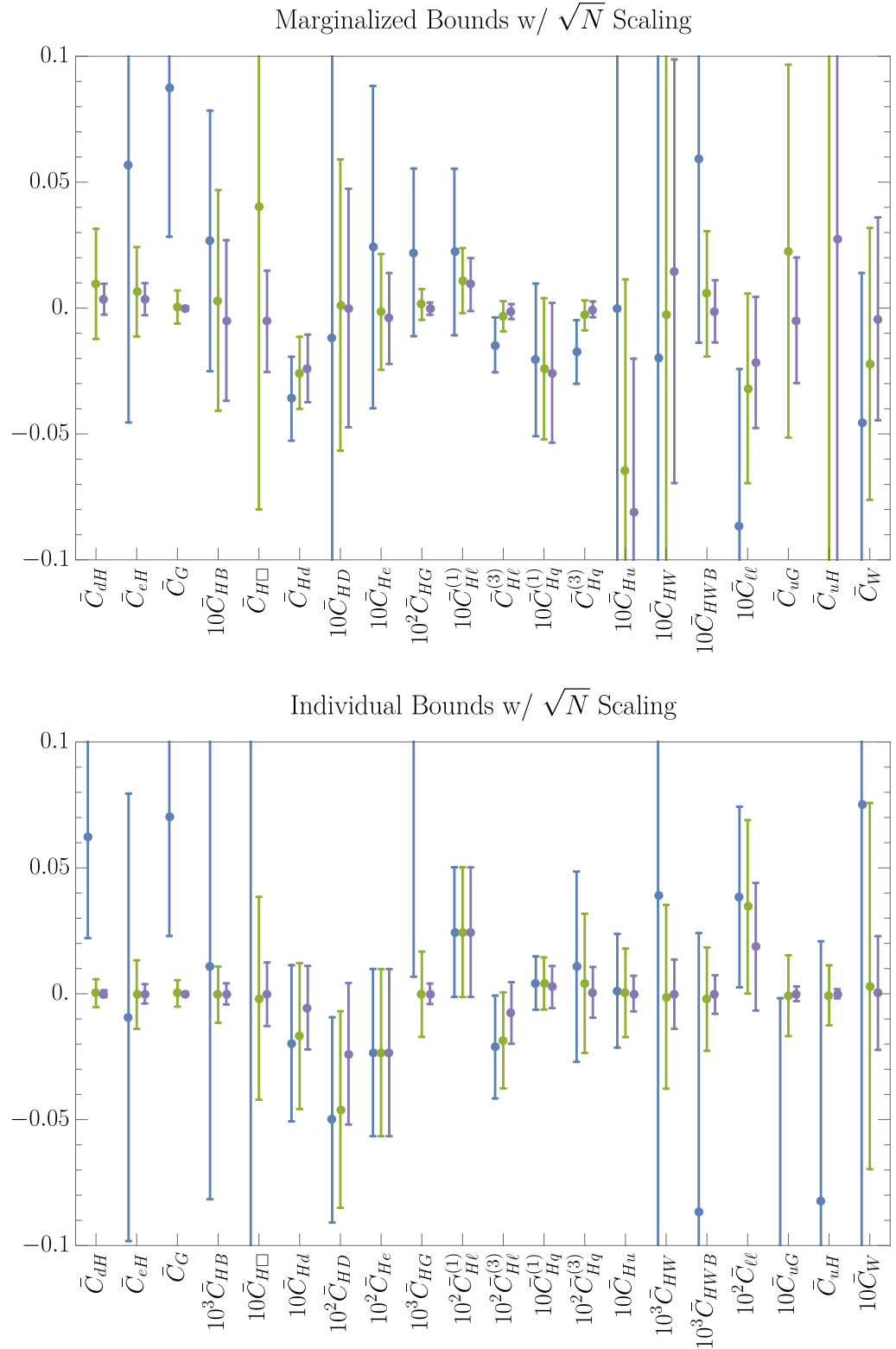


Fig. 94: Current bounds (blue), and projections with  $\sqrt{N}$  scaling for HL-LHC (green) and HE-LHC (purple) including all operators simultaneously (upper panel) and switching each operator on individually (lower panel). We display the best-fit values and 95% CL ranges.

## 9 Searches for beyond the standard model Higgs physics

*Make sure your contribution is in a separate file!*

### 9.1 Production of $t\bar{t}h$ and $t\bar{t}hh$ at the LHC in Composite Higgs models

Carlos Bautista,<sup>1,2</sup> Leonardo de Lima,<sup>3</sup> Ricardo D’Elia Matheus,<sup>1</sup> Eduardo Pontón,<sup>1,2</sup> Leônidas A. Fernandes do Prado,<sup>1,4</sup> and Aurore Savoy-Navarro<sup>4</sup>

<sup>1</sup>Instituto de Física Teórica – UNESP, São Paulo, Brazil

<sup>2</sup>ICTP South American Institute for Fundamental Research, São Paulo, Brazil

<sup>3</sup>Universidade Federal da Fronteira Sul, Realeza, Brazil

<sup>4</sup>IRFU-CEA, Université Paris-Saclay and CNRS-IN2P3, France

#### 9.1.1 Introduction

With the discovery of the Higgs boson [?, 19] the question of whether this resonance is a composite state, or rather the first observed scalar particle that appears elementary down to distances much shorter than its Compton wavelength, has gained new prominence. We consider the question of Higgs compositeness and the possible effects on the  $t\bar{t}h$  and  $t\bar{t}hh$  processes. The first one has already been observed [26, 27], and is consistent with the SM expectation, although with large uncertainties of order 20%. The second one is of particular interest for the models we consider, since one expects new charge 2/3 vectorlike “top partners” that can decay in the  $th$  channel. Resonance searches focusing on this decay channel have been presented in [?], and combined searches that consider the  $bW$ ,  $tZ$  and  $th$  channels already put strong constraints on such vectorlike resonances [?, ?].

In this work, we point out that the non-resonant  $t\bar{t}hh$  process is also of considerable interest in this context. Due to the already existing strong bounds on the vectorlike resonances, the non-resonant production very often accounts for a large fraction of the total  $t\bar{t}hh$  cross-section. Furthermore, it carries distinct information about the compositeness nature of the Higgs boson, as opposed to the indirect information connected to the existence of the heavy fermion resonances. We also point out that the non-resonant  $t\bar{t}hh$  process is closely connected to the  $t\bar{t}h$  process, but would be expected to display larger deviations from the SM expectation. We present here a first step in the analysis of such processes in the context of the 14 TeV High Luminosity phase of the LHC, and the possible High Energy LHC upgrade at 27 TeV. We explore these questions in the framework of the “Minimal Composite Higgs Models” (MCHM) [200], considering two possible realizations of the sector of fermionic resonances. Further details can be found in the companion paper [?].

#### 9.1.2 Theoretical Framework

The modern composite Higgs paradigm posits a new strongly coupled sector that spontaneously breaks a global symmetry  $\mathcal{G}$  down to a subgroup  $\mathcal{H}$ , thus generating a number of pseudo-Nambu-Goldstone bosons (pNGBs), some of which are identified with the Higgs doublet. The SM gauge group is contained in  $\mathcal{H}$  and electroweak symmetry breaking (EWSB) takes place only when the Higgs doublet acquires a vacuum expectation value (vev), a process that is dynamical and often calculable in such scenarios. In addition to a set of strong resonances of various spins, there is an “elementary” sector that mimics in its gauge quantum numbers the Standard Model (SM). The physical states are linear superpositions of the composite and elementary states, realizing the paradigm of partial compositeness, first proposed in [?]. We refer the reader to the full review in [?] for complete details. We restrict ourselves here to the MCHM scenarios, where  $\mathcal{G} = SO(5)$  and  $\mathcal{H} = SO(4)$ .

In this work, we focus on the resonances associated to the top sector, as these are the most relevant to the processes we study. We summarize here the essential features that enter into the phenomenological analysis, referring the reader to the companion work [?] for precise conventions and further details. Since

the fermionic sector is model dependent, we adopt two concrete realizations. Both share an elementary sector denoted by  $q_L$  and  $t_R$ , described by

$$\mathcal{L}_{\text{elem}} = \bar{q}_L iD q_L + \bar{t}_R iD t_R , \quad (138)$$

where  $D$  stands for the  $SU(3)_C \times SU(2)_L \times U(1)_Y$  covariant derivative.  $q_L$  and  $t_R$  transform as  $(3, 2, 1/6)$  and  $(3, 1, 2/3)$  under the SM gauge group.

### The MCHM<sub>5</sub>

In this “minimal” extension, one considers fermion resonances in a single **5** of  $SO(5)$ , which splits into a  $SO(4)$  4-plet,  $\Psi_4$ , and a  $SO(4)$  singlet,  $\Psi_1$ :

$$\Psi_4 \sim (X_{5/3}, X_{2/3}, T, B) ; \Psi_1 \sim \tilde{T} . \quad (139)$$

The states  $(X_{5/3}, X_{2/3})$  transform as a  $SU(2)_L$  doublet with exotic hypercharge  $Y = 7/6$ . The states  $(T, B)$  also transform as a  $SU(2)_L$  doublet and have hypercharge  $Y = 1/6$ , while  $\tilde{T}$  is a  $SU(2)_L$  singlet with hypercharge  $Y = 2/3$ . The composite sector is described by

$$\mathcal{L}_{\text{comp}}^{\text{5}} = \bar{\Psi}_4 iD \Psi_4 - M_4 \bar{\Psi}_4 \Psi_4 + \bar{\Psi}_1 iD \Psi_1 - M_1 \bar{\Psi}_1 \Psi_1 . \quad (140)$$

There is also the possibility of mixing between the composite and elementary states, described here by <sup>27</sup>

$$\mathcal{L}_{\text{mix}}^{\text{5}} = y_L f \bar{q}_L^{\text{5}} U [\Psi_4 + \Psi_1] + y_R f \bar{t}_R^{\text{5}} U [\Psi_4 + \Psi_1] + \text{h.c.} \quad (141)$$

where  $U$  parametrizes the Higgs field and  $f$  is the “Higgs decay constant”. All the features required for our analysis follow from the charge 2/3 fermion mass matrix, given in the  $\{\bar{t}_L, \bar{T}_L, \bar{X}_{2/3,L}, \bar{\tilde{T}}_L\}$  vs  $\{t_R, T_R, X_{2/3,R}, \tilde{T}_R\}$  basis by

$$\mathcal{M}_{2/3}^{\text{5}} = \begin{bmatrix} 0 & \frac{1}{2}y_L f(1 + \sqrt{1 - \xi}) & \frac{1}{2}y_L f(1 - \sqrt{1 - \xi}) & \frac{1}{\sqrt{2}}y_L f\sqrt{\xi} \\ -\frac{1}{\sqrt{2}}y_R f\sqrt{\xi} & -M_4 & 0 & 0 \\ \frac{1}{\sqrt{2}}y_R f\sqrt{\xi} & 0 & -M_4 & 0 \\ y_R f\sqrt{1 - \xi} & 0 & 0 & -M_1 \end{bmatrix} , \quad (142)$$

where  $\xi = v^2/f^2$  characterizes the deviations from a SM Higgs due to compositeness (here  $v = 246$  GeV). Consistency with current Higgs measurements results in  $\xi \lesssim 0.1$ , or  $f \gtrsim 800$  GeV [?, ?, ?, ?, 46, 74]. The remaining resonances have masses  $M_{X_{5/3}} = M_4$  and  $M_B = \sqrt{M_4^2 + y_L^2 f^2}$ .

### The MCHM<sub>14</sub>

In the second scenario, the composite states span a **14** of  $SO(5)$  [?, ?, ?, ?, ?, ?, ?, ?]. Under  $SO(4)$ , in addition to a 4-plet and a singlet, as in Eq. (139), we have an additional  $SO(4)$  nonet:

$$\Psi_9 \sim (U_{8/3}, U_{5/3}, U_{2/3}, Y_{5/3}, Y_{2/3}, Y_{-1/3}, Z_{2/3}, Z_{-1/3}, Z_{-4/3}) . \quad (143)$$

The  $U$ ’s,  $Y$ ’s and  $Z$ ’s transform as  $SU(2)_L$  triplets, with hypercharges  $Y = 5/3, 2/3$  and  $-1/3$ , respectively. The composite Lagrangian given in Eq. (140) is supplemented by terms involving  $\Psi_9$ :

$$\mathcal{L}_{\text{comp}}^{\text{14}} = \mathcal{L}_{\text{comp}}^{\text{5}} + \text{Tr} [\bar{\Psi}_9 iD \Psi_9] - M_9 \text{Tr} [\bar{\Psi}_9 \Psi_9] , \quad (144)$$

while the mixing with the elementary states is given by <sup>28</sup>

$$\mathcal{L}_{\text{mix}}^{\text{14}} = y_L f \text{Tr} [U^T \bar{Q}_L^{\text{14}} U \Psi_{14}] + y_R f \text{Tr} [U^T \bar{T}_R^{\text{14}} U \Psi_{14}] + \text{h.c.} \quad (145)$$

<sup>27</sup>In principle, one can choose different Yukawa couplings for the **4** and **1**. See [?].

<sup>28</sup>Here  $Q_L^{\text{14}}$  and  $T_R^{\text{14}}$  are convenient extensions of  $q_L$  and  $t_R$  that simplify the writing of the Lagrangian. See [?].

where  $\Psi_{14} \equiv \Psi_9 + \Psi_4 + \Psi_1$ .

The charge 2/3 mass matrix, in the  $\{\bar{t}_L, \bar{T}_L, \bar{X}_{2/3,L}, \bar{\tilde{T}}_L, \bar{U}_{2/3,L}, \bar{Y}_{2/3,L}, \bar{Z}_{2/3,L}\}$  vs  $\{t_R, T_R, X_{2/3,R}, \tilde{T}_R, U_{2/3,R}, Y_{2/3,R}, Z_{2/3,R}\}$  basis, is given by:

$$\mathcal{M}_{2/3}^{14} = \begin{bmatrix} 0 & \frac{1}{2}y_L f a_+ & -\frac{1}{2}y_L f a_- & -\frac{\sqrt{5}}{4}y_L f s_{2h} & -\frac{1}{2}y_L f b_- & -\frac{1}{2}y_L f s_{2h} & \frac{1}{4}y_L f b_+ \\ \frac{\sqrt{5}}{4}y_R f s_{2h} & -M_4 & 0 & 0 & 0 & 0 & 0 \\ -\frac{\sqrt{5}}{4}y_R f s_{2h} & 0 & -M_4 & 0 & 0 & 0 & 0 \\ y_R f \left(1 - \frac{5}{4}s_h^2\right) & 0 & 0 & -M_1 & 0 & 0 & 0 \\ \frac{\sqrt{5}}{4}y_R f s_h^2 & 0 & 0 & 0 & -M_9 & 0 & 0 \\ -\frac{\sqrt{5}}{4}y_R f s_h^2 & 0 & 0 & 0 & 0 & -M_9 & 0 \\ \frac{\sqrt{5}}{4}y_R f s_h^2 & 0 & 0 & 0 & 0 & 0 & -M_9 \end{bmatrix}, \quad (146)$$

where  $s_h^2 = \xi$ ,  $s_{2h} = 2\sqrt{\xi}\sqrt{1-\xi}$ ,  $a_{\pm} = 1 \pm \sqrt{1-\xi} - 2\xi$ ,  $b_{\pm} = \sqrt{\xi}(1 \pm \sqrt{1-\xi})$ .

We give the charge  $-1/3$  mass matrix in Ref. [?], as it plays a subdominant role. The remaining states have masses  $M_{X_{5/3}} = M_4$ ,  $M_{U_{8/3}} = M_{U_{5/3}} = M_{Y_{5/3}} = M_{Z_{-4/3}} = M_9$ .

An important distinction between the two scenarios is that when the mixing is dominated by the nonet, the leading order operator coupling the top quark to the Higgs doublet is the non-renormalizable operator  $\bar{q}_L \tilde{H} t_R H^\dagger H$ . In contrast, mixing through a 4-plet or singlet lead to the SM operator  $\bar{q}_L \tilde{H} t_R$  (plus corrections that are higher order in  $H/f$ ). In the former case the ratio of the top Yukawa coupling to the top mass is three times larger than in the second case. Cases where the nonet plays a comparable role to the 4-plet or singlet can then lead to interesting enhancements in the top Yukawa coupling, which are not present in the MCHM<sub>5</sub>.

### Higgs Decays

The scenarios under consideration can also affect the Higgs decays, and thus require a specification of how the remaining (light) fermions are treated. For concreteness, we assume that the RH bottom is associated with resonances in a **10** of  $SO(5)$  [?]. For the remaining fermions, we choose to replicate the scheme employed for the third family. We also assume that the lepton sector follows the same scheme as the quark sector. Furthermore, we assume that the mixing angles between the elementary and composite states associated with the light families are small, as in “anarchy” models of flavor.

Under the previous assumptions, one can express the partial widths as a rescaling of the corresponding SM widths. For the MCHM<sub>5</sub>, one finds [?]

$$\begin{aligned} \Gamma(h \rightarrow b\bar{b}) &= F_2(\xi)^2 \Gamma_{\text{SM}}(h \rightarrow b\bar{b}), \\ \Gamma(h \rightarrow c\bar{c}) &= F_1(\xi)^2 \Gamma_{\text{SM}}(h \rightarrow c\bar{c}), \\ \Gamma(h \rightarrow \tau^+ \tau^-) &= F_2(\xi)^2 \Gamma_{\text{SM}}(h \rightarrow \tau^+ \tau^-), \\ \Gamma(h \rightarrow VV) &= F_2(\xi)^2 \Gamma_{\text{SM}}(h \rightarrow VV), \\ \Gamma(h \rightarrow gg) &= F_1(\xi)^2 \Gamma_{\text{SM}}(h \rightarrow gg), \end{aligned} \quad (147)$$

where

$$F_1(\xi) = \frac{1 - 2\xi}{\sqrt{1 - \xi}}, \quad F_2(\xi) = \sqrt{1 - \xi}. \quad (148)$$

For the MCHM<sub>14</sub>, the bottom channel is controlled by  $F_1$  instead of  $F_2$ , and the  $ggh$  coupling is controlled by

$$c_g^{14} \approx \frac{4(1 - r_1)r_9 - (9r_1 + 23r_9 - 32r_1r_9)\xi + 4(3r_1 + 5r_9 - 8r_1r_9)\xi^2}{\sqrt{1 - \xi}[4(1 - r_1)r_9 - (3r_1 + 5r_9 - 8r_1r_9)\xi]}, \quad (149)$$

where  $r_1 = M_1/M_4$  and  $r_9 = M_9/M_4$ , instead of  $F_1(\xi)$ .

The total Higgs width in the MCHM models under consideration can then be written as

$$\begin{aligned}\Gamma_5(h) &= \left\{ F_2(\xi)^2 \left[ \text{BR}_{\text{SM}}(b\bar{b}) + \text{BR}_{\text{SM}}(\text{VV}) + \text{BR}_{\text{SM}}(\tau^+\tau^-) \right] \right. \\ &\quad \left. + F_1(\xi)^2 [\text{BR}_{\text{SM}}(gg) + \text{BR}_{\text{SM}}(c\bar{c})] \right\} \Gamma_{\text{SM}}(h),\end{aligned}\quad (150)$$

$$\begin{aligned}\Gamma_{14}(h) &= \left\{ F_2(\xi)^2 \left[ \text{BR}_{\text{SM}}(\text{VV}) + \text{BR}_{\text{SM}}(\tau^+\tau^-) \right] \right. \\ &\quad \left. + F_1(\xi)^2 [\text{BR}_{\text{SM}}(b\bar{b}) + \text{BR}_{\text{SM}}(c\bar{c})] + (c_g^{14})^2 \text{BR}_{\text{SM}}(gg) \right\} \Gamma_{\text{SM}}(h),\end{aligned}\quad (151)$$

and the branching fractions can also be written in terms of the functions  $F_1$ ,  $F_2$ ,  $c_g^{14}$ , and SM quantities. They are all that is needed to take into account the effects of compositeness in Higgs decays.

### 9.1.3 Parameter Space and Results

The parameters of the models are  $M_i$ ,  $f$ ,  $y_L$  and  $y_R$ . Taking into account the freedom to absorb phases through field redefinitions, one can see that there is only one physical phase in the  $\text{MCHM}_5$ , while there are two phases in the  $\text{MCHM}_{14}$ . For simplicity, we will take all parameters to be real, so that the free parameters can be taken as follows:

- $\text{MCHM}_5$ :  $f$ ,  $|M_1|$ ,  $|M_4|$ ,  $\text{sign}(M_1)$ ,  $y_L$  and  $y_R$ .
- $\text{MCHM}_{14}$ :  $f$ ,  $|M_1|$ ,  $|M_4|$ ,  $|M_9|$ ,  $\text{sign}(M_1)$ ,  $\text{sign}(M_4)$ ,  $y_L$  and  $y_R$ .

One of these parameters can be further fixed by requiring that the top mass be reproduced. We choose to fix  $y_R$  in this way. We use here the running top mass at the scale of the resonances, which will be typically around  $2 - 3$  TeV. We take  $\bar{m}_t = 150$  GeV. For  $t\bar{t}h$ , and also for the parts of  $t\bar{t}hh$  to be described in the following section, the relevant scales are of the order of a couple hundred GeV. We therefore distinguish between the high-scale running top mass (relevant for the diagonalization of the mass matrix), and a low scale running top mass, relevant to the physical processes of interest. We take for the latter the pole top mass of  $m_t = 173$  GeV, which also enters in kinematical quantities. To first approximation, this takes into account the running between the two scales. We take the Higgs mass as an independent parameter, referring the reader to [?] for further discussion on this point.

For the  $\text{MCHM}_5$ , we consider the following ranges for the parameters:

$$\begin{aligned}|M_1| &\in [800, 3000] \text{ GeV}, & M_4 &\in [1200, 3000] \text{ GeV}, \\ f &\in [800, 2000] \text{ GeV}, & y_L &\in [0.5, 3].\end{aligned}$$

For the  $\text{MCHM}_{14}$ , we use:

$$\begin{aligned}|M_1| &\in [800, 3000] \text{ GeV}, & |M_4| &\in [1200, 3000] \text{ GeV}, & M_9 &\in [1300, 4000] \text{ GeV}, \\ f &\in [800, 2000] \text{ GeV}, & y_L &\in [0.5, 3].\end{aligned}$$

We take an upper limit on  $y_L < 3$ , in order to remain in the (semi-) perturbative regime and thus justify the present tree-level analysis. For the same reason, we also check that  $y_R$ , as determined by the top mass, is below 4. In Fig. 95 we show the normalized top Yukawa coupling,  $y_{\text{top}}/y_{\text{top}}^{\text{SM}}$ , in the  $M_1$ - $M_4$  plane for both the  $\text{MCHM}_5$  and  $\text{MCHM}_{14}$  scenarios. We fix  $y_L = 2$  and  $f = 1200$  GeV, and  $M_9 = 2$  TeV for the  $\text{MCHM}_{14}$ . In the  $\text{MCHM}_5$ , the scaling with  $f$  is, to first approximation, given by the function  $F_1(\xi)$  in Eq. (148), while for the  $\text{MCHM}_{14}$  it is intertwined with the other parameters in a more complicated way. We see that the  $\text{MCHM}_5$  always displays a suppression of the top Yukawa coupling compared to the SM limit, while the  $\text{MCHM}_{14}$  can display an enhancement in certain regions of parameter space, as pointed

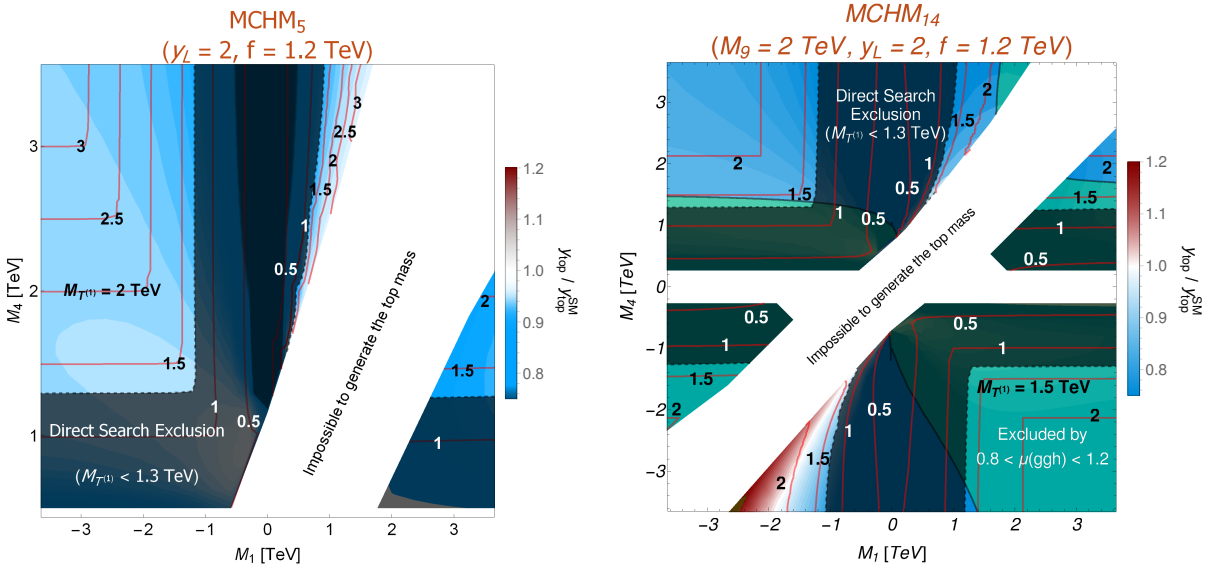


Fig. 95: Display of the values of the normalized top Yukawa coupling,  $y_{\text{top}} / y_{\text{top}}^{\text{SM}}$ , in the  $M_1$ - $M_4$  plane. Blue colors indicate a suppression and red colors an enhancement. Also shown the curves of constant  $M_{T^{(1)}}$ , the mass of the lightest  $Q = 2/3$  vectorlike resonance. The darker bands indicate the approximate current direct exclusion of top partner VLQ resonances, assuming decays into  $bW$ ,  $tZ$  and  $th$  [?, ?].

out in [?]. We also show in the figure, curves of constant  $M_{T^{(1)}}$  (red lines) and the approximate direct exclusion region (dark bands). The white area corresponds to the region in parameter space where it is not possible to reproduce the top quark mass. We also show the region where the  $ggh$  coupling deviates by more than 20% from unity, as this region is expected to be in tension with the current constraints on Higgs couplings [25].

#### 9.1.3.1 Implementation into Event Generator

We implement both models in FeynRules (v2.3) [201] and produce an associated UFO file for each model, that can be interfaced with MadGraph 5 (v2.6.2) [79]. The numerical input from the diagonalization of the mass matrices is then fed via a custom-written Python script into the param\_card.dat for processing within MG5. We simulate the  $t\bar{t}h$  and  $t\bar{t}hh$  processes in MG5. The output is then ready to be run through PYTHIA 8.2 [132], which takes care of the decays of the top quarks and the Higgs. We code the Higgs branching fractions, as described above, into Pythia. We also check that the deviations from the SM in the top quark properties are negligible, since the new physics is rather heavy. The output is then ready to pass through fast simulation [176] or the full simulation of the LHC experiments for HL-LHC.

#### 9.1.3.2 The $t\bar{t}h$ Process

To an excellent approximation, the  $t\bar{t}h$  process in the MCHM is related to the corresponding SM process by a simple rescaling:

$$\sigma_{\text{MCHM}}(t\bar{t}h) = \left( \frac{y_t}{y_t^{\text{SM}}} \right)^2 \sigma_{\text{SM}}(t\bar{t}h). \quad (152)$$

All the modifications due to Higgs compositeness, or mixing with vector-like fermions, enter only through the top Yukawa coupling. Therefore, only a modification in the total rate is expected, but not in kinematic distributions.

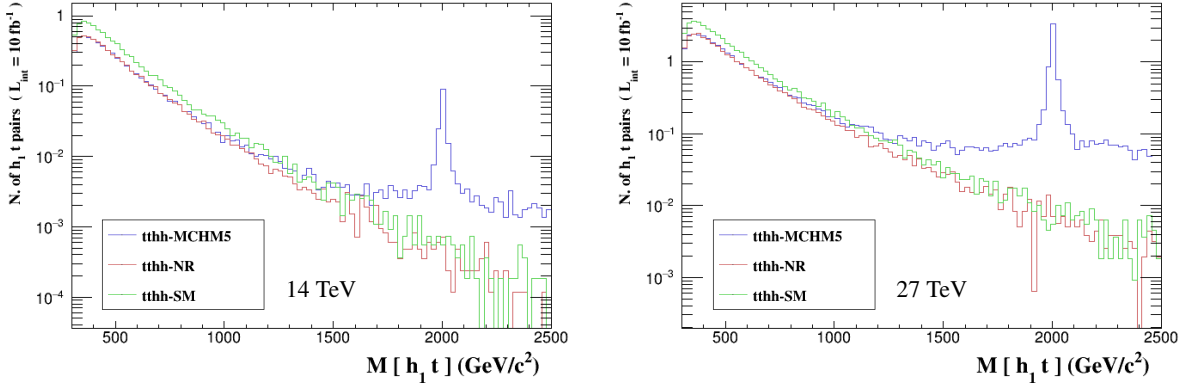


Fig. 96: Distribution of the invariant mass of the top quark and the hardest Higgs boson in the  $\text{MCHM}_5$  ( $M_1 = -2500 \text{ TeV}$ ,  $M_4 = 2 \text{ TeV}$ ,  $f = 1.8 \text{ TeV}$ ,  $y_L = 1$ ). The blue histogram shows the distribution of the full  $t\bar{t}hh$  process in the  $\text{MCHM}_5$ , while the NR-tthh cross-section is shown in red. For comparison, we also show in green the SM  $t\bar{t}hh$  distribution. Plots generated with MadAnalysis 5 [?].

#### 9.1.3.3 The $t\bar{t}hh$ Process

For the  $t\bar{t}hh$  process there are two qualitatively different contributions:

1. Resonant processes, involving the production and decay (in the  $t\bar{t}$  channel) of heavy vector-like states of charge 2/3 (top partners).
2. Non-resonant processes: these are defined by the diagrams that do not involve the production of the vector-like resonances.

The presence of resonant processes can lead to important enhancements in the  $t\bar{t}hh$  cross-section w.r.t. the SM, depending on their mass. The non-resonant process carries information that is distinct from the resonant part. It is therefore useful to define a “non-resonant cross-section” as obtained from this subset of diagrams, which we label as “NR-tthh”. One can similarly define a resonant cross section in terms of the diagrams involving QCD vector-like pair production. We find that, to an excellent approximation, the total  $t\bar{t}hh$  cross-section is given by the sum of these two cross-sections.

In Fig. 96 we show the  $ht$  invariant mass distribution for the resonant and non-resonant processes for a particular point in the  $\text{MCHM}_5$ . For comparison, we also show the SM  $t\bar{t}hh$  cross-section. We see that the NR-tthh follows the SM cross-section, but displays a suppression. We also see that the relative importance of the resonant process w.r.t. the non-resonant one increases with larger c.m. energies. The cross-section for both processes also increases significantly with the c.m. energy (by a factor of 7 in the total  $t\bar{t}hh$  cross-section when going from 14 to 27 TeV, and by a factor of 5 when restricted to NR-tthh).

#### 9.1.3.4 The Non-Resonant $t\bar{t}hh$ Process

The diagrams in the MCHM scenarios contributing to the NR-tthh process fall into three categories:

1. Those that involve only the  $t\bar{t}$  vertex.
2. Those that involve the trilinear Higgs self-interaction:  $\lambda = [(1 - 2\xi)/\sqrt{1 - \xi}] \lambda_{\text{SM}}$ .
3. Those that involve the  $t\bar{t}hh$  vertex (“double Higgs” Yukawa vertex).

The first two categories correspond to sets of *diagrams* that are identical to those in the SM. The third type involves diagrams that have no counterpart in the SM [202]. The latter is closely connected to the Higgs compositeness aspect of the MCHM scenarios, and it would therefore be extremely interesting if one could get information about such effects experimentally.

		MCHM <sub>5</sub>					MCHM <sub>14</sub>			
		Point 1	Point 2	Point 3	Point 4	Point 5	Point 1	Point 2	Point 3	Point 4
Parameters	M <sub>1</sub> (GeV)	-1317	800	-960	-3350	914	-1173	-1054	-1084	-1579
	M <sub>4</sub> (GeV)	1580	2311	1400	3000	2632	-1823	-1826	-1767	-2512
	M <sub>9</sub> (GeV)	-	-	-	-	-	1382	1448	2036	2714
	f(GeV)	969	896	1186	2450	1573	882	1032	1078	1298
	y <sub>L</sub>	1.66	1.80	0.88	1.00	2.36	1.98	1.93	2.95	2.71
	y <sub>R</sub>	0.62	1.95	0.87	0.85	2.41	3.90	2.78	2.67	2.46
$\mu(t\bar{t}h)$ (All Energies)		0.83	0.85	0.92	0.975	0.95	1.40	1.14	1.15	1.11
$\mu(t\bar{t}hh)$ (14 TeV)		1.13	0.57	2.96	0.68	0.65	3.31	2.14	1.19	0.92
$\mu(t\bar{t}hh)$ (27 TeV)		2.95	0.87	8.17	0.74	0.73	7.87	5.42	2.17	1.05
NR-t $\bar{t}$ hh/t $\bar{t}$ hh (14 TeV)		0.44	0.90	0.20	1.00	1.00	0.44	0.45	0.81	0.99
NR-t $\bar{t}$ hh/t $\bar{t}$ hh (27 TeV)		0.18	0.64	0.08	0.99	0.95	0.19	0.18	0.46	0.90
$M_{T^{(1)}}$ (TeV)		1.44	1.83	1.34	3.00	2.61	1.38	1.45	1.72	2.46
$M_{T^{(2)}}$ (TeV)		1.59	2.37	1.45	3.82	3.91	1.38	1.45	2.01	2.70
$M_{T^{(3)}}$ (TeV)		2.25	2.83	1.76	3.99	4.56	1.41	1.46	2.04	2.71
$M_{B^{(1)}}$ (TeV)		2.25	2.82	1.75	3.87	4.56	1.38	1.45	2.02	2.70
$M_{X_{5/3}}$ (TeV)		1.58	2.31	1.40	3.06	2.63	1.82	1.83	1.77	2.51
BR( $T^{(1)}$ $\rightarrow$ t h)		0.32	0.30	0.58	0.30	0.35	0.35	0.26	0.45	0.38
BR( $T^{(1)}$ $\rightarrow$ W <sup>+</sup> b)		0.46	0.46	0.09	0.01	0.10	0.40	0.50	0.10	0.10
BR( $T^{(1)}$ $\rightarrow$ t Z)		0.23	0.21	0.26	0.29	0.28	0.16	0.13	0.32	0.28
BR( $T^{(1)}$ $\rightarrow$ W <sup>+</sup> W <sup>-</sup> t)		0	0.05	0.07	0.38	0.26	0.09	0.10	0.13	0.24

Table 46: Sample points for MCHM<sub>5</sub> with M<sub>1</sub> M<sub>4</sub> same sign and opposite sign and for MCHM<sub>14</sub> with M<sub>1</sub> and M<sub>4</sub> both  $< 0$  and  $\mu(t\bar{t}h) > 1$ .

In order to get a sense for the relative importance of the different physical subprocesses, we simulate the NR-t $\bar{t}$ hh cross section turning off, in turn, the double Higgs Yukawa coupling and the trilinear coupling. We find that the effects of the double Higgs Yukawa coupling are typically at the couple to few percent level in MCHM<sub>5</sub> and MCHM<sub>14</sub> if  $\mu(t\bar{t}h) < 1$ , and at most 2% in MCHM<sub>14</sub> if  $\mu(t\bar{t}h) > 1$ , with a mild dependence on the c.m. energy (at 14 and 27 TeV) in all cases. We also find that the effect of the trilinear Higgs self-interaction can be around 15% in MCHM<sub>5</sub> and MCHM<sub>14</sub> if  $\mu(t\bar{t}h) < 1$ , and 10% in MCHM<sub>14</sub> if  $\mu(t\bar{t}h) > 1$  at a c.m. energy of 14 TeV, decreasing to a few percent at higher c.m. energies in all cases. For comparison, the effect of the trilinear Higgs self-interaction in the SM t $\bar{t}$ hh cross-section is about 20%, with a very mild c.m. energy dependence. Thus, the NR-t $\bar{t}$ hh (like the SM t $\bar{t}$ hh cross-section) is largely determined by the top Yukawa interaction, and the two are, to a first approximation, related by a scaling factor ( $y_t/y_t^{\text{SM}}$ )<sup>4</sup>. This explains the result seen in Fig. 96, with the suppression arising from the suppression of the top Yukawa coupling in the MCHM<sub>5</sub>.

The previous observation also leads to a strong correlation between the t $\bar{t}$ h and the NR-t $\bar{t}$ hh processes, as shown in Fig. 97. Due to the different scaling with the top Yukawa coupling, the deviations from the SM in the NR-t $\bar{t}$ hh process are larger than those in t $\bar{t}$ h.

#### 9.1.3.5 Set of Example Points

We show in Table 46 a number of points selected as examples that illustrate, in more detail, the properties of the MCHM<sub>5</sub> and MCHM<sub>14</sub>. These properties are reflected in Figs. 97, 98 and 99, where these points are indicated. The MCHM<sub>5</sub> points are labelled as P<sub>i</sub>, i=1 to 5, and MCHM<sub>14</sub> points as P' <sub>j</sub>, with j=1 to 4.

The points for the MCHM<sub>5</sub> exhibit a suppression in  $\mu(t\bar{t}h) \equiv \sigma(t\bar{t}h)/SM$  that ranges from about 15% (roughly at the current 95% C.L. limit [26,27]) to a few percent, a sensitivity that might be achievable by the end of the HL phase of the LHC run (Fig. 98,a). The smaller deviations from the SM are associated with larger values of f (Fig 98,a). The Table 19 and Fig 99 show that the t $\bar{t}$ hh process can exhibit an

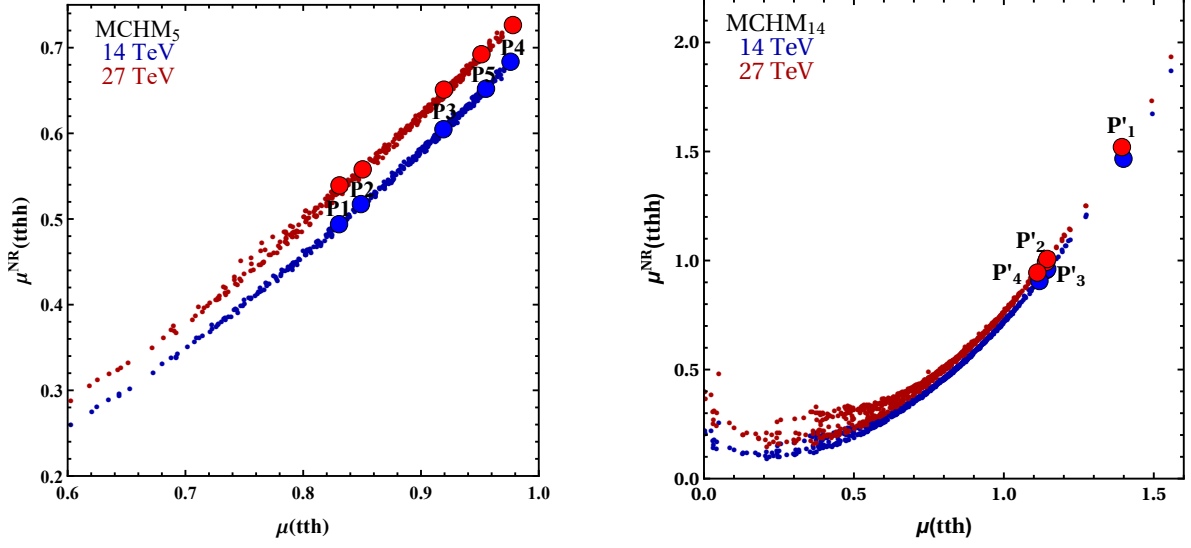


Fig. 97: Correlation between the normalized  $t\bar{t}h$  and non-resonant  $t\bar{t}hh$  cross-sections, for 14 and 27 TeV c.m. energies. The left (right) plots correspond to the MCHM<sub>5</sub> (MCHM<sub>14</sub>)

enhancement if the fermion resonances are light enough. As expected, this enhancement increases with increasing c.m. energy. For the points 2, 4 and 5 in the MCHM<sub>5</sub>, the resonant production is not enough to produce an enhancement in  $t\bar{t}hh$  compared to the SM, although these points correspond to two different cases; the resonances for Point 2 are slightly beyond the current direct limit whereas, on the contrary, much beyond that limit for points 4 and 5. In this case, the  $t\bar{t}hh$  process is easily dominated by the NR-tth process, as defined above. For completeness, Table 46 includes the spectrum of resonances, and the BRs for the lightest  $Q = 2/3$  one. It decays mostly into the standard  $th$ ,  $Wb$  and  $tZ$  channels (with BRs that are model dependent), but in some cases it has a non-negligible non-standard BRs, such as into the  $W^+W^-t$  channel.

The set of example points for MCHM<sub>14</sub> in Table 46 exhibits an enhancement of the top Yukawa coupling, due to the effect described in section 9.1.2 and reflected in Fig 98,b. These enhancements can easily be of the order of 10-20%. Interestingly, Point 1 shows that the enhancement can be as large as 40% (while being consistent with a sufficiently small deviation in the  $ggh$  vertex [?]). The four points display as well, an enhancement in the  $t\bar{t}h$  process. While about half of the rate is due to resonant production in Points 1 and 2, for points 3 and 4 the enhancement arises dominantly from the non-resonant process, reflecting the enhancement in the top Yukawa coupling. In Table 46 are displayed, the spectrum of the 5 resonances in the MCHM<sub>5</sub> and of the 3 lightest 2/3 resonances, the lightest B resonance and the lightest 5/3 resonance out of the total of 14 resonances of the MCHM<sub>14</sub>. All the selected points for MCHM<sub>14</sub> lie in the  $M_1 < 0$ ,  $M_4 < 0$  quadrant of the right panel of Fig. 95. The properties of the other quadrants are qualitatively rather similar to those of the MCHM<sub>5</sub> (see [?]).

#### 9.1.4 Experimental perspectives

A deviation from the SM in the  $t\bar{t}h$  production is an essential measurement for MCHM. An increase will reject the MCHM<sub>5</sub> scenario and greatly refine the areas of the parameter space where MCHM<sub>14</sub> would be valid. A deficit instead, would make MCHM<sub>5</sub> and MCHM<sub>14</sub> both possible. The measurement of this observable is expected to be achieved with 5% accuracy at the HL-LHC and thus with very high accuracy at HE-LHC. The  $t\bar{t}hh$  production process plays a major role in MCHM searches. Deviations from the SM expectation (deficit or increase) can be significant in both MCHM scenarios. The  $t\bar{t}hh$  production cross-section is around 1 fb at tree level whereas  $t\bar{t}h$  is about 500 times larger. Therefore the aim at HL-LHC will be to evidence this process and discover if a strong deviation from SM. For exploring MCHM,

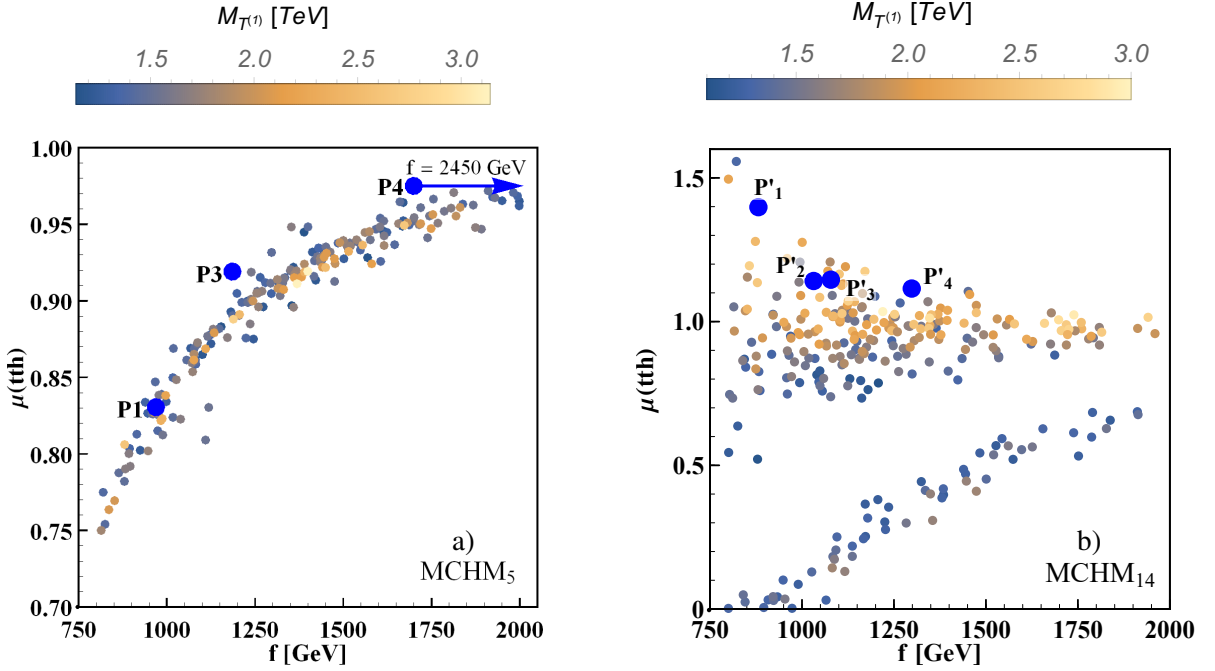


Fig. 98: The normalized  $t\bar{t}h$  cross-section as a function of  $f$ , for 14 and 27 TeV c.m. energies, with color coded the lightest vector-like mass. The left (right) plots correspond to Q2 of MCHM<sub>5</sub> (Q3 of MCHM<sub>14</sub>). The blue arrow indicates that the point P4 is outside the horizontal range of the plot with  $f=2450$  GeV.

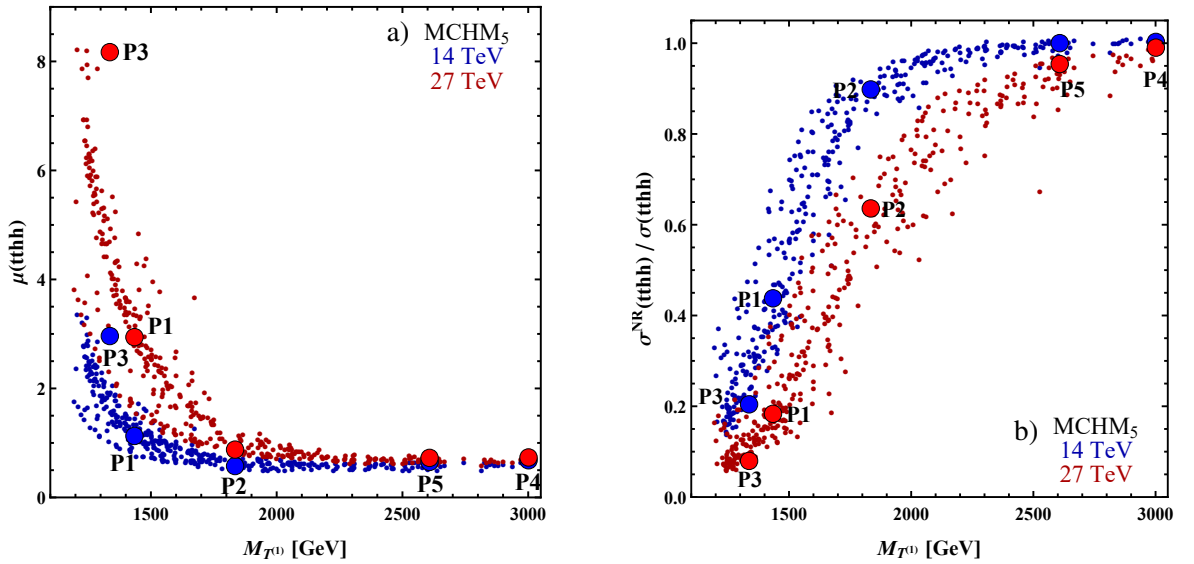


Fig. 99: The left plot shows the normalized  $t\bar{t}h$  cross-section as a function of the lightest  $Q = 2/3$  vector-like mass,  $T^{(1)}$  for 14 and 27 TeV c.m. energies for MCHM<sub>5</sub>. The right plot shows the ratio between the non-resonant  $t\bar{t}h$  cross section and the total  $t\bar{t}h$  cross section as a function of  $T^{(1)}$  for 14 and 27 TeV c.m. energies for MCHM<sub>5</sub>.

higher energy together with higher luminosity (HE-LHC) is really a plus if even not a need.

## 9.2 Exotic decays of the Higgs boson

### 9.2.1 First Level Track Jet Trigger for Displaced Jets at High Luminosity LHC

The high luminosity LHC program offers many exciting opportunities to search for rare processes. It is expected that the LHC will accumulate  $3 \text{ ab}^{-1}$  of proton-proton ( $p\ p$ ) collisions at 14 TeV. The CMS detector will undergo major upgrades to all subsystems, including the tracker [?], the barrel [?] and endcap [?] calorimeters, the muon system [?], and the trigger [?].

The bandwidth limitations of the first level (L1) trigger are one of the main problems facing current searches for exotic Higgs boson decays, as well as many other signals beyond the standard model (BSM). The process where the Higgs boson decays to two new light scalars that in turn decay to jets,  $H \rightarrow \phi\phi$ , is an important example. If the scalar  $\phi$  has a macroscopic decay length, the offline analysis has no background from SM processes, but the majority of the signal events do not get recorded because they fail to be selected by the L1 trigger. The main obstacle is the high rate for low transverse momentum jets, which is made worse by additional extraneous  $p\ p$  collisions in the high luminosity environment.

In this note, we investigate the capabilities of L1 track finding [?] to increase the L1 trigger efficiency for such signals. We focus on small or moderate decay lengths of the new particles, 1–50 mm, and assume, as is demonstrated by many analyses [?, ?, ?], that the offline selection can remove all SM backgrounds with only a moderate loss of efficiency.

The investigation has two major thrusts. First, we propose a jet clustering algorithm that uses the L1 tracks found with a primary vertex constraint. Second, we consider the extension of the L1 track finder to off-pointing tracks, and develop a jet lifetime tag for tracks with  $|\eta| < 1.0$ . Future work will include: expanding the off-pointing track finding at L1 to the full acceptance of the outer tracker; matching the track jets with high transverse energy ( $E_T$ ) deposits in the electromagnetic calorimeter; and finding new ways to evaluate track quality to suppress “fake” tracks that result from finding the wrong combination of track hits.

While in this study we focus on the specific Higgs boson decay to light scalars (see Ref. [?] for extensive review of physics motivations for such decays), the results and the proposed triggers are relevant for a broad spectrum of new physics searches, with or without macroscopic decay lengths.

#### 9.2.1.1 Signal and background simulation

In these studies, the Phase-2 CMS detector is simulated using GEANT 4 [?]. Event samples corresponding to 200 collisions per bunch crossing (pileup) [?] are used for the evaluation of trigger rates.

The following signal samples are considered:

1. Displaced single muons, generated with a uniform distribution of transverse momentum ( $p_T$ ) between 2 and 8 GeV, uniform in  $\eta$  between -1 and 1, and with impact parameter  $d_0$  distributed as a Gaussian with width  $\sigma = 2 \text{ cm}$ .
2. The decay of the SM Higgs boson  $H(125) \rightarrow \phi\phi \rightarrow b\bar{b}b\bar{b}$ , with  $\phi$  masses of 15, 30, and 60 GeV, and  $c\tau$  of 0, 1, and 5 cm. The production of the Higgs boson via gluon fusion is simulated by POHWEGV2.0 [?], while the hadronization and decay is performed by PYTHIAv8.205 [?].
3. The decay of a heavy SM-like Higgs boson with mass 250 GeV,  $H(250) \rightarrow \phi\phi \rightarrow b\bar{b}b\bar{b}$ , with  $\phi$  masses of 15, 30, and 60 GeV, and  $c\tau$  of 0, 1, and 5 cm. The production of the heavy SM-like Higgs boson via gluon fusion, its decay, and its hadronization are all simulated with PYTHIA8 [?].

#### 9.2.1.2 Track jets

The tracker is the most granular detector participating in the L1 decision, and therefore the most resilient to pileup. Track finding at L1 relies on selection at the front end of tracker hits that originated from high transverse momentum particles. This is achieved through use of the so-called  $p_T$ -modules consisting of

two sensors separated by a few mm [?]. A particle crossing a tracker module produces a pair of hits in the two sensors. Such pairs form a “stub” if the azimuthal difference between the hits in the two sensors of a module is consistent with a prompt track with  $p_T \gtrsim 2$  GeV.

In this section, we describe a simple jet clustering algorithm implementable in firmware, and compare it with anti- $k_t$  jets [?] with a size parameter of  $R = 0.3$ , as produced by FASTJET [?].

A simplified algorithm for L1 track jets is used to facilitate the firmware implementation for the L1 trigger applications. L1 track jets are found by grouping tracks in bins of  $z_o$ , the point of closest approach to the  $z$ -axis, for the tracks. The bins are overlapping, staggered by half a bin, so that each track ends up in two bins, eliminating inefficiencies at bin edges. In each  $z_o$  bin, the  $p_T$  of the tracks are summed in bins of  $\eta$  and azimuthal angle  $\phi$  with bin size  $0.2 \times 0.23$ . A simplified nearest-neighbor clustering is performed, and the total  $H_T = \sum p_T^{\text{trk}}$  in the  $z_o$  bin is calculated. The  $z_o$  bin with the highest  $H_T$  is chosen. Jets obtained through this algorithm are referred to as “TwoLayer Jets.” For the studies below,  $z_o$  bins with size 6 cm are used. Jets with  $E_T > 50$  (100) GeV are required to have at least two (three) tracks.

The track purity depends on the number of stubs in the track and the  $\chi^2$  of the track fit. High- $p_T$  tracks are much less pure than low- $p_T$  tracks, with fake tracks distributed approximately uniformly in  $1/p_T$  while real tracks are mostly low- $p_T$ . To mitigate the effect of high- $p_T$  fake tracks, any track with a reconstructed  $p_T$  above 200 GeV is assigned a  $p_T$  of 200 GeV. The track quality selection used in this analysis is summarized in Table 47.

Table 47: Track selection for jet finding. The  $\chi^2$  selections are per degree of freedom for a 4-parameter track fit.

track $p_T$	4 stubs	5 stubs	6 stubs
2–10 GeV	$\chi^2 < 15$	$\chi^2 < 15$	accept
10–50 GeV	reject	$\chi^2 < 10$	accept
>50 GeV	reject	$\chi^2 < 5$	$\chi^2 < 5$

We have verified that the TwoLayer trigger algorithm gives similar performance to a full jet clustering using the anti- $k_t$  algorithm with a size parameter  $R = 0.3$ , as implemented in FASTJET. Figure 100 shows the efficiency to reconstruct a track jet as function of the generator-level jet  $p_T$ . Figure 101 shows the calculated L1 trigger rates for an  $H_T$  trigger (scalar sum of  $p_T$  of all jets above threshold) and a quad-jet trigger (at least four jets above threshold) as a function of the threshold.  $H_T$  is computed from track jets with  $p_T > 5$  GeV.

The rates are computed based on a fixed number of colliding bunches. The trigger rate is computed as

$$\text{Rate} = \epsilon_{\text{LT}} N_{\text{bunches}} f_{\text{LHC}},$$

where  $N_{\text{bunches}} = 2750$  bunches for 25 nsbunch spacing operation,  $f_{\text{LHC}} = 11246$  Hz, and  $\epsilon_{\text{LT}}$  is the efficiency to pass a given L1 threshold as determined in simulation. For both the L1 trigger efficiency and rate, the performance of the TwoLayer hardware algorithm is compatible with the performance from the more sophisticated algorithm from FASTJET.

### 9.2.1.3 Displaced track finding

In this section, we briefly describe the performance of an algorithm for reconstruction of tracks with non-zero impact parameter. This approach extends the baseline L1 Track Trigger design to handle tracks with non-zero impact parameter and to include the impact parameter in the track fit. This enhanced design is feasible without greatly altering the track finding approach, but will require more FPGA computational power than the current proposal, which only considers only prompt tracks. Tracks passing the selection

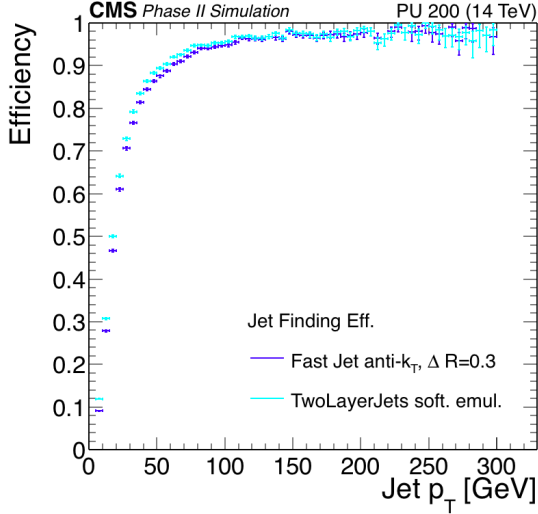


Fig. 100: The efficiency for a jet to give rise to a L1 track jet as a function of the generator-level  $p_T$  of the jet. The light and dark blue lines correspond to the trigger clustering (TwoLayer Jets) and anti- $k_t$  with  $R = 0.3$  (FASTJET), respectively.

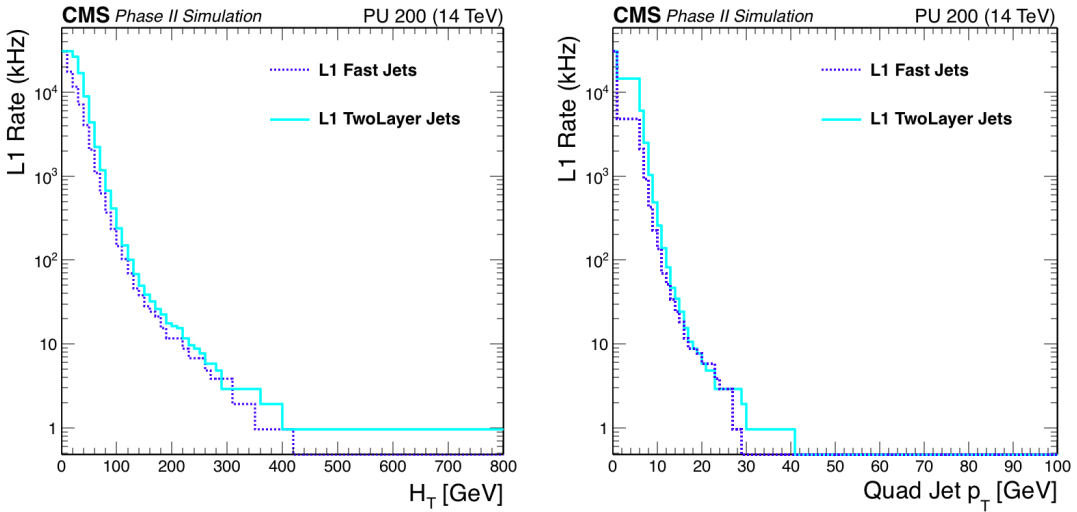


Fig. 101: Calculated L1 trigger rates for track jet based  $H_T$  (left) and quad-jet (right) triggers. The light and dark blue lines correspond to the trigger clustering (TwoLayer Jets) and anti- $k_t$  with  $R = 0.3$  (FASTJET), respectively.

are clustered using the same algorithm as described in Section 9.2.1.2, and clusters containing tracks with high impact parameters are flagged as displaced jets. Though the baseline design of the L1 Track Trigger currently is optimized to find prompt tracks, these studies show that an enhanced L1 Track Trigger can extend the L1 trigger acceptance to include new BSM physics signals.

A track with a sufficiently small impact parameter can produce a stub. For tracks with large  $p_T$  (i.e. large curvature radius  $\rho$ ) and small  $d_0$ , the bending angle  $\beta$  between the track and the prompt infinite momentum track, as shown in Fig. 102, is

$$\beta \approx \frac{r}{2\rho} - \frac{d_0}{r}.$$

Therefore, for a given  $d_0$ , one expects the stubs to be formed more efficiently as the radius of

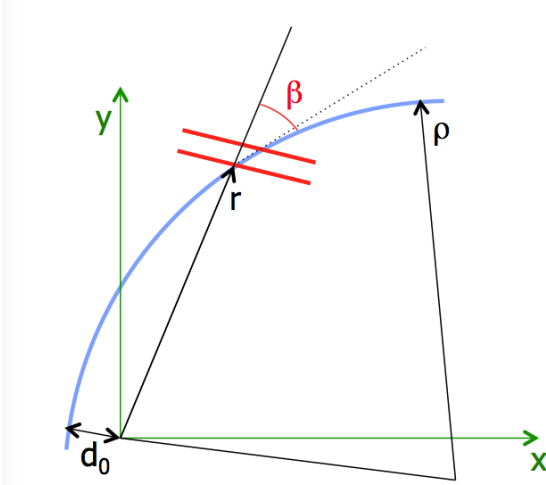


Fig. 102: A sketch of a track crossing a  $p_T$ -module.

the module  $r$  increases. Fig. 103 shows the efficiency for a displaced muon to produce a stub as a function of the signed transverse momentum and the impact parameter of the muon, as measured in the full GEANT 4-based simulation of the Phase-2 detector.

A special version of the tracklet algorithm [?] has been developed that is capable of reconstructing tracks with impact parameters of a few cm. For now, the reconstruction is limited to the barrel region ( $|\eta| < 1.0$ ). Preliminary feasibility studies show that the algorithm will have similar performance in the entire outer tracker coverage.

Fig. 104 shows the track reconstruction efficiency requiring at least four and at least five stubs on the track. As expected, allowing only four stubs on a track gives a higher efficiency for high impact parameter tracks.

For the extended track finding algorithm, two track fits are performed: a 3-parameter  $r\phi$  fit yielding  $1/\rho$ ,  $\phi_0$ , and  $d_0$ , and a 2-parameter  $rz$  fit yielding  $t$  and  $z_o$ . The bend consistency variable is defined as

$$\text{consistency} = \frac{1}{N_{\text{stubs}}} \sum_{i=1}^{N_{\text{stubs}}} \left( \frac{\beta_i - \beta_i^{\text{exp}}}{\sigma_i} \right)^2,$$

where  $N_{\text{stubs}}$  is the total number of stubs comprising the track,  $\beta_i$  and  $\beta_i^{\text{exp}}$  are the measured and expected bend angles for stub  $i$ , and  $\sigma_i$  is the expected bend angle resolution.

Two track categories are defined, loose and tight. The selection is summarized in Table 48.

Table 48: Track selection criteria for jet finding with extended L1 track finding.

$N_{\text{stubs}}$	Loose			Tight		
	$\chi^2_{r\phi}$	$\chi^2_{rz}$	consistency	$\chi^2_{r\phi}$	$\chi^2_{rz}$	consistency
4	<0.5	<0.5	<1.25			reject
$\geq 5$	<5.0	<2.5	<5.0	<3.5	<2.0	<4.0

A jet is required to have at least two tracks passing the tight selection. If two or more tight tracks in a jet have  $|d_0| > 0.1$  cm, the jet is tagged as a displaced jet.

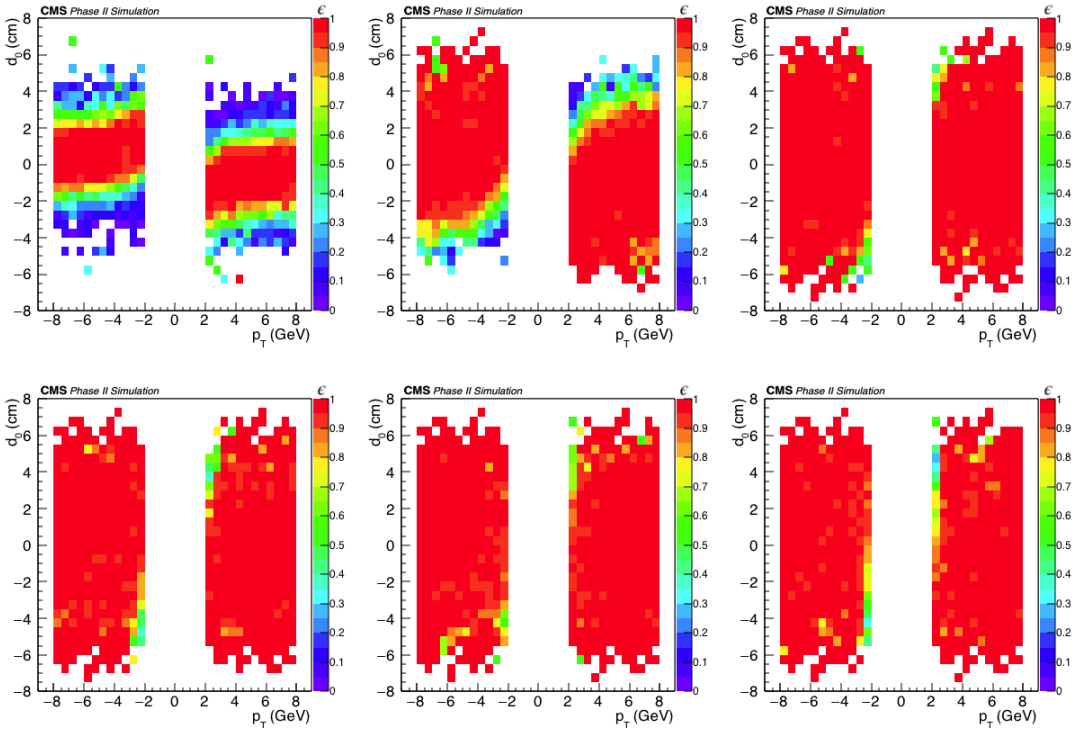


Fig. 103: The efficiency for a displaced muon to form stubs in the six barrel layers of the Phase-2 tracker, as a function of the signed muon  $p_T$  and impact parameter. The top row shows, from left to right, layers 1, 2, and 3; the bottom row shows layers 4, 5, and 6. The sample is comprised of 2000 muons generated with uniformly distributed transverse momentum between 2 and 8 GeV and pseudorapidity  $|\eta| < 1$ , and with the impact parameter  $d_0$  distributed as a Gaussian with width of 2 cm.

#### 9.2.1.4 Results

Figure 105 shows the rate of the track jet  $H_T$  trigger as a function of the efficiency of the heavy SM-like Higgs boson signal. While for prompt  $\phi$  decays one can realistically achieve 20% efficiency at an L1 rate of 25 kHz, the efficiency quickly drops with the decay length, since the displaced tracks are not reconstructed for  $d_0$  values above a few mm.

The rate for the  $H_T$  trigger using the extended track finding is shown in Fig. 106, with and without a requirement of at least one jet with a displaced tag. The displaced tag requirement suppresses the rate by more than an order of magnitude. The displaced tracking and the trigger that requires a jet with a displaced tag make the signals with low  $H_T$  accessible for displaced jets.

In order to compare the results with prompt and extended track reconstruction, one needs to make a correction for the rapidity coverage: prompt tracks are found in  $|\eta| < 2.4$ , while the extended track algorithm currently only reconstructs tracks in  $|\eta| < 1.0$ . For the feasible thresholds, the rate for  $|\eta| < 0.8$  and  $|\eta| < 2.4$  differ by a factor of five. To scale the efficiency for finding track jets to the full  $|\eta| < 2.4$  range, we derive a scale factor (SF) based on efficiency in the full  $\eta$  range and the central  $\eta$  range. The signal efficiency SFs range from 4–6, which is comparable to the increase in the L1 rate. We have confirmed that such extrapolation works for the track jets clustered with prompt tracks. Figure 107 shows the expected trigger rate as a function of efficiency for the SM and the heavy SM-like Higgs bosons.

The available bandwidth for the triggers described above, if implemented, will be decided as a part of the full trigger menu optimization. Here, we consider two cases, 5 and 25 kHz. The expected event yield for triggers using extended and prompt tracking are shown in Fig. 108, assuming branching

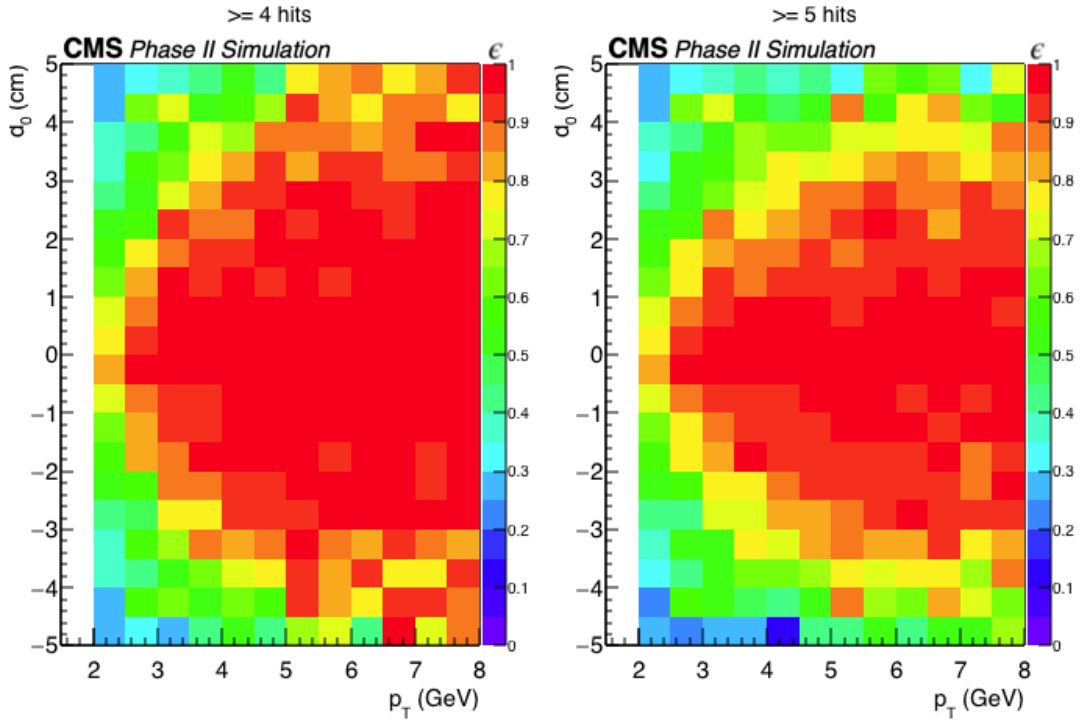


Fig. 104: The efficiency for a displaced muon to be reconstructed as a track with at least four stubs (left) and at least five stubs (right).

fraction  $\mathcal{B}[H \rightarrow \phi\phi] = 10^{-5}$  for the SM Higgs boson. For the heavy Higgs boson, the expected number of produced signal events is set to be the same as for the SM Higgs by requiring  $\sigma_{pp \rightarrow H(250)} \mathcal{B}[\Phi \rightarrow \phi\phi] = 10^{-5} \sigma_{pp \rightarrow H(125)}$ .

#### 9.2.1.5 Conclusion

We have studied the upgraded CMS detector's ability to trigger on events with long lived particles decaying into jets. Currently, such events pass the L1 trigger only if the total transverse energy in the event is above a few hundred GeV. This is an important blind spot for searches, especially for the rare exotic Higgs boson decays like  $H \rightarrow \phi\phi$ .

In this note, a new L1 trigger strategy based on the Phase-2 CMS detector's ability to find tracks at L1 is explored. Using L1 tracks for jet reconstruction significantly suppresses pile-up and allows to accept events with lower  $H_T$ . For the exotic Higgs decays considered, given the total Phase-2 dataset of  $3 \text{ ab}^{-1}$  and branching fraction of  $10^{-5}$ , CMS would collect  $\mathcal{O}(10)$  events, which should be sufficient for discovery. We also considered a plausible extension of the L1 track finder to consider tracks with impact parameters of a few cm. That approach improves the yield by more than an order of magnitude. The gains for the extended L1 track finding are even larger for the events with larger  $H_T$ , as demonstrated by the simulations of heavy Higgs boson decays.

#### 9.2.2 Exotic decays of the Higgs to $2b2\mu$

David Curtin<sup>1</sup>, Rouven Essig<sup>2</sup>, and Yi-Ming Zhong<sup>3</sup>

<sup>1</sup>*Department of Physics, University of Toronto, Toronto, ON M5S 1A7, Canada*

<sup>2</sup>*C.N. Yang Institute for Theoretical Physics, Stony Brook University, Stony Brook, NY 11794, USA*

<sup>3</sup>*Physics Department, Boston University, Boston, MA 02215, USA*

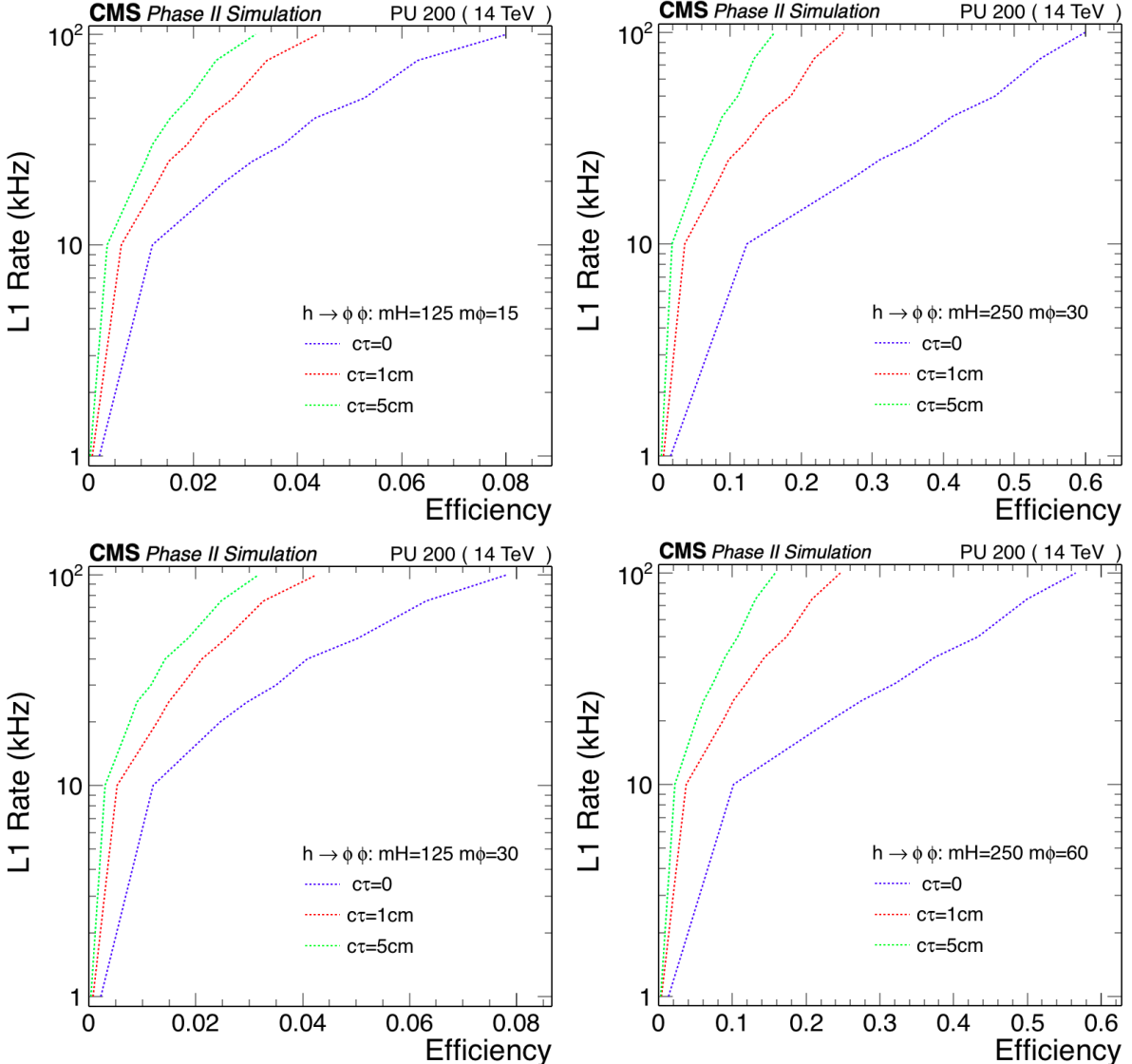


Fig. 105: The rate of the track jet  $H_T$  trigger as a function of signal efficiency for the SM Higgs boson (left) and the heavy SM-like Higgs boson (right) using prompt track finding.

Here we assess the potential of an exotic Higgs decay search for  $h \rightarrow 2X \rightarrow b\bar{b}\mu^+\mu^-$  to constrain theories with light CP-even ( $X = s$ ) and CP-odd ( $X = a$ ) singlet scalars. This decay channel may represent the best discovery avenue for many models, such as the 2HDM model with an additional complex scalar singlet (2HDM+S). It has competitive reach, and is less reliant on low- $p_T$   $b$ - and  $\tau$ -reconstruction compared to other channels like  $4b$ ,  $4\tau$ , and  $2\tau 2\mu$ .

To estimate the reach of  $h \rightarrow 2X \rightarrow b\bar{b}\mu^+\mu^-$  search at the 14 TeV LHC, we take  $X = a$  for simplicity. (Results for  $X = s$  should be similar.) The dominant backgrounds are Drell-Yan (DY) production with associated jets, i.e.,  $Z/\gamma^* + 2b/2c/2j$ , where  $Z/\gamma^*$  produces a muon pair. A secondary background arises from  $t\bar{t}$  production. Backgrounds from diboson production ( $ZZ, WW, WZ$ ) have small enough cross sections so that we can neglect them. It is also possible for QCD multi-jet events, with two jets being mis-identified as muons, to contribute to the background. We find this can be neglected for analysis with  $b$ -tags. Signal, as well as DY and  $t\bar{t}$  backgrounds, are simulated at LO by Sherpa 2.1.1 [?] for  $\sqrt{s} = 14$  TeV with the CT10 PDF, and matched up to three jets. The Higgs production cross section for the signal is normalized to the NLO gluon-fusion cross section  $\sigma_{ggF} \simeq 49.47 \text{ pb}^{-1}$  [?].

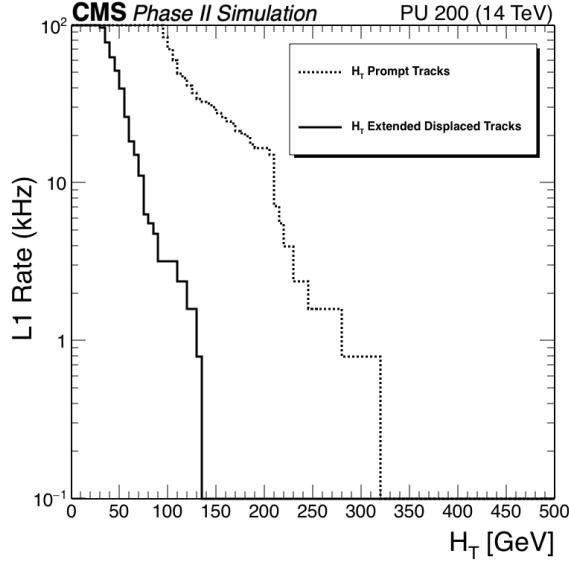


Fig. 106: The rate of the track jet  $H_T$  trigger using extended track finding with (solid line) and without (dashed line) a requirement of at least one jet with a displaced tag.

Two types of analyses have been included. A conventional analysis use standard anti- $k_t$  jets with a jet radius of  $R \sim 0.4$ . Two  $b$ -tags at 70%  $b$ -tagging efficiency working point [?] are imposed to the final states. A missing transverse energy cut of  $\cancel{E}_T < 30$  GeV suppresses  $t\bar{t}$  background. In addition we make use of the double-resonance structure of the signal by imposing invariant mass cuts

$$|m_{b_1 b_2 \mu_1 \mu_2} - m_h| < 15 \text{ GeV}, \quad |m_{b_1 b_2} - m_a| < 15 \text{ GeV}, \quad |m_{\mu_1 \mu_2} - m_a| < 1 \text{ GeV}, \quad (153)$$

separately for each  $m_a$ . After passing above cuts, we then perform a simple counting experiments to estimate the reach. The expected bounds are approximately independent of scalar mass for  $m_a \geq 30$  GeV. For  $m_a < 20$  GeV, the signal efficiency drops dramatically because the two  $b$ 's from the  $a$ -decay become collimated. Instead we adopt the mass drop tagger (MDT) [?], a jet substructure technique, to improve the search sensitivity for the low  $-m_a$  region. After clustering a  $b$ -tagged C/A jet with a jet radius of  $R = 0.8$ , we resolve its hardest subjets that satisfy the MDT criteria ( $\mu < 0.67$ ,  $y > 0.09$ ) by undoing the last step of the C/A clustering. We then apply the same missing energy and invariant mass cuts to the subjets as the conventional analysis.

The results of the combined substructure and conventional analysis are shown in Fig. 109. It shows a fairly flat sensitivity of  $\text{Br}(h \rightarrow 2a \rightarrow 2b2\mu) \lesssim \text{few} \times 10^{-4}$  for 14 TeV LHC with  $30 \text{ fb}^{-1}$  data in the range  $15 \text{ GeV} \leq m_a \leq 60 \text{ GeV}$ . With either  $300$  or  $3000 \text{ fb}^{-1}$  of data, the projected sensitivity increases to  $10^{-4}$ , and  $\text{few} \times 10^{-5}$ , respectively. For HE-LHC (27 TeV with  $15 \text{ ab}^{-1}$ ), we expected the number of signal and DY background events to be respectively increased by a factor of  $\sim 15$  and  $\sim 12$  in comparison with those of the HL-LHC (14 TeV with  $3 \text{ ab}^{-1}$ ). This yield reach estimates for HE-LHC to be  $\lesssim 10^{-5}$ , i.e., a factor of  $15/\sqrt{12} \approx 4$  better than those of the HL-LHC. In the same plot, we also show the 95% CL bounds from 13 TeV ATLAS analysis with  $36.1 \text{ fb}^{-1}$  data [?] as the black shaded region (assuming the Higgs production cross section to be the same as the SM prediction). For a range of  $m_a$  values, the ATLAS bounds are better than our projections by a factor of a few. This may due to more dedicated analysis techniques such as kinematic-likelihood fit [?], which improves the invariant mass resolutions. Based on above comparison, we expect the real HL-LHC and HE-LHC reach should be better than our conservative projections.

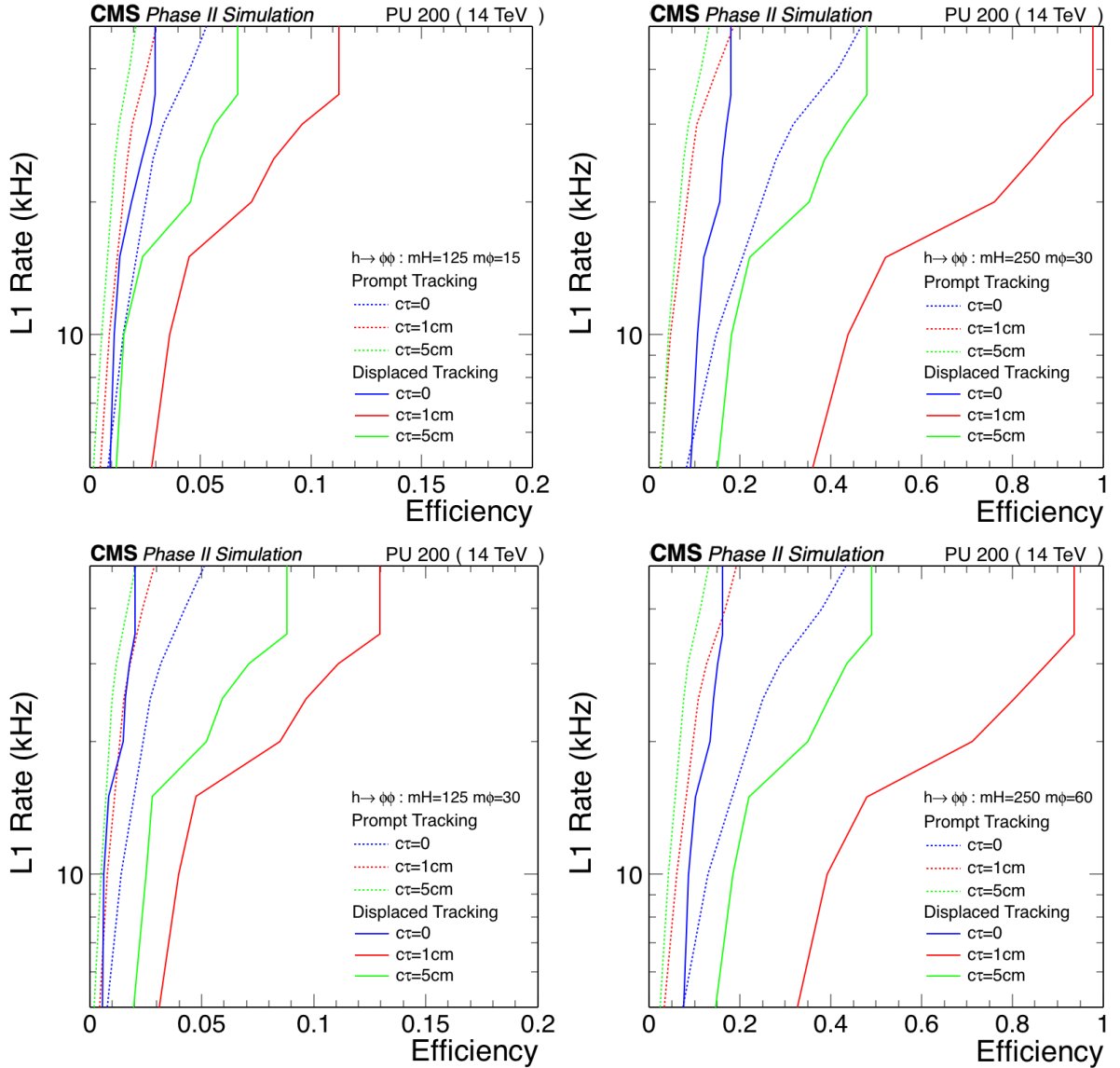


Fig. 107: The rate of the track jet  $H_T$  trigger as a function of signal efficiency using extended track finding for the SM Higgs (left) and the heavy SM-like Higgs (right). The extended track finding performance is extrapolated to the full outer tracker acceptance as described in text.

### 9.2.3 Exotic Higgs decays to ALPs: $h \rightarrow Za$ and $h \rightarrow aa$

Martin Bauer<sup>1</sup>, Matthias Neubert<sup>2,3</sup>, and Andrea Thamm<sup>4</sup>

<sup>1</sup>*Institut für Theoretische Physik, Universität Heidelberg Philosophenweg 16, 69120 Heidelberg, Germany*

<sup>2</sup>*PRISMA Cluster of Excellence & Mainz Institute for Theoretical Physics*

*Johannes Gutenberg University, 55099 Mainz, Germany*

<sup>3</sup>*Department of Physics & LEPP, Cornell University, Ithaca, NY 14853, USA*

<sup>4</sup>*CERN, Theoretical Physics Department, 1211 Geneva, Switzerland*

Here we discuss the exotic Higgs decays  $h \rightarrow aa$  and  $h \rightarrow Za$ , where  $a$  is a light pseudoscalar particle often called an axion-like particle (ALP). Its interactions with Standard Model (SM) particles are described by dimension-5 operators or higher when assuming that the ALP respects a shift symmetry

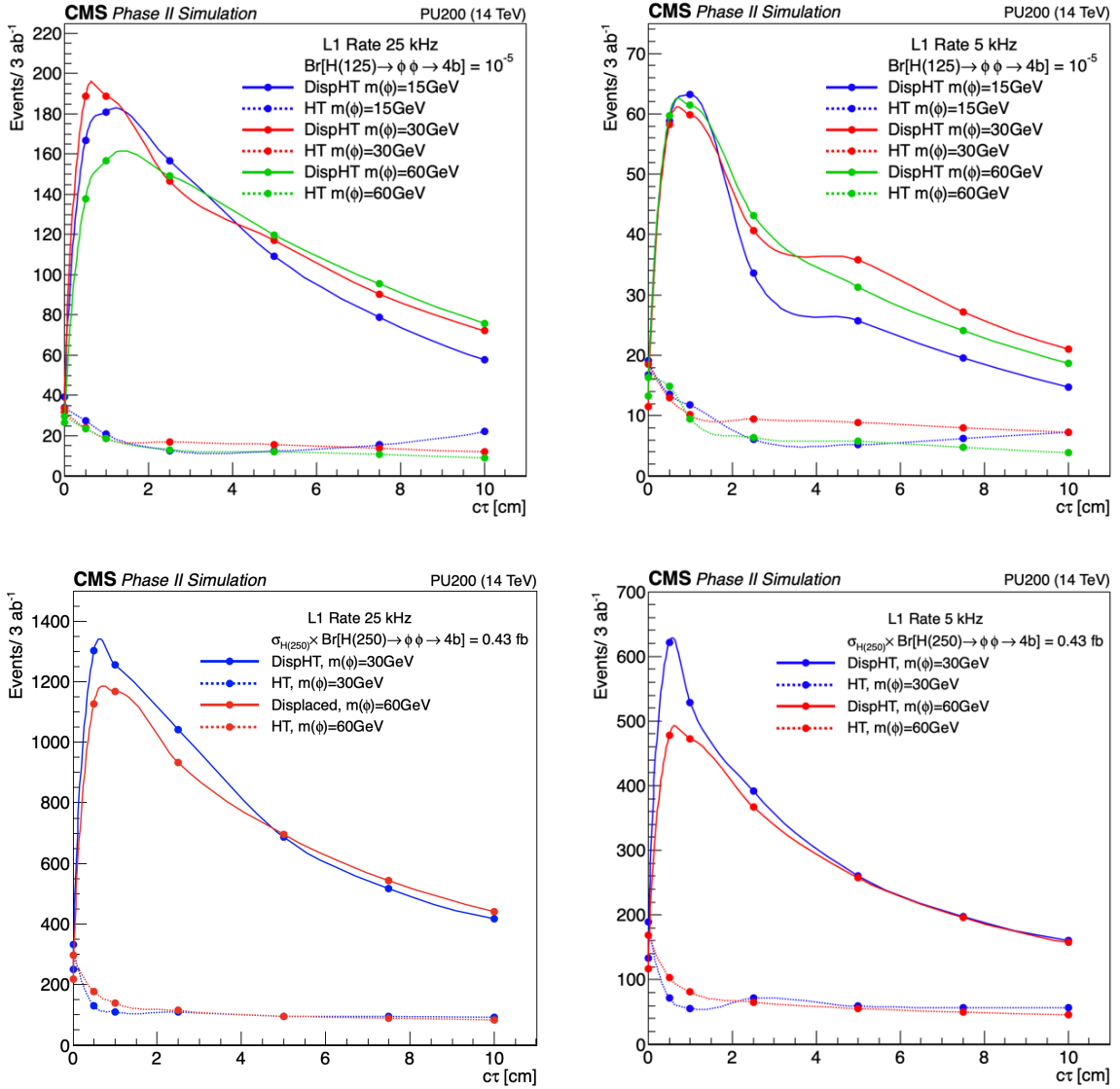


Fig. 108: This plot shows the number of triggered Higgs events (assuming  $\mathcal{B}[\text{H} \rightarrow \phi\phi] = 10^{-5}$ , corresponding to 1700 events) as a function of  $c\tau$  for two choices for the trigger rates: 25 kHz(left), 5 kHz(right). Two triggers are compared: one based on prompt track finding (dotted lines) and another that is based on extended track finding with a displaced jet tag (solid lines).

apart from a soft breaking through an explicit mass term [?]

$$\begin{aligned} \mathcal{L}_{\text{eff}}^{D \leq 5} = & \frac{1}{2} (\partial_\mu a)(\partial^\mu a) - \frac{m_{a,0}^2}{2} a^2 + \sum_f \frac{c_{ff}}{2} \frac{\partial^\mu a}{\Lambda} \bar{f} \gamma_\mu \gamma_5 f + g_s^2 C_{GG} \frac{a}{\Lambda} G_{\mu\nu}^A \tilde{G}^{\mu\nu,A} \\ & + e^2 C_{\gamma\gamma} \frac{a}{\Lambda} F_{\mu\nu} \tilde{F}^{\mu\nu} + \frac{2e^2}{s_w c_w} C_{\gamma Z} \frac{a}{\Lambda} F_{\mu\nu} \tilde{Z}^{\mu\nu} + \frac{e^2}{s_w^2 c_w^2} C_{ZZ} \frac{a}{\Lambda} Z_{\mu\nu} \tilde{Z}^{\mu\nu}, \end{aligned} \quad (154)$$

where  $m_{a,0}$  is the explicit symmetry breaking mass term,  $s_w$  and  $c_w$  are the sine and cosine of the weak mixing angle, respectively, and  $\Lambda$  sets the new physics scale and is related to the ALP decay constant by  $\Lambda/|C_{GG}| = 32\pi^2 f_a$ . Note that an exotic  $Z$ -decay  $Z \rightarrow \gamma a$  proceeds through the  $C_{\gamma Z}$  operator.

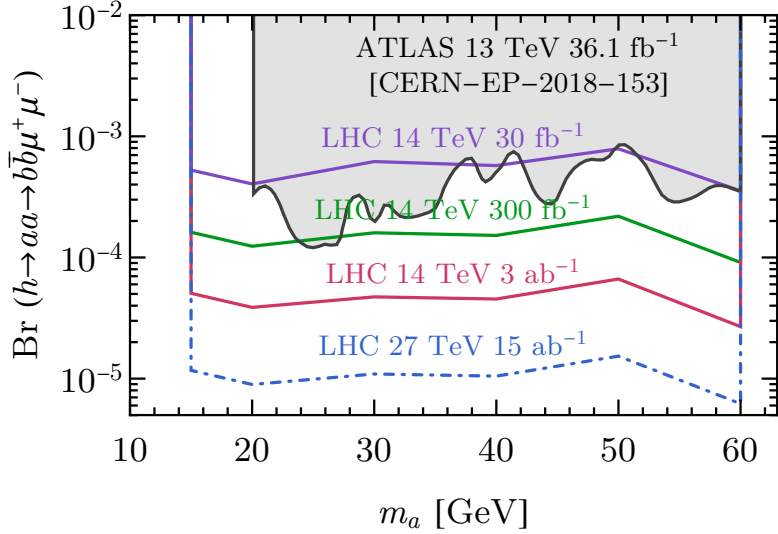


Fig. 109: Combined 95% CL projected reaches on  $\text{Br}(h \rightarrow aa \rightarrow b\bar{b}\mu^+\mu^-)$  for 30 (purple), 300 (green), and 3000 (red)  $\text{fb}^{-1}$  at 14 TeV [?] and  $15 \text{ ab}^{-1}$  at 27 TeV (dash-dotted blue). The 95% CL upper limits from 13 TeV ATLAS with  $36.1 \text{ fb}^{-1}$  data [?] is shown as the black shaded region.

Interactions with the Higgs boson,  $\phi$ , are described by the dimension-6 and 7 operators

$$\mathcal{L}_{\text{eff}}^{D \geq 6} = \frac{C_{ah}}{\Lambda^2} (\partial_\mu a)(\partial^\mu a) \phi^\dagger \phi + \frac{C_{Zh}}{\Lambda^3} (\partial^\mu a) \left( \phi^\dagger i D_\mu \phi + \text{h.c.} \right) \phi^\dagger \phi + \dots, \quad (155)$$

where the first operator mediates the decay  $h \rightarrow aa$ , while the second one is responsible for  $h \rightarrow Za$ . Note that a possible dimension-5 operator coupling the ALP to the Higgs current is redundant unless it is introduced by integrating out a heavy new particle which acquires most of its mass through electroweak symmetry breaking [?, ?, ?, ?]. The exotic Higgs decay rates into ALPs are given by

$$\Gamma(h \rightarrow Za) = \frac{m_h^3}{16\pi\Lambda^2} |C_{Zh}^{\text{eff}}|^2 \lambda^{3/2} \left( \frac{m_Z^2}{m_h^2}, \frac{m_a^2}{m_h^2} \right), \quad (156)$$

$$\Gamma(h \rightarrow aa) = \frac{m_h^3 v^2}{32\pi\Lambda^4} |C_{ah}^{\text{eff}}|^2 \left( 1 - \frac{2m_a^2}{m_h^2} \right)^2 \sqrt{1 - \frac{4m_a^2}{m_h^2}}, \quad (157)$$

where  $\lambda(x, y) = (1 - x - y)^2 - 4xy$  and we define  $C_{Zh}^{\text{eff}} = C_{Zh}^{(5)} + C_{Zh}v^2/2\Lambda^2$  to take into account possible contributions from a dimension-5 operator which originates from integrating out chiral heavy new physics. The relevant partial widths for this study are the decay into photons and leptons. For the derivation and one-loop contributions we refer the reader to [?]

$$\Gamma(a \rightarrow \gamma\gamma) = \frac{4\pi\alpha^2 m_a^3}{\Lambda^2} |C_{\gamma\gamma}^{\text{eff}}|^2, \quad (158)$$

$$\Gamma(a \rightarrow \ell^+ \ell^-) = \frac{m_a m_\ell^2}{8\pi\Lambda^2} |c_{\ell\ell}^{\text{eff}}|^2 \sqrt{1 - \frac{4m_\ell^2}{m_a^2}}. \quad (159)$$

Future hadron colliders can significantly surpass the reach of the LHC in searches for ALPs. In particular, searches for ALPs produced in exotic Higgs and  $Z$  decays profit from the higher center-of-mass energies and luminosities of the proposed high-energy LHC (HE-LHC), planned to replace the LHC in the LEP tunnel with  $\sqrt{s} = 27 \text{ TeV}$ , and the ambitious plans for a new generation of hadron

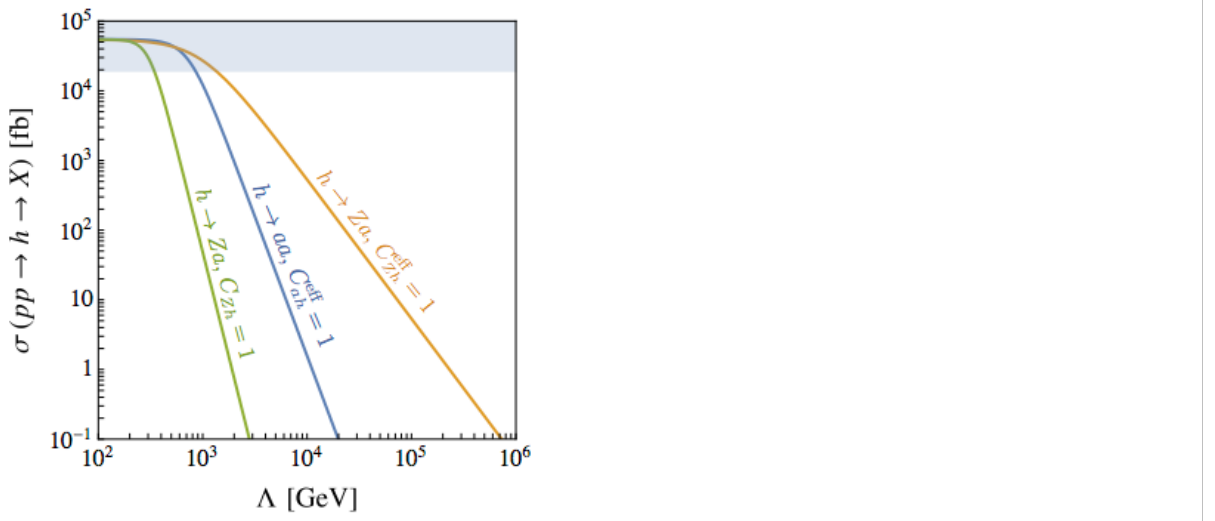


Fig. 110: Production cross sections of ALPs produced in Higgs decays at the LHC ( $\sqrt{s} = 14 \text{ TeV}$ ) versus the new-physics scale  $\Lambda$ . We set  $m_a = 0$  and fix the relevant Wilson coefficients to 1. For the green contour we fix  $C_{Zh}^{(5)} = 0$  and only consider the dimension-7 coupling in (155). The grey region is excluded by Higgs coupling measurements.

colliders with  $\sqrt{s} = 100 \text{ TeV}$  at CERN (FCC-hh) and in China (SPPC). As benchmark scenarios we assume integrated luminosities of  $3 \text{ ab}^{-1}$  at the LHC,  $15 \text{ ab}^{-1}$  at the HE-LHC and  $20 \text{ ab}^{-1}$  at the FCC-hh. At hadron colliders, ALP production in association with electroweak bosons suffers from large backgrounds. Previous studies of these processes have therefore focussed on invisibly decaying (or stable) ALPs, taking advantage of the missing-energy signature [?, ?]. In contrast, here we focus on ALPs produced in the decays of a Higgs boson,  $h \rightarrow Za$  and  $h \rightarrow aa$  (for more details see [?]).

Exotic decays are particularly interesting, because even small couplings can lead to appreciable branching ratios and be as large as several percent [?, ?]. This allows us to probe large new-physics scales  $\Lambda$ , as illustrated in Figure 110, where we show the cross sections of the processes  $pp \rightarrow h \rightarrow Za$  and  $pp \rightarrow h \rightarrow aa$  at the LHC with  $\sqrt{s} = 14 \text{ TeV}$ . The figure nicely reflects the different scalings of the dimension-5, 6, and 7 operators in the effective ALP Lagrangian. The shaded region is excluded by Higgs coupling measurements constraining general beyond the SM decays of the Higgs boson,  $\text{Br}(h \rightarrow \text{BSM}) < 0.34$  [25]. This leads to constraints on the coefficients  $|C_{Zh}^{\text{eff}}| < 0.72 (\Lambda/\text{TeV})$  and  $|C_{ah}^{\text{eff}}| < 1.34 (\Lambda/\text{TeV})^2$ .

Light or weakly coupled ALPs can be long-lived, and thus only a fraction of them decays inside the detector and can be reconstructed. The average ALP decay length perpendicular to the beam axis is given by

$$L_a^\perp(\theta) = \frac{\sqrt{\gamma_a^2 - 1}}{\Gamma_a} \sin \theta, \quad (160)$$

where  $\Gamma_a$  denotes the total width of the ALP,  $\theta$  is the scattering angle (in the center-of-mass frame) and  $\gamma_a$  specifies the relativistic boost factor. Using the fact that most Higgs bosons are produced in the forward direction at the LHC and approximating the ATLAS and CMS detectors (as well as future detectors) by infinitely long cylindrical tubes, we first perform a Lorentz boost to the rest frame of the decaying boson.

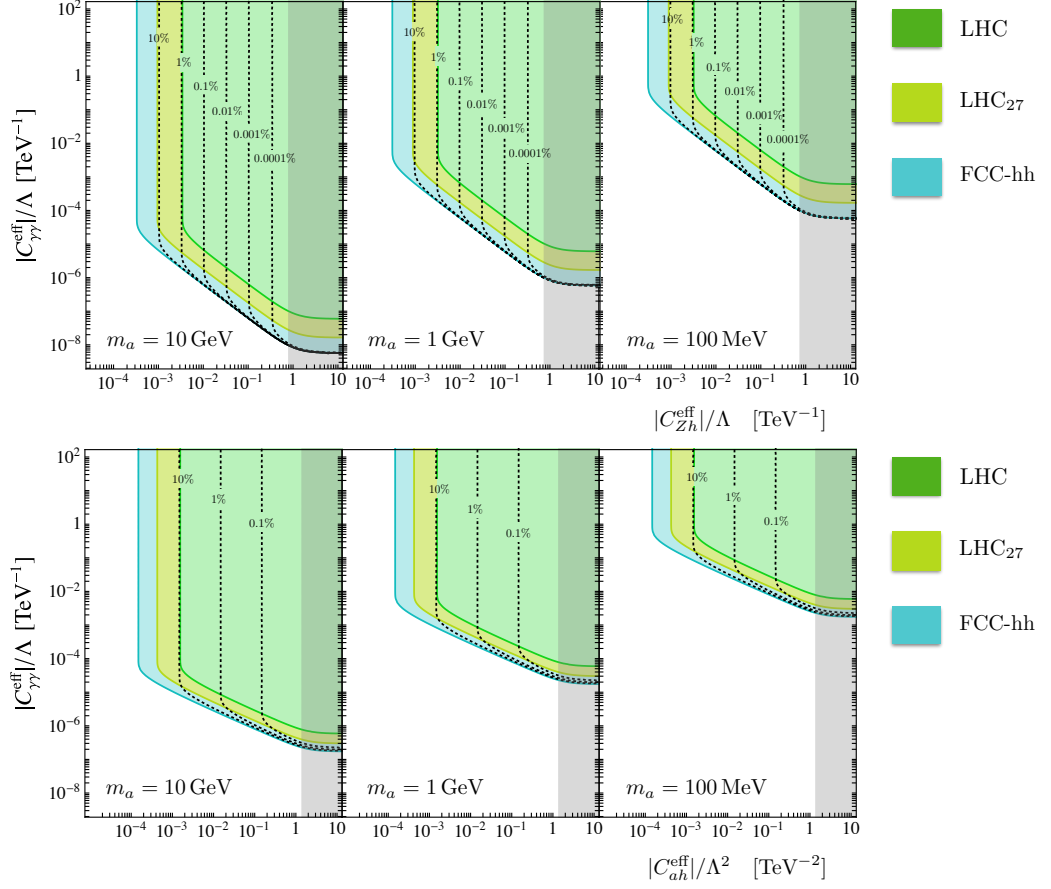


Fig. 111: Projected reach in searches for  $h \rightarrow Za \rightarrow \ell^+ \ell^- + 2\gamma$  and  $h \rightarrow aa \rightarrow 4\gamma$  decays with the LHC with  $3 \text{ ab}^{-1}$  (green), HE-LHC with  $15 \text{ ab}^{-1}$  (dark green) and a  $100 \text{ TeV}$  collider with  $20 \text{ ab}^{-1}$  (blue). The parameter region with the solid contours correspond to a branching ratio of  $\text{Br}(a \rightarrow \gamma\gamma) = 1$ , and the contours showing the reach for smaller branching ratios are dotted.

In this frame the relevant boost factors for the Higgs decay into ALPs are given by

$$\gamma_a = \begin{cases} \frac{m_h^2 - m_Z^2 + m_a^2}{2m_a m_h}, & \text{for } h \rightarrow Za, \\ \frac{m_h}{2m_a}, & \text{for } h \rightarrow aa. \end{cases} \quad (161)$$

We can compute the fraction of ALPs decaying before they have travelled a certain distance  $L_{\text{det}}$  from the beam axis, finding

$$\begin{aligned} f_{\text{dec}}^a &= \int_0^{\pi/2} d\theta \sin \theta \left( 1 - e^{-L_{\text{det}}/L_a^\perp(\theta)} \right), \\ f_{\text{dec}}^{aa} &= \int_0^{\pi/2} d\theta \sin \theta \left( 1 - e^{-L_{\text{det}}/L_a^\perp(\theta)} \right)^2. \end{aligned} \quad (162)$$

where  $f_{\text{dec}}^a$  is relevant for  $h \rightarrow Za$  decays and  $f_{\text{dec}}^{aa}$  applies to  $h \rightarrow aa$  decays.

For prompt ALP decays, we demand all final state particles to be detected in order to reconstruct the decaying SM particle. For the decay into photons we require the ALP to decay before the electromagnetic calorimeter which, at ATLAS and CMS, is situated approximately 1.5 m from the interaction

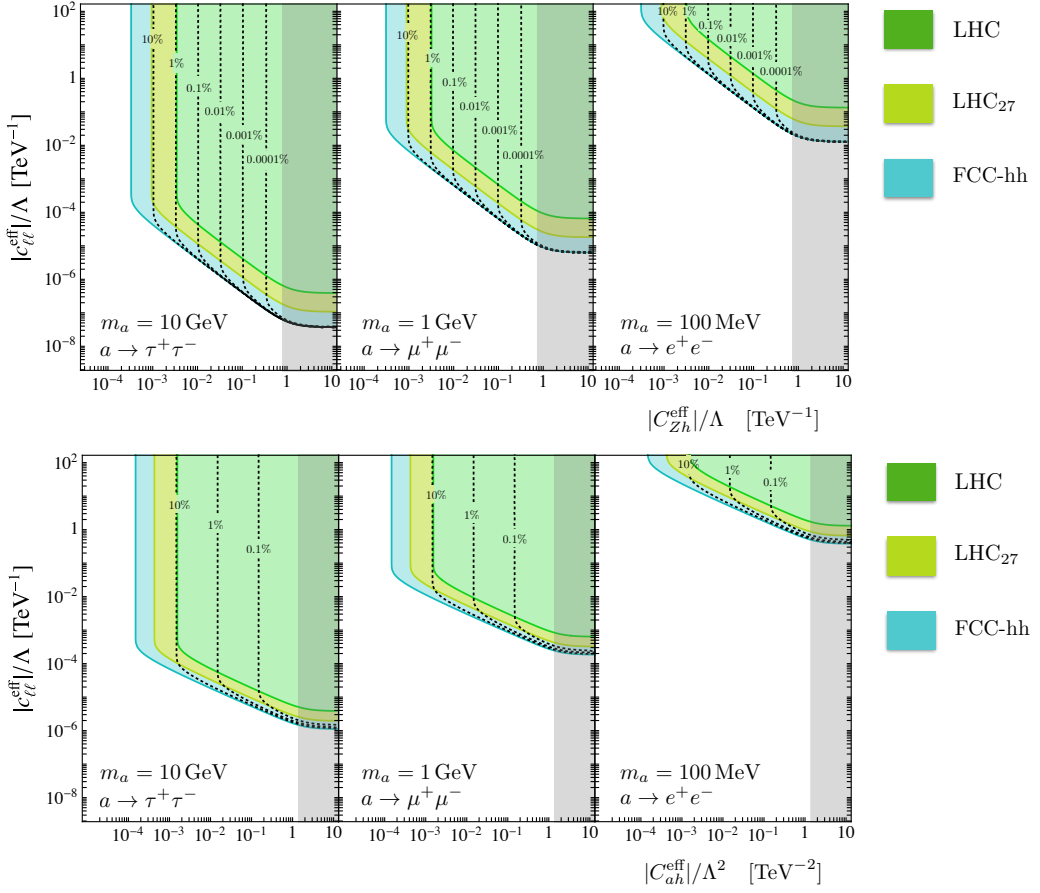


Fig. 112: Projected reach in searches for  $h \rightarrow Za \rightarrow \ell^+\ell^- + \ell^+\ell^-$  and  $h \rightarrow aa \rightarrow 4\ell$  decays with the LHC with  $3 \text{ ab}^{-1}$  (green), HE-LHC with  $15 \text{ ab}^{-1}$  (dark green) and a  $100 \text{ TeV}$  collider with  $20 \text{ ab}^{-1}$  (blue). The parameter region with the solid contours correspond to a branching ratio of  $\text{Br}(a \rightarrow \ell^+\ell^-) = 1$ , and the contours showing the reach for smaller branching ratios are dotted.

point, and we thus take  $L_{\text{det}} = 1.5 \text{ m}$ . Analogously, the ALP should decay before the inner tracker,  $L_{\text{det}} = 2 \text{ cm}$ , for an  $e^+e^-$  final state to be detected. We also require  $L_{\text{det}} = 2 \text{ cm}$  for muon and tau final states in order to take full advantage of the tracker information in reconstructing these events. We define the effective branching ratios

$$\text{Br}(h \rightarrow Za \rightarrow Y\bar{Y} + X\bar{X})|_{\text{eff}} = \text{Br}(h \rightarrow Za) \text{Br}(a \rightarrow X\bar{X}) f_{\text{dec}}^a \text{Br}(Z \rightarrow Y\bar{Y}), \quad (163)$$

$$\text{Br}(h \rightarrow aa \rightarrow X\bar{X} + X\bar{X})|_{\text{eff}} = \text{Br}(h \rightarrow aa) \text{Br}(a \rightarrow X\bar{X})^2 f_{\text{dec}}^{aa}, \quad (164)$$

where  $X = \gamma, e, \mu, \tau$  and  $Y = \ell$ , hadrons. Multiplying the effective branching ratios by the appropriate Higgs production cross section and luminosity allows us to derive results for a specific collider. The Higgs production cross section at  $14 \text{ TeV}$  is given by  $\sigma(pp \rightarrow h) = 54.61 \text{ pb}$  [?]. We use the reference cross section  $\sigma(gg \rightarrow h) = 146.6 \text{ pb}$  [?] at  $\sqrt{s} = 27 \text{ TeV}$ . At  $\sqrt{s} = 100 \text{ TeV}$ , the relevant cross section is  $\sigma(gg \rightarrow h) = 802 \text{ pb}$  [203]. We require 100 signal events, since this is what is typically needed to suppress backgrounds in new-physics searches with prompt Higgs decays [?, ?, 25] (see also [?] for further discussion). We do not take advantage of the additional background reduction obtained by cutting on a secondary vertex in the case where the ALP lifetime becomes appreciable. A dedicated analysis by the experimental collaborations including detailed simulations of the backgrounds is required to improve on our projections.

In Figure 111, we display the reach for observing 100 events at the LHC, HE-LHC and FCC-hh for searches for  $pp \rightarrow h \rightarrow Za \rightarrow \ell^+ \ell^- \gamma\gamma$  (upper panels) and  $pp \rightarrow h \rightarrow aa \rightarrow 4\gamma$  (lower panels) for  $m_a = 100$  MeV, 1 GeV and 10 GeV and  $\text{Br}(a \rightarrow \gamma\gamma) = 1$  in the  $|C_{Zh}^{\text{eff}}|/\Lambda - |C_{\gamma\gamma}^{\text{eff}}|/\Lambda$  and  $|C_{ah}^{\text{eff}}|/\Lambda^2 - |C_{\gamma\gamma}^{\text{eff}}|/\Lambda$  planes respectively. We further indicate the reach obtained in the case that  $\text{Br}(a \rightarrow \gamma\gamma) < 1$  by the dotted lines. For all considered ALP masses, the  $h \rightarrow Za$  decay could be observed at a 100 TeV collider for  $\text{Br}(a \rightarrow \gamma\gamma) \gtrsim 10^{-6}$  and the  $h \rightarrow aa$  decay could be fully reconstructed for  $\text{Br}(a \rightarrow \gamma\gamma) \gtrsim 0.01$ .

The results are similar for leptonic ALP decays. In Figure 112 we show the reach in the  $c_{\ell\ell}^{\text{eff}} - C_{Zh}^{\text{eff}}$  plane (upper row) and  $c_{\ell\ell}^{\text{eff}} - C_{ah}^{\text{eff}}$  plane (lower row).

#### 9.2.4 $h \rightarrow aa \rightarrow \mu\mu\mu\mu$

<sup>1</sup>Alfredo Castaneda<sup>1</sup>, Sven Dildick<sup>2</sup>, Luca Pernie<sup>2</sup> and Jamal Rorie<sup>3</sup>

<sup>1</sup>*Department of Physics and Astronomy, University of Sonora, Mexico*

<sup>2</sup>*Department of Physics and Astronomy, Texas A&M University, USA*

<sup>3</sup>*Department of Physics and Astronomy, Rice University, USA*

In this analysis, the search for a new light boson is focused on events where four final-state muons reconstruct to a pair of dimuons [?]. These dimuons must have a common decay vertex and a similar invariant mass. The dimuon mass is allowed to vary between between 0.25 and 8.5 GeV; their lifetimes can range up to  $c\tau = 100$  mm. Standard model backgrounds are reduced due to the dimuon vertex constraint and mass criteria as well as isolation requirements on the constituent muons. To avoid the introduction of bias between models in the trigger, we require the presence of a “high  $p_T$ ” muon: a muon with  $p_T > 17$  GeV located in the barrel region. The criteria are examined in the context of multiple models to ensure that there is no model sensitivity. The remaining background is sparse and is dominated by decays of b  $\bar{b}$  quarks, with small-to-negligible contributions from promptly produced J/ $\psi$  mesons and electroweak processes. This background is modeled with a two-dimensional template as a function of dimuon mass. The b  $\bar{b}$  contribution to the background template, normalized to unity, is shown in Fig. 113. Since the width of the new particle is expected to be extremely narrow, the signal shape for each mass point is modeled according to a Crystal Ball [?] function for which the width is solely determined by the resolution of the muon system. The template is used along with any observed events to extract a limit as part of modified frequentist procedure. This result can then be interpreted in the context of specific models.

The projected CL upper limits on  $\sigma(pp \rightarrow 2a + X)\mathcal{B}^2(a \rightarrow 2\mu)\alpha_{\text{gen}}$  for the  $h \rightarrow aa \rightarrow 4\mu$  analysis is shown in Fig. 114. The upper limits scale approximately as the inverse of the integrated luminosity. The results are interpreted in the NMSSM in Fig. 115, and in models with dark photons in Fig. 116, for the scenario with YR18 systematic uncertainties and using  $3000 \text{ fb}^{-1}$ . The results obtained using  $3000 \text{ fb}^{-1}$  with run 2 systematic uncertainties were not found to be significantly different.

Compared to the results in Ref. [?] obtained with  $36 \text{ fb}^{-1}$ , the limit on  $\sigma(pp \rightarrow h_{1,2} \rightarrow 2a_1)\mathcal{B}^2(a_1 \rightarrow 2\mu)$  is approximately a factor 80 smaller with integrated luminosity of  $3000 \text{ fb}^{-1}$  of data. In models with dark photons, more stringent limits were set on the kinetic mixing parameter  $\varepsilon$ . In addition, the search becomes more sensitive to models with  $\text{BR} = 0.1\%$  beyond the  $\rho$  meson mass.

They should be considered as lower bounds of the sensitivity of this analysis. The analysis methods used in the search on Run 2 data from 2016 were neither reviewed nor optimized for this projection. The methods do not consider anticipated improvements to the analysis techniques nor the effect of upgrades to the LHC and CMS hardware. The results are thus extremely conservative estimates.

This search is designed to have almost no background contribution. However, as this projection was made with non-optimized background modeling techniques, a non-trivial number of background events (primarily from bottom quark pair production, b  $\bar{b}$ ) enter the search region when the integrated luminosity is  $3000 \text{ fb}^{-1}$ . As such, the sensitivity is expected to be dominated by the background con-

# THIS IMAGE NEEDS TO BE REPLACED

Fig. 113: The 2D analytical template for distribution of the dimuon masses obtained using background-enriched data sample, normalized to unity.

tribution in this simple projection. The systematic uncertainties have a negligible effect on the model independent upper limit on the product of the cross section, the branching fraction, and the acceptance. The limits for scenario 2 with smaller systematic uncertainties are not significantly better than for scenario 1.

The search can also be extended to search for new bosons that are more massive. Searches could be performed for  $m_a$  up to 62.5 GeV. Preliminary studies indicate that the modeling of the leading background,  $b\bar{b}$ , would have to be revised.

This search may be improved considerably with the HL-LHC upgrade and upgrades to the CMS detector. The sensitivity to  $h \rightarrow aa \rightarrow \mu\mu\mu\mu$  events will increase as the center-of-mass energy increases from 13 to 14 TeV. The main production channel ggF will increase by as much as 12% [7]. Additional Higgs boson production modes, associated production and ttbarH, will improve the sensitivity as well.

Data taking with an upgraded tracker and muon system may potentially have a dramatic effect on the fiducial search region. The commissioning of new GEM-based detectors in the forward region could extend the fiducial region from  $|\eta| < 2.4$  to  $|\eta| < 2.8$ . In addition, the momentum assignment could improve significantly in the overlap and endcap region, so that high-pT dimuons may also be selected beyond  $|\eta| > 0.9$ .

The transverse displacement of the new light boson decay vertex,  $L_{xy}$ , was limited to 9.8 cm in the search with the 2016 data set. By making use of new muon finding techniques optimized for displacement in the L1 trigger, the high level trigger, and in offline reconstruction, the range of transverse displacement in which a new light boson decay can be detected may increase to 1–3 m. Such an increase in the range of  $L_{xy}$  would correspond to an upper limit on the kinetic mixing parameter  $\varepsilon$  as low as  $\varepsilon < 10^{-10}$ .

Finally, the object reconstruction and selection should be revised and optimized for signatures with dimuons in pp collision data at the HL-LHC.

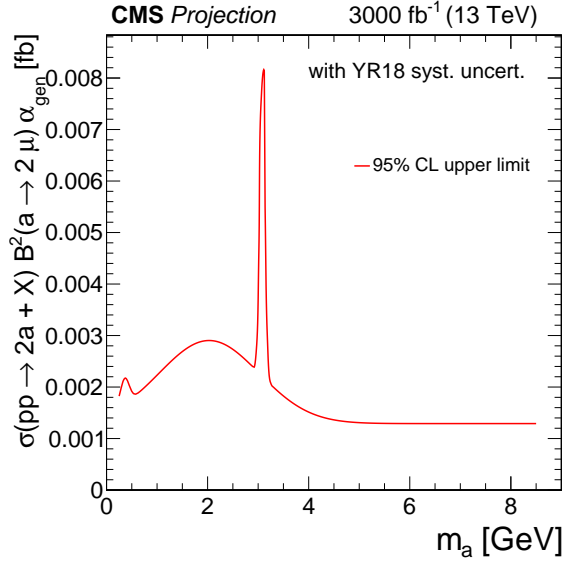


Fig. 114: Projected 95% C.L. upper limits on  $\sigma(pp \rightarrow 2a + X)B^2(a \rightarrow 2\mu)\alpha_{\text{gen}}$  over the range  $0.25 < m_a < 8.5$  GeV for  $3000 \text{ fb}^{-1}$  of data in the scenario with YR18 systematic uncertainties.

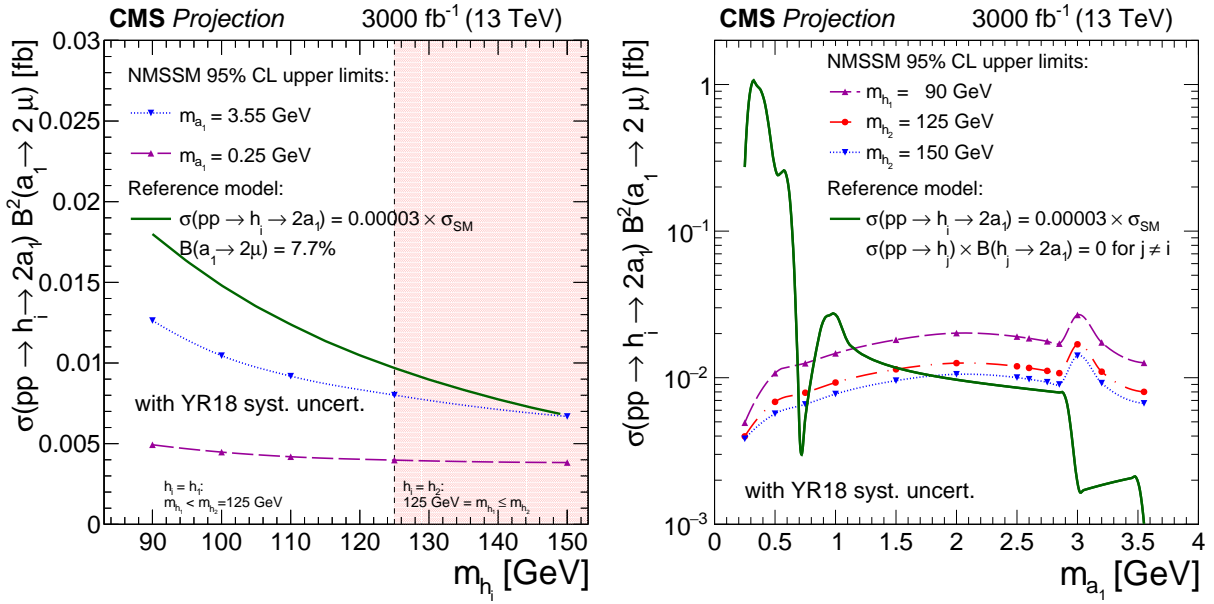


Fig. 115: Left: Projected 95% C.L. upper limits for  $3000 \text{ fb}^{-1}$  of data in the NMSSM benchmark model as functions of  $m_{h_{1,2}}$  on  $\sigma(pp \rightarrow h_{1,2} \rightarrow 2a_1)B^2(a_1 \rightarrow 2\mu)$  with  $m_{a_1} = 0.25$  GeV (dashed curve) and  $m_{a_1} = 3.55$  GeV (dotted curve). The limits are compared to a representative predicted rate (solid curve) obtained using a simplified model where  $\sigma(pp \rightarrow h_1) = \sigma_{\text{SM}}(m_{h_1})$  [?],  $\sigma(pp \rightarrow h_2)B(h_2 \rightarrow 2a_1) = 0$ ,  $B(h_1 \rightarrow 2a_1) = 0.3\%$ , and  $B(a_1 \rightarrow 2\mu) = 7.7\%$ . For the chosen  $B(a_1 \rightarrow 2\mu)$ , taken from Ref. [?],  $m_{h_1} = 2$  GeV and NMSSM parameter  $\tan \beta = 20$ . Right: Projected 95%

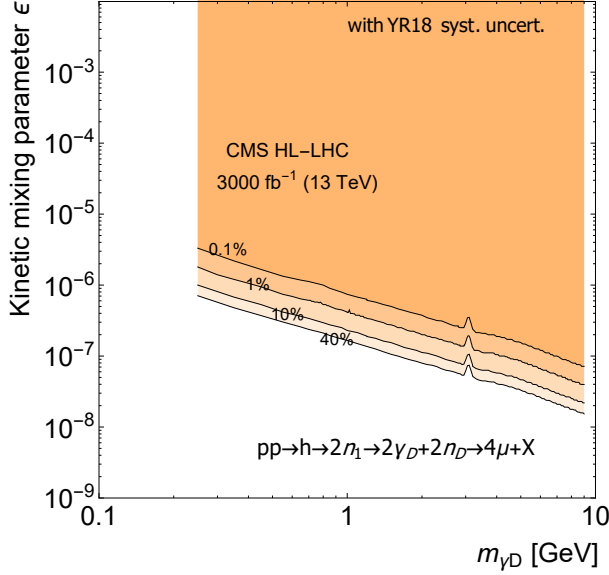


Fig. 116: Projected 95% C.L. upper limits (black solid curves) for  $3000 \text{ fb}^{-1}$  of data as interpreted in the dark SUSY benchmark model, where the process is  $\text{pp} \rightarrow \text{h} \rightarrow 2n_1 \rightarrow 2\gamma_D + 2n_D \rightarrow 4\mu + X$ , with  $m_{n_1} = 10 \text{ GeV}$  and  $m_{\gamma_D} = 1 \text{ GeV}$ . The limits are presented in the plane of the parameters ( $\varepsilon$  and  $m_{\gamma_D}$ ). The colored contours represent different values of  $\mathcal{B}(\text{h} \rightarrow 2\gamma_D + X)$  that range from 0.1 to 40%.

### 9.3 Searches for additional Higgs bosons in fermionic final states

#### 9.3.1 Projection of Run-2 CMS searches for MSSM and other heavy Higgs bosons

Analyses which search for MSSM Higgs bosons have been performed using the 2016 dataset with  $35.9 \text{ fb}^{-1}$  of data and have not shown any excess above the SM background [?, ?, ?]. However, so far the LHC has only collected a small fraction of its lifetime target integrated luminosity and several future measurements are sensitive to models beyond the SM not excluded by the current data. In particular analyses where the sensitivity is limited by statistical uncertainties will see a significantly extended reach in the coming years. Among these are searches for MSSM Higgs bosons.

The projection of the search for heavy Higgs bosons decaying into a pair of tau leptons to higher luminosities is documented in detail in the following. The projection is based on the most recent CMS publication of this analysis, performed using  $35.9 \text{ fb}^{-1}$  of data collected during 2016, at a centre-of-mass energy of 13 TeV [?], referred to as HIG-17-020 in the following. In HIG-17-020, all the details of the analysis, including simulation samples, background estimation methods, systematic uncertainties, and different interpretations are described. Only details of direct relevance to the projection are documented in the following.

The analysis is a direct search for a resonance decaying to two tau leptons. The following tau lepton decay mode combinations, called channels, are considered:  $\mu\tau_h$ ,  $e\tau_h$ ,  $\tau\tau$ , and  $e\mu$ , where  $\tau_{\text{had}}$  indicates a tau lepton decaying hadronically. In all of these channels, events are separated into those which contain at least one b-tagged jet and those which do not contain any b-tagged jets. The goal of this categorization is to increase the sensitivity to the dominant MSSM production modes, gluon fusion ( $ggH$ ) and production in association with b quarks ( $bbH$ ). The final discriminant is the total transverse mass, as defined in Ref. [?]. The signal hypotheses considered consist of additional Higgs bosons in the mass range of 90 GeV to 3.2 TeV.

A projection of this analysis is carried out by scaling all the signal and background processes to an integrated luminosity of  $3000 \text{ fb}^{-1}$ , expected to be collected at the high-luminosity LHC (HL-LHC). The upgrade and the expected performance of the CMS detector are described in detail in the Technical

Proposal and the Technical Design Reports for the Phase-II Upgrade of the CMS Detector [?, ?, ?, ?, ?]. The most recent CMS projection of the sensitivity to MSSM Higgs boson decays to a pair of tau leptons is reported in Ref. [?]. The results are presented in terms of model-independent limits on a heavy resonance decaying to two tau leptons, as well as interpreted in MSSM benchmark scenarios.

### 9.3.1.1 Projection methodology

Three scenarios are considered to project systematic uncertainties:

- Statistical uncertainties-only: All systematic uncertainties are neglected.
- Run 2 systematic uncertainties: All systematic uncertainties are constant with respect to luminosity, i.e. they are the same as for the 2016 results.
- YR18 systematic uncertainties: Systematic uncertainties improve with integrated luminosity, following a set of assumptions explained below.

For the YR18 scenario, selected systematic uncertainties are scaled down as a function of luminosity until they reach a certain minimum value. Specifically, all pre-fit uncertainties of experimental nature (including the statistical uncertainty in control regions and of simulation samples) are scaled proportionally to the square root of the integrated luminosity. The following minimum values are enforced:

- muon efficiency: 25% of the 2016 value, corresponding to an average absolute uncertainty of about 0.5%;
- electron,  $\tau_{\text{had}}$ , and b-tagging efficiency: 50% of the 2016 value, corresponding to an average absolute uncertainty of about 0.5%, 2.5%, and 1.0%, respectively.
- estimate of the background due to jets misreconstructed as  $\tau_{\text{had}}$  using a fake factor method [?], for the subset of its uncertainties which is not of a statistical nature: 50% of the 2016 values.
- luminosity uncertainty: minimum value 1%.
- theory uncertainties: halved with respect to the 2016 values, independently of the luminosity for all projections.

Note that for limits where the Higgs boson mass is above about 1 TeV, the statistical uncertainties are dominant and the choice of systematic uncertainty values has a negligible impact on the result.

The lightest Higgs boson  $h$  is excluded from the SM versus MSSM hypothesis test for the following reason: With increasing luminosity, the search will become sensitive to this boson. However, the current benchmark scenarios do not incorporate the properties of the  $h$  boson with the accuracy required at the time of the HL-LHC. Certainly the benchmark scenarios will evolve with time in this respect. Therefore the signal hypothesis includes only the heavy A and H bosons, to demonstrate the search potential only for these.

### 9.3.1.2 Model-independent limits

The model-independent limits on the cross section of the ggH and bbH production mechanisms with subsequent  $\tau\tau$  decays are shown in Fig. 117 for integrated luminosities of  $300 \text{ fb}^{-1}$  and  $3000 \text{ fb}^{-1}$ . For both production modes, the improvement at high mass is close to the statistical limit of scaling with the square root of the integrated luminosity, see Fig. 118. The improvement at very low mass is almost entirely due to the assumption of reduced systematic uncertainties, and not directly due to the additional collected data in the signal region. The difference between the Run 2 and YR18 scenarios is mostly due to the treatment of two kinds of systematic uncertainties of statistical nature, namely the uncertainties due to the number of simulated events and the number of events in data control regions.

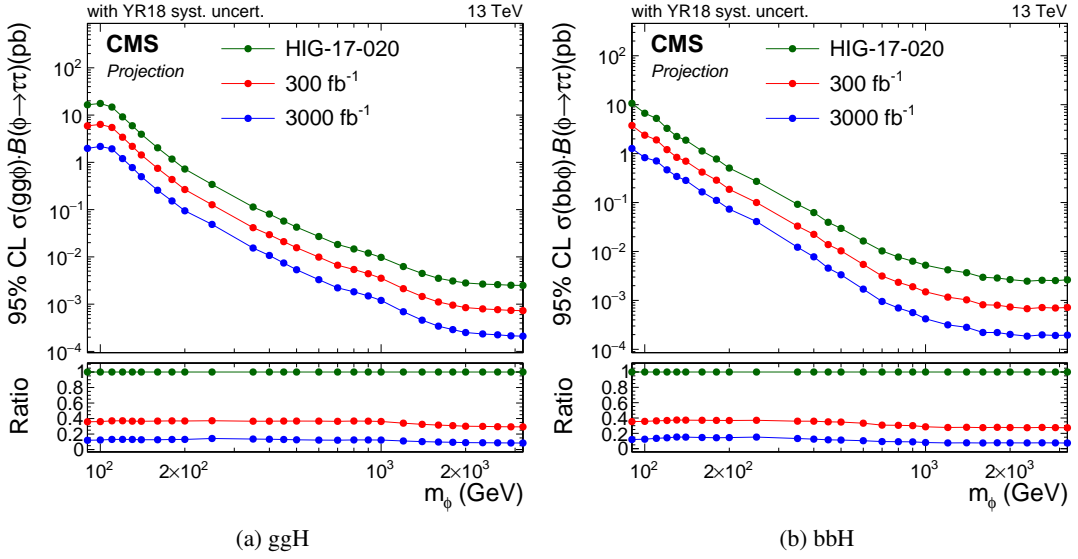


Fig. 117: Projection of expected model-independent limits based on 2016 data [?] for ggH and bbH production with subsequent  $H \rightarrow \tau\tau$  decays, with YR18 systematic uncertainties.

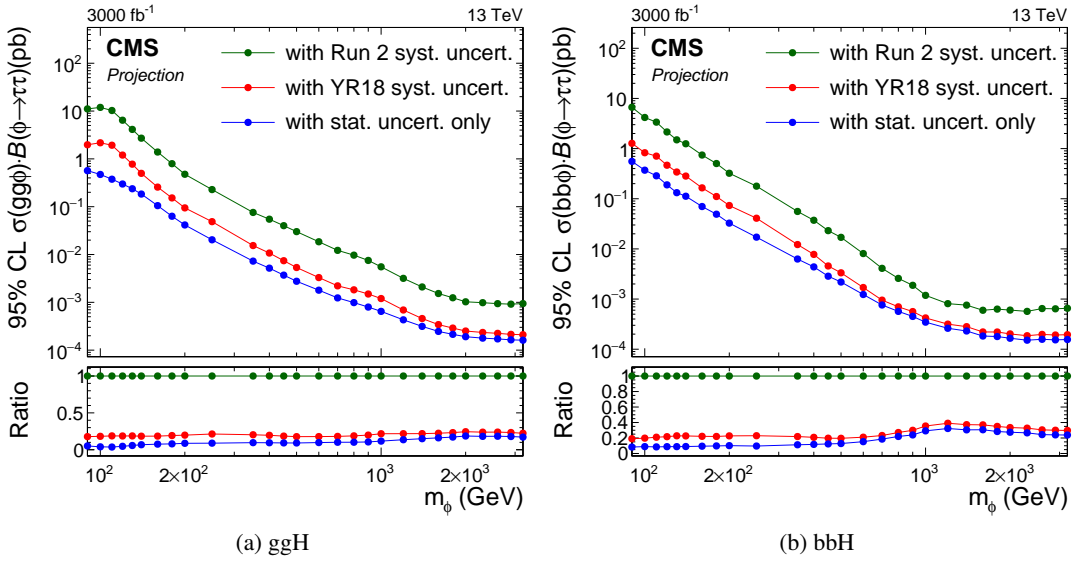


Fig. 118: Projection of expected model-independent limits based on 2016 data [?] for ggH and bbH production with subsequent  $H \rightarrow \tau\tau$  decays, comparing different scenarios for systematic uncertainties for an integrated luminosity of  $3000 \text{ fb}^{-1}$ .

### 9.3.1.3 Model-dependent limits

The di- $\tau$  lepton final state provides the most sensitive direct search for additional Higgs bosons predicted by the MSSM for intermediate and high values of  $\tan\beta$ , due to the enhanced coupling to down-type fermions.

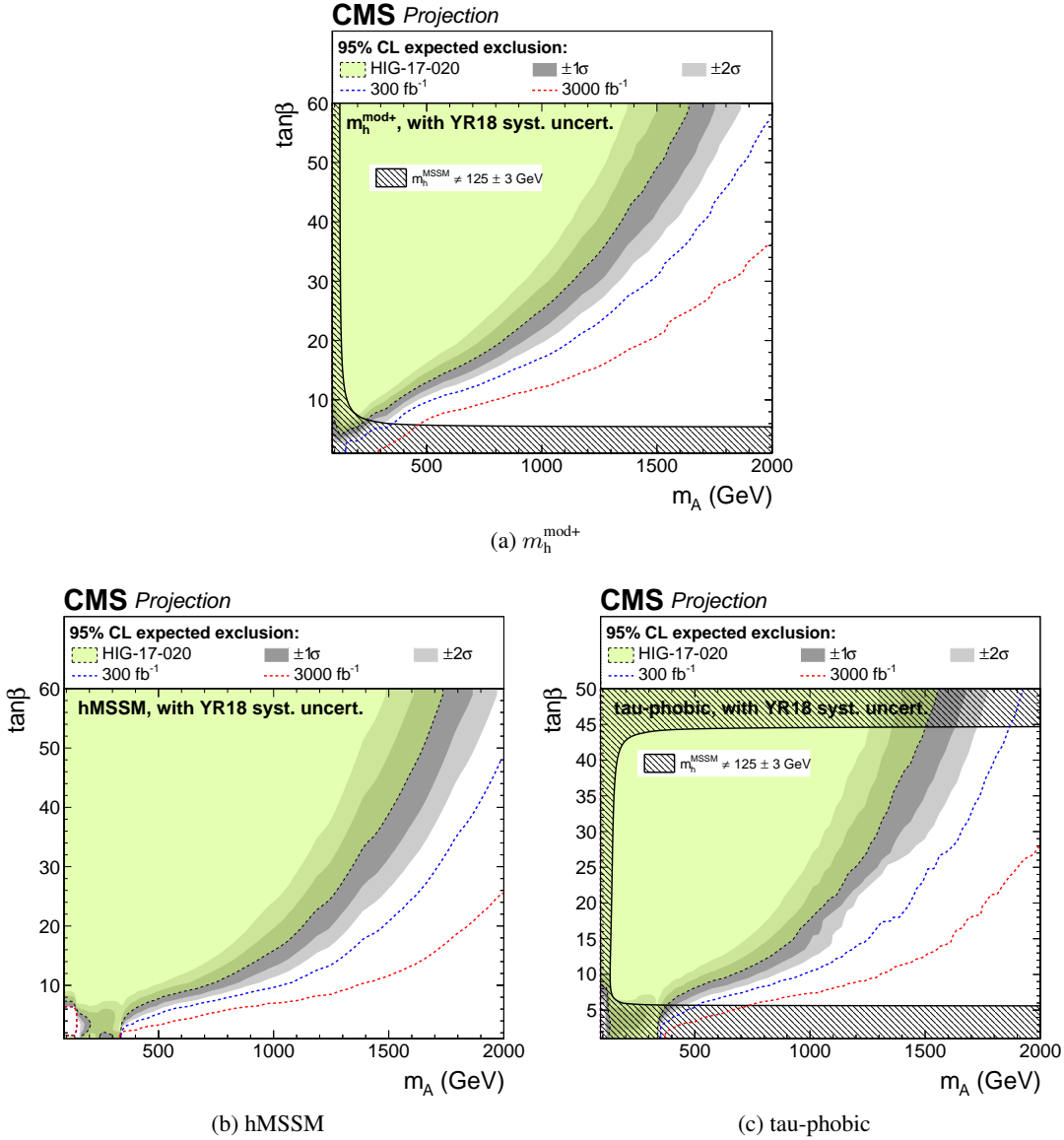


Fig. 119: Projection of expected MSSM  $H \rightarrow \tau\tau$  limits based on 2016 data [?] for different benchmark scenarios, with YR18 systematic uncertainties.

The analysis results are interpreted in terms of benchmark scenarios [?] based on the profile likelihood ratio of the background-only and the tested signal-plus-background hypotheses. For this purpose, the predictions from both production modes and both heavy neutral Higgs bosons are combined. Figure 119 shows the results for different benchmark scenarios. The sensitivity is extended to a mass of 2 TeV and  $\tan\beta$  values of about 30, depending on the scenario. Even at low mass, improvements are expected but in this case they are mostly due to reduced systematic uncertainties and not the additional data in the signal region.

### 9.3.1.4 Conclusions

HL-LHC projections of the most recent results of searches for MSSM Higgs bosons decaying to  $\tau$  leptons have been shown based on the 2016 dataset corresponding to a total integrated luminosity of  $35.9 \text{ fb}^{-1}$ . In terms of cross section, an order-of-magnitude increase of sensitivity is expected for neutral Higgs boson masses above 1 TeV since here the analysis is statistically limited by the available integrated luminosity. For lower masses, an improvement by approximately a factor of five is expected for realistic assumptions on the evolution of the systematic uncertainties. For the MSSM benchmarks, the sensitivity will reach up to Higgs boson masses of 2 TeV for values of  $\tan \beta$  of 36, 26, and 28 for the  $m_h^{\text{mod}+}$ , the hMSSM, and the tau-phobic scenario, respectively.

## 9.3.2 Projection of Run-2 ATLAS searches for MSSM heavy Higgs bosons

### 9.3.2.1 Introduction

The discovery of the Standard Model (SM) like Higgs boson [?, ?] at the Large Hadron Collider (LHC) [?] has provided important insight into the mechanism of electroweak symmetry breaking. However, it remains possible that the discovered particle is part of an extended scalar sector, a scenario that is favoured by a number of theoretical arguments [?, ?]. Searching for the extra Higgs boson is a principal goal of the High-Luminosity LHC (HL-LHC) programme [?]. The Minimal Supersymmetric Standard Model (MSSM) [?, ?, ?] is one of the most favored extension of the SM. Besides the SM-like Higgs boson, the MSSM requires two additional Higgs bosons: one CP-odd ( $A$ ) and one CP-even ( $H$ ), which are generically called  $\phi$ . At tree level, the MSSM Higgs sector depends on only two non-SM parameters, which can be chosen to be the mass of the CP-odd Higgs boson,  $m_A$ , and the ratio of the vacuum expectation values of the two Higgs doublets,  $\tan \beta$ . Beyond tree level, a number of additional parameters affect the Higgs sector, the choice of which defines various MSSM benchmark scenarios, such as  $m_h^{\text{mod}+}$  [?] and hMSSM [?, ?]. The couplings of the additional MSSM Higgs bosons to down-type fermions are enhanced with respect to the SM Higgs boson for large  $\tan \beta$  values, resulting in increased branching fractions to  $\tau$ -leptons and  $b$ -quarks, as well as a higher cross section for Higgs boson production in association with  $b$ -quarks.

The projections presented in this note are extrapolations of the recent results obtained by ATLAS using the Run 2 dataset [?]. The MSSM Higgs boson with masses of 0.2–SI2.25 TeV and  $\tan \beta$  of 1–58 is searched in the  $\tau_{\text{lep}}\tau_{\text{had}}$  and  $\tau_{\text{had}}\tau_{\text{had}}$  decay modes, where  $\tau_{\text{lep}}$  represents the leptonic decay of a  $\tau$ -lepton, whereas  $\tau_{\text{had}}$  represents the hadronic decay. The main production modes are gluon–gluon fusion (ggf) and in association with  $b$ -quarks ( $bb\phi$ ). To exploit the different production modes, events containing at least one  $b$ -tagged jet enter the  $b$ -tag category, while events containing no  $b$ -tagged jets enter the  $b$ -veto category. The total transverse mass ( $m_T^{\text{tot}}$ ) is used as the final discriminant between the signal and the background.

In making these extrapolations, the assumption is made that the planned upgrades to the ATLAS detector and improvements to reconstruction algorithms will mitigate the effects of higher pileup conditions, leading to the detector performance matching that of the current detector. Furthermore, the assumption is made that the analysis will be unchanged in terms of selection and statistical analysis technique. It is a rather pessimistic assumption given that the analysis will be improved to use new techniques and optimised to make the best use of larger datasets.

### 9.3.2.2 Extrapolation method

To account for the luminosity increase at HL-LHE, signal and background distributions are scaled by a factor of  $3000/36.1$ . Furthermore, the distributions also have to be corrected to account for the increase in collision energy. The parton-luminosity of gluon has a larger increase than that of the (anti-)quark when the collision energy  $\sqrt{s}$  goes from SI13 TeV to SI14 TeV. In this analysis, the initial states of the main background processes, i.e. multijet,  $W+\text{jet}$ ,  $Z/\gamma^*+\text{jet}$ ,  $t\bar{t}$ , single top-quark and diboson ( $WW$ ,  $WZ$

and  $ZZ$ ) production, involve both the quark and the gluon. For simplicity the number of expected events of all background distributions are corrected conservatively by 1.18, which accounts for the increase in cross-sections due to the change in gluon-luminosity [3]. Possible effects on the kinematics and the  $m_T^{\text{tot}}$  shape are neglected for this study. The scaled  $m_T^{\text{tot}}$  distributions are shown in Figure 120 and 121. These distributions are used in the statistical analysis. The pseudo-data used in the extrapolation is taken to be the sum of the background distributions.

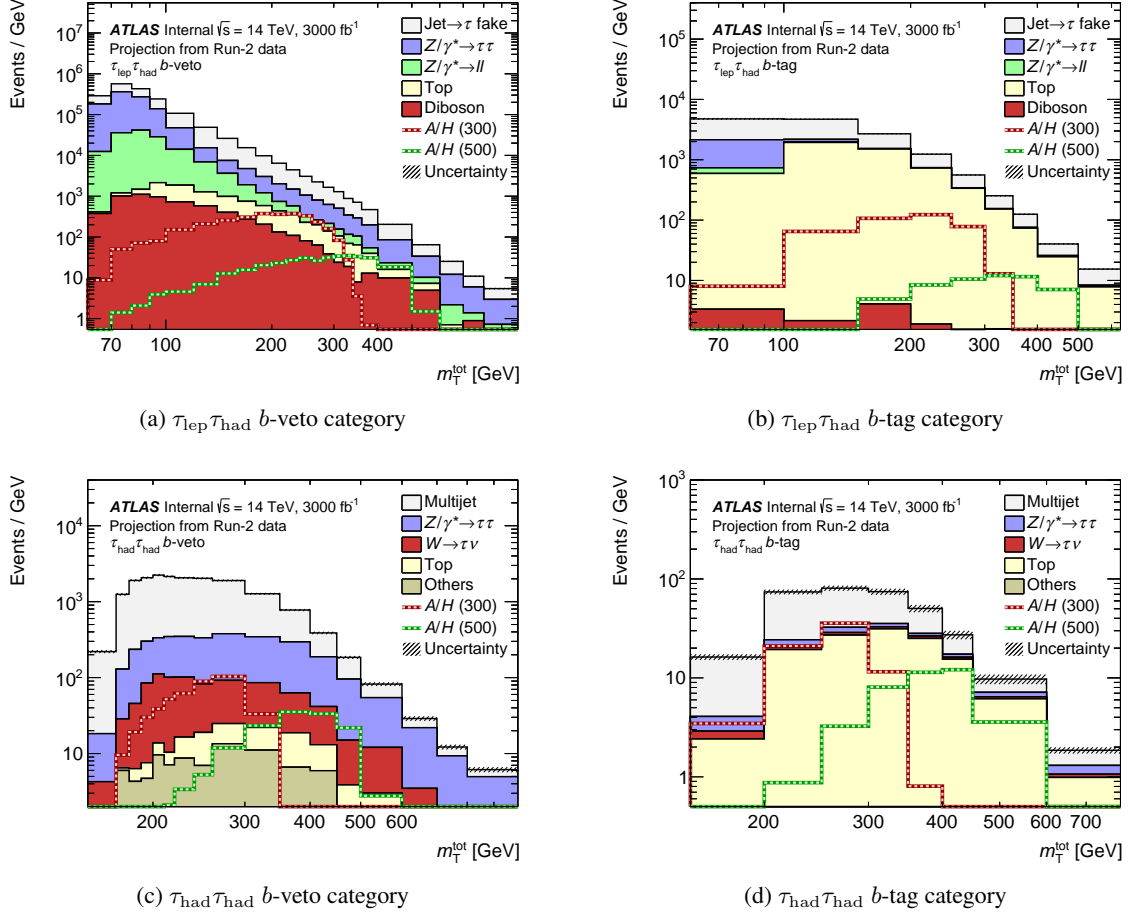


Fig. 120: Distributions of  $m_T^{\text{tot}}$  for each signal category. The style of the plot follows Ref. [?].

With the larger dataset at HL-LHC, the systematic uncertainties in this analysis are expected to be reduced. The systematic uncertainties associated with  $b$ -tagging,  $\tau_{\text{had-vis}}$  and theoretical uncertainties due to the missing higher order calculation, the PDF uncertainty, etc. are reduced according to Ref. [?]. The systematic uncertainties associated with the reconstruction and identification of the high- $p_T \tau_{\text{had-vis}}$  is reduced by a factor of 2 and is the dominant uncertainty for a heavy Higgs boson with mass  $m_\phi > 1 \text{ TeV}$ . The systematic uncertainty associated with the modeling of the jet to  $\tau_{\text{had-vis}}$  fake background is assumed to be the same as the current analysis. For the multijet background in  $\tau_{\text{had}}\tau_{\text{had}}$  channel, where the modeling of the jet to  $\tau_{\text{had-vis}}$  fake background is limited by the data sample size in the control region, this uncertainty is reduced by a factor of 2. The statistical uncertainties of the predicted signal and background distributions is determined by the size of the MC samples and the data sample in the failed  $\tau_{\text{had-vis}}$  identification control region (CR-1 in [?]). The impact of this statistical uncertainty is negligible in the Run 2 analysis. Assuming enough MC samples will be generated in HL-LHC, the uncertainties due to the sample size is ignored in this extrapolation study. The theoretical uncertainties, e.g. the signal acceptance uncertainties due to the missing higher order calculation, the PDF uncertainty,

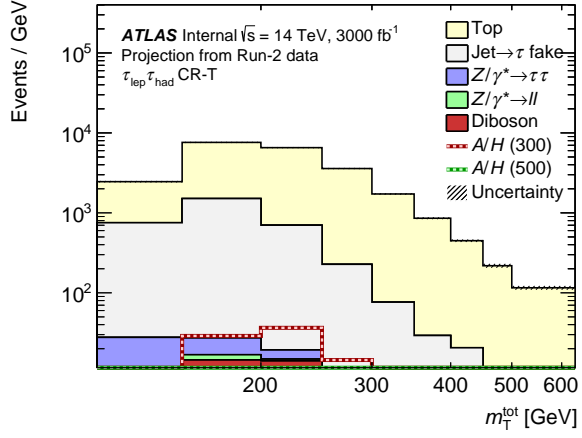


Fig. 121: Distribution of  $m_T^{\text{tot}}$  distributions in the top quark enriched control region of the  $\tau_{\text{lep}}\tau_{\text{had}}$  channel.

etc., are also assumed to be the same. The uncertainties associated to  $e$ ,  $\mu$ , jet,  $E_T^{\text{miss}}$  have minor impact to the analysis and are assumed to be the same for simplicity. This systematic uncertainty treatment scheme is defined as “Baseline”.

The statistical framework used to produce the Run-2 results is documented in Ref. [?] is adapted for this HL-LHC projection study. A likelihood function constructed as the product of Poisson probability terms is used. A term is included for each bin in the  $m_T^{\text{tot}}$  distributions from the  $\tau_{\text{lep}}\tau_{\text{had}}$  and  $\tau_{\text{had}}\tau_{\text{had}}$  signal regions, as well as the top control region.

### 9.3.2.3 Results

Assuming the data are found to be in good agreement with the predicted background, the results are given in terms of exclusion limits [?].

### 9.3.2.4 Cross section limits

Figure 122 shows the upper limits on the gluon–gluon fusion and  $b$ -quark associated production cross section times ditau branching fraction. To demonstrate the impact of systematics, the expected exclusion limits with different systematic uncertainty schemes are shown, as well as the current Run 2 results [?]. The peaking structure around  $m_\phi = 1$  TeV in figure 122 (a) is due to the impact of the high- $p_T$  tau systematic uncertainty.

### 9.3.2.5 MSSM interpretation

Results are interpreted in terms of the MSSM. Figure 123 shows regions in the  $m_\phi - \tan \beta$  plane excluded at 95% CL in the hMSSM and  $m_h^{\text{mod+}}$  scenarios. In the hMSSM scenario,  $\tan \beta > 1.0$  for  $m_\phi < 350$  GeV and  $\tan \beta > 15$  for  $m_\phi = 1.5$  TeV can be excluded at 95% CL. When  $m_\phi$  is above the  $\phi \rightarrow \bar{t}t$  threshold, this additional decay mode reduces the sensitivity of the  $A \rightarrow \tau\tau$  search for low  $\tan \beta$ . In the MSSM  $m_h^{\text{mod+}}$  scenario, the expected 95% CL upper limits exclude  $\tan \beta > 1$  for  $m_\phi < 350$  GeV and  $\tan \beta > 25$  for  $m_\phi = 1.5$  TeV.

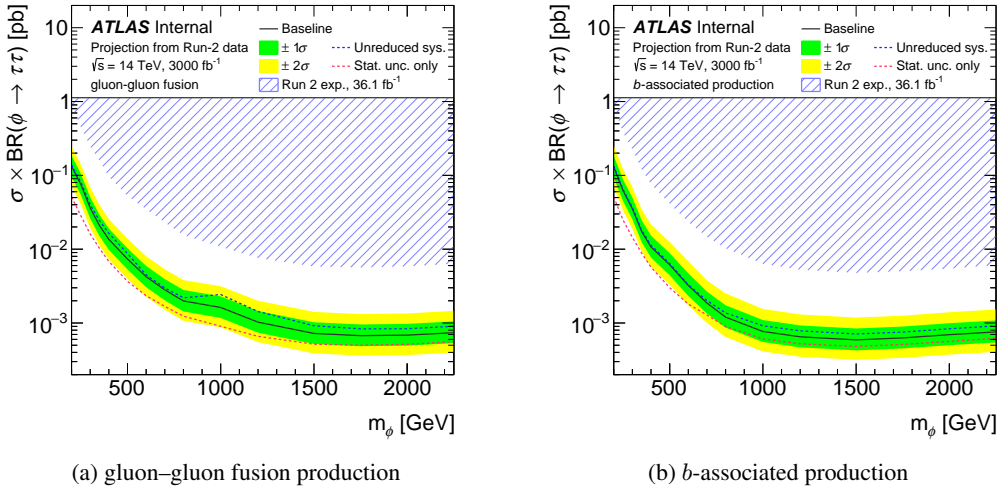


Fig. 122: Projected 95% CL upper limits on the production cross section times ditau branching fraction for a scalar boson produced via (a) gluon–gluon fusion and (b)  $b$ -associated production, as a function of scalar boson mass. The limits are calculated from a statistical combination of the  $\tau_e \tau_{\text{had}}$ ,  $\tau_\mu \tau_{\text{had}}$  and  $\tau_{\text{had}} \tau_{\text{had}}$  channels. “Baseline” uses the reduced systematic uncertainties scheme described in the text. “Unreduced sys.” uses the same systematic uncertainties as the Run 2 analysis while ignoring the statistical uncertainty due to the limited data size of the signal and backgrounds. “Stat. unc. only” represents the expected limit without considering any systematic uncertainty.

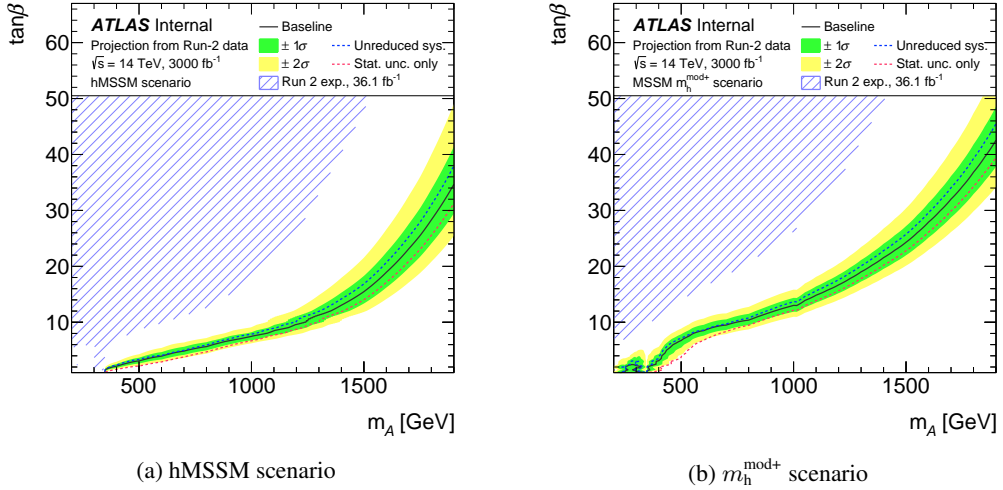


Fig. 123: Projected 95% CL limits on  $\tan \beta$  as a function of  $m_\phi$  in the MSSM (a) hMSSM and (b)  $m_h^{\text{mod}+}$  scenarios. “Baseline” uses the reduced systematic uncertainties scheme described in the text. “Unreduced sys.” uses the same systematic uncertainties as the Run 2 analysis while ignoring the statistical uncertainty due to the limited data size of the signal and backgrounds. “Stat. unc. only” represents the expected limit without considering any systematic uncertainty.

### 9.3.2.6 Conclusion

The  $H/A \rightarrow \tau\tau$  analysis documented in [?] have been extrapolated to estimate the sensitivity of the SI3000  $\text{fb}^{-1}$  of the HL-LHC dataset. Upper limits on the cross section for the production of scalar bosons times the branching fraction to ditau final states are set at 95% CL. A factor of 6 to 10 increase in

the sensitivity compared to the searches with the  $\text{SI}36.1 \text{ fb}^{-1}$  Run 2 data [?] is projected. The expected limits are in the range  $140\text{--}0.8 \text{ fb}$  ( $130\text{--}0.8 \text{ fb}$ ) for gluon-gluon fusion (b-associated) production of scalar bosons with masses of  $0.2\text{--}2.25 \text{ TeV}$ . In the context of the hMSSM scenario, the most stringent limits for the combined search exclude  $\tan \beta > 1.0$  for  $m_\phi < 300 \text{ GeV}$  and  $\tan \beta > 15$  for  $m_\phi = 1.5 \text{ TeV}$  at 95% CL. The systematic uncertainties degrade the model independent exclusion limit by more than a factor of 2 for  $m_\phi < 500 \text{ GeV}$  and about 40% for  $m_\phi = 2 \text{ TeV}$ . Especially, the uncertainty on high- $p_T \tau_{\text{had-vis}}$  reconstruction and identification is the dominant uncertainty at  $m_\phi > 1.0 \text{ TeV}$ .

### 9.3.3 HL-LHC projections of LHCb searches for 2HDM+S pseudoscalars

Martino Borsato<sup>1</sup>, Ulrich Haisch<sup>2,3,4</sup>, Jernej F. Kamenik<sup>5,6</sup>,  
Augustinas Malinauskas<sup>3</sup>, and Michael Spira<sup>7</sup>

<sup>1</sup>*Physikalisches Institut, Ruprecht-Karls-Universität Heidelberg, Heidelberg, Germany*

<sup>2</sup>*Max Planck Institute for Physics, Föhringer Ring 6, 80805 München, Germany*

<sup>3</sup>*Rudolf Peierls Centre for Theoretical Physics, University of Oxford, OX1 3NP Oxford, United Kingdom*

<sup>4</sup>*CERN, Theoretical Physics Department, CH-1211 Geneva 23, Switzerland*

<sup>5</sup>*Jožef Stefan Institute, Jamova 39, 1000 Ljubljana, Slovenia*

<sup>6</sup>*Faculty of Mathematics and Physics, University of Ljubljana, Jadranska 19, 1000 Ljubljana, Slovenia*

<sup>7</sup>*Paul Scherrer Institut, CH-5232 Villigen PSI, Switzerland*

Several well-motivated extensions of the Standard Model (SM) include a new pseudoscalar  $a$  with mass below the electroweak scale. A well-known example in the context of supersymmetry is the next-to-minimal supersymmetric SM, where this state can arise as a result of an approximate global  $U(1)_R$  symmetry [?]. Non-supersymmetric extensions featuring a light pseudoscalar include Little Higgs models, hidden valley scenarios (see [?], and references therein for details), and simplified models where a complex singlet scalar is coupled to the Higgs potential of the SM or the two-Higgs doublet model (2HDM). Light pseudoscalars have been searched via various collider signatures such as exotic decays of the  $125 \text{ GeV}$  scalar  $h$  discovered at the LHC (both  $h \rightarrow aa$  and  $h \rightarrow aZ$ ), radiative decays of bottomonium  $\Upsilon \rightarrow a\gamma$ , direct production from  $pp$  collisions in association with  $b$ -jets and also inclusively in  $pp \rightarrow a + X$ , where the main production mode is usually gluon-gluon fusion. The interplay of searches for exotic  $h$  decays and direct searches in  $pp$  collisions within 2HDM+S models depend on the 2HDM parameters  $\alpha, \beta$ , on the mixing angle  $\theta$ , on the physical spin-0 masses, and on the form of the scalar potential (see for instance [?] for further explanations).

Despite the significantly lower luminosity collected with respect to ATLAS and CMS, LHCb has proven to be capable of placing world-best limits for low-mass pseudoscalars produced in gluon-gluon fusion [?, ?], by searching simply for resonant pairs of opposite-sign muons [?, ?]. Indeed, a large fraction of these light pseudoscalars are produced with large boosts at the LHC and end up in the LHCb acceptance. On top of that, the LHCb detector is capable of triggering on muons with transverse momenta as low as  $1.8 \text{ GeV}$  ( $0.5 \text{ GeV}$ ) with the current (upgraded) trigger, greatly enhancing its acceptance to  $a \rightarrow \mu^+ \mu^-$  with respect to ATLAS and CMS. A key ingredient of this trigger, is the LHCb capability to efficiently reject the large background due to pion mis-identification thanks to online availability of offline-quality particle identification based on information from all sub-detectors [?, ?]. On top of that, the large boost of the pseudoscalar  $a$  in the forward region allows to separate muons coming from semileptonic  $B$  decays due to their displacement with respect to the  $pp$  collision vertex.

The HL-LHC sensitivity to prompt dimuon resonances in the context of dark photon searches at LHCb can be found in [?]. The kinematic selection used for the projection is inspired by [?] and rely on the improved performance expected after the upgrade of the LHCb trigger that will be implemented for LHC Run-3. Maintaining this exceptional performance in the HL-LHC era (i.e., with 10 times larger instantaneous luminosity) will require a redesign of the muon detector and is briefly discussed in [?].

In Figure 124, the limits on the dark photon parameter space presented in [?] are reinterpreted

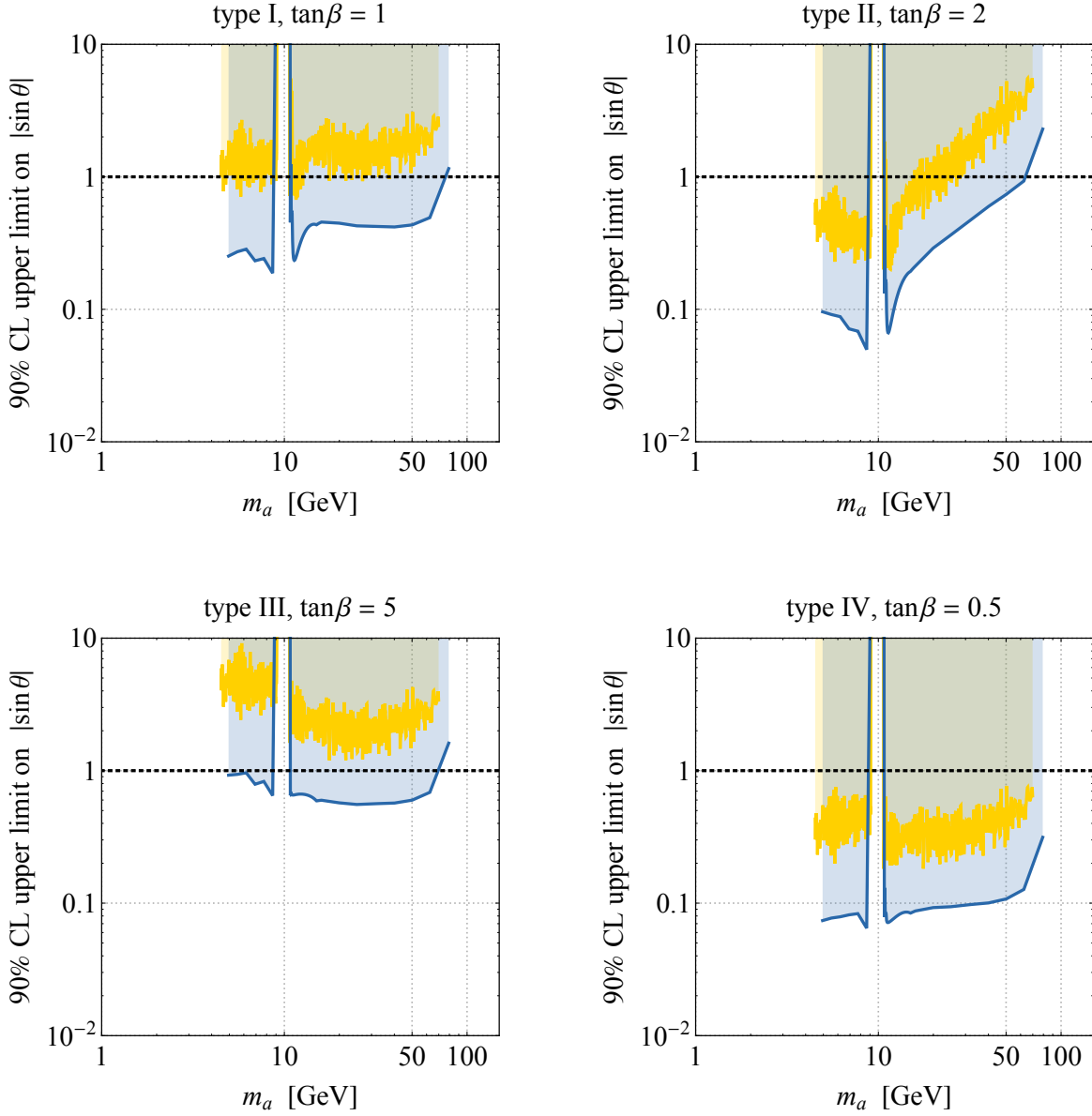


Fig. 124: Upper 90% CL limits on  $|\sin \theta|$  in the 2HDM+S of type I with  $\tan \beta = 1$  (top left), type II with  $\tan \beta = 2$  (top right), type III with  $\tan \beta = 5$  (bottom left) and type IV with  $\tan \beta = 0.5$  (bottom right). The yellow curves illustrate the results of a recast [?] of the LHCb search [?] performed with a data set corresponding to  $1.6 \text{ fb}^{-1}$  of 13 TeV  $pp$  collisions, while the blue contours are our projections to  $300 \text{ fb}^{-1}$  of 14 TeV  $pp$  collision data using the expected HL-LHC dark photon limits presented in [?].

in the context of the 2HDM+S, following the analysis strategy detailed in [?]. The production cross section of the pseudoscalar  $a$  and its decay rate to muons depend on the mixing angle  $\theta$ , on the parameter  $\tan \beta$  and on the type of the Yukawa sector of the considered 2HDM. Fixing  $\tan \beta$  and the type of the 2HDM, upper limits are placed on  $|\sin \theta|$  as a function of the pseudoscalar mass  $m_a$ . In all considered cases, LHCb searches in the HL-LHC era (blue contours) are found to be sensitive to values of  $|\sin \theta|$  well below 1 for a large range of  $m_a$  values between 5 GeV and 70 GeV. This represents a significant improvement over the LHC Run-2 results (yellow curves), where only in the 2HDM+S scenario of type IV with  $\tan \beta = 0.5$  it was possible to set physical meaningful bounds on the sine of the mixing angle

$\theta$ , i.e.,  $|\sin \theta| < 1$ , in the entire range of considered pseudoscalar masses. Notice that spin-0 states with masses around 10 GeV can be probed by searches for dimuon resonances in  $\Upsilon$  production [?, ?].

## 9.4 Searches for additional Higgs bosons in diboson final states

### 9.5 MSSM charged Higgs bosons

#### 9.5.1 Prospects for the observation of MSSM charged Higgs in the $\tau_h \nu$ channel at HL-LHC and HE-LHC

Amin Abouibrahim<sup>29</sup> and Pran Nath<sup>30</sup>

Department of Physics, Northeastern University, Boston, MA 02115-5000, USA

Here we discuss the potential of HL-LHC and HE-LHC for discovering a heavy charged Higgs boson [?] ( $m_{H^\pm} > m_t$ ) in a class of high scale models, specifically SUGRA models [?, ?, ?] (for a review see [?]) consistent with the experimental constraints on the light Higgs mass at  $\sim 125$  GeV and dark matter relic density (for a recent related work see [?]). We will focus on models where the radiative electroweak symmetry breaking is likely realized on the hyperbolic branch [?] and where the Higgs mixing parameter  $\mu$  can be relatively small. Specifically we consider supergravity models with non-universalities in the Higgs sector and in the gaugino sector so that the extended parameter space of the models we consider is given by  $m_0$ ,  $A_0$ ,  $m_1$ ,  $m_2$ ,  $m_3$ ,  $m_{H_u}^0$ ,  $m_{H_d}^0$ ,  $\tan\beta$ ,  $\text{sgn}(\mu)$ . Here  $m_0$  is the universal scalar mass,  $A_0$  is the universal trilinear coupling,  $m_1, m_2, m_3$  are the masses of the  $U(1)$ ,  $SU(2)$ , and  $SU(3)_C$  gauginos, and  $m_{H_u}^0$  and  $m_{H_d}^0$  are the masses of the up and down Higgs bosons all at the GUT scale. To satisfy the relic density constraint in these models often one needs coannihilation (see, e.g., [?, ?] and the references therein).

The largest production mode of the charged Higgs at hadron colliders is the one that proceeds in association with a top quark (and a low transverse momentum  $b$ -quark),  $pp \rightarrow t[b]H^\pm + X$ . This production mode can be realized in two schemes, namely, the four and five flavour schemes (4FS and 5FS, respectively), where in the former, the  $b$ -quark is produced in the final state and in the latter it is considered as part of the proton's sea of quarks and folded into the parton distribution functions (PDF). The cross-sections of the two production modes  $q\bar{q}, gg \rightarrow tbH^\pm$  (4FS) and  $gb \rightarrow tH^\pm$  (5FS), are evaluated at next-to-leading order (NLO) in QCD with `MadGraph_aMC@NLO-2.6.3` [79] using `FeynRules` [201] `UFO` files [?, 204] for the Type-II two Higgs doublet model (2HDM). The simulation is done at fixed order, i.e., no matching with parton shower. The couplings of the 2HDM are the same as in the MSSM, but when calculating production cross-sections in the MSSM, one should take into account the SUSY-QCD effects. In our case, gluinos and stops are rather heavy and thus their loop contributions to the cross-section are very minimal. In this case, the 2HDM is the decoupling limit of the MSSM and this justifies using the 2HDM code to calculate cross-sections. For the 5FS, the bottom Yukawa coupling is assumed to be non-zero and normalized to the on-shell running  $b$ -quark mass. In the 5FS, the process is initiated via gluon- $b$ -quark fusion while in the 4FS it proceeds through either quark-antiquark annihilation (small contribution) or gluon-gluon fusion. At finite order in perturbation theory, the cross-sections of the two schemes do not match due to the way the perturbative expansion is handled but one expects to get the same results for 4FS and 5FS when taking into account all orders in the perturbation. In order to combine both estimates of the cross-section, we use the Santander matching criterion [?] whereby

$$\sigma^{\text{matched}} = (\sigma^{4\text{FS}} + \alpha\sigma^{5\text{FS}})/1 + \alpha, \quad (165)$$

with  $\alpha = \ln\left(\frac{m_{H^\pm}}{\tilde{m}_b}\right) - 2$ . The uncertainties are combined as  $\delta\sigma^{\text{matched}} = \frac{\delta\sigma^{4\text{FS}} + \alpha\delta\sigma^{5\text{FS}}}{1 + \alpha}$ . The results are shown in Table 49.

---

<sup>29</sup>Email: a.abouibrahim@northeastern.edu

<sup>30</sup>Email: p.nath@northeastern.edu

Model	$\sigma_{\text{NLO}}^{\text{4FS}}(pp \rightarrow tbH^\pm)$		$\sigma_{\text{NLO}}^{\text{5FS}}(pp \rightarrow tH^\pm)$		$\sigma_{\text{NLO}}^{\text{matched}}$		$\mu_F = \mu_R$ (GeV)	$\bar{m}_b$
	14 TeV	27 TeV	14 TeV	27 TeV	14 TeV	27 TeV		
(a)	49.0 <sup>+12.6%</sup> <sub>-13.1%</sub>	272.8 <sup>+9.2%</sup> <sub>-10.3%</sub>	71.8 <sup>+6.6%</sup> <sub>-5.7%</sub>	397.1 <sup>+7.0%</sup> <sub>-6.6%</sub>	65.9 <sup>+8.1%</sup> <sub>-7.6%</sub>	365.4 <sup>+7.6%</sup> <sub>-7.5%</sub>	183.6	2.72
(b)	34.5 <sup>+10.6%</sup> <sub>-12.1%</sub>	204.6 <sup>+8.1%</sup> <sub>-9.6%</sub>	58.3 <sup>+7.0%</sup> <sub>-5.9%</sub>	336.1 <sup>+6.9%</sup> <sub>-6.5%</sub>	52.4 <sup>+7.9%</sup> <sub>-7.4%</sub>	303.5 <sup>+7.2%</sup> <sub>-7.3%</sub>	197.9	2.70
(c)	29.1 <sup>+11.1%</sup> <sub>-12.3%</sub>	175.9 <sup>+8.2%</sup> <sub>-9.7%</sub>	48.8 <sup>+6.7%</sup> <sub>-5.7%</sub>	285.9 <sup>+6.4%</sup> <sub>-6.0%</sub>	43.9 <sup>+7.8%</sup> <sub>-7.3%</sub>	259.0 <sup>+6.8%</sup> <sub>-6.9%</sub>	205.6	2.69
(d)	24.8 <sup>+10.9%</sup> <sub>-12.3%</sub>	149.9 <sup>+7.1%</sup> <sub>-9.1%</sub>	42.6 <sup>+6.3%</sup> <sub>-5.3%</sub>	264.8 <sup>+6.8%</sup> <sub>-6.2%</sub>	38.3 <sup>+7.4%</sup> <sub>-6.9%</sub>	237.2 <sup>+6.8%</sup> <sub>-6.9%</sub>	215.9	2.68
(e)	18.4 <sup>+11.2%</sup> <sub>-12.4%</sub>	120.1 <sup>+8.3%</sup> <sub>-9.8%</sub>	32.3 <sup>+5.9%</sup> <sub>-4.9%</sub>	206.7 <sup>+6.4%</sup> <sub>-6.0%</sub>	29.0 <sup>+7.1%</sup> <sub>-6.7%</sub>	186.3 <sup>+6.8%</sup> <sub>-6.9%</sub>	229.6	2.67
(f)	13.6 <sup>+11.3%</sup> <sub>-12.5%</sub>	93.2 <sup>+7.8%</sup> <sub>-9.5%</sub>	25.1 <sup>+6.1%</sup> <sub>-5.2%</sub>	169.6 <sup>+6.7%</sup> <sub>-6.0%</sub>	22.4 <sup>+7.3%</sup> <sub>-6.9%</sub>	152.1 <sup>+7.0%</sup> <sub>-6.8%</sub>	248.2	2.65
(g)	13.1 <sup>+10.5%</sup> <sub>-12%</sub>	95.8 <sup>+7.6%</sup> <sub>-9.5%</sub>	26.0 <sup>+6.2%</sup> <sub>-5.6%</sub>	185.1 <sup>+6.7%</sup> <sub>-6.0%</sub>	23.1 <sup>+7.2%</sup> <sub>-7.0%</sub>	165.0 <sup>+6.8%</sup> <sub>-6.8%</sub>	264.6	2.64
(h)	11.2 <sup>+10.3%</sup> <sub>-12.0%</sub>	85.1 <sup>+7.5%</sup> <sub>-9.4%</sub>	22.7 <sup>+6.1%</sup> <sub>-5.8%</sub>	168.3 <sup>+6.8%</sup> <sub>-5.9%</sub>	20.2 <sup>+7.0%</sup> <sub>-7.2%</sub>	149.9 <sup>+6.9%</sup> <sub>-6.7%</sub>	278.2	2.63
(i)	7.8 <sup>+11.7%</sup> <sub>-12.6%</sub>	61.1 <sup>+8.1%</sup> <sub>-9.8%</sub>	15.8 <sup>+6.0%</sup> <sub>-6.0%</sub>	121.0 <sup>+6.9%</sup> <sub>-6.0%</sub>	14.0 <sup>+7.2%</sup> <sub>-7.4%</sub>	107.9 <sup>+7.2%</sup> <sub>-6.8%</sub>	292.9	2.62
(j)	5.5 <sup>+12.6%</sup> <sub>-13.0%</sub>	48.9 <sup>+9.1%</sup> <sub>-10.3%</sub>	11.6 <sup>+6.7%</sup> <sub>-6.5%</sub>	99.4 <sup>+6.4%</sup> <sub>-5.5%</sub>	10.3 <sup>+7.9%</sup> <sub>-7.8%</sub>	88.7 <sup>+6.9%</sup> <sub>-6.5%</sub>	329.9	2.60

Table 49: The NLO production cross-sections, in fb, of the charged Higgs in association with a top (and bottom) quark in the five (and four) flavour schemes along with the matched values at  $\sqrt{s} = 14$  TeV and  $\sqrt{s} = 27$  TeV for the ten benchmark points in [?]. The running  $b$ -quark mass,  $\bar{m}_b$ , is also shown evaluated at the factorization and normalization scales,  $\mu_F = \mu_R = \frac{1}{3}(m_t + \bar{m}_b + m_{H^\pm})$ .

For the parameter points considered, the  $H^\pm \rightarrow \tau\nu$  channel has the smallest branching ratio but it is of interest since jets can be tau-tagged and the tau has leptonic and hadronic decay signatures. For the considered signal final states (fully hadronic), the SM backgrounds are mainly  $t\bar{t}$ ,  $t+\text{jets}$ ,  $W/Z/\gamma^*+\text{jets}$ , diboson production and QCD multijet events which can fake the hadronic tau decays. The simulation of the charged Higgs associated production,  $t[b]H^\pm$ , is done at fixed order in NLO while the SM backgrounds are done at LO (which are then normalized to their NLO values) using MadGraph interfaced with LHAPDF [16] and PYTHIA8 [132] which handles the showering and hadronization of the samples. For the SM backgrounds a five-flavor MLM matching [133] is performed on the samples. Detector simulation and event reconstruction is performed by DELPHES-3.4.2 [176] using the beta card for HL-LHC and HE-LHC studies.

The selection criteria depends on the flavour scheme under consideration. For the 4FS (5FS) we apply a lepton veto and at least five (four) jets, two (one) of which are (is) b-tagged and one is tau-tagged. To discriminate the signal from background we use gradient boosted decision trees (BDT), GradientBoost, which proves to be more powerful than the conventional cut-based analysis. A large set of variables have been tried in the BDT training and the ones which produced the best results were kept. The kinematic variables entering into the training of the BDTs are:

$$\begin{aligned} & E_T^{\text{miss}}, \quad E_T^{\text{miss}}/\sqrt{H_T}, \quad m_{T2}^{\text{jets}}, \quad m_T^\tau, \quad p_T^\tau, \quad E_T^{\text{miss}}/m_{\text{eff}}, \\ & m_T^{\min}(j_{1-2}, E_T^{\text{miss}}), \quad \Delta\phi(p_T^\tau, E_T^{\text{miss}}), \quad N_{\text{tracks}}^\tau, \quad \sum_{\text{tracks}} p_T. \end{aligned} \quad (166)$$

The training and testing of the samples is carried out using ROOT's [?] own TMVA (Toolkit for Multivariate Analysis) framework [?]. After the training and testing phase, the variable "BDT score" is created. We apply the selection criteria (as given in [?]) along with a BDT score cut  $> 0.95$  on the SM background and on each of the 4FS and 5FS signal samples to obtain the remaining cross-sections. The signal cross-sections are combined using Eq. (165) in order to evaluate the required minimum integrated luminosity for a  $\frac{S}{\sqrt{S+B}}$  discovery at the  $5\sigma$  level. The results for both the 14 and 27 TeV cases are shown in Fig. 125.

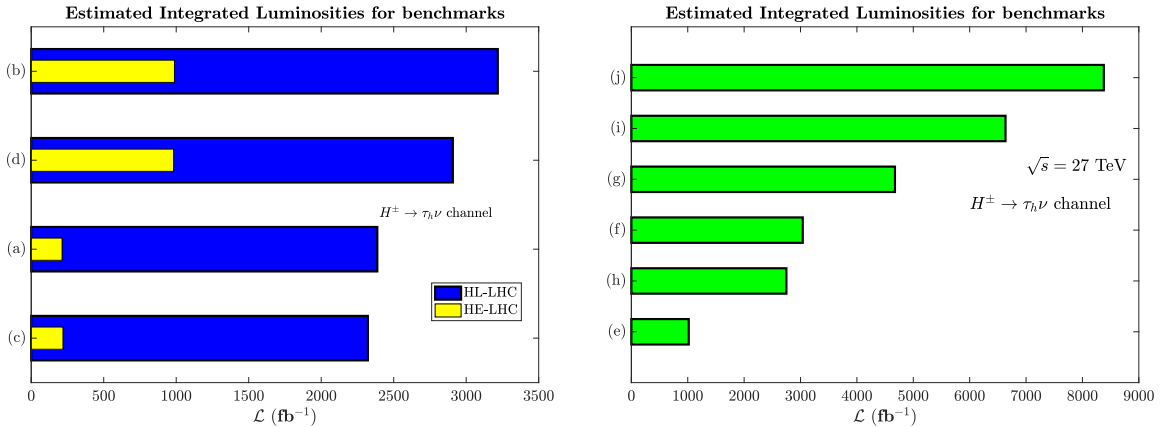


Fig. 125: The evaluated integrated luminosities,  $\mathcal{L}$  ( $\text{fb}^{-1}$ ), for ten benchmark points. Left plot: calculated  $\mathcal{L}$  for points discoverable at both HL-LHC and HE-LHC. Right plot: calculated  $\mathcal{L}$  for points discoverable only at HE-LHC.

One can see from Fig. 125 that four of the ten points may be discoverable at the HL-LHC as it nears the end of its run where a maximum integrated luminosity of  $3000 \text{ fb}^{-1}$  will be collected. Given the rate at which the HL-LHC will be collecting data, points (a)-(d) will require  $\sim 7$  years of running time. On the other hand, the results from the 27 TeV collider show that all points may be discoverable for integrated luminosities much less than  $15 \text{ ab}^{-1}$ . The HE-LHC will be collecting data at a rate of  $\sim 820 \text{ fb}^{-1}$  per year and with that points (a) and (c) may be discoverable within the first 3 months of operation, points (b), (d) and (e) may take  $\sim 1.2$  years, points (h) and (f)  $\sim 3.5$  years and the rest of the points  $> 6$  years.

**Acknowledgments:** This research was supported in part by the NSF Grant PHY-1620575.

## 9.6 Interference effects in heavy Higgs searches

31 32

The singlet SM extension serves as the simplest, yet elusive benchmark to test a sufficiently strong first-order phase transition compatible with the Higgs boson mass measurements at the LHC. The singlet without  $Z_2$  protection could mix with the SM Higgs and (in most cases) a promptly decaying scalar particle would provide a rich phenomenology at colliders. The singlet scalar could be produced resonantly and decay back to pairs of SM particles, dominantly into  $WW$ ,  $ZZ$ ,  $HH$  and  $t\bar{t}$ . The signal of a singlet scalar resonance decaying into  $HH$  is a smoking-gun for singlet enhanced EWPT [?, ?, ?, ?, ?, ?, ?, 7, 205].

Searches for resonant di-Higgs production have received much attention by both the ATLAS and CMS collaborations [?, ?, ?, 206–208]. In the case of a singlet resonance, constraints from SM precision measurements render these searches more challenging. From one side precision measurements imply that the singlet-doublet mixing parameter is constrained to be small over a large region of parameter space. From the other side, the singlet only couples to SM particles through mixing with the SM Higgs doublet.

<sup>31</sup> Authors: Marcela Carena<sup>a,b,c</sup>, and Zhen Liu<sup>a,d</sup>, Marc Riembau<sup>e,f</sup>

<sup>a</sup> Theoretical Physics Department, Fermi National Accelerator Laboratory, Batavia, Illinois, 60510, USA

<sup>b</sup> Enrico Fermi Institute, University of Chicago, Chicago, Illinois, 60637, USA

<sup>c</sup> Kavli Institute for Cosmological Physics, University of Chicago, Chicago, Illinois, 60637, USA

<sup>d</sup> Maryland Center for Fundamental Physics, Department of Physics, University of Maryland, College Park, MD 20742

<sup>e</sup> IFAE and BIST, Universitat Autònoma de Barcelona, E-08193 Bellaterra, Barcelona, Spain

<sup>f</sup> DESY, Notkestraße 85, D-22607 Hamburg, Germany

<sup>32</sup> This manuscript has been authored by Fermi Research Alliance, LLC under Contract No. DE-AC02-07CH11359 with the U.S. Department of Energy, Office of Science, Office of High Energy Physics. ZL is also supported by the NSF under Grant No. PHY1620074 and by the Maryland Center for Fundamental Physics (MCFP).

This results in a reduced di-Higgs production via singlet resonance decays. In particular, the singlet resonance amplitude becomes of the same order as the SM triangle and box diagram amplitudes. Most important, in this work we shall show that a large relative phase between the SM box diagram and the singlet triangle diagram becomes important. This special on-shell interference effect has been commonly overlooked in the literature and turns out to have important phenomenological implications. We shall choose the spontaneous  $Z_2$  breaking scenario of the SM plus singlet to demonstrate the importance of the novel on-shell interference effect for the resonant singlet scalar searches in the di-Higgs production mode.

### MODEL FRAMEWORK

We will consider the simplest extension of the SM that can assist the scalar potential to induce a strongly first-order electroweak phase transition, consisting of an additional real scalar singlet with a  $Z_2$  symmetry. The scalar potential of the model can be written as

$$V(s, \phi) = -\mu^2 \phi^\dagger \phi - \frac{1}{2} \mu_s^2 s^2 + \lambda (\phi^\dagger \phi)^2 + \frac{\lambda_s}{4} s^4 + \frac{\lambda_{s\phi}}{2} s^2 \phi^\dagger \phi, \quad (167)$$

where  $\phi$  is the SM doublet<sup>33</sup> and  $s$  represents the new real singlet field. In the above, we adopt the conventional normalization for the couplings of the SM doublets and match the other couplings with the singlet with identical normalization. We allow for spontaneous  $Z_2$  breaking with the singlet  $s$  acquiring a vacuum expectation value (vev)  $v_s$ , since this case allows for interesting collider phenomenology of interference effects. As we shall show later, the (on-shell) interference effects commonly exist for loop-induced processes in BSM phenomenology and it is the focus of this paper. The CP even neutral component  $h$  of the Higgs doublet field  $\phi$  mixes with the real singlet scalar  $s$ , defining the new mass eigenstates  $H$  and  $S$

$$\begin{pmatrix} h \\ s \end{pmatrix} = \begin{pmatrix} \cos \theta & \sin \theta \\ -\sin \theta & \cos \theta \end{pmatrix} \begin{pmatrix} H \\ S \end{pmatrix}, \quad (168)$$

where  $\theta$  is the mixing angle between these fields. The five free parameters in Eq. (167) can be traded by the two boundary conditions

$$m_H = 125 \text{ GeV}, \quad v = 246 \text{ GeV} \quad (169)$$

and the three “physical” parameters,

$$m_S, \quad \tan \beta (\equiv \frac{v_s}{v}), \quad \text{and } \sin \theta, \quad (170)$$

where  $\tan \beta$  characterizes the ratio between the vevs of the doublet and the singlet scalar fields, respectively. Detailed relations between the bare parameters and physical parameters can be found in Ref. [?].

### ENHANCING THE DI-HIGGS SIGNAL VIA INTERFERENCE EFFECTS

The on-shell interference effect may enhance or suppress the conventional Breit-Wigner resonance production. Examples in Higgs physics known in the literature, such as  $gg \rightarrow h \rightarrow \gamma\gamma$  [?] and  $gg \rightarrow H \rightarrow t\bar{t}$  [?], are both destructive. We discuss in detail in this section the on-shell interference effect between the resonant singlet amplitude and the SM di-Higgs box diagram. We shall show that in the singlet extension of the SM considered in this paper, the on-shell interference effect is generically constructive and could be large in magnitude, thus enhances the signal production rate.

The interference effect between two generic amplitudes can be denoted as nonresonant amplitude  $A_{nr}$  and resonant amplitude  $A_{res}$ . The resonant amplitude  $A_{res}$ , defined as

$$A_{res} = a_{res} \frac{\hat{s}}{\hat{s} - m^2 + i\Gamma m}, \quad (171)$$

---

<sup>33</sup>  $\phi^T = (G^+, \frac{1}{\sqrt{2}}(h + iG^0 + v))$ , where  $G^{\pm,0}$  are the Goldstone modes.

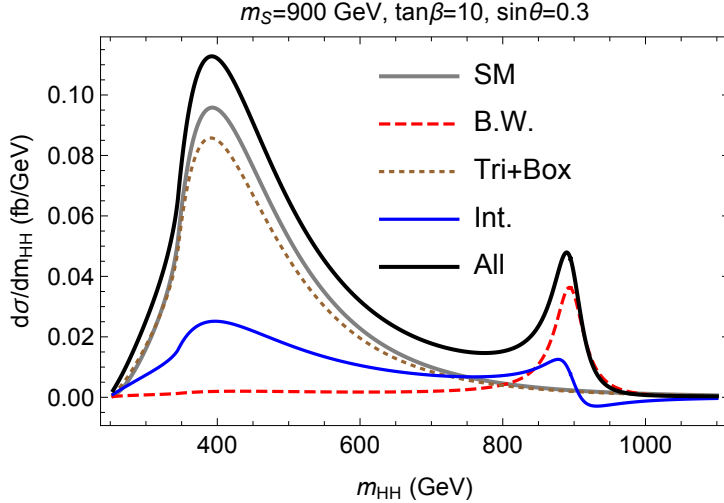


Fig. 126: The differential di-Higgs distribution for a benchmark point of the singlet extension of the SM shown in linear scale and over a broad range of the di-Higgs invariant mass. The full results for the SM and the singlet SM extension are shown by the gray and black curves, respectively. In the singlet extension of the SM, the contributions from the resonant singlet diagram, the nonresonant diagram and the interference between them are shown in red (dashed), brown (dotted) and blue curves, respectively.

has a pole in the region of interest and we parametrize it as the product of a fast varying piece containing its propagator and a slowly varying piece  $a_{res}$  that generically is a product of couplings and loop-functions. The general interference effect can then be parametrized as [?, ?],

$$\begin{aligned}
 |\mathcal{M}|_{int}^2 &= 2\Re(A_{res} \times A_{nr}^*) = 2(\mathcal{I}_{int} + \mathcal{R}_{int}), \\
 \mathcal{R}_{int} &\equiv |A_{nr}| |a_{res}| \frac{\hat{s}(\hat{s} - m^2)}{(\hat{s} - m^2)^2 + \Gamma^2 m^2} \cos(\delta_{res} - \delta_{nr}) \\
 \mathcal{I}_{int} &\equiv |A_{nr}| |a_{res}| \frac{\hat{s}\Gamma m}{(\hat{s} - m^2)^2 + \Gamma^2 m^2} \sin(\delta_{res} - \delta_{nr}),
 \end{aligned} \tag{172}$$

where  $\delta_{res}$  and  $\delta_{nr}$  denote the complex phases of  $a_{res}$  and  $A_{nr}$ , respectively.

The special interference effect  $\mathcal{I}_{int}$  only appears between the singlet resonant diagram and the SM box diagram. This interference effect is proportional to the relative phase between the loop functions  $\sin(\delta_{\triangleright} - \delta_{\square})$  and the imaginary part of the scalar propagator which is sizable near the scalar mass pole.

### Differential distribution

We present in this section our analysis of the differential distribution of the Higgs pair invariant mass to estimate the relevance of the interference effects discussed in the previous section. We choose one of the best channels,  $pp \rightarrow HH \rightarrow b\bar{b}\gamma\gamma$ , as the benchmark channel to present the details of our analysis. Furthermore, we discuss another phenomenologically relevant piece of interference in the far off-shell region of the singlet scalar. We display the discovery and exclusion reach for both HL-LHC and HE-LHC for various values of  $\tan \beta$  in the  $m_S$ - $\sin \theta$  plane.

In Fig. 126 we display the differential cross section as a function of the Higgs pair invariant mass for a benchmark point with a heavy scalar mass of 900 GeV, mixing angle  $\sin \theta = 0.3$  and  $\tan \beta = 10$ . The differential cross section is shown in linear scale for a broad range of di-Higgs invariant masses, including the low invariant mass regime favored by parton distribution functions at hadron colliders.

We choose this benchmark to show well the separation of the scalar resonance peak and the threshold enhancement peak above the  $t\bar{t}$ -threshold. The SM Higgs pair invariant mass distribution is given

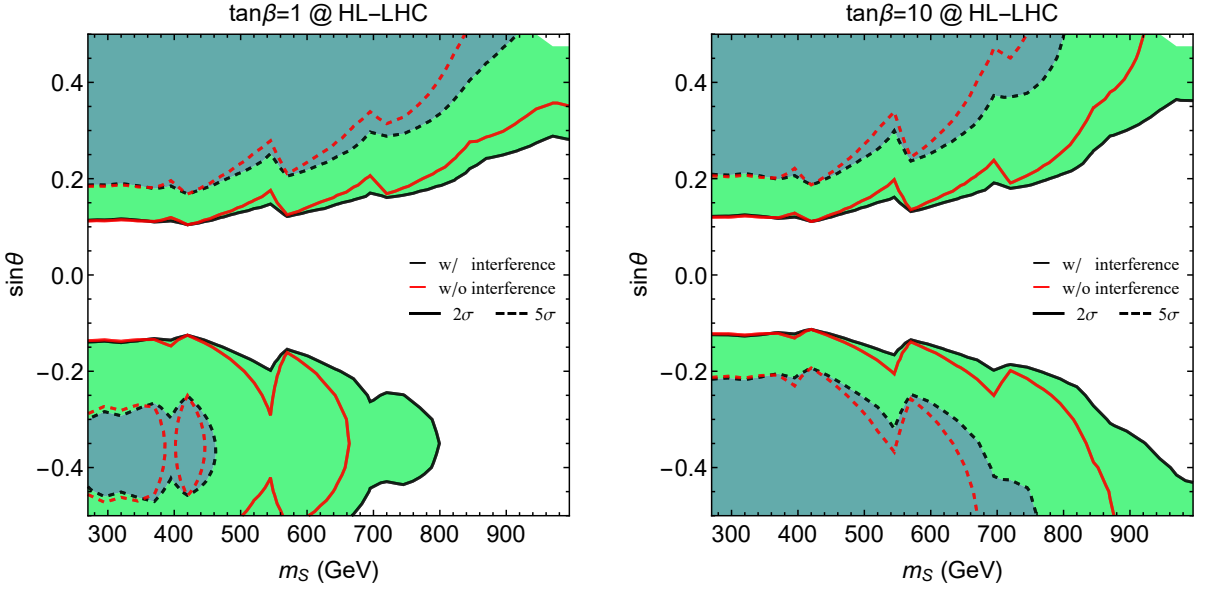


Fig. 127: Projected exclusion and discovery limits at HL-LHC in the  $m_S$ - $\sin \theta$  plane with the line-shape analysis detailed in the text for  $\tan \beta = 1$  (left panel) and  $\tan \beta = 10$  (right panel). The shaded regions bounded by dashed/solid curves are within the discovery/exclusion reach of the HL-LHC. The black and red lines represent the projection with and without the inclusion of the interference effects between the singlet resonance diagram and the SM Higgs pair diagram, respectively.

by the gray curve while the black curve depicts the di-Higgs invariant mass distribution from the singlet extension of the SM. It is informative to present all three pieces that contribute to the full result of the di-Higgs production, namely, the resonance contribution (red, dashed curve), the SM nonresonance contribution (box and triangle diagrams given by the brown, dotted curve), and the interference between them (blue curve). Note that the small difference between the “Tri+Box” and the “SM” line shapes is caused by the doublet-singlet scalar mixing, which leads to a  $\cos \theta$  suppression of the SM-like Higgs coupling to top quarks as well as a modified SM-like Higgs trilinear coupling  $\lambda_{HHH}$ . We observe that the full results show an important enhancement in the di-Higgs production across a large range of invariant masses. This behavior is anticipated from the decomposition analysis in the previous section. There is a clear net effect from the interference curve shown in blue. Close to the the scalar mass pole at 900 GeV, the on-shell interference effect enhances the Breit-Wigner resonances peak (red, dashed curve) by about 25%. Off-the resonance peak, and especially at the threshold peak, the interference term (blue curve) enhances the cross section quite sizably as well. Hence, a combined differential analysis in the Higgs pair invariant mass is crucial in probing the singlet extension of the SM.

### ***Discovery and exclusion reach at the HL- and HE-LHC***

Using the analysis detailed in Ref. [?] through the  $pp \rightarrow HH \rightarrow \gamma\gamma b\bar{b}$  channel, we obtain the discovery and exclusion projections for the HL-LHC and HE-LHC. In Fig. 127 we show the projected 2- $\sigma$  exclusion and 5- $\sigma$  discovery reach for the HL-LHC in the  $m_S$ - $\sin \theta$  plane for  $\tan \beta = 1$  (left panel) and  $\tan \beta = 10$  (right panel) in solid and dashed curves, respectively. The shaded regions are within the reach of the HL-LHC for discovery and exclusion projections. To demonstrate the relevance of the interference effects discussed in the previous sections, we show both the results obtained with and without the inclusion of the interference effects in black and red contours, respectively.

We observe in Fig. 127 that the inclusion of the interference effects extend the projections in a

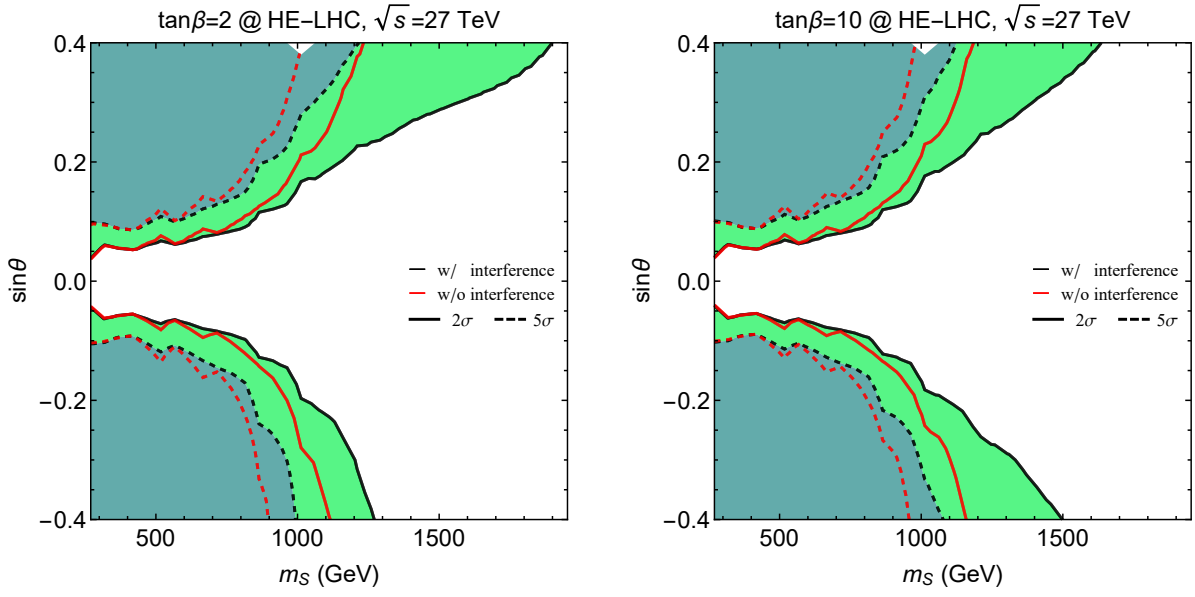


Fig. 128: Similar to Fig. 127, projected exclusion and discovery limits at HE-LHC with 27 TeV center of mass energy and an integrated luminosity of  $10 \text{ ab}^{-1}$  for  $\tan\beta = 2$  (left panel) and  $\tan\beta = 10$  (right panel).

relevant way. For example, considering the  $\tan\beta = 10$  case in the right panel for  $\sin\theta \simeq 0.35$  the interference effect increase the exclusion limit on  $m_S$  from 850 GeV to 1000 GeV. Note that the on-shell interference effect is larger for heavier scalar mass  $m_S$ .

In Fig. 128 we show the projections for the HE-LHC in a analogous fashion as in Fig. 127. The discovery and exclusion reach for heavy scalars can be significantly extended by the HE-LHC operating at 27 TeV center of mass energy with  $10 \text{ ab}^{-1}$  of integrated luminosity. We show the results for  $\tan\beta = 2$  (left panel) and  $\tan\beta = 10$  (right panel). For example, considering the  $\tan\beta = 2$  case in the right panel of Fig. 128, for  $\sin\theta \simeq 0.35$  the exclusion reach increases from 1200 to 1800 GeV, once more showing the importance of including the on-shell interference effects.

### Summary and outlook

In this study, we analyze the interference effects in the  $gg \rightarrow HH$  process in the presence of a heavy scalar resonance. We focus on the novel effect of the on-shell interference contribution and discuss it in detail considering the framework of the singlet extension of the SM with spontaneous  $Z_2$  breaking. The interference pattern between the resonant heavy scalar contribution and the SM nonresonant triangle and box contributions show interesting features. We highlight the constructive on-shell interference effect that uniquely arises between the heavy scalar resonance diagram and the SM box diagram, due to a large relative phase between the loop functions involved. We observe that the on-shell interference effect can be as large as 40% of the Breit-Wigner resonance contribution and enhances notably the total signal strength, making it necessary taking into account in heavy singlet searches.

To better evaluate the phenomenological implications of the interference effects in the di-Higgs searches, we carried out a line-shape analysis in the  $gg \rightarrow HH \rightarrow \gamma\gamma b\bar{b}$  channel, taking into account both the on-shell and off-shell interference contributions. We find that both for the HL-LHC and HE-LHC, the proper inclusion of the interference effects increases the discovery and exclusion reach significantly.

## 9.7 All contributions below: Move your contribution to a separate file!

## 9.8 Interpretation of the Higgs couplings in terms of Composite Higgs models

L. Vecchi

Theoretical Particle Physics Laboratory, Institute of Physics, EPFL, Lausanne, Switzerland

### 9.8.1 Introduction

- Composite Higgs (CH) models provide a natural solution to the hierarchy problem. Main assumption: a strong sector generates a light scalar  $H$  (with the same charges of the SM Higgs doublet) that breaks  $SU(2) \times U(1)$ .
- Several realizations of the CH proposed in the literature predict the existence of additional light particles beyond the Higgs, e.g. scalars in non-minimal  $G \rightarrow H$ , a dilaton in nearly-conformal models, fermion resonances to reduce the fine-tuning, vector resonances in Little Higgs models. Here however we will assume that all exotic particles are heavy enough to be directly inaccessible. Within this assumption, an effective field theory formalism becomes reliable.
- The main goal of this section is to (1) review what are the most important corrections to the Higgs couplings that are expected if the Higgs is a composite state; (2) estimate the sensitivity of the HL and HE-LHC on the CH picture. We will focus on modifications of the Higgs couplings (as opposed to off-shell rates like double-Higgs production or  $VV \rightarrow VV, hh$  scattering).
- Up to dimension 6, the operators that can potentially impact on-shell processes involving the Higgs boson are collected in table 50. Note that  $O_r = H^\dagger H (D_\mu H)^\dagger D^\mu H$  is not part of the set because equivalent to a linear combination of  $\sum_\psi \mathcal{O}_\psi$  and  $\mathcal{O}_{H,6}$ . Similarly,  $gg' H^\dagger \sigma^i H W_{\mu\nu}^i B^{\mu\nu}$  and  $g^2 H^\dagger H W_{\mu\nu}^i W^{i\mu\nu}$ , as well as their CP-odd versions, are not independent. Finally, there is a set of operators involving the Higgs doublet that are severely constrained by precision data, and for this reason are expected to be negligible in our analysis. These include  $O_T = \frac{1}{2} (H^\dagger \overleftrightarrow{D}_\mu H)(H^\dagger \overleftrightarrow{D}^\mu H)$ , current-current interactions  $H^\dagger \overleftrightarrow{D}^\mu H \bar{\psi} \gamma^\mu \psi$  and  $H^\dagger \tau^a \overleftrightarrow{D}^\mu H \bar{\psi} \gamma^\mu \tau^a \psi$  containing non-universal couplings to the SM fermions  $\psi$ , and dipole operators. The coefficient of the operator  $O_T$  contributes to the EW  $T$  parameter, and may be suppressed assuming the strong sector respects a custodial  $SU(2)$  symmetry. The current-current operators are constrained by LEP and the non-observation of rare flavor-violating processes. Dipole operators are severely constrained by measurements of dipole moments. (The only exception is provided by those interactions involving the top...)

### 9.8.2 Modified Higgs couplings

- The observables that are mostly affected by the new operators are shown in the third column of table 50. An estimate of the various Wilson coefficients in concrete CH models reveals that (1) corrections to  $h \rightarrow VV^*$  are typically dominated by  $\mathcal{O}_{H,\psi}$ , (2) corrections to the radiative processes  $h \rightarrow gg, \gamma\gamma, Z^0\gamma$  are controlled by  $\mathcal{O}_{H,\psi}$  if the Higgs is a Nambu-Goldstone mode and receive important contributions also from  $\mathcal{O}_{g,\gamma}$  if  $H$  is an accidentally resonance. The bottom line is that the reduced set of operators

$$\delta\mathcal{L}_{\text{eff}} = \frac{g_*^2}{m_*^2} c_H \mathcal{O}_H + \frac{g_*^2}{m_*^2} \sum_\psi c_\psi \mathcal{O}_\psi + \frac{1}{m_*^2} c_g \mathcal{O}_g + \frac{1}{m_*^2} c_\gamma \mathcal{O}_\gamma, \quad (173)$$

can be used to characterize the most common signatures of realistic CH models.

- A few benchmark models in which the coefficients can be reliably estimated is presented. For example, a  $O(5)/O(4)$  CH model with fermions in some representation of  $O(5)$ . The possible existence of additional symmetries (custodial symmetry,  $G \rightarrow H$ ,  $T$ -parity, etc.) has implications on the Wilson coefficients.

Operator name	Operator definition	Main On-shell (Higgs)
$\mathcal{O}_H$	$\frac{1}{2} \partial_\mu (H^\dagger H) \partial^\mu (H^\dagger H)$	$h \rightarrow \psi\bar{\psi}, VV^*$
$\mathcal{O}_T$	$\frac{1}{2} (H^\dagger \overleftrightarrow{D}_\mu H) (H^\dagger \overleftrightarrow{D}^\mu H)$	$h \rightarrow ZZ^*$
$\mathcal{O}_6$	$\lambda_h (H^\dagger H)^3$	off-shell $h^* \leftrightarrow hh$
$\mathcal{O}_\psi$	$y_\psi \bar{\psi}_L H \psi_R (H^\dagger H)$	$h \rightarrow \psi\bar{\psi}$
$\mathcal{O}_W$	$\frac{i}{2} g (H^\dagger \sigma^i \overleftrightarrow{D}_\mu H) (D_\nu W^{\mu\nu})^i$	$h \rightarrow VV^*$
$\mathcal{O}_B$	$\frac{i}{2} g' (H^\dagger \overleftrightarrow{D}_\mu H) (\partial_\nu B^{\mu\nu})$	$h \rightarrow VV^*$
$\mathcal{O}_{HW}$	$ig (D^\mu H)^\dagger \sigma^i (D^\nu H) W_{\mu\nu}^i$	$h \rightarrow VV^*, \gamma Z$
$\mathcal{O}_{HB}$	$ig' (D^\mu H)^\dagger (D^\nu H) B_{\mu\nu}$	$h \rightarrow VV^*, \gamma Z$
$\mathcal{O}_g$	$g_s^2 H^\dagger H G_{\mu\nu}^a G^{a\mu\nu}$	$h \rightarrow gg$
$\mathcal{O}_\gamma$	$g'^2 H^\dagger H B_{\mu\nu} B^{\mu\nu}$	$h \rightarrow \gamma\gamma, \gamma Z^0, Z^0 Z^0$

Table 50: List of the most relevant dimension-6 operators in the study of modified Higgs couplings in CH models. We use the basis of [75]. Here  $y_\psi$  are the SM Yukawa couplings and  $V = Z^0, W^\pm$ . CP-odd versions of  $HW, HB, \gamma, g$  can be obtained by replacing one field strength with the corresponding dual,  $F^{\mu\nu} \rightarrow \frac{1}{2}\epsilon^{\mu\nu\alpha\beta}F_{\alpha\beta}$ . The third column shows the dominant on-shell Higgs processes that the operator contributes to.

- We can now match the Wilson coefficients derived above onto a Lagrangian for the physical Higgs (see e.g. [?]):

$$\begin{aligned}
\mathcal{L}_h = & \frac{1}{2} \partial_\mu h \partial^\mu h - \frac{1}{2} m_h^2 h^2 \\
& + \left[ m_W^2 W_\mu^+ W^{-\mu} + \frac{1}{2} m_Z^2 Z_\mu Z^\mu \right] \left( 1 + c_V \frac{h}{v} + \dots \right) \\
& - \sum_{\psi=u,d,l} m_\psi \bar{\psi} \psi \left( 1 + c_\psi \frac{h}{v} + \dots \right) \\
& + \left[ \frac{1}{2} c_{gg} G_{\mu\nu}^a G^{a\mu\nu} + \frac{1}{2} c_{\gamma\gamma} \gamma_{\mu\nu} \gamma^{\mu\nu} + \frac{1}{2} c_{ZZ} Z_{\mu\nu} Z^{\mu\nu} + c_{Z\gamma} Z_{\mu\nu} \gamma^{\mu\nu} \right] \frac{h}{v} \\
& + \dots
\end{aligned} \tag{174}$$

with the modified Higgs couplings defined by

$$\begin{aligned}
c_V &= 1 - \frac{c_H}{2} \xi \\
c_\psi &= 1 - \left( \frac{c_H}{2} + c_\psi \right) \xi \\
c_{gg} &= 2 \frac{g_s^2}{g_*^2} \xi c_g \\
c_{\gamma\gamma} &= -\frac{c_{Z\gamma}}{\tan \theta_W} = \frac{c_{ZZ}}{\tan^2 \theta_W} = 2 \frac{e^2}{g_*^2} \xi c_\gamma
\end{aligned} \tag{175}$$

and

$$\xi \equiv \frac{g_*^2 v^2}{m_*^2}. \tag{176}$$

- We can then present the expected reach of the HL and HE LHC on the modified Higgs couplings. **This is where some experimental input would be appreciated.** We can briefly compare it with current constraints and proposed experiments.

- Using (174) (175) under the generic and reasonable assumption  $c_{H,\psi} = 1$ , the limits on the modified Higgs couplings translate into an indirect sensitivity on the new physics scale  $m_*$  as a function of the size of the coupling  $g_*$ . We will show a plot that should quantify how a direct bound on the modified Higgs couplings + no direct access to new physics translates into a bound on the new physics parameters.
- I will finally comment on the fact that  $c_V \neq 1$  also leads to exotic contributions to the electroweak precision parameters (e.g.  $S, T$ ). However, these probes on the new physics are *indirect* and significantly depend on corrections at the cutoff scale (where new model-dependent particles are expected to emerge). Hence, while *indirect* bounds can be used to derive very stringent constraints, *direct* probes of the Higgs couplings provide a more robust and model-independent access to the new physics scale and coupling.

## 9.9 Interpretation of the Higgs couplings in terms of SUSY models

## 9.10 Direct and indirect sensitivity to heavy Higgs bosons using MSSM benchmark scenarios

by Philip Bechtle, Sven Heinemeyer, Stefan Liebler, Tim Stefaniak and Georg Weiglein

### **Introduction**

The LHC keeps measuring the properties of the discovered Higgs boson with increasing precision. So far the measured properties are, within current experimental and theoretical uncertainties, in agreement with the predictions of the Standard Model (SM) [25]. The Minimal Supersymmetric Standard Model (MSSM) [?, ?, ?] is one of the best studied models with an extended Higgs sector. It predicts two scalar partners for all SM fermions as well as fermionic partners to all SM bosons. Contrary to the case of the SM, the MSSM contains two Higgs doublets. This results in five physical Higgs bosons instead of the single Higgs boson in the SM. In the absence of  $\mathcal{CP}$ -violating phases, these are the light and heavy  $\mathcal{CP}$ -even Higgs bosons,  $h$  and  $H$ , the  $\mathcal{CP}$ -odd Higgs boson,  $A$ , and the charged Higgs bosons,  $H^\pm$ .

In order to facilitate collider searches for the additional MSSM Higgs bosons, a set of new benchmark scenarios for MSSM Higgs boson searches at the LHC have been proposed recently [?]. The scenarios are compatible – at least over wide portions of their parameter space – with the most recent LHC results for the Higgs-boson properties and the bounds on masses and couplings of new particles. Each scenario contains one  $\mathcal{CP}$ -even scalar with mass around 125 GeV and SM-like couplings. However, the scenarios differ importantly in the phenomenology of the additional, so far undetected Higgs bosons.

The search for the additional Higgs bosons will continue at the LHC Run 3 and subsequently at the HL-LHC. These benchmark scenarios, due to their distinct phenomenology of the additional Higgs bosons, serve well to assess the reach of current and future colliders. The reach can either be direct, via the search for new Higgs bosons, or indirectly, via the precise measurements of the properties of the Higgs boson at  $\sim 125$  GeV.

### **Experimental and theoretical input**

In order to analyze the potential of the HL-LHC in the exploration of the MSSM Higgs sector we evaluate the direct and indirect physics reach in two of the benchmark scenarios proposed in Ref. [?]. The first scenario is the  $M_h^{125}$ : it is characterized by relatively heavy superparticles, such that the Higgs phenomenology at the LHC resembles that of a Two-Higgs-Doublet-Model (2HDM) with MSSM-inspired Higgs couplings. The second scenario is the  $M_h^{125}(\tilde{\chi})$ . It is characterized by light electroweakinos (EWinos), resulting in large decay rates of the heavy Higgs bosons  $H$  and  $A$  into charginos and neutralinos, thus diminishing the event yield of the  $\tau^+ \tau^-$  final state signatures that are used to search for the additional Higgs bosons at the LHC. In addition, the branching ratios of the Higgs boson at 125 GeV into a pair of photons is enhanced for small values of  $\tan \beta$  due to the EWinos present in the loop.

We assess the reach of direct LHC searches in the  $\tau^+\tau^-$  final state by applying the HL-LHC projected 95% CL limits from the CMS experiment [add reference to corresponding Section in the YR report].<sup>34</sup> CMS evaluated these projections both for the  $m_h^{\text{mod}+}$  scenario [?] and for one-dimensional (marginalized) cross section limits on either the gluon fusion or  $b\bar{b}$ -associated production mode. We implemented the latter in the program HiggsBounds [?, ?, ?, ?, ?] to obtain the projected 95% CL exclusion in our scenarios.

We estimate the indirect reach through Higgs rate measurements by using detailed HL-LHC signal strength projections for the individual Higgs production times decay modes, including the corresponding correlation matrix, as evaluated by the CMS experiment [add reference to corresponding Section in the YR report]. We doubled these projected measurements to account for similar future ATLAS measurements. We furthermore take cross-correlations of theoretical rate uncertainties between future ATLAS and CMS measurements into account. All this is done with the use of the program HiggsSignals [?]. We provide projections for both scenarios S1 and S2, where the theory uncertainties are kept at their current values, or halved, respectively.

The theory predictions are obtained from FeynHiggs [?, ?, ?, ?, ?, ?, ?, ?], as well as from SusHi [?, ?, ?, ?, ?, ?, ?, ?, 209–211] for gluon fusion and matched predictions for bottom-quark annihilation [?, ?, ?, ?]. We determine the theoretical uncertainties on the Higgs production cross sections as in Ref. [?]. Thus, we include renormalization- and factorization-scale uncertainties, PDF+ $\alpha_s$  uncertainties as well as parametric and matching uncertainties for the  $\tau^+\tau^-$  exclusion, see Ref. [?] for details. For the light Higgs rate measurements we use the SM uncertainties following Ref. [7].

### **Projected HL-LHC reach**

Our projections in the  $M_h^{125}$  and the  $M_h^{125}(\tilde{\chi})$  scenario in the  $(M_A, \tan \beta)$  plane are presented in the left and right column of Fig. 129, respectively. In the upper (lower) row we show the results in the S1 (S2) scenario. We furthermore include the current limits (magenta lines) for the direct and indirect reach of the LHC in the two benchmark scenarios, as evaluated in Ref. [?].

Within the  $M_h^{125}$  scenario the reach via measurements of the Higgs signal strengths extends to  $M_A$  values of around 900 (1000) GeV for S1 (S2). The horizontal contour excluding  $\tan \beta$  values less than 6 is due to the light Higgs mass being below 122 GeV. Hence, this boundary is not changing between S1 and S2 in the  $M_h^{125}$  scenario. The direct heavy Higgs searches in the  $\tau^+\tau^-$  final state will probe the parameter space up to  $M_A \leq 2000$  (2400) GeV in S1 (S2) for  $\tan \beta = 50$ , and up to  $M_A \leq 1600$  (1900) GeV at  $\tan \beta = 20$ .

The picture is somewhat different in the  $M_h^{125}(\tilde{\chi})$  scenario. Here the large branching ratio of the heavy neutral Higgs boson decaying to charginos and neutralinos leads to a strongly reduced direct reach of heavy Higgs to  $\tau^+\tau^-$  searches. While at large values of  $\tan \beta \sim 50$  the reach is only slightly weaker than in the  $M_h^{125}$  scenario, at  $\tan \beta = 20$  it is significantly reduced to  $M_A \leq 1250$  (1550) GeV for S1 (S2). In order to overcome this, dedicated searches for the decays of  $H$  and  $A$  to charginos and neutralinos will have to be devised. On the other hand, Higgs rate measurements are an important complementary probe. In S1 they exclude  $M_A \leq 1000$  GeV and  $\tan \beta \leq 9$ . While the bound in  $M_A$  is induced through Higgs coupling modifications arising from non-decoupling, values of  $\tan \beta \leq 9$  feature a too-large enhancement of the  $h \rightarrow \gamma\gamma$  partial width. In the optimistic scenario S2 with reduced theoretical uncertainties these limits improve further to  $M_A \geq 1100$  GeV and  $\tan \beta \gtrsim 16$ , respectively. In that case the combination of direct and indirect bounds yields a lower limit of  $M_A \geq 1300$  GeV in the  $M_h^{125}(\tilde{\chi})$  scenario.

In summary, the HL-LHC has the potential, using the combined direct and indirect reach, to probe the MSSM Higgs sector up to  $M_A \sim 1000$  GeV and possibly beyond, depending on the details of the MSSM scenario. Values larger than that, as predicted, e.g., by GUT based models [?, ?, ?, ?, ?, ?, ?] or

---

<sup>34</sup>We thank Martin Flechl for helpful discussions.

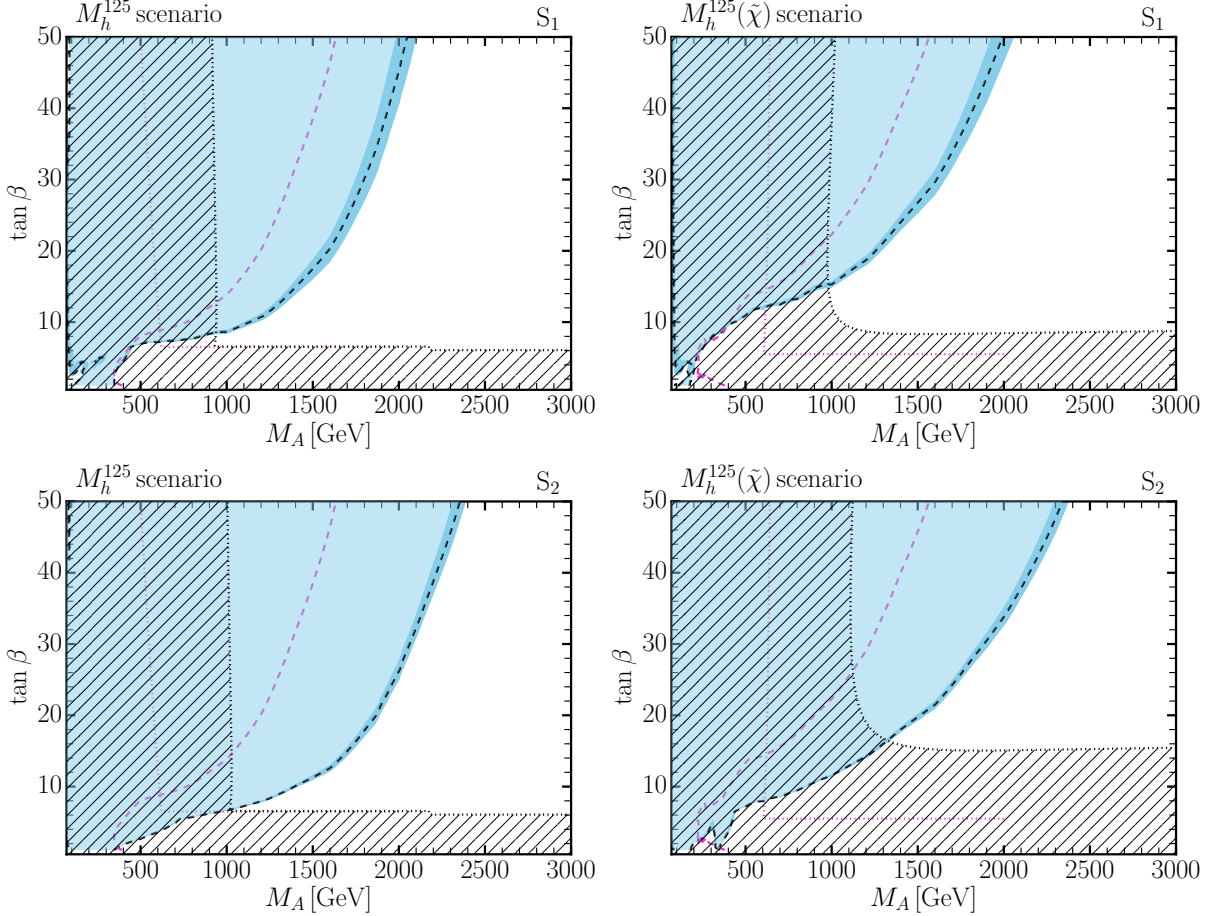


Fig. 129: HL-LHC projections in the  $M_h^{125}$  (left) and  $M_h^{125}(\tilde{\chi})$  (right) scenario for the projection scenario S1 (top) and S2 (bottom). The dashed black curve and blue filled region indicate the HL-LHC reach via direct heavy Higgs searches in the  $\tau^+\tau^-$  channel (with the dark blue region indicating the theoretical uncertainty), whereas the magenta dashed curve shows the current exclusion. The current and future HL-LHC sensitivity via combined ATLAS and CMS Higgs rate measurements is shown as magenta and black dotted contours, respectively (the latter being accompanied with a hatching of the prospectively excluded region).

Finite Unified Theories [?, ?, ?], or allowed by global fits of the phenomenological MSSM [?, ?] would remain uncovered. To explore these regions an energy upgrade and/or refined Higgs signal strength measurements (e.g. at an  $e^+e^-$  collider [?]) will be necessary.

## 9.11 Searches for low mass Higgs bosons (below 120 GeV)

### 9.11.1 Introduction

Many extensions of the Standard Model (SM) Higgs sector allow for new charged and neutral Higgs bosons that can be lighter than the Higgs boson discovered [?, 19] at  $\approx 125$  GeV. However, as the observed (heavier) Higgs boson shows itself to be increasingly SM-like [?] in its couplings to  $WW$  and  $ZZ$  pairs [?, ?, ?, ?, ?, 25], as well as to fermions [?, ?], we are in general pushed into an ‘alignment without decoupling’ limit [?, 149], which has been examined in a number of recent studies [?, ?, ?, ?, ?, ?, ?, ?, ?]. In this limit, the 125 GeV Higgs boson has SM like couplings without having to decouple the other Higgs bosons which might be present allowing them to be lighter than 125 GeV. In what follows we work in

the alignment without decoupling limit focusing on new Higgs bosons in the mass range  $65 - 120$  GeV, between the SM-like Higgs mass and its two body decay threshold.

In two Higgs doublet models (2HDM) alignment occurs when one of the neutral CP-even Higgs mass eigenstates is approximately aligned in field space with the direction of the vacuum expectation value (*vev*) [?, ?]. For non-doublet electroweak multiplets (as well as singlets [?]), one obtains an ‘aligned’ SM-like Higgs when the non-doublet [?, ?] Higgs *vev* is small, which typically also suppresses the Higgs mixing angle [?, ?]. Furthermore, in the singlet and non-doublet multiplet cases, the new Higgs bosons are (at least approximately) fermiophobic, making them generically harder to detect [?, ?, ?, ?] either directly or indirectly as we discuss more below.

In this review we summarize the relevant experimental constraints on light Higgs bosons in the mass range  $65 - 120$  GeV. We also discuss models which can realize light Higgs bosons and highlight promising search signals at the LHC. This includes searching for deviations in Higgs couplings since, as emphasized in [?], even in the deep alignment regime where one might naively expect everything to be very SM-like, precise measurements of the 125 GeV Higgs boson signal strengths could uncover the existence of an extended Higgs sector. Some projections for a high luminosity/high energy LHC are also made. The aim is to encourage new experimental analysis, targeting specifically searches for light Higgs bosons at the HL/HE-LHC.

### 9.11.2 Experimental constraints on light Higgs bosons

In the mass range and alignment limit we consider, the most relevant constraints for the *anti-aligned* neutral Higgs bosons but with significant couplings to SM fermions, come from CMS  $b\bar{b}X$  with  $X \rightarrow \tau\bar{\tau}$  searches [?] as well as ATLAS [?] and CMS [?] searches for  $X \rightarrow \tau\bar{\tau}$  decays in both the  $gg \rightarrow X$  and  $b\bar{b}X$  production modes. Similarly, the searches in the diphoton channel place important bounds [?, ?].<sup>35</sup> A recent CMS search [?] for new resonances decaying to a  $Z$  boson and a light resonance, followed by  $Z \rightarrow \ell\bar{\ell}$  and the light resonance decaying to  $b\bar{b}$  or  $\tau\bar{\tau}$  pairs, has also been shown to impose severe constraints [?] on light CP-even neutral Higgs bosons. Direct searches at LEP for light neutral Higgs states produced in pairs or in association with a  $Z$  boson are also relevant [?, ?, ?], setting relevant limits on the couplings of the light Higgs to SM gauge bosons. For the charged Higgs bosons, LEP searches [?] and  $B$ -physics constraints from  $R_b$ ,  $\epsilon_K$ ,  $\Delta m_B$ ,  $B \rightarrow X_s\gamma$ , and  $B \rightarrow \tau\nu$  [?, ?, ?, ?, ?] measurements impose the most stringent constraints. These limits apply to all 2HDMs and impose particularly severe constraints on *non-type-I* 2HDMs [?] in which there is no fermiophobic limit.

As emphasized in numerous studies [?, ?, ?, ?, ?], the above limits are less stringent (most limits can be rescaled) when the Higgs bosons have highly suppressed couplings to SM fermions as can happen in the type-I 2HDM [?] in the large  $\tan\beta$  limit [?]. For non-doublet extended Higgs sectors one automatically has suppressed couplings to SM fermions when the non-doublet *vev* is small (or mixing angle in the case of singlets) since they only enter (if at all) through mixing with the SM-like Higgs boson [?]. In the case of fermiophobia, the most robust probes of neutral Higgs bosons are inclusive diphoton [?, ?, ?] and multiphoton searches [?, ?, ?] which utilize the Drell-Yan pair production channel of a charged and neutral Higgs boson. Constraints from electroweak (EW) precision data [?, ?] also apply with the primary effect being that the neutral and charged Higgs bosons are constrained to be not too different in mass.

### 9.11.3 Models with light Higgs bosons

A number of recent studies of the alignment without decoupling limit in 2HDMs have been performed which consider the case where the SM-like Higgs boson is not the lightest scalar. As shown in [?, ?, ?, ?, ?, ?, ?, ?], for type-I 2HDMs there are regions of parameter space where, along with the light CP-even scalar, both the charged and neutral CP-odd Higgs bosons can be below the SM-like Higgs mass

---

<sup>35</sup>It is interesting to note that the CMS search in the diphoton channel [?] shows an excess of events at  $\sim 96$  GeV, in the same mass range where the LEP searches in the  $b\bar{b}$  final state observed a  $2\sigma$  excess [?].

while satisfying the constraints discussed above. This is in contrast to type-II 2HDM, where combined constraints from  $B$  meson decays [?] and EW precision constraints [212] require the charged and CP-odd neutral Higgs bosons to be much heavier than the mass range we consider here. Within the MSSM however, the additional particle content results in substantially weaker limits from  $B$  meson decays and EW data. In general the allowed regions of parameter space in the type-I 2HDM is much larger than in other 2HDMs [?, ?], again due to the presence of a fermiophobic limit at large  $\tan\beta$  which opens up more regions of parameter space.

In the MSSM which is a type-II 2HDM, the alignment without decoupling limit [?] requires accidental cancellations between tree level and radiative corrections in the Higgs mass matrix [?, ?]. It was shown that a tuning of  $\sim 10\%$  is sufficient to find agreement with the Higgs-boson rate measurements [?]. Depending on the level of alignment required, this can lead to a highly constrained parameter space, especially in the case where the SM-like Higgs is the heavier of the CP-even neutral scalars. In particular, after accounting for all relevant experimental constraints (as well as theoretical uncertainties) recent studies [?] of the alignment without decoupling limit of the MSSM [?] defined a benchmark plane of allowed parameter space with  $\tan\beta \sim 5 - 6$  (and very large values of  $\mu$ ) in which the light CP-even Higgs can be between  $\sim 60 - 100$  GeV if the charged Higgs mass is between  $\sim 170 - 185$  GeV and the neutral CP-odd Higgs is  $\sim 130 - 140$  GeV. Still larger allowed regions are expected in a global scan, as performed in [?]. Recent studies of the NMSSM [?, ?] and  $\mu\nu$ SSM [?] have also examined the alignment without decoupling limit finding a larger allowed parameter space than in the MSSM due to an additional gauge singlet Higgs (or right handed scalar neutrino).

For models with non-doublet multiplets the most well known are those involving electroweak triplets. In particular, Higgs triplet models with custodial symmetry [?], as in the famous Georgi-Machacek (GM) model [?, ?, ?, ?, ?] or its supersymmetric incarnations [?, ?, ?], have been well studied due to their ability to easily satisfy constraints from electroweak precision data. Recent studies [?, ?, ?] have shown that GM-like models can allow for light neutral and charged scalars below the SM-like Higgs boson mass. In the alignment limit implied by Higgs coupling measurements, the triplet Higgs  $v_{ev}$  is constrained to be small though it can still much larger than non-custodial cases [?, ?] which are constrained by measurements of the  $\rho$  parameter. Custodial symmetry also ensures that the neutral and charged components of the Higgs multiplet have (at least approximately) degenerate masses, making them more difficult to detect due to soft decay products [?, ?]. For these anti-aligned and fermiophobic Higgs bosons, recent studies have emphasized di- and multi-photon searches [?, ?, ?, ?] as robust probes of this scenario.

#### 9.11.4 Phenomenology of light anti-aligned Higgs bosons

In the alignment limit, single electroweak production mechanisms for the additional ‘anti-aligned’ neutral Higgs bosons (or small  $v_{ev}$  and Higgs mixing for non-doublets), such as vector boson fusion (VBF) or associated vector boson production, necessarily become suppressed. Thus the dominant production mechanisms become gluon fusion or associated  $b\bar{b}$  production when there is a significant coupling to SM quarks. However, these production mechanisms become suppressed when the couplings to fermions are negligible<sup>36</sup>, as can happen in type-I 2HDM in the large  $\tan\beta$  limit [?] or non-doublet electroweak sectors which are generically fermiophobic. The same is true for the light charged Higgs bosons production channels  $t \rightarrow H^\pm b$  and  $pp \rightarrow H^\pm tb$  which are also obsolete in the fermiophobic limit. Note that for charged scalars coming from larger than doublet representations we can also have  $W^\pm Z \rightarrow H^\pm$  VBF production, but this is again suppressed in the small non-doublet  $v_{ev}$  and Higgs mixing limit.

---

<sup>36</sup>Of course if they couple to some not too heavy colored BSM particles, gluon fusion could open back up.

#### 9.11.4.1 Pair Production as a discovery channel

A different option that offers new experimental opportunities is the Drell-Yan Higgs pair production mechanism. Any extension of the SM Higgs sector by electroweak charged scalars will possess the pair production channels mediated by  $W$  and  $Z$  bosons and which are not present in the SM. Furthermore, as emphasized in [?, ?, ?, ?, ?, ?], even in the alignment and fermiophobic limits, this production mechanism is not suppressed and can be as large as  $\sim 10 \text{ pb}$  at 13 TeV and  $\sim 50 \text{ pb}$  and 27 TeV in the mass range we consider (see ??). Thus, Drell-Yan Higgs pair production can be as large or even dominate over single production mechanisms, for both charged and neutral Higgs bosons. Despite this, the Drell-Yan Higgs pair production mechanism has been largely overlooked in experimental searches with the lone exception being a recent CDF analysis of Tevatron four photon data [?] searching for fermiophobic Higgs bosons.

The Drell-Yan pair production mechanism is mediated by the vector-Higgs-Higgs coupling. In the alignment limit, this will have vertices that are maximized in this limit and depend only on electroweak couplings and quantum numbers, while some vertices will go to zero depending on which Higgs pairs are being produced [?, ?, ?, ?, ?, ?]. Thus for the non-zero cases the vertex can be written schematically as,

$$g_{WH_M^\pm H_N^0} \equiv ig C_N(p_1 - p_2)^\mu, \quad g_{ZH_M^0 H_N^0} \equiv i \frac{g}{c_W} C_N(p_1 - p_2)^\mu, \quad (177)$$

where  $C_N$  is fixed by the  $SU(2)_L \times U(1)_Y$  representation [?, ?, ?, ?, ?, ?] and  $p_1, p_2$  are the four momenta of the incoming and outgoing scalar momenta. Here  $H_N^0$  stands for any neutral Higgs boson and can include CP-even or CP-odd and similarly for  $H_M^\pm$  in the case of charged Higgs bosons. There is also a photon mediated channel when both Higgs bosons are charged, but we focus on cases where at least one is neutral. In ?? we show the leading order  $q\bar{q} \rightarrow V \rightarrow H_M^{\pm,0} H_N^0$  (including *pdfs*) cross section  $\times C_N^{-2}$  for the  $W$  mediated (blue solid) and  $Z$  mediated (black dashed) channels at the LHC with  $\sqrt{s} = 13 \text{ TeV}$  (left) and  $\sqrt{s} = 27 \text{ TeV}$  (right) in the mass range  $60 - 125 \text{ GeV}$ . They are computed with Madgraph [79] using a modified version of the GM model implementation of [?] and rescaling appropriately. There are also NLO contributions which may generate  $\gtrsim \mathcal{O}(1)$  K-factors for Higgs pair production [?, ?, 213], but are not included. We show four cases for mass splittings of  $\Delta M \equiv M_{H_M^{\pm,0}} - M_{H_N^0} = 0, 100, 200, 300 \text{ GeV}$  as labeled in plot.

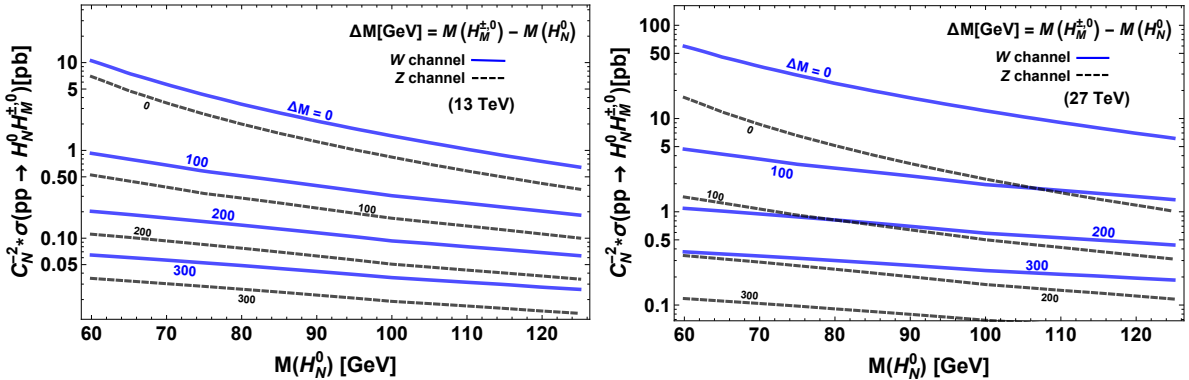


Fig. 130: Leading order cross sections (with *pdfs*) for the  $q\bar{q} \rightarrow V \rightarrow H_M^{\pm,0} H_N^0$  Higgs pair production mechanism mediated by  $W$  (blue solid) and  $Z$  (black dashed) bosons at the LHC for  $\sqrt{s} = 13 \text{ TeV}$  (left) and  $\sqrt{s} = 27 \text{ TeV}$  (right) in the mass range  $60 - 125 \text{ GeV}$ . We show three cases for mass splittings  $\Delta M \equiv M_{H_M^{\pm,0}} - M_{H_N^0} = 0, 100, 200, 300 \text{ GeV}$  as labeled in plot and have factored out an overall group theory factor  $C_N$  (see ??). The curves for a particular model can be obtained by rescaling with  $(C_N)^2$  which is fixed by the  $SU(2)_L \times U(1)_Y$  representation.

The dominant decay modes of the neutral Higgs bosons will be to  $b\bar{b}$  and  $\tau\bar{\tau}$  when there is a sig-

nificant coupling to SM fermions. In the fermiophobic case, the Higgs bosons can have large branching ratios into EW gauge bosons and in particular photons at low masses. The less emphasized  $Z\gamma$  channel may also offer promising opportunities [?]. Inclusive searches for resonances can then be combined with the Drell-Yan production channel to put relatively robust bounds on branching ratios in extended Higgs sectors as done in [?, ?] for the case of decays into diphotons. For the charged Higgs bosons comking Drell-Yan pair production with decays into  $W\gamma$  [?, ?] or four photon signals [?] offer promising search channels.

#### 9.11.4.2 Suggestions for searches at the HL/HE-LHC

We briefly summarize search strategies for (anti)-aligned light Higgs bosons at the (HL/HE) LHC. This is in addition to continuing and updating current searches in the mass range we consider, including  $\tau\tau$ ,  $\gamma\gamma$ ,  $b\bar{b}$  searches based on gluon fusion and  $\tau\tau$  searches based on associated  $b\bar{b}$  production [?, ?, ?] as well as recent CMS searches [?] for  $A \rightarrow Zh$  with  $Z \rightarrow \ell\bar{\ell}$  and  $h \rightarrow \tau\tau, bb$ .

- Push current conventional Higgs searches in  $WW$  and  $ZZ$ , which currently [?, ?] do not go below  $\sim 130$  GeV, to as low a mass as possible, ideally down to  $\sim 65$  GeV. As emphasized in [?, ?], this can help to rule out cases of a fermiophobic Higgs boson with suppressed couplings to photons, which could otherwise escape detection. Similarly, heavier Higgs bosons with the “remaining” coupling to SM gauge bosons could be detected.
- Combine *inclusive* searches for resonances with the ‘universal’ Drell-Yan Higgs pair production channel to put robust bounds on allowed branching ratios to  $\tau\tau$ ,  $b\bar{b}$ ,  $Z\gamma$  and  $\gamma\gamma$  final states. In the alignment limit, these bounds depend only on electroweak couplings and can be applied to any extended Higgs boson sector (with appropriate rescaling), in some cases providing the strongest limits [?, ?].
- Utilizing the Drell-Yan Higgs pair production mechanism, dedicated LHC searches for more optimized, but model dependent signals such as  $4\gamma + V^*$  [?, ?, ?],  $4\gamma + V^*V^*$  [?],  $3\gamma + V^*$  where in the last case dedicated phenomenological studies are lacking.
- Search for  $\tau\tau$ ,  $b\bar{b}$ , or  $\gamma\gamma$  plus missing energy as well as mono photon or mono lepton plus missing energy final states to cover cases where neutral Higgs may have an invisible decay. In particular the  $\gamma\gamma$  channel appears to be very promising (especially in view of a potential signal at  $\sim 96$  GeV [?]).

## 9.12 Sensitivity to heavy Higgs bosons from the 2HDM in "Higgs-to-Higgs" decays

K. Mimasu<sup>1</sup>, Jose Miguel No<sup>2</sup>

<sup>1</sup>Universite catholique de Louvain, Chemin du Cyclotron, 2, B-1348 Louvain-la-Neuve, Belgium

<sup>2</sup>Instituto de Fisica Teorica, IFT-UAM/CSIC, Cantoblanco, 28049, Madrid, Spain

#### 9.12.1 Introduction

Searches for heavy scalars are highly complementarity to coupling measurements of the 125 GeV Higgs  $h$  as probes of extended Higgs sectors. For 2HDM scenarios, di-boson search channels  $H \rightarrow WW$ ,  $ZZ$ ,  $hh$  probe the parameter space for which the 125 GeV Higgs is not SM-like, in combination with Higgs coupling measurements. However for a SM-like 125 GeV Higgs, corresponding to the alignment limit of 2HDMs [149], these channels suffer a significant loss in sensitivity since the couplings  $HVV$  ( $V = W^\pm, Z$ ) and  $Hhh$  vanish in such a limit. In this case, searches for heavy scalars through non-standard decay channels [?, ?, ?, ?] as well as through fermionic decay channels [?, ?] become the primary avenue to find these new states, and are crucial to cover the parameter space of aligned 2HDMs.

For Higgs sectors with several new states beyond the SM, as in the 2HDM, non-standard “Higgs-to-Higgs” decays occur between these BSM scalars for sizable splittings among them, yielding the leading probe of aligned 2HDM scenarios in this case [?]. Focusing here in the 2HDM neutral scalars

$A/H$ , such signatures include  $A/H \rightarrow ZH/A$  ( $Z \rightarrow \ell\ell$ ,  $H/A \rightarrow \bar{b}b, \tau\tau$ ) [?, ?] and  $H \rightarrow AA \rightarrow b\bar{b}b\bar{b}, b\bar{b}\tau\tau$  [214]. There exists a very strong interplay between these and searches for  $H/A$  in fermionic decay channels, mainly  $H/A \rightarrow \tau\tau$ , depending on the mass splitting among the new scalars.

### 9.12.2 2HDM Summary

Relevant aspects of the 2HDM (overlap with Carlos and Nausheen's contribution) Consider a general 2HDM scalar potential with a softly broken  $\mathbb{Z}_2$  symmetry (and no CP violation)

$$\begin{aligned} V(H_1, H_2) = & \mu_1^2 |H_1|^2 + \mu_2^2 |H_2|^2 - \mu^2 \left[ H_1^\dagger H_2 + \text{h.c.} \right] + \frac{\lambda_1}{2} |H_1|^4 + \frac{\lambda_2}{2} |H_2|^4 \\ & + \lambda_3 |H_1|^2 |H_2|^2 + \lambda_4 \left| H_1^\dagger H_2 \right|^2 + \frac{\lambda_5}{2} \left[ \left( H_1^\dagger H_2 \right)^2 + \text{h.c.} \right]. \end{aligned} \quad (178)$$

Physical scalar sector of a 2HDM comprised of  $h$  (which we assume here to be the 125 GeV Higgs),  $H$ ,  $A$  and  $H^\pm$ . Types of 2HDM, regarding the couplings of the two doublets  $H_{1,2}$  to fermions: By convention, up-type quarks couple to  $H_2$ . In Type I 2HDM all the other fermions also couple to  $H_2$ , while for Type II down-type quarks and leptons couple<sup>37</sup> to  $H_1$ . Parameters  $t_\beta \equiv \tan \beta$  and  $c_{\beta-\alpha} \equiv \cos(\beta - \alpha)$  control strength of the couplings of  $h$ ,  $H$ ,  $A$  to gauge bosons and fermions. We denote the couplings normalized to the SM values (of  $h_{\text{SM}}$ ) by  $\kappa$ -factors ( $\kappa_V$  for gauge bosons,  $\kappa_u$  for up-type quarks,  $\kappa_d$  for down-type quarks,  $\kappa_\ell$  for charged leptons), which read

$$\text{Type I : } \left\{ \begin{array}{l} \kappa_V^h = s_{\beta-\alpha} \\ \kappa_u^h = \kappa_d^h = \kappa_\ell^h = t_\beta^{-1} c_{\beta-\alpha} + s_{\beta-\alpha} \\ \kappa_V^H = -c_{\beta-\alpha} \\ \kappa_u^H = \kappa_d^H = \kappa_\ell^H = t_\beta^{-1} s_{\beta-\alpha} - c_{\beta-\alpha} \\ \kappa_u^A = -\kappa_d^A = -\kappa_\ell^A = t_\beta^{-1} \end{array} \right. \quad \text{Type II : } \left\{ \begin{array}{l} \kappa_V^h = s_{\beta-\alpha} \\ \kappa_u^h = t_\beta^{-1} c_{\beta-\alpha} + s_{\beta-\alpha} \\ \kappa_d^h = \kappa_\ell^h = s_{\beta-\alpha} - t_\beta c_{\beta-\alpha} \\ \kappa_V^H = -c_{\beta-\alpha} \\ \kappa_u^H = t_\beta^{-1} s_{\beta-\alpha} - c_{\beta-\alpha} \\ \kappa_d^H = \kappa_\ell^H = -t_\beta s_{\beta-\alpha} - c_{\beta-\alpha} \\ \kappa_u^A = t_\beta^{-1} \\ \kappa_d^A = \kappa_\ell^A = t_\beta \end{array} \right. \quad (179)$$

For  $c_{\beta-\alpha} \rightarrow 0$  (alignment limit [149])  $h$  has SM-like couplings to gauge bosons and fermions ( $\kappa_i^h \rightarrow 1$ , yielding  $h \rightarrow h_{\text{SM}}$ ), while the coupling of  $H$  to gauge bosons  $V = W^\pm, Z$  vanishes ( $\kappa_V^H \rightarrow 0$ ).

### 9.12.3 $m_A > m_H$ : searches for $A \rightarrow ZH$

Here we obtain the present limits on the 2HDM in the alignment limit from the  $\sqrt{s} = 13$  TeV ATLAS  $A \rightarrow ZH$  search [?] with  $36.1 \text{ fb}^{-1}$  (there are also CMS searches at 8 TeV with  $19.8 \text{ fb}^{-1}$  [?] and at 13 TeV with  $2.3 \text{ fb}^{-1}$  [?]) in the  $\ell\ell b\bar{b}$  final state, and present sensitivity projections of this search for HL-LHC and HE-LHC. The present limits and future projections are derived in the  $(m_A, m_H, \tan\beta)$  parameter space.

For the HL-LHC, we first perform a sensitivity projection to  $\sqrt{s} = 13$  TeV with  $\mathcal{L} = 3000 \text{ fb}^{-1}$ , for  $m_A = m_H + 100 \text{ GeV}$ ,  $m_A = m_H + 200 \text{ GeV}$ ,  $m_A = m_H + 300 \text{ GeV}$  as benchmarks. In figure 131 (left) our sensitivity projection is obtained through a  $\sqrt{\mathcal{L}}$  rescaling of the present ATLAS expected sensitivity, assuming that the background uncertainties are statistically dominated. In figure 131 (right) we instead assume a  $x\%$  of background systematics (coming dominantly from  $Z + \text{jets}$ ) in our projections, and use xxx as signal significance.

Mind the region where  $\Gamma_A/m_A > 20\%$ !

<sup>37</sup>Two more possibilities (depending on coupling of leptons w.r.t. down-type quarks), but we focus here on Types I and II.

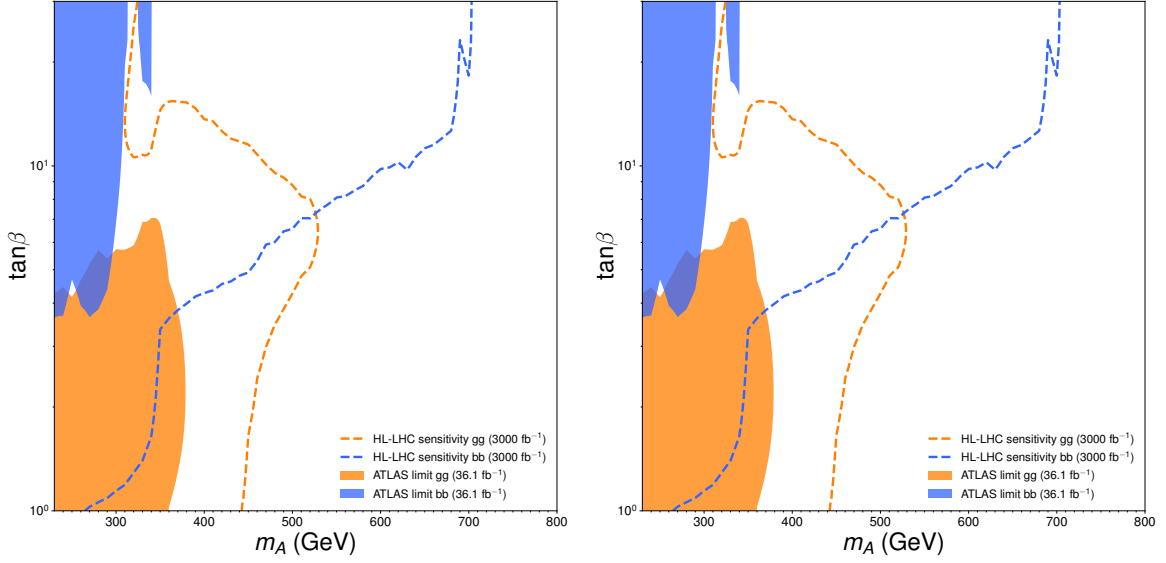


Fig. 131: Left: Present (solid) and projected (dashed) 95% C.L. exclusion sensitivity for  $pp \rightarrow A \rightarrow ZH \rightarrow \ell\ell b\bar{b}$  in the in the  $(m_A, \tan\beta)$  plane for  $m_A = m_H + 100$  GeV, from gluon fusion (orange) and  $bb$ -associated production (blue). Right: (Placeholder for the limits with systematics).

#### 9.12.4 $m_H > m_A$ : searches for $H \rightarrow ZA$ and $H \rightarrow AA$

The analysis above can be also applied to  $H \rightarrow ZA$ , bearing in mind the possibility of the competing decay  $H \rightarrow AA$ . For  $H \rightarrow AA$  there are no present ATLAS/CMS experimental studies<sup>38</sup> but there is an existing sensitivity study [214] based on the 13 TeV resonant di-Higgs CMS analysis [?] (see also [215]).

Following [214], we particularize the search  $H \rightarrow AA \rightarrow 4b$  for  $m_A \in [65, 290]$  GeV (for which the multijet background is provided by CMS) and  $m_H \in [m_H^{\min}, m_H^{\max}] = [3.2 \times m_A, 9.6 \times m_A]$  (MMR selection of [?], validated in [214]). The 95% C.L. cross section times branching ratio exclusion sensitivity (in fb) for  $pp \rightarrow H \rightarrow AA \rightarrow b\bar{b}b\bar{b}$  in the  $(m_H, m_A)$  plane, for LHC 13 TeV with an integrated luminosity of  $35.9 \text{ fb}^{-1}$  is given in Figure 132. We Convert this into the 2HDM parameter space in Figure...

Regarding extrapolation to HL-LHC and HE-LHC...

Mind the region where  $\Gamma_H/m_H > 20\%$ !

#### 9.12.5 Interplay with $H/A \rightarrow \tau\tau$

In order to study the interplay of the above searches with heavy scalar searches in fermionic decay modes like  $H/A \rightarrow \tau\tau$ , we translate the model-independent HL-LHC and HE-LHC sensitivity projections for  $\phi \rightarrow \tau\tau$  from section (9.6.3) to the  $m_\phi, \tan\beta$  plane (with  $\phi = H/A$ ) of the 2HDM (here assume one scalar at a time? should be a fair assumption if  $|m_A - m_H| \gg \delta m_{\tau\tau}$ , with  $\delta m_{\tau\tau}$  the invariant mass resolution of the analysis) using *SusHi* [209] and *2HDMC* [150], assuming  $\cos(\beta - \alpha) = 0$ .

<sup>38</sup>We however note there are existing LHC analyses for  $h \rightarrow AA$ , with  $h$  the 125 GeV Higgs boson (see e.g. [?]).

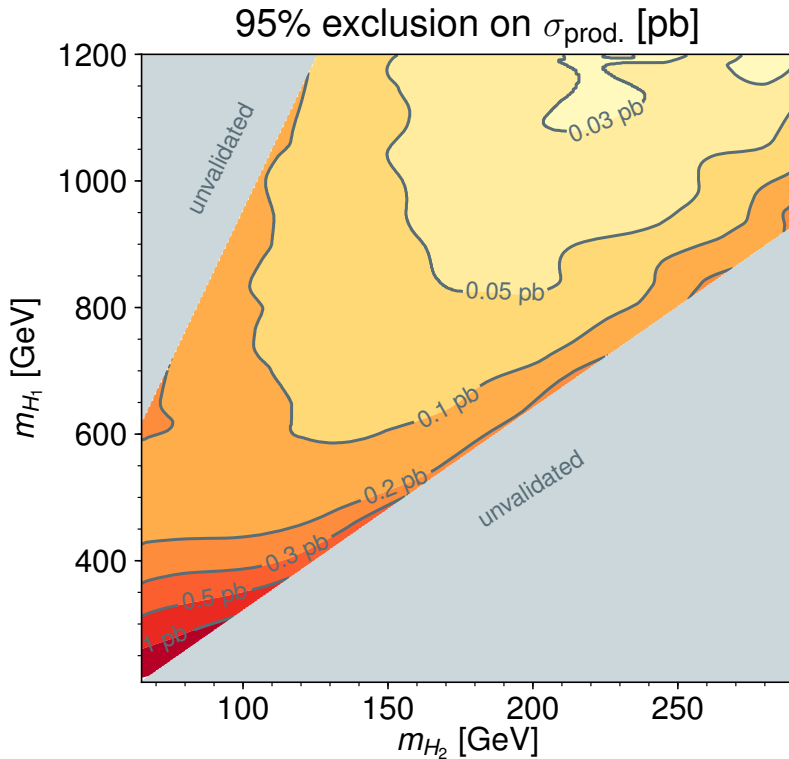


Fig. 132: Estimated 95% C.L.  $\sigma \times \text{BR}$  exclusion sensitivity for  $pp \rightarrow H \rightarrow AA \rightarrow b\bar{b}b\bar{b}$  in the ( $m_{H_1} = m_H$ ,  $m_{H_2} = m_A$ ) plane for LHC 13 TeV with an integrated luminosity of  $35.9 \text{ fb}^{-1}$  (Placeholder for the 2HDM interpretation of these limits).

## 10 Conclusions and Outlook

## References

- [1] M. Mangano, *Physics at the FCC-hh, a 100 TeV pp collider*. CERN Yellow Reports: Monographs. CERN, Geneva, 2017. <https://cds.cern.ch/record/2270978>.
- [2] LHC Higgs Cross Section Working Group Collaboration, A. David, A. Denner, M. Duehrssen, M. Grazzini, C. Grojean, G. Passarino, M. Schumacher, M. Spira, G. Weiglein, and M. Zanetti, *LHC HXSWG interim recommendations to explore the coupling structure of a Higgs-like particle*, arXiv:1209.0040 [hep-ph].
- [3] LHC Higgs Cross Section Working Group Collaboration, J. R. Andersen et al., *Handbook of LHC Higgs Cross Sections: 3. Higgs Properties*, arXiv:1307.1347 [hep-ph].
- [4] J. Gao, L. Harland-Lang, and J. Rojo, *The Structure of the Proton in the LHC Precision Era*, Phys. Rept. **742** (2018) 1–121, arXiv:1709.04922 [hep-ph].
- [5] J. Rojo et al., *The PDF4LHC report on PDFs and LHC data: Results from Run I and preparation for Run II*, J. Phys. **G42** (2015) 103103, arXiv:1507.00556 [hep-ph].
- [6] W. Beenakker, C. Borschensky, M. Kramer, A. Kulesza, E. Laenen, S. Marzani, and J. Rojo, *NLO+NLL squark and gluino production cross-sections with threshold-improved parton distributions*, Eur. Phys. J. **C76** (2016) no. 2, 53, arXiv:1510.00375 [hep-ph].
- [7] LHC Higgs Cross Section Working Group Collaboration, D. de Florian et al., *Handbook of LHC Higgs Cross Sections: 4. Deciphering the Nature of the Higgs Sector*, arXiv:1610.07922 [hep-ph].
- [8] NNPDF Collaboration, R. D. Ball et al., *Parton distributions from high-precision collider data*, Eur. Phys. J. **C77** (2017) no. 10, 663, arXiv:1706.00428 [hep-ph].
- [9] S. Alekhin, J. Blümlein, S. Moch, and R. Placakyte, *Parton distribution functions,  $\alpha_s$ , and heavy-quark masses for LHC Run II*, Phys. Rev. **D96** (2017) no. 1, 014011, arXiv:1701.05838 [hep-ph].
- [10] M. Czakon, N. P. Hartland, A. Mitov, E. R. Nocera, and J. Rojo, *Pinning down the large-x gluon with NNLO top-quark pair differential distributions*, JHEP **04** (2017) 044, arXiv:1611.08609 [hep-ph].
- [11] J. M. Campbell, J. Rojo, E. Slade, and C. Williams, *Direct photon production and PDF fits reloaded*, Eur. Phys. J. **C78** (2018) no. 6, 470, arXiv:1802.03021 [hep-ph].
- [12] R. Gauld, J. Rojo, L. Rottoli, and J. Talbert, *Charm production in the forward region: constraints on the small-x gluon and backgrounds for neutrino astronomy*, JHEP **11** (2015) 009, arXiv:1506.08025 [hep-ph].
- [13] R. Gauld and J. Rojo, *Precision determination of the small-x gluon from charm production at LHCb*, Phys. Rev. Lett. **118** (2017) no. 7, 072001, arXiv:1610.09373 [hep-ph].
- [14] R. A. Khalek, S. Bailey, J. Gao, L. Harland-Lang, and J. Rojo, *Towards Ultimate Parton Distributions at the High-Luminosity LHC*, arXiv:1810.03639 [hep-ph].
- [15] J. Butterworth et al., *PDF4LHC recommendations for LHC Run II*, arXiv:1510.03865 [hep-ph].
- [16] A. Buckley, J. Ferrando, S. Lloyd, K. Nordström, B. Page, M. Rüfenacht, M. Schönher, and G. Watt, *LHAPDF6: parton density access in the LHC precision era*, Eur. Phys. J. **C75** (2015) 132, arXiv:1412.7420 [hep-ph].
- [17] *Recommendations for Systematic Uncertainties at HL-LHC.*,  
<https://twiki.cern.ch/twiki/bin/view/LHCPhysics/HLELHCCommonSystematics>. Currently collected in a Twiki page, numbers will go either in a YR Appendix or in a standalone note.
- [18] ATLAS Collaboration, T. A. collaboration, *Measurements of Higgs boson properties in the diphoton decay channel using  $80\text{ fb}^{-1}$  of pp collision data at  $\sqrt{s} = 13\text{ TeV}$  with the ATLAS*

*detector, .*

- [19] ATLAS Collaboration, G. Aad et al., *Observation of a new particle in the search for the Standard Model Higgs boson with the ATLAS detector at the LHC*, Phys. Lett. **B716** (2012) 1–29, arXiv:1207.7214 [hep-ex].
- [20] P. D. Dauncey, M. Kenzie, N. Wardle, and G. J. Davies, *Handling uncertainties in background shapes*, JINST **10** (2015) no. 04, P04015, arXiv:1408.6865 [physics.data-an].
- [21] ATLAS Collaboration, The ATLAS Collaboration, *Measurements of the Higgs boson production, fiducial and differential cross sections in the  $4\ell$  decay channel at  $\sqrt{s} = 13$  TeV with the ATLAS detector, .*
- [22] The ATLAS Collaboration, *Measurements of gluon-gluon fusion and vector-boson fusion Higgs boson production cross-sections in the  $H \rightarrow WW^* \rightarrow e\nu\mu\nu$  decay channel in pp collisions at  $\sqrt{s} = 13$  TeV with the ATLAS detector*, arXiv:1808.09054 [hep-ex].
- [23] CMS Collaboration, A. M. Sirunyan et al., *Observation of Higgs boson decay to bottom quarks*, Phys. Rev. Lett. **121** (2018) no. 12, 121801, arXiv:1808.08242 [hep-ex].
- [24] CMS Collaboration, *Evidence for the Higgs boson decay to a bottom quark-antiquark pair*, Phys. Lett. B **780** (2018) 501, arXiv:1709.07497 [hep-ex].
- [25] ATLAS, CMS Collaboration, G. Aad et al., *Measurements of the Higgs boson production and decay rates and constraints on its couplings from a combined ATLAS and CMS analysis of the LHC pp collision data at  $\sqrt{s} = 7$  and 8 TeV*, JHEP **08** (2016) 045, arXiv:1606.02266 [hep-ex].
- [26] ATLAS Collaboration, M. Aaboud et al., *Observation of Higgs boson production in association with a top quark pair at the LHC with the ATLAS detector*, 2018.
- [27] CMS Collaboration, A. M. Sirunyan et al., *Observation of  $t\bar{t}H$  production*, Phys. Rev. Lett. **120** (2018) no. 23, 231801, arXiv:1804.02610 [hep-ex].
- [28] ATLAS Collaboration, M. Aaboud et al., *Search for the standard model Higgs boson produced in association with top quarks and decaying into a  $b\bar{b}$  pair in pp collisions at  $\sqrt{s} = 13$  TeV with the ATLAS detector*, Phys. Rev. **D97** (2018) no. 7, 072016, arXiv:1712.08895 [hep-ex].
- [29] CMS Collaboration, A. M. Sirunyan et al., *Search for  $t\bar{t}H$  production in the  $H \rightarrow b\bar{b}$  decay channel with leptonic  $t\bar{t}$  decays in proton-proton collisions at  $\sqrt{s} = 13$  TeV*, arXiv:1804.03682 [hep-ex]. Submitted to JHEP.
- [30] ATLAS Collaboration, M. Aaboud et al., *Evidence for the associated production of the Higgs boson and a top quark pair with the ATLAS detector*, Phys. Rev. **D97** (2018) 072003, arXiv:1712.08891 [hep-ex].
- [31] ATLAS Collaboration, *to be published*, ATLAS-PHYS-PUB-2018-XY, CERN, Geneva, 2018.
- [32] CMS Collaboration, *PAS in preparation*, . CMS-PAS-FTR-2018-011.
- [33] CMS Collaboration, *Search for the associated production of a Higgs boson and a single top quark in pp collisions at  $\sqrt{s} = 13$  TeV*, CMS Physics Analysis Summary CMS-PAS-HIG-18-009, CERN, Geneva, 2018. <http://cds.cern.ch/record/2628662>.
- [34] CMS Collaboration, *Search for production of a Higgs boson and a single top quark in multilepton final states in proton collisions at  $\sqrt{s} = 13$  TeV*, CMS Physics Analysis Summary CMS-PAS-HIG-17-005, CERN, Geneva, 2017. <https://cds.cern.ch/record/2264553>.
- [35] CMS Collaboration, CMS Collaboration, *Search for the  $tH(H \rightarrow b\bar{b})$  process at  $\sqrt{s} = 13$  TeV and study of Higgs boson couplings*, CMS Physics Analysis Summary CMS-PAS-HIG-17-016, 2017. <http://cms.cern.ch/icMS/analysisadmin/cadilines?line=HIG-17-016>.
- [36] CMS Collaboration, *Measurements of properties of the Higgs boson decaying into the four-lepton final state in pp collisions at  $\sqrt{s} = 13$  TeV*, JHEP **11** (2017) 47, arXiv:1706.09936 [hep-ex].
- [37] CMS Collaboration, *Measurements of Higgs boson production and couplings using decays to a*

*W boson pair in pp collisions at 13 TeV*, CMS Physics Analysis Summary CMS-PAS-HIG-16-042, 2018. Submitted to *Phys. Lett. B*.

- [38] CMS Collaboration, *Observation of the Higgs boson decay to a pair of  $\tau$  leptons with the CMS detector*, Phys. Lett. B **779** (2018) 283, arXiv:1708.00373 [hep-ex].
- [39] CMS Collaboration, *Inclusive search for a highly boosted Higgs boson decaying to a bottom quark-antiquark pair*, Phys. Rev. Lett. **120** (2018) 071802, arXiv:1709.05543 [hep-ex].
- [40] CMS Collaboration, A. M. Sirunyan et al., *Search for  $t\bar{t}H$  production in the  $H \rightarrow b\bar{b}$  decay channel with leptonic  $t\bar{t}$  decays in proton-proton collisions at  $\sqrt{s} = 13$  TeV*, Submitted to *JHEP*, 2018.
- [41] CMS Collaboration, *Search for  $t\bar{t}H$  production in the all-jet final state in proton-proton collisions at  $\sqrt{s} = 13$  TeV*, JHEP **06** (2018) 101, arXiv:1803.06986 [hep-ex].
- [42] CMS Collaboration, *Search for the standard model Higgs boson decaying to two muons in pp collisions at  $\sqrt{s} = 13$  TeV*, CMS Physics Analysis Summary CMS-PAS-HIG-17-019, 2017. Submitted to *Phys. Rev. Lett.*
- [43] CMS Collaboration, *Combined measurements of Higgs boson couplings in proton-proton collisions at  $\sqrt{s} = 13$  TeV*, Submitted to *Eur. Phys. J. C*, 2018.
- [44] G. Buchalla, O. Cata, A. Celis, and C. Krause, *Fitting Higgs Data with Nonlinear Effective Theory*, Eur. Phys. J. **C76** (2016) no. 5, 233, arXiv:1511.00988 [hep-ph].
- [45] G. Buchalla, O. Cata, A. Celis, and C. Krause, *Note on Anomalous Higgs-Boson Couplings in Effective Field Theory*, Phys. Lett. **B750** (2015) 298–301, arXiv:1504.01707 [hep-ph].
- [46] J. de Blas, O. Eberhardt, and C. Krause, *Current and future constraints on Higgs couplings in the nonlinear Effective Theory*, arXiv:1803.00939 [hep-ph].
- [47] A. Dobado and M. J. Herrero, *Phenomenological Lagrangian Approach to the Symmetry Breaking Sector of the Standard Model*, Phys. Lett. **B228** (1989) 495–502.
- [48] A. Dobado and M. J. Herrero, *Testing the Hypothesis of Strongly Interacting Longitudinal Weak Bosons in Electron - Positron Collisions at Tev Energies*, Phys. Lett. **B233** (1989) 505–511.
- [49] A. Dobado, D. Espriu, and M. J. Herrero, *Chiral Lagrangians as a tool to probe the symmetry breaking sector of the SM at LEP*, Phys. Lett. **B255** (1991) 405–414.
- [50] A. Dobado, M. J. Herrero, and J. Terron, *The Role of Chiral Lagrangians in Strongly Interacting  $W(l)$   $W(l)$  Signals at pp Supercolliders*, Z. Phys. **C50** (1991) 205–220.
- [51] D. Espriu and M. J. Herrero, *Chiral Lagrangians and precision tests of the symmetry breaking sector of the Standard Model*, Nucl. Phys. **B373** (1992) 117–168.
- [52] M. J. Herrero and E. Ruiz Morales, *The Electroweak chiral Lagrangian for the Standard Model with a heavy Higgs*, Nucl. Phys. **B418** (1994) 431–455, arXiv:hep-ph/9308276 [hep-ph].
- [53] M. J. Herrero and E. Ruiz Morales, *Nonddecoupling effects of the SM higgs boson to one loop*, Nucl. Phys. **B437** (1995) 319–355, arXiv:hep-ph/9411207 [hep-ph].
- [54] F. Feruglio, *The Chiral approach to the electroweak interactions*, Int. J. Mod. Phys. **A8** (1993) 4937–4972, arXiv:hep-ph/9301281 [hep-ph].
- [55] J. Bagger, V. D. Barger, K.-m. Cheung, J. F. Gunion, T. Han, G. A. Ladinsky, R. Rosenfeld, and C. P. Yuan, *The Strongly interacting  $W W$  system: Gold plated modes*, Phys. Rev. **D49** (1994) 1246–1264, arXiv:hep-ph/9306256 [hep-ph].
- [56] V. Kouvassilopoulos and R. S. Chivukula, *The Phenomenology of a nonstandard Higgs boson in  $W(L)$   $W(L)$  scattering*, Phys. Rev. **D50** (1994) 3218–3234, arXiv:hep-ph/9312317 [hep-ph].
- [57] C. P. Burgess, J. Matias, and M. Pospelov, *A Higgs or not a Higgs? What to do if you discover a new scalar particle*, Int. J. Mod. Phys. **A17** (2002) 1841–1918, arXiv:hep-ph/9912459 [hep-ph].

- [58] L.-M. Wang and Q. Wang, *Electroweak chiral Lagrangian for neutral Higgs boson*, Chin. Phys. Lett. **25** (2008) 1984, arXiv:hep-ph/0605104 [hep-ph].
- [59] B. Grinstein and M. Trott, *A Higgs-Higgs bound state due to new physics at a TeV*, Phys. Rev. **D76** (2007) 073002, arXiv:0704.1505 [hep-ph].
- [60] A. Azatov, R. Contino, and J. Galloway, *Model-Independent Bounds on a Light Higgs*, JHEP **04** (2012) 127, arXiv:1202.3415 [hep-ph]. [Erratum: JHEP04,140(2013)].
- [61] R. Alonso, M. B. Gavela, L. Merlo, S. Rigolin, and J. Yepes, *The Effective Chiral Lagrangian for a Light Dynamical "Higgs Particle"*, Phys. Lett. **B722** (2013) 330–335, arXiv:1212.3305 [hep-ph]. [Erratum: Phys. Lett.B726,926(2013)].
- [62] G. Buchalla and O. Cata, *Effective Theory of a Dynamically Broken Electroweak Standard Model at NLO*, JHEP **07** (2012) 101, arXiv:1203.6510 [hep-ph].
- [63] G. Buchalla, O. Cata, and C. Krause, *Complete Electroweak Chiral Lagrangian with a Light Higgs at NLO*, Nucl. Phys. **B880** (2014) 552–573, arXiv:1307.5017 [hep-ph]. [Erratum: Nucl. Phys.B913,475(2016)].
- [64] G. Buchalla, O. Cata, and C. Krause, *On the Power Counting in Effective Field Theories*, Phys. Lett. **B731** (2014) 80–86, arXiv:1312.5624 [hep-ph].
- [65] F.-K. Guo, P. Ruiz-Femenia, and J. J. Sanz-Cillero, *One loop renormalization of the electroweak chiral Lagrangian with a light Higgs boson*, Phys. Rev. **D92** (2015) 074005, arXiv:1506.04204 [hep-ph].
- [66] G. Buchalla, O. Cata, A. Celis, M. Knecht, and C. Krause, *Complete One-Loop Renormalization of the Higgs-Electroweak Chiral Lagrangian*, Nucl. Phys. **B928** (2018) 93–106, arXiv:1710.06412 [hep-ph].
- [67] R. Alonso, K. Kanshin, and S. Saa, *Renormalization group evolution of Higgs effective field theory*, Phys. Rev. **D97** (2018) no. 3, 035010, arXiv:1710.06848 [hep-ph].
- [68] G. Buchalla, O. Cata, A. Celis, and C. Krause, *Comment on "Analysis of General Power Counting Rules in Effective Field Theory"*, arXiv:1603.03062 [hep-ph].
- [69] R. Gröber, M. Mühlleitner, M. Spira, and J. Streicher, *NLO QCD Corrections to Higgs Pair Production including Dimension-6 Operators*, JHEP **09** (2015) 092, arXiv:1504.06577 [hep-ph].
- [70] J. H. Kim, Y. Sakaki, and M. Son, *Combined analysis of double Higgs production via gluon fusion at the HL-LHC in the effective field theory approach*, arXiv:1801.06093 [hep-ph].
- [71] G. Buchalla, M. Capozzi, A. Celis, G. Heinrich, and L. Scyboz, *Higgs boson pair production in non-linear Effective Field Theory with full  $m_t$ -dependence at NLO QCD*, arXiv:1806.05162 [hep-ph].
- [72] M. Ghezzi, R. Gomez-Ambrosio, G. Passarino, and S. Uccirati, *NLO Higgs effective field theory and  $\kappa$ -framework*, JHEP **07** (2015) 175, arXiv:1505.03706 [hep-ph].
- [73] I. Brivio and M. Trott, *The Standard Model as an Effective Field Theory*, arXiv:1706.08945 [hep-ph].
- [74] G. Buchalla, O. Cata, and C. Krause, *A Systematic Approach to the SILH Lagrangian*, Nucl. Phys. **B894** (2015) 602–620, arXiv:1412.6356 [hep-ph].
- [75] G. F. Giudice, C. Grojean, A. Pomarol, and R. Rattazzi, *The Strongly-Interacting Light Higgs*, JHEP **06** (2007) 045, arXiv:hep-ph/0703164 [hep-ph].
- [76] HEPfit Collaboration, *HEPfit: a Code for the Combination of Indirect and Direct Constraints on High Energy Physics Models*, . in preparation.
- [77] HEPfit Collaboration, <http://hepfit.roma1.infn.it>.
- [78] ATLAS Collaboration, G. Aad et al., *Measurements of the Higgs boson production and decay rates and coupling strengths using pp collision data at  $\sqrt{s} = 7$  and 8 TeV in the ATLAS*

- experiment*, Eur. Phys. J. **C76** (2016) no. 1, 6, arXiv:1507.04548 [hep-ex].
- [79] J. Alwall, R. Frederix, S. Frixione, V. Hirschi, F. Maltoni, O. Mattelaer, H. S. Shao, T. Stelzer, P. Torrielli, and M. Zaro, *The automated computation of tree-level and next-to-leading order differential cross sections, and their matching to parton shower simulations*, JHEP **07** (2014) 079, arXiv:1405.0301 [hep-ph].
- [80] R. Frederix, S. Frixione, V. Hirschi, F. Maltoni, O. Mattelaer, P. Torrielli, E. Vryonidou, and M. Zaro, *Higgs pair production at the LHC with NLO and parton-shower effects*, Phys. Lett. **B732** (2014) 142–149, arXiv:1401.7340 [hep-ph].
- [81] S. Borowka, N. Greiner, G. Heinrich, S. P. Jones, M. Kerner, J. Schlenk, and T. Zirke, *Full top quark mass dependence in Higgs boson pair production at NLO*, JHEP **10** (2016) 107, arXiv:1608.04798 [hep-ph].
- [82] G. Heinrich, S. P. Jones, M. Kerner, G. Luisoni, and E. Vryonidou, *NLO predictions for Higgs boson pair production with full top quark mass dependence matched to parton showers*, JHEP **08** (2017) 088, arXiv:1703.09252 [hep-ph].
- [83] S. Borowka, N. Greiner, G. Heinrich, S. Jones, M. Kerner, J. Schlenk, U. Schubert, and T. Zirke, *Higgs Boson Pair Production in Gluon Fusion at Next-to-Leading Order with Full Top-Quark Mass Dependence*, Phys. Rev. Lett. **117** (2016) no. 1, 012001, arXiv:1604.06447 [hep-ph]. [Erratum: Phys. Rev. Lett.117,no.7,079901(2016)].
- [84] S. Alioli, P. Nason, C. Oleari, and E. Re, *A general framework for implementing NLO calculations in shower Monte Carlo programs: the POWHEG BOX*, JHEP **06** (2010) 043, arXiv:1002.2581 [hep-ph].
- [85] S. Dulat, T.-J. Hou, J. Gao, M. Guzzi, J. Huston, P. Nadolsky, J. Pumplin, C. Schmidt, D. Stump, and C. P. Yuan, *New parton distribution functions from a global analysis of quantum chromodynamics*, Phys. Rev. **D93** (2016) no. 3, 033006, arXiv:1506.07443 [hep-ph].
- [86] L. A. Harland-Lang, A. D. Martin, P. Motylinski, and R. S. Thorne, *Parton distributions in the LHC era: MMHT 2014 PDFs*, Eur. Phys. J. **C75** (2015) no. 5, 204, arXiv:1412.3989 [hep-ph].
- [87] A. Carvalho, M. Dall’Osso, T. Dorigo, F. Goertz, C. A. Gottardo, and M. Tosi, *Higgs Pair Production: Choosing Benchmarks With Cluster Analysis*, JHEP **04** (2016) 126, arXiv:1507.02245 [hep-ph].
- [88] A. Carvalho, M. Dall’Osso, P. De Castro Manzano, T. Dorigo, F. Goertz, M. Gouzevich, and M. Tosi, *Analytical parametrization and shape classification of anomalous HH production in the EFT approach*, arXiv:1608.06578 [hep-ph].
- [89] CMS Collaboration, *Combined measurements of the Higgs boson’s couplings at  $\sqrt{s} = 13 \text{ TeV}$* , , CERN, Geneva, 2018. <https://cds.cern.ch/record/2308127>.
- [90] CMS Collaboration, *Combination of searches for Higgs boson pair production in proton-proton collisions at  $\sqrt{s} = 13 \text{ TeV}$* , CMS-PAS-HIG-17-030, CERN, Geneva, 2018. <https://cds.cern.ch/record/2628486>.
- [91] ATLAS Collaboration, *Combination of searches for Higgs boson pairs in pp collisions at 13 TeV with the ATLAS experiment.*, ATLAS-CONF-2018-043, CERN, Geneva, Sep, 2018. <https://cds.cern.ch/record/2638212>.
- [92] A. Azatov, R. Contino, G. Panico, and M. Son, *Effective field theory analysis of double Higgs boson production via gluon fusion*, Phys. Rev. **D92** (2015) no. 3, 035001, arXiv:1502.00539 [hep-ph].
- [93] D. de Florian, I. Fabre, and J. Mazzitelli, *Higgs boson pair production at NNLO in QCD including dimension 6 operators*, JHEP **10** (2017) 215, arXiv:1704.05700 [hep-ph].
- [94] A. Collaboration, *Technical Design Report for the ATLAS Inner Tracker Pixel Detector*, . <https://cds.cern.ch/record/2285585>.

- [95] *PUB note in preparation*, .
- [96] *Run 2 paper in preparation*, CERN-EP-2018-164.
- [97] CMS Collaboration, *Higgs pair production at the High Luminosity LHC*, .
- [98] CMS Collaboration, *Projected performance of Higgs analyses at the HL-LHC for ECFA 2016*, .
- [99] A. Adhikary, S. Banerjee, R. K. Barman, B. Bhattacherjee, and S. Niyogi, *Revisiting the non-resonant Higgs pair production at the HL-LHC*, Physics **2018** (2018) 116, arXiv:1712.05346 [hep-ph].
- [100] J. H. Kim, K. Kong, K. T. Matchev, and M. Park, *Measuring the Triple Higgs Self-Interaction at the Large Hadron Collider*, arXiv:1807.11498 [hep-ph].
- [101] C. G. Lester and D. J. Summers, *Measuring masses of semiinvisibly decaying particles pair produced at hadron colliders*, Phys. Lett. **B463** (1999) 99–103, arXiv:hep-ph/9906349 [hep-ph].
- [102] M. Burns, K. Kong, K. T. Matchev, and M. Park, *Using Subsystem MT2 for Complete Mass Determinations in Decay Chains with Missing Energy at Hadron Colliders*, JHEP **03** (2009) 143, arXiv:0810.5576 [hep-ph].
- [103] A. J. Barr, T. J. Khoo, P. Konar, K. Kong, C. G. Lester, K. T. Matchev, and M. Park, *Guide to transverse projections and mass-constraining variables*, Phys. Rev. **D84** (2011) 095031, arXiv:1105.2977 [hep-ph].
- [104] P. Konar, K. Kong, and K. T. Matchev,  $\sqrt{\hat{s}}_{min}$ : *A Global inclusive variable for determining the mass scale of new physics in events with missing energy at hadron colliders*, JHEP **03** (2009) 085, arXiv:0812.1042 [hep-ph].
- [105] P. Konar, K. Kong, K. T. Matchev, and M. Park, *RECO level  $\sqrt{s}_{min}$  and subsystem  $\sqrt{s}_{min}$ : Improved global inclusive variables for measuring the new physics mass scale in  $\cancel{E}_T$  events at hadron colliders*, JHEP **06** (2011) 041, arXiv:1006.0653 [hep-ph].
- [106] M. L. Graesser and J. Shelton, *Hunting Mixed Top Squark Decays*, Phys. Rev. Lett. **111** (2013) no. 12, 121802, arXiv:1212.4495 [hep-ph].
- [107] W. S. Cho, D. Kim, K. T. Matchev, and M. Park, *Probing Resonance Decays to Two Visible and Multiple Invisible Particles*, Phys. Rev. Lett. **112** (2014) no. 21, 211801, arXiv:1206.1546 [hep-ph].
- [108] D. Debnath, D. Kim, J. H. Kim, K. Kong, and K. T. Matchev, *Resolving Combinatorial Ambiguities in Dilepton  $t\bar{t}$  Event Topologies with Constrained  $M_2$  Variables*, Phys. Rev. **D96** (2017) no. 7, 076005, arXiv:1706.04995 [hep-ph].
- [109] P. Konar, K. Kong, K. T. Matchev, and M. Park, *Superpartner Mass Measurement Technique using 1D Orthogonal Decompositions of the Cambridge Transverse Mass Variable  $M_{T2}$* , Phys. Rev. Lett. **105** (2010) 051802, arXiv:0910.3679 [hep-ph].
- [110] P. Konar, K. Kong, K. T. Matchev, and M. Park, *Dark Matter Particle Spectroscopy at the LHC: Generalizing  $M(T2)$  to Asymmetric Event Topologies*, JHEP **04** (2010) 086, arXiv:0911.4126 [hep-ph].
- [111] W. S. Cho, K. Choi, Y. G. Kim, and C. B. Park, *Gluino Stransverse Mass*, Phys. Rev. Lett. **100** (2008) 171801, arXiv:0709.0288 [hep-ph].
- [112] CMS Collaboration, A. M. Sirunyan et al., *Identification of heavy-flavour jets with the CMS detector in pp collisions at 13 TeV*, JINST **13** (2018) no. 05, P05011, arXiv:1712.07158 [physics.ins-det].
- [113] ATLAS Collaboration, *Projected sensitivity to non-resonant Higgs boson pair production in the  $b\bar{b}b\bar{b}$  final state using proton-proton collisions at HL-LHC with the ATLAS detector*, .
- [114] F. Kling, T. Plehn, and P. Schichtel, *Maximizing the significance in Higgs boson pair analyses*, Phys. Rev. **D95** (2017) no. 3, 035026, arXiv:1607.07441 [hep-ph].

- [115] ATLAS Collaboration, *Study of the double Higgs production channel  $H(\rightarrow b\bar{b})H(\rightarrow \gamma\gamma)$  with the ATLAS experiment at the HL-LHC*, , CERN, Geneva, Jan, 2017.  
<https://cds.cern.ch/record/2243387>.
- [116] M. Grazzini, G. Heinrich, S. Jones, S. Kallweit, M. Kerner, J. M. Lindert, and J. Mazzitelli, *Higgs boson pair production at NNLO with top quark mass effects*, JHEP **05** (2018) 059, arXiv:1803.02463 [hep-ph].
- [117] A. Mitov, *Top pair production at a future 27 TeV HE-LHC*, HE/HL-LHC Workshop, CERN.
- [118] F. Demartin, F. Maltoni, K. Mawatari, B. Page, and M. Zaro, *Higgs characterisation at NLO in QCD: CP properties of the top-quark Yukawa interaction*, Eur. Phys. J. **C74** (2014) no. 9, 3065, arXiv:1407.5089 [hep-ph].
- [119] D. Gonçalves, T. Han, F. Kling, T. Plehn, and M. Takeuchi, *Higgs Pair Production at Future Hadron Colliders: From Kinematics to Dynamics*, arXiv:1802.04319 [hep-ph].
- [120] A. Alves, T. Ghosh, and K. Sinha, *Can We Discover Double Higgs Production at the LHC?*, Phys. Rev. **D96** (2017) no. 3, 035022, arXiv:1704.07395 [hep-ph].
- [121] D. de Florian and J. Mazzitelli, *Two-loop virtual corrections to Higgs pair production*, Phys. Lett. **B724** (2013) 306–309, arXiv:1305.5206 [hep-ph].
- [122] S. Bergstra, R. Bardenet, Y. Bengio, and B. Kégl, *Algorithms for hyper-parameter optimization.*, Advances in Neural Information Processing Systems (2011) 2546.
- [123] S. Bergstra, D. Yamins, and D. Cox, *Hyperopt: A Python Library for Optimizing the Hyperparameters of Machine Learning Algorithms.*, Proceedings of the 12th PYTHON in Science Conference, SciPy 2013 (2013) .
- [124] HyperOpt software package: <https://github.com/jberg/hyperopt> .
- [125] ATLAS Collaboration, G. Aad et al., *Search For Higgs Boson Pair Production in the  $\gamma\gamma b\bar{b}$  Final State using pp Collision Data at  $\sqrt{s} = 8$  TeV from the ATLAS Detector*, Phys. Rev. Lett. **114** (2015) no. 8, 081802, arXiv:1406.5053 [hep-ex].
- [126] *Prospects for measuring Higgs pair production in the channel  $H(\rightarrow \gamma\gamma)H(\rightarrow b\bar{b})$  using the ATLAS detector at the HL-LHC*, , CERN, Geneva, Oct, 2014.  
<http://cds.cern.ch/record/1956733>.
- [127] R. Contino et al., *Physics at a 100 TeV pp collider: Higgs and EW symmetry breaking studies*, CERN Yellow Report (2017) no. 3, 255–440, arXiv:1606.09408 [hep-ph].
- [128] S. Homiller and P. Meade, *Measurement of the Triple Higgs Coupling at a HE-LHC*, to appear (2018) .
- [129] V. Hirschi and O. Mattelaer, *Automated event generation for loop-induced processes*, JHEP **10** (2015) 146, arXiv:1507.00020 [hep-ph].
- [130] NNPDF Collaboration, R. D. Ball et al., *Parton distributions for the LHC Run II*, JHEP **04** (2015) 040, arXiv:1410.8849 [hep-ph].
- [131] P. Artoisenet, R. Frederix, O. Mattelaer, and R. Rietkerk, *Automatic spin-entangled decays of heavy resonances in Monte Carlo simulations*, JHEP **03** (2013) 015, arXiv:1212.3460 [hep-ph].
- [132] T. Sjöstrand, S. Ask, J. R. Christiansen, R. Corke, N. Desai, P. Ilten, S. Mrenna, S. Prestel, C. O. Rasmussen, and P. Z. Skands, *An Introduction to PYTHIA 8.2*, Comput. Phys. Commun. **191** (2015) 159–177, arXiv:1410.3012 [hep-ph].
- [133] M. L. Mangano, M. Moretti, F. Piccinini, and M. Treccani, *Matching matrix elements and shower evolution for top-quark production in hadronic collisions*, JHEP **01** (2007) 013, arXiv:hep-ph/0611129 [hep-ph].
- [134] J. Alwall et al., *Comparative study of various algorithms for the merging of parton showers and matrix elements in hadronic collisions*, Eur. Phys. J. **C53** (2008) 473–500, arXiv:0706.2569

[hep-ph].

- [135] M. McCullough, *An Indirect Model-Dependent Probe of the Higgs Self-Coupling*, Phys. Rev. **D90** (2014) no. 1, 015001, arXiv:1312.3322 [hep-ph]. [Erratum: Phys. Rev.D92,no.3,039903(2015)].
- [136] M. Gorbahn and U. Haisch, *Indirect probes of the trilinear Higgs coupling:  $gg \rightarrow h$  and  $h \rightarrow \gamma\gamma$* , arXiv:1607.03773 [hep-ph].
- [137] G. Degrassi, P. P. Giardino, F. Maltoni, and D. Pagani, *Probing the Higgs self coupling via single Higgs production at the LHC*, arXiv:1607.04251 [hep-ph].
- [138] W. Bizon, M. Gorbahn, U. Haisch, and G. Zanderighi, *Constraints on the trilinear Higgs coupling from vector boson fusion and associated Higgs production at the LHC*, JHEP **07** (2017) 083, arXiv:1610.05771 [hep-ph].
- [139] S. Di Vita, C. Grojean, G. Panico, M. Riembau, and T. Vantalon, *A global view on the Higgs self-coupling*, JHEP **09** (2017) 069, arXiv:1704.01953 [hep-ph].
- [140] T. Barklow, K. Fujii, S. Jung, M. E. Peskin, and J. Tian, *Model-Independent Determination of the Triple Higgs Coupling at e+e- Colliders*, Phys. Rev. **D97** (2018) no. 5, 053004, arXiv:1708.09079 [hep-ph].
- [141] F. Maltoni, D. Pagani, A. Shivaji, and X. Zhao, *Trilinear Higgs coupling determination via single-Higgs differential measurements at the LHC*, Eur. Phys. J. **C77** (2017) no. 12, 887, arXiv:1709.08649 [hep-ph].
- [142] S. Di Vita, G. Durieux, C. Grojean, J. Gu, Z. Liu, G. Panico, M. Riembau, and T. Vantalon, *A global view on the Higgs self-coupling at lepton colliders*, JHEP **02** (2018) 178, arXiv:1711.03978 [hep-ph].
- [143] F. Maltoni, D. Pagani, and X. Zhao, *Constraining the Higgs self-couplings at  $e^+e^-$  colliders*, JHEP **07** (2018) 087, arXiv:1802.07616 [hep-ph].
- [144] G. Degrassi, M. Fedele, and P. P. Giardino, *Constraints on the trilinear Higgs self coupling from precision observables*, JHEP **04** (2017) 155, arXiv:1702.01737 [hep-ph].
- [145] G. D. Kribs, A. Maier, H. Rzehak, M. Spannowsky, and P. Waite, *Electroweak oblique parameters as a probe of the trilinear Higgs boson self-interaction*, Phys. Rev. **D95** (2017) no. 9, 093004, arXiv:1702.07678 [hep-ph].
- [146] L. Di Luzio, R. Gröber, and M. Spannowsky, *Maxi-sizing the trilinear Higgs self-coupling: how large could it be?*, Eur. Phys. J. **C77** (2017) no. 11, 788, arXiv:1704.02311 [hep-ph].
- [147] M. Bauer, M. Carena, and A. Carmona, *Higgs Pair Production as a Signal of Enhanced Yukawa Couplings*, Phys. Rev. Lett. **121** (2018) no. 2, 021801, arXiv:1801.00363 [hep-ph].
- [148] F. Boudjema and A. Semenov, *Measurements of the SUSY Higgs selfcouplings and the reconstruction of the Higgs potential*, Phys. Rev. **D66** (2002) 095007, arXiv:hep-ph/0201219 [hep-ph].
- [149] J. F. Gunion and H. E. Haber, *The CP conserving two Higgs doublet model: The Approach to the decoupling limit*, Phys. Rev. **D67** (2003) 075019, arXiv:hep-ph/0207010 [hep-ph].
- [150] D. Eriksson, J. Rathsman, and O. Stal, *2HDMC: Two-Higgs-Doublet Model Calculator Physics and Manual*, Comput. Phys. Commun. **181** (2010) 189–205, arXiv:0902.0851 [hep-ph].
- [151] R. Franceschini, G. Panico, A. Pomarol, F. Riva, and A. Wulzer, *Electroweak Precision Tests in High-Energy Diboson Processes*, JHEP **02** (2018) 111, arXiv:1712.01310 [hep-ph].
- [152] R. S. Gupta, A. Pomarol, and F. Riva, *BSM Primary Effects*, Phys. Rev. **D91** (2015) no. 3, 035001, arXiv:1405.0181 [hep-ph].
- [153] A. Pomarol, *Higgs Physics*, in *Proceedings, 2014 European School of High-Energy Physics (ESHEP 2014): Garderen, The Netherlands, June 18 - July 01 2014*, pp. 59–77. 2016. arXiv:1412.4410 [hep-ph].

<http://inspirehep.net/record/1334375/files/arXiv:1412.4410.pdf>.

- [154] B. Grzadkowski, M. Iskrzynski, M. Misiak, and J. Rosiek, *Dimension-Six Terms in the Standard Model Lagrangian*, JHEP **10** (2010) 085, arXiv:1008.4884 [hep-ph].
- [155] J. M. Butterworth, A. R. Davison, M. Rubin, and G. P. Salam, *Jet substructure as a new Higgs search channel at the LHC*, Phys. Rev. Lett. **100** (2008) 242001, arXiv:0802.2470 [hep-ph].
- [156] S. Banerjee, C. Englert, R. S. Gupta, and M. Spannowsky, *Probing Electroweak Precision Physics via boosted Higgs-strahlung at the LHC*, arXiv:1807.01796 [hep-ph].
- [157] ALEPH Collaboration, DELPHI Collaboration, L3 Collaboration, OPAL Collaboration, LEP TGC Working Group, *A Combination of Preliminary Results on Gauge Boson Couplings Measured by the LEP experiments*, LEPEWWG-TGC-2003-01. DELPHI-2003-068-PHYS-936. L3-Note-2826. LEPEWWG-2006-01. OPAL-TN-739. ALEPH-2006-016-CONF-2003-012, CERN, Geneva, Jan, 2003. <https://cds.cern.ch/record/2285934>. 2003 Summer Conferences.
- [158] A. Falkowski and F. Riva, *Model-independent precision constraints on dimension-6 operators*, JHEP **02** (2015) 039, arXiv:1411.0669 [hep-ph].
- [159] M. Baak, M. Goebel, J. Haller, A. Hoecker, D. Kennedy, R. Kogler, K. Moenig, M. Schott, and J. Stelzer, *The Electroweak Fit of the Standard Model after the Discovery of a New Boson at the LHC*, Eur. Phys. J. **C72** (2012) 2205, arXiv:1209.2716 [hep-ph].
- [160] R. Barbieri, A. Pomarol, R. Rattazzi, and A. Strumia, *Electroweak symmetry breaking after LEP-1 and LEP-2*, Nucl. Phys. **B703** (2004) 127–146, arXiv:hep-ph/0405040 [hep-ph].
- [161] R. Franceschini, G. Panico, A. Pomarol, F. Riva, and A. Wulzer, *Electroweak Precision Tests in High-Energy Diboson Processes*, JHEP **02** (2018) 111, arXiv:1712.01310 [hep-ph].
- [162] G. Panico, F. Riva, and A. Wulzer, *Diboson Interference Resurrection*, Phys. Lett. **B776** (2018) 473–480, arXiv:1708.07823 [hep-ph].
- [163] A. Azatov, J. Elias-Miro, Y. Reyimuaji, and E. Venturini, *Novel measurements of anomalous triple gauge couplings for the LHC*, JHEP **10** (2017) 027, arXiv:1707.08060 [hep-ph].
- [164] M. S. Chanowitz and M. K. Gaillard, *The TeV Physics of Strongly Interacting W's and Z's*, Nucl. Phys. **B261** (1985) 379–431.
- [165] A. Wulzer, *An Equivalent Gauge and the Equivalence Theorem*, Nucl. Phys. **B885** (2014) 97–126, arXiv:1309.6055 [hep-ph].
- [166] ATLAS Collaboration, G. Aad et al., *Measurements of  $W^\pm Z$  production cross sections in pp collisions at  $\sqrt{s} = 8$  TeV with the ATLAS detector and limits on anomalous gauge boson self-couplings*, Phys. Rev. **D93** (2016) no. 9, 092004, arXiv:1603.02151 [hep-ex].
- [167] ATLAS Collaboration, G. Aad et al., *Measurement of the double-differential high-mass Drell-Yan cross section in pp collisions at  $\sqrt{s} = 8$  TeV with the ATLAS detector*, JHEP **08** (2016) 009, arXiv:1606.01736 [hep-ex].
- [168] ATLAS Collaboration, T. A. collaboration, *Electron efficiency measurements with the ATLAS detector using the 2015 LHC proton-proton collision data*.
- [169] F. Campanario, R. Roth, and D. Zeppenfeld, *QCD radiation in  $WH$  and  $WZ$  production and anomalous coupling measurements*, Phys. Rev. **D91** (2015) 054039, arXiv:1410.4840 [hep-ph].
- [170] J. Ellis, P. Roloff, V. Sanz, and T. You, *Dimension-6 Operator Analysis of the CLIC Sensitivity to New Physics*, JHEP **05** (2017) 096, arXiv:1701.04804 [hep-ph].
- [171] D. Racco, A. Wulzer, and F. Zwirner, *Robust collider limits on heavy-mediator Dark Matter*, JHEP **05** (2015) 009, arXiv:1502.04701 [hep-ph].
- [172] F. Pobbe, A. Wulzer, and M. Zanetti, *Setting limits on Effective Field Theories: the case of Dark Matter*, JHEP **08** (2017) 074, arXiv:1704.00736 [hep-ph].

- [173] A. Biekotter, A. Knochel, M. Krämer, D. Liu, and F. Riva, *Vices and virtues of Higgs effective field theories at large energy*, Phys. Rev. **D91** (2015) 055029, arXiv:1406.7320 [hep-ph].
- [174] A. Azatov, R. Contino, C. S. Machado, and F. Riva, *Helicity selection rules and noninterference for BSM amplitudes*, Phys. Rev. **D95** (2017) no. 6, 065014, arXiv:1607.05236 [hep-ph].
- [175] U. Baur, T. Han, and J. Ohnemus, *Amplitude zeros in W+ Z production*, Phys. Rev. Lett. **72** (1994) 3941–3944, arXiv:hep-ph/9403248 [hep-ph].
- [176] DELPHES 3 Collaboration, J. de Favereau, C. Delaere, P. Demin, A. Giammanco, V. Lemaître, A. Mertens, and M. Selvaggi, *DELPHES 3, A modular framework for fast simulation of a generic collider experiment*, JHEP **02** (2014) 057, arXiv:1307.6346 [hep-ex].
- [177] R. Contino, C. Grojean, M. Moretti, F. Piccinini, and R. Rattazzi, *Strong Double Higgs Production at the LHC*, JHEP **05** (2010) 089, arXiv:1002.1011 [hep-ph].
- [178] M. J. Dolan, C. Englert, N. Greiner, and M. Spannowsky, *Further on up the road: hhjj production at the LHC*, Phys. Rev. Lett. **112** (2014) 101802, arXiv:1310.1084 [hep-ph].
- [179] M. J. Dolan, C. Englert, N. Greiner, K. Nordstrom, and M. Spannowsky, *hhjj production at the LHC*, Eur. Phys. J. **C75** (2015) no. 8, 387, arXiv:1506.08008 [hep-ph].
- [180] M. Gouzevitch, A. Oliveira, J. Rojo, R. Rosenfeld, G. P. Salam, and V. Sanz, *Scale-invariant resonance tagging in multijet events and new physics in Higgs pair production*, JHEP **07** (2013) 148, arXiv:1303.6636 [hep-ph].
- [181] J. K. Behr, D. Bortoletto, J. A. Frost, N. P. Hartland, C. Issever, and J. Rojo, *Boosting Higgs pair production in the bbbb final state with multivariate techniques*, Eur. Phys. J. **C76** (2016) no. 7, 386, arXiv:1512.08928 [hep-ph].
- [182] M. Cacciari, G. P. Salam, and G. Soyez, *FastJet User Manual*, Eur. Phys. J. **C72** (2012) 1896, arXiv:1111.6097 [hep-ph].
- [183] R. Contino, A. Falkowski, F. Goertz, C. Grojean, and F. Riva, *On the Validity of the Effective Field Theory Approach to SM Precision Tests*, JHEP **07** (2016) 144, arXiv:1604.06444 [hep-ph].
- [184] J. Kalinowski, P. Kozow, S. Pokorski, J. Rosiek, M. Szleper, and S. Tkaczyk, *Same-sign WW scattering at the LHC: can we discover BSM effects before discovering new states?*, Eur. Phys. J. **C78** (2018) no. 5, 403, arXiv:1802.02366 [hep-ph].
- [185] CMS Collaboration, A. M. Sirunyan et al., *Measurement of vector boson scattering and constraints on anomalous quartic couplings from events with four leptons and two jets in proton-proton collisions at  $\sqrt{s} = 13$  TeV*, Phys. Lett. **B774** (2017) 682–705, arXiv:1708.02812 [hep-ex].
- [186] R. Gomez-Ambrosio, *Studies of Dimension-Six EFT effects in Vector Boson Scattering*, arXiv:1809.04189 [hep-ph].
- [187] E. E. Jenkins, A. V. Manohar, and M. Trott, *Renormalization Group Evolution of the Standard Model Dimension Six Operators I: Formalism and lambda Dependence*, JHEP **10** (2013) 087, arXiv:1308.2627 [hep-ph].
- [188] CMS Collaboration, A. M. Sirunyan et al., *Measurement of differential cross sections for Z boson pair production in association with jets at  $\sqrt{s} = 8$  and 13 TeV*, arXiv:1806.11073 [hep-ex].
- [189] S. Alioli, F. Caola, G. Luisoni, and R. Rüntsch, *ZZ production in gluon fusion at NLO matched to parton-shower*, Phys. Rev. **D95** (2017) no. 3, 034042, arXiv:1609.09719 [hep-ph].
- [190] S. Catani and M. H. Seymour, *A General algorithm for calculating jet cross-sections in NLO QCD*, Nucl. Phys. **B485** (1997) 291–419, arXiv:hep-ph/9605323 [hep-ph]. [Erratum: Nucl. Phys.B510,503(1998)].

- [191] M. Bauer, M. Carena, and K. Gemmeler, *Creating the fermion mass hierarchies with multiple Higgs bosons*, Phys. Rev. **D94** (2016) no. 11, 115030, arXiv:1512.03458 [hep-ph].
- [192] M. Bauer, M. Carena, and K. Gemmeler, *Flavor from the Electroweak Scale*, JHEP **11** (2015) 016, arXiv:1506.01719 [hep-ph].
- [193] M. Bauer, S. Casagrande, U. Haisch, and M. Neubert, *Flavor Physics in the Randall-Sundrum Model: II. Tree-Level Weak-Interaction Processes*, JHEP **09** (2010) 017, arXiv:0912.1625 [hep-ph].
- [194] D. B. Kaplan, *Flavor at SSC energies: A New mechanism for dynamically generated fermion masses*, Nucl. Phys. **B365** (1991) 259–278.
- [195] J. de Blas, M. Ciuchini, E. Franco, S. Mishima, M. Pierini, L. Reina, and L. Silvestrini, *Electroweak precision observables and Higgs-boson signal strengths in the Standard Model and beyond: present and future*, JHEP **12** (2016) 135, arXiv:1608.01509 [hep-ph].
- [196] T. Sjostrand, S. Mrenna, and P. Z. Skands, *PYTHIA 6.4 Physics and Manual*, JHEP **05** (2006) 026, arXiv:hep-ph/0603175 [hep-ph].
- [197] M. Buschmann, D. Goncalves, S. Kuttimalai, M. Schönherr, F. Krauss, and T. Plehn, *Mass Effects in the Higgs-Gluon Coupling: Boosted vs Off-Shell Production*, JHEP **02** (2015) 038, arXiv:1410.5806 [hep-ph].
- [198] J. Ellis, C. W. Murphy, V. Sanz, and T. You, *Updated Global SMEFT Fit to Higgs, Diboson and Electroweak Data*, arXiv:1803.03252 [hep-ph].
- [199] SLD Electroweak Group, DELPHI, ALEPH, SLD, SLD Heavy Flavour Group, OPAL, LEP Electroweak Working Group, L3 Collaboration, S. Schael et al., *Precision electroweak measurements on the  $Z$  resonance*, Phys. Rept. **427** (2006) 257–454, arXiv:hep-ex/0509008 [hep-ex].
- [200] K. Agashe, R. Contino, and A. Pomarol, *The Minimal composite Higgs model*, Nucl. Phys. **B719** (2005) 165–187, arXiv:hep-ph/0412089 [hep-ph].
- [201] A. Alloul, N. D. Christensen, C. Degrande, C. Duhr, and B. Fuks, *FeynRules 2.0 - A complete toolbox for tree-level phenomenology*, Comput. Phys. Commun. **185** (2014) 2250–2300, arXiv:1310.1921 [hep-ph].
- [202] R. Contino, M. Ghezzi, M. Moretti, G. Panico, F. Piccinini, and A. Wulzer, *Anomalous Couplings in Double Higgs Production*, JHEP **08** (2012) 154, arXiv:1205.5444 [hep-ph].
- [203] M. L. Mangano et al., *Physics at a 100 TeV pp collider: Standard Model processes*, arXiv:1607.01831 [hep-ph].
- [204] C. Degrande, C. Duhr, B. Fuks, D. Grellscheid, O. Mattelaer, and T. Reiter, *UFO - The Universal FeynRules Output*, Comput. Phys. Commun. **183** (2012) 1201–1214, arXiv:1108.2040 [hep-ph].
- [205] S. Dawson and I. M. Lewis, *NLO corrections to double Higgs boson production in the Higgs singlet model*, Phys. Rev. **D92** (2015) no. 9, 094023, arXiv:1508.05397 [hep-ph].
- [206] ATLAS Collaboration, M. Aaboud et al., *Search for pair production of Higgs bosons in the  $b\bar{b}b\bar{b}$  final state using proton–proton collisions at  $\sqrt{s} = 13$  TeV with the ATLAS detector*, arXiv:1606.04782 [hep-ex].
- [207] ATLAS Collaboration, G. Aad et al., *Searches for Higgs boson pair production in the  $hh \rightarrow b\bar{b}\tau\tau, \gamma\gamma WW^*, \gamma\gamma bb, bbbb$  channels with the ATLAS detector*, Phys. Rev. **D92** (2015) 092004, arXiv:1509.04670 [hep-ex].
- [208] CMS Collaboration, *Search for Higgs boson pair production in the final state containing two photons and two bottom quarks in proton-proton collisions at  $\sqrt{s} = 13$  TeV*, CMS-PAS-HIG-17-008, CERN, Geneva, 2017. <https://cds.cern.ch/record/2273383>.
- [209] R. V. Harlander, S. Liebler, and H. Mantler, *SusHi: A program for the calculation of Higgs*

- production in gluon fusion and bottom-quark annihilation in the Standard Model and the MSSM*, Comput. Phys. Commun. **184** (2013) 1605–1617, arXiv:1212.3249 [hep-ph].
- [210] R. V. Harlander, S. Liebler, and H. Mantler, *SusHi Bento: Beyond NNLO and the heavy-top limit*, arXiv:1605.03190 [hep-ph].
- [211] R. Harlander and P. Kant, *Higgs production and decay: Analytic results at next-to-leading order QCD*, JHEP **12** (2005) 015, arXiv:hep-ph/0509189 [hep-ph].
- [212] M. E. Peskin and T. Takeuchi, *Estimation of oblique electroweak corrections*, Phys. Rev. **D46** (1992) 381–409.
- [213] S. Dawson, S. Dittmaier, and M. Spira, *Neutral Higgs boson pair production at hadron colliders: QCD corrections*, Phys. Rev. **D58** (1998) 115012, arXiv:hep-ph/9805244 [hep-ph].
- [214] G. Brooijmans et al., *Les Houches 2017: Physics at TeV Colliders New Physics Working Group Report*, in *10th Les Houches Workshop on Physics at TeV Colliders (PhysTeV 2017) Les Houches, France, June 5-23, 2017*. 2018. arXiv:1803.10379 [hep-ph].  
<http://inspirehep.net/record/1664565/files/1803.10379.pdf>.
- [215] CMS Collaboration, *Search for resonant pair production of Higgs bosons decaying to two bottom quark-antiquark pairs in proton-proton collisions at 13 TeV*, CMS-PAS-HIG-16-002, 2016.